

A nighttime photograph of a city skyline, featuring a prominent, illuminated skyscraper with a unique, curved facade. The building is lit up with warm yellow lights, contrasting with the dark blue night sky. Other buildings and city lights are visible in the background, creating a vibrant urban scene.

Ali Bumajdad
Walid Bouhamra
Osamah A. Alsayegh
Hasan A. Kamal
Salem Falah Alhajraf
Editors

Gulf Conference on Sustainable Built Environment



Springer

Gulf Conference on Sustainable Built Environment

Ali Bumajdad • Walid Bouhamra
Osamah A. Alsayegh • Hasan A. Kamal
Salem Falah Alhajraf
Editors

Gulf Conference on Sustainable Built Environment

 Springer

Editors

Ali Bumajdad
Department of Chemistry
Kuwait University
Kuwait City, Kuwait

Walid Bouhamra
Gulf University for Science and Technology
Kuwait City, Kuwait

Osamah A. Alsayegh
Kuwait Institute for Scientific Research
Kuwait City, Kuwait

Hasan A. Kamal
Kuwait Institute for Scientific Research
Kuwait Municipal Council
Kuwait City, Kuwait

Salem Falah Alhajraf
Kuwait Foundation for the Advancement
of Sciences
Kuwait City, Kuwait

ISBN 978-3-030-39733-3

ISBN 978-3-030-39734-0 (eBook)

<https://doi.org/10.1007/978-3-030-39734-0>

© Springer Nature Switzerland AG 2020

This work is subject to copyright. All rights are reserved by the Publisher, whether the whole or part of the material is concerned, specifically the rights of translation, reprinting, reuse of illustrations, recitation, broadcasting, reproduction on microfilms or in any other physical way, and transmission or information storage and retrieval, electronic adaptation, computer software, or by similar or dissimilar methodology now known or hereafter developed.

The use of general descriptive names, registered names, trademarks, service marks, etc. in this publication does not imply, even in the absence of a specific statement, that such names are exempt from the relevant protective laws and regulations and therefore free for general use.

The publisher, the authors, and the editors are safe to assume that the advice and information in this book are believed to be true and accurate at the date of publication. Neither the publisher nor the authors or the editors give a warranty, expressed or implied, with respect to the material contained herein or for any errors or omissions that may have been made. The publisher remains neutral with regard to jurisdictional claims in published maps and institutional affiliations.

This Springer imprint is published by the registered company Springer Nature Switzerland AG
The registered company address is: Gewerbestrasse 11, 6330 Cham, Switzerland

Foreword

The subject of this conference—the sustainability of the built environment, especially in the context of climate change risk—highlights the importance of international collaboration and the future of research universities.

To address the climate change risk—almost certainly the greatest risk that humanity faces in the twenty-first century—we must find ways to reduce urban resource intensity: by closing material loops, by electrifying our cities with low-carbon energy, and by reducing the carbon intensity of supply chains. Today, cities consume about 75% of primary energy and account for 50–60% of the world’s greenhouse gas emissions. In addition, cities directly and indirectly drive most of the material flows that serve the world’s population. By 2050, according to an estimate by the United Nations, the world’s urban population will have increased by more than 2.5 billion, with almost 90% of this increase occurring in Asia and Africa—continents that will be most in need of innovation for a sustainable future.

This is an enormous challenge for all of our societies and also for our universities. The modern research university is mostly about advancing knowledge and educating a wide range of students to play active roles out in the world. But beyond these roles, I believe that universities also need to see themselves as leaders in solving problems for the benefit of the world. And in order to respond effectively to the tremendous global challenge of environmental sustainability, I believe that it will be necessary for our research universities to greatly increase their efforts to collaborate across national borders.

Of course, universities around the world have been internationalizing their educational and research activities for decades. Students have been seeking more high-quality opportunities to learn about and engage with the world. Faculty members have been finding more opportunities to collaborate with international colleagues. In many countries, enrollment of students from overseas has been growing, and student mobility has been increasing.

All this has occurred during a period in which national economies have also been globalizing. Indeed, the same dynamics that have been shaping the development of the global economy have also been central to the internationalization of the universities: growing cross-border economic, social, and cultural connections; greater

individual and corporate mobility; increased trade and capital flows; and instantaneous, globe-spanning transmission of information. Universities have thrived in the rules-based, increasingly open, and increasingly connected global economy.

Today, however, the ideas, the values, and the policies that have been driving globalization are under greater stress than at any time in the last several decades, even as the importance of international cooperation in research and education in many fields, including infrastructure sustainability, has continued to grow.

Some things have not changed. The core commitments of the global university community to open intellectual exchange, to the free flow of ideas and people, and to international collaboration in scholarship and problem-solving are as strong as they have ever been. But unfolding economic and political developments around the world point towards a more challenging international environment than the one we in the university research community have grown accustomed to.

There is no standard template or roadmap for what to do. Each university will need to design its own strategy and programs, based on a realistic estimate of its own capabilities and constraints, its external environment, and the values and principles that are most important to its community. At MIT, our mission is to develop in our students the ability and the passion to work wisely, creatively, and effectively for the benefit of humankind. Engaging internationally and achieving international impact are central to achieving that mission. In recent years, we have been experimenting with a number of new approaches, each with the potential to strengthen our contributions to research and education in the field of sustainability, and each of them opening up more opportunities to work internationally. We are grateful to the Kuwait Foundation for the Advancement of Science (KFAS) for making possible the successful collaboration between MIT, KISR, and Kuwait University that was the subject of this conference, and more broadly for KFAS's strong support of research collaborations between MIT and Kuwait over a period of many years.

September 16, 2019

Massachusetts Institute of Technology
Cambridge, MA, USA

Richard Lester

Contents

Part I Sustainable Built Environment: An Overview

Roadmap for a Sustainable Built Environment: A Science-Based Multidisciplinary Research	3
Oral Büyüköztürk	
Kuwait-MIT Collaborative Signature Project: Sustainability of Kuwait's Built Environment	15
Hasan A. Kamal	

Part II Sustainable Construction Materials

Challenges and Opportunities for Concrete in the Digital Era	27
Henri Van Damme	
Sustainability of Carbon Fiber-Reinforced Polymers in Construction	57
Urs Meier	
On the Behaviour of Recycled Aggregate Concrete Incorporating Slag	77
Moetaz El-Hawary, Anwar Al-Yaqout, and Khallad Nouh	
Ecological Cementitious Material Based on Combination Between Natural Pozzolan and Polymer Admixture	93
Mohammed Hussein Khudhair, Abdulsamad Mohammed Alhousali, Bouchra El Hilal, Rachid Hsissou, Mohamed Berradi, Ahmed Mohammed Al-Anweh, Mohamed Salahdine Elyoubi, and Ahmad Elharfi	
Modeling the Rutting Behavior of Asphalt Mixtures Obtained by Accelerated Testing Device	109
Taha A. Ahmed and Mohammad H. Yassin	

Design and Manufacturing a Miniature Reynolds Apparatus for Testing Nanofluids	123
Ahmad Sedaghat, Hayder Salem, Seyed Amir Abbas Oloomi, Leila Borvayeh, Masoud Rashidi, Abbas Amini, Samira Ghafoori, Jessica Cheska Lopez, and Girish Kaimal Mohanan	
Effect of Aluminosilicate Nanoparticles on Cement Blends Containing Volcanic Ash and Metakaolin	145
Rehab Masmoudi, Ali Bumajdad, and Kunal Kupwade-Patil	
Compressed Earth Blocks: A Sustainable Construction Alternative	157
Ahmad S. Saad, Fahad M. Al-Enezi, Hamad A. Al-Sayab, Zuhair H. Al-Zayed, Fares H. Awwad, and Sarah N. Al-Muhanna	
Historic Heritage Protection as Part of Sustainable Growth	169
Jadwiga W. Lukaszewicz and Jerzy P. Lukaszewicz	
Archaeological Science in the Arabian Gulf: A Study of Bronze Age Pottery from Kuwait Using Portable X-Ray Fluorescence (pXRF)	185
Hasan J. Ashkanani	
Part III Structural Monitoring, Assessment, and Engineering	
Sustainable Design of Earthquake-Resistant Buildings Through Case Studies	213
Sassan Mohasseb, Niloufar Ghazanfari, and Mona Alizadeh	
Experimental Verification of Inelastic Energy Demand Spectrum Using SDOF Steel Specimens on Shaking Table	253
Hümeýra Börekçi, Cem Yalçın, and Ercan Yüksel	
Image-Based Dynamic Response Measurement of a Full-Scale, Multistory Structure Tested on a Shake Table	261
Ferit Yardımcı, Cem Yalçın, and Ercan Yüksel	
Determination of Input Energy Profile in Structures Through Seismic Interferometry	269
Burak Horoz, Cem Yalçın, and Ercan Yüksel	
Structural Health Monitoring System for Al-Hamra Tower in Kuwait City	279
Jamal Al-Qazweeni, Jafarali Parol, Hasan A. Kamal, Abdullah Al-Enezi, Ammar Bin-Nakhi, Hao Sun, and Oral Büyüköztürk	
Part IV Energy Efficiency and Life Cycle Analysis	
Disaster Resilience and Sustainability of Infrastructures: Relationships and Quantification Methods	289
Bilal M. Ayyub	

What Can GCC Countries Learn from Well-Established Green Power Markets in Other Countries?	309
Leila Dagher, Jenny Heeter, and Mohamad Hussein Mansour	
Analysis of Optimal Energy Performance for Commercial Buildings in the GCC Region.	329
Fatemah Ashraf, Benjamin Park, and Moncef Krarti	
Nanocomposite Windows Converting Solar Power into Electricity for Self-Sustaining Buildings.	367
A. M. Darwish, S. S. Sarkisov, and D. N. Patel	
Atrium Design and the Science of Daylighting: A Comparative Field Study	383
Sadiqa Al Awadh and Ihab Elzeyadi	
Early Adopter Nation for Electric Vehicles: The Case of Iceland	401
Andri Ottesen and Sumaya Banna	
3D Numerical Modeling for Assessing the Energy Performance of Single-Zone Buildings with and Without Phase Change Materials.	419
Hamed H. Saber and Ali E. Hajiah	
Role of Green Buildings in Reduction of Energy Consumption.	439
Mohamed F. Hamoda	
Long-Term Energy and Moisture Performance of Reflective and Non-reflective Roofing Systems with and Without Phase Change Materials Under Kuwaiti Climates.	453
Ali E. Hajiah and Hamed H. Saber	
Gender Differences in Thermal Comfort and Satisfaction in Offices in GCC and Asia	483
Madhavi Indraganti	
Part V Educational Issues	
Exploiting Building Information Model and Other Technologies in Facilities Management of an Educational Facility.	501
Mohamed M. Salem, Taha A. Ahmed, Anas A. AlSarmini, and Sana A. El-Azzeh	
Shifting the Learning of Engineering Mechanics and Dynamics Paradigm from Hands-On Experiments to Mobile Virtual Labs	515
Anwar Alroomi	
Index.	523

Part I
Sustainable Built Environment:
An Overview

Roadmap for a Sustainable Built Environment: A Science-Based Multidisciplinary Research



Oral Büyüköztürk

1 Introduction

This first MIT-Kuwait institutional Signature Project is a collaborative and multidisciplinary research effort between MIT and Kuwaiti researchers aiming at the development of innovative methods and solutions for the sustainability of Kuwait's built environment. With a three-level multi-scale approach of materials, buildings, and urban neighborhoods, the effort represents a wide scope leadership activity in science and engineering through world-class research. The project started on February 1, 2013, and ended on July 31, 2017.

The overall objective of the MIT-Kuwait Signature Project is to develop innovative solutions and methodologies to design, evaluate, and improve the sustainability of Kuwait's built environment and establish a new paradigm in engineering design. These solutions and methodologies are directed toward both improvement of the existing buildings and infrastructure and for creating sustainable designs of new systems. The project approach includes three well-defined, interrelated research focus areas including nanoengineered construction materials, performance-based engineering and reliability of buildings, and energy efficiency and life cycle performance of construction materials and buildings in Kuwait. The project activity at MIT spans the departments of Civil and Environmental Engineering, Earth, Atmospheric and Planetary Sciences, Architecture, and Nuclear Science and Engineering. The participating institutions in Kuwait include the Kuwait Institute for Scientific Research (KISR) and Kuwait University (KU). The project has promoted collaboration between MIT and Kuwaiti researchers as well as a strong interaction among the participating departments at MIT and between KISR and KU within Kuwait.

O. Büyüköztürk (✉)

Department of Civil and Environmental Engineering, Massachusetts Institute of Technology, Cambridge, MA, USA

e-mail: obuyuk@mit.edu

© Springer Nature Switzerland AG 2020

A. Bumajdad et al. (eds.), *Gulf Conference on Sustainable Built Environment*, https://doi.org/10.1007/978-3-030-39734-0_1

2 Focus Areas

Based on the overall goal of the project, three distinct but related focus research areas have been defined for this signature project: (a) nanoengineered sustainable construction materials for durability in aggressive environments, (b) ground motion modeling and structural monitoring for performance-based engineering and reliability, and (c) enhanced operational energy efficiency and life cycle performance of buildings and cities in Kuwait (refer to Fig. 1).

The goal of Focus Area A is to develop a science-based design for durable and sustainable concrete materials and structures for extreme environments in Kuwait and the Gulf region. This is achieved through a combined and evolutionary approach involving experiments with sustainable micro- and nanocement additives as well as computational multi-scale modeling and simulation of material design extending the engineering design space to the fundamental levels as a basis for durable and sustainable construction materials. The goal of Focus Area B is to ensure the safety and reliability of Kuwait’s built environment, including tall buildings, against natural forces such as earthquakes, winds, and climate factors. The study includes computational modeling for building performance, determining characteristics (amplitude, frequency, duration) of ground motion due to local and regional earthquakes, instrumenting and monitoring the response of selected tall buildings, and correlating the measurements with the model-based predictions. The goal of Focus

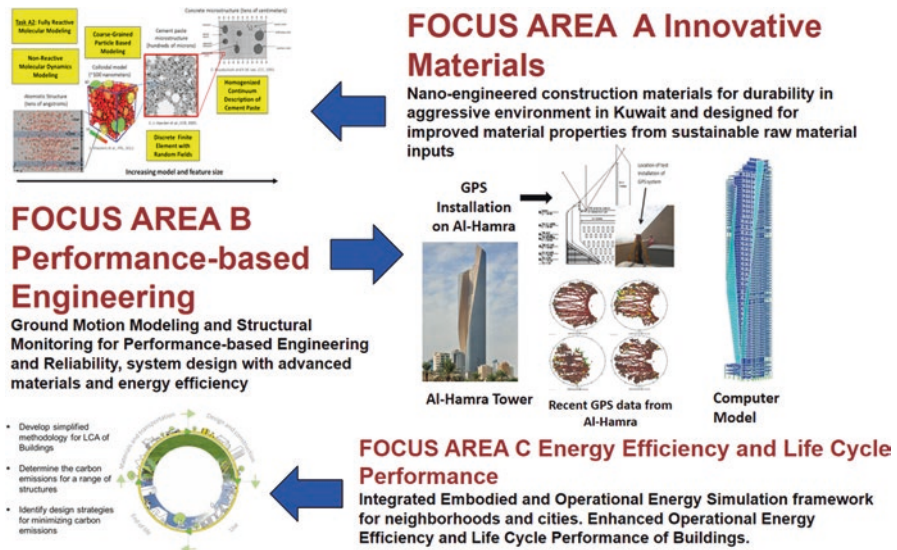


Fig. 1 Three related focus areas of research as part of the main pillars of the Signature Project

Area C is to develop innovative solutions and methodologies for the sustainability of Kuwait's built environment in the area of energy efficiency and life cycle performance. These solutions are directed toward both improvements of existing buildings and neighborhoods and the creation of more sustainable building designs and urban planning for new resilient cities.

In what follows, we highlight several major achievements for the focus areas.

2.1 Focus Area A: Nanoengineered Sustainable Construction Materials for Durability in Aggressive Environments

To address this challenge, the overall objective of the MIT Focus Area A group is to develop a bottom-up multi-scale framework for investigating the influence of additives on cement paste at multiple length scales as a basis for designing more durable cementitious materials for the Kuwait environment. The framework described below is a first implementation for seamlessly connecting atomistic and continuum behavior in cementitious materials and provides a foundation for future exploration and innovation. The development of this framework is supported by experimental studies, including joint studies conducted collaboratively by researchers at MIT and Kuwait. These experiments allow us to determine the impact of additives such as volcanic ash, nanosilica, silica fume, and metakaolin on the formation and durability of cement paste materials. Where appropriate, these experiments also provide inputs to computational models.

Large volcanic resources are available in the region of Saudi Arabia. Kuwait being a neighbor to Saudi Arabia used the volcanic ash from Saudi Arabia since Kuwait's goal was to use locally available materials for preparing eco-friendly cements and concretes for the Gulf region. Volcanic ash-based concretes were designed by varying the particle size, and its effect on hydration was examined via synchrotron and beamline techniques [1, 2]. Enhanced strength and durability properties were detected when 30% of Portland cement was substituted with 6 μm volcanic ash [3]. In addition, the pore structure was densified when silica fume was added with volcanic ash thus providing durable and sustainable solutions for building new infrastructure in the Gulf region [4].

In addition to experimental research, computational modeling was performed to examine the cohesive–frictional interactions of hardened cement paste microstructure with and without additives [5]. The cohesive–frictional force field (CFFF) along with coarse-graining approach provided an essential connection between nanoscale molecular interactions and macroscale continuum behavior for hydrated cementitious materials [6, 7].

2.2 Focus Area B: Ground Motion Modeling and Structural Monitoring for Performance-Based Engineering and Reliability

The goal of Focus Area B was to ensure the safety and reliability of Kuwait's built environment, including tall buildings, against natural forces such as earthquakes, winds, and climate factors. The study includes computational modeling for building performance, determining characteristics (amplitude, frequency, duration) of ground motion due to local and regional earthquakes, and instrumenting and monitoring the response of selected tall buildings and correlating the measurements with the model-based predictions. In particular, significant work has been completed in ground motion simulation, development of a full-scale finite element analysis model for the Al Hamra Tower with extensive data processing algorithms, and GPS installation and data collection and processing. Seismic instrumentation design and planning for the Al Hamra building was accomplished.

The Al Hamra Tower represents the tallest sculptured concrete structure in the world located in Kuwait City. A detailed study of this unique structure has been made by using a high-fidelity computational model with ETABS for structural health monitoring applications [8]. The tower is made of cast-in-place reinforced concrete with a core of shear walls and two curved shear walls running the height of the building (approximately 413 m with 86 floors in total). Interesting static and dynamic characteristics of the tower are described. System identification, interferometry-based wave propagation analysis, and wave-based damage detection are performed using synthetic data. This computational study serves as a basis for correlating the field monitoring data with the predictive model of the building.

Ground motion in Kuwait from regional and local earthquakes was examined to evaluate the effects on tall buildings [9]. In recent years, the construction of tall buildings has been increasing in many countries, including Kuwait and other Gulf states. These tall buildings are especially sensitive to ground shaking due to long-period seismic surface waves. Although Kuwait is relatively aseismic, it has been affected by large ($M_w > 6$) regional earthquakes in the Zagros Fold–Thrust Belt (ZFTB). Accurate ground motion prediction for large earthquakes is important to assess the seismic hazard to tall buildings. An analysis is performed of the observed ground motions due to two earthquakes widely felt in Kuwait: the August 18, 2014, M_w 6.2 earthquake, 360 km NNE of Kuwait City, and the November 12, 2017, M_w 7.3 earthquake, 642 km NNE of Kuwait City. The peak spectral displacement periods of the ground motion from the August 18, 2014, M_w 6.2 earthquake matched well with the ambient vibration spectra of the tallest building—the Al Hamra Tower. Ground motions from potential regional and local earthquakes are calculated using a velocity model obtained by matching the observed seismograms of the 2014 and 2017 earthquakes. Our study shows that a significant source of seismic hazard to tall buildings in Kuwait comes from the regional tectonic earthquakes. However, local earthquakes in Kuwait have the potential to generate high peak ground accelerations ($\sim 98 \text{ cm/s}^2$) close to their epicenters.

Global positioning systems (GPS) have been used for long-term monitoring of deformation for tectonic applications for many decades. Our recently published

study shows the global positioning system (GPS) measured response of the tallest building in Kuwait, the Al Hamra Tower, to the November 12, 2017, M_w 7.3 earthquake, 642 km to the north, on the Iran–Iraq border [10]. Nearby GPS and seismic stations measure the ground motion near the building. The ground motions have amplitudes of ~ 40 mm, while the top of the building moves by up to 160 mm. The building motion continues with levels greater than the noise level of the GPS measurement for about 15 min after the earthquake. After the ground motion excitation ends, the building motion decays with a time constant of ~ 2 min, and the beat between the two lowest frequency modes of deformation of the building can be seen. There are two large amplitude peaks in the building motion with magnitudes of 120 and 160 mm. The timing of the peaks is consistent with ground excitation in an 8.3–6.5 s period (120–180 mHz) band, which covers the 7.25 and 5.81 s periods (138 and 172 mHz frequencies) of the fundamental modes of the building. The ground motions in this band show two large pulses of the excitation, which have timing consistent with the large amplitude building signals. The response of the top of the building is amplified by an order magnitude over the ground motions in this band. There is no apparent permanent displacement of the top of the tower.

2.3 Focus Area C: Enhanced Operational Energy Efficiency and Life Cycle Performance of Buildings and Cities in Kuwait

A major part of Focus Area C research involved in examining the embodied energy studies from material to building scale [11]. One common strategy for reducing CO₂ emission is by replacing Portland cement with supplementary cementitious materials (SCM). Moreover, the reduction in CO₂ emission due to the usage of SCM significantly contributes to the life cycle greenhouse gas (GHG) emissions and Embodied Energy (EE) of the concrete. The effect on embodied energy (EE) of concrete is studied when Ordinary Portland Cement (OPC) is partially replaced with natural Pozzolanic Volcanic Ash (VA) at the material and the building scale. The work aims to demonstrate potential improvements to the EE of buildings by comparing the EE of the cement mix with VA replacement to that of baseline case of traditional concrete. Embodied energy coefficients (EEC) express the EE of each building product in megajoules (MJ) per kg of material. Hardened cement paste made with up to 50% of the OPC replaced by volcanic ash with a mean particle size of either 17 or 6 mm is considered. Replacement of OPC with volcanic ash decreases the EEC; however, the mix design must be engineered considering the volcanic ash composition to maintain the optimum mechanical strength. Grinding the volcanic ash from 17 mm to 6 mm led to increased compressive strength when replacing up to 40% of OPC with 6-mm-sized volcanic ash. An average of 16% decrease in EEC values can be achieved when 40% OPC was replaced with VA. On a building scale, the initial EE is the energy consumed related to the extraction, production, and transportation of materials. For buildings with an average structural material quantity (SMQ, expressed in mass of material per area) value of approximately 2000 kg/

m², a 16% decrease in EE value was observed among a sample set of 26 residential and commercial buildings when 50% of OPC is replaced with VA. The demonstrated reduction in EE values was calculated when natural supplementary cementitious materials (SCM) such as volcanic ash are used as a partial replacement to OPC, and it can be adapted to design and build energy-efficient systems tailored for structural and nonstructural applications.

3 Project Team and Activities

The first MIT-Kuwait Signature Project (SP1) was conducted under the leadership of the Principal Investigator Professor Oral Buyukozturk, with Dr. Kunal Kupwade-Patil as project manager and Dr. Hasan Kamal as the coordinator of the Kuwait work. The project activity at MIT spans the departments of Civil and Environmental Engineering, Earth, Atmospheric and Planetary Sciences, Architecture, and Nuclear Science and Engineering. The participating research institutions in Kuwait are KISR and KU. The project has successfully promoted collaboration between MIT and Kuwaiti researchers as well as a strong interaction among the participating departments at MIT and between KISR and KU within Kuwait. The project involved 37 Kuwaiti researchers including 6 Co-PIs and 24 MIT researchers including 6 Co-PIs, with an overall total of 61 researchers (refer to Table 1).

3.1 Students

Student involvement including research and academic theses was one of the major aspects of SP1:

- Doctoral students: 7, 6 MIT Ph.D. theses and 1 Ph.D. thesis from KU were completed.
- Master of Science students: 6 master's theses were completed from Kuwait.
- Bachelor of Science: 1 MIT thesis was completed from MIT.

3.2 Capacity Building

The primary objective of the signature project was to perform high-level collaborative research to develop innovative solutions and methodologies for evaluating and improving sustainability of Kuwait's built environment and to establish a new paradigm in engineering design.

However, in this process the project has also undertaken and delivered a significant knowledge transfer/capacity building activities. These activities involved holding

Table 1 Research team members from MIT and Kuwait

MIT	Kuwait
<i>Focus Area A: Innovative materials</i>	
Prof. Oral Buyukozturk (CEE), PI	Prof. Ali Bumajdad (KU), Co-PI
Prof. Markus Buehler (CEE), Co-PI	Eng. Suad Al-Bahar (KISR), Co-PI
Prof. Sidney Yip (NSE), Co-PI	Dr. Adel Husain (KISR), Co-I
Dr. Kunal Kupwade-Patil (CEE)	Dr. Saud Al-Otaibi (KISR)
Steven D. Palkovic (CEE), Ph.D. student	Dr. Jayasree Chakkamalayth (KISR)
Dieter B. Brommer (MechE), Ph.D. student	Dr. Abdul Salam Al-Hazza (KISR)
Cheahuychou Mao (freshman)	Mohammad F. Abdulsalam (KISR)
Stephanie Chin (freshman)	Anfal F. Al-Aibani (KISR)
Maranda L. Johnston (DMSE), Senior	Dr. Antony Joseph (KISR)
	Abdullah Jamsheer (KU), Ph.D. student
	Rehab Masmoudi (KU), M.S. student
<i>Focus Area B: Performance-based engineering</i>	
Prof. Nafi Toksoz (EAPS), Co-PI	Dr. Hasan Kamal (KISR), Co-PI
Prof. Tom Herring (EAPS), Co-PI	Eng. Jamal Al-Qazweeni (KISR), Co-I
Prof. Oral Buyukozturk (CEE), PI	Dr. Abdullah Al-Enezi (KISR)
Dr. German Prieto, (EAPS)	Dr. Ammar E. A. Ben-Nakhi (KU)
Dr. Hao Sun, (CEE)	Dr. Jafarali Parol (KISR)
Dr. Sadi Kuleli (EAPS)	Safaa Abdulsalam (KISR)
Chen Gu (EAPS), Ph.D. student	Farah Al-Jeri (KISR)
Martina Coccia (EAPS), Ph.D. student	Mahmoud Taha (KISR)
Dr. Aurelien Mordret, (EAPS)	Mona Alsaffar (KISR)
	Osama A.I. Eid (KISR)
	Meshal Adel Abdulsalam (KU)
<i>Focus Area C: Energy efficiency and life cycle analysis</i>	
Prof. Christoph Reinhart (Architecture), Co-PI	Dr. Ali E. Hajiah (KISR), Co-PI
Prof. John Ochsendorf (Architecture), Co-PI	Prof. Adil K. Al-Mumin (KU), Co-PI
Carlos Cerezo (Architecture), Ph.D. student	Mohammad Sebzali (KISR)
Nathaniel Jones (Architecture), Ph.D. student	Zainab Murtadhawni (KISR)
Zahraa Nazim Saiyed (Architecture), M.S.	Ahmad Al-Ghadban (KISR)
Catherine De Wolf (Architecture), Ph.D. student	M. Al Mulla (KISR)
	M. Mousawi (KISR)
	M. Alawadhi (KISR)
	A. Abdulrahim (KISR)
	F. Alalawi (KISR)
	R. Alforaih (KISR)
	A. Al-Mazeedi (KU), M.S. student
	S. Al-Ibrahim (KU), M.S. student
	R. Al Najjar (KU), M.S. student
	S. Abbas Al Mohri (KU), M.S. student

well-organized workshops, developing skills through special training sessions, and providing analysis codes and tools. The following is a brief summary of activities:

- Number of project workshops: 15
- Special training sessions: 30
- Analysis codes and tools: 22
- Total number of capacity building activities: 67
- Scientific publications: 82

Extensive capacity building: The project has been effective in capacity building by training researchers, and students from Kuwait, in performing sophisticated experimentation, high-fidelity computational modeling, sensing, and data processing. Many students from Kuwait University have been closely engaged in the project, which also led to the initiation of a new postgraduate program in Material Science and Engineering at KU.

3.3 Outreach

MIT and Kuwaiti teams have successfully organized three major outreach activities in Kuwait:

1. Kuwait 2030: A Blueprint for Managing Kuwait's Building-Related Energy Needs, December 3, 2015
2. Al Hamra Day, January 17, 2016
3. Outreach Day-Signature Project "Sustainably of Kuwait's Built Environment," April 25, 2016

As a final product of the SP1, a major conference has been organized jointly by MIT and Kuwait on "Gulf Conference on Sustainable Built Environment." This conference was held in Kuwait from March 10–13, 2019.

3.4 Educational Impact

As a result of the SP1 project, a new postgraduate program related to Material Science and Engineering was proposed to Kuwait University. Four thrust areas are being initiated in (1) construction materials, (2) polymeric materials, (3) bio- and nanomaterials, and (4) electronic materials.

This initiative together with all the other educational training of students and research staff will open new directions in the education of future students who will be motivated by science and applications of scientific knowledge to the improvement of existing built environment and design of new durable infrastructure.

3.5 Potential for Industry Development

The methodologies, solutions, and tools developed through this multidisciplinary project have many components potential for industry use and commercialization in the field of construction materials, sensor technologies, energy-efficient construction, buildings, and cities. Opportunities exist for follow-up projects and start-ups in the assessment of buildings, oil field deformations, and motions, as well as in the use of innovative and sustainable materials in construction. The SP1 investigators have already been contacted by some industry representatives for further application projects.

3.6 Managerial Challenges

In addition to the scientific challenges, the project with its 12 Co-PIs and total 61 researchers has undertaken significant managerial challenges. Although some difficulties related to the personnel have been encountered (e.g., internal conflicts within and among groups, nonuniform performance levels, communication, budget management, unresolved NDA issues), at the end, a good engagement and effective collaboration has been achieved with established processes, norms of writing and reporting, and open communication channels.

We can state that all teams engaged in this project have now developed a sense of accomplishment and success, and with the created potential and experience, we believe that the project represents a model for a large-scale interdisciplinary research conduct with all its scientific and management challenges.

3.7 Benefits of the First Signature Project Between MIT and Kuwait

The benefits of this unique, multidisciplinary, multi-team project to Kuwait as well as to the general scientific community are many. We emphasize some highlights below:

- Successful delivery of scientifically high-quality research in broad but coherent areas of study concerning sustainability of Kuwait's built environment. The overall collaboration has contributed to expanding research vision with significant research and educational experience.
- The knowledge and methodologies developed as a basis for real-life implementation directly contributing to the industrial development and benefitting existing physical infrastructure for better performance and for building future infrastructure projects.

- Extensive capacity building: The project has been effective in capacity building by training researchers, and students, from Kuwait in performing sophisticated experimentation, high-fidelity computational modeling, sensing, and data processing. Many students from Kuwait University have been closely engaged in the project, which also led to the initiation of a new postgraduate program in Material Science and Engineering at KU.
- An essential added value of our project is to provide the intellectual framework and background for the required mechanisms for follow-up projects for both continued scientific research and for technology transfer and start-up activities contributing to industrial, economic, and social developments in Kuwait.

4 Gulf Conference on Sustainable Built Environment

As an output of the successful completion of the first MIT-Kuwait Signature Project, the Gulf Conference on Sustainable Built Environment was held from March 10–13, 2019, in Kuwait. In this conference, developments, methods, and results of the SP1 were presented. Additionally, the Gulf Conference on Sustainable Built Environment provided an international platform giving the opportunity to the engineers, scientists, distinguished speakers, and all attendees to discuss research needs and application areas for sustainable development of future infrastructure as well as for retrofitting existing systems. In view of the grand societal and engineering challenges, such as expected population growth, increase in carbon emissions, need for sustainable materials and systems, impact of climate change, and complexity of new infrastructure systems, the developed capabilities and new engineering approaches are extremely timely and provide a road map for future engineering projects. The results obtained from this project through a world-class collaborative research are applicable not only to Kuwait and the Gulf region but to many other regions of the world.

5 Conclusions

The first MIT-Kuwait Signature Project (SP1) is a collaborative and multidisciplinary research between MIT and Kuwaiti researchers aiming at the development of innovative methods and solutions for the sustainability of Kuwait's built environment. With a three-level multi-scale approach of materials (Focus Area A), buildings (Focus Area B), and urban neighborhoods (Focus Area C), the effort represents a wide scope leadership activity in science and engineering through a world-class research.

Integrated knowledge developed from the project has led to synergetic results forming a fundamental basis for intellectual development contributing to education, industrial competitiveness, and economic growth in Kuwait. In Focus Area A,

microstructural characterization work has been completed by all parties using advanced experimentation techniques. Computational material modeling studies have been completed in parallel with the experimental work including investigation on the atomistic mechanical behavior of C-S-H under mixed-mode loading and multi-scale description of cement paste systems incorporating volcanic ash. In Focus Area B, significant work has been completed in ground motion simulation, development of a full-scale finite element analysis model for the Al Hamra Tower with extensive data processing algorithms, and GPS installation and data collection and processing. Seismic instrumentation design and planning for the Al Hamra building has been accomplished. In Focus Area C, the work has been completed in developing and adapting approaches to comprehensively model the operational and embodied energy content for buildings and neighborhoods in Kuwait City using the developed simulation models.

The collaborative work between MIT and Kuwaiti teams resulted in productive research as well as extensive publications and other activities including capacity building, student involvement, and outreach. From this research 82 publications have resulted, including published journal papers, conference papers, and academic theses. The overall activity has contributed to KU and KISR in advancing their research vision and agenda.

The project has successfully promoted collaboration between MIT and Kuwaiti researchers as well as a strong interaction among the participating departments at MIT and between KISR and KU within Kuwait. The project involved 37 Kuwaiti researchers including 6 Co-PIs and 24 MIT researchers including 6 Co-PIs, with an overall total of 61 researchers. Integrated knowledge developed from the project has led to synergetic results forming a fundamental basis for intellectual development contributing to education, industrial competitiveness, and economic growth of Kuwait.

It is anticipated that the outcomes of this unique project with developed methodologies and innovations will lead to effective infrastructure solutions and sustainability of the built environment. The published material from this project will represent a major reference in infrastructure science and engineering for many years to come.

Acknowledgment This project was sponsored by the Kuwait Foundation for the Advancement of Sciences (KFAS). I would like to thank Dr. Adnan Shihab-Eldin for his support of this project. I express my sincere thanks to Professor M. Nafi Toksöz for his role in the initiation of this project and for his valuable contributions. Thanks are due to Dr. Hasan Kamal of KISR for his contributions to the initiation and realization of this project and for his collaboration in the conduct and coordination of the work. Advice and suggestions of Professor Sidney Yip have been inspirational throughout the course of the project, and his technical contributions have been essential. Dr. Kunal Kupwade-Patil skillfully served as a researcher and the project manager and assisted me in organizing and managing the activities of this challenging project.

This unique project could not have been possible without the hard work and creativity of our undergraduate and graduate students, postdocs, researchers, and colleagues, in all participating institutions, who dedicated their time and efforts. We acknowledge the evaluation and advice of external panel review members during the course of the work by Professor Urs Meier, Swiss Federal Laboratories for Materials Science and Technology (EMPA); Professor Christian Grosse, Technical University of Munich; and Dr. Franca Trubiano, University of Pennsylvania.

References

1. Kupwade-Patil K, Tyagi M, Brown CM, Büyüköztürk O (2016) Water dynamics in cement paste at early age prepared with pozzolanic volcanic ash and Ordinary Portland Cement using quasielastic neutron scattering. *Cem Concr Res* 86:55–62
2. Kupwade-Patil K, Chin S, Ilavsky J, Andrews RN, Bumajdad A, Büyüköztürk O (2018) Hydration kinetics and morphology of cement pastes with pozzolanic volcanic ash studied via synchrotron-based techniques. *J Mater Sci* 53:1743–1757
3. Kupwade-Patil K, Chin SH, Johnston ML, Maragh J, Masic A, Büyüköztürk O (2018) Particle size effect of volcanic ash towards developing engineered Portland cements. *J Mater Civil Eng* 30:04018190:04018191-04018114
4. Kupwade-Patil K, Palkovic SD, Bumajdad A, Soriano C, Büyüköztürk O (2018) Use of silica fume and natural volcanic ash as a replacement to Portland cement: Micro and pore structural investigation using NMR, XRD, FTIR and X-ray microtomography. *Construct Build Mater* 158:574–590
5. Palkovic SD, Kupwade-Patil K, Yip S, Büyüköztürk O (2018) Random field finite element models with cohesive-frictional interactions of a hardened cement paste microstructure. *J Mech Phys Solids* 119:349–368
6. Palkovic SD, Yip S, Büyüköztürk O (2017) A cohesive-frictional force field (CFFF) for colloidal calcium-silicate-hydrates. *J Mech Phys Solids* 109:160–177
7. Palkovic SD, Yip S, Büyüköztürk O (2017) Constitutive response of calcium-silicate-hydrate layers under combined loading. *J Am Ceram Soc* 100:713–723
8. Sun H, Al-Qazweeni J, Parol J, Kamal H, Chen Z, Büyüköztürk O (2019) Computational modeling of a unique tower in Kuwait for structural health monitoring: Numerical investigations. *Struct Control Health Monit* 26:e2317
9. Gu C, Prieto GA, Al-Enezi A, Al-Jeri F, Al-Qazweeni J, Kamal H, Kuleli S, Mordret A, Büyüköztürk O, Toksöz MN (2018) Ground motion in Kuwait from regional and local earthquakes: potential effects on tall buildings. *Pure Appl Geophys* 175:4183–4195
10. Herring T, Gu C, Nafi Toksöz M, Parol J, Al-Enezi A, Al-Jeri F, Al-Qazweeni J, Kamal H, Büyüköztürk O (2018) GPS measured response of a tall building due to a distant Mw 7.3 earthquake. *Seismol Res Lett* 90:149–159
11. Kupwade-Patil K, De Wolf C, Chin S, Ochsendorf J, Hajjah AE, Al-Mumin A, Büyüköztürk O (2018) Impact of embodied energy on materials/buildings with partial replacement of ordinary Portland Cement (OPC) by natural pozzolanic volcanic ash. *J Clean Prod* 177:547–554

Kuwait-MIT Collaborative Signature Project: Sustainability of Kuwait's Built Environment

Hasan A. Kamal

1 Introduction

Infrastructure of the State of Kuwait is the fundamental facilities and systems serving the state, including the services and facilities necessary for its economy to function. Infrastructure is composed of public and private physical improvements such as roads, bridges, tunnels, water supply, sewers, electrical grids, and telecommunications (including Internet connectivity and broadband speeds). Sustainability of the infrastructure facilities, and their efficiency, poses a key societal challenge in Kuwait which is directly related to other challenges of a nation including environment, energy, economy, education, and security.

In the last 15 years, a vast urban development has been noticed in Kuwait due to various reasons, especially in the capital downtown area. These developments have been generally along the lines of building high-rise and tall buildings in this region with unique environmental, geotechnical, and seismic conditions that significantly affect the performance and safety of these special structures (Fig. 1).

These buildings are affected by near and far seismic sources, by the impact of developed and developing vast petroleum fields, as well as by the desert and ocean environment including wind, high temperatures, and corrosive elements, which may cause material deterioration, damage, or failure to these structures. The first Kuwait-MIT collaborative project was developed to address aforementioned issues. In this paper, a short overview of the background of the Kuwait-MIT Signature Project is outlined, which consisted of three main interrelated thrust areas.

H. A. Kamal (✉)

Kuwait Institute for Scientific Research, Kuwait Municipal Council, Kuwait City, Kuwait
e-mail: hkamal@kisir.edu.kw



Fig. 1 Tall buildings in Kuwait City

2 Third Kuwait Master Plan

The Master Plan of the state of Kuwait is the general framework that defines the future urban policies that reflect the vision and objectives of the political, economic, social, and environmental state on different land uses within a specified period from 25 to 30 years old. Accordingly, future urban policies are determined with implementation plans, in parallel with future expected population growth in the State, which is planned to take place within the proposed new towns and settlements outside the metropolitan area. The State of Kuwait is favored by its natural resources and strategic location. The First Kuwait Master Plan was developed in the 1950s, the Second in the 1970s, and the Third in 2008 [1].

The Third Kuwait Master Plan (3KMP) proposed to develop new cities with a long-term vision of becoming a regional trade and financial center. 3KMP considered many factors; one among them is the population growth of Kuwait. Figure 2 shows the age pyramid for Kuwait by 2030. It should be noted that by 2030, approximately 65% of the total Kuwaiti population will be in age below 35 years, indicating that the country has young population and needs to heavily invest in the infrastructure systems, increase the capacity provided services, and generate new employment opportunities. In the Kuwait-MIT Signature Project, local capacity building was an important goal. Hence, several on-the-job trainings were planned in the project and implemented.

Based on various considerations, the 3KMP proposed the national physical plan for Kuwait (Fig. 3). The Silk City project in northeast Kuwait is spearheading the vision and one of the largest infrastructure projects in Kuwait. In 2010, the Sheikh Jaber causeway project was just in the initial planning phase (one of the largest infrastructure projects constructed in the GCC region), which is completed in mid-2019. The causeway project provides new strategic highway routes to facilitate planned development to the north of Kuwait City and comprises two discrete elements.

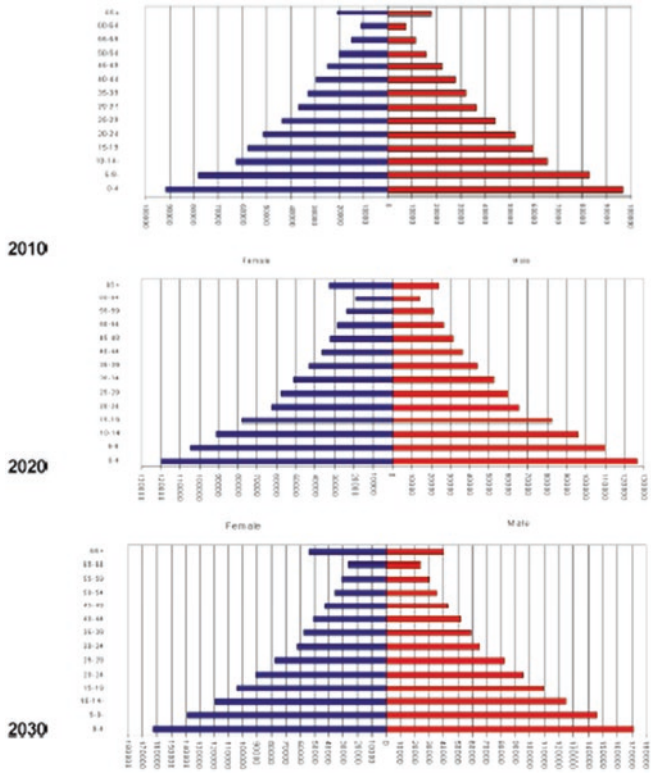


Fig. 2 Age pyramid for Kuwaiti population in 2010–2020–2030

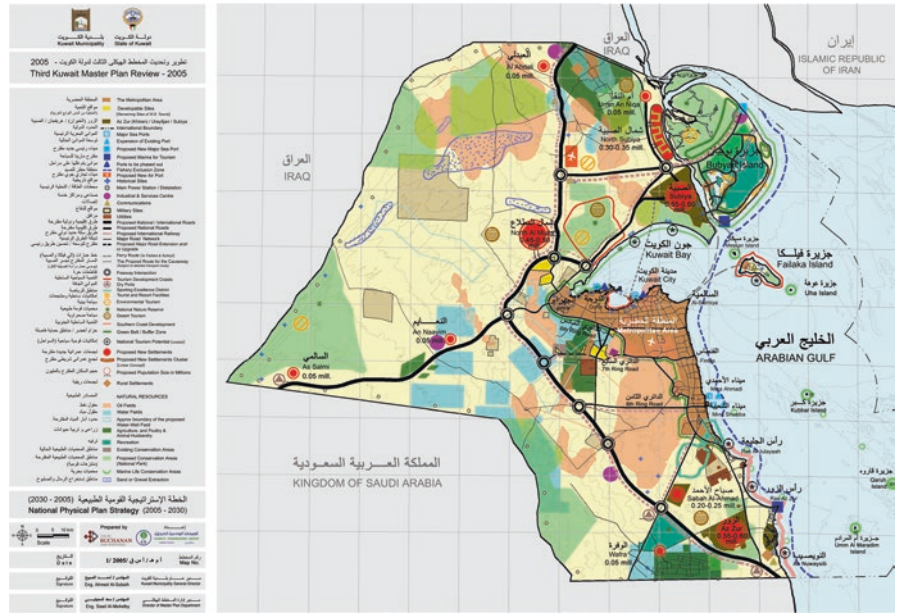


Fig. 3 Kuwait national physical plan

In summary, Kuwait is planning to invest in the country's infrastructure development by 2030. It is worth noting that most of the new development is planned in the northern side of Kuwait where the ground is more exposed to earthquake shock from Iran and Iraq side. Our recent study showed that seismic activities in the Iran–Iraq border can shake vibrations in buildings all over Kuwait. There were no prior studies carried out in Kuwait examining the effect of regional earthquakes on infrastructures in Kuwait. Hence, while developing the Kuwait-MIT collaborative project, this issue was considered and given prime importance.

3 Kuwait Seismic Condition

Kuwait is located in the northeastern corner of the Arabian Peninsula and in the northwestern extremity of the Arabian Gulf. It is characterized as a typical desert environment with prolonged dry summers with extremely high temperatures and high evaporation rates. In addition to the hot temperature, the sea environment from the Arabian Gulf produces chloride elements which are corrosive for the built infrastructures.

It is important to consider the seismic loading in buildings and infrastructure during the design phase to ensure that in the event of earthquakes, human lives are protected, damage is limited, and structures important for civil protection remain operational. Significant earthquakes in and around Kuwait that could cause potential damages to buildings are presented Fig. 4. Several earthquakes were recorded in Kuwait by the Kuwait National Seismic Network during 1997–2019 at KISR

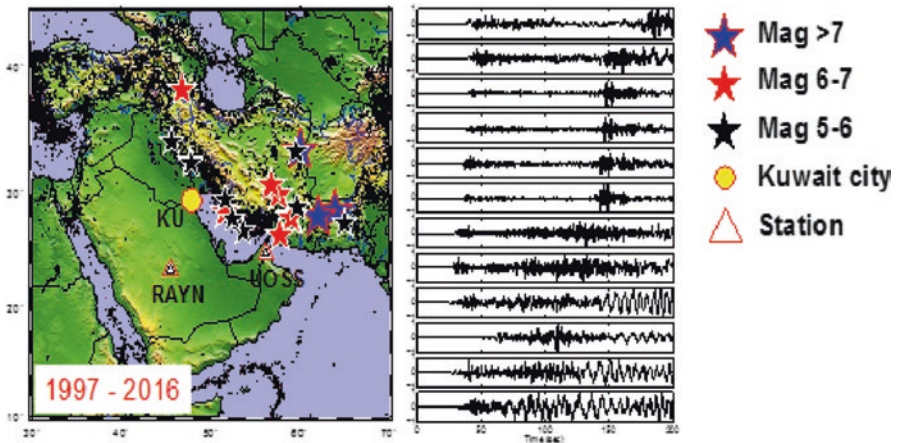


Fig. 4 Significant earthquakes in Kuwait and around that could cause potential damages in buildings

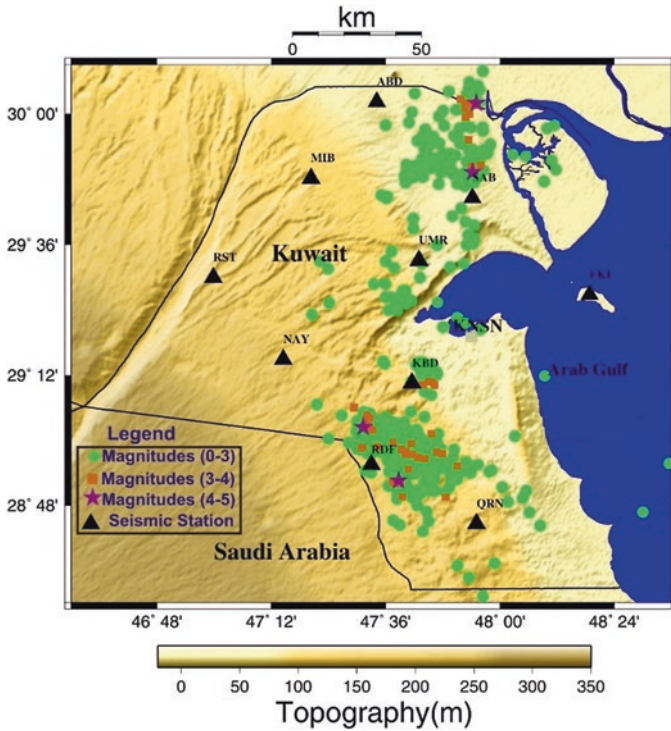


Fig. 5 Recorded earthquakes in Kuwait by the Kuwait National Seismic Network during 1997–2019 (KISR)

(Fig. 5). The earthquake epicenters are concentrated primarily to the north and to the south of Kuwait City. The largest earthquakes in Kuwait in the past two decades were the magnitude $M = 4.8$ event in East Bubiyan Island and the $M = 4.7$ event in the Minagish area in 1993 [2].

Kuwait is located in the vicinity of an active seismic zone. There are construction regulations that enforce designers to consider the seismic load in the design of structures of all sizes. Long span and tall structures are more vulnerable to short and long seismic waves, which affect the safety of such structures. Wind load has a major dynamic effect on the comfort, serviceability, and performance of tall buildings.

Kuwait experiences extreme temperature in winter and summer. Due to this harsh environment, together with the other effects of possible seismic activity and high winds, as well as increased demand in service conditions due to the population increase, serious deterioration may be manifested in the performance and serviceability of the civil infrastructure systems raising concerns for safety [3, 4].

4 Kuwait-MIT Center for Natural Resources and the Environment

The mission of Kuwait-MIT Center for Natural Resources and the Environment (CNRE) is to foster collaborations in research and education between the Massachusetts Institute of Technology (MIT) and institutions in Kuwait (KISR and KU). The Center is funded by the Kuwait Foundation for the Advancement of Sciences (KFAS).

Kuwait-MIT Collaborative Signature Project (“Sustainability of Kuwait’s Built Environment) is an outcome of a Visiting Scientist Exchange Program. During the initial stages of developing a collaborative project with MIT, it was decided to align the collaborative projects with the 3KMP. Considering these factors three interrelated focus areas of research study relevant to Kuwait were proposed:

- Focus Area A: Innovative materials (nanoengineered construction materials)
- Focus Area B: Performance-based engineering and reliability
- Focus Area C: Energy efficiency and life cycle analysis

5 Major Achievements of the Collaborative Project

At a large scale, the project integrated knowledge developed from the project has led to synergetic results forming a fundamental basis for intellectual development and capacity building contributing to education, industrial competitiveness, and economic growth of Kuwait.

In Focus Area A, microstructural characterization work was performed by all groups using advanced experimentation techniques. Computational material modeling studies progressed in parallel with the experimental work including investigation on the atomistic mechanical behavior of C-S-H under mixed-mode loading and multi-scale description of cement paste systems incorporating volcanic ash [5].

In Focus Area B, studies focused on ground motion modeling and effects of ground motions on tall buildings in Kuwait. This area of research also introduced structural health monitoring system for the first time in Kuwait, a modern technique to monitor the structural condition of the infrastructures in order to accurately qualify the actual behavior of civil engineering structures over time, combining continuous measurements taken on site with statistical and mathematical analyses and models. The exhaustive measurements taken over time provide an overview of the actual effects of different phenomena on the structures. The method can then identify the infrastructure’s real characteristics and study their evolution. Novel mathematical algorithms were developed in order to apply for the structural health monitoring systems.

The recent seismic actions in the region strongly indicate that more research work needed to be initiated on seismic effect on buildings and infrastructures due to

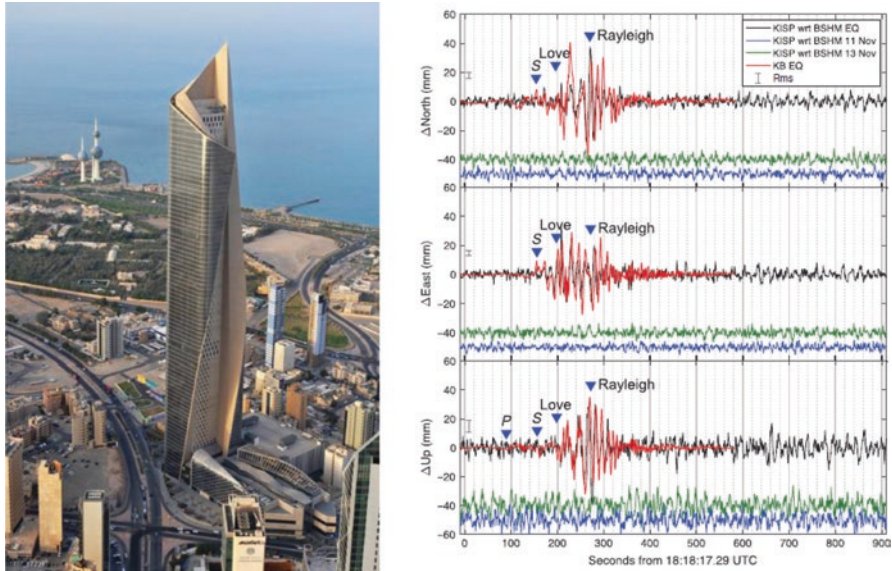


Fig. 6 Measured vibration in the Al Hamra Tower due to a distant 7.3 M_w earthquake which originated from the Iran–Iraq border in November 2017

local and regional earthquakes in Kuwait [6]. This is especially important when the Kuwait 2035 Development Plan is considered as the government is investing in building new residential neighborhoods, bridges, tall buildings, multipurpose industrial cities, etc. These buildings and infrastructures should be designed for seismic load considering the local Kuwait conditions incorporating seismic history, soil conditions, type of construction, important buildings, etc.

The global positioning system (GPS) is used to monitor earthquake response of the tallest building in Kuwait (Al Hamra Tower). It was demonstrated that GPS can be used for deformation monitoring under ambient and seismic loading conditions. The response of the Al Hamra Tower due to the 7.3 M_w earthquake which occurred on 12 November 2017 in the Iran–Iraq border, 642 km away from Kuwait City, was measured using the GPS [7]. It is observed that the building vibrated for more than 10 min, while the earthquake lasted only for a few seconds (Fig. 6).

In Focus Area C, the work has been completed in developing and adapting MIT's approach to comprehensively model the operational and embodied energy content for buildings and neighborhoods in Kuwait City using the developed simulation models.

Extensive trainings were given to young Kuwaiti professionals in all the three research areas. Several joint workshops were conducted in the USA at MIT and in Kuwait at KISR (Figs. 7 and 8 shown in Appendix). Many reports and publications were developed in addition to follow-up proposals of research projects.

6 Conclusions

In general, the collaborative research project between Kuwait and MIT research groups resulted in productive research, incubation of new research areas in Kuwait, as well as extensive publications and other activities including capacity building, student involvement, and outreach. The overall project activity has contributed to Kuwait University and Kuwait Institute for Scientific Research in advancing their research vision and schema with a significant research and collaborative educational experience.

7. Appendix



Fig. 7 Joint workshops conducted in Kuwait (KISR) 2013, 2014, and 2015



Fig. 8 Joint workshops conducted in the USA (MIT) 2013, 2014, and 2015

References

1. Kuwait Municipality (2008) Third Kuwait master plan. Kuwait Municipality, Kuwait City
2. Al-Sarawi MA (1980) Tertiary faulting beneath Wadi Al-Batin, Kuwait. *Geol Soc Am* 91(1):610–618
3. Buyukozturk O, Tuakta C, Lau D (2008) Durability of cementitious materials. in: 11th international conference on the durability of building materials and components, Istanbul, Turkey, 11 May 2008, pp 11–14
4. Buyukozturk O, Lau D (2007) High performance concrete: fundamentals and application. In: The international conference on developments and application of concrete technology, 28–30 Nov 2007, Istanbul
5. Büyükoztürk O, Kamal H, Toksöz MN (eds) (2018) Sustainability of Kuwait's built environment. MIT, Kuwait City
6. Gu C, Prieto GA, Al-Enezi A, Al-Jeri F, Al-Qazweeni J, Kamal H, Kuleli S, Mordret A, Büyükoztürk O, Toksöz MN (2018) Ground motion in Kuwait from regional and local earthquakes: potential effects on tall buildings. *Pure Appl Geophys* 2018:1–13
7. Herring T, Gu C, Nafi Toksöz M, Parol J, Al-Enezi A, Al-Jeri F, Al-Qazweeni J, Kamal H, Büyükoztürk O (2018) GPS measured response of a tall building due to a distant Mw 7.3 earthquake. *Seismol Res Lett* 90(1):149–159

Part II
Sustainable Construction Materials

Challenges and Opportunities for Concrete in the Digital Era



Henri Van Damme

1 The Present State of Affairs

Unloved by the majority and yet ubiquitous, concrete is the backbone of our modern built environment. More concrete is produced than any other synthetic material on earth. Twice as much concrete and mortar is used in construction—roughly 35 billion tons [1]—as the total of all other industrial building materials including wood [2], steel [3, 4], plastic [5], and aluminum [6]. Roads, bridges, tunnels, dams, power plants, ports, airports, dikes and seawalls, waste- and freshwater plants and networks—all these infrastructures rely on the extensive use of concrete, just like schools, hospitals, and public and commercial buildings. There seems to be no other currently known material available in the quantities required to meet the global demand for building and infrastructure.

Although the word concrete is a generic term that applies to any granular composite to which cohesion is provided thanks to a binding phase—bitumen, clay, epoxy, lime, etc.—modern concrete relies almost exclusively on the use of Portland cement or its variants. Not surprisingly considering the success of concrete, the global demand for cement has seen an unprecedented growth in the last half-century, especially since the turn of the third millennium (Fig. 1). In relative terms, the increase of cement demand is surpassed by that of plastic [10] (Fig. 1), but in absolute terms, cement remains by far the largest industrially manufactured product. There is a wide consensus that this exceptional growth of cement and concrete consumption on the global scale is temporary and due to a handful of actors only among the emerging countries, China in particular [7, 8]. But there are also good reasons to consider that a slower but lasting growth will go on for long. Developed countries face the challenge of maintaining and upgrading their extensive but aging transport, power, water, and telecommunication networks, whereas many developing countries

H. Van Damme (✉)

Ecole de Physique et Chimie Industrielles de Paris (ESPCI Paris), Paris, France

e-mail: henri.vandamme@espci.fr; henrivd@mit.edu

© Springer Nature Switzerland AG 2020

A. Bumajdad et al. (eds.), *Gulf Conference on Sustainable Built Environment*,
https://doi.org/10.1007/978-3-030-39734-0_3

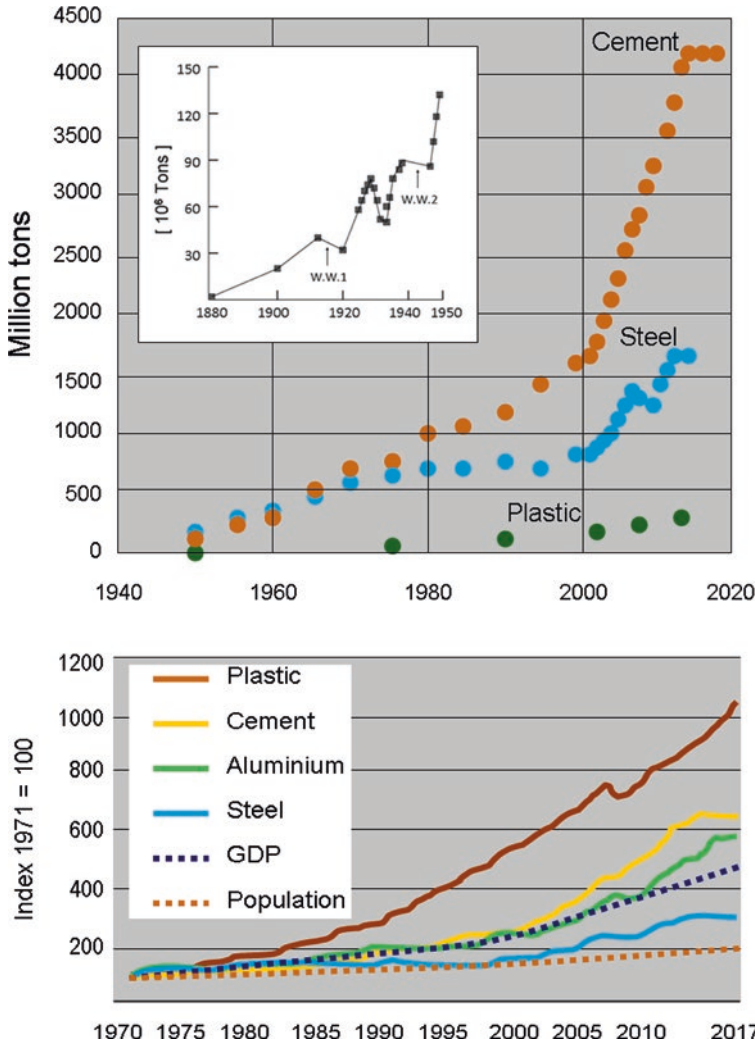


Fig. 1 Top: comparative evolution of the post-WWII global cement, steel, and plastic productions (data from [3–5, 7, 8]). The inset shows the earlier cement production [9]. Bottom: relative evolution of the world demand for plastic, cement, aluminum, and steel, as compared to the evolution of the world population and gross GDP, starting from the year 1971 [10]

still dedicate a large fraction of their national income to satisfy basic human development needs like access to water, sanitation, electricity, and affordable housing. Altogether, this is likely to drive a lasting increase of concrete demand for decades to come.

In parallel with its galloping dissemination, concrete has made tremendous technical progress. The late nineteenth-century mixes of aggregates, cement, and water, produced on site, had a compressive strength of the order of 20 MPa, and they were

rammed in a barely wet and rather stiff state either between movable forms to make walls or on a falsework to make arches. Contemporary concrete with a predefined compressive strength between 50 and 200 MPa (Fig. 2) is now routinely produced in ready-mixed plants and delivered on site in a much more workable state. Vibration, which was for many decades a compulsory step for proper filling of rebar-congested formworks, is no longer necessary with the advent of self-placing concrete (also termed self-compacting or self-leveling concrete). Even ultrahigh-performance concrete (UHPC) remains highly flowable in spite its very high solid volume fraction.

The two key ingredients of this progress are the quasi-homeopathic introduction of deflocculating agents on the one hand and the controlled addition of fines in the granular formulation on the other hand. By avoiding the formation of aggregates of cement particles in particular, the former—water-reducing agents or superplasticizers [12]—allow for a more efficient use of the suspending solution in hydrodynamic terms (or, equivalently, avoid the formation of hydrodynamic dead zones). The latter—nanosilica, silica fume, limestone fillers, etc.—extend and improve the continuity of the particle size distribution, thereby allowing for a denser and stronger hierarchical packing structure of the hardened solid phase. Interestingly, deflocculation, which is primarily intended to improve workability, has also a beneficial influence on strength, whereas the addition of fines, which is primarily targeting mechanical properties, has also a beneficial impact on rheological behavior [13].

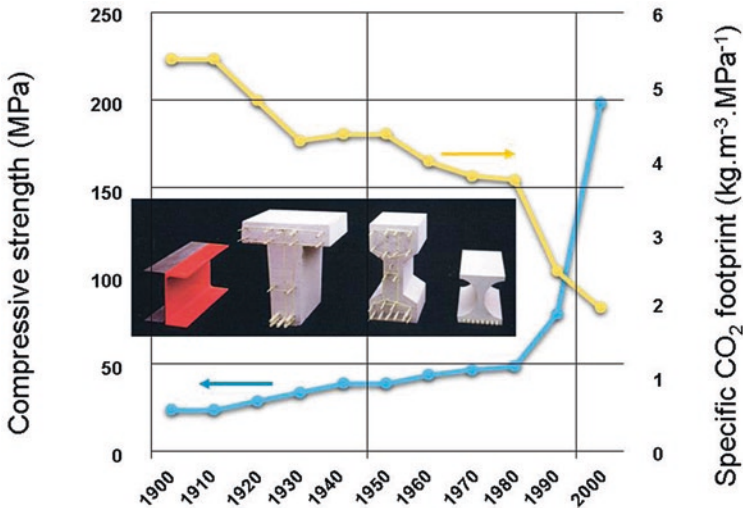


Fig. 2 Evolution of the compressive strength and average specific carbon dioxide footprint of concrete during the twentieth and early twenty-first century [11]. The four beams on the inset have the same load-bearing capacity. The first is made of mild steel. The second is made of classical reinforced concrete with iron rebars, as it was used in the 1930s. The third is made of prestressed high-performance concrete, with both rebars and prestressing cables. The last one is in fiber-reinforced ultrahigh-performance concrete (UHPC), without any rebar, but with prestressing cables. It is only slightly heavier per unit length than the steel beam (+20%), whereas the more classical concretes are much heavier (+450% and +400%, respectively) (courtesy: Ph. Gégout, Bouygues)

This synergetic control of rheology in the fresh state and strength in the hardened state is still a matter of active research [14, 15].

Better placement and less capillary porosity are not only improving strength. They are also improving durability. Voids are the gates through which aggressive agents—salts, chloride ions, and carbon dioxide in particular—penetrate the material and induce the chemical changes, at the reinforcement–matrix interface in particular, which may ultimately lead to the loss of structural integrity. Thanks to a drastic reduction of porosity, the contractual life span of concrete structures is now exceeding 100 years.

The manufacture of Portland cement itself—or, more exactly, of ordinary Portland cement (OPC), containing over 90% Portland cement clinker—has also made valuable progress in environmental terms, thanks to improvement in kiln efficiencies, choice in fuel type, and reduction in electricity requirements (mainly for crushing). As a result, the production of OPC generates now on average ~ 0.840 kg CO₂/kg of clinker, as compared to ~ 1 kg CO₂/kg of clinker a few decades ago [16]. Unfortunately, the emissions due to limestone decomposition during calcination—the so-called process emissions—can hardly be decreased without changing the composition of the product. This leaves clinker substitution by low-carbon mineral additions and/or so-called supplementary cementitious materials (SCM) as the simplest and most efficient strategy for further reduction in carbon footprint [17, 18]. With the present level of clinker substitution, cement production is still the third largest source of anthropogenic emissions of carbon dioxide, after fossil fuel oxidation and land-use change [19]. With ~ 1.45 Gt CO₂ in 2016, cement process emissions are equivalent to about 4% of all emissions from fossil fuels [19]. The “energy” emissions add a further 60% on top of these process emissions.

In contrast with the technical aspects, the social picture is less engaging. Alternatively lauded or execrated, concrete is also the most controversial among all building materials. Widely perceived as dull and repetitive, concrete is blamed for its contribution to carbon emissions and climate change and to a variety of environmental problems like loss of farmland and increased vulnerability to natural hazards (flash floods in particular, due to increased imperviousness of soils), destruction of landscapes, loss of biodiversity, destruction of social link, loss of traditional constructive cultures, or depletion of natural resources, sand in particular [20, 21]. Taken together, it is an extraordinarily severe indictment that concrete is facing.

The construction industry itself does not benefit from a much better image. The world is covered with a wealth of iconic buildings and impressive civil engineering works that are true architectural and technical feats, in Asia and in the Gulf region in particular. Yet, construction is still considered by many as the low-tech end of the industrial landscape. One reason for this poor image could be the notoriously low productivity of the construction sector. In terms of value added by construction workers per hour of work, construction is indeed performing below other major economic sectors like agriculture, manufacturing, wholesale, and retail (or even mining) [22] (Fig. 3). Today, construction-related spending accounts for about ten trillion USD, which amounts to 13% of global GDP [22]. Yet, labor-productivity growth has averaged only 1% a year in the past 20 years, compared with 2.8% for

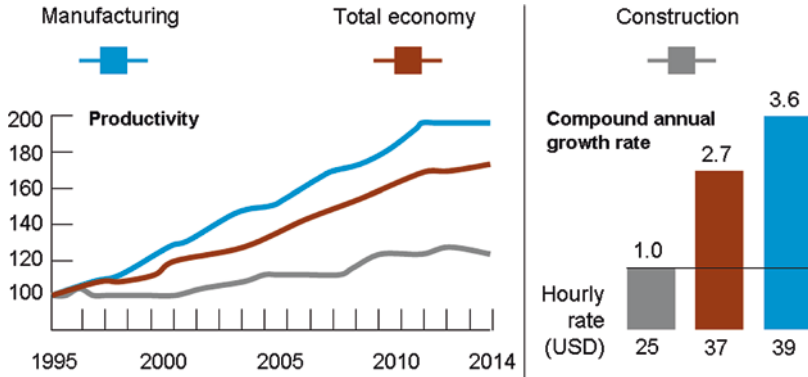


Fig. 3 Left: evolution of the productivity, defined as the real gross value added per hour worked by person engaged in 2005 USD. Index 100 is the value in 1995. Right: compound annual growth rate, 1995–2014 (%). Calculations are based on a sample of 41 countries that generate 96% of global GDP [22]

the total world economy and 3.6% for the manufacturing industry. Actually, it seems that the construction sector’s productivity has seen a consistent decline or, at best, a stagnation since the late 1960s [22]. While the manufacturing sector has implemented entirely new concepts of flow, modularized and standardized designs, and aggressively automated to increase production, the construction industry still relies on traditional methods for many projects [22].

So, we are left with the following general question: What can we do to tackle the environmental and technical weaknesses of the concrete-related construction sector and bring it as close as possible to full sustainability and to productivity standards close to those of the manufacturing industry? This contribution is a brief inventory of the most straightforward actions that we can take, either in the formulation of concrete or in its implementation method. Most opportunities are related to the advent of digital technologies in one way or another. Therefore, it is worth having a first look at the ongoing digital (r)evolution in materials science and design.

2 The Digital Context

The science of materials, as well as the way we design new materials and the way we choose materials to design and build structures, is currently undergoing deep transformations. At the industrial scale, we are living the onset of what Klaus Schwab called the Fourth Industrial Revolution [23], while others consider that it is just in the continuity of the Third Revolution [24]. In the four-revolution scheme of the World Economic Forum [23], the first revolution—that is, the one which increased by several powers of ten our capacity to do work—is the coal, water and steam revolution. The second revolution—the one that led to mass production of goods, cars in particular—is the one associated with the generalization of electricity

and the division of work. The third came with the introduction of electronics, computers, and information technology. It led to automation in production, improving further the affordable access to goods, including high-tech ones. Now a fourth revolution is building on the third, disrupting not only production but also services. All aspects of every day's life are impacted, including education and health care (Fig. 4). It is based on generalized connectivity, big data (BD) collection, and artificial intelligence (AI).

Somewhat similarly, Agrawal and Choudhary identified four different stages or paradigms in the evolution of materials science [25]. For a very long time, science was based on fortuitous or provoked observations and on empirical correlations between these observations. The early science of metals and alloys, and that of hydraulic binders (Roman cement), belongs to this paradigm. Then came the time of theoretical models and generalized correlations in the form of mathematical equations or “laws.” The laws of thermodynamics or those of the mechanics of solids are good examples of this category. However, not every problem of the real world is amenable to the analytical solution of a theoretical model. In those situations, the advent of computers offered a radically different approach by allowing for the simulation of real-world complex phenomena. Grand canonical Monte Carlo simulations, molecular dynamics (MD), and density functional theory (DFT) are typical methods of this computational science.

Actually, experiments, theory, or simulation is not mutually exclusive. They form the common toolbox of researchers in almost every scientific field and in materials science in particular. Together, they have generated a vast amount of data. In turn, this wealth of available data of different types—not in every field though—is now giving rise to a new paradigm which is (big) data-driven science. Big data analytics is the use of advanced analytic techniques against very large, diverse data



Fig. 4 The four industrial revolutions, according to Klaus Schwab (World Economic Forum) [23]

sets that include structured, semi-structured, and unstructured data, from different sources and in different sizes. The data may have unknown inconsistencies, they may have parts that are missing, and they may be unreliable. All this makes big data analytics a challenging exercise (Fig. 5).

Materials science is still far from having data sets as big as those found in human sciences or in nuclear physics for instance or as heterogeneous as those found in the marketing business, but the development of molecular modeling and high-throughput experimental methods like time-resolved synchrotron spectroscopy and imaging methods is rapidly increasing the number of structural and property data. In parallel, large-scale initiatives like the Materials Genome Initiative (MGI) are promoting their open accessibility [26].

Extracting useful information from large and heterogeneous data sets requires the use of specific methods. Like bioinformatics some time ago for the wealth of data coming from genomics, proteomics, and synthetic biology, materials informatics has to develop the methods of data-driven materials science and engineering [27, 28]. Keys in this type of approach are the predictive modeling algorithms of machine learning that enable rapid predictions based purely on existing data rather than by new experimentation or computer simulations [29, 30].

The working frame of materials informatics is the familiar “composition–structure–property” sequence of laboratory materials research to which, in order to be closer to the real world, “processing” has to be added on the uphill side and “performance” on the downhill side [25, 31, 32]. This CPSPP sequence (Fig. 6) can be scrolled through deductively from left to right or inductively from right to left.

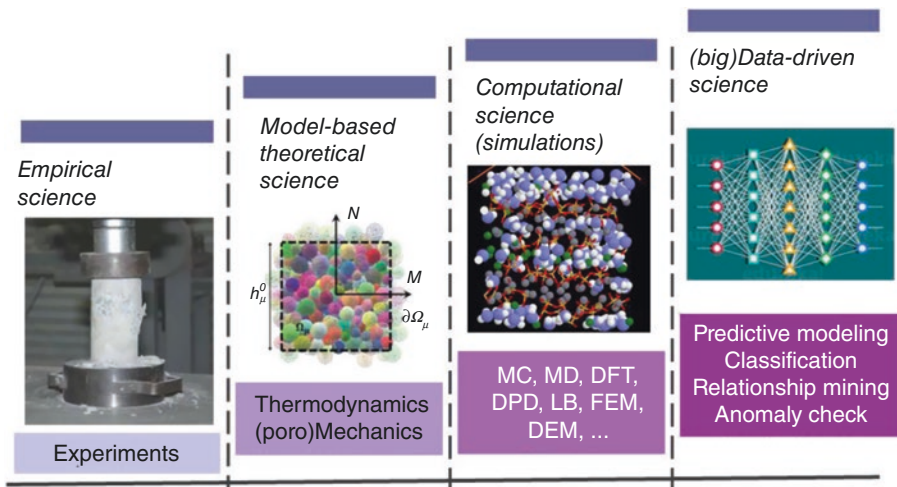


Fig. 5 The four paradigms of science, illustrated for cement and concrete science (Adapted from [25])

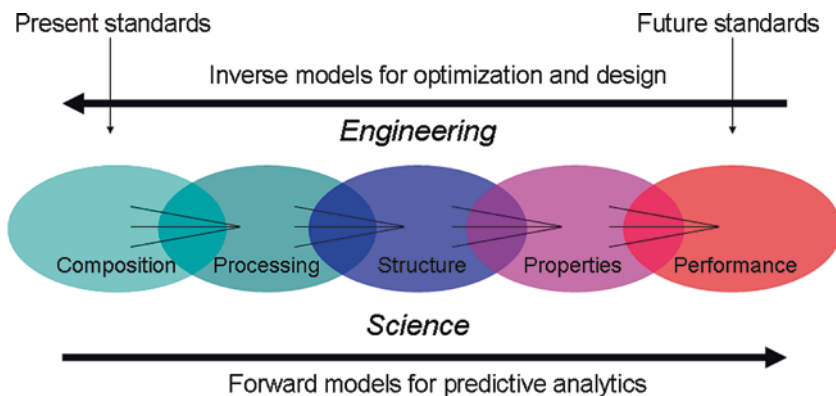


Fig. 6 The composition–processing–structure–property–performance sequence covered deductively from left to right in materials science and inductively from right to left in materials engineering. Materials informatics can help us go both ways with predictive or optimization modeling (Cartoon adapted from [25])

The former is typical of a science-based approach relating causes to effects, whereas the latter is more in line with an engineering approach going from goals to means [25, 31].

Machine learning algorithms can be used both ways. Forward (left to right) models allow for the rapid prediction of properties and performance given the composition, processing, and structure information. Inverse (right to left) models are algorithms allowing for the optimization of a property or performance within a given composition, processing, and structure parameter space or, alternatively, in new materials space. Materials informatics, i.e., big data collection coupled with machine learning, is still far from being a mature field, but it has the potential to revolutionize the way we choose and optimize existing materials and the way we discover new materials. The number of reported applications is growing at an extraordinary rate. Concrete science and engineering cannot afford to stay away from this revolution.

3 What Can We Do?

We now go back to our initial aim which is to identify possible strategies for improving the image, the environmental impact, and the productivity of construction with concrete, while simultaneously maintaining or—better—increasing mechanical and durability performance. Nine lines of action may rather easily be identified, which can be classified in two major categories: those which deal with improvement of concrete itself (Sects. 3.1–3.4 hereafter) and those which deal with improvement in the way we use it (Sects. 3.5–3.9).

3.1 *Nanoengineering the Cohesive Hydrates (C-(A)-S-H)*

Among all the “hydrates” that the reaction of Portland cement with water is producing, calcium silicate hydrate is the most abundant and the most important. It controls to a large extent the properties of the hardened cement paste, including its mechanical properties [33], and may be considered as the real glue of our built environment. Surprisingly, in contrast with the wealth of efforts and debate devoted to the atomic structure and nanoscale physical–chemical properties (density, porosity, water adsorption, etc.) of this poorly organized material, only a handful of teams have been tackling its mechanical properties (stiffness, cohesion, adhesion, creep, strength, etc.) in the same range of length scales, either experimentally or computationally. Yet, engineering the mechanical properties of C-S-H is a strategy that cannot be ignored, considering the direct relationship between the properties of concrete and those of C-S-H (this doesn’t mean that the “quality” of C-S-H is the sole factor in concrete properties). The following examples will illustrate the type of nanoengineering that can be achieved, either computationally or experimentally.

3.1.1 Atomic-Scale Engineering

The first example is based on a computational approach and makes use of the rigidity theory of trusses which goes back to the great J.C. Maxwell. While Maxwell’s theory was intended to be applied to mechanical systems of nodes and bars like the Eiffel Tower for instance, the theory has been extensively used in recent decades to disordered molecular networks [34], following the pioneering work of Phillips and Thorpe [35, 36]. Nodes are replaced by atoms, and the bar tensions are replaced by the most relevant two-body radial (stretching) and three-body angular (bending) interactions at molecular level.

The basic principle of rigidity theory—also termed topological constraint theory—is to compare the number of mechanical constraints, n_c , to the number of degrees of freedom, n_{dof} , per node ($n_{\text{dof}} = 3$ in our 3D world). Structures fulfilling $n_c = n_{\text{dof}}$ are said to be isostatic. Structures with $n_c < n_{\text{dof}}$ are floppy, whereas those with $n_c > n_{\text{dof}}$ like in the Eiffel Tower, with redundant bars, are “stressed-rigid.” In glasses, the isostatic state is associated with remarkable properties like a stress-free character, very weak aging phenomena, or a fracture toughness maximum [37].

The application to rigidity to C-S-H is not straightforward, due to the inhomogeneous character of its structure (pseudo-2D, internal interfaces with broken “bonds,” and variable coordination numbers). This makes the determination of the number of constraints much less obvious than in homogeneous and isotropic networks where it is easily derived from the average coordination number. The problem was solved thanks to a molecular dynamics (MD)-based constraint-counting algorithm. Indeed, intact constraints are characterized by small MD excursions, whereas broken constraints are characterized by large excursions [37]. Then, by following the MD atomic trajectories in more than 150 simulated C-S-H compositions with variable

Ca/Si ratio, they were able to identify a rigidity transition from a flexible to a stressed-rigid domain at $\text{Ca/Si} = 1.5$ (Fig. 7), which is significantly below the average Ca/Si ratio in hardened Portland cement (1.75) [41].

The compositional dependence of hardness, fracture toughness, and creep was also calculated. Remarkably, a clear maximum of fracture toughness and creep modulus was obtained around the isostatic composition (Fig. 7) [39, 40]. This result was confirmed by experimental measurements. To our best knowledge, this is the first example of a computational science-based optimal prediction in concrete science. The next problem is clearly to obtain this optimal composition by simple and reliable means in real construction conditions.

3.1.2 Mesoscale Engineering

In parallel with the previous type of approach which aims to optimize C-S-H by nanoengineering its structure at the very atomic scale, an increasing number of predictive modeling studies is devoted to the mesoscale arrangement of its nanoscale structural units [42–48]. Despite some debate about their shape (nanoglobules or nanoplatelets?), there is now a wide consensus that C-S-H precipitates—that is, nucleates and grows—in the form of nanoparticles which themselves, as they are continuously formed, aggregate to form the C-S-H “gel” which will ultimately fill the capillary voids. The mesoscale domain is the wide range of length scales between the size of the nanoparticles and that of the capillary voids.

The predictive modeling of the way the C-S-H gel progressively fills the capillary void space and connects the particles of the concrete mix—aggregates, residual cement particles, fines, nano-additions—is important because it provides a lever for controlling the kinetics of the early strength rise, including the yield stress in the fresh state.

A priori, the way the nucleation–growth–aggregation process takes place may be controlled by a number of factors including (1) the solution composition and supersaturation, which control the overall kinetics of nucleation and growth; (2) the concentration gradients, which control *where* the next nanoparticles will form; (3) the surface properties of the nanoparticles which, together with the interstitial solution composition, controls the attractive–repulsive interactions between nanoparticles; and (4) diffusive motion (Fig. 8).

Of crucial importance in the modeling algorithm is the decision to introduce or not diffusive (Brownian) motions. This question is seldom considered. Yet, it is of crucial importance for the gel structure. Basically, two options have been considered. In the first option, new particles are formed by secondary nucleation around primary particles [48]. Anisotropic shapes may also be used [46]. Not surprisingly, this leads to liquid crystalline-like order (nematic, smectic, or discotic), reminiscent of the type of order observed by TEM or AFM (but without the dynamics found in real liquid crystals) (Fig. 8).

The second option is to introduce new hydrate nanoparticles randomly in the void space, as in homogeneous nucleation, at a rate determined by the free energy

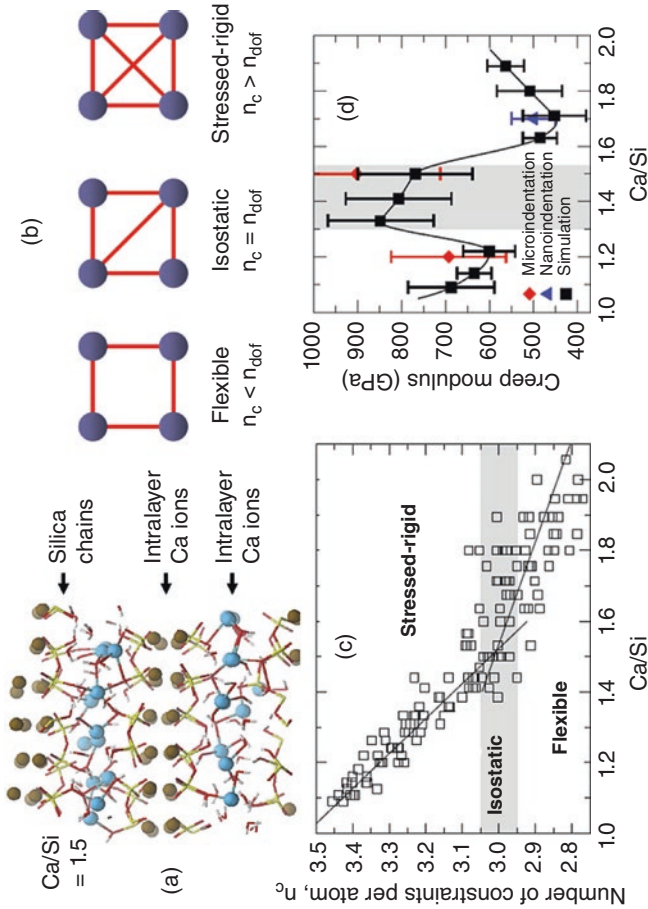


Fig. 7 Topological constraint theory applied to C-S-H. (a) A molecular model of C-S-H with $\text{Ca/Si} = 1.5$ [38]; (b) illustration of the crossover from flexible to isostatic and stressed-rigid networks as the number of constraints applied to the nodes reaches and surpasses the number of degrees of freedom; (c) the number of constraints per atom in C-S-H as a function of composition, determined by molecular dynamics [39]; and (d) compositional dependence of the resistance to creep in C-S-H. The maximum of creep modulus is reached around the isostatic composition [40]

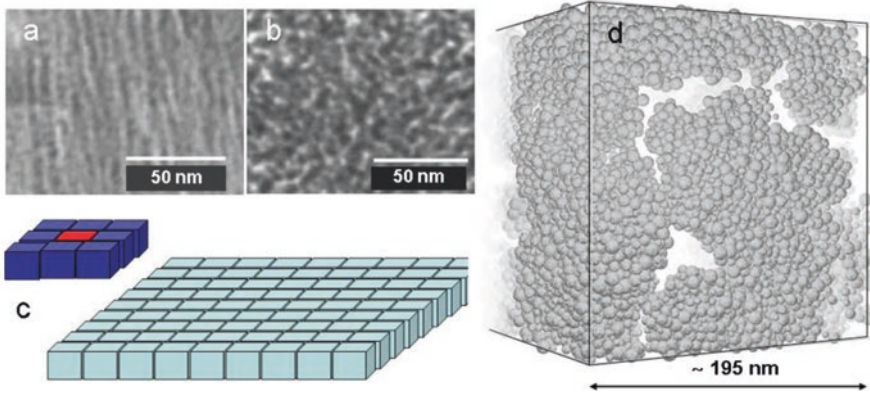


Fig. 8 The meso-structure of C-S-H and its modeling. (a, b) TEM micrographs of outer and inner C-S-H product, respectively, in a hardened C_3S paste [49]; (c) cartoon illustrating the formation of a C-S-H foil by repeated secondary nucleation around a primary nucleus; the (limited) growth of each crystallite is not shown (Adapted from [48]); (d) the model C-S-H solid formed by thermodynamically controlled precipitation, followed by MD-modeled rearrangements driven by realistic interaction potentials [44]

gain associated to their production and to allow them to move and aggregate in the interaction energy landscape of the whole system using molecular dynamics (MD) [43]. Using interaction potentials inspired by those determined experimentally by AFM measurements, this leads to a meso-structure which is more disordered than in the first option but still contains elongated aggregates with a parameter-dependent thickness. These aggregates eventually branch and percolate into a gel network [43, 44] (Fig. 8d). Remarkably, the calculated small-angle scattering intensity $I(q)$ is scaling as q^{-3} , in good agreement with neutron scattering data obtained on a hardened cement paste. Furthermore, the evolution of the calculated modulus and hardness as a function of packing fraction (the fractional volume of capillary space occupied by hydrates) are also in agreement with those obtained by nanoindentation on real cement samples [46].

The computational models of C-S-H meso-structure are still far from having delivered all their potential. One important reason for this is that, as far as hydration is concerned, the first-order parameter controlling the mechanical properties of concrete is the *amount* of hydrates, not their meso-structure [15]. So, there is little hope to improve significantly the strength of concrete by optimizing the meso-structure of the hydrates. However, provided the nucleation and growth *kinetics* of the nanoparticles is explicitly included in the models via the molecular details of their surface chemistry, mesoscale models may well prove to become the most efficient way to predict the gelation and hardening kinetics of cementitious pastes and to design new accelerating or retarding agents.

3.1.3 Bioinspired Engineering

Most natural high mechanical-performance materials like bone, nacre, wood, tendon, or spider silk owe their properties to one of the following features, or to both: (1) a hierarchical structure, from nano- to macroscale, and/or (2) a hybrid composition, associating a majority inorganic phase with a minority organic phase of biopolymers. These strategies—hybridization in particular—are followed in an increasingly wide family of materials, including clay- and cement-based composites [50–53].

Actually, in the case of cement-based materials, improving the mechanical properties by incorporating synthetic polymers has been a permanent quest of chemists for more than 40 years. This nature-inspired strategy has led to remarkable results. With calcium-aluminate cement and PVA, it led to the development of the so-called macro-defect-free (MDF) composite cement with a flexural strength of up to 70 MPa [54]. Recently, highly oriented mesocrystalline deposits of C-S-H could be prepared by careful destabilization of an initially fully dispersed suspension of C-S-H nano-foils ($\sim 60 \times 30 \times 5 \text{ nm}^3$) [55]. Total dispersion was obtained using copolymer dispersants selected from a phage display assay [56, 57]. The colloidal suspension was then gently destabilized by changing the chemical conditions (pH, polymer/C-S-H ratio) of the medium and inducing a slow particle attachment process. During deposition, from ~ 5 to $\sim 20\%$ (wt%) of polymer are incorporated in the material (Fig. 9).

Tests performed on micro-cantilevers milled from these deposits revealed an amazing bending strength approaching 200 MPa, which is close to that of nacre, and outperforms the flexural strength of ordinary concrete by a factor of 40 to 100 [55]. Unfortunately, fracture remains brittle. In spite of the scientific beauty of this nanochemical feat, progress is clearly still needed before both strength and ductility could be reached with polymer contents compatible with material availability (a 10 wt% polymer content with respect to cement on global scale would correspond to a doubling of the world polymer production), not considering cost issues.

3.2 Better Cement with Less Clinker

A simple and effective strategy to reduce the global warming potential of Portland cement-based concrete is to use cement in which a less carbon-intensive fine mineral material is substituted for part of the clinker, hopefully without loss or even improvement of durability and mechanical performance. It is usual to distinguish reactive substitutes from less reactive or inert substitutes. The former are usually referred to as “supplementary cementitious materials” or SCM, while the latter are usually termed “fillers.” Actually, there is no such thing as a totally inert addition. All fine mineral additions interfere to some extent with the hydration process, be it

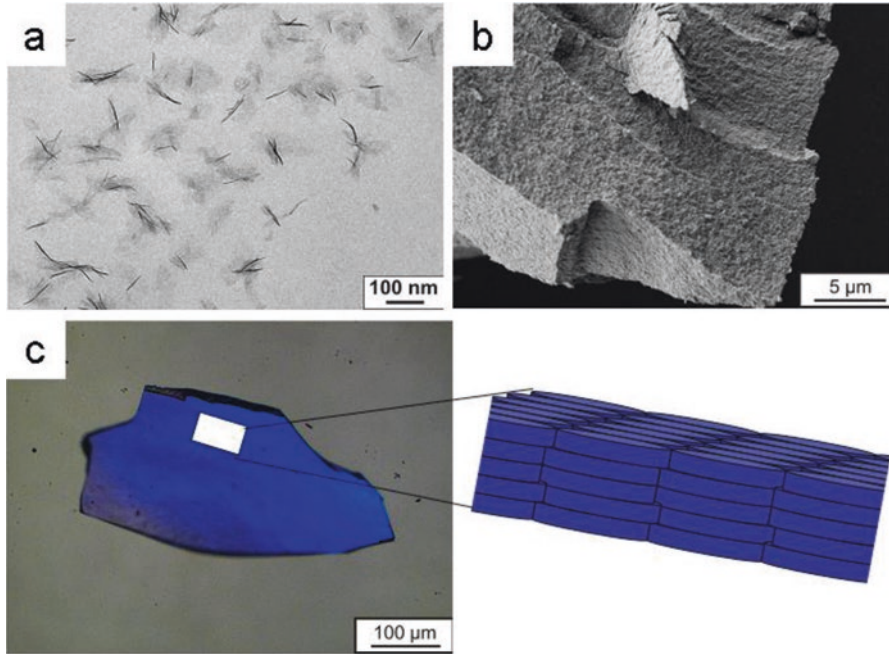


Fig. 9 C-S-H/polymer meso-composite with extraordinary bending strength. A colloidal C-S-H suspension (a) is gently destabilized and allowed to settle, leading to highly oriented deposits (b). The homogeneous color in polarized optical microscopy (c) indicates very high orientational disclotic order (c) (Idealized in the cartoon; adapted from [55])

by accelerating or retarding nucleation only. In this section we concentrate on the reactive “SCM effect.” A review of supplementary cementitious materials can be found in [58], and a more detailed discussion of the current and projected availability of SCMs and fillers can be found in [1, 17].

The major families of SCM are silica fume (SF), fly ashes (FA), granulated blast furnace slag (GBFS), metakaolin (MK), and crushed limestone. SF is a byproduct of silicon and ferrosilicon alloys metallurgy. It is formed by oxidation of silicon vapor in the electrical furnace exhaust gases. Similarly, FA is the condensed form of the noncombustible part of coal in the exhaust gases of coal-fired plants. Both SF and FA are spherical particles, of sub- μm size for SF and of larger size, comparable to that of the cement grains ($\sim 50 \mu\text{m}$) for FA. Two classes of FA may be distinguished (class F and class C), according to their low or high lime content, respectively. GBFS is the residue of cast iron production from the high temperature melting of iron ores with flux materials (Ca and Mg carbonates) and coke. Finally, MK is the product of kaolin dehydroxylation. SF, FA, BFS, and MK are essentially amorphous materials.

In spite of their clinker-diluting effect, SCM are able to maintain the level of durability and mechanical performance of unblended cement, thanks to their composition and their amorphous character (for SF, FA, BFS, and MK) which favor

reactivity. A key parameter to understand the reactivity of SCM is their Lewis basicity (or acidity), that is, their ability to donate (or accept) an electron pair. The larger the difference in basicity between two reactant compounds, the stronger will be their tendency to form covalent bonds. The concept has been applied to cement-relevant oxides, and it provides a convenient way to understand the reactivity of SCM in a Portland cement environment [59, 60].

In a $\text{CaO-Al}_2\text{O}_3\text{-SiO}_2$ composition diagram (Fig. 10), slag is not very far from clinker and lies on the high basicity corner of the diagram. It contains ~40% CaO , ~35% SiO_2 , and it is itself a hydraulic material, like clinker, but it reacts more slowly. It forms a variety of hydrates similar to those formed by neat Portland cement.

On the other hand, silica fume, fly ash, and metakaolin are closer to the acidic side of the phase diagram. They have no hydraulic character, but they share with volcanic ashes the ability to react with lime and to produce C-(A)-S-H-type hydrates. Most volcanic ashes are glassy silica-aluminas, and upon reaction with lime, they produce a hydrate which writes C-A-S-H, in which silicon is partially substituted by aluminum. Fly ash and metakaolin (and similar types of calcined clays) have also a high alumina content, and they produce the same type of C-A-S-H hydrate. On the other hand, fume silica, which is almost pure amorphous SiO_2 , produces essentially Al-free C-S-H. Finally, crushed limestone is neither hydraulic nor pozzolanic, but its surface is able to nucleate C-S-H hydrates [61]. Thus, whether by their hydraulic (GBFS), pozzolanic (SF, FA, MK), or nucleating properties (limestone), the addition of SCMs to clinker or the substitution of SCMs for clinker leads basically to the same result: as much or even more hydrates than in unblended cement.

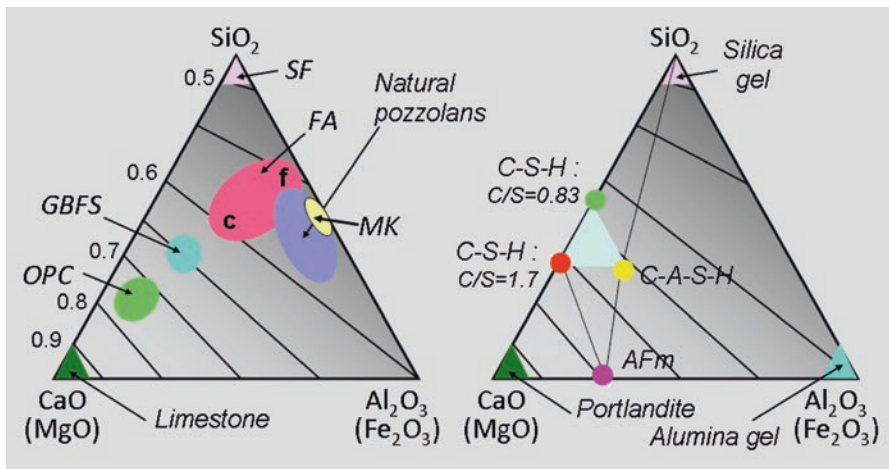


Fig. 10 Left: compositional diagram (wt%) showing the position of the most important SCMs with respect to Portland cement. Isobasicity lines are superimposed starting (highest basicity) from the lower left corner and decreasing to the top and to the right. The potential for an acid–base reaction between two oxides in the diagram increases with the distance between the isobasicity lines on which they are located. Right: hydrate phases (Adapted from [59, 60])

A particularly promising strategy is the *co*-substitution of clinker with limestone and a source of reactive alumina. Limestone reacts with available alumina to form carboaluminate phases which contribute to strength and durability [1, 17, 62, 63]. Metakaolinite is a suitable source of reactive alumina, but calcined kaolinitic clays with a kaolinite content down to 40% can do the job, at a much lower cost. Kaolinite-rich clays are widely available in many places, especially in intertropical regions. This is the basis for the so-called LC³ blended cement [64]. Co-substitution allows for much higher degrees of substitution than with either clay or limestone alone, down to clinker contents around 50%. The development of LC³-type mixes may well prove to be a decisive step toward sustainability [18].

3.3 Better Concrete with Less Cement

Concrete is primarily a cohesive–frictional granular pile. So far (Sects. 3.1 and 3.2), we discussed possible actions dealing with the cohesive and adhesive binding phase, but the structure of the granular pile itself is an important source of optimization. It controls the way the applied stress propagates and possibly concentrates, leading to failure. At first order, strength is controlled by the average packing density or solid volume fraction ρ , i.e., the fraction of total volume occupied by the solid particles. The porosity ϕ , i.e., the fraction of total volume occupied by voids, is just $1 - \rho$.

It has long been known that the minimum residual porosity of a fresh concrete formulation is scaling as a power law of the width of the particle size distribution ([15] and refs. therein):

$$\phi \propto (r_{\min} / r_{\max})^{\alpha} \quad (1)$$

In this relationship, r_{\min} and r_{\max} are the size of the smallest and largest particle populations, respectively. The exponent α is generally close to 0.2. Ultrahigh-performance concretes may have a very broad and continuous particle size distribution, especially toward the lower end of the size spectrum, and this confers to these materials a very high durability, in addition to their exceptional strength (Fig. 11) [66].

Going beyond simple scaling relations like Eq. 1 and optimizing the concrete granular formulation under given constraints for aggregates, sand, filler, fines, and colloidal additions properties and availability are not an easy task, and a number of quantitative proportioning methods have been proposed [67]. Cement itself is introducing a particular population of particles in the system. An interesting attempt to quantitatively assess the quality of the fit between the cement and the other particle populations is to calculate the so-called binder intensity index, *bi*, as proposed by Damineli et al. [68, 69]. This index measures the total amount of binder necessary to deliver one unit of a given performance indicator, e.g., 1 MPa of compressive strength. It reads.

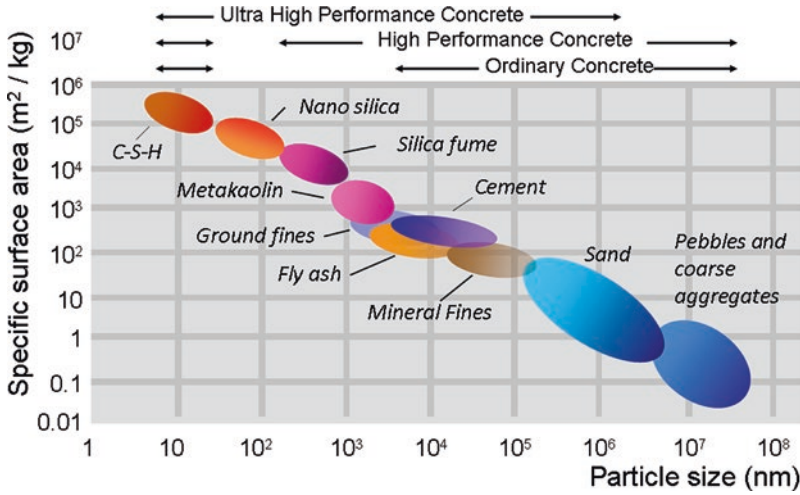


Fig. 11 A surface area vs. particle size plot for the different granular populations—aggregates, fillers, cement, and hydrates—used in modern concretes. C-S-H is the main product of reaction of Portland cement with water (Adapted from [15, 65])

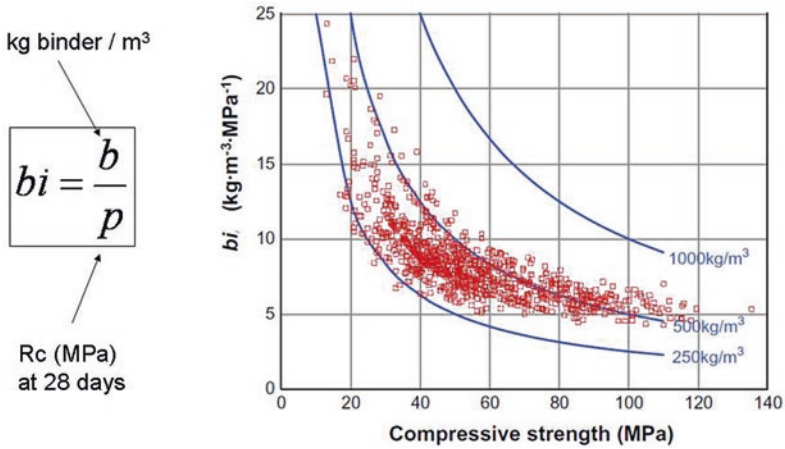


Fig. 12 Binder intensity index as a function of 28 days compressive strength for close to 1000 concretes of international origin (From [69])

$$bi = \frac{b}{p} \tag{2}$$

where b is the total consumption of binder ($\text{kg}\cdot\text{m}^{-3}$) and p is the performance requirement, e.g., compressive strength after curing. Figure 12 illustrates the distribution of bi_{cs} as a function of the compressive strength for close to 1000 different

concretes of international origin [69]. A first interesting observation relates to the scatter of the b_i values, which is very broad on the low-performance side of the data points cloud but becomes considerably narrower toward the high-performance end. This illustrates the fact that poor strength performances can be obtained in many different ways (i.e., with many different formulations), while high-performance concrete obeys more accurate formulation rules.

A second observation is that the average binder intensity index tends clearly to decrease with the increase in compressive strength, down to a plateau value of about $5 \text{ kg cement m}^{-3} \text{ MPa}^{-1}$. This shows that cement is best used in high-performance mixes, using superplasticizers and addition of fines, in order to have a quasi-continuous distribution of particle size (Fig. 11). However, in this type of concrete, the width and continuity of the particle size distribution are further improved by using a water/cement ratio well below the minimum required for complete hydration, which leaves a significant fraction of cement particles unhydrated. Thus, in this type of mix, cement is not only a source of hydrates. It behaves also as filler, and it occupies a slot in the particle size distribution which otherwise would be empty. This is an efficient strategy in terms of strength, but it is not the best choice in terms of environmental impact.

On the theoretical side, the conclusion of this section is rather straightforward. Good concrete with a reduced carbon footprint can be obtained with much lower cement content than in ordinary practice, provided its granular and colloidal formulation is optimized. On the practical side, things are not that simple, for several reasons. First, a significant part of the particle size distribution—cement, SCM, and fillers—is currently imposed by the cement producers. Second, the design of an optimal formulation for a given application, taking into account the available aggregates and additions, is a highly technical operation, the theoretical basis of which is still under development. Finally, a minimum of cement content well above what could be achieved with an optimized granular formulation may be imposed by regulations. A possible step in the right direction may be the widespread introduction of digital—possibly AI-based—formulation methods, concomitantly with the introduction with performance-based standards.

3.4 Use Locally Available Materials and Skills

As far as construction is concerned, our world is an extraordinarily diverse showroom of resourceful and frugal answers to local material and environmental constraints [70, 71]. This intrinsically vernacular character of traditional construction materials and techniques—to use with measure what is locally available and recyclable and invent locally optimized solutions—is contrasting with the evolution of the modern construction sector, privileging a limited choice of materials and constructive solutions. This out-of-context character of the present construction sector is reinforced by the often composition-based norms and standards system (Fig. 6) which in its time was a useful way to inject technical knowledge, reliability, and

safety in construction practice but which is also a confession of our inability to deal with contextual diversity and constitutes an exceedingly rigid straitjacket for innovation.

A topic on which construction would clearly benefit from adaptation to local conditions is that of SCM. There is no point to force the use of only one or a very limited number of clinker substitutes on the global scale. While fly ash and blast furnace slag may be good and widely available substitutes in some parts of the world, calcined clays, volcanic ashes, or vegetable ashes may be a better choice in other places. Sand itself would benefit from a better ability to use local resources. Too often—even in sand-rich regions like the Middle East and the Emirates—sand is still transported over long distances in order to comply with rigid formulation rules. Rather than doing this at a large environmental cost, a more rationally sound solution would be to learn how to use local resources.

To close this brief section, it is important to remember that the most widely and locally available eco-friendly construction material is raw (crude, unfired) “earth” or soil. In many respects, raw earth is nothing but a natural concrete, the fine (less than 2 μm) clay fraction playing the cohesive and adhesive role that cement hydrates play in normal concrete [72]. Raw earth has been used as a construction material for thousands of years on a worldwide scale, and it is still extensively in use today. It led to a remarkable variety of vernacular construction techniques including wattle and daub, cob, mud brick or compressed earth block masonry, and rammed earth. It is estimated that more than two billion people are currently living in earthen dwellings and that about 10% of the world heritage properties incorporate earthen structures [73].

Earth construction offers significant environmental advantages ([72] and refs. therein). The raw material is soil or, more exactly, subsoil (the use of the organic-rich topsoil horizon, if any, should be reserved for agriculture). It is infinitely recyclable. No energy-intensive manufacturing is needed. Processing is kept to a minimum. Earth buildings perform very well hygrothermally thanks to their relatively low thermal conductivity, large thermal mass and strong “breathability” (easy water/vapor phase change and transport). When taken together, these features lead to good comfort, remarkably small embodied energy, and light environmental impact.

Not surprisingly, with the increased awareness of environmental and energetic issues, earth construction is gaining renewed interest. Several attempts have been made to transfer to earthen construction the technologies used in cement concrete construction, like casting in place, prefabrication, or even 3D printing. One important objective is to design a mix suitable for making the earth pourable in a formwork while allowing for the removal of the formwork in a time much shorter than what simple air-drying would have permitted (Fig. 13). Based on the informed use of clay dispersants (fluidizers) and flocculants (stiffeners), impressive progress has been made in recent years [72, 74, 75].

Skills and traditions in earthen construction are particularly strong in the Middle East. It would be a pity for the Gulf Region countries not to be part of the strong science-based revival of earthen construction that is presently going on.



Fig. 13 Concrete technologies applied to construction with raw earth. Left: slab fabrication with ready-mixed pourable earth formulated with only ~10% water and clay dispersants (University of Mokpo, South Korea). Right: assembling pre-fabricated rammed earth elements during construction of the Ricola Herb Center, Switzerland (Jacques Herzog and Pierre de Meuron Architects; Engineering: Lehm Ton Erde GmbH)

3.5 *Smart Design: Topology Optimization, Architectural Geometry, and Origamics*

Nature is full of complex, often hierarchical structures which succeed in optimizing simultaneously mechanical, optical, hydrodynamic, etc. properties and economy of material use. They are a fountain of inspiration for architects and engineers [76–78]. Typical examples are the cellular structure of trabecular bone, the hierarchical structure of nacre, or the ribbed structure of some large leaves which has been an obvious source of inspiration for Pier Luigi Nervi for his amazingly thin floors and roofs which owe their stiffness to their ribbed structure (Fig. 14).

What nature achieved through natural evolution, engineers may try to accomplish through *topology optimization*, also called *generative design*. Topology optimization is a mathematical method that optimizes material layout within a given design space, for a given set of loads, boundary conditions, and constraints [80, 81]. The design can attain any shape within the design space. Optimizing a form regarding its own weight and force distribution leads generally to pseudo-organically grown structures (Fig. 14a, b).

Due to the free forms that naturally emerge from this, the result is often difficult to build or to manufacture. 3D printing may be a solution (see Sect. 3.7), but recent developments suggest that transformational progress may also come from theoretical research in *architectural geometry* [82, 83]. A key ingredient of architectural geometry is discrete differential geometry [84] which aims at transforming ideal free-form surfaces into buildable structures. This often means panelization, i.e., finding a collection of smaller flat or curved polyhedral elements that can be assembled to the desired free-form meshes with planar or curved faces and, desirably, with torsion-free nodes in the support structure. Steel-and-glass or wood-and-wood are the most frequently encountered combinations, but ultrahigh-performance-fiber-

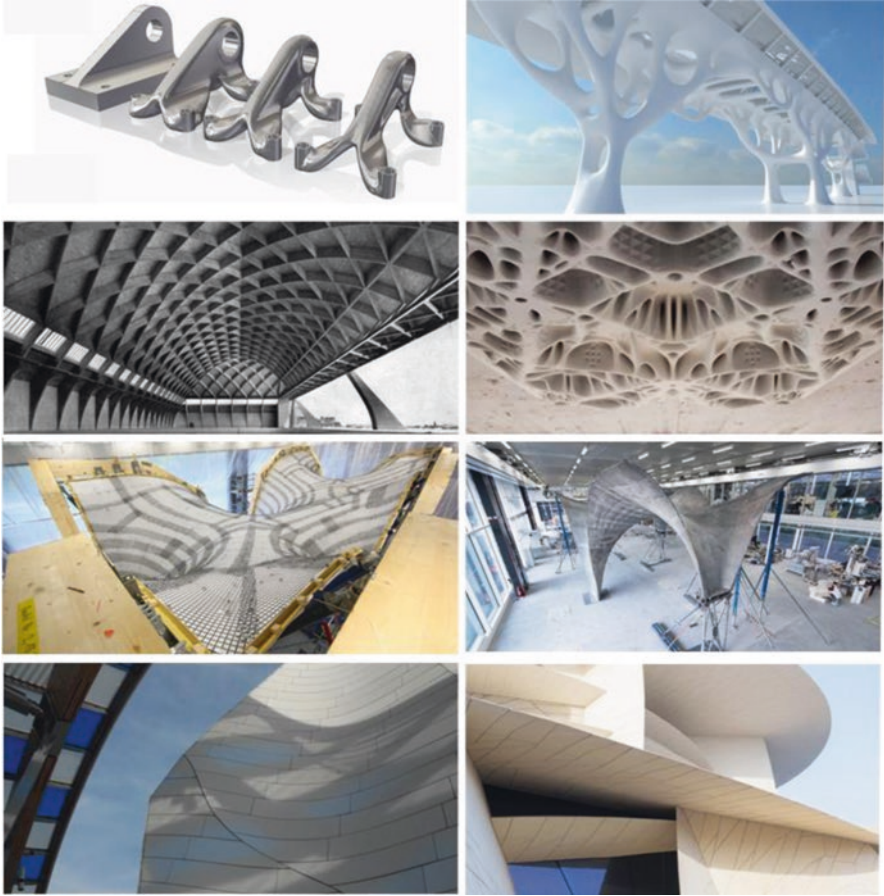


Fig. 14 From left to right and from top to bottom: (1) an example of topology optimization applied to a fastening element (GrabCAD model library, Frustum, Siemens); (2) an artist's view of a hypothetical optimized viaduct; (3) aircraft hangar, Orvieto, Italy, designed by architect-engineer Pier Luigi Nervi in 1935; the “ribs” stiffen the vault which would otherwise be much thicker; (4) a complex 3D-printed optimized slab (A. Jipa, M. Bernhard, M.A. Meibodi, B. Dillenburger, ETH Zurich); (5) the frame used to build the ultrathin double-curved concrete structure on the right. The frame is made off a net of steel cables and a polymer fabric stretched into a reusable scaffolding structure (Ph. Block's group, ETH Zurich) [79]; (6) The final self-standing ultrathin structure obtained by spraying concrete on the polymer fabric (Ph. Block's group, ETH Zurich); (7) a curved wall of curved ultrahigh-performance fiber-reinforced concrete (UHPFRC) panels, Louis Vuitton Foundation building in Paris (architect Frank Gehry); (8) the panelized UHPFRC petals of the National Museum of Qatar, Doha (architect Jean Nouvel)

reinforced concrete (UHPFRC) panels are also perfectly adapted to free-form architecture (Fig. 14).

On the other hand, *origamics*, the art of folding paper, has recently emerged as a method for creating deployable and reconfigurable structures [85, 86]. It is at the center of an intense exploration activity for (possible) applications as diverse as

solar arrays, deployable curtain walls for light control, self-foldable robots, or self-deployable stent grafts, just to name a few. It is a common experience that folding makes sheets more rigid. However, folded sheets are not yet structures [87]. They tend to be flexible, and because folding is reversible, they need to be locked into a fixed configuration in order to behave as a real structure. Therefore, conferring load-bearing characteristics to a deployable origami-patterned structure is tricky business.

Origami patterning is certainly an interesting method for conferring dynamic properties to building facades, but it is also an interesting approach for manufacturing formworks able to cast complex shapes, with potentially much less labor than with traditional formworks. It has been suggested that, together, topology optimization, architectural geometry, and origami patterning may well become, on equal foot with printing, privileged methods for building optimally designed structures in concrete, using reconfigurable formworks.

3.6 *Toward Rebar-Free Concrete*

Conventional reinforcement—especially passive reinforcement—has many advantages. It is an inexpensive and robust technology. It is easy to build on site, with minimum training. It provides tensile strength, ductility, and crack growth resistance. Whatever the future cement and concrete technologies, the need for reinforcement will probably not disappear soon.

Yet, conventional reinforcement has serious drawbacks, in particular in terms of workforce needs and productivity. While *robotic placement, bending, and welding* could be a solution, either on site or in the prefabrication plant [88, 89], other approaches taking advantage from digital technologies may be considered. For instance, digital methods may help in designing structures with minimal levels of tension or even *compression-only structures*, with much reduced reinforcement needs [90, 91].

Autonomous assembly of the reinforcement units is another, radically different approach [92]. The concept of autonomous assembly may be viewed as a generalization of the concept of self-organization or self-assembly which has been widely popularized as a key concept in our understanding of life and many other natural phenomena [93]. It is currently intensively explored in the context of fabrication, architecture or structural engineering under various names like “designer matter” [94], “aleatory architecture” [95], or “aggregate architecture” [96]. A common underlying idea is that, with properly designed building blocks, functionality may emerge from the interaction of a large number of building blocks during the assembly process which, in the simplest case, may be totally random.

Jammed assemblies of non-convex particles represent a particularly clear example of this type of system [97]. Ordinary non-cohesive and convex particles, like dry sand for instance, exhibit solid-like behavior only when they reach the jamming limit by confinement. Think of ground coffee packed under vacuum. The coffee grains are so densely packed by the atmospheric pressure on the pack envelope that



Fig. 15 Entangled assemblages of non-convex particles which could provide self-assembled reinforcement for concrete. Left: an aggregate of staples. Pick one; take them all. Right: a self-standing structure of Z-shaped particles (Kieran Murphy, Leah Roth, Heinrich Jaeger, Project Z-Form)

the bag cannot be deformed. Things are very different with non-convex particles able to entangle, like staples or paperclips for instance. Just throwing them randomly in an open vessel is enough to build an intricate cohesive assembly that can be easily removed from the vessel (Fig. 15). Jamming is reached by “geometric cohesion” or “self-confinement” [98].

On the experimental side, U-shaped, Z-shaped, and star-shaped particles have been shown to exhibit strong self-confinement. They make it possible to create free-standing walls and columns, or even overhangs and domes, by simply pouring the particles into a mold and removing the mold as soon as it is full [99]. By changing the number of segments, the segment length, and the angles between segments, the degree of entanglement may be fine-tuned. Robotic arms may even be used to grasp handfuls of particles and to build the structural element without the need of mold [100]. Here we suggest that random aggregates of non-convex particles provide also an interesting alternative to traditional passive reinforcement.

3.7 *Robotic Construction*

Digital technologies are already present in the construction sector via the widespread use of CAD (computer-aided design) software in the architectural phase. Contrasting with this, they are only scarcely present in the construction phase itself, which is still essentially based on human manpower. The construction sector is still far from the massive move toward robotic methods observed in the manufacturing industry. Yet, robots are fully present in architectural research [101], and an increasing number of laboratories, companies, or consortia are experimenting and developing robotic methods suitable for either prefabrication or on-site construction with concrete [102]. Formwork-free 3D printing by multilayer addition of extruded layers [103], often called contour crafting after the seminal work of B. Khoshnevis

[104], is the most widely explored method, but particle-bed printing [105], initiated by E. Dini [106], is an interesting alternative in prefabrication. In parallel, robotic manufacturing of the steel reinforcement is also explored [89].

Fast additive manufacturing with fresh concrete or mortar is still a challenge. It requires an accurate control of the fresh paste rheological behavior [107] and, most important, of its so-called structural buildup kinetics, that is, the rate of yield stress increase once an extruded layer has been laid down [108]. Structural buildup determines the rate at which layers can be piled on top of each other without buckling, while still allowing for good adhesion between layers.

Rapidity of construction is often put forward as the main advantage of robotic construction, but this is far from being obvious. When massive production of simple building or infrastructure elements is concerned, classical prefabrication techniques with formworks remain very competitive. The real benefit from using robotic printing technologies must be looked for elsewhere, not necessarily in the way (faster, cheaper, etc.) we build but more likely in *what* we build. Not many quantitative assessments have been made so far, but a key finding is that robotic construction produces high environmental benefits compared to conventional construction when complex structures are built [109]. As a matter of fact, with robotic 3D-printing technologies, additional complexity can be achieved without additional environmental costs, so the potential benefit of digital fabrication increases proportionally to the level of complexity of the structure. This is the perfect incentive for implementing the smart design methods summarized in Sect. 3.5 (topology optimization, architectural geometry, origamics), provided a real benefit is obtained in terms of environmental impact, productivity, and/or human well-being (Fig. 16).



Fig. 16 3D-printed UHPC curved wall (left) and free-form structure (right) (XTreeE and LafargeHolcim)

3.8 *Toward a Data-Based Circular Economy of Concrete*

Digital technologies are not only present in the architectural design phase of buildings and infrastructures. They are also increasingly used all along the life of a project via the so-called Building Information Modeling (BIM) process. BIM is generally understood as a variety of digital methods able to represent building elements in terms of their 3D geometric (structural) and nongeometric (functional) attributes and relationships [110, 111]. All the information is stored as a heterogeneous database. BIM allows for building behavior and aging simulation, project management, and operational collaboration between stakeholders (Fig. 17). It is aiming to enhance interorganizational collaboration, thereby enhancing productivity while improving design, construction, and maintenance practices [110, 111].

Concrete is ubiquitously present in buildings and infrastructures, but, so far, it is remaining astonishingly absent from BIM platforms, at least in explicit form. Yet, if the climate change mitigation objectives of the construction sector are to be met, an effective tool for optimizing the production and use of concrete according to environmental criteria is urgently needed. All the components of the cement and concrete value chain have to be taken into account [112], some of them addressed in this contribution, including raw materials availability and use, clinker production, SCM and aggregates availability and properties, concrete formulation, transporta-

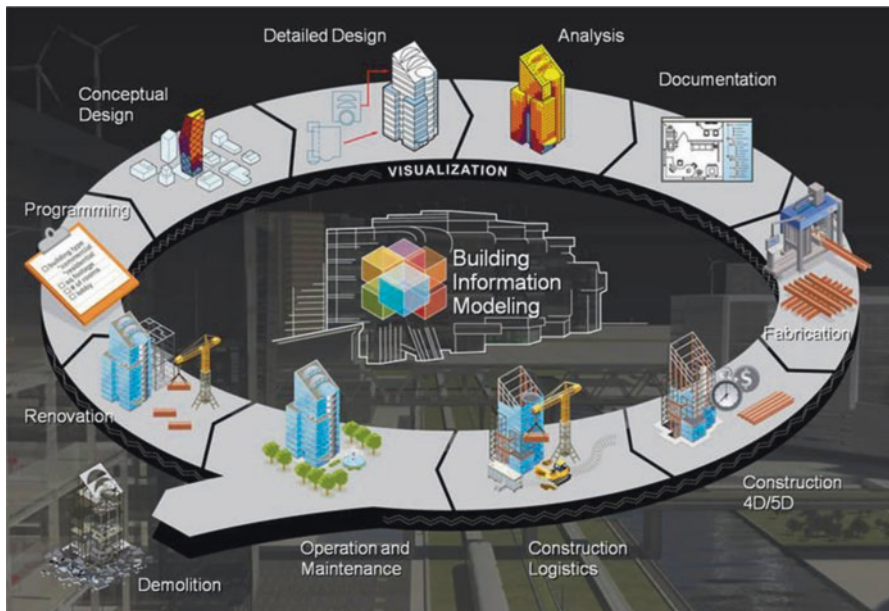


Fig. 17 Schematic representation of the various aspects of a building’s life cycle included in BIM methods (www.buildipedia.com)

tion, architectural design, construction method, recycling, etc. Considering the diversity of input information, the tool that we need can only be a digital and statistical BIM-like platform. Most probably, it will make extensive use of machine learning methods to link big data-type inputs to performance-based standards. Unfortunately, in spite of the millions of concrete mixes prepared and used every day all over the world, very few data are collected, and even less are shared. The final suggestion of this paper is that, with reference to Sect. 2 and Figs. 4, 5, and 6, the time has come for the concrete industry to make its own digital revolution.

Acknowledgements The author would like to thank Prof. Ali Bumajdad for his invitation and the Kuwait Foundation for the Advancement of Sciences for financial support.

References

1. Scrivener KL, John VM, Gartner EM (2016) Eco-efficient cements: potential, economically viable solutions for a low-CO₂, cement-based materials industry. *Cement Concrete Res* 114:2–26. United Nations Environment Program. www.unep.org
2. Ramage MH, Burrige H, Busse-Wicher M, Fereday G, Reynolds T, Shah DU, Wu G, Yu L, Fleming P, Densley-Tingley D, Allwood J, Dupree P, Linden PF, Scherman O (2017) The wood from the trees. The use of timber in construction. *Renew Sust Energy Rev* 68:333–359
3. World Steel Association (WSA). Steel statistical yearbooks 1978 to 2016. www.worldsteel.org/steel-by-topic/statistics/steel-statistical-yearbook-.html.
4. U.S. Geological Survey (USGS). Iron and steel statistics and information. https://minerals.usgs.gov/minerals/pubs/commodity/iron_&_steel/mcs-2018-feste.pdf
5. Geyer R, Jambeck JR, Law KL (2017) Production, use, and fate of all plastics ever made. *Sci Adv* 3:e1700782. Supplementary material, <http://advances.sciencemag.org/cgi/content/full/3/7/e1700782/DC1>
6. U.S. Geological Survey (USGS). Aluminium statistics and information. <https://minerals.usgs.gov/minerals/pubs/commodity/aluminum/mcs-2018-alumi.pdf>
7. U.S. Geological Survey (USGS). Cement statistics and information. <https://minerals.usgs.gov/minerals/pubs/commodity/cement/>
8. CEMBUREAU (2016) Activity report. <https://cembureau.eu/media/1635/activity-report-2016.pdf>
9. Idorn GM (1997) Concrete progress from antiquity to third millennium. Thomas Telford, London
10. IEA (2019) Material efficiency in clean energy transitions. International Energy Agency report, March 2019. <https://www.iea.org/publications/reports/MaterialEfficiencyinCleanEnergyTransitions/>
11. Ulm F-J (2012) Concrete innovation potential. *Beton Stahlbetonbau* 107:504–509
12. Aitcin P-C, Flatt R (eds) (2016) Science and technology of concrete admixtures. Woodhead Publishing, Amsterdam
13. Okamura H, Ozawa K (1995) Mix-design for self-compacting concrete. *Concrete Library JSCE* 25:107–120
14. Chateau X (2012) Particle packing and the rheology of concrete. In: Roussel N (ed) *Understanding the rheology of concrete*. Woodhead Publishing, Cambridge, pp 117–143
15. Van Damme H (2018) Concrete material science: past, present, and future innovations. *Cem Concr Res* 112:5–24
16. WBCSD (2016) Cement sustainability initiative, getting the numbers right, project emissions report 2014. <http://www.gnr-project.org/>

17. UN Environment KL, Scrivener VM, John EMG (2018) Eco-efficient cements: potential economically viable solutions for a low-CO₂ cement-based materials industry. *Cem Concr Res* 114:2–26
18. Miller SA, John VM, Pacca SA, Horvath A (2018) Carbon dioxide reduction potential in the global cement industry by 2050. *Cem Concr Res* 114:115–124
19. Torres A, Brandt J, Lear K, Liu J (2017) A looming tragedy of the sand commons. *Science* 357(6355):970–971
20. Andrew RM (2018) Global CO₂ emissions from cement production. *Earth Syst Sci Data* 10:195–217. <https://doi.org/10.5194/essd-10-195-2018>
21. UNEP Global Environmental Alert Service (GEAS) (2014) Sand, rarer than one thinks. www.unep.org/geas/
22. Barbosa F, Woetzel J, Mischke J, Riberinho MJ, Sridhar M, Parsons M, Bertram N, Brown S. Reinventing construction: a route to higher productivity. McKinsey report, Feb 2017. <https://www.mckinsey.com/~media/McKinsey/Industries/Capital>
23. Schwab K (2013) The fourth industrial revolution – what it means and how to respond. World Economic Forum
24. Rifkin J (2011) The third industrial revolution – how lateral power is transforming energy, the economy, and the world. Palgrave MacMillan, London
25. Agrawal A, Choudhary A (2016) Perspective: materials informatics and big data: realization of the “fourth paradigm” of science in materials science. *Materials* 4:053208
26. NSTC National Science and Technology Council (2014) Office of Science and Technology Policy report. Materials genome initiative – strategic plan. NSTC National Science and Technology Council, Washington, DC
27. Rajan K (2015) Materials informatics: the materials “gene” and big data. *Annu Rev Mater Res* 45:171–193
28. Takahashi K, Tanaka Y (2016) Materials informatics: a journey toward material design and synthesis. *Dalton Trans* 45:10497–10499
29. Ramprasad R, Batra R, Pilia G, Mannodi-Kanakthodi A, Kim C (2017) Machine learning in materials informatics: recent applications and prospects. *Comput Mater* 3:54. <https://doi.org/10.1038/s41524-017-0056-5>
30. Butler KT, Davies DW, Cartwright H, Isayev O, Walsh A (2018) Machine learning for molecular and materials science. *Nature* 559:547–555
31. Olson GB (1997) Computational design of hierarchically structured materials. *Science* 277:1237–1242
32. Kalidindi SR, De Graef M (2015) Materials data science: current status and future outlook. *Annu Rev Mater Res* 45:171–193
33. Powers TC (1958) Structure and physical properties of hardened portland cement paste. *J Am Ceram Soc* 41:1–6
34. Micoulaut M, Yue Y (2017) Material functionalities from molecular rigidity: Maxwell’s modern legacy. *MRS Bull* 42:18–22
35. Phillips JC (1979) Topology of covalent non-crystalline solids, I and II. *J Non-Cryst Solids* 34:153–181. 43, 37–77 (1981)
36. Thorpe MF (1983) Continuous deformations in random networks. *J Non-Cryst Solids* 57:355–370
37. Bauchy M, Abdolhosseini Qomi MJ, Bichara C, Ulm F-J, Pellenq RJ-M (2014) Nanoscale structure of cement: viewpoint of rigidity theory. *J Phys Chem C* 118:12485–12493
38. Abdolhosseini Qomi MJ, Krakowiak KJ, Bauchy M, Stewart KL, Shahsavari R, Jagannathan D, Brommer DB, Baronnet A, Buehler MJ, Yip S, Ulm F-J, Van Vliet KJ, Pellenq RJ-M (2014) Combinatorial molecular optimization of cement hydrates. *Nat Commun* 5:4960. <https://doi.org/10.1038/ncomms5960>
39. Bauchy M (2017) Nanoengineering of concrete via topological constraint theory. *MRS Bull* 42:50–54

40. Pignatelli I, Kumar A, Alizadeh R, Le Pape Y, Bauchy M, Sant G (2016) Does a dissolution-precipitation mechanism explain concrete creep in moist environment? *J Chem Phys* 145:054701
41. Bauchy M, Abdolhosseini Qomi MJ, Bichara C, Ulm F-J, Pellenq RJ-M (2015) Rigidity transition in materials: hardness is driven by weak atomic constraints. *Phys Rev Lett* 114:125502
42. Gonzalez-Teresa R, Dolado JS, Ayuela A, Gimel JC (2013) Nanoscale texture development of C-S-H gel: a computational model for nucleation and growth. *Appl Phys Lett* 103:234105. <https://doi.org/10.1063/1.4838396>
43. Ioannidou K, Pellenq RJ-M, Del Gado E (2014) Controlling local packing and growth in calcium-silicate-hydrate gels. *Soft Matter* 10:1121–1133
44. Ioannidou K, Krakowiak KJ, Bauchy M, Hoover CG, Masoero E, Yip S, Ulm F-J, Levitz P, Pellenq RJ-M, Del Gado E (2016) Mesoscale texture of cement hydrates. *Proc Natl Acad Sci U S A* 113:2029–2034
45. Ioannidou K, Kanduc M, Li L, Frenkel D, Dobnikar J, Del Gado E (2016) The crucial effect of early-age gelation on the mechanical properties of cement hydrates. *Nat Commun* 7:12106
46. Delhorme M, Labbez C, Turesson M, Lesniewska E, Woodward CE, Jönsson B (2016) Aggregation of calcium silicate hydrate nanoplatelets. *Langmuir* 32:2058–2066
47. Shvab I, Brochard L, Manzano H, Masoero E (2017) Precipitation mechanisms of mesoporous nanoparticle aggregates: off-lattice, coarse-grained, kinetic simulations. *Cryst Growth Des* 17:1316–1327
48. Andalibi MR, Kumar A, Srinivasan B, Bowen P, Scrivener K, Ludwig C, Testino A (2018) On the mesoscale mechanism of synthetic calcium-silicate-hydrate precipitation: a population balance modeling approach. *J Mater Chem A* 6:363–373
49. Richardson IG (2004) Tobermorite/jennite- and tobermorite/calcium hydroxide-based models for the structure of C-S-H: applicability to hardened pastes of tricalcium silicate, β -dicalcium silicate, Portland cement, and blends of Portland cement with blast-furnace slag, metakaolin, or silica fume. *Cem Concr Res* 34:1733–1777
50. Minet J, Abramson S, Bresson B, Sanchez C, Montouillout V, Lequeux N (2004) New layered calcium organosilicate hybrids with covalently linked organic functionalities. *Chem Mater* 16:3955–3962
51. Minet J, Abramson S, Bresson B, Van Damme H, Lequeux N (2006) Organic calcium silicate hybrids : a new approach to cement-based nanocomposites. *J Mater Chem* 16:1379–1386
52. Pellenq RJ-M, Lequeux N, Van Damme H (2008) Engineering the bonding scheme in C-S-H: the ionic-covalent framework. *Cem Concr Res* 38:159–174
53. Palkovic SD, Brommer DB, Kupwade-Patil K, Masic A, Buehler MJ, Büyükköztürk O (2016) Roadmap across the mesoscale for durable and sustainable cement paste – a bioinspired approach. *Constr Build Mater* 115:13–31
54. Birchall JD, Howard AJ, Kendall K (1981) Flexural strength and porosity of cements. *Nature* 289:388–390
55. Picker A, Nicoleau L, Burhard Z, Bill J, Zlotnikov I, Labez C, Nonat A, Cölfen H (2017) Mesocrystalline calcium silicate hydrate: a bioinspired route toward elastic concrete materials. *Sci Adv* 3:e1701216
56. Nicoleau L, Gädt T, Chitu L, Maier G, Paris O (2013) Oriented aggregation of calcium silicate hydrate platelets by the use of comb-like copolymers. *Soft Matter* 9:4864–4874
57. Rieger J, Kellermeier M, Nicoleau L (2014) Formation of nanoparticles and nanostructures – an industrial perspective on CaCO₃, cement, and polymers. *Angew Chem Int Ed* 53:12380–12396
58. Lothenbach B, Scrivener K, Hooton RD (2011) Supplementary cementitious materials. *Cem Concr Res* 41:1244–1256
59. Dent-Glasser LS, Duffly JA (1987) Analysis and prediction of acid-base reactions between oxides and oxysalts using the optical basicity concept. *J Chem Soc Dalton Trans* 1987:2323–2328

60. Gartner EM, Macphee DE (2011) A physico-chemical basis for novel cementitious binders. *Cem Concr Res* 41:736–749
61. Jiang S, Van Damme H (1998) Influence of fillers on textural and mechanical properties of C3S pastes. In: Colombat P, Grimmer A-R, Zanni H, Sozzani P (eds) Nuclear magnetic resonance spectroscopy of cement-based materials. Springer, Berlin, pp 379–386
62. Matschei T, Lothenbach B, Glasser FP (2007) The role of calcium carbonate in cement hydration. *Cem Concr Res* 37:551–558
63. Lothenbach B (2008) Influence of limestone on the hydration of Portland cements. *Cement Concrete Res* 38:848–860
64. Scivener K, Martirena F, Bishnoi S, Maity S (2018) Calcined clay limestone cements (LC³). *Cem Concr Res* 114:49–56
65. Sobolev K, Ferrada Gutiérrez M (2005) How nanotechnology can change the concrete world. *Am Ceram Soc Bull* 84:14–18
66. Vernet CP (2004) Ultra-durable concretes: structure at the micro- and nanoscale. *Mater Res Soc Bull* 29:324–327
67. de Larrard F, Concrete Mixture Proportioning: A scientific approach (1999) Modern Concrete Technology series, N°9. E & FN SPON, London
68. Damineli BL, Kemeid FM, Aguiar PS, John VM (2010) Measuring the eco-efficiency of cement use. *Cem Concr Comp* 32:555–562
69. Damineli BL, Pileggi RG, John VM (2013) Lower binder intensity eco-efficient concretes. In: Pacheco-Torgal F, Jalali S, Labrincha J, John VM (eds) Eco-efficient concrete. Woodhead Publishing in Materials, Cambridge, pp 26–44
70. Rudofsky B (1987) Architecture without architects – a short introduction to non-pedigreed architecture. University of New Mexico Press, Albuquerque
71. Olivier P (2003) Dwellings. Phaidon Press Ltd, London
72. Van Damme H, Houben H (2018) Earth concrete. Stabilization revisited. *Cem Concr Res* 114:90–102
73. Eloundou L, Joffroy T (2013) Earthen architecture in today’s World, in Proceedings of the UNESCO international colloquium on the conservation of world heritage earthen architecture. UNESCO Publishing, Paris. www.whc.unesco.org/en/series/36/
74. Moevius M, Jorand Y, Olagnon C, Maximilien S, Anger R, Fontaine L, Arnaud L (2016) Earthen construction: an increase of the mechanical strength by optimizing the dispersion of the binder phase. *Mater Struct* 49:1555–1568
75. Landrou G, Brumaud C, Winnefeld F, Flatt RJ, Habert G (2016) Lime as an anti-plasticizer for self-compacting clay concrete. *Materials* 9:330. <https://doi.org/10.3390/ma9050330>
76. Pawlin M (2011) Biomimicry in architecture. RIBA Publishing, London
77. Vincent J (2010) New materials and natural design. In: Allen R (ed) Bulletproof feathers. how science uses nature’s secrets to design cutting-edge technology. University of Chicago Press, Chicago, IL, pp 132–171
78. Cranford SW, Buehler MJ (2012) Biomaterialomics. Springer, New York, NY
79. Veenendaal D, Block P (2014) *Eng Struct* 75:39–50
80. Mirzendehtel AM, Suresh K (2017) A hands-on introduction to topology optimization. CreateSpace Independent Publishing Platform, Scotts Valley, CA
81. Zhu J, Gao T (2016) Topology optimization in engineering structure design. Elsevier, Amsterdam
82. Pottmann H, Asperl A, Hofer M, Kilian A (2007) Architectural geometry. Bentley Institute Press, Exton, PA
83. Pottmann H, Eigensatz M, Vaxman A, Wallner J (2015) Architectural geometry. *Comput Graph* 47:145–164
84. Bobenko AI, Suris YB (2009) Discrete differential geometry: integrable structure, graduate studies in mathematics. *Am Math Soc* 98:404
85. Stewart I (2007) Mathematics: some assembly needed. *Nature* 448:419

86. Reis PM, Lopez Jimenez F, Marthelot J (2015) Transforming architectures inspired by origami. *Proc Natl Acad Sci U S A* 112:12234–12235
87. Lebé A (2015) From folds to structures, a review. *Int J Space Struct* 30:55–74
88. Buchli J, Gifftalher M, Kumara N, Lussi M, Sandy T, Dörfler K, Hack N (2018) Digital in-situ fabrication – challenges and opportunities for robotic in situ fabrication in architecture, construction, and beyond. *Cem Concr Res* 112:66–75
89. Asprone D, Menna C, Bos FP, Salet TAM, Mata-Falcón J, Kaufmann W (2018) Rethinking reinforcement for digital fabrication with concrete. *Cem Concr Res* 112:111–121
90. Block P, Van Mele T, Rippmann M (2017) Compressive assemblies. *Archit Des* 248:104–109
91. Schwartz J (2018) Graphic statics and their potential for digital design and fabrication with concrete. *Cem Concr Res* 112:122–135
92. S. Tibbits, From automated to autonomous assembly S. Tibbits Autonomous assembly architectural design profile no. 248 Wiley Hoboken, NJ, 87(4), 7–15 (2017).
93. Whitesides GM, Grzybowski B (2002) Self-assembly at all scales. *Science* 295:2418–2421
94. Reis PM, Jaeger HM, van Hecke M (2015) Designer matter: a perspective. *Extreme Mech Lett* 5:25–29
95. Keller S, Jaeger HM (2016) Aleatory architectures. *Granular Matter* 18:paper 29
96. Dierichs K, Menges A (2012) Aggregate structures: material and machine computation of designed granular substances. *Archit Des* 82:74–81
97. Jaeger HM (2015) Toward jamming by design. *Soft Matter* 11:12–27
98. Franklin SV (2012) Geometric cohesion in granular materials. *Phys Today* 65(9):70
99. Murphy KA, Reiser N, Choksy D, Singer CE, Jaeger HM (2016) Freestanding loadbearing structures with Z-shaped particles. *Granular Matter* 18:paper 26
100. Zhao Y, Liu K, Zheng M, Barés J, Dierichs K, Menges A, Behringer RP (2016) Packings of 3D stars: stability and structure. *Granular Matter* 84:paper 24
101. Gramazio F, Kohler M (2008) Digital materiality in architecture. Lars Müller Publishers, Baden
102. Flatt RJ, Wangler T, Guest (eds) (2018) Special issue of *Cem Concr Res* 112
103. Buswell RA, Leal de Silva WR, Jones SZ, Dirrenberger J (2018) 3D printing using concrete extrusion: a roadmap for research. *Cem Concr Res* 112:37–49
104. Khoshnevis B, Hwang D, Yao K-T, Yeh Z (2006) Mega-scale fabrication by contour crafting. *Int J Industr Syst Eng* 1:301e320
105. Lowke D, Dini E, Perrot A, Weger D, Gehlen C, Dillenburger D (2018) Particle-bed 3D printing in concrete construction – possibilities and challenges. *Cem Concr Res* 112:50–65
106. Cesaretti G, Dini E, De Kestelier D, Colla V, Pambaguian L (2014) Building components for an outpost on the lunar soil by means of a novel 3D printing technology. *Acta Astronaut* 93:430–450
107. Roussel N (2018) Rheological requirements for printable concretes. *Cem Concr Res* 112:76–85
108. Reiter, Wangler T, Roussel N, Flatt RJ (2018) The role of early age structural build-up in digital fabrication with concrete. *Cem Concr Res* 112:86–95
109. Agusti-Juan I, Müller F, Hack N, Wangler T, Haber G (2017) Potential benefits of digital fabrication for complex structures: environmental assessment of a robotically fabricated concrete wall. *J Clean Prod* 154:330–340
110. Miettinen R, Paaola S (2014) Beyond the BIM utopia: approaches to the development and implementation of building information modelling. *Autom Constr* 43:84–91
111. Ghaffarianhoseini A, Tookey J, Ghaffarianhosini A, Naismith N, Azhar S, Efimova O, Raahemifar K (2017) Building information modelling (BIM) uptake: clear benefits, understanding its implementation, risks and challenges. *Renew Sust Energy Rev* 75:1046–1053
112. Favier A, Scrivener K, Habert G (2019) Decarbonizing the cement and construction sector: integration of the full value chain to reach net zero emissions in Europe. *IOP Conf Ser Earth Environ Sci* 225:012009

Sustainability of Carbon Fiber-Reinforced Polymers in Construction



Urs Meier

1 Trigger of Need of CFRP Research for Applications in Construction

The Kurt Schumacher Bridge crossing the river Rhine in Mannheim–Ludwigshafen was world’s first cable-stayed bridge with parallel steel wire bundles as stay cables. The design of stay cables is in general stiffness—and not strength driven. Therefore, the designer Professor Fritz Leonhardt cared for a high axial stiffness of the stays. In the past the stays were produced from spiral steel strands or locked-coil steel ropes, with an axial modulus of elasticity of only 160 GPa or even less. This is a reduction of 24% compared to the modulus of a straight steel wire. Since World War II, parallel wire bundles (PWB) made of steel have successfully been used for post-tensioning and prestressing of concrete structures. However, in such applications, opposite to stay cables, fatigue requirements are relatively low. Therefore, the HiAm (high amplitude) anchorage system that satisfies high fatigue requirements had been developed for stay cables [1, 2]. In such a system, the steel wires of the cable are spread out into the cone of a steel socket and are anchored by means of mechanically formed buttonheads at the end of the termination. The spaces between the wires in the anchorage cone are filled with a steel ball/epoxy compound that prevents fretting and the ingress of air or moisture, and it improves the fatigue resistance of the anchorage. The results of the Empa full-scale fatigue experiments were fully satisfactory [3, 4]. But after only 17 years in service, severe corrosion and many broken wires outside of the anchorage system had been detected at the stays of the Kurt Schumacher Bridge in Mannheim [5]. There was certain disillusionment, since during the construction in 1970, modern, innovative corrosion protection measures had very carefully been applied. This was for the Empa team that had

U. Meier (✉)

Empa, Swiss Federal Laboratories for Materials Science and Technology,

Dübendorf, Switzerland

e-mail: urs.meier@empa.ch

strongly been involved in this first application of parallel steel wire bundles, one reason to consider alternative materials. At the same time, visions had been developed for long-span lightweight bridges made of CFRP [6]. Therefore, it was decided to create parallel wire bundles made of pultruded CFRP wires. The production of such wires was at that time already state of the art. The key issue was the development of an anchorage system that would allow using the high strength of the extremely anisotropic CFRP wires. The difficulties were much greater than expected at the beginning.

2 CFRP Tendons

The outstanding mechanical properties of CFRP wires with strength of 3000 MPa or more are only valid in the longitudinal direction. The lateral properties including interlaminar shear are relatively poor being below 100 MPa. This makes it very difficult to anchor CFRP parallel wire bundles and obtain the full static and fatigue strength of the wires. Empa researchers have been developing CFRP cables using a conical resin-cast termination analogous to the HiAm system. The evaluation of the casting material to fill the space between the cone of the termination and the CFRP wires was finally the key to the problem. This casting material, also called load transfer media (LTM), has to satisfy multiple requirements: (1) the load should be transferred without reduction of the high long-term static and fatigue strength of the CFRP wires due to the connection and (2) galvanic corrosion between the CFRP wires and the steel cone of the termination must be avoided. It would harm the steel cone. Therefore, the LTM must be an electrical insulator. The conical shape inside the socket provides the necessary radial pressure to increase the interlaminar shear strength of the CFRP wires. The concept is demonstrated in Fig. 1a, b using for this example a one-wire system. If the LTM over the whole length of the sockets is a material with high elastic modulus, this will avoid creep, but there will be a high shear stress concentration at the load side of the termination on the surface of the CFRP wire (Fig. 1a). This shear peak causes delamination and pullout or tensile failure far below the strength of the CFRP wire. One could avoid this shear peak by the use of a soft low-modulus material. However, this would cause creep and an early stress rupture.

The best design is shown in Fig. 1b. The LTM is a gradient material. At the load side of the termination, the modulus of elasticity is low and continuously increases until reaching a maximum at the end of the termination.

The LTM is composed of aluminum oxide ceramic (Al_2O_3) granules with a typical diameter of 2 mm. All granules have the same size. To get a low modulus of the LTM, the granules are coated with a thick layer of epoxy resin and cured before application (Fig. 2, left, top). Hence, shrinkage can be avoided later in the socket. To obtain a medium modulus, the granules are coated with a thin layer. To reach a high

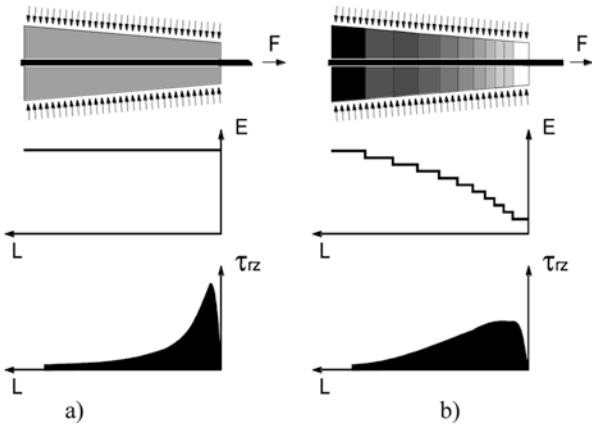


Fig. 1 (a, b) Stress buildup in LTM

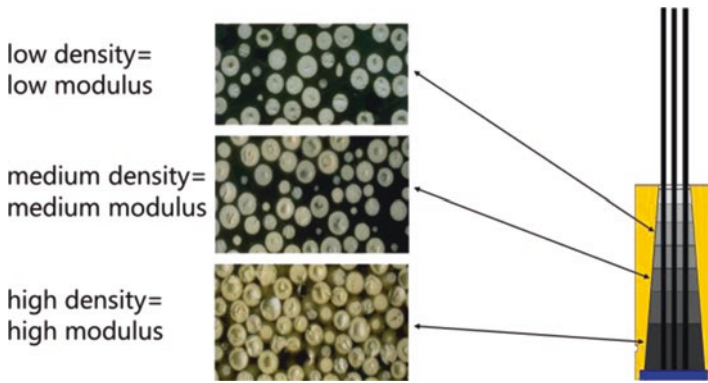


Fig. 2 Gradient anchorage system for CFRP wires

modulus, the granules are filled into the socket without any coating (Fig. 2 left, bottom). With this method the modulus of the LTM can be designed tailor-made. The holes between the granules are after all filled by vacuum-assisted resin transfer molding with epoxy resin [7]. The development of this gradient anchorage started in the early 1980s. At the beginning there were many flops and failures. The sponsoring research agencies and supporting industries started to doubt on the feasibility.

3 CFRP Strips for Strengthening

3.1 *Opposition Against the Brittle Material CFRP*

On one side were the described difficulties with the anchorage system for the CFRP wires. On the other side was also something like an “ideological problem.” In the 1950s advanced civil engineering research started to promote “plastic-design” in steel-reinforced concrete and in steel structures [8]. Until the 1980s this “philosophy” of plastic design gained worldwide very high acceptance [9]. Therefore, many civil engineering professors rejected the idea to use the brittle, linear elastic CFRPs that show not any ductility. Having brittle materials in mind, they thought on glass and did not realize that CFRPs are a composite material with very little scatter in strength. Opposite to them, Professor Bruno Thürlimann, one of the pioneers of the plastic design theory, persuaded the responsible Swiss Commission for Technology and Innovation (CTI) to give the modern material CFRP a chance in construction and to continue to finance the CFRP project for parallel wire bundles nevertheless. After the Empa researchers promised the industry to run in parallel a research and development project about strengthening of steel-reinforced concrete structures with thin CFRP laminates, the industry also continued the support.

Since the early 1970s, flexural and shear strengthening of steel-reinforced concrete structures with externally bonded steel plates are well established. This technique shows in a noncorrosive environment very good long-term behavior [10]. However, for outdoor applications, it has limited use, because of corrosion of the steel plates and technical problems in installing them over long spans. In 1987, after 5 years of research and development work, it was possible to prove in the laboratory that strengthening of concrete structures with CFRP laminates is feasible [11, 12]. It took another 6 years until the world’s first application of CFRP in construction happened.

3.2 *Ibach Bridge Near Lucerne: World’s First Application of CFRP in Construction*

The strengthening technique using CFRP laminates (Fig. 3) was applied for the first time outside of the laboratory in July 1991, for the repair of the Ibach Bridge that crosses the Emme River, the Reuss River, and Highway E35 (Amsterdam to Rome) near the city of Lucerne [12]. This bridge was completed in 1969. It is designed as a continuous, multispan box beam with a total length of 228 m. The damaged span of the bridge (Fig. 4) has a length of 39 m. The box section is 16 m wide, with a central, longitudinal web. Core borings were performed to mount new traffic signals. In the process, a steel posttensioning tendon in the outer web was accidentally damaged, with several of its wires completely severed by means of an oxygen lance.



Fig. 3 CFRP laminates are going to be prepared for the application on the soffit of the Ibach Bridge



Fig. 4 Loading test on Ibach Bridge after strengthening with CFRP laminates

As a result, the granting of authorizations for special, heavy convoys across the bridge was suspended until after completion of the repair work.

Since the damaged span crosses Highway E35, the traffic lanes in the direction of Lucerne on this highway had to be closed during the repair work, which could therefore only be conducted at night. All the work could be carried out from a mobile platform, thus eliminating the need for expensive scaffolding. The experts participating in the repair of the Ibach Bridge were pleasantly surprised about the simplicity of applying the 2-mm-thick and 150-mm-wide CFRP laminates. Considering that 175 kg of steel plates that had to be brought to a difficult-to-reach

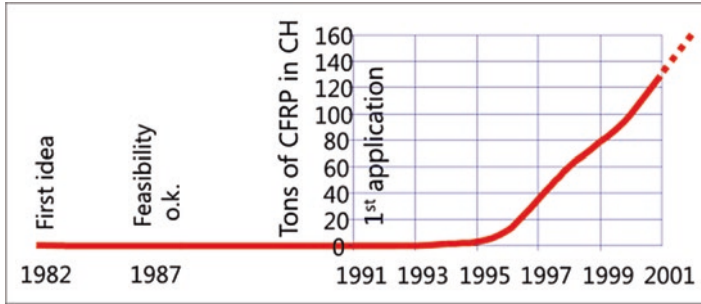


Fig. 5 First part of chronological development of CFRP strengthening; tons of CFRP laminates applied in Switzerland until 2001

construction site could be replaced by a mere 6.2 kg of CFRP, the concept and the price of CFRP were no longer so prohibitive. Furthermore, it must be kept in mind that in the strengthening application considered, material cost is only about 20% of the total compared to 80% for the labor cost. The very easy handling strongly reduces the labor cost. This was the key for the afterward upcoming worldwide commercial breakthrough for this kind of application of CFRP in civil engineering.

This application has been monitored, and the bond between the CFRP laminates and the concrete soffit of the bridge is after 28 years still perfect. The CFRP laminates look after brushing off the dirt like new. Meanwhile, strengthening with CFRP laminates is worldwide state of the art. Hundreds of thousands of structures have been strengthened since 1991 with this technique. Figure 5 shows the chronological development of CFRP strengthening in the first phase. From the first idea to the proof of feasibility, it took 5 years. Afterward, the promoters of the technique had to wait another 4 years until the first application happened. Then they had to be patient again during 4 years until commercial takeoff took place, first in Switzerland, then in North America, and finally worldwide.

4 Proof of Reliability

4.1 Cable-Stayed Stork Bridge in Winterthur

The success of the CFRP strengthening technique helped to slim down critical comments on the brittle CFRP. But apart from the price, the lack of extensive empirical data on CFRP parallel wire bundles continued to inhibit their acceptance. Even if sponsors were to be found to finance the use of CFRP as an alternative to steel cables, no authority wanted to run the risk of approving large-scale use of a relatively untried anchorage system. This problem was only to be solved by the incorporation of individual CFRP cable components in existing or new bridges and the long-term monitoring of their performance in practice. Given that the linear thermal



Fig. 6 Stork Bridge, Winterthur, with two CFRP stay cables installed in 1996. Load-carrying capacity of each cable: 12 MN

expansion coefficient of CFRP in longitudinal direction is zero, the parallel use of steel and CFRP cable is only possible in certain situations. The first suitable opportunity to test the material arose in 1996 in connection with the Stork Bridge (Fig. 6), a 124-m-span, two-lane road bridge across 14 tracks at Winterthur railway station. Here, for the first time ever, two CFRP stay cables (Fig. 7), each with a load capacity of 12 MN, were installed [13]. As the longitudinal main girders of this cable-stayed bridge are due to little depth very flexible, the varying thermal expansion coefficients of the cable materials did not pose insuperable problems. Both the CFRP cables and the adjacent steel cables are being continually monitored by Empa staff. So far results have met up with the high expectations and will become increasingly important in building confidence in years to come.

4.2 Continuous Two-Span Road Bridge Verdasio

The refurbishment of the Verdasio Bridge (Figs. 8 and 9) represented the first attempt to make practical use of the results of extensive Empa experiments performed in the mid-1990s on continuous two-span girders prestressed with CFRP cables [14].

Smooth wires were, however, used in place of the CFRP strands described in the relevant publication [14], with an anchorage system similar to that of the Stork Bridge [7, 13]. Four cables each comprising nineteen 5-mm-diameter CFRP wires

Fig. 7 Cross-section of CFRP parallel wire bundle with 241 wires of 5 mm diameter used as stay cable at Stork Bridge

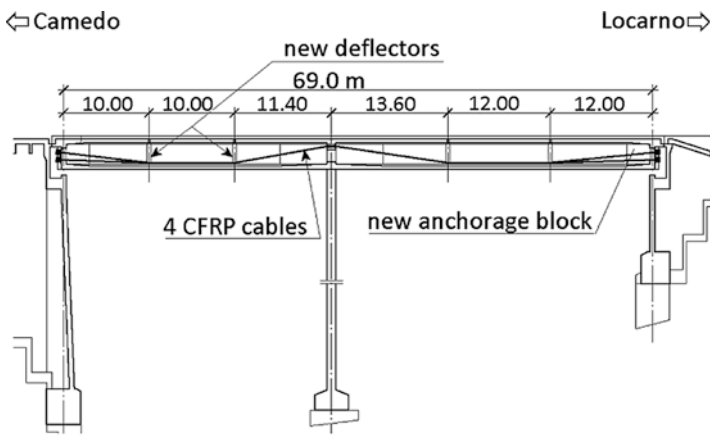
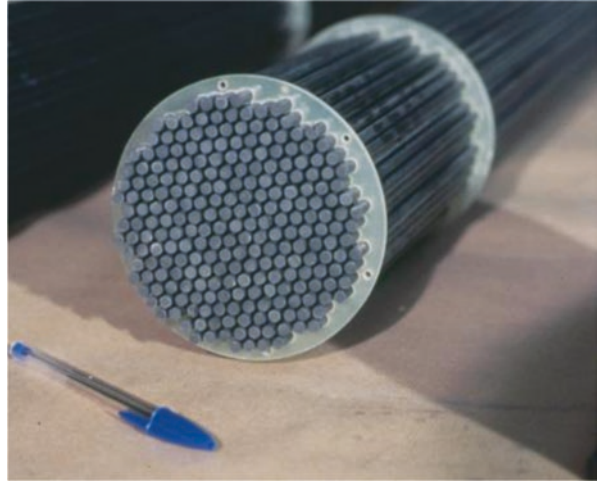


Fig. 8 Longitudinal section

were used for external posttensioning inside of the box girder to replace corroded steel cross-sections. The main problem in this application was to carry the cable around relatively tight-bending radii of 4.5 m, as CFRP wires are sensitive to transverse stresses due to their composition. However, the series of experiments with two-span girders described in [14] with 3.0 m radii at the center support suggested that a satisfactory solution was found to this problem in Verdasio. The results of the long-term monitoring over a period of 20 years are very satisfying. There is, except for the first year, no creep in the anchorage and also with the very high sustained stress of 1800 MPa no stress relaxation [15].

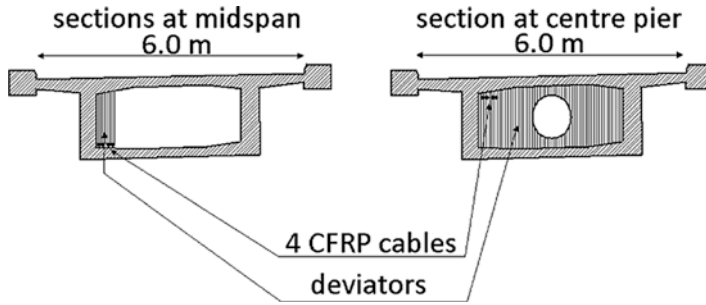


Fig. 9 Cross-sections



Fig. 10 Kleine Emme Bridge

4.3 Pedestrian Bridge Kleine Emme Near Lucerne

A further bridge project in Switzerland using CFRP parallel wire bundles followed in quick succession in late autumn 1998. Here too, the aim was to gather experience from practical CFRP cable applications over a longer period of time in order to promote confidence in the material. Two CFRP cables produced by a BBR/Empa team were used as bottom chord for the bridge over the Kleine Emme River (Fig. 10) described in detail in [15].

This project saw the first ever use of CFRP wires with integrated optical fiber sensors for this kind of application. Two parallel wire cables, each comprising 91 5-mm-thick CFRP wires, were then produced at Empa, wound onto 2.5-m-diameter reels and transported to Emmen. Since October 1998, these cables have tensioned the bottom chord of the new bridge over the Kleine Emme River near Emmenbrücke. The 47-m-span pedestrian bridge over the Kleine Emme is significant for the future development of CFRP cable in two respects: firstly in view of the innovative use of sensors and secondly due to the sustained high stress of 1350 MPa on the cables. So far the monitoring results have met up with the high expectations [15].

4.4 Posttensioned Dintelhaven Highway Bridge in Rotterdam

In 2001 two highway bridges over the River Dintelhaven in the harbor area of Rotterdam were opened to traffic. Both are concrete box girder bridges. The main span of the bridge with CFRP parallel wire tendons is about 185 m [16]. Four external tendons each with 91 CFRP wires of 5 mm diameter have been applied beside to conventional steel tendons (Fig. 11).

The tendons have been anchored similar to the cables of Stork, Verdasio, and Kleine Emme Bridge according to [7]. The project is the result of an initiative that was started in 1994 by the Civil Engineering Division of the Dutch Ministry of Transport and Public Works and the CUR (Dutch Centre for Civil Engineering Research and Codes). In order to guide the activities, with regard to the application of the CFRP tendons in the Dintelhaven Bridge, experiments were carried out at TNO Building and Construction Research, focusing upon the long- and short-term behavior of the CFRP wires and tendons [17]. In this paper, the results of these tests are presented. Moreover, in the paper, attention is paid to the manufacturing of the tendons, as well as the installation of the tendons in the bridge.

5 Update 2019 for Visions of the 1970s and 1980s.

5.1 The Arctic City

The Institute for Lightweight Structures (IL) at the University of Stuttgart published under the leadership of Frei Otto and in cooperation with Kenzo Tange and Urtec, Tokyo and Ove Arup and Partners, London, in 1971 the project study “City in the Arctic” [18]. The research was sponsored by the Farbwerke Hoechst, at that time one of the biggest companies of Germany’s chemical industry.

The city was planned to lie under a dome of a transparent inflated skin that covers without support an area of 3 km² and offers a moderate climate (Fig. 12). Further information is given in Table 1. Calculations for the supporting structure, which spans a record distance, were made by the engineering firm of Ove Arup and Partners in London [18].

There was a load-carrying polyester cable net planned to pull the transparent polymer membrane down with square meshes of 10 m side length. The cables with

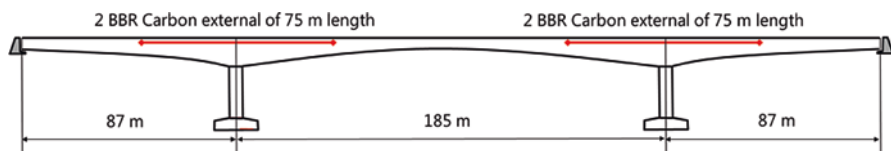
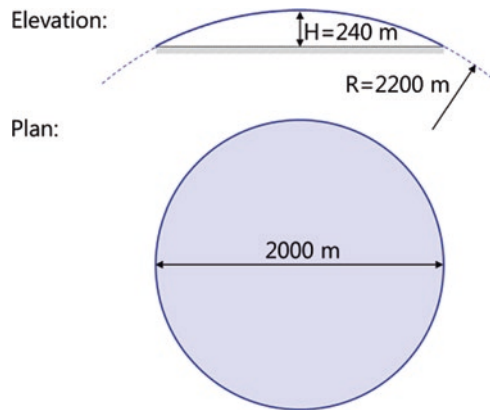


Fig. 11 Longitudinal section of Dintelhaven Bridge with CFRP posttensioning cables of 1420 MPa sustained stress

Fig. 12 Dome of Artic City**Table 1** Technical data dome of Artic City

Property	Unit	Year 1971	Year 2019
Tendon material		PES	CFRP
Working load	[kN]	2700	2700
Ultimate load	[kN]	35800	4500
Partial safety factor γ	[-]	13	1.67
Tendon diameter	[mm]	270	44
Mass per unit length	[kg/m ^l]	40	2.3

a diameter of 270 mm were designed as polyester fiber (PES) bundles (Trevira impregnated with PVC). The cables had to be such thick to reduce the stresses and avoid creep of the polyester fibers due to sustained loading. The mass-per-unit length of such a cable would have been 40 kg/m. After the good experiences with CFRP cables as seen in previous sections, the proposal of 1971 was redesigned with CFRP cables. The results for the year 2019 are given in Table 1. These numbers demonstrate that the advancement of materials technology within more than four decades is impressive. There is a reduction of mass for the cable net of 94%. Beside that there is a much higher, nearly “unlimited,” longevity for CFRP tendons than for PES tendons. The CFRP tendons face no corrosion, no stress corrosion, no stress relaxation, respectively, creep, and have outstanding fatigue properties. The total length of all CFRP cables needed for the square meshes of 10 m side length amounts to 650 km. This results in a total mass of 1500 metric tons. Assuming a price of 40 US\$ per kg CFRP cable, the total cable cost would result in 60 Mio. US\$. The project of the “Arctic City” is, from a technical point of view, not far from realization, if needed. However, it may be that such a super dome will be first somewhere in a desert and not in the Arctic. Frei Otto suggested that already in the project study “Shadow in the Desert” in 1972 [19], and Dubai has in 2014 announced plans to build the first climate-controlled city on the planet covering 4.5 km². Heat and humidity regulation by an evaporation mechanism is a possibility for reducing air temperature and increasing humidity within the air-supported dome. The principle

is as follows: The warm external air enters through a nozzle into a depressurizing chamber where pressure decrease is induced by a fan. Inside the chamber, water is injected into the air mass at a regulated rate. Then the cooled and moistened air passes into the air-supported dome. Solar radiant energy present in the dome will be absorbed while simultaneously warming the air and adjusting the humidity to the desired amount. This idea is schematized in Fig. 13. In a future project, there are also additional advanced means available to control the climate inside of such a pneumatic structure. Fifty percentage of the surface of the dome could be covered with flexible, ultrathin, lightweight solar panels to produce electric energy for the air-conditioning system and the other half with flexible, lightweight electrochromic foils between ETFE foils for transmission control of solar radiation (Fig. 14).

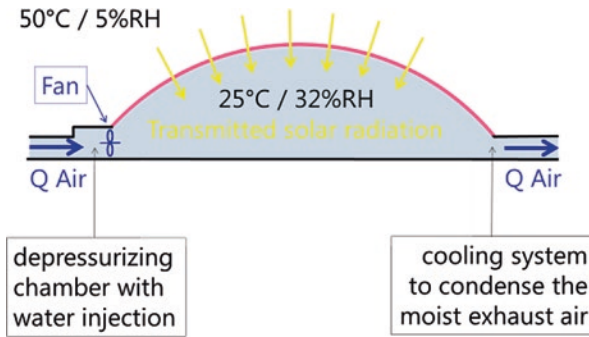


Fig. 13 By [19] proposed concept for climate control

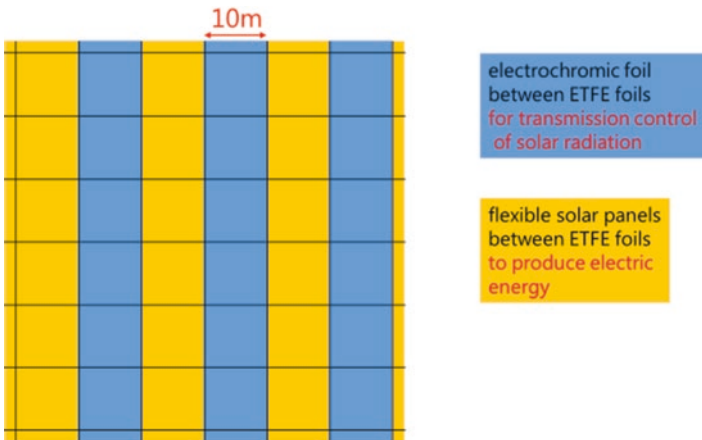


Fig. 14 Fifty percentage of the surface of the dome could be covered with solar panels to produce electric energy and the other half with electrochromic foils between ETFE foils for transmission control of solar radiation

5.2 CFRP Bridges Across the Strait of Gibraltar

In 1980 Spain and Morocco signed a scientific and technical cooperation agreement for the joint study of the feasibility of a fixed link across the Strait of Gibraltar. In the following years, many proposals for suspended bridges and tunnels have been presented. Based on the insight that with the use of lightweight CFRP cables, the limiting span of a suspended bridge could be a multiple of that of steel, the paper “Proposal for a Carbon Fibre-Reinforced Composite Bridge Across the Strait of Gibraltar at Its Narrowest Site” was published in 1987 [6]. A main span of 8400 m is for such a bridge needed. From the static point of view, this seems today feasible, however, absolutely not yet from the dynamic side. The needed active mitigation systems for damping of oscillations, e.g., due to wind loads are by far not yet ready for use [20]. Assuming an allowable stress of 1800 MPa is guaranteed for CFRP cables, 22000 metric tons would be needed. With a price of 40\$ per kg CFRP cable, the total cable cost would result in 880 Mio. \$. Lin [21] proposed in 1991 the bridge sketched in Fig. 15 crossing the Strait of Gibraltar also at the narrowest site, however, with two main spans and with steel cables. In this case according to [6, 22], the use of CFRP for the cables would be less expensive than that of steel cables. The “breakeven span” that means the span where the application of CFRP is more economic than that of steel amounts to about 4.1 km.

5.3 Submersible Tunnel Across the Strait of Gibraltar

Kaempfen [23] proposed in 1989 a submerged tunnel with a tube of circular cross-section as a fixed link across the Strait of Gibraltar. This cross-section is a sandwich construction with skins of glass fiber-reinforced polymers (GFRP) and a concrete core (Figs. 16 and 17). The tube would consist of 348 cylindrical double-wall tube sections made entirely of glass fiber-reinforced polyester resin designed to be mechanically connected by a pair of composite mechanical coupling structures. The tube was designed to handle the combined concentrated load of two freight trains each having a length of 450 m and a combined mass of 1100 metric tons. The cou-

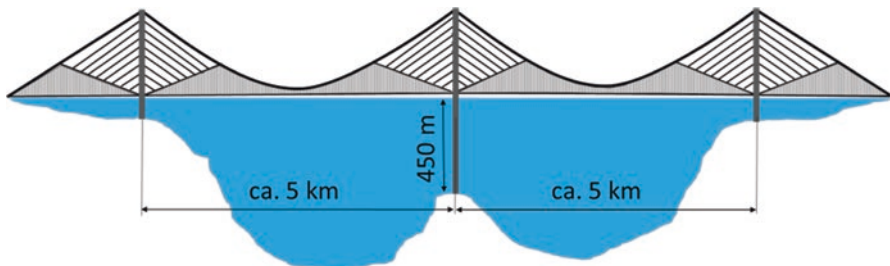


Fig. 15 Suspension bridge across the Strait of Gibraltar, 1991, proposed by Lin [21]

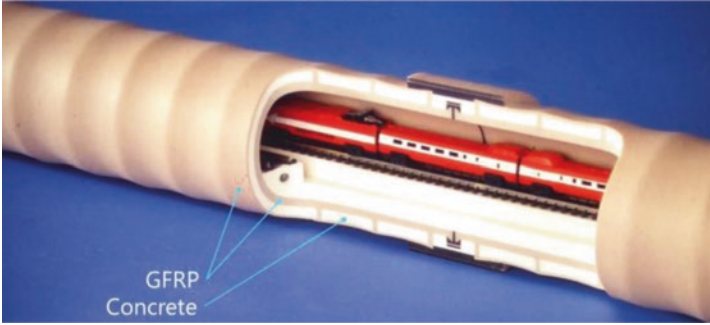
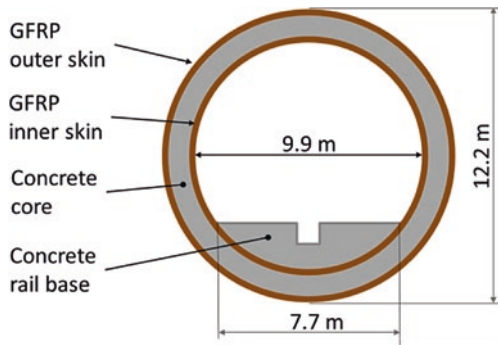


Fig. 16 Model of proposed submerged tunnel

Fig. 17 Cross-section of tunnel tube



pler assembly used to connect the outer wall structure is described in all details in [23]. The sections would be fabricated on shore in a 180-m-long factory adjacent to the seashore and connected to a floating tube string that would be anchored and then filled with enough seawater to provide the negative buoyancy to allow it to slowly sink into place. After the tube has been properly positioned on the sea floor, it would be permanently anchored by CFRP cables attached to the ribs (Fig. 16) comprising each tube section. It was expected that the total cost to complete the submerged tunnel railroad link between Europe and Africa would not exceed \$1 billion [24] and that it would require no more than 4 years to make.

In the 1989 proposition of Kaempfen, it was foreseen to produce segments of 73 m and to connect them. Such connections are difficult, prone to failure, and expensive. An alternative would be a submerged floating tunnel (SFT) across the Strait of Gibraltar at its narrowest site (14 km) beneath its water surface without any joints. Therefore, a continuous tunnel tube should be produced. A combination of continuous filament winding and application of shotcrete and fiber spaying would allow the production of a 14 km tube in one piece. Such a machine can be described as follows: at the start there is a 40-m-long circular horizontal steel tube with 12 m diameter as mandrel. It is at the beginning clamped as cantilever beam. The outside of this circular mandrel is fully covered with an endless helical wound-moving steel

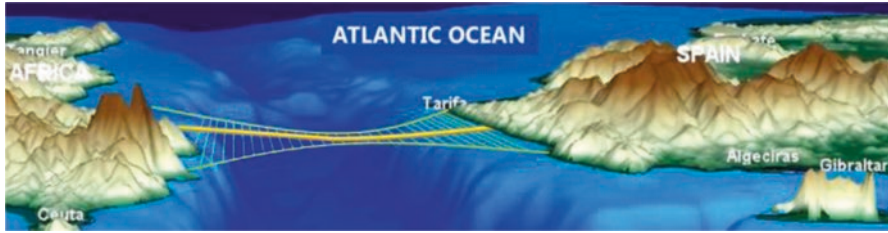
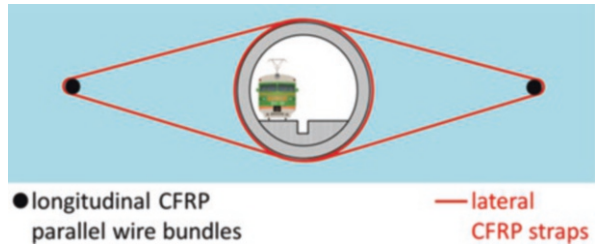


Fig. 18 Gibraltar strait crossing: vision submerged floating tunnel at narrowest site stabilized with CFRP cables

Fig. 19 Cross-section of floating tube stabilized with CFRP cables and straps



tape. It is endless because at the end of the mandrel, it returns inside the mandrel back to the start. Therefore, the surface of the mandrel is rotating and at the same time longitudinally moving forward. Along the mandrel are stations delivering glass fiber rovings impregnated with polyester resin that are going to be wound on this rotating and forward-moving surface in different angles. Inside the mandrel is another cantilever tube that can be rotated and also moved in longitudinal direction. It is equipped with two nozzles, one for shotcrete and one for glass fiber and polyester spraying. As soon as the outer skin is cured leaving the mandrel, the shotcrete nozzle will produce the core, and finally the inner wall will be sprayed with GFRP. This composite tunnel tube would be fabricated on one shore and continuously be pulled across the strait. The tethered type of submerged floating tunnel is due to the large depth of 900 m and the submarine traffic between the Atlantic Ocean and the Mediterranean Sea not feasible. A horizontal plane of CFRP cables, like suspension bridge where the two vertical cable planes have been unfolded into a horizontal plane, will be needed. It is sketched in Figs. 18 and 19. It must stabilize the floating tunnel tube against the flow of the Atlantic water pouring into the Mediterranean Sea and against the flow of the tide.

6 About the Sustainability of CFRP

What is the environmental impact of carbon fibers and therefore CFRP? Steel people often compare that the average CO₂ intensity for steel is 2 tons of CO₂ per 1 ton of steel and 20 tons of CO₂ for 1 ton of carbon fibers. This comparison based on



Fig. 20 Bowstring arch bridge fully supported by filigree but very powerful CFRP tendons

mass is not correct; it must be based on volumes. Then the relationship is 16 tons of CO_2 for 1 m^3 of steel and 30 tons of CO_2 for 1 m^3 of carbon fibers. This is still in favor of steel, but we have also to consider that carbon fibers do not corrode, degrade, rust, or fatigue. That means they have a much longer life cycle, e.g., as tendons on a suspended bridge, so they potentially only have to be produced once where steel tendons would have to be replaced multiple times. That makes its full life cycle impact look a lot better.

Already more than 10 years ago Empa researchers demonstrated with the project “Environmental-Friendly Footbridge Made of CFRP, GFRP, and Timber” that it is possible to make already today use of CFRP in an environmentally sustainable way [25]. It is a bowstring arch bridge where the outward-directed horizontal forces of the arch are borne as tensile forces by the CFRP bottom chord (string). The arched bridge deck was made out of glulam in lateral direction pretensioned with 30-mm-wide and only 0.12-mm-thick thermoplastic CFRP tapes. The bowstring arch bridge concept was realized with six longitudinal arranged CFRP strings and the above described glulam plate for the finally arch-shaped bridge slab (Fig. 20). The strings are composed of nonlaminated pin-loaded thermoplastic CFRP strap elements. The stiffness EA of each bowstring is 18 MN. It was the first time that such tendons were applied in a bridge construction. It is interesting to compare the volume fractions of the materials used for the whole bowstring arch bridge. The volume fraction of the glulam arched deck amounts to 93.8%, that of GFRP for the posts and struts to 5.9% and that of all CFRP tendons to only 0.3%. By the increase of timber consumption, the global CO_2 balance is favorable in two ways: (1) the use of timber in construction constitutes long-term storage of CO_2 ; (2) the use of timber in construction avoids the direct CO_2 emission due to production of steel or concrete. With a volume fraction of 94% of wood is this type of bridge therefore from an environmental point of view very sustainable. The sentence “Never before has a strengthening method done so much with so little” coined by the writer during a lecture tour through the

Unites States in 1997 for the promotion of CFRP rehabilitation systems can in this case also be transferred to new construction. This example shows clearly that with little, but powerful, CFRP, a lot can be moved.

Vision for the future: raw materials for carbon fibers are polymers. Such polymers can nowadays be produced from captured CO₂ [26] instead of refined oil. When the energy-intensive carbonizing process of the polymer fibers is driven by renewable energy sources, it is even enabling a negative CO₂ emission technology. Latest research shows that it may be possible to produce carbon fibers directly from captured CO₂ without the indirect route via polymer fibers [27].

7 What Is Next?

Since most civil engineers got within the last decades confident with CFRP for rehabilitation, it is time now to go also ahead in new construction. Next will be a network arch bridge with all hangers made from CFRP. The use of welded steel sections for hangers of network arches combined with hanger layouts, which were tuned for minimum fatigue stress range and for avoidance of hangers getting slack, leads to technical challenges that could not always be solved entirely satisfactory in the near past [28].

Based on extensive full-scale fatigue experiments and the practical experiences described in the previous section “Proof of Reliability,” Empa researchers wrote in 2017 a comprehensive assessment to the responsible German building authorities to get an approval for the use of CFRP hangers for the network arch bridge of 107 m span for a double-track city railway shown in Fig. 21 [29]. The approval was given in April 2018. Construction will happen in 2019/2020. This will be a pilot project of a new scale. This medium-span railway bridge will fully rely on CFRP hangers. These hangers are exposed to very high-fatigue cycles. Since CFRPs show excellent fatigue behavior, the required hanger section drops to about 25% of what would be needed in steel [28].



Fig. 21 Network arch bridge designed by Schlaich Bergermann Partner for the city public transport operator Stuttgarter Straßenbahnen (SSB) fully suspended on CFRP hangers. Source of rendering: Stuttgarter Straßenbahnen AG

8 Final Remarks

- From year to year, obtain CFRP applications in civil engineering nowadays a higher acceptance. This is the result of more than 20 years of very positive practical experience with applications in rehabilitation and strengthening.
- Megastructures like the “Arctic City” or “Shadow in the Desert” with CFRP cables are from a technical point of view not far from realization [30].
- The technology of active mitigation of wind-induced vibrations for very long-span suspended bridges is not yet ready for large-scale applications. There is much more research work required. Another question is, if the civil engineering community will accept active mitigation, when is it ready for use? Without active mitigation, very long-span lightweight bridges made of CFRP cannot be realized.
- The suspension bridge proposed by Lin across the Strait of Gibraltar might be feasible without active mitigation. In such a case, the application of CFRP cables would be by far more economic and sustainable than steel cables. More than 70% of the volumes of such a large superstructure are cables.
- The outlined 14 km submerged floating tunnel (SFT) would be by far the most economic and sustainable solution for a fixed link across the Strait of Gibraltar. The SFT concept was first conceived at the beginning of the twentieth century with conventional materials, but no actual project was undertaken until recently. In this case, it is not a confidence problem with CFRP; it is missing experience with the SFT concept.
- The “network arch bridge” might be the trigger for broader use of CFRP cables in construction, similar as Ibach Bridge was the landmark for commercial takeoff for the use of CFRP in rehabilitation and strengthening.
- May be within 10 years, we will see megastructures based on CFRP like the air-supported dome as described in the project “Arctic City.” For long-span suspended bridges, we will have to wait at least two decades until the second generation of CFRP pilot projects like the mentioned “network arch bridge” demonstrates to be reliable and economic.
- Today most CFRP applications in construction are sustainable because only small amounts are needed for the same task in comparison to classical materials and CFRPs last much longer. There is a high probability that in the future, based on a CFRP production of captured CO₂, even a negative CO₂ footprint is possible.

References

1. Andrä W, Zellner W (1969) Die Bautechnik 46:263–268. and 309–315
2. Andrä W, Saul R (1974) Die Bautechnik 51:289–298. 332–340 and 371–373
3. Meier U, Rösli A (1971) Schweizer Bauz 89:81–86
4. Meier U (1971) Schweizer Bauz 89:375–380

5. Watson St CC, Stafford D (1988) *Civil Eng* 58:38–41
6. Meier U (1987) *Proc Instn Mech Eng IMechE* 201B2:73–78
7. Meier U, Kim P, Meier H (1998) Anchorage device for high-performance fiber composite cables. US Patent 5713169
8. Beedle LS, Thürlimann B, Ketter RL (1955) American Institute of Steel Construction. Plastic design in structural steel, lecture notes. Lehigh University Press, Lehigh, p 66
9. Thürlimann B (1979) *IABSE Rep Work Comm* 28:71–90
10. Ladner M, Pralong J, Weder Ch (1990) *Geklebte Bewehrung: Bemessung und Erfahrungen*, EMPA-Bericht Nr. 116/5
11. Meier U (1987) *Mater Tech* 15:125–128
12. Meier U (1992) *Strut Eng Int* 2:7–12
13. Meier U, Meier H (1996) *J. Modern Plast* 73:87
14. Maissen A (2000) *Struct Eng Int* 10:117–120
15. Meier U, Brönnimann R, Anderegg P (2016) In: Teng JG, Dai J (eds) *Proceedings of the eighth international conference on fibre-reinforced polymer (FRP) composites in civil engineering (CICE)*, pp 1069–1074
16. Vervuurt AHJM, Kaptijn N, Grundlehner WB (2003) *Struct Concrete* 4:1–11
17. Vervuurt AHJM, Hordijk DA (2001) Carbon fibre based tendons with the pilot project “Dintelven Bridge”, TNO-report 2000-CON-BM R3008
18. Otto F, Tange K, Rice P et al (1971) Project study city in the Arctic, IL 2, Information of the Institute for Lightweight Structures (IL). University Stuttgart, Stuttgart
19. Otto F et al (1972) Project study shadow in the desert, IL 7 Information of the Institute for Lightweight Structures (IL). University Stuttgart, Stuttgart
20. Boberg M, Feltrin G, Martinoli A (2015) A novel bridge section model endowed with actively controlled flap arrays mitigating wind impact, *ieee international conference on robotics and automation (ICRA)*
21. Lin TY, Chow P (1991) *Struct Eng Int* 1(2):53–58
22. Meier U (2012) *Arab J Sci Eng* 37:399–411
23. Kaempfen CE (1989) Transportation research record (TRR) 1223. Transportation Research Board (TRB), Washington, DC, pp 107–116
24. Weber J (1990) Scientist’s fiberglass composite is promoted for \$1-billion tunnel. *Los Angeles Times* of May 10
25. Meier U, Brönnimann R, Widmann R, Winistörfer A, Irniger P, Deuring M (2013) Environmental-friendly footbridge made of CFRP, GFRP and timber. Presented at the 19th international conference on composite materials (ICCM19), Montreal, QC. pp 6260–6267.
26. Fernández-Dacosta C et al (2017) *J CO2 Util* 21:405–422
27. Esrafilzadeh D et al (2019) *Nat Commun* 10:Article number: 865
28. Haspel L (2019) *Stahlbau* 88:153–159
29. Meier U (2017) Gutachterliche Stellungnahme zur Erlangung einer Zustimmung im Einzelfall (ZiE) für die Verwendung von Carbonstangen als Hänger bei der Netzwerkbogenbrücke über die A8 in Stuttgart beim zweiten Teilabschnitt des Stadtbahnprojektes Linie U6
30. Meier U (2018) An update of past visions of fiber reinforced megastructures, report IABSE symposium tomorrow’s megastructures, nantes. ISBN: 978-3-85748-161-1, pp S8-1–S8-8

On the Behaviour of Recycled Aggregate Concrete Incorporating Slag



Moetaz El-Hawary, Anwar Al-Yaqout, and Khallad Nouh

1 Introduction

Previous studies [1–5] tested the mechanical behaviour of concretes containing recycled aggregates. The mechanical properties of RAC with varying replacement ratios (below 30%) was comparable to that containing natural aggregates (NAC), but further testing was required to establish the confidence in the material for specific cases.

Although many authors published several publications on the durability of concrete containing recycled coarse aggregates [6–11], the durability of RCA, especially in hot weather, still needs more investigation. Although recycled aggregates have many environmental advantages in concrete, the workability of RAC needs additional water compared to normal aggregates. Fresh properties and compressive strength of RAC are slightly less than that of the regular concrete [12, 13]. Furthermore, the rate of reinforcement corrosion, the rate of carbonation, and concrete permeability of RAC for a specific (w/c) ratio are higher than that of NAC [12, 13].

Ground granulated blast-furnace slag (GGBS) can be utilized as a cement supplementary material in numerous concrete structures [14–16]. It supplies more chloride diffusion resistance and sulphate attack resistance and reduces the harmful of alkali–silica reactivity [17]. On the other hand, it is not useful to add mineral slag in concrete, if high early strength is required [18–21]. In the past, moderate replacement levels of GGBS were used in concrete; in summer 20–25%, in winter 15–20% [22]. Nowadays, the common replacement levels for appropriate strength concrete can reach 20–50% [22].

Earlier researches have been made on the mechanical and durability characteristics of RAC mixed with supplementary cementitious materials (SCM).

M. El-Hawary (✉) · A. Al-Yaqout · K. Nouh
Kuwait University, Safat, Kuwait
e-mail: a.ottesen@ack.edu.kw

Qasrawi [23] studied the mechanical characteristics of ordinary concrete that utilize steel slag aggregate or recycled coarse aggregate. Results indicated that the fresh properties of concrete had been deteriorated when utilizing steel slag aggregate or recycled coarse aggregate. While steel slag aggregate enhanced the mechanical characteristics of concrete, the recycled coarse aggregate reduced them.

Limbachiya et al. [24] studied different concrete mixtures that contain mineral admixtures. These mixes were (a) control mix, (b) 70% GGBS, (c) 50% fly ash, (d) 50% GGBS, and (e) 25% fly ash and 25% GGBS. Results indicated that the addition of 50% GGBS as a cement replacement had the highest mechanical properties efficiency. GGBS was mostly useful for concrete made with RA and could minimize the losses of strength. On the other hand, utilizing RA showed little growth in chloride diffusion coefficient and permeability coefficient. Furthermore, 50% FA mix showed comparatively low efficiency for both the mixture proportions and materials utilized in that research.

Ann et al. [25] used mineral slag (GGBS) and fuel ash (pulverized) to enhance the durability and strength RAC. Results showed that the incorporation of 65% GGBS and 30% fuel ash improved the compressive strength to the grade of control mix. Moreover, the limitation of oxygen and water penetration in concrete had kept the corrosion rate of 30% fuel ash and 65% slag at a lower grade.

The current research aims to investigate the durability of recycled aggregate concrete (RAC). The utilization of GGBS as a partial replacement of cement is one method that can improve the durability characteristics of concrete containing recycled aggregate. The results of testing compressive strength, drying shrinkage, water absorption, water penetration, alkali silica reactivity, alkali carbonate reactivity, and sulphate content of various proportions of recycled aggregate concrete combined with 25% of GGBS as a cement replacement are reported and discussed in this paper.

2 Materials

2.1 *Materials and Mixture Design*

2.1.1 Binders

Ordinary Portland cement (Type I) is utilized in all mixtures, and it was supplied by Kuwait Portland Cement Company (KPCC). It is produced in accordance with the American standard (ASTM C150-11). A single source of ground granulated blast slag (GGBS) was provided by the ACICO Industries Company (ACC) conforming to BS EN 6699 and ASTM C 989-05 and was used as 25% replacement by weight of PC. Table 1 shows the physical properties and chemical composition of Portland cement (OPC) and GGBS.

Table 1 Chemical composition of (OPC) and GGBS

Ingredients	Percentage (%)	
	PC	GGBS
SiO ₂ (%)	20.83	33.60
Al ₂ O ₃ (%)	4.44	12.50
Fe ₂ O ₃ (%)	3.53	0.52
CaO (%)	64.55	42.50
MgO (%)	1.45	7.52
SO ₃	2.52	1.68
C ₃ S	62.30	–
C ₂ S	12.70	1.26
C ₃ A	5.80	–
Alkalies	0.65	0.48
Chlorides	0.01	0.01
Loss of ignition	1.41	0.02
Density (g/cm ³)	–	2.98
Specific surface (m ² /kg)	322	542.5

Table 2 Physical properties of the aggregates

Aggregates	S.G (SSD)	S.G (OD)	A (wt.%)	MC (%)	FM	CD (OD) (kg/m ³)
Sand	2.59	2.57	1.13	0.91	2.46	–
3/4" NA	2.65	2.62	1.25	0.381	–	
1/2" NA	2.62	2.59	1.21	0.71	–	1609.7
3/8" NA	2.69	2.66	1.24	0.5	–	1645.43
3/4" RA	2.47	2.38	4.09	1.24	–	1264
1/2" RA	2.43	2.31	5.14	3.36	–	1208
3/8" RA	2.39	2.25	6.12	3.5	–	1151

Where S.G (OD) is bulk-specific gravity (oven dry), S.G (SSD) is bulk-specific gravity (SSD), MC the moisture content (%), A the water absorption (wt.%), FM the fineness modulus, and CD (OD) the oven-dry compacted density (kg/m³)

2.1.2 Aggregates

The fine aggregate consisted of natural sand, which was obtained from domestic quarries in Kuwait. Table 2 displays the physical characteristics of the fine aggregate (sand). The ordinary coarse aggregate used was gabbro (crushed stone) of three various grades of 3/8" (9.5 mm), 1/2" (12.7 mm), and 3/4" (19.05 mm). These aggregates were imported from Ras Al Khaimah in the United Arab Emirates. Table 2 shows the physical characteristics of the natural coarse aggregates. The recycled aggregate (RA) utilized in this research was acquired from waste concrete and is commercially available in Kuwait. The physical characteristics of the recycled coarse aggregates with three various grades are shown in Table 2. All aggregates were used at the saturated surface dry condition. Absorption and specific gravity of the aggregates were measured according to ASTM (C128) and ASTM

(C127), respectively. The gradings of natural and recycled aggregates were determined according to ASTM C33. The aggregates grade distributions are shown in Fig. 1. Regular tap water was utilized as mixing water.

2.2 Concrete Mixes

Six concrete mixes were prepared and cast in the lab using a rotating mixer. The mix proportions were calculated using the absolute volume method. In all concrete mixtures, a fixed water/cementitious (w/c) ratio of 0.35 was used. Concrete mixture I utilized RA as coarse aggregate, and the mixture was designated as RA100%, (OPC with 100% recycled aggregate). In mixes II, and III, 50% and 0% of the aggregates were recycled aggregates, while the remaining aggregates were natural coarse aggregate (NAC). The mixes were designated as RA50% (OPC with 50% recycled aggregate) and RA0% (control, OPC with 0% recycled aggregate). The next three mixtures were prepared as the previous ones but with 25% GGBS as cement replacements. The mixes were designated as RA100% S (100% recycled aggregate with 25% GGBS), RA50% S (50% recycled aggregate with 25% GGBS), and RA0% S (0% RA with 25% GGBS). Table 3 reports the mix proportions of all mixes. Seven hundred and five kilogram of sand was used for all mixes.

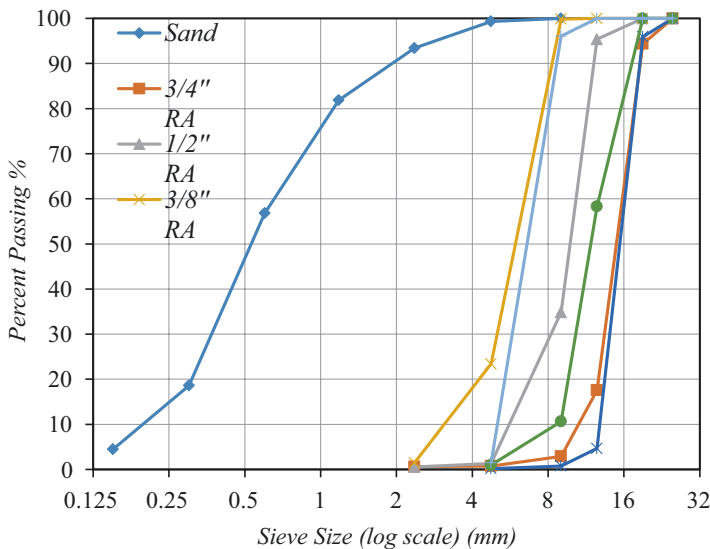


Fig. 1 Aggregates grading

Table 3 Mixture proportions for 1 m³ concrete

Mix name	RA%	Ingredient (kg/m ³)					
		PC	GGBS	Water	3/8"	1/2"	3/4"
RA100%	100	410	0	143.5	0 (NA)	0 (NA)	0 (NA)
					500 (RA)	340 (RA)	260 (RA)
RA50%	50	410	0	143.5	250 (NA)	170 (NA)	130 (NA)
					250 (RA)	170 (RA)	130 (RA)
RA0%	0	410	0	143.5	500 (NA)	340 (NA)	260 (NA)
					0 (RA)	0 (RA)	0 (RA)
RA100% S	100	307.5	102.5	143.5	0 (NA)	0 (NA)	0 (NA)
					500 (RA)	340 (RA)	260 (RA)
RA50% S	50	307.5	102.5	143.5	250 (NA)	170 (NA)	130 (NA)
					250 (RA)	170 (RA)	130 (RA)
RA0% S	0	307.5	102.5	143.5	500 (NA)	340 (NA)	260 (NA)
					0 (RA)	0 (RA)	0 (RA)

2.3 Preparation, Casting, and Curing Regimes for Specimens

The concrete cubes samples of size 150 mm were prepared to determine the compressive strength and absorption. Moreover, 200 × 200 × 120 mm concrete discs were used for water permeability test. Concrete cylinders of 150 mm by 300 mm were cast for compressive strength, and 75 × 75 × 285 mm prisms were cast for ASR, ACR, sulphate content, and drying shrinkage test (DST). The samples were cast according to ASTM C192. The fresh properties were then determined: air content according to (ASTM C231) and slump according to (ASTM C143). Wet burlap and polyethylene sheet were utilized to reduce evaporation. Samples were cured for 24 h in lab environment then were de-moulded and put in a water till the day of testing.

3 Experimental Program

3.1 Compressive Strength Test

Compressive strength at 28 days was determined by using cylinders with diameter 150 mm and height 300 mm according to ASTM C39. In addition, the 150 mm cubes were examined by a compression testing machine. The load was applied at a rate of 13,000 N/s for cubes and 5.4 kN/mm for cylinders.

3.2 *Water Penetration Test*

The water penetration test under pressure mentioned in BS EN 12390-8 was used to measure the depth of penetration of water under pressure. Specimens of dimensions $200 \times 200 \times 120$ mm were used after 28 days of curing, which were placed in a penetration cell and then subjected to 0.5 MPa water pressure on bottom surface. After 3 days of exposure, specimens were removed and split into two halves, vertically to the surface, to evaluate the water depth inside the concrete.

3.3 *Water Absorption Test*

This test determines the absorption in the hardened concrete sample according to ASTM C 642-13. Hundred and fifty millimeter concrete cubes were cast and placed for 28 days in water curing tank. Cores of size 150 mm (height) by 70 mm (diameter) were drilled from each cube and were then oven dried for 72 h at 100°C till the mass became fixed. All the specimens were held to cool to the laboratory temperature and weighted (M_{OD}). Specimens then were set on a water griddle at a temperature of 22°C in 5 ± 1 mm deep for half an hour and weighted again, and the absorption is measured (M_{S}).

$$W\% = \frac{M_{\text{S}} \times M_{\text{OD}}}{M_{\text{OD}}} \times 100$$

3.4 *Drying Shrinkage Test*

The $75 \times 75 \times 285$ mm concrete prisms were cast for determining the drying shrinkage. Stainless steel pins were used on opposite direction to measure the length of each specimens. After de-moulding, the specimens were set in chamber at $50 \pm 5\%$ humidity and $23 \pm 2^\circ\text{C}$, according to ASTM C157, for about 210 days. Comparator was used to indicate the change in length of the prisms, and frequent readings were taken.

3.5 *Alkali Silica Reactivity*

ASTM C 1293 specifies the alkali silica reactivity test to determine the expansion length. Two $75 \times 75 \times 285$ mm concrete prisms were used for each mixture. Forty gram of sodium hydroxide was dissolved in 1 L of distilled water to prepare a

solution of 1 N NaOH, so that the solution volume was four times the volume of samples. All prisms were cast, cured in a water tank, and then stored in 100% relative humidity at 38 °C after de-moulding. A length comparator was used to measure the expansion at 1, 7, and 28 days and subsequently at 3, 6, 9, and 12 months of age. According to ASTM C 1293, if the average expansion is equal to or larger than 0.04% at 1 year, the aggregate could be categorized as potentially deleteriously reactive.

3.6 Sulphate Attack

The durability of concrete containing natural or recycled aggregate that is exposed to sulphate solution was achieved by immersing concrete prisms with sizes 75 × 75 × 285 mm in a 50 g/L Na₂SO₄ at room temperature. The prisms were cured for 28 days before being placed in the sulphate solution. The change in length readings were taken after 7, 28, and 56 days and 3, 6, 9, and 12 months of exposure to the sulphate solution. This test was conducted according to ASTM C 1012.

4 Results and Discussion

4.1 Workability

Table 4 shows the slump of each concrete mixture. As the amount of recycled aggregates increases, the workability decreases due to the high amount of water demand and also to the increase in the aggregate angularity. This agrees with the results obtained from previous researches. A similar tendency was also found for GGBS mixtures, in general. The workability of concrete was improved by using 25% GGBS as a cement replacement in recycled aggregate concrete.

In addition, Table 4 illustrates the results of the air content for the several concrete mixtures. The percentage of air content increased with the increase in the recycled aggregates percentage. The increase was more than 50% for 100% recycled

Table 4 Slump and air content for all mixtures

Mixture code	RCA%	Slump (mm)	Air content (%)
RA 100%	100	20	3.1
RA 50%	50	25	2.5
RA 0%	0	108	2
RA 100% S	100	57	2.8
RA 50% S	50	160	2.2
RA 0% S	0	51	2.1

aggregates. The mortar layer that covers the recycled aggregate may be the reason to increase the air content in recycled aggregate concrete.

It has been observed that mixes of 25% GGBS partial cement replacement showed a similar trend.

4.2 Compressive Strength

Figure 2 shows the results of compressive strength at 28 days of recycled aggregate concrete. The compressive strength changed from 35.5 to 42.4 MPa at 28 days for concrete specimens without slag and from 35.6 to 54.7 MPa at 28 days for concrete specimens containing slag, depending on test and aggregate type.

4.2.1 Recycled Coarse Aggregate (RCA)

The compressive strength was reduced in concrete mixtures that contain recycled aggregate as shown in Fig. 2. As the amount of recycled coarse aggregate increase, the reduction in compressive strength increases. It is visible that the compressive

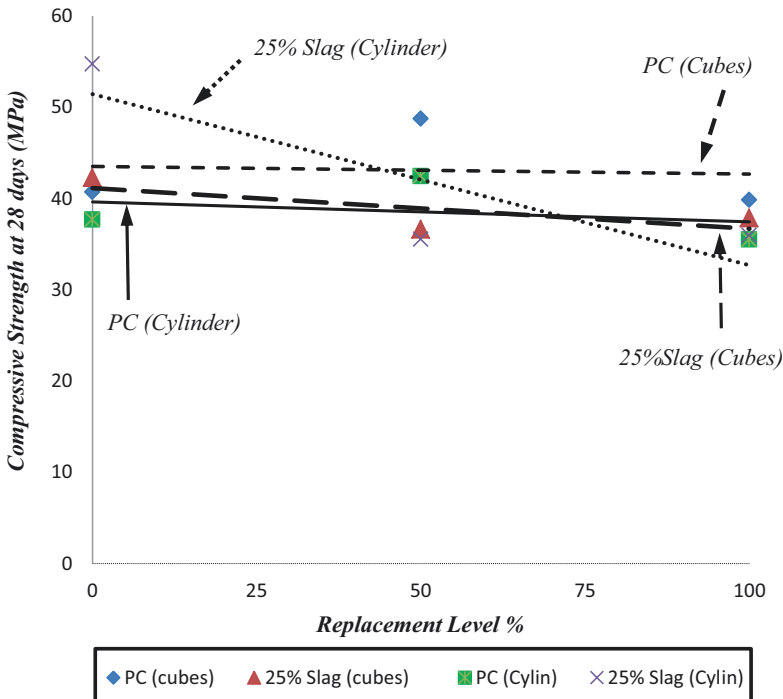


Fig. 2 Compressive strength at 28 days

strength of concrete that contains 100% recycled aggregate was the lowest at 28 days, whereas replacement with 50% RA and 0% RA increased the compressive strength by about 19% and 6%, respectively, compared with 100% RA. Limbachiya et al. [24] found that this fluctuation in the attitude of concrete mixtures prepared with the recycled coarse aggregate could be referred to the different parameters of the aggregate. The quantity and density of mortar layer stuck on the recycled aggregate are the main parameters influencing the strength of concrete. In addition, this RCA could have various primary moisture, which might impact on the cement hydration approach. This primary moisture can reduce the compressive strength at the beginning, while it could be helpful for long-period cement hydration.

4.2.2 Introducing 25% GGBS

As 25% of GGBS is added as a cement replacement of PC in concrete mixtures, the compressive strength of concrete cylinders containing recycled coarse aggregate is improved in general, as shown in Fig. 2. There is increase in strength of up to 45% and 1.41% for the RA0% S and RA100% S mixes compared with the same mixes without GGBS, respectively, while the reduction in strength is less than 16% for the RA50% S mix compared with the RA50% mix. This is because concretes containing GGBS are effective in improving the compressive strength of concrete at a long term, while it is not utilized in applications where high early compressive strength is desired.

4.3 Water Penetration

Figure 3 illustrates the water penetration depth under pressure for various concrete mixtures. The use of 50% RA and 100% RA seems to reduce water penetration considerably by more than 35% and 42%, respectively, compared with the control mix (0% RA).

In contrast, the combination of RCA with 25% GGBS led to a significant increase in water penetration. There is an increase in penetration depth of more than 50% for RA50% S mix compared with the RA50% mix. The higher water penetration of the recycled aggregate concrete mixtures is certainly combined with the mortar in the recycled coarse aggregates. Remaining mortar in recycled aggregate concrete serves as a channel for water transfer.

4.4 Water Absorption by Immersion

The test results indicated that the increase in the recycled aggregate amount produced an increase in absorption as shown in Fig. 4. When the amount of RA was 100%, the absorption was increased by 70% compared to that of 0% recycled

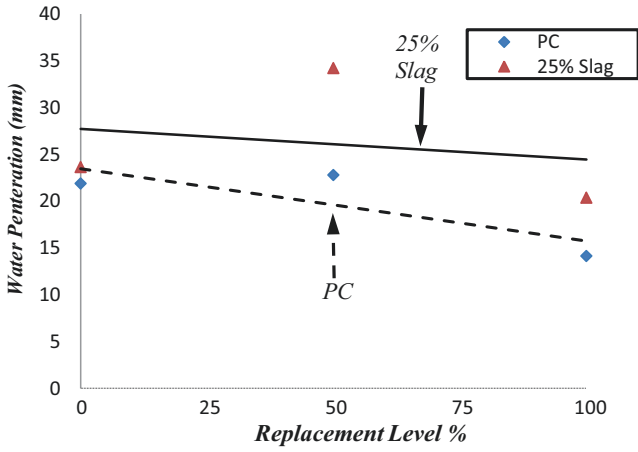


Fig. 3 Maximum water penetration under pressure

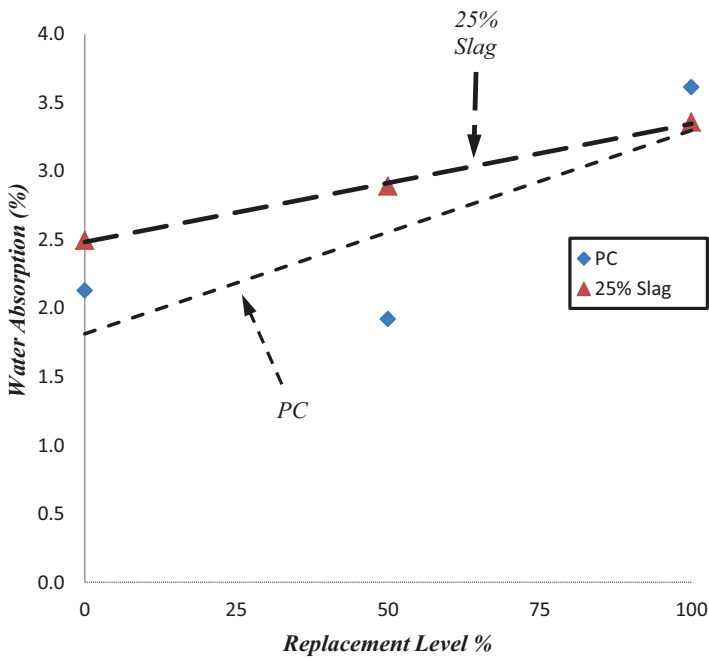


Fig. 4 Water absorption by immersion

aggregate. This is because the higher pressure in concrete was produced due to the higher absorption rate of the RA.

Furthermore, the influence of 25% GGBS on the water absorption in recycled aggregate concrete was determined. There is a reduction in water absorption of 7% for RA100% S mix compared with the RA100% mix.

4.5 Drying Shrinkage

Figure 5 shows the measurements of the drying shrinkage of concrete mixes determined after 210 days. It is evident that the utilization of recycled aggregate increased the drying shrinkage of concretes. The increase in drying shrinkage is proportional to the increase in the recycled aggregate ratio. The use of 100% RA increased drying shrinkage considerably by more than 32% compared with the nominal mix (0% RA). This might be due to the existence of ancient mortar and the lower restraining capacity of recycled aggregate particles.

Water cement ratio (w/c), initial aggregates, and admixtures are the main factors affecting drying shrinkage. However, it could be seen that the inclusion of 25% GGBS in concrete mixes that contain natural and recycled aggregate displayed higher drying shrinkage values compared to the normal control mixes. The pozzolanic reaction between mineral slag and $Ca(OH)_2$ could yield more amount of C-S-H gel.

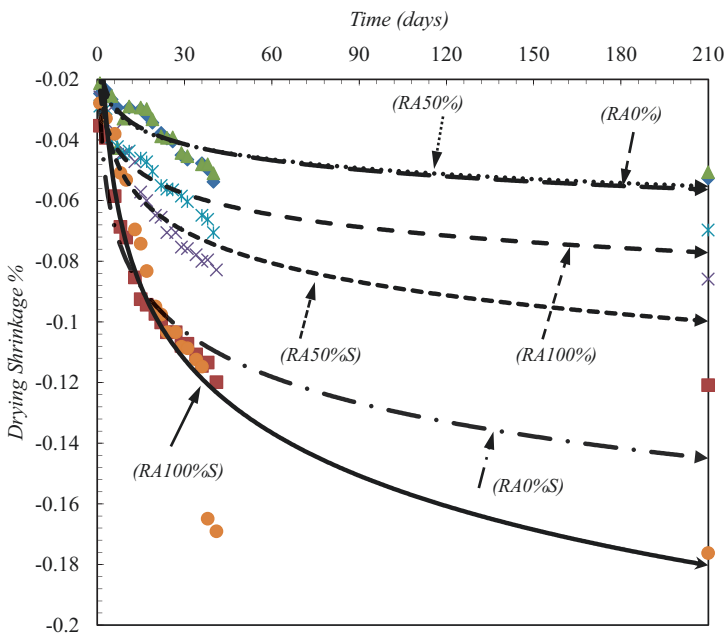


Fig. 5 Drying shrinkage for all specimens

4.6 Alkali Silica Reactivity

Expansion results using the concrete prism test for the natural and recycled aggregate concrete mixtures after 1 year are illustrated in Fig. 6. The expansion of the concrete control mix (RA0%) and RA50% was about 0.022% at 1 year, approximately half of the acceptable expansion of 0.04%. The use of 100% RA seems to increase the expansion considerably by more than 100% compared with the control mix (0% RA) expansions. The study showed that a water to cement ratio (w/c) of 0.45 and a maximum aggregate size of 5/8 inch for RA allowed a satisfactory ASR resistance.

However, the addition of 25% GGBS in RAC provided a substantial decrease in expansion compared to the concrete mixtures without slag. The use of 25% GGBS reduced expansion for 0% RA, 50% RA, and 100% RA mixes to 0.0008%, 0.01%, and 0.02%, after 1 year, respectively, which are below the 0.04% limit.

4.7 Sulphate Resistance

ASTM C1012 indicates that the cement can be classified as moderate sulphate resistance (MSR) if the maximum expansion of prisms after 6 months is below 0.1%, while it is highly sulphate resistance (HSR) when it is below 0.05% after 6 months or below 0.1% after 1 year.

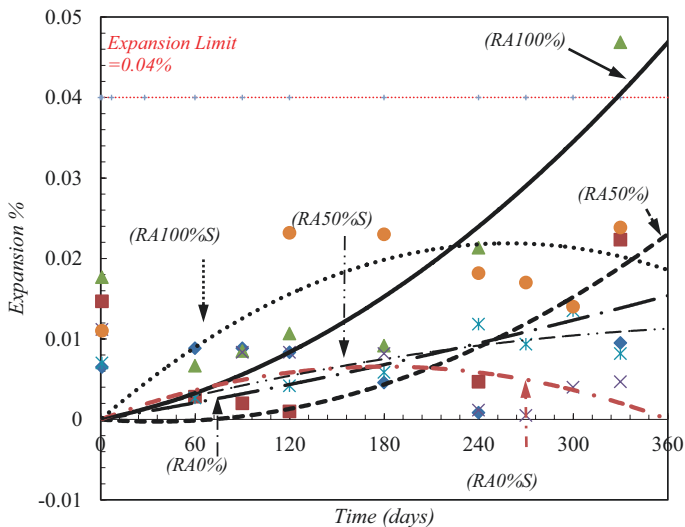


Fig. 6 Expansion due to alkali silica reactivity

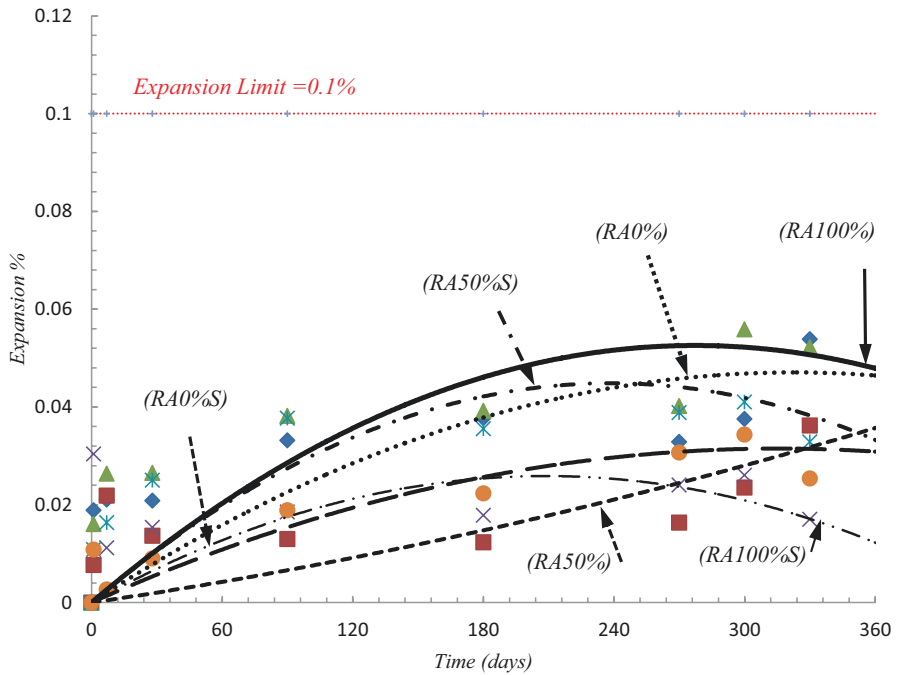


Fig. 7 Expansion due to sulphate attack

Figure 7 shows the expansion and the exposure time of the NAC and RAC prisms exposed to the 5% Na₂SO₄ solution. The preliminary increase in expansion for concrete mixtures is due to hydration reaction progressing. After 1 year of exposure, the RA0%, RA50% and 100%, RA mixtures displayed a significant expansion of 0.053%, 0.040, and 0.051% respectively.

Mixes that contain 25% GGBS with and without RCA showed better resistance to sulphate attack than those which contain PC only. The total expansion exhibited by sulphate attack was 0.034%, 0.04%, and 0.009% for RA0% S, RA50% S, and RA100% S concrete mixes, respectively.

5 Conclusions

An experimental program was conducted to investigate the effect of using 25% GGBS as partial cement replacement on the durability performance of concrete containing different ratios of recycled aggregates. The main conclusions are as follows:

- The 28-day compressive strength of concrete mixtures containing recycled aggregate is generally below that of conventional concrete mixtures. The intro-

duction of enhanced 25% GGBS improved the compressive strength of recycled aggregate concrete.

- Resistance to water penetration improved with the increase in RCA proportions. However, the incorporation of 25% GGBS has an adverse influence on resisting the water penetration of RAC mixes.
- As the replacement ratio of recycled aggregates rises, water absorption by immersion increases. The use of 25% GGBS as cement replacement reduced the water absorption for RAC mixes.
- The drying shrinkage values of the RAC made with 25% GGBS were higher than those of the control mixes without slag. The introduction of recycled aggregates in general increases the drying shrinkage values.
- All concrete mixes utilizing 25% GGBS, with the incorporation of RAC, were effective in reducing the ASR expansion of RAC after 1 year.
- The results indicated that the introduction of 25% GGBS as partial cement replacement improved the sulphate resistance of the recycled aggregate concrete (RAC).
- Overall, the addition of GGBS proved to be effective in increasing the compressive strength and reducing water absorption, alkali aggregate reactivity, and sulphate attack in recycled aggregate concrete.
- The use of recycled aggregates results in a sustainable concrete as it reduces solid waste and reduces quarrying for new aggregates. The introduction of GGBS, however, greatly increase the sustainability of concrete as it reduces the amount of cement, which results in a noticeable reduction in carbon dioxide emission.
- Additional research is needed to investigate the effect of higher percentages of GGBS on the durability of concrete, especially in hot weather and marine environments.

Acknowledgement The research presented in this paper (RE01/14) was supported by Kuwait University, and this support is thankfully acknowledged. The laboratory analyses conducted by the General Facility of the College of Science and Nanotechnology Research Facilities at Kuwait University is also gratefully acknowledged.

References

1. Vázquez E (2004) Draft of Spanish regulations for the use of recycled aggregate in the production of structural concrete. In: Hendriks CF, Janssen GMT (eds) International RILEM Conference on the use of recycled materials in buildings and structures, vol 2, pp 511–525
2. Butler L, Tighe S, West J (2013) Guidelines for selection and use of coarse recycled-concrete aggregates in structural concrete. *Transport Res Record* 2335:3–12
3. Parekh DN, Modhera CD (2011) Assessment of recycled aggregate concrete. *J Eng Res Stud* 2(1):1–9
4. Knaack AM, Kurama YC (2013) Design of concrete mixtures with recycled concrete aggregates. *ACI Mater J* 110(5):483–494

5. Rahal K (2007) Mechanical properties of concrete with recycled coarse aggregate. *Build Environ* 42(1):407–415
6. Xiao J, Lu D, Ying J (2013) Durability of recycled aggregate concrete: an overview. *J Adv Concr Technol* 11(12):347–359
7. Pečur IB, Štürmer N, Milovanović B (2014) Durability properties of recycled aggregate concrete. In: RILEM International workshop on performance-based specification and control of concrete durability
8. Haque M, Al-Yaqout A, Sreekala V, El-Hawary M (2014) Characteristics of recycled aggregate concretes produced in Kuwait: a case study. *J Eng Res* 2(4):15–31
9. Al-Sanad S, El-Hawary M (2010) Recycling and waste management of building rubbles in Kuwait. In: 25th International Conference on Solid waste technology and management. Windsor University, Philadelphia, PA
10. Al-Otaibi S, El-Hawary M, Abdul-Jaleel A (2010) Recycling crushed concrete fines to produce lime–silica bricks. In: *Proceedings of the Institution of Civil Engineers-Waste and Resource Management*, vol 163(3). Thomas Telford Ltd., London, pp 123–127
11. El-Hawary M, Al-Otaibi S (2010) Durability assessment of concrete containing recycled aggregates. In: *The International conference on future concrete*, Doha, Qatar, p 10
12. Thomas C, Setién J, Polanco J, Alaejos P, De Juan MS (2013) Durability of recycled aggregate concrete. *Constr Build Mater* 40:1054–1065
13. Padmini AK, Ramamurthy K, Mathews MS (2009) Influence of parent concrete on the properties of recycled aggregate concrete. *Constr Build Mater* 23(2):829–836
14. Barnett SJ, Soutsos MN, Millard SG, Bungey JH (2006) Strength development of mortars containing ground granulated blast-furnace slag: effect of curing temperature and determination of apparent activation energies. *Cem Concr Res* 36(3):434–440
15. American Concrete Institute (2003) Report of ACI Committee 233. Slag cement in concrete and mortar ACI 233R-03. American Concrete Institute, Farmington Hills, MI
16. Bijen J (1996) Blast furnace slag cement for durable marine structures. Stichting Beton Prisma, Biezenmortel, Netherlands
17. Wild S, Kinuthia JM, Robinson RB, Humphreys I (1996) Effects of ground granulated blast furnace slag (GGBS) on the strength and swelling properties of lime-stabilized kaolinite in the presence of sulphates. *Clay Miner* 31(3):423–433
18. Song HW, Saraswathy V (2006) Studies on the corrosion resistance of reinforced steel in concrete with ground granulated blast-furnace slag—an overview. *J Hazard Mater* 138(2):226–233
19. Tan K, Pu X (1998) Strengthening effects of finely ground fly ash, granulated blast furnace slag, and their combination. *Cem Concr Res* 28(12):1819–1825
20. Park CK, Noh MH, Park TH (2005) Rheological properties of cementitious materials containing mineral admixtures. *Cem Concr Res* 35(5):842–849
21. Aldea CM, Young F, Wang K, Shah SP (2000) Effects of curing conditions on properties of concrete using slag replacement. *Cem Concr Res* 30(3):465–472
22. Hooton RD (2000) Canadian use of ground granulated blast-furnace slag as a supplementary cementing material for enhanced performance of concrete. *Can J Civ Eng* 27(4):754–760
23. Qasrawi H (2014) The use of steel slag aggregates to enhance the mechanical properties of recycled aggregate concrete and retain the environment. *Constr Build Mater* 54:298–304
24. Limbachiya M, Meddah MS, Ouchagour Y (2012) Use of recycled concrete aggregate in fly-ash concrete. *Constr Build Mater* 27(1):439–449
25. Ann KY, Moon H, Kim YB, Ryou J (2008) Durability of recycled aggregate concrete using pozzolanic materials. *Waste Manag* 28(6):993–999

Ecological Cementitious Material Based on Combination Between Natural Pozzolan and Polymer Admixture



Mohammed Hussein Khudhair, Abdulsamad Mohammed Alhousali, Bouchra El Hilal, Rachid Hsissou, Mohamed Berradi, Ahmed Mohammed Al-Anweh, Mohamed Salahdine Elyoubi, and Ahmad Elharfi

1 Introduction

The valorization of natural pozzolan using it in cement formulation and concrete has economic and environmental benefits: to minimize the CO₂ emission into the atmosphere, to reduce the consumption of raw materials and energy, and to improve the physical properties and mechanical performance. The fine particles of this addition contribute to reducing the porosity and capillary absorption of concrete while improving the physical and mechanical properties [1–9].

M. H. Khudhair (✉)

Faculty of Engineering and Information Technology, Amran University, Amran, Yemen

Laboratory of Cement and Quality Control of Amran Cement Plant of Yemen, Amran, Yemen

Laboratory of Agro Resources Polymers and Process Engineering, Faculty of Sciences, Ibn Tofail University, Kenitra, Morocco

Laboratory of Chemistry of Solid State, Faculty of Science, Ibn Tofail University, Kenitra, Morocco

A. M. Alhousali

Laboratory of Engineering Science and Modeling, Team of Engineering Science, Safety and Entrepreneurial Science, Faculty of Science, Ibn Tofail University, Kenitra, Morocco

B. El Hilal · R. Hsissou · M. Berradi · A. Elharfi

Laboratory of Agro Resources Polymers and Process Engineering, Faculty of Sciences, Ibn Tofail University, Kenitra, Morocco

A. M. Al-Anweh

Faculty of Engineering and Information Technology, Amran University, Amran, Yemen

Laboratory of Cement and Quality Control of Amran Cement Plant of Yemen, Amran, Yemen

M. S. Elyoubi

Laboratory of Chemistry of Solid State, Faculty of Science, Ibn Tofail University, Kenitra, Morocco

The incorporation of the polymeric admixture of polycarboxylate into concrete formulated by natural pozzolan has the advantage of being done as late as possible during the mixing of concrete, minimizing the amount of mixing water, improving the rheological properties of cement paste, and, subsequently, increasing its mechanical of compressive strength [1–3, 10, 11]. The combination of organic and inorganic additions makes it possible to increase the rate of hydration of mortars and concretes while modifying the *W/C* ratio and improving the mechanical performance, namely, the compactness and the capillary absorption [2, 4, 10–14].

In this work, different formulations have been elaborated while partly substituting the clinker by natural pozzolan in various percentages ranging from 5% to 40% by weight of cement with a step of 5% in presence of 3.5% of the polymeric admixture of polycarboxylate. The influences of incorporation of these additions on physical properties and mechanical performances in the fresh and hardened state have been studied.

The obtained results from the different formulations elaborated show that the partly substitution of clinker by natural pozzolan in presence of admixture of polycarboxylate allowed us to develop new durable hydraulic binder with improved physical–chemical and mechanical properties while reducing the cost of production, minimizing the CO₂ emissions into the atmosphere, decreasing the use of mixing water, and improving the physical properties and mechanical performance of concrete in fresh cement paste and hardened state.

2 Materials and Methods

2.1 Material

2.1.1 Cement

The type of cement used in this work is CMI-42.5 from the plant Amran in Yemen. The chemical and mineralogical compositions of clinker, gypsum, and cement used determined by XF and XRD are presented in Tables 1 and 2 and Fig. 1.

Table 1 Elementary chemical compositions of clinker, gypsum, and cement in weight of atomic

Names	CaO	SiO ₂	Al ₂ O ₃	Fe ₂ O ₃	MgO	SO ₃	K ₂ O	Na ₂ O	Cl ⁻
Clinker	62.76	21	5.84	3	1.96	0.9	1.21	0.2	0.02
Gypsum	33.4	0.7	0.36	0.09	0.63	47.2	0.03	0.1	0.01
Cement	61.29	19.99	5.57	2.85	1.89	3.22	1.15	0.2	0.02

Table 2 Mineralogical composition of clinker

Chemical name	Mineral name	Chemical formula	Cement nomenclature	Content
Tricalcium silicate	Alite	CaO ₃ SiO ₅	C ₃ S	47.70
Dicalcium silicate	Balite	CaO ₂ SiO ₄	C ₂ S	25.10
Aluminate tricalcium	Aluminate	CaO ₃ Al ₂ O ₂	C ₃ A	10.40
Tetracalcium aluminoferrite	Ferrite	CaO ₄ Al ₂ O ₃ Fe ₂ O ₃	C ₄ AF	9.10

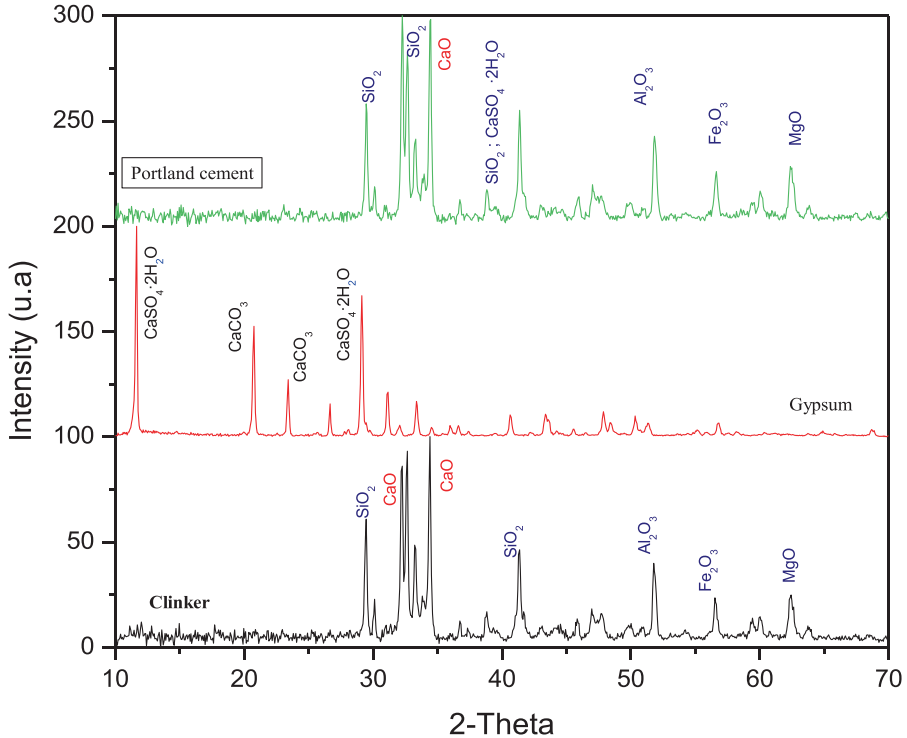


Fig. 1 Spectrum of XRD analysis of clinker, gypsum, and cement

2.1.2 Natural Pozzolan

This is a material of a volcanic origin, extracted from Amran of Yemen deposit. The analysis results by X fluorescence of PN are represented in Table 3. The PN used in this work is a local available material in our country with very high quantity.

From the results shown in Table 3, we observed that PN contained 8.8% of lime (CaO), 41.43% of silica (SiO_2), 16.16% of alumina (Al_2O_3), 9.41% iron of (Fe_2O_3), and 4.79% of magnesia (MgO). These pozzolans have a black color, a specific surface Blaine $4576 \text{ cm}^2 \text{ g}^{-1}$, a density 2.81, and size of particles lower than $50 \mu\text{m}$.

The results of mineralogical analysis by X-ray diffraction of natural pozzolan of Amran, Yemen, are represented in Fig. 2.

From Fig. 2, we have noticed that the natural pozzolan reveals the strong presence of feldspar, plagioclase (anorthite, $\text{CaO} \cdot \text{Al}_2\text{O}_3 \cdot 2\text{SiO}_2$), followed by the pyroxene (augite, $(\text{Mg,Fe})_2 \cdot 2\text{SiO}_6$), then volcanic glass of analcime (zeolite) chlorite ($6\text{Mg}_5 \cdot \text{AlSi}_3 \cdot \text{O}_{10}$) (OH), and some traces of hematite— Fe_2O_3 also as the magnetite, Fe_2O_3 OTF as well as the biotite, $2\text{K}(\text{Fe,Mg})_3 \text{AlSi}_{10}(\text{OH})$ and traces of minerals: basalts, dolomites, calcite, clays, etc.

Table 3 Elementary chemical compositions and physical properties of natural pozzolan in weight of atomic

Names	CaO	SiO ₂	Al ₂ O ₃	Fe ₂ O ₃	MgO	SO ₃	K ₂ O	Na ₂ O	Cl ⁻	LOI	Color	Particles size (µm)	Specific surface (cm ² g ⁻¹)	ρ
Content	8.8	41.43	16.16	9.41	4.79	0.13	0.9	3.47	0.04	14.87	Black	50 µm	4576	2.81

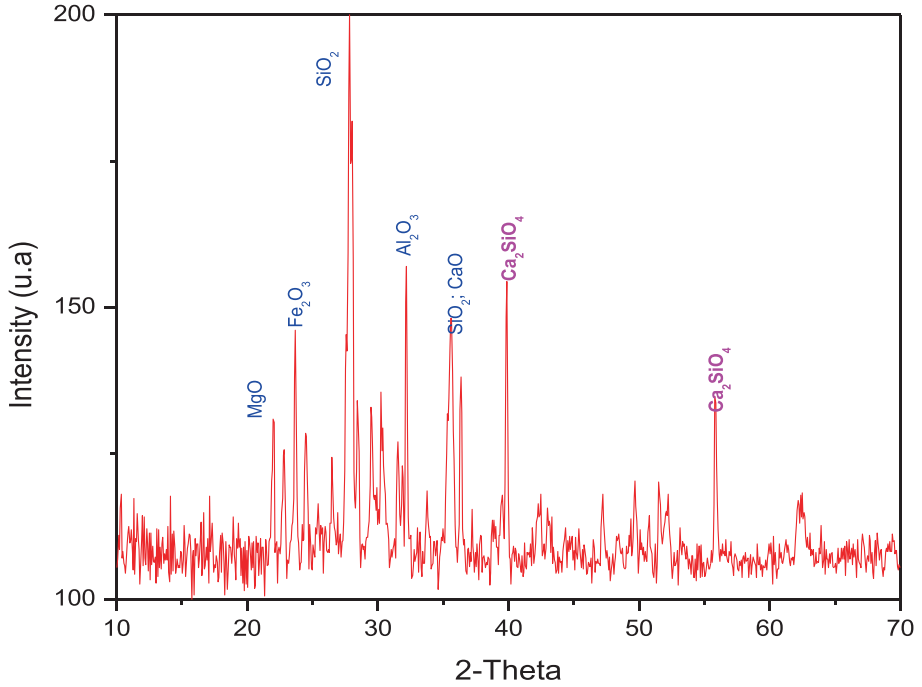


Fig. 2 Spectrum of XRD analysis of PN

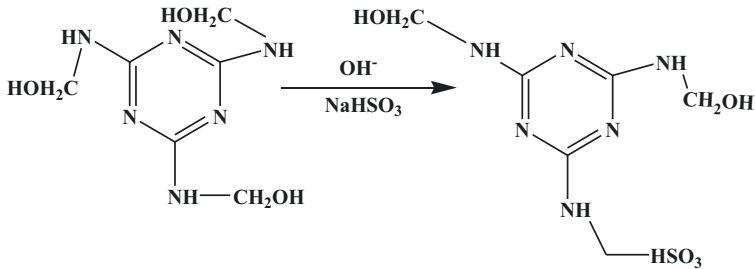


Fig. 3 Chemical structure of sulfone-poly-melamine

2.1.3 Polymeric Admixtures

The polymeric admixtures used are polymers in liquid form, prepared especially for cement industry and concrete. They are based on sodium or sulfonated naphthalene-formaldehyde, Fig. 3, or sulfonated melamine formaldehyde, Fig. 4.

The physical properties of polymeric admixtures are collected in Table 4.

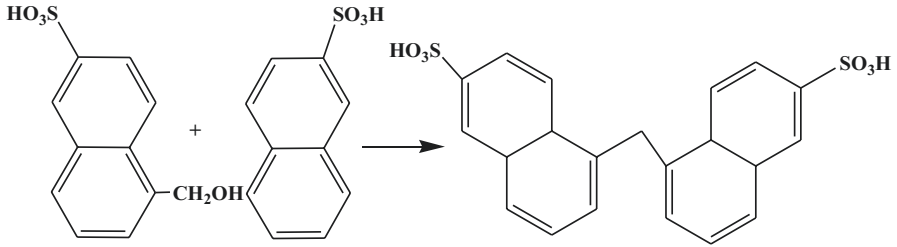


Fig. 4 Chemical structure of sulfone-poly-naphthalene

Table 4 Physical properties of PAS

Name	Nature	Color	Density	Area training (%)	Chloride content
Polymeric admixtures	Liquid	Brown	1.23	0.50–1.00	Nil

2.1.4 Mixing Water

To mix our mixture, we used a tap water (wells).

2.1.5 Sand

To prepare our mortar, we have used standard sand delivered by the new French company of Littoral, conferring to the norm EN 196-1.

2.2 Methods

To achieve the objective of our study, we have prepared a reference mortar without additions whose composition is inspired by that of the normal mortar defined by the norm EN 196-1, with a quantity of water adjusted to obtain a reference consistency. And another mortar with mineral additions and superplasticizers, always keeping the standardized consistency, was fixed. For each mortar having acquired this consistency, we have prepared prismatic specimens with dimensions $40 \times 40 \times 160 \text{ mm}^3$. The compressive strengths were measured at a young age (2 days), in median age (7 days), and long term (28 days) using a bending test machine to break the specimen into two halves, and each party is responsible of the subject of compressive using a hydraulic testing machine. The value of the resistance is considered as the average of the crushing stress of three test pieces (six halves).

The formulations of different tests prepared for elaboration of new ecological cementitious material, while still maintaining the content of gypsum to 5% of total weight of cement with addition of PN, are presented in Table 5.

Table 5 Formulation matrix of cement at base of PN

Content %	0	5	10	15	20	25	30	35	40
Cement (%)	100	95	90	85	80	75	70	65	60
PN (%)	0	5	10	15	20	25	30	35	40

2.2.1 Porosity Methods

The concrete is a porous material; this porosity plays an important role in the mechanisms of concrete damage; it is complex since it spreads on different scales and results from different phenomena. However, the porous nature of concrete is very important since the resistance of the latter is related to its porosity. In general, it can be seen that the more porous the concrete, the higher its permeability and the lower its compressive strength. This is the simplest method for measuring the porosity. It measures the amount of water that can circulate in the network of interconnected pores of the material. The procedure is that recommended by Ollivier [14]. It requires three weighings:

- The mass of the saturated sample M_{sat} when the sample is out of water.
- The hydrostatic mass M_{hyd} corresponding to the mass of the sample in water.
- The dry mass M_{sec} of the sample after stabilization of its mass in an oven.

The weighing must be carried out on a sample which has not undergone a prior saturation/desaturation cycle, in order to avoid the influence of a removal of cement matrix following this preliminary cycle. The apparent volume V_{app} (in m^3) of the sample is calculated from the saturated masses M_{sat} (in kg) and hydrostatic masses M_{hyd} (in kg) thanks to the buoyancy of Archimedes according to the Eq. (1)

$$M_{\text{hyd}} = M_{\text{sat}} - \rho_{\text{water}} \times V_{\text{app}} \quad (1)$$

where ρ_{water} is the density of water (1000 kg m^{-3}).

Assuming then that the interconnected pores are saturated with water, the porosity η is calculated of sample by Eq. (2).

$$\eta = \frac{V_{\text{vides}}}{V_{\text{app}}} = \frac{M_{\text{sat}} - M_{\text{sec}}}{M_{\text{sat}} - M_{\text{hyd}}} \quad (2)$$

2.2.2 Capillary Absorption Methods

The water absorption test consists following by weighing the quantity of water absorbed by a previously dried specimen and allows the indirect characterization of capillary porosity. There is no standard for this test, and several procedures are proposed in the literature. We followed a variant of the procedure proposed by the AFREM [15] after having optimized the preconditioning of the specimens.

Table 7 Physical and chemical properties of the cement

Content	Loss on ignition	Free lime	Fineness		Surface specific Blaine	Density	W/C	Setting time	
			45 μm	90 μm				Initial	Final
0	1.59	0.5	12.5	1.5	3240	3.14	0.5	60	90
5	1.62	0.55	13.7	1.7	3250	3.13	0.49	60	90
10	1.88	0.58	14.5	1.8	3260	3.12	0.48	70	100
15	2.00	0.6	15.3	1.9	3290	3.11	0.47	75	110
20	2.04	0.63	18	2	3340	3.09	0.45	80	120
25	2.25	0.65	19.5	2.1	3420	3.06	0.44	90	130
30	2.28	0.68	22	2.2	3510	3.04	0.42	120	160
35	2.42	0.71	24	2.3	3600	3.02	0.4	120	170
40	2.54	0.74	27	2.4	3630	3.00	0.4	130	180

From the results shown in Table 7, we observed that the loss on ignition value is increased as function of percentage of PN. This increase is mainly due to the expelled water and oxidizable elements present including our addition. In addition, we noticed that the insoluble residue rate of cement is increased as function of percentage of PN. This increase is essentially due to the residues present in pozzolan. Moreover, we detected that the fineness by saving sizes methods (45 and 90 μm) of cement increases with addition of PN; this increase is usually due to the fineness of PN, which facilitates the hydration of mixture during mixing. In addition, we observed that the fineness of cement increase with addition of PN. This increase is habitually due to the fineness of PN, which facilitates the hydration of mixture during mixing and filling the void between the particles of cement and that of aggregate on one hand and on the other hand is to improve the physical and mechanical properties thereafter. However, we illustrate that there is a decrease in density of cement with PN by cement witness report. This decrease is logically explained by the fact that adding of PN that replaces clinker has a lower real density, which enabled us to manufacture a cementitious material which is very light and durable. Similarly, we have realized that the W/C ratio decreases with increasing the percentages of PN. This decrease is normally due to the chemical and mineralogical compositions of PN, which is poor in CaO; the presence of a low fraction of CaO influencing on the phenomenon of pozzolan hydration in this mineral phase to a tendency to have a water demand decreased and, on the other hand, related to the fineness of the addition of PN. However, we remark that setting time (initial and final) increases in function the quantity of PN in the cement matrix; this increase is usually due to the chemical/mineralogical compositions and physical properties of PN and also the slow pozzolanic reaction of the mixture.

3.1.3 Mechanical Properties

Figure 5 explains the compressive strength of mortar based on different percentages of addition of PN add as a function of age in days.

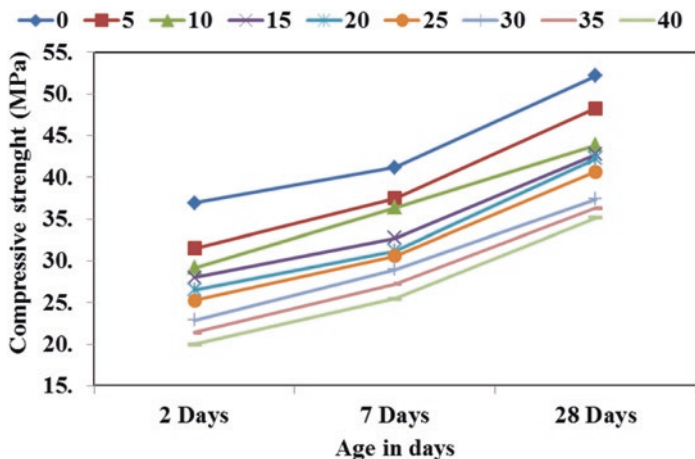


Fig. 5 Compressive strength of cement mortar formulated by different percentages PN add

According to Fig. 5, we identified that the compressive strength of all mortars at a base of PN is progressively increasing with age and does not fall. But it decreases with the increase in the percentage of PN.

In order to improve the physical properties and mechanical performance of mortar or concrete formulated by natural pozzolan, we have incorporated into the different formulation matrix 3.5% of polymeric admixture of polycarboxylate (PAP).

3.2 Mechanical Properties of Mortar and/or Concrete in Hardened State

3.2.1 Porosity

Figure 6 illustrates the porosity of cement mortar as a function of mass fraction of natural pozzolan with 3.5% of polymeric admixture of polycarboxylate.

From Fig. 6, we have established that the porosity of cement mortar formulated by different percentage of PN add with and without of 3.5% of polymeric admixture of polycarboxylate increases. This increase is explained by the fact that the addition of natural pozzolan (very fine materials) fills the voids between the cement and the aggregate particles (PN case). In the second case (PN + PAP), we noticed an increase in the compactness. These increases are due to the effect of the combination between the admixture and pozzolan that is to disperse the cement grains and fill the interstitial voids.

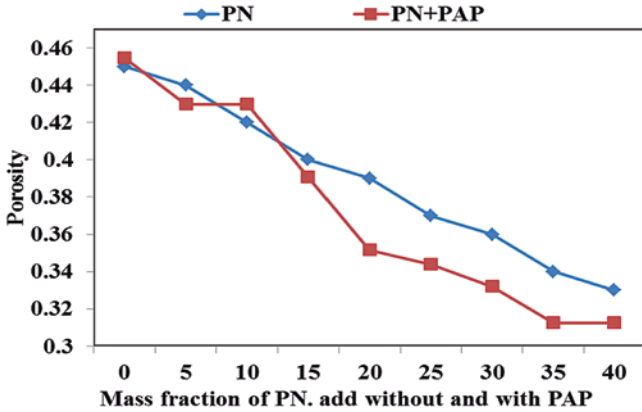


Fig. 6 Porosity of cement mortar formulated by different percentage of PN add with and without PAP

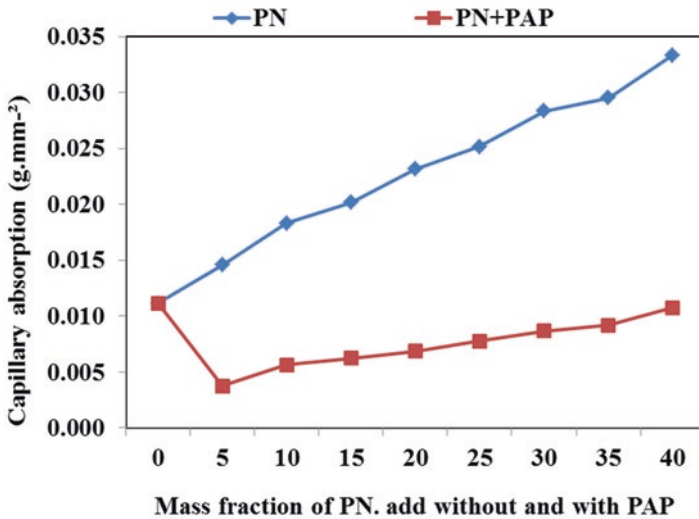


Fig. 7 Capillary absorption of cement mortar formulated by different percentage of PN add with and without PAP

3.2.2 Capillary Absorption

Figure 7 shows the capillary absorption of cement mortar as a function of mass fraction of natural pozzolan with 3.5% of polymeric admixture of polycarboxylate.

From the results presented in Fig. 7, we observed that the capillary absorption of cement mortar formulated by PN increases compared to the control mortar. On the other hand, we have noticed that the incorporation of 3.5% of polymeric admixture of polycarboxylate reduces the capillary absorption. This decrease can be explained

on one hand by the initial role of superplasticizers which disperses the cement grains from each other. On the other hand, it relates to the fineness of mineral addition which fills the voids between the particles and contributes to reduce of capillary absorption of concrete in hardened state.

3.2.3 Compressive Strength

Figure 8 explains the compressive strength of mortar based on different percentages of addition of PN add in presence of 3.5% of polymeric admixture of polycarboxylate.

From Fig. 8 we have observed that the compressive strengths of all mortars formulated by natural pozzolan in combination with 3.5% of polymeric admixture of polycarboxylate increase steadily and show no drop. These increases are related to the role of polymeric admixture of polycarboxylate, which disperses the cement grains from each other (physical–chemical effects).

3.2.4 Gain of Compressive Strength

Figure 9 displays the gain compressive strength at 28 days of mortar based on different percentages of addition of PN add in the presence of 3.5% of polymeric admixture of polycarboxylate.

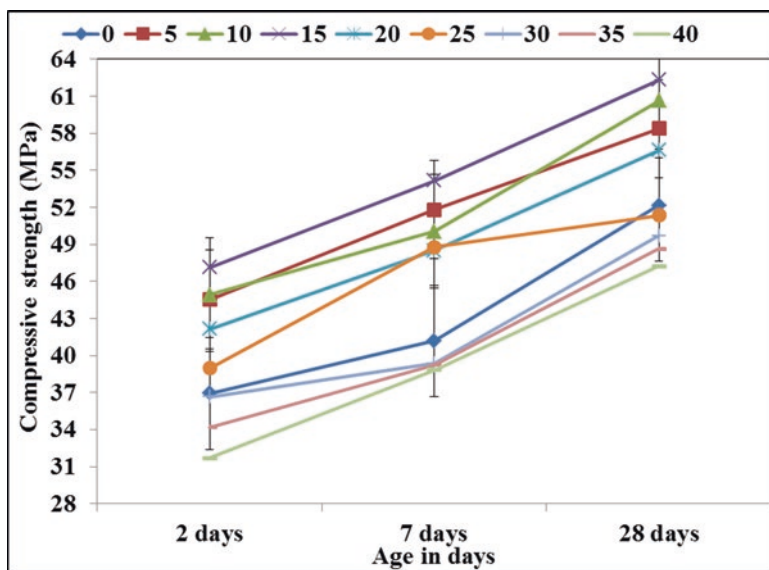


Fig. 8 Compressive strength of cement mortar formulated by different percentages of PN add with and without PAP

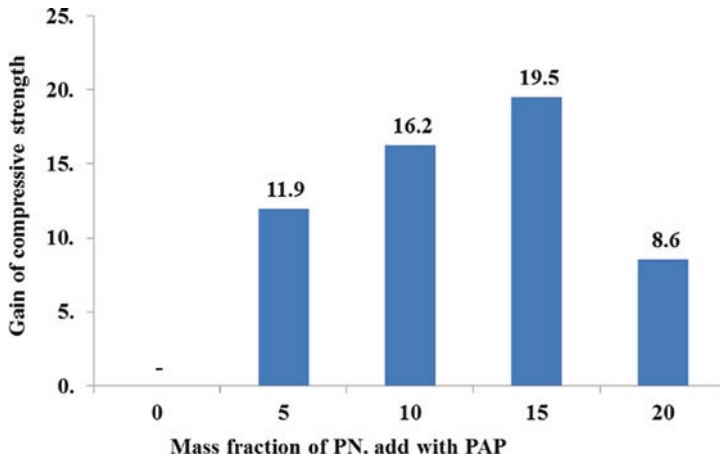


Fig. 9 Gain of compressive strength at 28 days of mortar formulated by different percentages PN add with PAP

According to Fig. 9, we detected that the gain of compressive strength increases with the mass fraction of PN increased in the presence of 3.5% of polymeric admixture of polycarboxylate. These increases are related to the role of polymeric admixture of polycarboxylate, which disperses the cement grains from each other.

4 Conclusion

In this work, we studied the influence of partially substitution of clinker by natural pozzolan at various percentages ranging from 5% to 40% by weight of cement with a step of 5% in the presence of 3.5% of the polymeric admixture of polycarboxylate. The influences of the incorporation of these additions on physical properties of fresh cement paste and mechanical performances in the hardened state have been studied.

The obtained results from the various formulations elaborated show that the granular, physical–chemical, and microstructural effects have been observed. These effects influence the physical–chemical and mechanical properties, namely, the reduction of the quantity of water used. Similarly, the density decreases. In addition, the fineness of the specific surface and the setting time were increased with the increase in the percentages of pozzolan with the superplasticizers. We found that the capillary absorption decreased. However, the compactness increases with increasing the mass fraction of natural pozzolan with superplasticizers (granular and microstructural effects). We have also observed that the mechanical of compressive strengths at a young age (2 days), median age (7 days) and long-term (28 days) have been improved as a function of the increase in the percentage of pozzolan in presence of 3.5% of the polymeric admixture of polycarboxylate in the mix, that is main that Physical-chemical and mechanical effects of the pozzolan i t was effective.

Our study contributes to valorize an abundant mineral resource in combination with the superplasticizers in cement manufacturing, allowing us to develop a new durable concrete with improved physical and mechanical properties and thus represents a great economic and environmental interest:

- Reduction in cost of the cement production.
- Minimization the emissions of CO₂ into the atmosphere.
- Decrease the use of mixing water.

Acknowledgments The authors are pleased to acknowledge all engineers and employees of the laboratory of cement and quality control of Amran cement plant of Yemen for providing the facilities for the research.

References

1. Khudhair MHR, El Harfi A (2016) Formulation of the cement kiln dust (CKD) in concrete: studies of the physical-chemical and mechanical properties. *Int J ChemTechRes* 9(12):695–704
2. Khudhair MHR, El Hilal B, El Youbi MS, El Harfi A (2017) Development and study of physical, chemical and mechanical properties of a new formulation of cement of a varying percentage of natural pozzolan. *J Chem Technol Metall* 52(5):873–884
3. Khudhair MH, Elyoubi MS, Elharfi A (2017) Development of a new hydraulic binder (composite cement) based on a mixture of natural Pozzolan active ‘PN’ and Pure Limestone ‘PLime’: study of the physical-chemical and mechanical properties. *J Mater Environ Sci* 8(3):902–910
4. Khudhair MHR, Elyoubi MS, Elharfi A (2017) Development of a new cementations material eco-friendly of the environment: study of physical and mechanical properties. *J Mater Environ Sci* 8(7):2302–2310
5. Khudhair MHR, Elyoubi MS, Elharfi A (2017) Experimental study and modeling the rupture model of a new hydraulic binder based on the combination of inorganic additions by the response surface methodology. *J Mater Environ Sci* 8(6):1978–1989
6. Scrivener KL, John VM, Gartner EM (2018) Eco-efficient cements: potential economically viable solutions for a low-CO₂ cement-based materials industry. *Cem Concr Res* 114:2–26
7. Plank J, Schroefl C, Gruber M, Lesti M, Sieber R (2009) Effectiveness of polycarboxylate superplasticizers in ultra-high strength concrete: the importance of PCE compatibility with silica fume. *J Adv Concr Technol* 7(1):5–12
8. Pacheco-Torgal F, Cabeza LF, Labrincha J, De Magalhaes AG (2014) Eco-efficient construction and building materials: life cycle assessment (LCA), eco-labelling and case studies. Woodhead Publishing, Cambridge, UK
9. Rojas M, Frías M (2013) Natural pozzolans in eco-efficient concrete. In: *Eco-efficient concrete*. Woodhead Publishing, Cambridge, UK, pp 83–104. <https://doi.org/10.1533/9780857098993.2.83>
10. Khudhair MH, Elyoubi MS, Elharfi Ahmed A (2017) Study of the influence of a high water-reducing super plasticizer and accelerator of setting time on the physical properties and mechanical performance of mortars and concretes. *Res J Pharm Biol Chem Sci* 8(3):1698–1712
11. Khudhair MH, Elyoubi MS, Elharfi AEA (2017) Formulation and characterization of a new ecological cementitious material at base of different percentage of limestone fillers: study of physical-chemical and mechanical properties. *J Mater Environ Sci* 8(11):3973–3985
12. Toledano-Prados M, Lorenzo-Pesqueira M, González-Fonteboia B, Seara-Paz S (2013) Effect of polycarboxylate superplasticizers on large amounts of fly ash cements. *Constr Build Mater* 48:628–635

13. Khudhair MH, Elyoubi MS, Elharfi A (2018) New eco-friendly hydraulic binder based on a combination of inorganic additions and organic admixture: formulation and characterization, *Mor. J Chem* 6(2):259–271
14. Ollivier JP, Baron J (1997) *Les bétons: bases et données pour leur formulation*. Eyrolles, Paris
15. Ollivier J-P, Torrenti J-M (2008) La structure poreuse des betons et les proprietes de transfert. *Durabilité Bétons* 1:1–60

Modeling the Rutting Behavior of Asphalt Mixtures Obtained by Accelerated Testing Device

Taha A. Ahmed and Mohammad H. Yassin

1 Introduction and Background

It's with no doubt that the prediction of the structural response of asphalt mixtures to different loads has been a challenge over the years. That's due to the fact that the common method of doing so is to subject the asphalt mixtures to diverse laboratory tests and use the data to generate a simulation model. Although this has been done in countless number over the years, the generated simulation models were never up to the level of the desired accuracy. For that matter, this study aims at producing a successful and representative FE model that can simulate various asphalt admixtures and predict their behavior over the long run of their life span. The experimental work in this study was extracted from the work of Ahmed et al. with results derived from an ongoing research project [1, 2].

1.1 Rutting

A permanent deformation can be characterized as the aggregation of small amount of unrecoverable strains due to the traffic load on the pavement, also known as rutting. Rutting develops when the asphalt layer underneath traffic loading consolidates and/or there is a sidelong movement of the hot-mix asphalt (HMA). This results in reducing the life expectancy of the asphalt mix. As of late, the potential for rutting has expanded rapidly due to the nonstop increase in traffic volumes. Permanent deformation in the surface layer and plastic deformation of the subgrade layer due to excessive compaction are two causes of developing rutting. Figure 1 shows rutting examples [3].

T. A. Ahmed (✉) · M. H. Yassin
Civil Engineering Department, Australian College of Kuwait, Kuwait, Kuwait
e-mail: t.ahmed@ack.edu.kw; m.yassin@ack.edu.kw



Fig. 1 Severe mix rutting (left), mix rutting (middle), and rutting in the wheel path (right) [3]

Several researches have been conducted with the aim of investigating which test method has the highest potential to evaluate the possibility of asphalt mix rutting. Those methods can be characterized as follow [4, 5]:

Static creep test (AASHTO TP9): A static load is applied to an asphalt sample; then the resulting plastic strain or deformation is measured. The creep test can be conducted under confined, unconfined, or diametral conditions. The measured deformation is correlated to the rutting potential, where a large number of plastic deformations indicates higher rutting potential.

Repeated load test: A repeated load is applied at a specific frequency to an asphalt test sample until the sample fails. Then, the sample's recoverable and plastic strains are measured. The test results from these tests correlate reasonably with the in-service pavement rutting measurements.

Simulative tests—laboratory wheel-tracking device: The wheel-tracking devices provide reasonable correlated results to the in-service pavement rutting measurements. This test tries to simulate the actual rutting development in the pavement by rolling a small loaded wheel device repeatedly across prepared asphalt samples and measuring the resulted rut depth.

Regarding the US loaded wheel testers, test trials were conducted and reviewed by Cooley et al. [6]. It was found that taking the temperature and environmental conditions into consideration will improve the accuracy of the results. Also, wheel-tracking devices can be utilized to assess the impact of asphalt binder type on the rutting resistance of the asphalt pavement. Lastly, test parameters such as load, number of wheel passes, and temperature can affect the results.

1.2 Finite Element Method

Finite element method (FEM) is widely used in the engineering field as it provides practical solutions by using the numerical technique.

Various FEM models have been used in previous researches. Some of these studies and their findings are discussed below.

A study done by Zaghoul and White [7] analyzed the flexibility of pavement when it was introduced to moving loads by using three-dimensional (3D) dynamic

finite element program. Their study showed that FEM can be utilized to predict the structural behavior of pavements when dynamic loading is applied [8].

A study by Bahia et al. [9] proposed a microstructure model of asphalt mixture using FEM code to study the permanent deformation of asphalt pavement. The aggregates were defined as circular objects, and both the aggregates and asphalt binder were defined as linear elastic materials. With these assumptions, the pavement deformation and strain distribution in relation to the nonlinear behavior of asphalt pavement can be assessed.

2 Research Methodology

Simulative models were a common methodology to study the structural behavior of various asphalt pavement mixes. The results from these models are not very effective due to the complexity of the stresses and strains of the asphalt mix.

In this study, a computational model was established to simulate the APA test in order to predict the rutting potential of the HMA mixture with the general-purpose finite element package ANSYS. The model was created using a viscoelastic plastic material and a three-dimensional (3D) finite element (FE) approach.

The dynamic modulus master curve was used to obtain the viscoelastic parameters used in the ANSYS model, while a power law model was used to represent the plastic parameters of the asphalt material. The power law model parameters were obtained using the least-square optimization routine. The research methodology is summarized in the following tasks.

2.1 *Task I: Measuring the Mechanical and the Rutting Performance Properties of the Asphalt Mixture*

In this task, the mechanical properties of the asphalt mixtures were extracted from the E^* master curves which were developed based on the test results obtained earlier. The test was conducted as per AASHTO T378 test standard “Standard Method of Test for Determining the Dynamic Modulus and Flow Number for Asphalt Mixtures Using the Asphalt Mixture Performance Tester (AMPT)” [10].

2.2 *Task II: Establishing the Material Model*

The material models consisted of two parts: viscoelastic and plastic. The viscoelastic part is represented by the dynamic modulus E^* (at the APA test temperature and loading frequency) and Poisson’s and damping ratios. The plastic part is represented by a creep model.

The rate-dependent general time-hardening creep model embedded in ANSYS was used to represent the material plastic properties. The model can be represented by the following equation [11]:

$$\epsilon_{cr} = C_1 \sigma^{C_2} t^{C_3+1} e^{\frac{-C_4}{T}} \quad (1)$$

where

ϵ_{cr} = creep strain

σ = equivalent stress

t = time

T = temperature

C_1 – C_4 are the model constants

The loading frequency was calculated based on the proposed approach by Imad L. Al-Qadi et al. [12]. In his study, a Fourier analysis of vehicular loading pulse was conducted to determine the loading frequency at the pavement surface. The loading frequency, f , can be calculated using the following equation:

$$f = \frac{\nu}{\lambda} \quad (2)$$

where

ν = vehicle speed

λ = wavelength of pavement roughness

The APA test loading frequency is 1 cycle per second. Based on the dimensions of the test settings (see Fig. 2), the loading frequency results in a vehicular speed of 0.6 m/s. Since this is a simulative test and not a full-scale pavement, the wavelength of pavement roughness can be simply set to the minimum value of 0.5 m. Thus, based on these assumptions, the loading frequency was calculated as 1.2 Hz.

2.3 Task III: Establishing the Boundary Conditions and Mesh Size

During the APA test, the cylindrical specimens are confined within a hard mold. The mold restrains the movement in the radial direction of the specimen [13]. Therefore, it was treated as a rigid confinement due to the fact that its stiffness in the radial direction is much higher than the HMA samples. The base of the mold also restrains the movement in the vertical direction. However, the sides of the specimens were considered to slide freely to displace vertically with respect to the sidewall. For these reasons, the nodes at the bottom of the model were restrained by fixed support,

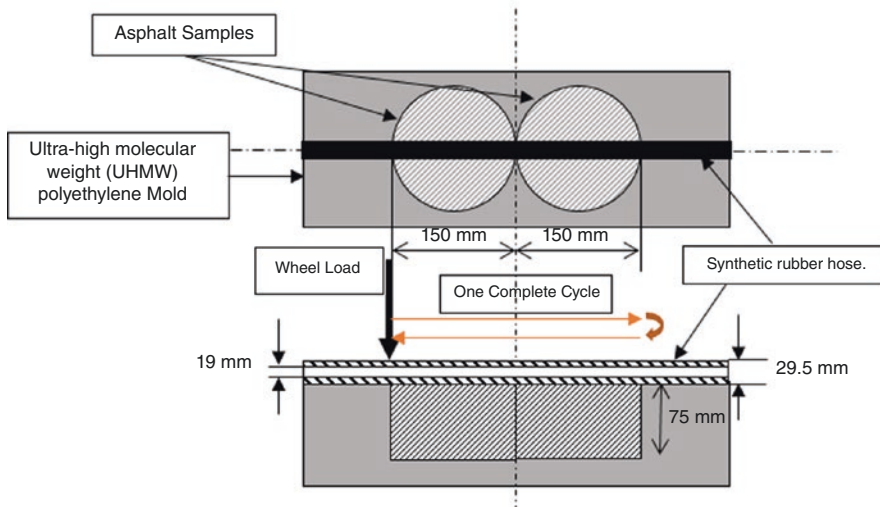
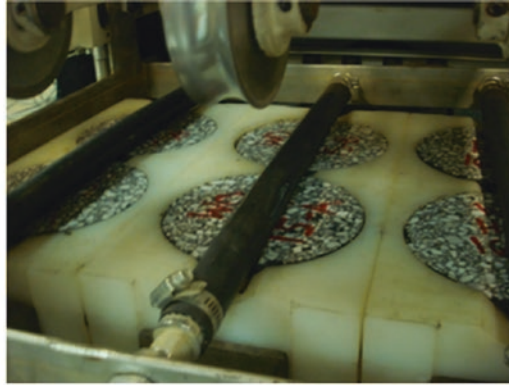
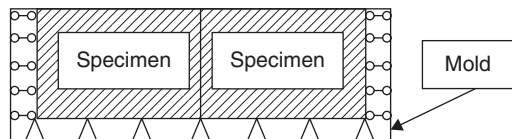


Fig. 2 Asphalt pavement analyzer (APA) test settings

Fig. 3 Boundary conditions of the asphalt pavement analyzer (APA) test



while the nodes over the sidewalls of the specimens were restrained with rollers in the vertical direction only. The boundary conditions of the specimens are shown in Fig. 3.

The APA test is conducted simultaneously on identical pairs of cylindrical specimens. Therefore, only one specimen was considered for the analysis. Based on previously performed studies, a relatively coarse mesh is proved to produce a

satisfactory FE simulation model for the asphalt pavement specimens [14, 15]. After several trials, the mesh size was selected to be 15.0 mm, which has resulted in a total number of 3562 elements.

2.4 Task IV: Establishing the Loading Method

The wheel load in the APA test is 45.4 kg (100 lb), and the contact area between the wheel and the hose has an elliptical shape with dimensions of 50 × 13 mm.

The APA test requires applying 8000 load repetitions before the specimen’s rut depth reaches 20 mm. Otherwise, the test will be terminated at 20 mm rut depth. Simulating 8000 loading cycles will be very difficult and may not be feasible. Therefore, an alternative method based on the work done by Milne et al. [16, 17] was adopted. This method includes a modified time-based load function to represent the applied moving load to the test specimens as shown in Fig. 4 and Table 1.

Due to very intensive nature of load computations, only 100 loading cycles were examined initially in order to test the accuracy of the model. This was increased later to 200 loading cycles in order to achieve higher accuracy.

Fig. 4 Time-based load function

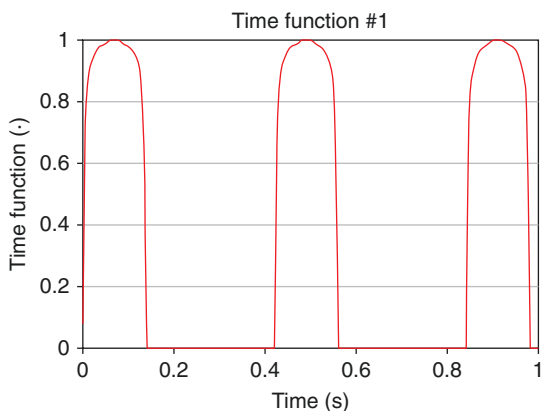


Table 1 Applicable stress inputs for ANSYS FE model with time-based load function

Stress direction	100% of maximum stress
Weight and tensioning tire surface:	
• Vertical stress zz	• 0.7 MPa (contact pressure = 100 psi)
• Lateral stress yy	• 0.105 MPa (15% of vertical stress zz)
• Rolling friction stress xx	• 0.0 (ignored due to its very small value)

2.5 Task V: Verifying the Model

The FEA results were verified against the experimental results obtained for three HMA different mixes. Statistical analysis was conducted to confirm the reasonableness of the obtained results and the variation among the three mixtures.

3 Results and Analysis

The aim of this study was to establish a well-validated FE model, which can be used to supplement the APA test in cases where APA device is not available. This model can easily predict the rutting behavior of the asphalt pavement in the field. In order to complete the model, laboratory tests were used to obtain the material models parameters, which were input to the ANSYS model.

3.1 Mechanical and Rutting Properties of the Evaluated Mixtures

The mechanical properties of the evaluated asphalt mixtures were extracted from the E^* master curves developed using the test results obtained from AASHTO T378 test standard. Three different hot-mix asphalt (HMA) mixtures were evaluated named as HMA, Advera, and Evotherm mixtures. HMA is a hot-mix asphalt mixture, while Advera and Evotherm are warm-mix asphalt (WMA) mixtures. The three HMA mixtures were designed according to South Dakota Department of Transportation (SDDOT) superpave requirements [1, 2]. The aggregate gradation used for the three mixtures and their mix design summaries are shown in Fig. 5 and Table 2, respectively. Table 3 presents a summary of the mechanical properties of the three mixtures at APA test temperature of (64 °C) [1, 2, 18].

The rutting performance properties were obtained using asphalt pavement analyzer (APA) tests. APA test was performed at the high temperature of asphalt PG (64-28), i.e., at 64 °C. The APA test results were used to establish a two-material plastic model. Figure 6 shows the APA test results, respectively, for the three asphalt mixtures [1, 2].

3.2 Power Law Model Results

As mentioned earlier, the rate-dependent general time-hardening creep model embedded in ANSYS was used to simulate the material plastic properties.

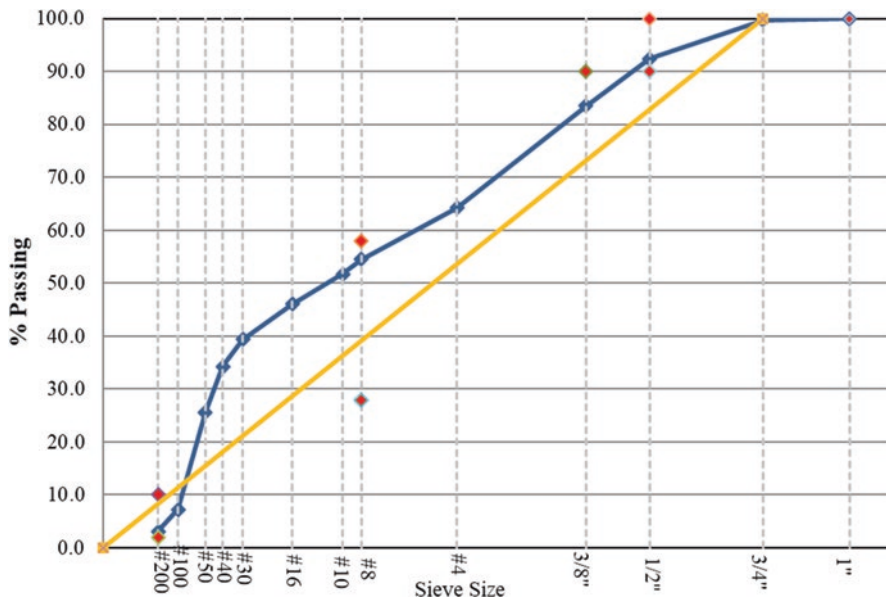


Fig. 5 Mixtures’ aggregate gradation [1, 2]

Table 2 Summary of mix designs [1, 2]

Properties	HMA	Advera	Evotherm	SDDOT Spec.
Aggregate type	Quartzite	Quartzite	Quartzite	–
Asphalt binder performance grade	PG 64-28	PG 64-28	PG 64-28	–
Nominal maximum aggregate size (mm)	19.0	19.0	19.0	–
Design binder content (%)	6.0	6.0	6.0	–
Mix/compaction temp. (°F)	325/300	250/225	250/225	–
Max theoretical specific gravity (G_{mm})	2.415	2.415	2.415	–
% G_{mm} at N_{des}	95.5	95.5	95.5	96 (±0.5)
VMA (%)	17.08	16.76	17.01	14.0% min.
VFA (%)	73.33	75.04	73.71	65–78
Dust proportion (P0.075/P _{bc})	0.72	0.72	0.72	0.6–1.4

Table 3 Summary of the mechanical properties of the evaluated mixtures at 64 °C [1, 2]

Property	Mix type		
	HMA	Advera	Evotherm
Loading frequency (Hz)	1.20	1.20	1.20
Dynamic modulus E^* (MPa)	67.57	72.40	71.71
Poisson’s ratio	0.35	0.35	0.35

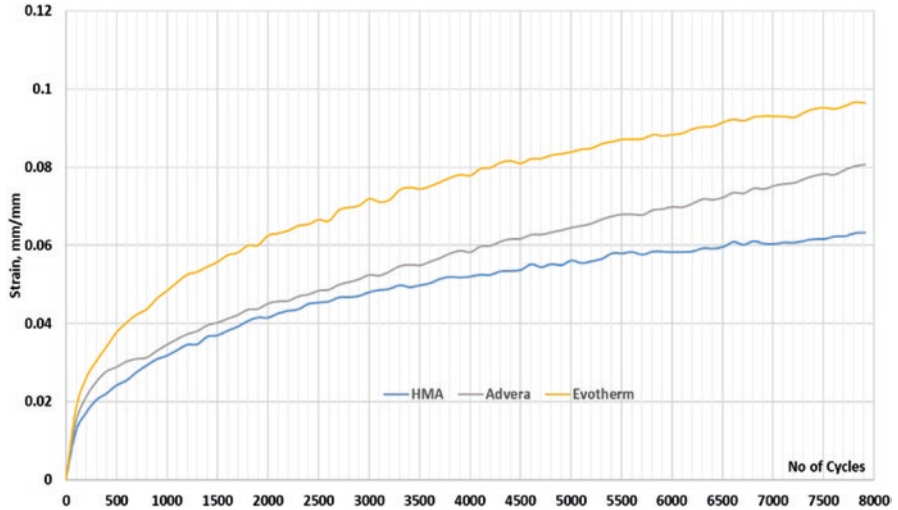


Fig. 6 APA test results for HMA (left), Advera (middle), and Evotherm (right) mixtures [1, 2]

Table 4 Power law model parameters

Constant	Mix type		
	HMA	Advera	Evotherm
C ₁	0.0088	0.0319	0.0032
C ₂	2.6871	3.6386	1.8831
C ₃	0.3283	0.3991	0.3389
C ₄	0	0	0

In order to eliminate the temperature effect, all mechanical parameters were entered at the given APA test temperature, and the model parameter C₄, which accounts for temperature effects, was set to 0. The remaining model constants, C₁–C₃, were obtained by optimizing the APA test results using the least-square optimization method. Table 4 represents the optimization results for the power law model.

3.3 Strain Results

Figure 7 illustrates the obtained strain results from the FE ANSYS simulation at 100 and 200 loading cycles compared to the actual measured strain from the APA test.

As it can be seen from Fig. 7, ANSYS results are very close to the actual measured ones from the APA test. Additionally, by looking at the deformation values obtained from both APA test and FE analysis, listed in Table 5, it can be seen that

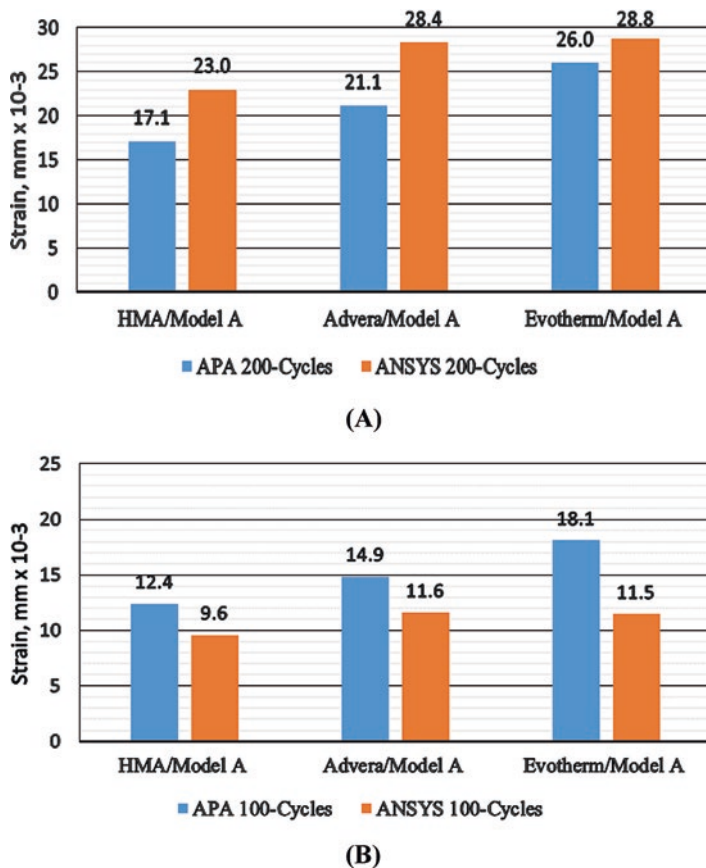


Fig. 7 Strain data analysis after 100 (a) and 200 (b) loading cycles

for some of the ANSYS strain values, it might appear that the percent of error values is higher than normal; however, this is acceptable when comparing micro strain values. The strains in this study vary between 9.1×10^{-3} and 18.1×10^{-3} for the case of 100 loading cycles and between 17.1×10^{-3} and 28.8×10^{-3} for the case of 200 loading cycles.

Figure 8 illustrates final deformed specimen of HMA after completing the FE ANSYS analysis at 200 cycles versus a typical deformed specimen from the APA test. It can be seen that the deformed pattern obtained by FE ANSYS analysis is identical to the one resulted from APA test.

Table 5 Deformation analysis of the evaluated mixtures

Mix type	Cycle/time (s)	APA, average deflection (mm)	ANSYS average deflection (mm)	Error (%)
HMA	100	0.93	0.94	0.57
	200	1.28	1.49	15.69
Advera	100	1.11	0.75	33.06
	200	1.59	1.76	11.03
Evotherm	100	1.36	1.03	23.94
	200	1.95	1.84	5.54

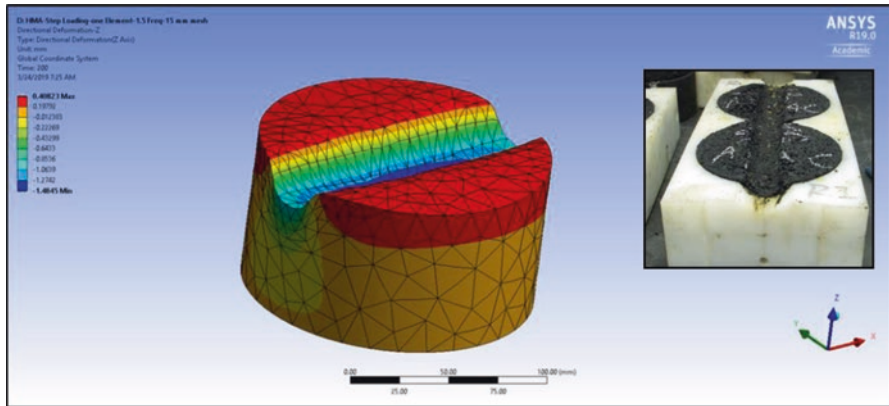


Fig. 8 Deformed HMA specimen after FE ANSYS analysis

4 Summary of the Findings

In general, the FE simulation of the rutting behavior for asphalt pavement was successfully completed using the commercial software package ANSYS 19.0.

4.1 Conclusions

The conclusions of the study can be listed as follows:

- Power law model provides more accurate results, which is similar to the APA-obtained ones (compressive) when modeling the creep in asphalt.
- A reasonably sized coarse mesh can be used for this simulation to accelerate the analysis time without compromising the accuracy of the results.
- Minimum loading cycles required for this simulation is 200, and a haversine load function can be used to simulate the load.

- A successful FE model was able to predict the rutting performance of different asphalt mixtures at various temperatures. The one variable in each FE model is the dynamic modulus (E^*), which can be extracted using the E^* -master curve at the required temperature and frequency.
- The temperature effect can be covered by inputting the dynamic modulus (E^*), at the required test temperature.
- This model can be used as a rapid inexpensive substitute for cumbersome laboratory techniques.

4.2 Recommendations for Future Work

Similarly, other pavement structural behaviors can be simulated using the same FE procedure presented in this study. As an example, the AASHTO T 321 test, “Determining the Fatigue Life of Compacted Hot-Mix Asphalt (HMA) Subjected to Repeated Flexural Bending,” can be simulated using the fatigue tool in ANSYS software package. The data obtained from the lab test can be compared with the FE analysis results obtained from ANSYS model.

Acknowledgments The authors of this paper would like to acknowledge the great support of the Australian College of Kuwait in sponsoring this research study.

References

1. Ahmed TA (2011) Laboratory evaluation of warm mix asphalt mixtures in South Dakota, USA. MSc Thesis, University of Nevada, Reno
2. Ahmed TA, Hajj EY, Sebaaly PE, Majerus N (2013) Influence of aggregate source and warm-mix technologies on the mechanical properties of asphalt mixtures. *Adv Civil Eng Mater* 2(1):1–19
3. Pavement Interactive. Pavement management, pavement distresses, flexible pavement distress, rutting. <http://www.pavementinteractive.org/article/rutting/>. Accessed Oct 2017
4. Brown ER, Kandhal PS, Zhang J (2001) Performance testing for hot mix asphalt. NCAT Report No. 01-05. National Center for Asphalt Technology, Auburn
5. Pavement Interactive. HMA performance tests. <http://www.pavementinteractive.org/article/hma-performance-tests/>. Accessed Oct 2016
6. Cooley LA, Kandhal PS, Buchanan MS, Fee F, Epps A (2000) Loaded wheel testers in the United States: state of the practice. NCAT Report No. 2000-4. National Center for Asphalt Technology, Auburn
7. Zaghoul S, White T (1993) Use of a three-dimensional, dynamic finite element program for analysis of flexible pavement. *Transp Res Rec* 1388:60–69
8. Cho YH, McCullough BF, Weissmann J (1996) Considerations on finite-element method application in pavement structural analysis. *Transp Res Rec* 1539:96–101
9. Bahia HU, Zhai H, Bonnetti K, Kose S (1999) Non-linear viscoelastic and fatigue properties of asphalt binders. *J Assoc Asphalt Paving Technol* 68:1–34

10. AASHTO T378 (2017) Standard method of test for determining the dynamic modulus and flow number for asphalt mixtures using the asphalt mixture performance tester (AMPT). American Association of State Highway and Transportation Officials, Washington, DC
11. ANSYS, Inc (2017) ANSYS mechanical APDL material reference. Release 18.1
12. Al-Qadi IL, Xie W, Elseifi MA (2008) Frequency determination from vehicular loading time pulse to predict appropriate complex modulus in MEPDG. In: Annual meeting, Association of Asphalt Paving Technologists, 2008, Philadelphia, vol 77, pp 739–772
13. AASHTO T 340 (2017) Standard method of test for determining rutting susceptibility of hot mix asphalt (HMA) using the asphalt pavement analyzer (APA). American Association of State Highway and Transportation Officials, Washington, DC
14. Wang Y (2007) Digital simulative test of asphalt mixtures using finite element method and X-ray tomography images. PhD (Doctor of Philosophy) thesis, Virginia Polytechnic Institute and State University
15. MILAD Ghorban Ebrahimi (2015) Investigation of viscoelastic behaviour and permanent deformation modelling for New Zealand hot mix asphalts. PhD (Doctor of Philosophy) thesis, University of Canterbury
16. Milne TI, Huurman M, van de Ven MFC, Jenkins KJ, Scarpas A, Kasbergen C (2004) Towards mechanistic behaviour of flexible road surfacing seals using a prototype FEM Model. In: Proceedings of the 8th Conference on asphalt pavements for Southern Africa (CAPSA'04), Sun City, South Africa, September, 2004
17. Milne T, Jenkins K (2005) Towards modelling road surfacing seal performance: performance testing and mechanistic behavioural model. *J South Afr Inst Civil Eng* 47(3):2–13
18. Ahmed TAH (2014) Investigating the rutting and moisture sensitivity of warm mix asphalt with varying contents of recycled asphalt pavement. PhD (Doctor of Philosophy) thesis, University of Iowa

Design and Manufacturing a Miniature Reynolds Apparatus for Testing Nanofluids



Ahmad Sedaghat, Hayder Salem, Seyed Amir Abbas Oloomi, Leila Borvayeh, Masoud Rashidi, Abbas Amini, Samira Ghafoori, Jessica Cheska Lopez, and Girish Kaimal Mohanan

1 Introduction

In the ongoing research in the oil and gas industry, reservoirs, pipelines, and pumping equipment are susceptible to precipitation of particles and chemicals that can reduce the life cycle and increase maintenance times and costs. There is a continuous demand for decreasing friction of fluids on pipelines and rotating systems to improve efficiency and increase the life cycle of systems particularly those with moving parts. In addition, the energy loss in countless growing engineering systems has raised concerns for supplying energy demands in the near future. It is an attractive field of research for cutting costs and increasing the life cycle of equipment in the oil and gas industry while reducing energy consumption. Nanoparticles may play an important role to reduce friction and wear of fluid in pipes and also moving parts in well drilling and bearing systems and also to enhance heat transfer efficiency of such systems.

In drilling fluids which are oil-based mud (OBM) and water-based mud (WBM), the nanoparticles can be added as lubrication additives. The most common drilling

A. Sedaghat (✉) · H. Salem · A. Amini
Mechanical Engineering Department, Australian College of Kuwait, Kuwait, Kuwait
e-mail: a.sedaghat@ack.edu.kw

S. A. A. Oloomi
Department of Mechanical Engineering, Yazd Branch, Islamic Azad University, Yazd, Iran

L. Borvayeh
Mathematics Department, Australian College of Kuwait, Kuwait, Kuwait

M. Rashidi · S. Ghafoori
Petroleum Engineering Department, Australian College of Kuwait, Kuwait, Kuwait

J. C. Lopez · G. K. Mohanan
Fluid Mechanics Laboratory, Australian College of Kuwait, Kuwait, Kuwait

fluid is the OBM since it provides improved lubrication compared to WBM [1]. This is due to the nonpolar properties of oil which allow the particles to move without any attraction or repulsion, whereas WBM is naturally ionic and charged which makes it a less desirable lubrication [2].

In general, the skin friction in pipeline systems may affect the efficiency and performance of the system. To save energy, the skin friction must be reduced. In order to do such process, many solutions have been proposed [3]. The common solution for reducing the skin friction in the engineering field is to improve rheological properties of lubricants.

The application of various nanoparticles showed improvement in the plastic deformation, temperature distribution, and friction effects. Many experimental studies revealed wear and friction reduction effects of nanofluids [4, 5], using metal [6–8], metal oxides [9, 10], and nonmetal [11–13] nanoparticles.

Pottuz et al. [14] have used carbon nanotubes in poly α -alpin oil. Scanning electron microscopy (SEM) with high-quality imaging was used to study characteristics of carbon nanotubes. The study showed that the anti-wear properties of nanotube particles under boundary lubrication condition and with laminar flow regime were better than graphite powder. Lee et al. [15] conducted experiments on friction characteristics of graphite nanoparticle-based fluids ($0.00022 \text{ m}^2/\text{s}$ at $40 \text{ }^\circ\text{C}$). It was observed that the friction factor was reduced.

Hwang et al. [16] investigated the effect of shape and size of different nanoparticles in mineral oils. The nanoparticles studied were graphite, graphite nanofibers, carbon black, and carbon nanotubes. It was observed that using spherical shapes of particles has significantly decreased the friction factor. It was suggested that these nanoparticles play a rule on prevention of direct contact of surfaces. But the fiber nanoparticles were reported to result in unfavorable effects on friction factor where friction forces occur at contact surfaces of mechanical systems such as rings, disks, and bearings.

Jahns [2] conducted experimental studies on friction reduction by using nanoparticles such as alumina, titania, and silica in drilling mud, and the effect of nanoparticles on friction and wear was reported. Different volumetric concentrations of nanofluid at different temperatures were investigated to examine lubrication efficiency of the drilling mud. The experimental measurements were conducted using pin on disk apparatus and modular compact rheometer (MCR) to measure metal-to-metal friction factor. In pin on disk experiments, results showed that the titania and silica nanofluids decreased the friction factor by 47%, whereas the alumina nanofluid effect was not significant. In general, it is believed that nanoparticles affect the friction by acting as ball bearings between the surfaces or create slipping films between the surfaces in contact [17].

The objectives of this project are to design, manufacture, test, and calibrate a Reynolds apparatus to study nanofluid flows in laminar and turbulent flows, to measure precipitation effects, and to measure skin friction reduction in flows inside a transparent pipe. Two pressure sensors may be used to determine skin friction and also effects of nanoparticle precipitation. The system should operate for a long time

duration, and time series of pressure and temperature data should be stored using a microprocessor such as Arduino. All components should be high quality and capable of long-run operation. The accumulation of nanoparticles and growth of them on the tube surface will be evaluated from the data.

In this paper, first a miniature tube viscometer (Reynolds apparatus) is built to measure rheological properties of nanofluids at low-speed laminar flows using very small amount of nanofluid of order of milliliters. The Reynolds apparatus will then be applied for turbulent flows. CFD simulations are explained here for the designed system to assess accuracy of the miniature Reynolds apparatus. An in-house MATLAB code is also developed for solving governing laminar non-Newtonian fluid equations using the pressure and flow rate measurements.

2 Rheological Properties of Nanofluids

The flow of non-Newtonian fluids in industrial applications is widely encountered, such as in food or/and petroleum industry. These fluids are transported via pipelines, where pressure drop is observed. Reducing the skin friction can be achieved by improving rheological properties of lubricants. One approach is by utilizing nanoparticles in pipelines and lubrication systems. Ghazvini et al. [18] investigated the effects of utilizing nanodiamond as an additive to engine oil in laminar pipe flow. The pressure-drop measurements showed significant increase due to addition of nanopowder to engine oil. Esmailzadeh et al. [19] experimentally investigated the hydrodynamics and heat transfer characteristics of γ - Al_2O_3 /water under laminar flow inside a horizontal tube. No significant change of friction factor for nanofluids in comparison with base fluid was found.

Lin et al. [20] conducted numerical simulations of polyalphaolefins- Al_2O_3 nanofluids containing cylindrical nanoparticles in a laminar pipe flow by solving the Navier–Stokes equation with term of cylindrical nanoparticles. They found that the relationships between the friction factor and the nanoparticle volume concentration as well as particle aspect ratio are dependent on the Reynolds number. They continued their study for turbulent flow [21]. They found that friction factors increase with the increase of particle volume concentrations and particle diameter and with the decrease of Reynolds number.

Boertz et al. [22] and Minakov et al. [23] experimentally studied the rheological behavior of nanofluids based from consideration of several tens of nanofluids based on water, ethylene glycol, and engine oil, containing particles of different oxides and diamond. In some cases, it was shown that when increasing nanoparticle concentration, rheological behavior of nanofluids becomes non-Newtonian and is well described by power law fluid models or Herschel–Bulkley fluids. They have also studied the influence of nanoparticle size and material, as well as the nature of the base fluid on the rheological behavior of nanofluids.

3 Methodology

The objectives of this project are to design, manufacture, test, and calibrate a miniature Reynolds apparatus to measure pressure drop across a transparent pipe. A typical Reynolds apparatus and measuring equipment has high capacity of 40 L for the constant head tank and 60 L of sump tank.

In this project, the volume of fluid in the tank should be 1 L or lower to minimize the required nanoparticles materials for testing up to 5% volumetric concentration. Pressure drops in laminar and turbulent nanofluid flows are measured using sensors at the beginning and end of the transparent tube. A temperature sensor will be utilized for changes of temperature over time in long run of the system. The effects of nanoparticles in reducing skin friction and the coagulations effects of nanoparticles to the tube surface will be investigated. An additional feature may be added such as study two-phase flows by adding a compressor to supply air into water stream in the tube. Then, nanofluids in single- and two-phase flows may be investigated. The goal of this project at first is to measure rheological properties of nanofluids. The viscosity of nanofluids, precipitation of nanoparticles to the tube surface, and the skin friction coefficient reduction of nanofluid flows are of major interest in this project.

Further studies revealed that a peristaltic pump could operate with very little liquid and provide small flow rate of 0–15 L/h, to provide laminar flow in a 4 mm acrylic-polyvinyl chloride “acrylic-pvc” tube. A 6 V DC dosing peristaltic pump with flow rate of 0–100 mL/min and rotational speed of 0.1–100 rpm was selected. However, this tiny pump heats up quickly and cannot be used for long run. Two-diameter-size acrylic-pvc tubes of 4 and 8 mm were purchased. Figure 1 shows the pipe length and pipe diameters for a total volume of 500 mL. As it can be seen, for a pipe diameter of 4 mm, the length of pipe can reach 40 m to be filled with 500 mL, and for a pipe diameter of 8 mm, the length of pipe can reach 10 m. In building the Reynolds apparatus, we may use up to 5-m-long tubes; therefore, the amount of nanofluid can be less, keeping in mind that the same amount of liquids should remain in the container tank for pumping. 3D prints are used to produce pressure ports and also pipe supports (see Figs. 13, 14 and 15 in Appendix).

In order to produce fully developed laminar and turbulent pipe flows, the measurement section must be well away from the entry section of the pipe. Munson et al. [24] suggested the following entry length formulas for laminar and turbulent flows:

$$\frac{L}{D} = 0.06 \text{ Re} \quad \text{for laminar flows} \quad (1)$$

$$\frac{L}{D} = 4.4 (\text{Re})^{1/6} \quad \text{for turbulent flows} \quad (2)$$

In Eqs. (1) and (2), L (m) is the pipe length, D (m) is the pipe diameter, and Re is the Reynolds number defined by

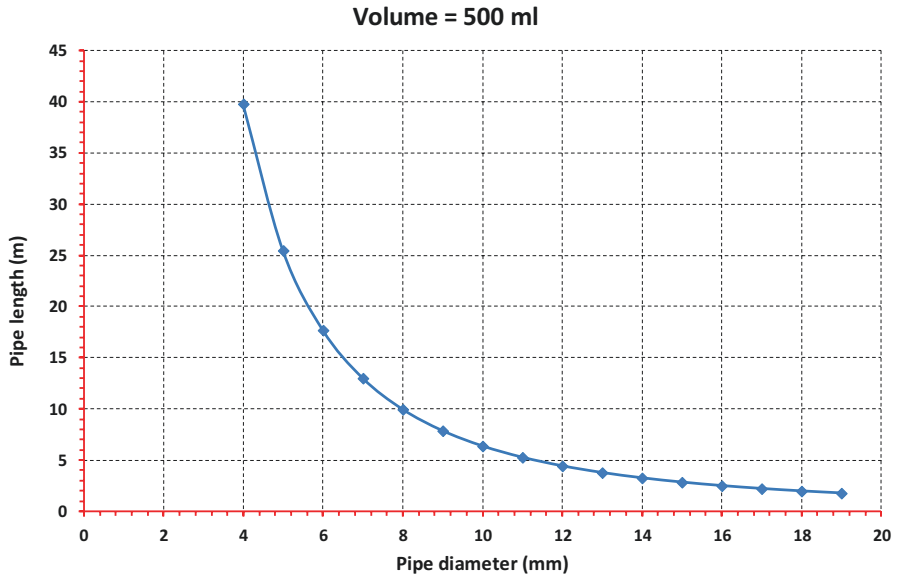


Fig. 1 Variation of length of pipe versus pipe diameter

$$Re = \frac{\rho V D}{\mu} \tag{3}$$

In Eq. (3), ρ (kg/m³) is the fluid density, V (m/s) is the fluid velocity, D (m) is the pipe diameter, and μ (Pa s) is the dynamic or molecular viscosity. Reynolds number is a dimensionless number widely used in fluid dynamics.

The required entry lengths for fully developed laminar flows in 4 and 8 mm pipes are shown in Fig. 2. As observed in Fig. 2, the entry length is about 0.5 m for pipe diameter of 4 mm and about 1.0 m for the pipe diameter of 8 mm. Figure 3 shows the turbulent entry lengths for 4 and 8 mm pipe flows for Reynolds numbers from 3000 to 10⁵. These lengths are much lower than the laminar pipe flows as seen in Fig. 3. Hence, the pipe diameter 4 mm may be used for laminar flow measurements, while pipe diameter 8 mm may be used for turbulent flows.

On this basis, two acrylic pipes with length of 2 m and inner pipe diameters of 4 and 8 mm were purchased. For both of the tubes, after the first meter of the pipe with distance of 20 cm, four small holes sizes of 0.5 mm are created using controlled drilling speeds to ensure smooth and scratch-free inner surfaces. This allows liquids to diffuse out of the main stream pipe for pressure measurements (see Appendix). In this sense, the pipes flows are free from disturbances of any measuring device.

The pressure drop for laminar flows can be obtained by [24]

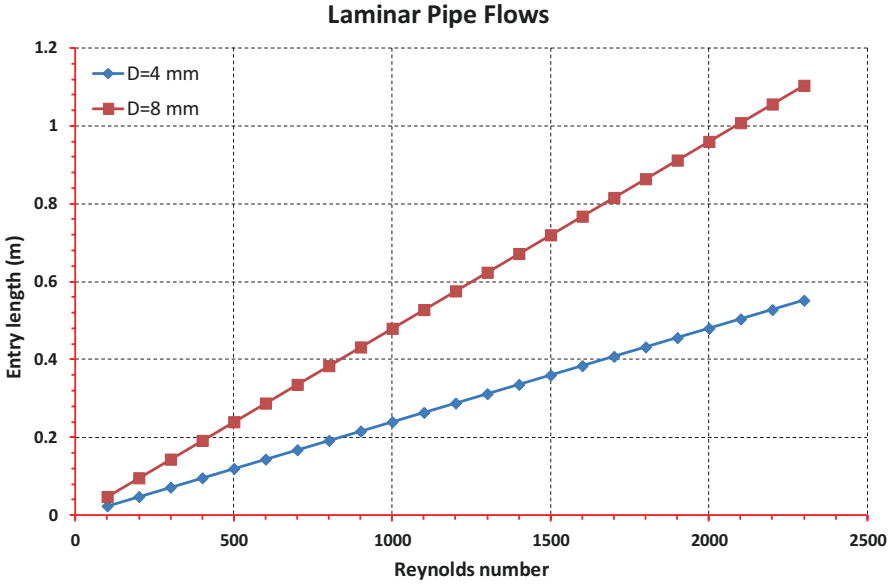


Fig. 2 Laminar entry lengths versus Reynolds number for 4 and 8 mm pipe diameters

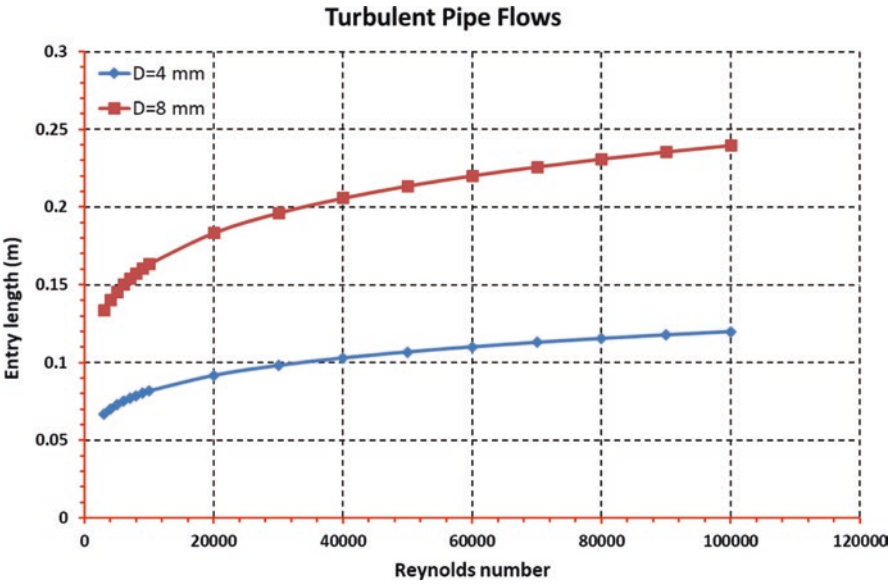


Fig. 3 Turbulent entry lengths versus Reynolds number for 4 and 8 mm pipe diameters

$$\Delta p = \frac{1}{2} \rho V^2 \left(f \frac{L}{D} \right) \quad f = \frac{64}{\text{Re}} \quad \text{for laminar flows} \quad (4)$$

In Eq. (4), Δp (Pa) is the pressure drop due to fluid friction with the inner pipe wet surfaces, ρ (kg/m³) is the fluid density, V (m/s) is the fluid velocity, D (m) is the pipe diameter, L (m) is the length of the pipe, f is the friction factor, and Re is the Reynolds number.

For the $L = 200$ mm and $D = 4$ mm, the pressure drops in laminar Newtonian fluid flows are calculated and shown in Fig. 4. As seen in Fig. 4, the pressure varies within a range of 100 Pa. For non-Newtonian fluids and also nanofluids, this may differ, so a pressure sensor with the range and accuracy of 150 ± 1 Pa may be suitable for our application.

For the $L = 200$ mm, $D = 8$ mm, and assuming a very smooth pipe, the pressure drops in turbulent fluid flows are calculated by Eq. (5) using the Colebrook equation for the friction factor, f , given by [24]

$$\frac{1}{\sqrt{f}} = -2.0 \log \left(\frac{\varepsilon/D}{3.7} + \frac{2.51}{\text{Re} \sqrt{f}} \right) \quad \text{for turbulent pipe flows} \quad (5)$$

In Eq. (5), ε (m) is the pipe inner surface roughness, D (m) is the inner pipe diameter, and Re is the Reynolds number. The roughness for drawn tubing, glass, and plastic is usually taken 0.0015–0.01 mm.

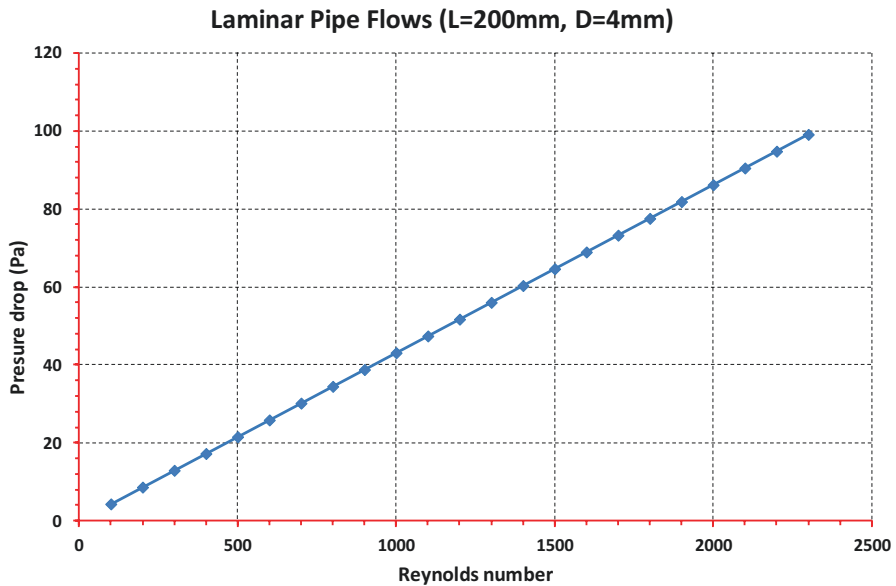


Fig. 4 Pressure drop in laminar pipe flows for $L = 200$ mm and $D = 4$ mm

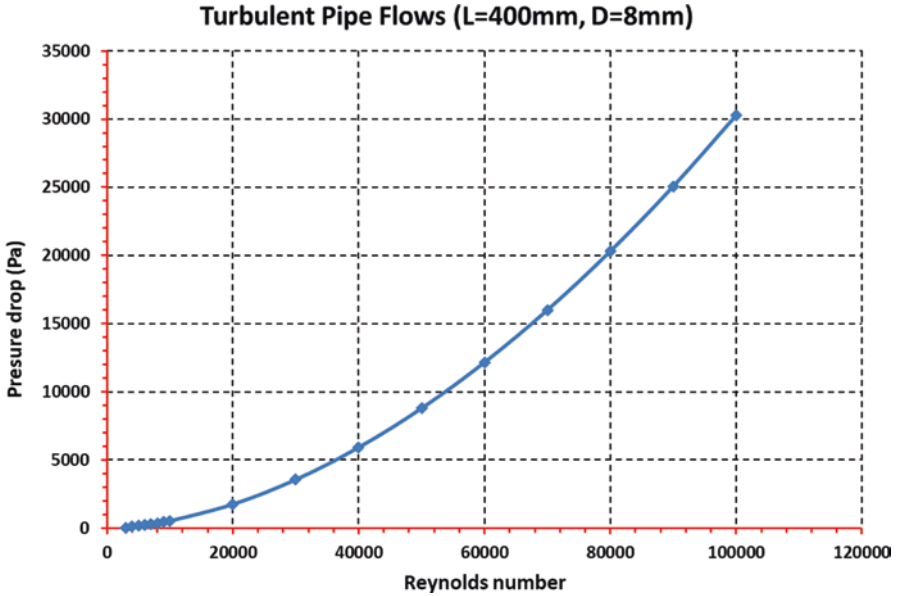


Fig. 5 Pressure drop in turbulent smooth pipe flows for $L = 200$ mm and $D = 8$ mm

As shown in Fig. 5, we may need a different pressure sensor with a range of 15 kPa for Reynolds numbers from 3000 up to 10^5 .

Furthermore, in our design we did not use any valves to control flow rate which may cause distortion to the flow stream; instead an electric controller is used to control the speed of the peristaltic pump. Figure 6 shows the schematic of the designed Reynolds apparatus for testing nanofluids.

The developed Reynolds apparatus can be used for multiple purposes. The present research has focused on determining rheological properties of Newtonian and non-Newtonian laminar nanofluid flows. CFD simulations and the developed in-house MATLAB code are explained in the next sections. An Arduino code was calibrated for the flow meter to correctly measure flow rates. The pressure sensors were tested with its calibrator (shown in Fig. 16 Appendix). Work is in progress to design customized sensors for this tiny application.

4 Results and Analysis

4.1 Fluid Models

The fluid behavior of non-Newtonian fluids may be best described by the Herschel–Bulkley (H-B) model given by [25]

$$\tau = \tau_0 + K \dot{\gamma}^n \quad \text{Herschel–Bulkley model} \quad (6)$$

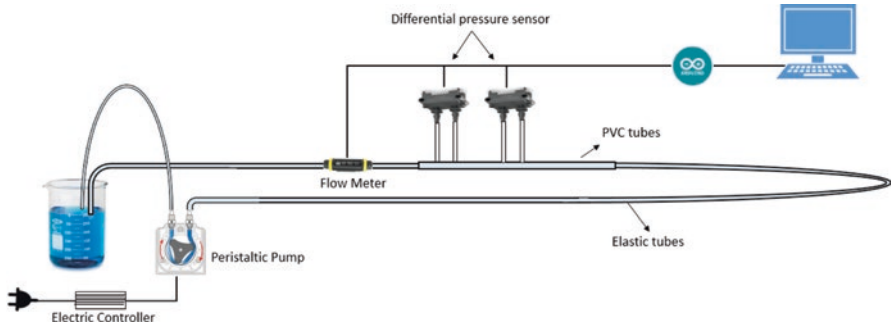


Fig. 6 Schematic of the developed Reynolds apparatus

In this model, τ (Pa) is the fluid shear stress, τ_0 (Pa) is the fluid yield stress or yield point, K (Pa s^{*n*}) is the viscosity coefficient, $\dot{\gamma}$ (s⁻¹) is the fluid strain rate, and n is the power law constant.

For the power law model for non-Newtonian fluids, by setting $\tau_0 = 0$, the H-B model is simplified to [25]

$$\tau = K\dot{\gamma}^n \quad \text{Power law model} \tag{7}$$

For $0 < n < 1$, the power law fluid is called pseudoplastic, and for $n > 1$, the fluid is called dilatants.

For $n = 1$ and $K = \eta$, the H-B model reduces to non-Newtonian fluids called Bingham plastic described by [25]

$$\tau = \tau_0 + \eta\dot{\gamma} \quad \text{Bingham plastic model} \tag{8}$$

In Eq. (8), η (Pa s) is called the apparent viscosity.

By setting $\tau_0 = 0$ and $K = \mu$, the well-known Newtonian fluid model is obtained:

$$\tau = \mu\dot{\gamma} \quad \text{Newtonian fluid model} \tag{9}$$

In Eq. (9), μ (Pa s) is the dynamic or molecular viscosity.

The objective of this study is to find the rheological characteristics of all the fluid models described by τ_0 , K , and n . This is the ultimate goal of any viscometer to obtain these three terms accurately for any type of fluids. This can be achieved by measuring pressure drops and flow velocity and solving the laminar flow equations described in the next subsection.

4.2 Laminar Fluid Flows

The shear stress on the wet inner surface of pipe flows is expressed by the dimensionless Darcy–Weisbach friction factor as follows [25]:

$$\tau = \left(\frac{1}{8} \rho V^2 \right) f \quad \text{Darcy–Weisbach friction factor} \quad (10)$$

In Eq. (10), for laminar Herschel–Bulkley (H-B) fluid flows, the Darcy–Weisbach friction factor is rewritten by [25]

$$f = \frac{64}{\psi \text{Re}} \quad \text{Friction factor for laminar Herschel–Bulkley (H-B) fluid flows} \quad (11)$$

In Eq. (11), Re is the generalized Reynolds number for the H-B fluid flows redefined by [25]

$$\text{Re} = \frac{8\rho V^{2-n} D^n}{K} \left(\frac{n}{2(1+3n)} \right)^n \quad \text{The generalized Reynolds number} \quad (12)$$

and the Reynolds factor ψ is given by [25]

$$\psi = (1+3n)^n (1-\xi_0)^{1+n} \left[\frac{(1-\xi_0)^n}{(1+3n)} + \frac{2\xi_0(1-\xi_0)}{(1+2n)} + \frac{\xi_0^2}{(1+n)} \right]^n \quad \text{The Reynolds factor} \quad (13)$$

In Eq. (13), ξ_0 is the dimensionless form of the yield stress given by [25]

$$\xi_0 = \frac{\tau_0}{\left(\frac{1}{2} \rho V^2 \right) f} \quad \text{The dimensionless yield stress} \quad (14)$$

Provided from the experimental apparatus three measurements for the friction factor, (f_1 f_2 f_3), and flow velocities (V_1 V_2 V_3), one can numerically solve for three fluid unknowns K , n , and τ_0 . This has been done by an in-house developed MATLAB code provided in the Appendix. By careful selection of initial values for three rheological properties of H-B fluid flows, i.e., K , n , and τ_0 , a set of three non-linear equations are solved by MATLAB for providing the converged values for the three unknowns.

5 CFD Simulations

A number of flow simulations were conducted for Newtonian water-based fluids using different nanoparticle size Al_2O_3 at different volumetric concentrations, although the results for the non-Newtonian nanofluids are only presented here.

5.1 Non-Newtonian Fluid Flow Simulations

The Bingham non-Newtonian laminar fluid flows are simulated here with Al_2O_3 nanoparticles at different volume concentrations of 0.04 and 0.06 in ANSYS Fluent. The pipe flow simulations are carried out for a smooth pipe with length of 2 m and inner diameter of 4 mm. The base fluid for the Bingham non-Newtonian fluid is ethylene glycol. The laminar Reynolds numbers of 500, 1000, and 1600 are investigated, and the results are presented here.

For the Bingham non-Newtonian nanofluids, the fluid properties are determined as follows:

$$\rho_{\text{nf}} = (1 - \phi)\rho_f + \phi\rho_p \quad \text{The density of nanofluid} \quad (15)$$

In Eq. (15), ρ_{nf} (kg/m^3) is the density of nanofluid, ϕ is the volume concentration, ρ_f (kg/m^3) is the density of the base fluid, and ρ_p (kg/m^3) is the density of nanoparticles.

$$(\rho C_p)_{\text{nf}} = (1 - \phi)(\rho C_p)_f + \phi(\rho C_p)_p \quad \text{The heat capacity of nanofluid} \quad (16)$$

Here, C_p ($\text{J}/\text{kg K}$) is the heat capacity.

The viscosity of nanofluids is determined by [26].

$$\frac{\mu_{\text{nf}}}{\mu_f} = 1 + \left(\frac{\rho_p V_b d_p^2}{72 N \delta} \right) \quad \text{The viscosity of nanofluid} \quad (17)$$

In Eq. (17), μ_{nf} (Pa s) is the viscosity of nanofluid, μ_f (Pa s) is the viscosity of the base fluid, and the rest of terms are given by [26].

$$V_b = \frac{1}{d_p} \sqrt{\frac{18k_b T}{\pi \rho_p d_p}} \quad \text{The free molecular speed of nanoparticles} \quad (18)$$

$$\delta = d_p \left[\frac{\pi}{6\phi} \right]^{1/3} \quad \text{The free molecular distance of nanoparticles} \quad (19)$$

$$N = (c_1\phi + c_2)d_p + (c_3\phi + c_4) \quad (20)$$

$$c_1 = -1.133 \times 10^{-6}, c_2 = -2.771 \times 10^{-6}, c_3 = 9.0 \times 10^{-8}, c_4 = -3.93 \times 10^{-7} \quad (21)$$

For the Bingham non-Newtonian fluid, the yield stress and the shear rate are set constant with the values of $\tau_0 = 0.38 \text{ Pa}$ and $\gamma (\text{s}^{-1}) = 20$, respectively. The thermo-physical properties of the base fluid and three different nanoparticles are given in Table 1.

Table 1 Thermophysical properties of the base fluid and some nanoparticles [27, 28]

Materials	ρ (kg/m ³)	C_p (J/kg k)	K (W/mk)	$\beta \times 10^{-5}$	σ (S/m)
Ethylene-glycol	1114	2415	0.252	57	5.5×10^{-6}
Copper oxide (CuO)	6510	540	540	0.85	5.96×10^7
Alumina (Al ₂ O ₃)	3790	765	765	0.85	3.5×10^7
Titania (TiO ₂)	4250	686.2	686.2	0.9	2.38×10^6

Table 2 Rheological properties of the Al₂O₃ nanofluid [23]

ϕ (%)	Al ₂ O ₃	
	τ_0 (mPa)	k_v (mPa s ⁿ)
4	121.8	57.67
6	382.3	140.0

Table 3 Friction factor for the Al₂O₃ nanofluid with nanoparticles size of 120 nm

Re	ϕ	f (analytical)	f (CFD)	ϕ	f (analytical)	f (CFD)
500	0.04	0.13	0.131907	0.06	0.1329	0.135479
1000	0.04	0.064	0.066895	0.06	0.065	0.067786
1600	0.04	0.04	0.042685	0.06	0.04048	0.043026

Table 4 Friction factor for the Al₂O₃ nanofluid with nanoparticles size of 150 nm

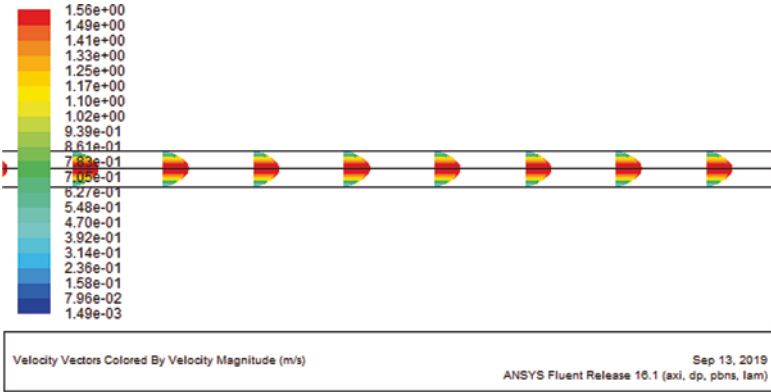
Re	ϕ	f (analytical)	f (CFD)	ϕ	f (analytical)	f (CFD)
500	0.04	0.129	0.131568	0.06	0.132	0.134601
1000	0.04	0.06425	0.06682	0.06	0.065	0.067565
1600	0.04	0.04	0.04266	0.06	0.04039	0.042942

Friction factors in Bingham non-Newtonian fluid are determined from Eq. (11) assuming the following factors listed in Table 2.

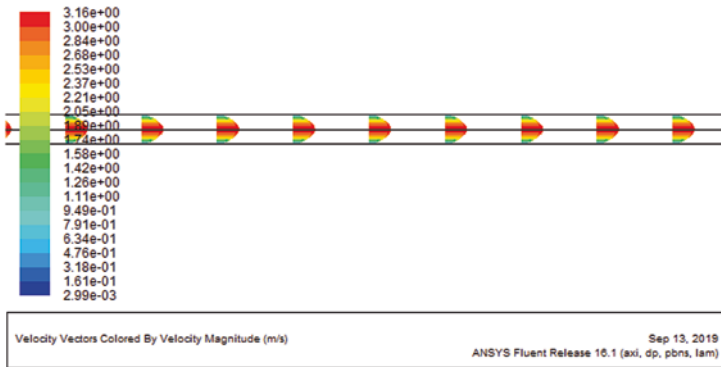
Results from the analytical expression in Eq. (11) for the friction factor, f (determine), are compared with the results from the ANSYS Fluent CFD simulations, f (CFD), in Tables 3 and 4 for nanoparticle sizes of 120 nm and 150 nm, respectively, and volumetric concentrations of 0.04 and 0.06.

The volume fraction of nanoparticles is related to the increased viscosity at high-volume fraction of nanoparticles. High values of the volume fraction cause the fluid to become more viscous which causes the velocity to attenuate accordingly. When the concentration increases, the nanoparticles make an agglomeration within the suspension. This consequently results in the increase of internal shear stress in nanofluid because of the greater force needed for dissipating the solid element of the dispersion and hence an increase in viscosity.

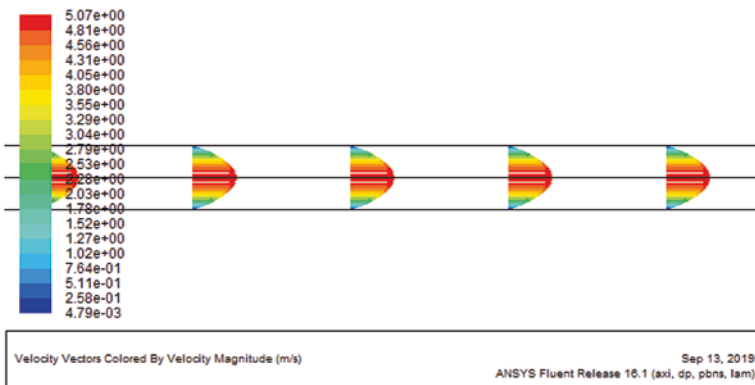
Figure 7 shows the velocity vectors for the non-Newtonian fluid condition of $D = 120$ nm and $\phi = 0.06$. The figure shows exact parabolic velocity profiles and the



(a)



(b)



(c)

Fig. 7 Velocity vectors for laminar non-Newtonian fluid flow condition of $D = 120$ nm and $\phi = 0.06$, (a) $Re = 500$, (b) $Re = 1000$, and (c) $Re = 1600$

no-slip condition on the pipe solid surface. Also, the fully developed condition is satisfied by showing the same velocity profiles across the length of tube.

Figure 8 shows pressure contours for the non-Newtonian fluid condition of $D = 120$ nm and $\phi = 0.06$. The pressure is uniform in each cross-section, and pressure drop across the tube is so marginal that no obvious distinction can be seen in change of contour colors. The results show also that the static pressure depends on Reynolds number and increases by increase of Reynolds number.

Figure 9 shows the velocity vectors for the non-Newtonian fluid condition of $D = 150$ nm and $\phi = 0.06$. Compared with Fig. 7, the same flow behaviors are observed except that the magnitude of maximum velocities in the center of tube was increased by increase of nanoparticle size from 120 to 150 nm. This may be correlated to increase of viscosity in the nanofluid with increased size of nanoparticles.

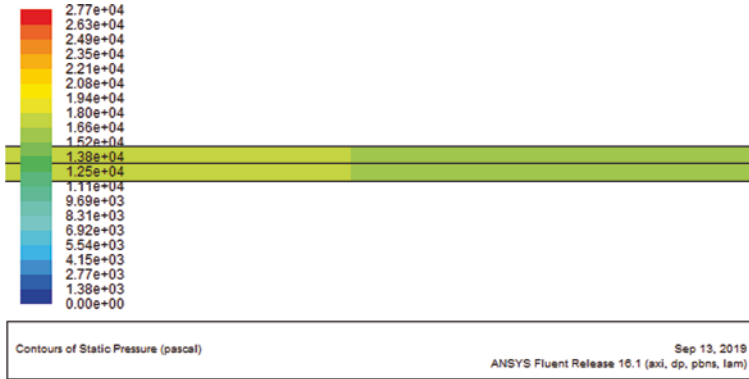
It can also be seen that the smaller particle sizes contribute to the compressed layer significantly more than the larger particles. This is due to the exceedingly increasing specific surface area of nanoparticles with decreasing size allowing for the formation of more nanostructure. However, with decreasing particle size at constant volume fraction, the rate of aggregation is increased due to the average interparticle distance decreasing, causing the effects of Van der Waals force to become more prominent (Figs. 7 and 9).

Figure 10 shows pressure contours, for the non-Newtonian fluid condition of $D = 150$ nm and $\phi = 0.06$. The same behavior is observed as seen in Fig. 8. However, by increased size of nanoparticles compared with Fig. 8, the static pressure has also increased. These changes are discussed with more detail in Figs. 11 and 12.

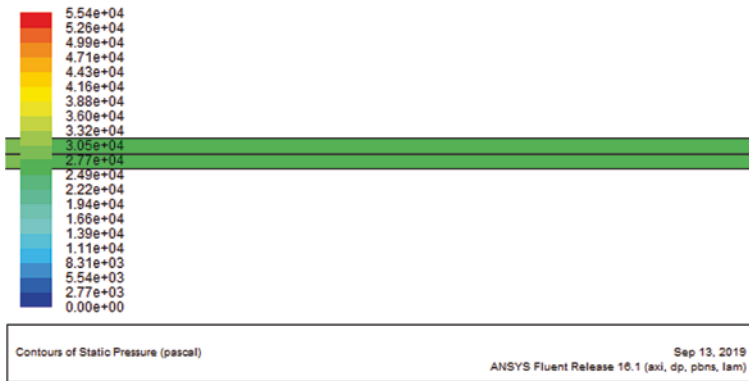
Figure 11 compares static pressure for the non-Newtonian fluid condition of $D = 120$ nm and $\phi = 0.06$ at different Reynolds numbers. It is observed that the pressure drops are linearly correlated with the length of the tube. The viscosity of nanofluids depends not only on the concentration of nanoparticles but also their size. Particles, starting from a certain critical size, actively interact with each other. In addition to this, the fluid near the nanoparticles is structured. Therefore, if nanoparticles are sufficiently small, the whole dispersion fluid is structured. For this reason, we should expect that a possible change of rheological behavior of nanofluids should depend also on the size of nanoparticles. Increasing the nanoparticle sizes increases interaction with each other and then increasing the static pressure as shown in Fig. 12.

6 Summary of Findings

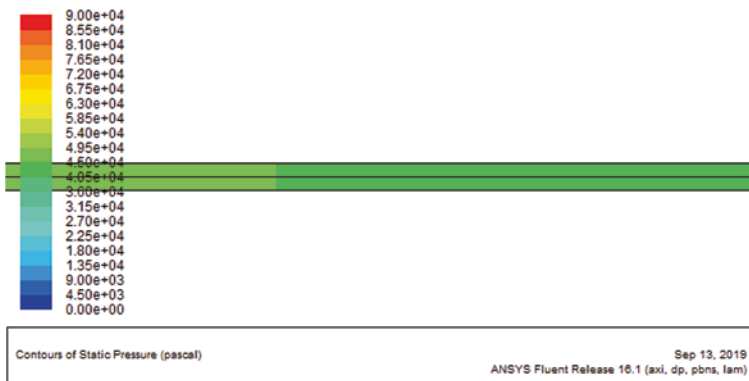
A miniature Reynolds apparatus has been designed and built to study rheological properties of Newtonian and non-Newtonian nanofluid flows in pipes. Initial 3D prints for pressure ports were found to be porous and not suitable to withhold fluid leakage; therefore, pressurized connecting ports were installed successfully to measure pressure drops in the pipe system with minimal interferences particularly for the laminar fluid flows. Custom-built pressure sensors are needed to measure very



(a)

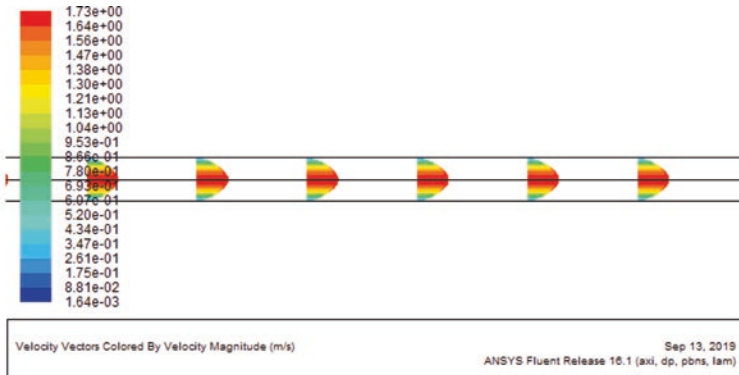


(b)

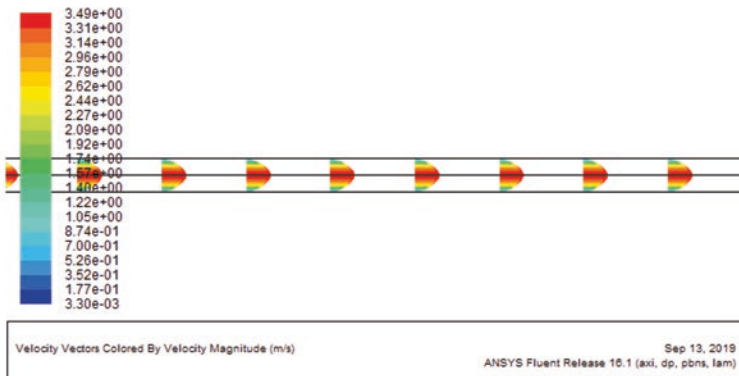


(c)

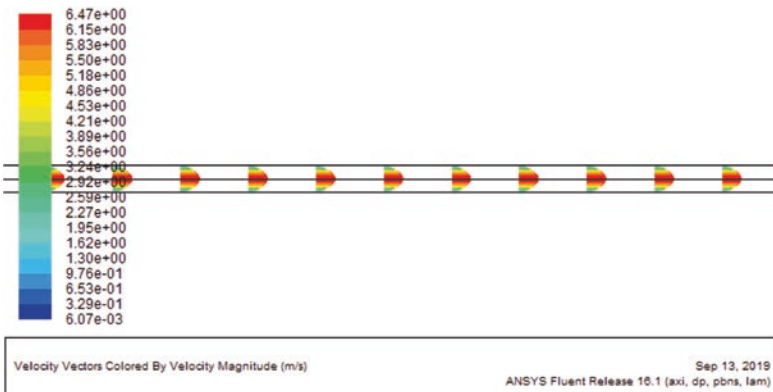
Fig. 8 Pressure contours for laminar non-Newtonian fluid flow condition of $D = 120$ nm and $\phi = 0.06$, (a) $Re = 500$, (b) $Re = 1000$, and (c) $Re = 1600$



(a)

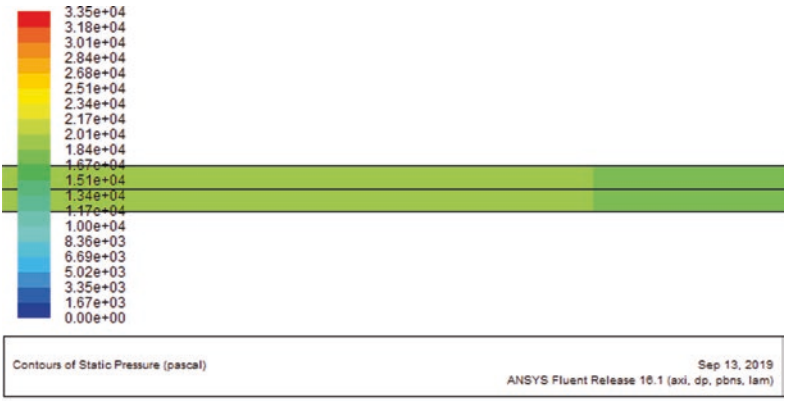


(b)

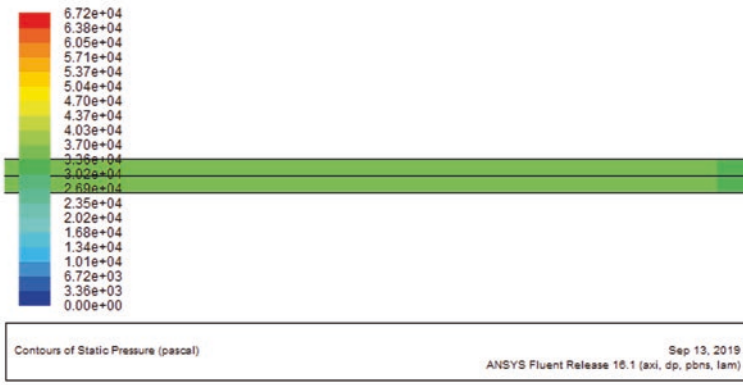


(c)

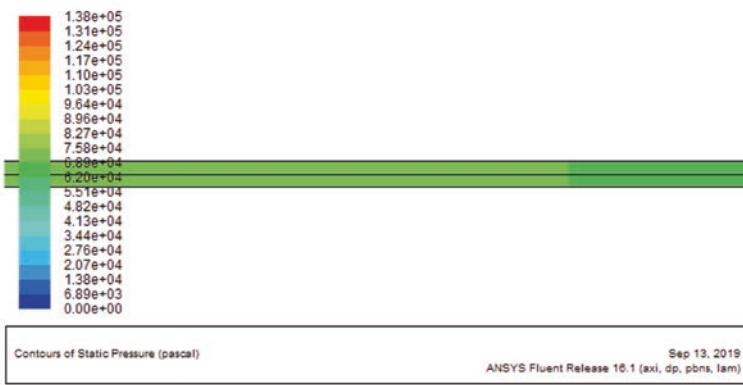
Fig. 9 Velocity vectors for laminar non-Newtonian fluid flow condition of $D = 150$ nm and $\phi = 0.06$, (a) $Re = 500$, (b) $Re = 1000$, and (c) $Re = 1600$



(a)



(b)



(c)

Fig. 10 Pressure contours for laminar non-Newtonian fluid flow condition of $D = 150$ nm and $\phi = 0.06$, (a) $Re = 500$, (b) $Re = 1000$, and (c) $Re = 1600$

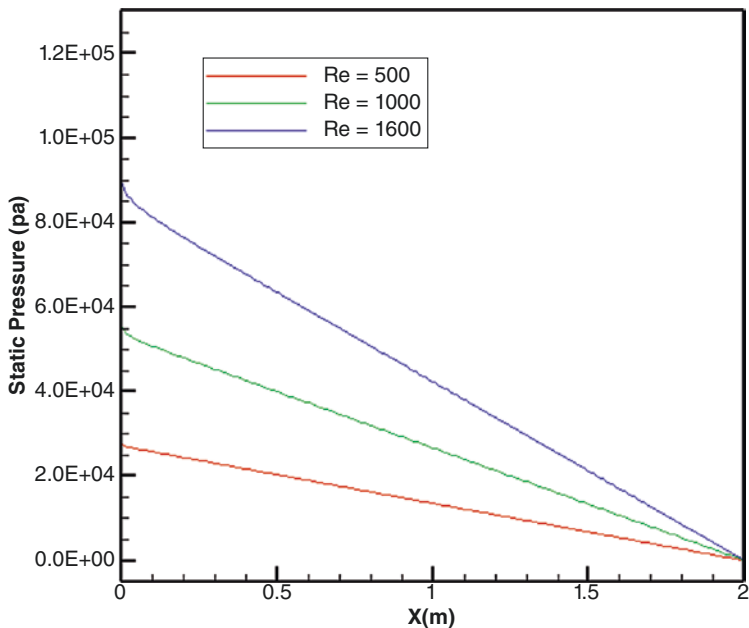


Fig. 11 Static pressure for laminar non-Newtonian fluid flow condition of $D = 120$ nm and $\phi = 0.06$

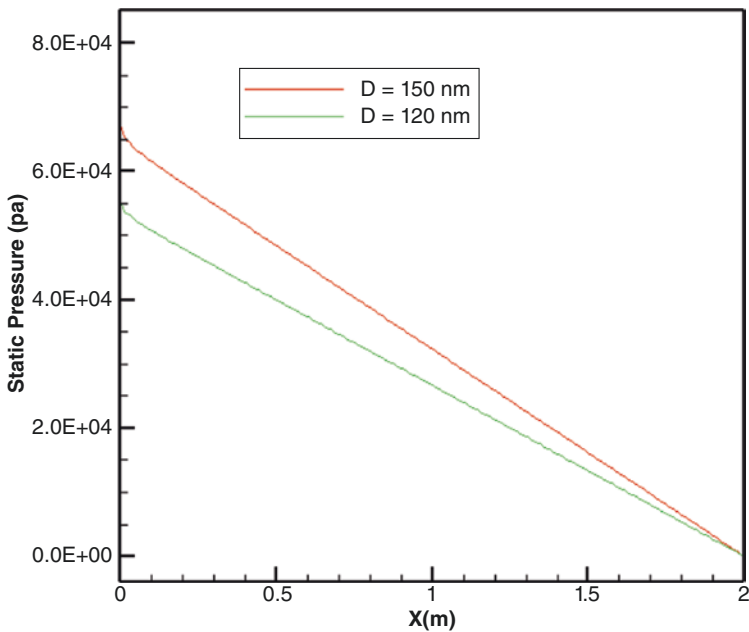


Fig. 12 Static pressure for laminar non-Newtonian fluid flow condition of $Re = 1000$, $D = 150$ nm, $D = 120$ nm, and $\phi = 0.06$

low pressure drops of below 150 Pa for laminar flow measurements. Also, peristaltic pump used here heats up quickly and cannot be used for long runs. Flow meter in several measurements were calibrated and compared well with manual volume flow rate measurements. Analytical and CFD simulations conducted for non-Newtonian nanofluid flows show good match, hence the methodology programmed in MATLAB for deriving rheological properties of nanofluids from the measured pressure drops and flow rates of the miniature Reynolds apparatus.

Appendix: 3D Solidworks Drawings

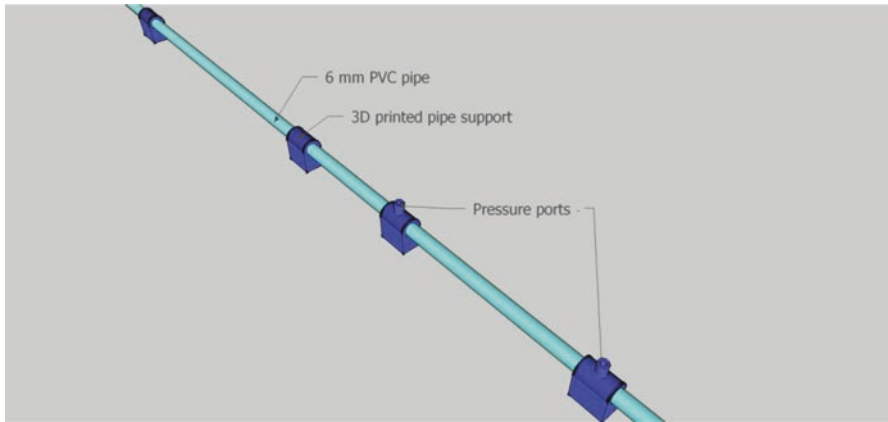


Fig. 13 3D drawing of the acrylic PVC (transparent) tube and pressure ports and supports

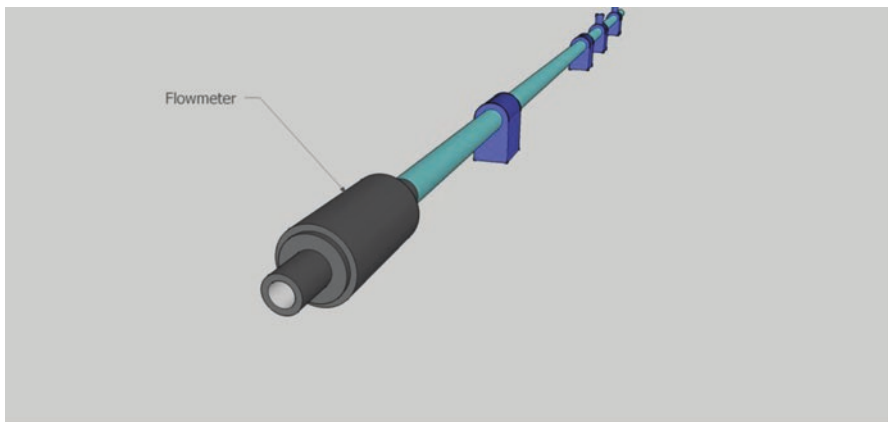


Fig. 14 3D drawing of the assembly of flow meter with the acrylic PVC (transparent) tube

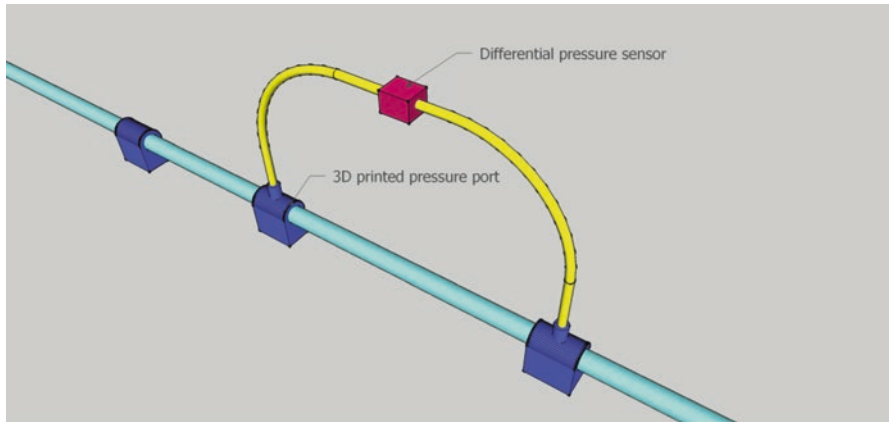


Fig. 15 3D drawing of the assembly of the differential pressure sensor with the acrylic PVC (transparent) tube

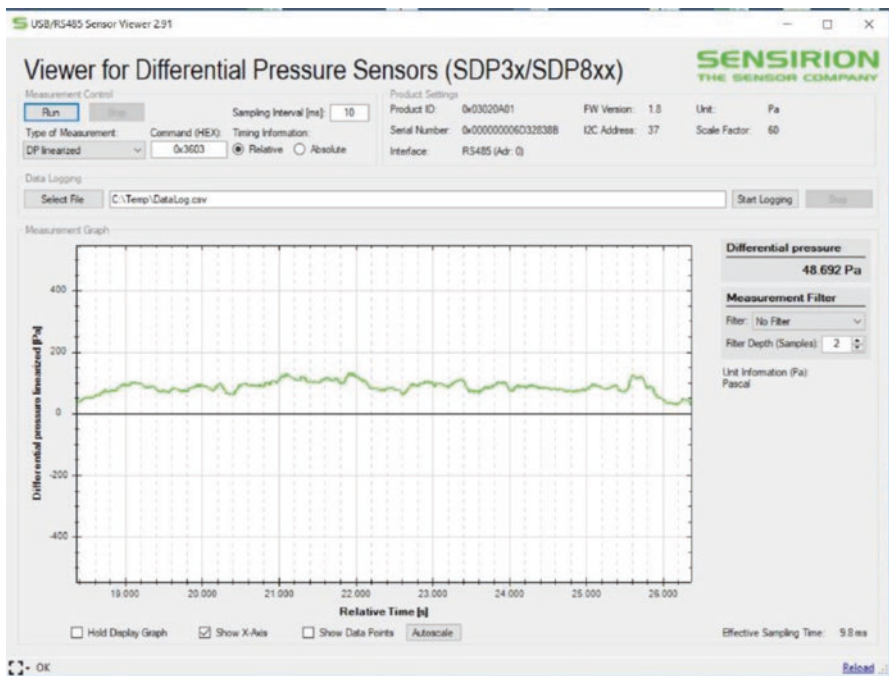


Fig. 16 Snapshot of pressure sensor measurements

References

1. Samuel RH (2010) Friction factors: what are they for torque, drag, vibration, drill ahead and transient surge/swab analysis. Society of Petroleum Engineers, IADC/SPE Drilling Conference and Exhibition, 2–4 Feb 2010, New Orleans, Louisiana, USA
2. Jahns C (2014) Friction reduction by using nanoparticles in oil-based mud. M.Sc. thesis, Department of Petroleum Engineering and Applied Geophysics, Norwegian University of Science and Technology
3. Jirkovsky L, Bo-ot LM (2014) Taylor–Couette flow and a molecule dependent transport equation. *Physica A Stat Mech Appl* 415(1):205–209
4. Tang Z, Li S (2014) A review of recent developments of friction modifiers for liquid lubricants (2007–present). *Curr Opin Solid State Mater* 18:119–139
5. Qiu S, Zhou Z, Dong J, Chen G (2001) Preparation of Ni nanoparticles and evaluation of their tribological performance as potential additives in oils. *ASME J Tribol* 123:441–443
6. Chou R, Battez AH, Cabello JJ, Viesca JL, Osorio A, Sagastume A (2010) Tribological behavior of polyalphaolefin with the addition of nickel nanoparticles. *Tribol Int* 43:2327–2332
7. Sánchez López JC, Abad MD, Kolodziejczyk L, Guerrero E, Fernández A (2011) Surface-modified Pd and Au nanoparticles for anti-wear applications. *Tribol Int* 44:720–726
8. Hernández Battez A, González R, Viesca JL, Fernández JE, Díaz Fernández JM, Machado A (2008) CuO, ZrO₂ and ZnO nanoparticles as antiwear additive in oil lubricants. *Wear* 265:422–428
9. Zhou GH, Zhu Y, Wang X, Xia M, Zhang Y, Ding H (2013) Sliding tribological properties of 0.45% carbon steel lubricated with Fe₃O₄ magnetic nanoparticle additives in base oil. *Wear* 301:753–757
10. Wu YY, Tsui WC, Liu TC (2007) Experimental analysis of tribological properties of lubricating oils with nanoparticle additives. *Wear* 262:819–825
11. Chou C, Lee S (2010) Tribological behavior of nanodiamond-dispersed lubricants on carbon steels and aluminum alloy. *Wear* 269:757–762
12. Elomaa O, Oksanen J, Hakala TJ, Shenderova O, Koskinen J (2014) A comparison of tribological properties of evenly distributed and agglomerated diamond nanoparticles in lubricated high-load steel–steel contact. *Tribol Int* 71:62–68
13. Pak BC, Cho Y (1998) Hydrodynamic and heat transfer study of dispersed fluids with submicron metallic oxide particle. *Exp Heat Transfer* 11(2):151–170
14. Pottuz LJ, Vacher B, Ohmae N, Martin JM, Epicier T (2008) Anti-wear and friction reducing mechanisms of carbon nano-onions as lubricant additives. *Tribol Lett* 30:69–80
15. Lee CG, Hwang JY, Choi YM, Lee JK, Choi C, Oh JM (2009) A study on the tribological characteristics of graphite nano lubricants. *Int J Precis Eng Manuf* 10(1):85–90
16. Hwang JY, Lee CG, Choi YM, Cheong S, Kim D, Lee K, Lee J, Kim HC (2011) Effect of the size and morphology of particles dispersed in nano-oil on friction performance between rotating discs. *Mech Sci Technol* 25:2853–2857
17. Wang XB, Liu WM (2013) Nanoparticle-based lubricant additives. Springer, Boston, MA
18. Ghazvini M, Akhavan-Behabadi MA, Rasouli E, Raisee E (2012) Heat transfer properties of nanodiamond–engine oil nanofluid in laminar flow. *Heat Transfer Eng* 33(6):525–532. <https://doi.org/10.1080/01457632.2012.624858>
19. Esmailzadeh E, Almohammadi H, Nasiri Vatan S, Omrani AN (2013) Experimental investigation of hydrodynamics and heat transfer characteristics of γ -Al₂O₃/water under laminar flow inside a horizontal tube. *Int J Therm Sci* 63:31–37. <https://doi.org/10.1016/j.ijthermalsci.2012.07.001>
20. Lin JZ, Xia Y, Ku XK (2014) Friction factor and heat transfer of nanofluids containing cylindrical nanoparticles in laminar pipe flow. *J Appl Phys* 116(13):133513-1–133513-11. <https://doi.org/10.1063/1.4896949>

21. Lin JZ, Xia Y, Ku XK (2016) Flow and heat transfer characteristics of nanofluids containing rod-like particles in a turbulent pipe flow. *Int J Heat Mass Transfer* 93:57–66. <https://doi.org/10.1016/j.ijheatmasstransfer.2015.09.088>
22. Boertz H, Baars AJ, Cieřliński JT, Smolen S (2018) Numerical study of turbulent flow and heat transfer of nanofluids in pipes. *Heat Transfer Eng* 39(3):241–251. <https://doi.org/10.1080/01457632.2017.1295739>
23. Minakov AV, Rudyak VY, Pryazhnikov MI (2018) Rheological behavior of water and ethylene glycol based nanofluids containing oxide nanoparticles. *Colloids Surf A Physicochem Eng Asp* 554:279–285
24. Munson BR, Huebsch WW, Rothmayer AP (2012) *Fundamentals of fluid mechanics*, 7th edn. Wiley, Hoboken, NJ
25. Garcia EJ, Steffe JF (1987) Comparison of friction factor equations for non-Newtonian fluids in pipe flow. *J Food Process Eng* 9:93–120
26. Mishra PC, Mukherjee S, Nayak SK, Panda A (2014) A brief review on viscosity of nanofluids. *Int Nano Lett* 4(4):109–120. <https://doi.org/10.1007/s40089-014-0126-3>
27. Kwak K, Chongyoun K (2005) Viscosity and thermal conductivity of copper oxide nanofluid dispersed in ethylene glycol. *Korea-Aust Rheol J* 17(2):35–40
28. Pastoriza-Gallego M, Lugo L, Legido J, Pieiro M (2011) Thermal conductivity and viscosity measurements of ethylene glycol-based Al₂O₃ nanofluids. *Nanoscale Res Lett* 6(221):1–11

Effect of Aluminosilicate Nanoparticles on Cement Blends Containing Volcanic Ash and Metakaolin

Rehab Masmoudi, Ali Bumajdad, and Kunal Kupwade-Patil

1 Background

Volcanic ash is one of the most common pozzolanic cement additives that provides enhanced strength and durability properties [1]. Additionally, SiO_2 and Al_2O_3 nanoparticles increase pozzolanic reactivity when added in small fractions to the Portland cement-based systems [2, 3]. Enhancement in compressive strength was observed when 2% of OPC was replaced with a combination of SiO_2 and Al_2O_3 nanoparticles [4, 5], whereas other study showed an increase in tensile and flexural strength with a replacement ratio of up to 3% [6]. In the work performed by Oltulu et al. [7], a replacement ratio of 1.25% containing equal amounts of Al_2O_3 and SiO_2 nanoparticles showed an optimum increase in compressive strength among all other single replacements except for 1.25% nano- SiO_2 , where these findings are corroborated by the minimal pore volume studied by water permeability [6, 7]. The binary composite incorporation in concrete also revealed a higher resistance toward shear, bending, and abrasion [5].

Metakaolin is another common supplementary cementitious material used for various cementing applications as it can be effectively used to control the rheological properties of modern-day cements. Metakaolin is a natural aluminosilicate, and it enhances the cementitious binder by producing aluminum-based crystalline gels, commonly known as the calcium-aluminum-silicate-hydrate (C-A-S-H) gels [8]. Similarly, zeolites are among the most aluminosilicates-rich pozzolanas with highly

R. Masmoudi
Department of Chemistry, Kuwait University, Safat, Kuwait

A. Bumajdad (✉)
Department of Chemistry, Kuwait University, Kuwait City, Kuwait
e-mail: a.bumajdad@ku.edu.kw

K. Kupwade-Patil
Laboratory for Infrastructure Science and Sustainability, Department of Civil and Environmental Engineering, Massachusetts Institute of Technology, Cambridge, MA, USA

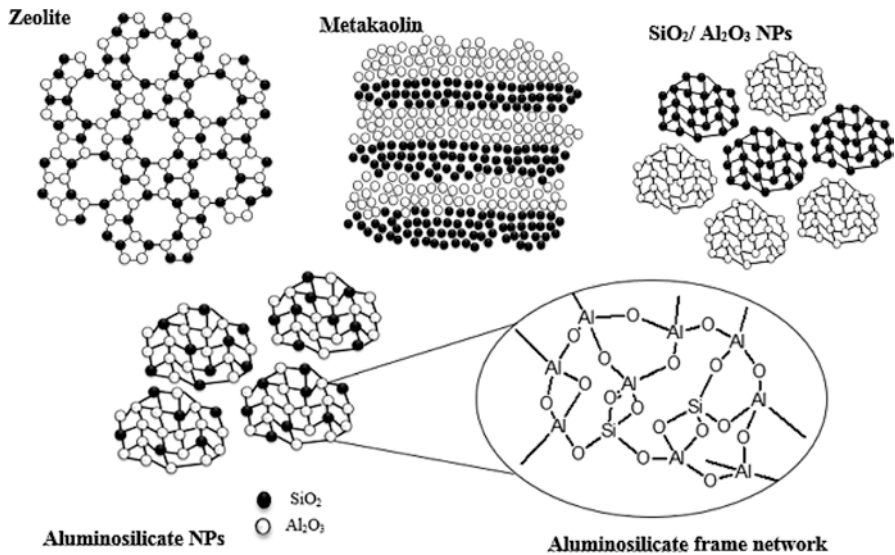


Fig. 1 Illustrative comparison of natural and synthetic material with SiO₂ and Al₂O₃ species

ordered system, also studied for their effect on concrete durability and performance. Investigations on the effect of zeolites on concrete showed that optimum replacement ratios are up to 10% [9]. Although metakaolin, zeolite, nano-SiO₂/nano-Al₂O₃ binary mix, and aluminosilicate NPs all acquire SiO₂ and Al₂O₃ species, they differ in their molecular structural arrangement that goes down to the atomistic level (see Fig. 1).

This work harnesses the chemical and physical combination of silica and alumina using volcanic ash, metakaolin, and aluminosilicate nanoparticles while examining the effect of aluminosilicate at the micro- and nanoscale.

2 Experimental Procedure

2.1 Materials and Methods

The aluminosilicates were prepared using the procedural protocol originated by Al-Omani et al. [10] for recovering titania nanoparticles except that the temperature used for recovering the aluminosilicate nanoparticles was 550 °C rather than 450 °C. Three compositions of aluminosilicate NPs were prepared in which precursor amounts (TEOS and aluminum ethoxide) were varied alternatively to obtain composites with Si:Al ratios of 3:7, 5:5, and 7:3 abbreviated as (3SA), (5SA), and (7SA), respectively. The cement paste specimens were prepared with the compositions shown in Fig. 2 with the corresponding test performed, where volcanic ash was obtained from the Super Burkani factory in Jeddah-Medina Province, Saudi

Arabia, and metakaolin from Advanced Cement Technologies, St. Blaine WA, USA. All cement paste mixtures were hydrated with a *w/c* ratio of 0.5 and studied by Raman during their freshly hydrated state and by nanoindentation and BET using water/nitrogen analysis at their hardened state (*w/c* = 0.4).

2.2 Characterization of Aluminosilicate NPs

According to our XPS data, the high Si 2p binding energy is more characteristic for SiO₂ which was observed for 7SA at 103.09 eV. This energy shift decreases in response to increasing the aluminum content and reaches a value of 102.70 eV, which is more characteristic to aluminosilicates and related to Si-O-Al bond [10]. TEM micrographs revealed more crystallization with decreasing Si:Al ratio (see Fig. 3).

HR TEM micrographs for the synthesized nanoparticles corroborate the previous findings. Crystallization of alumina becomes easier at lower temperature leading to the reduction in the particle size. From this standpoint, the amorphous layer surrounding the agglomerated portion was observed from HR TEM images, as shown in Fig. 4, and may belong to SiO₂ surrounding some crystalline phases of Al₂O₃.

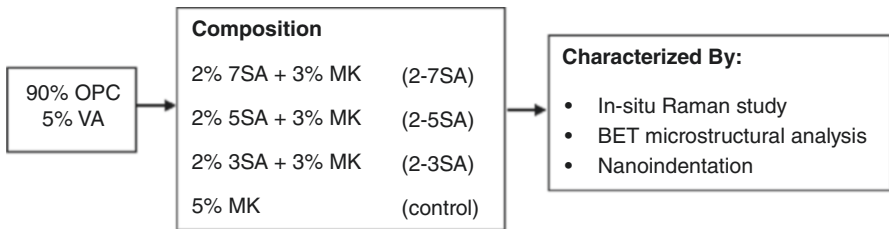


Fig. 2 Working scheme outlining the combinations of cement pastes prepared with volcanic ash, metakaolin, and different aluminosilicate NPs with the corresponding test performed (Note: volcanic ash size used will be represented in a parenthesis, e.g. 17 μm volcanic ash is denoted as (17 VA))

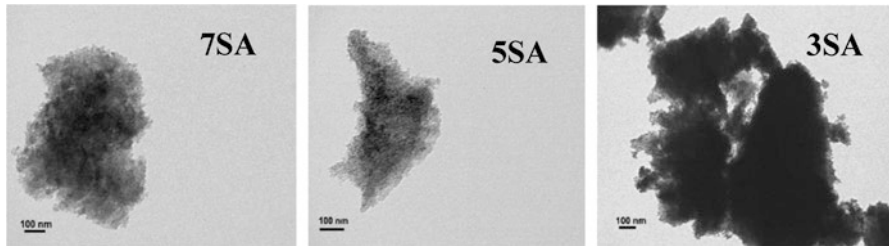


Fig. 3 TEM micrographs of the three aluminosilicate NPs recovered from aramid hybrid films at 550 °C compositions

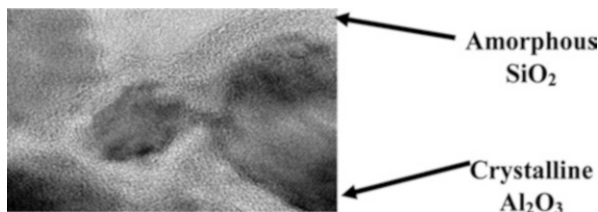


Fig. 4 HR TEM micrograph of aluminosilicate NPs (3SA) depicting the layering of amorphous SiO_2 over Al_2O_3

Table 1 BET parameters determined from N_2 adsorption–desorption isotherms for metakaolin and aluminosilicate NPs recovered from aramid hybrid films

Sample	Surface area (m^2/g)	Pore volume (cm^3/g)	Average pore size (nm)
Metakaolin	17.0	0.052	12.1
$\text{Al}_2\text{O}_3^{\text{a}}$	294.9	0.319	4.3
3SA	381.0	0.416	4.4
5SA	429.8	0.498	4.6
7SA	450.3	0.529	4.7
SiO_2^{b}	810.3	0.839	4.1

^aCourtesy from Dr. Shamsun Nahar

^bCourtesy from Abdullah Haddad (M.Sc. student)

Surface areas obtained by N_2 adsorption test of the three aluminosilicate NPs are in gradual increase with increasing SiO_2 over Al_2O_3 content, and all composites showed higher surface area than metakaolin (see Table 1).

3 Discussion

3.1 In Situ Raman Study

In situ Raman spectroscopy measurements are effective in tracking the extent of pozzolanic reaction by the evolution of Raman band at $\sim 360 \text{ cm}^{-1}$ designated for $\text{Ca}(\text{OH})_2$ or by the broad bands in the region $600\text{--}700 \text{ cm}^{-1}$ designated to deformation of Ca-O polyhedral [11, 12]. The combinations shown in Fig. 1 were recorded for their spectra at 1 h interval for 12 h, then after 24, 36, and 48 h (see Fig. 5). Control (17 μm VA) sample developed aluminate phases such as monosulfoaluminate, gypsum, and aragonite, whereas insoluble anhydrite was more evident for control (6 μm VA) which proves the effect of VA particle size on variations of sulfate phases and carbonation events. Additionally, incorporation of aluminosilicate NPs affected the resultant sulfate phases. For instance, 2-7SA (17 μm VA) revealed formation of ettringite, whereas 2-7SA (6 μm VA) showed evolution of insoluble anhydrite [13]. Although bands of ettringite and insoluble anhydrite are similar, ettringite

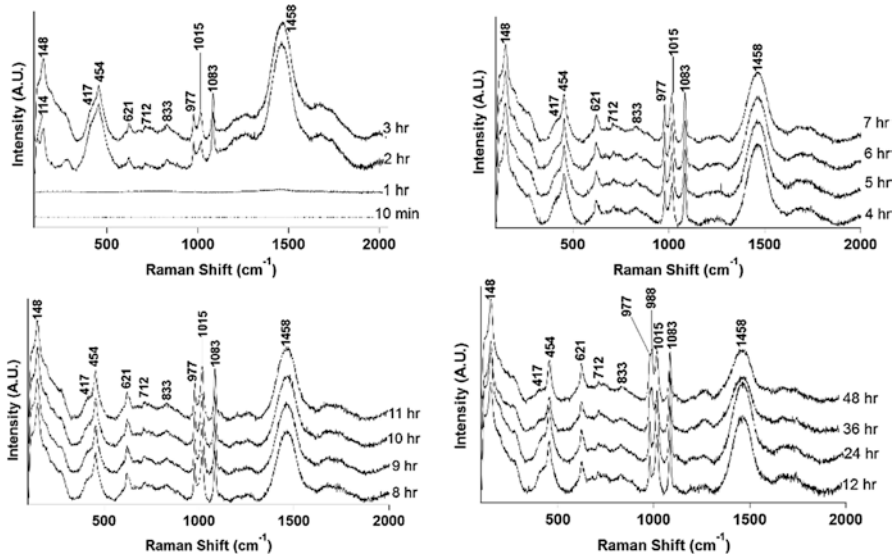


Fig. 5 Raman shifts collected for control paste containing 17 μm volcanic ash during 48 h of hydration

can be distinguished from insoluble anhydrite from the strong signals at 980–1002 cm⁻¹. Spectra of 2-5SA samples with both sizes of volcanic ash are quite similar and revealed the sulfate phase in the form of ettringite. Aragonite is a carbonate phase that has evolved upon decreasing both Si:Al ratio and volcanic ash particle size, as it is the case for 2-3SA containing 6 μm VA. Additionally, the volcanic ash particle size resulted in varying the sulfate phase evolved from 2-3SA (see Table 2 for summary of band assignment and phases evolved for all samples).

3.2 BET Microstructural Analysis

N₂ molecules are not accessible to all pores, mainly excluding ones below 2–4 nm in radii, whereas H₂O vapor acquires a smaller molecule size and a dipole that facilitates its penetration to interlayer spaces [19]. On the light of this understanding, we used the ratio of total pore volume found from both adsorbates (N₂ and H₂O) to infer how much volume is accessible to nitrogen compared to water vapor and therefore to estimate the total large to capillary pores and correlate them to compressive strength (see Fig. 6). It is expected that the lower V_{N₂}/V_{H₂O} is accompanied with higher compressive strength and vice versa for V_{H₂O} - V_{N₂}. The lowest value of V_{N₂}/V_{H₂O} was found to be for 2-7SA (6 VA), followed by 2-5SA (6 VA), and then control (6 VA). The same trend goes for V_{H₂O} - V_{N₂} value; highest value was found

Table 2 Predominant phases detected during the course of hydration by Raman spectroscopy of cement pastes prepared with volcanic ash, metakaolin, and aluminosilicate NPs

Sample	Raman shift (cm ⁻¹)	Assignment	Possible phases	Ref.
Control (17 μm VA)	977, 988	ν_1 [SO ₄]	Monosulfoaluminate	[14]
	454	ν_2 [SO ₄]		
	621	ν_4 [SO ₄]		
	800–1015	Symmetrical stretching of Si-O-Si	C-S-H	[13]
	1083	ν_1 [CO ₃]	Aragonite	[15]
	712	ν_1 [CO ₃]		
	1015	ν_1 [SO ₄]	Gypsum	[16]
	417	ν_2 [SO ₄]		
Control (6 μm VA)	1024	ν_1 (SiO ₄) symmetric stretching of Q ² : Si-O(Ca) and/or Si-O(H)	C-S-H	[13]
	451	Internal deformation of silicate tetrahedra		
	1083	ν_1 [CO ₃]	Carbonate (amorphous CaCO ₃)	[12]
	420	ν_2 [SO ₄]	Insoluble anhydrite	[12, 13]
	490			
	632	ν_2 [SO ₄]		
	1122	ν_4 [SO ₄]		
	1163			
2-7SA (17 μm VA)	1002	ν_1 [SiO ₄]	C-S-H	[13]
	428	ν_2 [SiO ₄] for Q ²		
	489	ν_4 [SiO ₄]		
	983	ν_1 [SO ₄]	Ettringite	[13, 14]
	442	ν_2 [SO ₄]		
	1083, 1139	ν_3 [SO ₄]		
	630	ν_4 [SO ₄]		
2-7SA (6 μm VA)	1022	Symmetrical stretching band for Si-O	C-S-H	[13]
	672	Symmetrical stretching for Si-O-Si bridges		
	450	Internal deformation of silicate tetrahedra		
	1022	ν_1 [SO ₄]	Insoluble anhydrite	[14]
	422, 492	ν_2 [SO ₄]		
	1142, 1164	ν_3 [SO ₄]		
	630	ν_4 [SO ₄]		
2-5SA (17 and 6 μm VA)	611–661	Deformation of Ca-O polyhedra	Ca(OH) ₂ or/and CSH	[17]
	430–493	Bending modes of terminal Si-O		[13]

(continued)

Table 2 (continued)

Sample	Raman shift (cm ⁻¹)	Assignment	Possible phases	Ref.
	1002–1005	$\nu_1[\text{SO}_4]$	Ettringite	[14]
	980–983			
	441–444	$\nu_2[\text{SO}_4]$		
	1139, 1166	$\nu_3[\text{SO}_4]$		
	622–625	$\nu_4[\text{SO}_4]$		
	1025	$\nu_1[\text{SiO}_4]$	C-S-H	[13]
2-3SA (17 μm)	422–492	Bending modes of terminal Si-O	C-S-H	[13]
	453	Internal deformation of silicate tetrahedral		
	675	Symmetrical stretching band Si-O		
	1025	$\nu_1[\text{SiO}_4]$	C-S-H	[13]
	980, 1002	$\nu_1[\text{SO}_4]$	Ettringite	[14]
	1142, 1166	$\nu_3[\text{SO}_4]$		
	630	Deformation of Ca-O polyhedra	Ca(OH) ₂ or/and CSH	[17]
2-3SA (6 μm VA)	1083	$\nu_1[\text{CO}_3]$	Aragonite	[18]
	147, 197			
	1022	$\nu_1[\text{SiO}_4]$	C-S-H	[13]
	672	Si-O symmetrical stretching band		
	422–492	Bending modes of terminal Si-O		
	1022	$\nu_1[\text{SO}_4]$	Insoluble anhydrite	[13, 16]
	422, 492	$\nu_2[\text{SO}_4]$		
	1144, 1164	$\nu_3[\text{SO}_4]$		
	630	$\nu_4[\text{SO}_4]$		

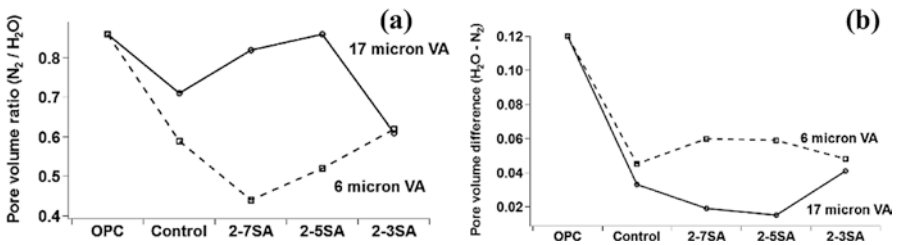


Fig. 6 Pore volume ratio (a) and pore volume difference (b) using N₂ and H₂O adsorbates

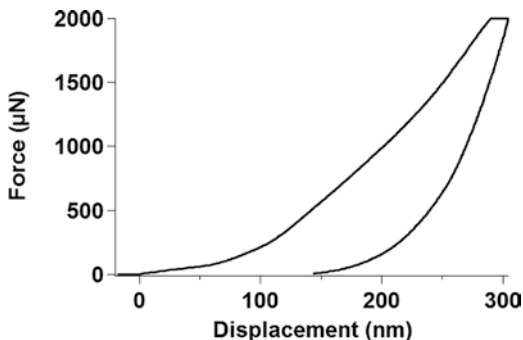
for 2-7SA (6 VA), followed by 2-5SA (6 VA), then control (6VA), 2-3SA (6 VA) and 2-3SA (17 VA) where the latter three are in proximity.

3.3 Nanoindentation Test

A typical load–displacement curve (also called *P-H* curve) for 2-3SA (6 μm VA) is shown in Fig. 7. Irregular curves which might have resulted from voids were discarded. The curve is initiated by increasing the load constantly followed by constant holding (where material suffers creeping), then constant unloading. The applied loading is associated with permanent plastic deformation and temporary elastic deformation, where the latter is recovered as indenter starts unloading [20]. The initial slope of elastic unloading allows inferring two mechanical properties: modulus (*M*) and hardness (*H*) [21, 22]. It was suggested by Doerner and Nix that the unloading stiffness can be obtained from a linear fit of the upper one-third of the unloading curve [23]. However, the hardness calculated by this method can be different than that when directly determining the size of residual hardness impression. Oliver et al. [21] described a simple power law relation to avoid the deviation resulting from (1) difference in stiffness between first and last unloading and (2) significant variation in the stiffness resulting from final unloading which depends on how much of the curve is used to fit [21]. However, the analysis must be complemented with SEM for assessing homogenous C-S-H regions.

Hardness and modulus obtained from averaged mapped areas showed that all combinations with 6 μm volcanic ash inclusion were associated with higher hardness than their counterparts containing 17 μm volcanic ash (see Fig. 8). The overall trend of hardness is in agreement with that found in BET microstructural analysis which significantly corroborates our findings. It can be found from modulus values that all blends, except for 2-7SA (17 VA) and 2-3SA (6 VA), fall within the same region found for high-stiffness C-S-H (25–35 GPa) and for calcium hydroxide (35–45 GPa) [24]. The incorporation of metakaolin and aluminosilicate NPs both revealed a significant enhancement in overall hardness and modulus, except for 2-7SA (17 VA), which showed very little improvement. The represented hardness

Fig. 7 Load–displacement curve for cement paste mixture 2-3SA containing 6 μm volcanic ash



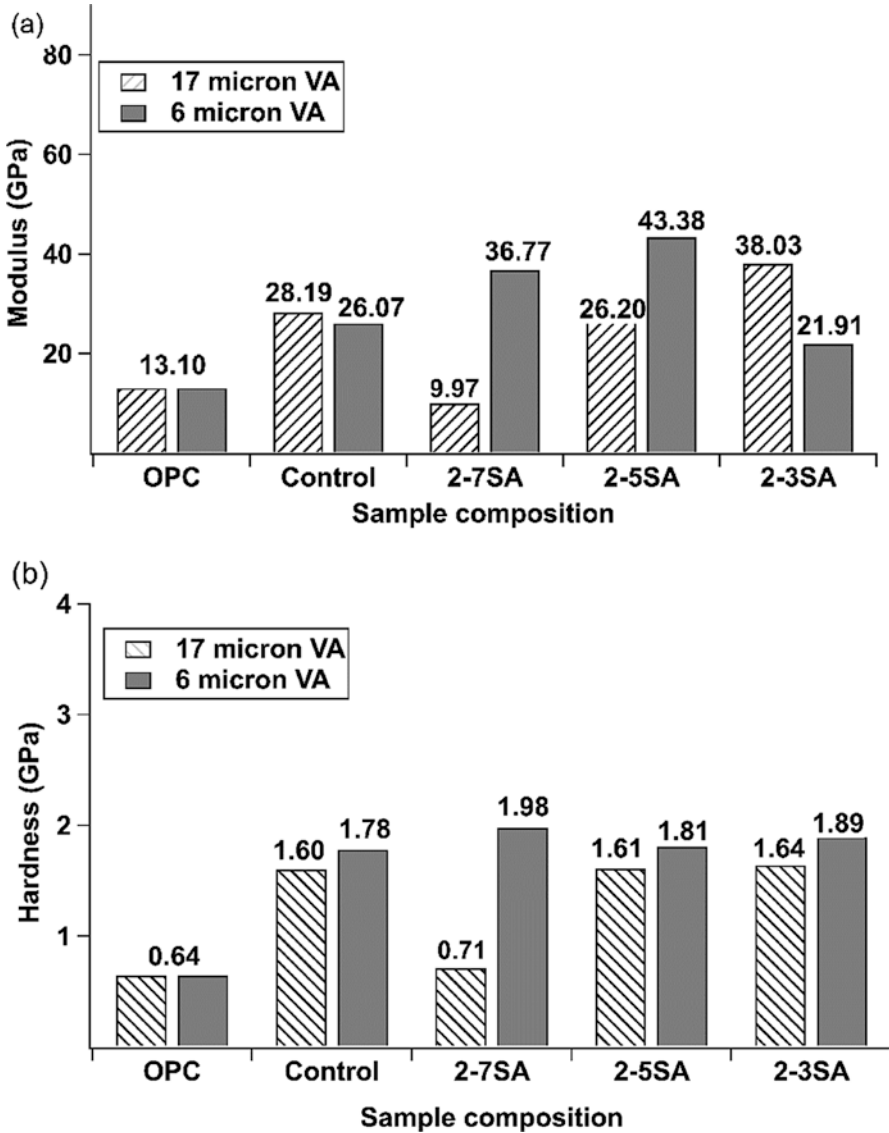


Fig. 8 Effect of aluminosilicate, metakaolin, and volcanic ash collectively on (a) modulus and (b) hardness on hardened cement pastes cured for 28 days

and modulus values for 2-7SA (6 VA) and 2-5SA (6 VA) were even greater than those reported in previous studies [25, 26]. The increased hardness and modulus of control samples over plain OPC can be attributed to C-A-S-H phases formed upon incorporating metakaolin. However, aluminosilicate NPs revealed only enhanced performance (for 17 μm VA) over metakaolin when Si:Al ratio was the smallest. This anomalous behavior can be ascribed to leached silica resulting from fast con-

sumption of portlandite by 7SA and 5SA resulting in lower strength. Contrarily, the strength was enhanced for all 6 μm VA samples over their corresponding control samples with the opposite trend, which could be due to higher association degree of fine VA in the reactivity at early stage. Further investigation by compression test is highly recommended.

4 Conclusion

In this work, aluminosilicate NPs were successfully prepared using aramid support and examined for their effect on cement performance. Lower Si:Al ratio resulted in higher crystallization event and slower reactivity. The aluminosilicate species greatly influenced the early hydration of cement according to Raman spectra, where the composition of aluminosilicate NPs and volcanic ash particle size influenced the evolution of sulfate-based phases. The formation of aluminum-based phases by micro- and nano-aluminosilicates corresponded to higher pore structure uniformity. Yet, the choice of composition of aluminosilicate NPs and their supporting additives is highly critical for cement strength. Fast-reacting aluminosilicate NPs were found to be best associated with fine volcanic ash to minimize silica leaching events and engender optimal strength enhancement.

Acknowledgments The authors gratefully acknowledge the College of Graduate Studies (CGS), Kuwait University, Research Sector Project Unit (RSPU): Project No. (GS 01/01), Nanoscopy Center, Nanotechnology Lab Project No. GE01/07, and Dr. Shamsun Nahar for their support and funds.

References

1. Kupwade-Patil K, Al-Aibani AF, Abdulsalam MF, Mao C, Bumajdad A, Palkovic SD, Büyükköztürk O (2016) Microstructure of cement paste with natural pozzolanic volcanic ash and Portland cement at different stages of curing. *Constr Build Mater* 113:423–441
2. Kupwade-Patil K, Cardenas H (2013) Electrokinetic nanoparticle treatment for corrosion remediation on simulated reinforced bridge deck. *J Nanopart Res* 15:1–16
3. Jamsheer AF, Kupwade-Patil K, Büyükköztürk O, Bumajdad A (2018) Analysis of engineered cement paste using silica nanoparticles and metakaolin using ^{29}Si NMR, water adsorption and synchrotron X-ray diffraction. *Constr Build Mater* 180:698–709
4. Silva JV, Ismael R, Carmo RNF, Lourenço C, Soldado E, Costa H, Júlio E (2016) Influence of nano- SiO_2 and nano- Al_2O_3 additions on the shear strength and the bending moment capacity of RC beams. *Constr Build Mater* 123:35–46
5. Ismael R, Silva JV, Carmo RNF, Soldado E, Lourenço C, Costa H, Júlio E (2016) Influence of nano- SiO_2 and nano- Al_2O_3 additions on steel-to-concrete bonding. *Constr Build Mater* 125:1080–1092
6. Rashad AM (2013) A synopsis about the effect of nano- Al_2O_3 , nano- Fe_2O_3 , nano- Fe_3O_4 and nano-clay on some properties of cementitious materials – a short guide for civil engineer. *Mater Des (1980–2015)* 52:143–157

7. Oltulu M, Şahin R (2013) Effect of nano-SiO₂, nano-Al₂O₃ and nano-Fe₂O₃ powders on compressive strengths and capillary water absorption of cement mortar containing fly ash: a comparative study. *Energy Buildings* 58:292–301
8. Siddique R, Klaus J (2009) Influence of metakaolin on the properties of mortar and concrete: a review. *Appl Clay Sci* 43:392–400
9. Valipour M, Pargar F, Shekarchi M, Khani S (2013) Comparing a natural pozzolan, zeolite, to metakaolin and silica fume in terms of their effect on the durability characteristics of concrete: a laboratory study. *Constr Build Mater* 41:879–888
10. Al-Omani SJ, Bumajdad A, Al Sagheer FA, Zaki MI (2012) Surface and related bulk properties of titania nanoparticles recovered from aramid–titania hybrid films: a novel attempt. *Mater Res Bull* 47:3308–3316
11. Garbev K, Stemmermann P, Black L, Breen C, Yarwood J, Gasharova B (2007) Structural features of C–S–H(I) and its carbonation in air—a Raman spectroscopic study. Part I: Fresh phases. *J Am Ceram Soc* 90:900–907
12. Black L, Breen C, Yarwood J, Garbev K, Stemmermann P, Gasharova B (2007) Structural features of C–S–H(I) and its carbonation in air—a Raman spectroscopic study. Part II: Carbonated phases. *J Am Ceram Soc* 90:908–917
13. Black L (2009) Raman spectroscopy of cementitious materials. *Spectrosc Inorg Organometall Compounds* 40:72–127
14. Renaudin G, Segni R, Mentel D, Nedelec J-M, Leroux F, Taviot-Gueho C (2007) A Raman study of the sulfated cement hydrates: Ettringite and monosulfoaluminate. *J Adv Concr Technol* 5:299–312
15. Black L, Breen C, Yarwood J, Deng CS, Phipps J, Maitland G (2006) Hydration of tricalcium aluminate (C₃A) in the presence and absence of gypsum—studied by Raman spectroscopy and X-ray diffraction. *J Mater Chem* 16:1263–1272
16. Bensted J (1976) Uses of Raman spectroscopy in cement chemistry. *J Am Ceram Soc* 59:140–143
17. Kirkpatrick RJ, Yarger JL, McMillan PF, Ping Y, Cong X (1997) Raman spectroscopy of C-S-H, tobermorite, and jennite. *Adv Cem Based Mater* 5:93–99
18. Ibáñez J, Artús L, Cuscó R, López Á, Menéndez E, Andrade MC (2007) Hydration and carbonation of monoclinic C₂S and C₃S studied by Raman spectroscopy. *J Raman Spectrosc* 38:61–67
19. Rouquerol J, Rouquerol F, Llewellyn P, Maurin G, Sing KSW (2013) Adsorption by powders and porous solids: principles, methodology and applications. Elsevier Science, Amsterdam
20. Zhu W, Hughes JJ, Bicanic N, Pearce CJ (2007) Nanoindentation mapping of mechanical properties of cement paste and natural rocks. *Mater Charact* 58:1189–1198
21. Oliver WC, Pharr GM (1992) An improved technique for determining hardness and elastic modulus using load and displacement sensing indentation experiments. *J Mater Res* 7:1564–1583
22. Palkovic SD, Kupwade-Patil K, Yip S, Büyüköztürk O (2018) Random field finite element models with cohesive-frictional interactions of a hardened cement paste microstructure. *J Mech Phys Solids* 119:349–368
23. Doerner MF, Nix WD (1986) A method for interpreting the data from depth-sensing indentation instruments. *J Mater Res* 1:601–609
24. Constantinides G, Ulm FJ, Van Vliet K (2003) On the use of nanoindentation for cementitious materials. *Mater Struct* 36:191–196
25. Hou P, Kawashima S, Kong D, Corr DJ, Qian J, Shah SP (2013) Modification effects of colloidal nanoSiO₂ on cement hydration and its gel property. *Compos Part B* 45:440–448
26. Zyganitidis I, Stefanidou M, Kalfagiannis N, Logothetidis S (2011) Nanomechanical characterization of cement-based pastes enriched with SiO₂ nanoparticles. *Mater Sci Eng B* 176:1580–1584

Compressed Earth Blocks: A Sustainable Construction Alternative



Ahmad S. Saad, Fahad M. Al-Enezi, Hamad A. Al-Sayab,
Zuhair H. Al-Zayed, Fares H. Awwad, and Sarah N. Al-Muhanna

1 Introduction

The accelerated construction and building industry in the GCC countries and the Middle East is one of the biggest contributors to the high per capita carbon dioxide emission of these regions [1]. Using compressed earth blocks (CEB) in construction of load-bearing walls introduces a sustainable alternative technique that can significantly help reduce the building's environmental impacts. CEBs are blocks that are made from a mixture of native soil and stabilizers, compressed at high pressure to form the blocks. Excavated soil on site can be molded and used directly. This would reduce emissions and transportation costs compared to reinforced concrete, in addition to the cost of the material and its availability.

CEBs have been widely used in load-bearing wall systems to carry structural loads in low-rise buildings [2]. Soil suitability to produce CEB is based on its plasticity, cohesion strength, grading, and the ability to be compacted. These criteria are to ensure suitable bonding between particles [3]. Optimum moisture content in the mixture is also required to reach the highest unit weight of the soil [2]. Cement or lime can be used as stabilizers to enhance the adhesion property of the mixture [4].

Soil is available in large quantities in most regions, specially countries such as Kuwait in the Middle East which makes it inexpensive and affordable. No specialized equipment is required in construction, which means less energy consumption. This technique is also advantageous for its fire resistance and its low thermal conductivity and porosity which provides suitable indoor atmosphere and contributes to long-term energy savings. CEB walls have the natural ability to absorb and release moisture and regulate humidity of the air on the outer face of the blocks because it

A. S. Saad (✉) · F. M. Al-Enezi · H. A. Al-Sayab · Z. H. Al-Zayed · F. H. Awwad
S. N. Al-Muhanna
Civil Engineering Department, Australian College of Kuwait, Kuwait, Kuwait
e-mail: a.said@ack.edu.kw

contains a breathable material. However, organic and synthetic fibers in addition to other types of stabilizers can improve its ability to withstand weather conditions [5].

Deboucha and Hashim [5] also stated that “Low energy input in processing and handling soil-only about 1% of the energy required manufacturing and processing the same volume of cement concrete” which is considered as one of the advantages of CEBs over regular concrete production.

CEB production also has some disadvantages, especially in the Middle East. This includes its low specific strength compared to the widely used concrete production. In addition, it has low popularity among stakeholders in the region, which makes it not among the engineers’ first choices as a construction technique.

Plant fibers can also be used as a reinforcement to the CEB in order to control shrinkage cracking by dispersing tension all over the block. It also enhances drying duration as it creates a path to the surface of the block which allows water to leave easily, in addition to developing tensile strength in the block [6].

2 Site Investigation

A recommended range of soil gradation was set by Boubekeur and Houben [3] for the selection of soils for CEB production. The granular composition (gradation graphs) of soils that falls within the recommended shaded area in most cases gave satisfactory results. Their study specified that the limits of the recommended shaded area (shown in Fig. 1) are approximate. A sample falling outside the recommended

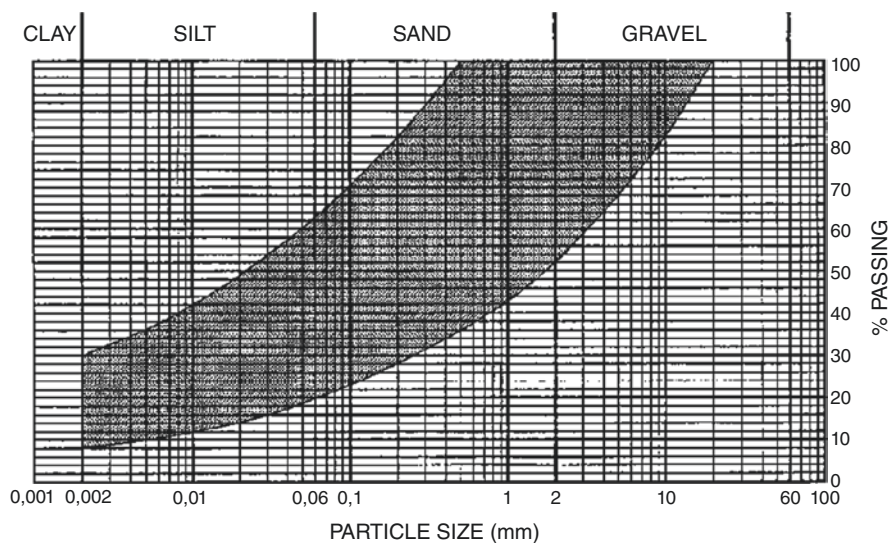


Fig. 1 Recommended range of soil gradation [3]

range does not deem it unacceptable, though it (the sample) will require further testing and alternations in the physical properties to use in CEB production. Alternations can include the addition of clay or fine sand for a gap-graded sample.

Based on the reconnaissance soil survey done [7] (shown in Figs. 2 and 3), soil samples were collected from Sadda, Kar Al-Maru, Sabriya, Al-Sulaibikhat, Jaber

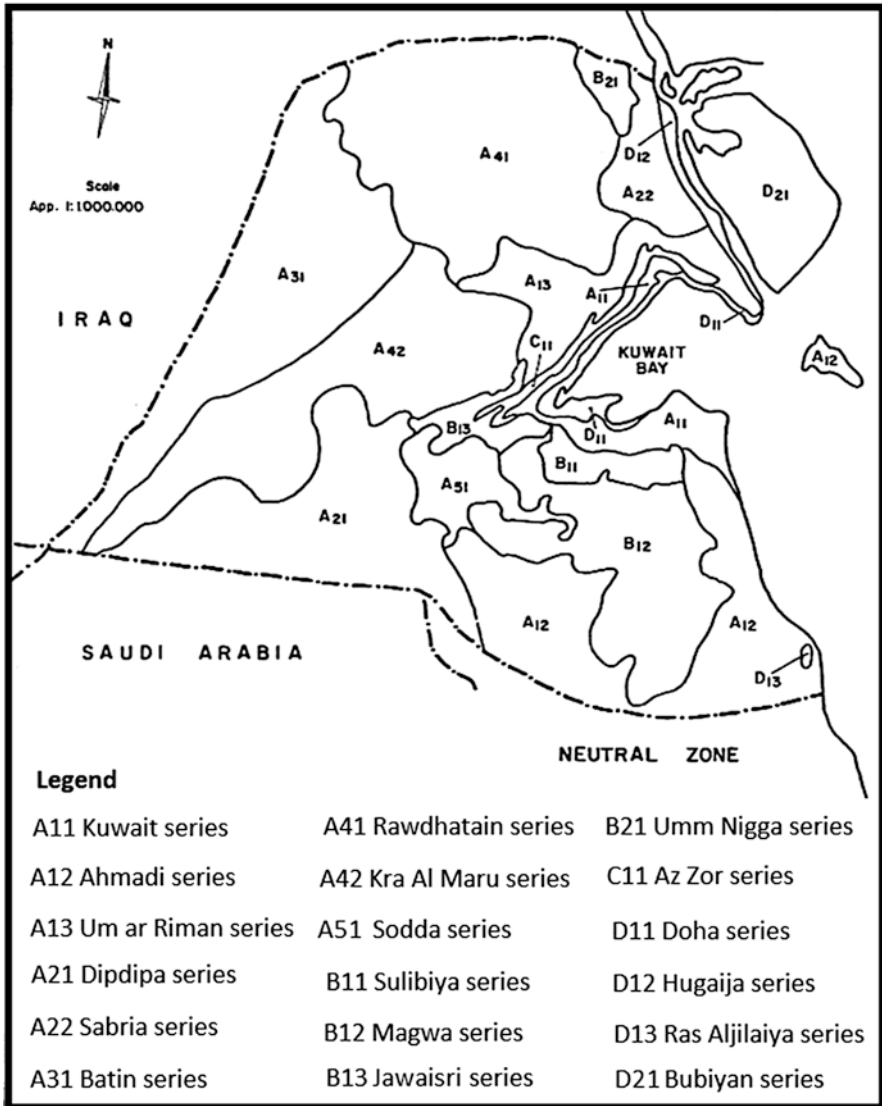


Fig. 2 Soil series marked on Kuwait map [7]

Soil Series	Profile No.	Depth (cm)	Texture			
			Gravel %	Sand %	Silt %	Clay %
Kuwait	2	0-18	7.78	82.32	10.30	7.38
		18-50	2.93	88.36	5.15	6.49
		50-100	3.67	88.79	2.60	8.61
		100-148	10.36	90.74	1.67	7.59
Ahmadi	11	0-14	6.20	91.15	4.80	4.05
		14-41	3.81	93.24	2.70	4.06
		41-94	18.63	91.28	2.80	5.92
		94-120	10.60	91.28	3.35	5.37
		120-155	13.45	93.88	2.31	3.81
Umm ar Rimam	21	0-5	-	75.00	13.00	12.00
		5-23	-	73.00	10.00	17.00
		23-55	-	74.00	13.00	13.00
		55-100	-	74.00	14.00	12.00
		100-120+	-	64.00	23.00	13.00
Dibaiiba	36	0-20	-	76.00	15.00	9.00
		20-50	-	78.00	11.00	11.00
		50-80	-	80.00	11.00	9.00
		80-130	-	84.00	14.00	2.00
Sabriya	39	0-18	-	79.00	10.00	11.00
		18-45	-	79.00	10.00	11.00
		45-90	-	61.00	26.00	13.00

Fig. 3 Percentages of soil particles [7]

AL-Ahmad, Al-Doha, and Northwest Sulaibikhat as illustrated in the maps in Figs. 4 and 5. The collected samples varied in depth depending on the soil properties (cemented or loose). Samples were collected at 0.25, 0.50, or 0.80 m below surface level to reach the native soil.

Sieve analyses of the collected soil samples were done in accordance with the ASTM Standard for Particle-Size Analysis of Soil ASTM D422-63 [9] and ASTM D1140-17 [10]. The results of the soil gradation in comparison with the recommended range of Boubekeur and Houben [3] are shown in Figs. 6, 7, 8, 9, 10 and 11. The best location that contained soil with gradation falling within the limits was Sabriya location. This research study continued with block produced from the collected soil from this location.



Fig. 4 Map 1 of the State of Kuwait with sample locations [8])

3 Mix Designs

3.1 Stabilizers

Different stabilizers have been used in the past in the production of CEBs. The main objective of these stabilizers is to increase the dry compressive strength of the blocks, which enhances their mechanical performance in addition to minimizing their porosity to reduce shrinkage [11].

Cement stabilization is most effective on sandy soils with low plasticity as it reacts much quicker. The soil sample must not include lumps, gravel, and stone. The presence of organic matter and sulfate could hinder the effect of cement stabilization. On the other hand, iron oxides guarantee a better stabilization with the soil particles. Blocks should be cured for at least 7 days covered with waterproof plastic sheets and sheltered from direct sunlight and wind. After 28 days of curing, there won't be any further substantial changes to the strength of the block [11]. In fact,

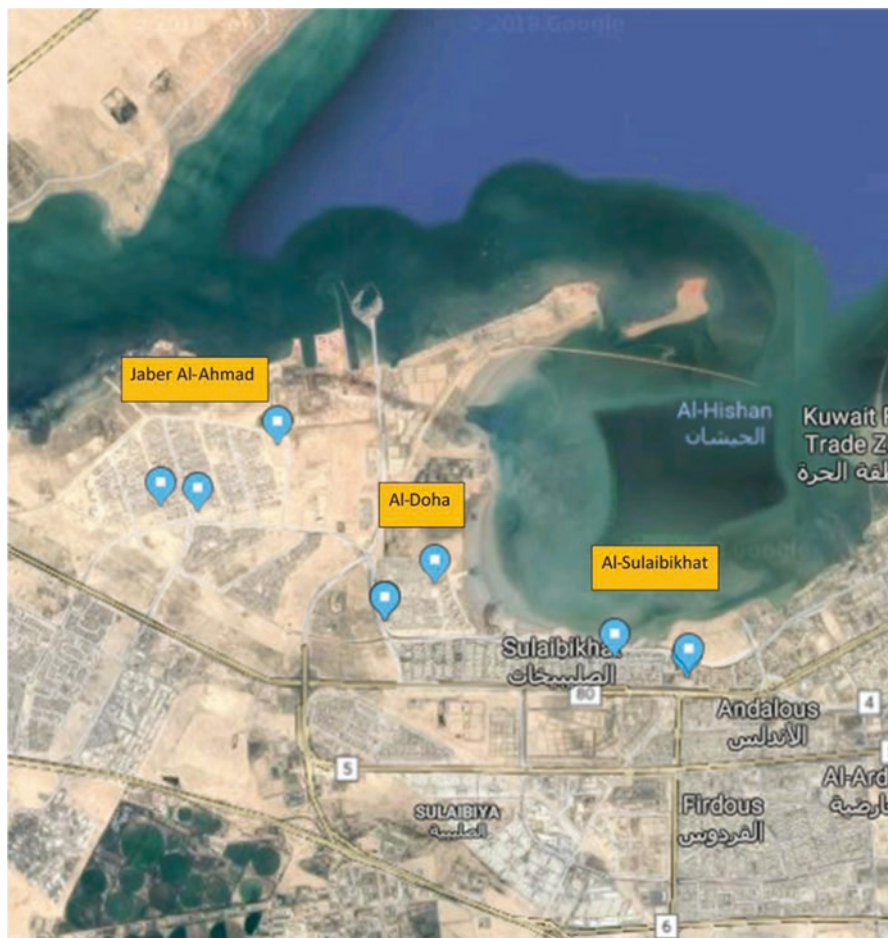


Fig. 5 Map 2 of sample locations [8]

researchers are still investigating the impact of using stabilizers as part of CEB production. A recent study by Van Damme and Houben [12] proved that using Portland cement as a stabilizer mildly improved the mechanical properties of CEB in comparison to the high environmental impact caused.

Bituminous emulsions are usually formed of 55% bitumen, 43–44% water, and 1–2% emulsifying agent. The emulsifying agent's main role is to bind the bitumen and water; water facilitates the mix between clay particles and bitumen. Bitumen emulsion is most suitable for soil with high clay content and well-graded sand, as its main goal is to coat the surface of the soil particles. The amount required to successfully stabilize the CEB depends on the texture of the soil used (see Table 1).

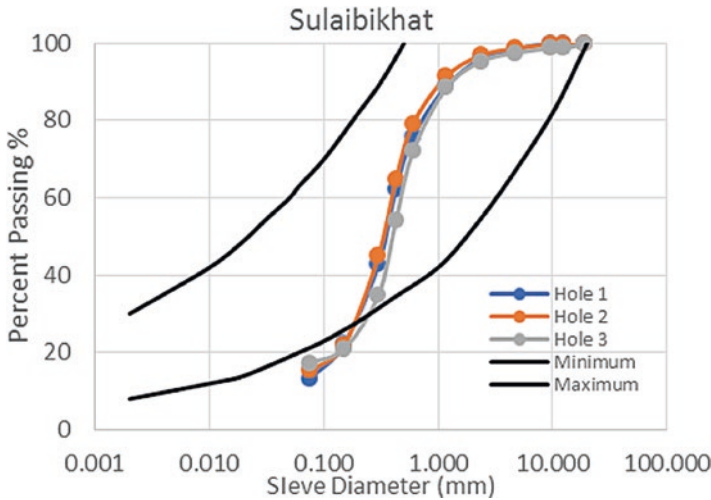


Fig. 6 Gradation for Sulaibikhat samples

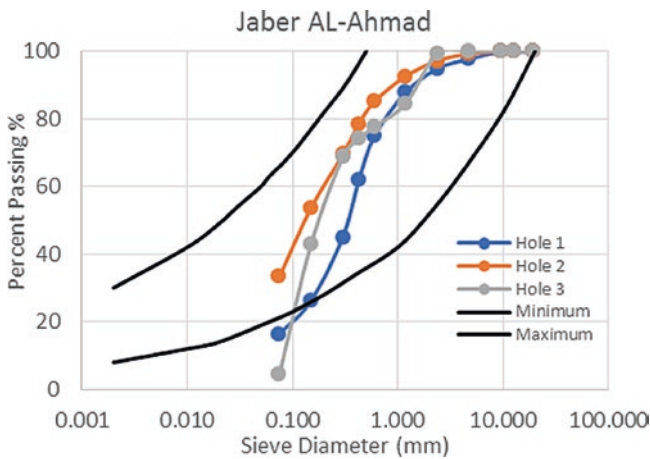


Fig. 7 Gradation for Jaber Al-Ahmad samples

Addition of natural/artificial fibers to the mixture of the CEB may result in the prevention of any shrinkage cracking occurrence. Fibers disperse the tension through the blocks. In addition, it improves the drying by providing a trail for moisture drainage toward the external surface of the block, decreases the density of the blocks, and improves the tensile strength of the block [11]. Date tree fiber (DTF) is chosen to be the reinforcement of the CEB in this study because of its availability in Kuwait. DTF is considered to be a waste material with large amounts, regularly cropped (once or twice a year) from the date trees. Therefore, using the fiber as a reinforcement is an environmentally friendly solution for a local waste material.

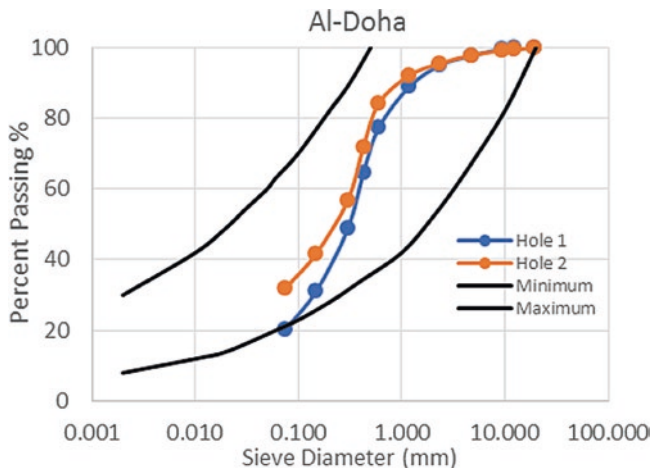


Fig. 8 Gradation for Al-Doha samples

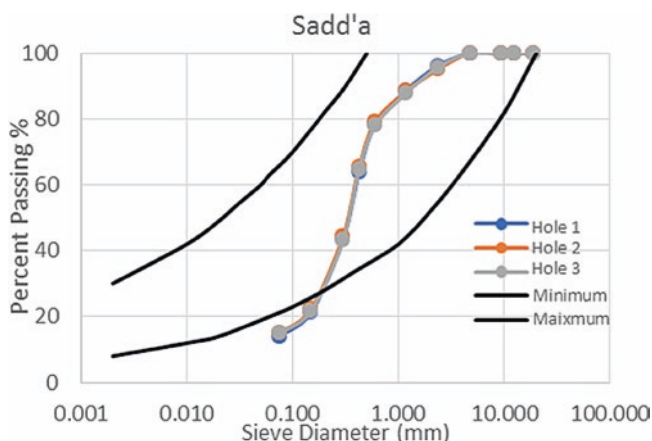


Fig. 9 Gradation for Sadd'a samples

3.2 Testing Protocol

In this study, the chosen block size was 217.5 mm × 140 mm × 90 mm. These dimensions were selected based on the size of the compression machine that was used for the production of the blocks. Molding pressure of 16.0 MPa was applied to form the blocks. After the soil (from Sabriya) was dried, stabilizers were added and hand mixed thoroughly; 2% of cement was added to all mixtures in order to counter the possible effect of organic matter on the adhesive properties [4]. A 10% of water

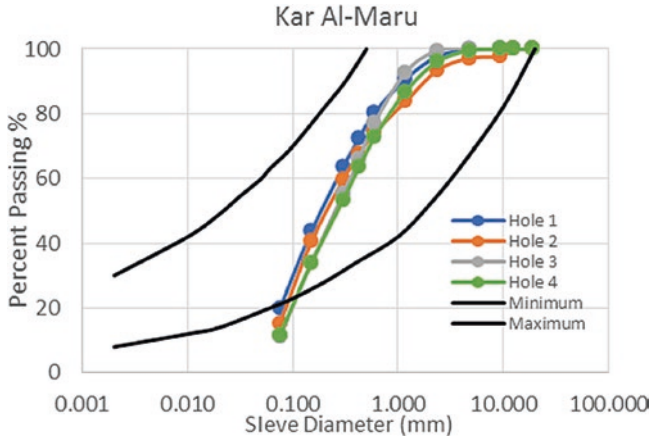


Fig. 10 Gradation for Kar Al-Marou samples

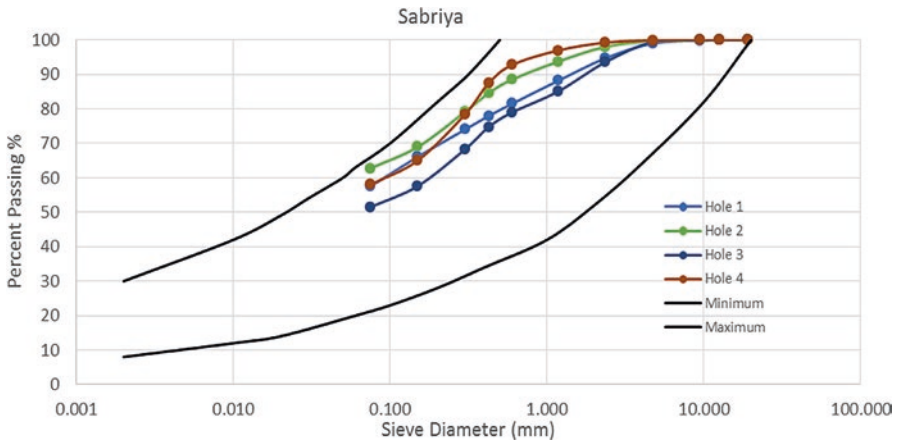


Fig. 11 Gradation for Sabriya samples

Table 1 Recommended bitumen emulsion content [11]

Soil	Percentage (%) of emulsion by weight
Soil with high sand content (over 50% sand)	4–6
Soil with medium sand content (approximately 50% sand)	7–12
Fine clay (below 50% sand)	13–20

Table 2 Different blocks produced for the study (at 16.0 MPa molding pressure)

Mix design	7 Curing days	28 Curing days
Reference block (2% cement)	3	3
Cement (8%)	3	3
DTF (1%)	3	3
Bitumen emulsion (8%)	3	3

Table 3 Compressive strength test results of the blocks

Mixture	7 Days (MPa)	28 Days (MPa)
Reference block (2% cement)	3.45	8.04
Cement (8%)	7.48	10.86
DTF (1%)	6.22	8.35
Bitumen emulsion (8%)	2.98	3.83

(by weight) was added to the mix (soil + stabilizers); this percent was chosen as it was found to be the optimum moisture content (OMC) of the soil using the modified proctor test [13]. Table 2 shows the blocks that were produced for testing using different stabilizers.

4 Results

The average compressive strength of the three blocks from each mixture was obtained at 7 and 28 curing days as shown in Table 3 and illustrated in Fig. 12.

5 Discussion

The highest result obtained through compressive strength test was 10.86 MPa after 28 days of curing. The mixture contained 8% of cement as a stabilizer. Adding date tree fiber in small percentages in terms of weight increased the compressive strength by 44% compared to the reference block (after 7 curing days); however, the compressive strength did not increase after 28 curing days proportionally. Date tree fibers enhanced the blocks after failure by keeping the cracked pieces intact. Bitumen emulsion had no positive enhancements to the compressive strength of the blocks when used as a stabilizer. An ongoing study is investigating other percentages of stabilizers and different mix designs for the production of CEBs in the State of Kuwait.

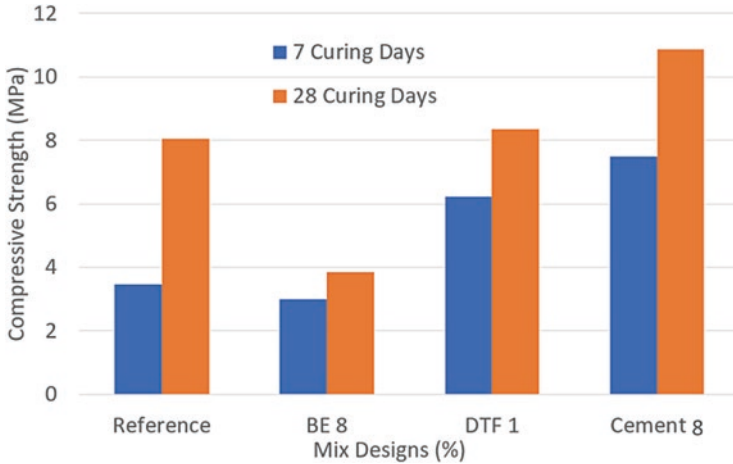


Fig. 12 Average compressive strength of the blocks

6 Future Work

- More investigation in terms of different stabilizers for 7 and 28 curing days
- Using bitumen emulsion as a coating material to the blocks rather than a stabilizer
- Adding sand to the mixture design percentages to study its effect
- Testing the flexural strength of the CEB and the effect of DTF on the flexural strength
- The effect of water on the CEB in terms of erosion, permeability, and absorption in addition to its wet compressive strength
- Studying the effect of interlocking CEBs on the total compressive strength of walls
- The thermal and audio insulation properties should be investigated in more detail

7 Conclusion

This ongoing research study aims at evaluating the applicability of using compressed earth blocks as a sustainable alternative construction technique in the state of Kuwait and the GCC region. The study started by evaluating different soils in Kuwait and concluded that the best soil that can be used is in the northern region of Kuwait, near Sabriya area and Bubiyan Island. The soil gradation of this region fell within the recommended gradation limits set by previous studies. In addition, CEBs were produced with mix designs using different stabilizers and evaluated through dry compressive strength. The obtained strength using 8.0% cement as a stabilizer

was the best. Using bitumen emulsion as a stabilizer decreased the compressive strength of the block. However, using it as a coating material for water proofing is under investigation. Using DTF as a stabilizer did not enhance the compressive strength significantly but enhanced the failure mode by keeping the block intact after failure due to its tension capacity. More ongoing studies on the topic is being done by researchers in the Australian College of Kuwait.

References

1. World Resources Institute (2014) World Resources Institute | Climate Analysis Indicator. <https://www.wri.org/>. Accessed 12 Jun 2017
2. Rigassi V (1995) Compressed earth blocks: manual of production. GATE (German Appropriate Technology Exchange), Germany
3. Boubekeur S, Houben H (1998) Compressed earth blocks: standards. Center for the Development of Industry; CRATerre-EAG, France
4. Mukerji K (1994) Stabilizers and mortars for compressed earth blocks. GATE (German Appropriate Technology Exchange), Germany
5. Deboucha S, Hashim R (2010) A review on bricks and stabilized compressed earth blocks. Academicjournals.org. <https://academicjournals.org>. Accessed 5 Feb 2018
6. Houben H, Guillaud H (1994) Earth construction: a comprehensive guide. ITDG Publishing, London, UK
7. Food and Agriculture Organization (FAO) of the United Nations (1969). Reconnaissance Soil Survey, A Report to the Government of Kuwait. Available at: <http://www.fao.org/3/88418e/88418e.pdf>. [accessed 21Aug. 2019]
8. Google Maps (2018). Kuwait Map. Available at: <https://www.google.com/maps/place/Kuwait/@29.3117863,46.4146205,8z/data=!3m1!4b1!4m5!3m4!1s0x3fc5363fbee51a1:0x74726bcd92d8edd2!8m2!3d29.31166!4d47.481766>. [accessed 10 Sept. 2018]
9. ASTM D422-63 (2007) E2, Standard test method for particle-size analysis of soils (Withdrawn 2016). ASTM International, West Conshohocken, PA. www.astm.org
10. ASTM D1140-17 (2017) Standard test methods for determining the amount of material finer than 75- μ m, Sieve in soils by washing, vol 200. ASTM International, West Conshohocken, PA. www.astm.org
11. Rigassi V (1985) Compressed earth blocks: manual of production. CRATerre-EAG, MISEREOR, Aus der Arbeit von GATE, Deutsche Gesellschaft für Technische Zusammenarbeit (GTZ) GmbH, Eschborn, Germany
12. Van Damme H, Houben H (2018) Earth concrete, stabilization revisited. Cement and concrete research. Sciencedirect.com. <https://www.sciencedirect.com>. Accessed 21 Aug 2019
13. ASTM D1557 (2017) Standard test methods for laboratory compaction characteristics of soil using modified effort. ASTM International, West Conshohocken, PA. www.astm.org

Historic Heritage Protection as Part of Sustainable Growth



Jadwiga W. Lukaszewicz and Jerzy P. Lukaszewicz

1 Introduction

According to some definitions, the term “sustainability” may be understood differently despite some clear definitions like “Sustainability is the process of people maintaining change in a balanced environment, in which the exploitation of resources, the direction of investments, the orientation of technological development and institutional change are all in harmony and enhance both current and future potential to meet human needs and aspirations” [1]. It may be also stated that “Sustainable development is the development that meets the needs of the present without compromising the ability of future generations to meet their own needs” [2]. The definitions/descriptions are very general, and as always, in such a case, some specific domains may be outlined within this area with respect to kind of phenomena and ideas occurring in the real life: sustainable environment, sustainable economy and technologies, sustainable social and cultural relationships, and sustainable politics [3, 4]. The most common view is that sustainability is attributed to environmental issues like climate change which recently bothers the societies around the world. Among all cited aspects of “sustainability,” environmental issues belong to the most well-known and exploited in science, politics, and everyday life. Societal aspects like a proper balance between the past and the present is less understood and discussed. However, every nation and every man inherit a certain amount of knowledge, information, and material artifacts from previous generations. Personal self-confidence in many cases relies on the relationships among people, events, and material objects from the past.

J. W. Lukaszewicz (✉)

Institute of Archaeology, Faculty of History, Nicolaus Copernicus University, Torun, Poland
e-mail: jwluk@umk.pl

J. P. Lukaszewicz

Centre for Modern Interdisciplinary Technologies, Nicolaus Copernicus University,
Torun, Poland

The relevance of and respect for the past have been noted by prominent historic figures like Winston Churchill (“The more we look back, the more we see the future”), George Orwell (“Whoever controls the past has power over the Future”), and many others.

Beside ideas and other nonmaterial heritage, every single man, every nation, and the mankind as a whole inherited material remaining, some of distinguished artistic meaning. All these items, despite of their artistic value, have a symbolic meaning as a magic bridge connecting us with the past events, places, and generations. This is a basic reason to undertake intensive actions against permanent deterioration of historic monuments and to undertake appropriate measures to reestablish the original shape and appearance of those historic artifacts which have been destroyed upon the passing of time.

2 Defining and Identification of Historic Architectonic Sites

Care on historic heritage is not only associated with mental, cultural, and administrative reasons; it also has a business component too. As a result of worldwide attention, awareness of the necessity of historic heritage protection is spreading to almost every country on the globe. However, historic heritage planning, protection, and restoration are governed by rules which were developed by conservators and restorers over nearly 250 years. This knowledge grew gradually and is full of contradictory points of view and continuously changing materials and methods applied to preservation and restoration of historic objects. Among all material objects inherited from past generations, the most outstanding and visible is architecture (buildings and building systems, gardens, etc.) and outdoor exposed single objects like sculptures and architectonic decorative details.

Firstly, the term historic object should be defined. Even in the ancient times, philosophers tried to define what a historic monument is. According to Plato and Aristotle, a monument (historic and artistic) “is a place where an idea and matter met and were transformed into beauty.” Following this statement, it may be concluded that each monument is the synthesis of the “material” and the “idea.” “Idea” may be also regarded as the form of matter which more commonly is understood as appearance. Besides this rather philosophical point of view, there are more exact definitions which became widely accepted in the recent years. The legal acts existing in some countries are the sources of such definitions. For example, in Poland the following definition may be cited after the Heritage Protection Legal Act (Law of 23.02.2003, Art. 3, Item 1): “A historical monument is a piece of real estate (immovable property) or a movable property, their parts or groups, which have been created by man or as a result of human activity and which constitute a testimony of the bygone epoch or event, whose preservation is of social interest due to its inherent historical, artistic or scientific value” [5]. The general definition is split in more detailed categories in the same Legal Act (Art. 6 Par. 1 Point 1), i.e., the following immovable monuments are subject to protection and care regardless of the state of preservation:

- (a) Cultural landscapes
- (b) Urban and rural layouts and construction teams
- (c) Architecture and construction departments
- (d) Defense construction departments
- (e) Technical facilities, in particular mines, steel mills, power plants, and other industrial plants
- (f) Cemeteries
- (g) Parks, gardens, and other forms of designed greenery
- (h) Places commemorating historical events or the activities of outstanding personalities or institutions

The protection may also apply to geographical, historical, or traditional names of a construction object, square, street, or settlement unit (Article 6 (2)).

Besides this general formulation, Conservation and Restoration State Service plays a crucial role (established in Poland in 1918), and among others, it is responsible for assembling detailed list of historic monuments in the whole country. The list of national heritage contains basic information on the object like exact name, location, owner's name and location, documented state of preservation, list of conservation/restoration works completed along with documentation of the works, list of aids (private and state) invested for conservation/restoration of the monument, etc.

The list is designed and updated after a careful expert evaluation of its artistic, historic, and emotional value. In such situation one may also say that a historic monument is the object which is listed as national heritage. Later in time the status of a historic monument can be extended to new categories of objects. Beside palaces, castles, old houses, old towns and villages, and temples which were at first identified as historic monuments, new types of objects are nowadays included as national heritage, like old factories, technical installations, old roads, parks, etc.

National treasury lists like the one mentioned in the case of Poland exist in many countries, particularly in Europe. In the global scale, analogous list of world scale heritage or treasures has been assembled by United Nations Educational, Scientific, and Cultural Organization (UNESCO) World Heritage Committee [6]. For a heritage treasure to become a status of World Heritage Site, it must be unique regarding specific geographical and/or historical features and has a special cultural or physical significance. Such objects in practice may be an ancient ruin or historical structure, building, city, complex, desert, forest, island, lake, monument, mountain, or wilderness area. Additionally, such a site should serve as evidence of intellectual or natural history of the planet and mankind. Sites are demarcated by UNESCO as protected zones. The whole program was started during the Convention Concerning the Protection of the World's Cultural and Natural Heritage. Then, the documents were accepted by the General Conference of UNESCO on 16 November 1972. Nowadays, 193 states have ratified the convention. The currently updated UNESCO list contains 1121 sites around the world, divided in 2 general categories: cultural (869) and natural (213). Some sites of mixed nature (39) have been also included. The sites are located in 167 countries. Among them the most "rich" are China (55 objects), Italy (55 objects), Spain (48 objects), Germany (46 objects), France (45 objects), India

(38 objects), and Mexico (35 objects). Similar classification may be formulated with respect to a geographic regions/zones/continents (Table 1).

Regarding the Gulf Conference on Sustainable Built Environment (Kuwait, 10–13 March 2019) and the origin countries of the most of attendees, it might be interesting to note which and how Middle East Sates participate on the list (Table 2).

Table 1 Geographic displacement of UNESCO heritage sites [6]

Area	Type of the site			Total
	Cultural	Natural	Mixed	
Africa	53	38	5	96
Arab States	78	5	3	86
Asia/Pacific Region	189	67	12	268
Europe/North America	453	65	11	529
Latin America/Caribbean Zone	96	38	8	141
Total	869	213	39	1121

Table 2 UNESCO heritage sites in the Gulf Region [6]

Country	Cultural/natural site
Bahrain	Ancient Qal'at al-Bahrain Harbor City and Capital of Dilmun; Muharraq Island, Qal'at Bu Mahir Fortress; coastal and offshore pearling sites
United Arab Emirates	Cultural sites of Al Ain (Hafit, Hili, Bidaa Bint Saud, and oases areas)
Yemen	Historic town of Zabid; Old City of Sana'a; Old Walled City of Shibam; Socotra
Iran	Armenian monastic ensembles of Iran; Bam and its cultural landscape; Bisotun; cultural landscape of Maymand; Gonbad-e Qabus; Golestan Palace; Lut Desert; Masjed-e Jame of Isfahan; Naqsh-e Jahan Square; Pasargadae; Persepolis; Shahr-e Sukhteh; Sheikh Safi al-din Khanegah and Shrine Ensemble in Ardabil; Shushtar historical hydraulic system; Soltaniyeh; Susa; Tabriz historic bazaar; complex; Takht-e Soleyman; Tchogha Zanbil; The Persian Garden; The Persian Qanat; Historic City of Yazad
Iraq	Ashur (Qal'at Sherqat); Erbil Citadel; Hatra; Samarra Archaeological City; The Ahwar of Southern Iraq
Oman	Aflaj irrigation systems of Oman; archaeological sites of Bat, Al-Khutm and Al-Ayn; Bahla Fort; Land of Frankincense
Qatar	Al Zubarah
Saudi Arabia	Al-Hijr archaeological site (Madain Salih); At-Turaif District in ad-Dir'iyah; historic Jeddah; Rock Art of the Hail Region

The complete list of UNESCO Heritage Site involves sites/monuments in well-preserved states as well as sites which are in very poor condition and need a conservation/restoration intervention, sometimes very urgently

3 Rules of Restoration and Conservation of Historic Architectonic Objects

The need for preservation and protection of cultural heritage has clearly existed for centuries, but there has been little knowledge of how to organize and perform such actions while taking into account the complicated factors of human intuition, politics, and religion. Quite recently, i.e., in the nineteenth century, the first systematic and science-based conservation/restoration concepts were formulated. From the very beginning, conservation/restoration of historic heritage was full of contradictions. The first theoretical principles of stone monument restoration were created in parallel by Eugene Emmanuel Viollet-le-Duc (1814–1879) and John Ruskin (1819–1900) [7]. Viollet-le-Duc advised an intensive transformation in order to return an object to its stylistic purity but also advised an individual approach to each artifact. Ruskin presented a totally opposite view and believed that any restoring/reconstruction of a historical monument is “a lie, from the beginning to the end.” He advocated only preservation works aimed at maintaining the monument in its current state. Thus, several important questions were raised and needed to be answered:

- What are the rules and the intensity of restorer’s intervention?
- Should the rules be consistent regardless of the kind and state of monuments?
- What is the acceptable scope of restorers’ intervention?
- Is the medical principle “*primum non nocere*” applicable to the protection/reconstruction of historical heritage?

In the recent decades, the international community of restorers and conservators undertook unification steps toward the elaboration of a universal attitude to historic heritage protection. Two fundamental documents were formulated and commonly accepted:

- The Athens Charter
- The Venice Charter

The Charters clearly define the acceptable scope of conservation and restoration works [8, 9]. The Athens Charter was adopted at the First International Congress of Architects and Technicians of Historic Monuments in Athens (Greece) in 1931. Seven general topics were formulated and described during the Congress covering the following issues:

- Doctrines. General principles
- Administrative and legislative measures regarding historical monuments
- Aesthetic enhancement of ancient monuments
- Restoration of monuments
- The deterioration of ancient monuments
- The technique of conservation
- The conservation of monuments and international collaboration.

This document is often called “Carta del Restauero” and still is like a Bible for those who care about historical heritage. Naturally, the primary point of view had to be modified and supplemented later in 1964 by the formulation of The Venice Charter for the Conservation and Restoration of Monuments and Sites by ICOMOS—International Council on Monuments and Sites (established during the founding congress in 1965 in Warsaw and Kraków in Poland).

The Venice Charter formulated clearly the aim of conservation and restoration as “The intention in conserving and restoring monuments is to safeguard them no less as works of art than as historical evidence.”

Due to numerous wars, fights, and natural disasters, the problem of monument reconstruction has become a crucial issue of national and international significance. Poland has a broad and long experience in the reconstruction and restoration of cities destroyed during World War II. Reconstructions of old towns of Warsaw, Gdańsk, and Wrocław are spectacular examples. The highest level of reconstruction works has found worldwide recognition through the listing of the Warsaw Old Town on the UNESOCO Heritage list in 1980 despite enormous war damages.

Additionally, in 2018 a Warsaw Recommendation document had listed principal rules of historic city reconstruction and recovery [10]. The rules allow for far-reaching reconstruction only if adequate documentation of the original state exists.

Both Charters should also serve as a text book for administration officers who are not professional restorers/conservators but are responsible for heritage protection.

4 Examples of Diversified Restoration and Conservation of Architectonic Monuments in Poland

Contemporary conservation and restoration of historical objects must obey the conclusions of the Venice Charter and the Athens Charter in all works undertaken to protect historical heritage regarding original state and appearance. However, the conservation and restoration works should also consider individual features of a monument as well as its future role in society. It makes a substantial difference if a historic object to be reestablished and protected has a very high artistic, historic, and emotional value. In such a case, restoration intervention should be moderate and oriented toward intensive protection of the original appearance of the remaining object. In case of moderate or low aesthetic value, the scale of permissible conservation/restoration intervention may be larger. The photos below show two apparently similar historic buildings, i.e., a palace and a castle, which were reestablished from ruins. The first architectonic monument is a nineteenth-century local landlord palace in Turzno (central Poland—Figs. 1, 2, and 3). The photos document the state of preservation before restoration works started and the current outside appearance of the palace as well as an example room. The Palace of Turzno has a moderate artistic, historic, and sentimental value, and many similar palaces may be found in Poland. Moreover, no key historic events happened in this place. Therefore, the restoration



Fig. 1 Part of Turzno Palace before restoration works. (With the permission of the copyright holder R. Predenkiewicz)



Fig. 2 A part of Turzno Palace after restoration. (With the permission of the copyright holder R. Predenkiewicz)



Fig. 3 An example hotel room in the Turzno Palace: concert hall. (With the permission of the copyright holder R. Predenkiewicz)

works targeted the reestablishment of the palace's original, i.e., nineteenth-century external appearance, while the interior was adopted to its new function. The Turzno Palace was converted into a luxury hotel having all necessary facilities for the visitors (a four-star hotel). This far-reaching intervention was also motivated by the fact that no original equipment, furnishing, and outfit survived from the past. All restoration works received the approval from District Conservator Office and were performed under an appropriate and established expert supervision.

In contrast to the Turzno Palace, the restoration of the Royal Castle in Warsaw (Poland) was much more focused on the preservation of original equipment, furnishings, and outfittings. The Castle has a long history (starting from the fourteenth century) and was a place of many nationally significant historic events. Thus, the Royal Castle is definitely an important and unquestionable part of Poland's history. The Castle was bombed, ruined, and burned by the Nazi army during World War II (Figs. 4, 5, 6, and 7). For nearly 30 years after World War II, its state was much worse than the state of Turzno Palace. Despite this fact the Royal Castle's exterior as well as interior were reestablished to nearly original state. This was possible since there were rich photographic and technical archives documenting the Castle's state before World War II. This archive material served as a pattern for restoration works. The rooms were reconstructed in Baroque and Classicist style, and many of the original architectonic details were incorporated during the restoration works. The furnishings and exposed pieces of art (sculptures, paintings) are originals dated mainly from the sixteenth to eighteenth centuries. In this way the Royal Castle is well suited to its contemporary function, i.e., a national museum and art gallery.



Fig. 4 The Royal Castle in Warsaw (Poland): the state after bombing in 1939. (Free access archive photograph)



Fig. 5 The Royal Castle in Warsaw (Poland): the state after World War II (1945). (With the permission of the copyright holder Narodowy Instytut Dziedzictwa (National Heritage Board Poland))



Fig. 6 The Royal Castle in Warsaw (Poland): the state after renovation (2017). (Author P. Ostrowski. With the permission of the copyright holder Narodowy Instytut Dziedzictwa (National Heritage Board Poland))

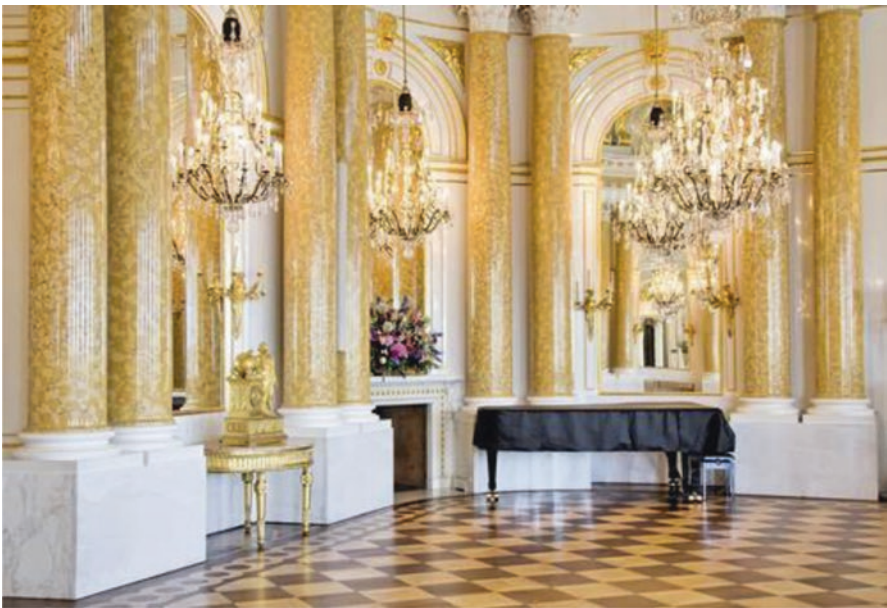


Fig. 7 The Royal Castle in Warsaw (Poland): the ballroom after restoration. (With the permission of copyright holder www.photogenica.pl)

These two examples show how complex restoration/conservation works can be and how individual decisions on the depth of restoration intervention must rely on different factors.

5 Selected Financial Aspects of Architectonic Monument Restoration and Conservation

The differences in the concept of restoration of both historic sites (Palace of Turzno and Royal Castle in Warsaw) illustrate the different roles that daily operations and available financial resources can play in restoration and conservation. The Palace of Turzno would have difficulties to obtain complete state financial assistance to cover its restoration and subsequent maintenance. Thus, the Palace was restored with the participation of a private investor/owner who was also interested in financial self-reliance of the Palace after the restoration is completed. The concept of a luxury hotel as business background was decided from early beginning. The constant inflow of revenues allows the historic object to be maintained in a vital state which can affect other reconstruction works: the palace chapel and garden. Turzno Palace is an instructive example on how to reconcile the historic heritage preservation goal with a contemporary function which eliminates the need for public support to cover daily maintenance. The Palace project has resulted in nearly 40 working places in the rural area which is an important social achievement.

Obviously, the artistic and historic value of the Royal Palace in Warsaw and the manner in which it was restored determined its every day operation. The Castle was restored using state funds mainly supplemented by some small private donations. The Castle is constantly receiving yearly state support for its operation. Together with the ticketing revenue, it is able to cover all expenses. The Royal Castle is also a good example of how to reconcile the restoration concept with the role of a national treasure in which any commercial support is not accepted.

Given the example of the Royal Castle in Warsaw, one may gain a false impression that restoration/conservation/maintenance of high-value historic architectonic objects is a source of permanent and sometimes increasing public expenses. However, there are convincing examples showing that the care for heritage may boost business and employment in a historic site. Torun (middle Poland) is a Gothic city established by Teutonic Knights in 1232 (Figs. 8, 9, 10, 11, 12, and 13). The city itself has nearly 200,000 inhabitants and is located on the bank of the largest Polish river Vistula. In the medieval era, Torun played a crucial role in the country's trade which was the source of huge revenues partly invested in the construction of monumental churches and houses. From these times Torun inherited its major architectonic monuments: the Cathedral of St. John the Evangelist and John the Baptist, St. Mary's church, St. James's church, the Old Town Hall, Leaning Tower of Torun, Ruins of thirteenth-century Teutonic Knights' castle, House at the sign of the Star, and Copernicus House. In contrast to other historic cities in Poland, Torun avoided



Fig. 8 The panorama of medieval Torun Old Town across the Vistula River. (Copyright by J. W. Lukaszewicz)



Fig. 9 Architectonic historic monuments of Torun: the Leaning Tower. (Copyright by J. W. Lukaszewicz)



Fig. 10 Architectonic historic monuments of Torun: the Gothic Town Hall. (Copyright by J. W. Lukaszewicz)



Fig. 11 Architectonic historic monuments of Torun: the Copernicus House. (Copyright by J. W. Lukaszewicz)



Fig. 12 Architectonic historic monuments of Torun: the outside view of the Cathedral of SS. John the Evangelist and John the Baptist after protective conservation (no intensive reconstruction works). (Copyright by J. W. Lukaszewicz)



Fig. 13 Architectonic historic monuments of Torun: the interior of the Cathedral of SS. John the Evangelist and John the Baptist after protective conservation (no intensive reconstruction works). (Copyright by J. W. Lukaszewicz)

substantial destruction in World War II. The Old Town area where all important architectural monuments are located is in original state, and no substantial reconstructions were needed. Only protective measures were performed starting from the early sixties of the twentieth century. This fact attracted the attention of UNESCO experts who decided to enroll Torun Old Town (including all the mentioned historic buildings) to the UNESCO World Cultural and Natural Heritage List in 1997. This act was a triggering event for attracting domestic and international tourism. Over the last 22 years, Torun improved its tourist infrastructure along with protective conservation works. All the above-listed medieval building underwent such works, particularly after Poland joined the European Union. Torun is, besides Krakow, Gdansk, Warsaw, and Malbork, one the major tourist attractions of Poland. In 2018 more than 2,350,000 tourists visited Torun, i.e., nearly 11 visitors per city inhabitant [11]. Rough estimations show that more than 600 mln PLN come to the city (local tax), city institutions (museums), and private business (hotels, restaurants, shopping) from the visitors. Tourism incomes are an important part of the local economy and play an important role in the labor market. The tourist revenue boosted private investment in the renovation of more ordinary houses which then serve as hotels, restaurants, and shops. Such privately renovated houses are technically sound and kept in a good state without any public financial assistance. The tourism delivers notable income to the city budget which cares for environmental issues caused by increased in flow of people as well as for renovation of streets and the city green (parks and woods).

Torun is an excellent example how well-protected heritage can positively influence contemporary livelihood from several points of view.

6 Conclusions

Protection and restoration of historic architectonic sties are part of a modern sustainable society which must maintain a proper balance between the past and the present. It covers human expectations from past generations as a part of its own cultural identity. While Europe, Asia, and America are rich in historic sites under UNESCO protection, the Gulf Countries also have inherited many such objects of primary importance to mankind. These sites need to be preserved for the future generations. Moreover, new sites should be identified, restored, and protected.

References

1. HEC Global Learning Centre. <https://www.globalfootprints.org/sustainability/>
2. International Institute for Sustainable Development. <https://www.iisd.org/topic/sustainable-development>
3. James P, Magee L, Scerri A, Steger MB (2015) Urban sustainability in theory and practice. Routledge, London

4. Magee L, Scerri A, James P, Thom JA, Padgham L, Hickmott S, Deng H, Cahill F (2013) Reframing social sustainability reporting: towards an engaged approach. *Environ Dev Sustain* 15:225–243. <https://doi.org/10.1007/s10668-012-9384-2>
5. Kancelaria Sejmu RP. <http://prawo.sejm.gov.pl/isap.nsf/down-load.xsp/WDU20031621568/U/D20031568Lj.pdf>
6. UNESCO. <https://whc.unesco.org/en/list/>
7. Lukaszewicz JW (2018) Ethics and basic principles of restoring historical stone monuments. *Heritage Future* 1:105–113
8. ICOMOS. <https://www.icomos.org/en/167-the-athens-charter-for-the-restoration-of-historic-monuments>
9. ICOMOS. https://www.icomos.org/charters/venice_e.pdf
10. Marcinkowska M, Lipska D (2018) Warsaw recommendation on recovery and reconstruction of cultural heritage. National Heritage Board of Poland, Warsaw. ISBN 978-83-66160-14-9
11. Osrodek Informacji Turystycznej. <https://visitatorun.com/pl/page/monitoring-ruchoturystycznego>

Archaeological Science in the Arabian Gulf: A Study of Bronze Age Pottery from Kuwait Using Portable X-Ray Fluorescence (pXRF)



Hasan J. Ashkanani

1 Introduction

Dilmun was an early civilization that was located in the contemporary Kingdom of Bahrain. Its inhabitants developed technical skills, formed economic and political units, and expressed themselves in art and cultural materials beginning in the third millennium BC [1, 2, p. 15]. By the second millennium BC, Dilmun culture has been clearly identified geographically on Bahrain, Failaka Island (Kuwait), and Tarut on the eastern coast of Saudi Arabia [1, 3]. Strategically, Dilmun was located on the sea route between Mesopotamian, Magan, and the Indus Valley. Thus, it developed a strong political, economic, and cultural interaction confirmed by the archaeological record (Fig. 1).

Significantly, there is Sumerian literature that referred to Dilmun as both a trade center and the region in which the god of freshwater, *Inzak*, was worshipped [4, p. 59]. Early scholars purported that ancient Dilmun was indeed modern Bahrain based on Old Babylonian cuneiform inscriptions that were recovered from Bahrain. These inscriptions mentioned a servant of the god *Inzak* [5, p. 31]. In 1928, some scholars presented additional support to the earlier argument based on additional textual evidence [5, p. 31]. They linked the Dilmun with Bahrain based upon an earlier translation of the Sumerian paradise myths, which make a connection between the deities *Enki* and *Ninhursag* with the existence of freshwater springs in Dilmun [5, p. 31]. Peter Bruce Cornwall, a young American scholar, addressed the Dilmun identity issue with his research, carried out in 1940 and 1941. His dissertation was an analysis of textual evidence in Bahrain along with other burial mounds on Bahrain Island from the Bronze Age [6].

H. J. Ashkanani (✉)

Anthropological Archaeology, Department of Sociology and Social Work,
College of Social Sciences, Kuwait University, Kuwait, Kuwait
e-mail: Hasan.ashkanani@ku.edu.kw

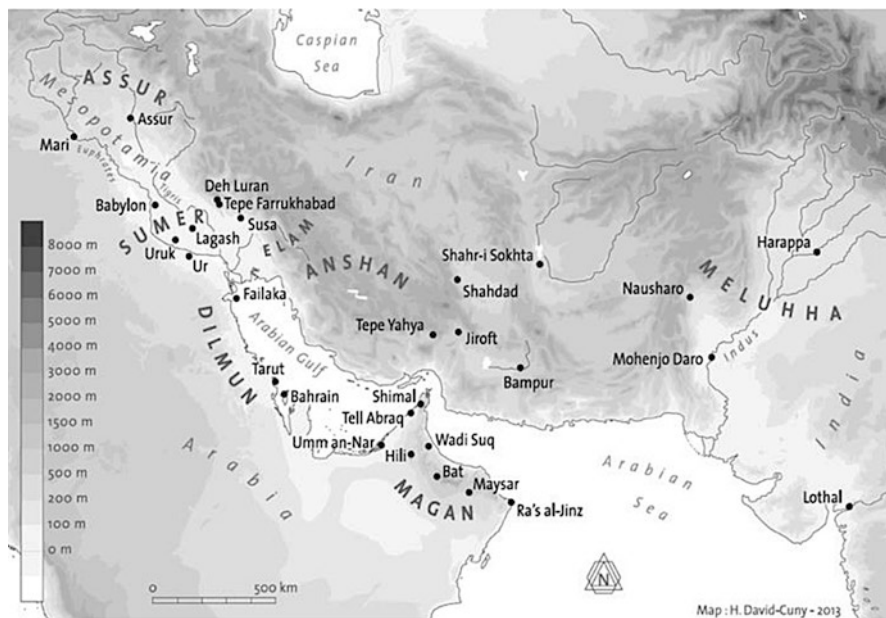


Fig. 1 Map of the Arabian Gulf and adjacent regions showing the major sites and locations mentioned in this text

The Dilmun culture underwent some notable changes during the Bronze Age. The oldest Bronze Age sites on Failaka Island coincide with the Barbar (City) II period in Bahrain (ca. 2050–1750 BC.). The astonishing expansion during the Barbar II period has been noted in all aspects of life. Bahrain replaced the Eastern Province as the center of the Dilmun polity and transformed into an active trade port, after an expansion in settlement pattern. Qala'at (Bahrain) became a small, urbanized trading port and a fortified capital with a small surrounding wall extending over more than 30 hectares.

By the end of the third millennium BC, planned residential settlements with notable architectural features (i.e., temples, municipal buildings, etc.) marked great economic growth and sociopolitical development. Furthermore, numerous burial complexes and “Royal Mounds” in Bahrain have been dated to the early second millennium BC, suggesting the emergence of a stratified social hierarchy. The latter suggests that a centralized administration existed that controlled this growth through various means. Thus, this inquiry seeks to explore whether the distribution of Barbar wares was one of the mechanisms used to control the economic growth of the Dilmun trade network. Also, this study seeks to explore whether a connection between the presence of nonlocal wares and far-distance staples in elite contexts on Failaka Island can be used to infer the pronouncement of status, power, and prestige.

This inquiry examines the production of pottery in the Dilmun territory (i.e., Failaka Island, Kuwait, and Bahrain) during the Bronze Age. Furthermore, this study investigates the provenance of Dilmun ceramic production as well as nonlocal

wares that were exchanged in Dilmun territories. Specifically, it examines the standardization of chemical composition of ceramic sherds from Dilmun sites on Failaka Island and Bahrain using a nondestructive portable X-ray fluorescence spectrometer (pXRF) and petrographic thin-section analysis. The petrographic thin-section analysis was carried out as a complementary tool to investigate the mineralogical composition of Dilmun wares and far-distance pottery of the first third of the second millennium BC.

The aims of this study included the following: (1) to explore the development of pottery production; (2) to determine if standardized production recipes were used for Barbar wares; (3) to link provenance sources to production sites, namely, to see if a specific site had access to nonlocal pottery; and (4) to determine if the standardization of provenance sources and production techniques of Barbar wares could be used to suggest Dilmun's elites having had sociopolitical authority in the region.

The study of ceramic characterization (i.e., craft specialization, production, etc.) was used in this research to explore the political and social complexity of the Dilmun. Specifically, the chemical and mineralogical characterization of Barbar ceramics of the Dilmun were investigated as another line of evidence to discuss the Dilmun's emerging presence in the Arabian Gulf during the second millennium BC. The data generated from a characterization study could be juxtaposed alongside other evidence, such as different burial mounds, distribution of nonlocal goods and items, and differential housing. In addition to the attempt made by archaeologists to study the development of Barbar pottery morphologically, this study is designed to contribute to the discussion about the mechanisms of power shifts.

1.1 Kuwait Archaeology Toward Scientific Perspective

The growing participation of Dilmun in the Arabian Gulf trade network was parallel to other sociopolitical and economic developments that occurred in the late third millennium, ca. 2050 BC. The development of stone work, planned settlement patterns, pottery production, temple building, royal burial mounds, and standardized stamp seals accompanied the Dilmun political hegemony in the beginning of the second millennium BC.

The shift in pottery production techniques at Dilmun, from chain style in the pre-Barbar to a well-fired hand- and wheel-made in the Barbar Period, could have been an important factor in the evolution of Dilmun sociopolitical complexity. Højlund [7] has characterized pre-Barbar period pottery production at the Qala'at site as exclusively handmade, with irregularity and unevenness in the rim, nick, and body regions. However, during Barbar Period II in the early second millennium, use of the wheel technique increased at the Qala'at site in addition to the handmade pottery. Also, imitations of imported goblets were introduced, implying the acceptance of innovations in Dilmun pottery production [7]. The wheel-turntable pottery has a limited number of styles and a small repertoire of luxury productions, suggesting craft specialization and standardization in production [8].

During the Barbar Period (2050–1800 BC), the red-ridged ware, a Barbar type, became widespread in Bahrain. Furthermore, this increase coincided with a decrease in Mesopotamian pottery and a disappearance of southeastern (Umm an-Nar) pottery types [3, 5, 7]. New shapes of pottery were developed in this period and other shapes became much more dominant [7, 9]. The Barbar Period wares were hand-made red-brownish, and hard-fired, with yellowish slip covering the outer surface. Painted pottery was introduced in this period, both local and imported, particularly the “Eastern Tradition” wares from Iran and the Indus Valley [3, 5, 7].

The Barbar type wares that have been found on Failaka Island represent a wide range of Barbar ware types, such as shouldered vessels, neck or neckless ridged jars, plates, goblets, bowls, and cooking pots. Furthermore, the Barbar Period II pottery, particularly the IIB phase (ca. 1950 BC), is parallel to the pottery of the Barbar Temple’s Period IIB and Failaka pottery, Period 1. The pottery production of this period is consistent with Barbar Period IIA in general with such commonality in wheel-made pottery for the large jars, suggesting an improvement in skills [8].

This study seeks to build upon previous typological studies and inquiries into trade and exchange to explore the emergence of Dilmun sociopolitical authority. Using pXRF and petrographic thin analysis, I explore the provenance of ceramics recovered from Dilmun sites on Failaka Island, Kuwait, and Bahrain.

Theoretically, this study addresses the political economy of ancient Dilmun in the second millennium BC and examines the level of sociopolitical complexity. The standardized appearance of the pottery strongly suggests that Barbar wares were mass-produced by professionals and had shifted gradually from a household level of pottery production. The shift in ceramic craft production was parallel with increasing sociopolitical complexity. Therefore, I intend to examine Dilmun ceramics from Failaka Island sites to determine if standardized production recipes (chemical and mineralogical compositions) were used for Barbar wares. I am suggesting that Dilmun elites may have controlled the production and distribution of Barbar wares as a part of their other economic activities that are associated with their emerging sociopolitical authority.

Also, the centralized administration’s officers and elites of Failaka may have been seeking to monopolize prestige items (i.e., nonlocal pottery, other exotic items, etc.) to increase their status. This provenance study has been able to characterize to some degree the level of involvement of the centralized administration in ceramic production. Control of raw materials, production techniques, and the distribution of finished products, as well as the very lives of the craft specialists [10, p. 15], support the aspirations of an emerging centralized authority and elite group.

Although many studies have been conducted on the ancient Arabian Gulf trade network during the Bronze Age, very little attention has been given to Kuwaiti Bronze Age ceramics and ceramic technology. Previous works were descriptive excavation reports and typological studies that reported site information and significant recoveries [9, 11–16]. These studies focused on describing the archaeological materials, such as Dilmun and Sumerian stamp seals and ceramics. Typological studies provided generalizations about cultural affiliation and chronological schematics. Through this characterization study, I intend to contribute data that allows

for interpretations that can reach beyond the descriptive nature of typological studies.

1.2 Failaka Island: A Key of Dilmun Power

Failaka Island currently belongs to the State of Kuwait and lies 20 km east of the mainland of Kuwait and opposite Kuwait Bay (Fig. 2). Its area is approximately 43 km², which is roughly half the size of Manhattan, New York; its maximum length is 14 km and is roughly 6 km wide [17, p. 9]. The island is flat, apart from a small hill 9 m above sea level in the extreme western part.

The island, roughly rectangular in shape, is adjacent to Meskan Island to the northwest, while O'ha Island is adjacent to the southeast. Failaka Island is mostly sandy with some rocky coastlines. The Shbija mound is considered the highest point at about 9 m above sea level [17, p. 9]. The entire shoreline of Failaka is considered to be a natural port, where ships used to be protected during storms.

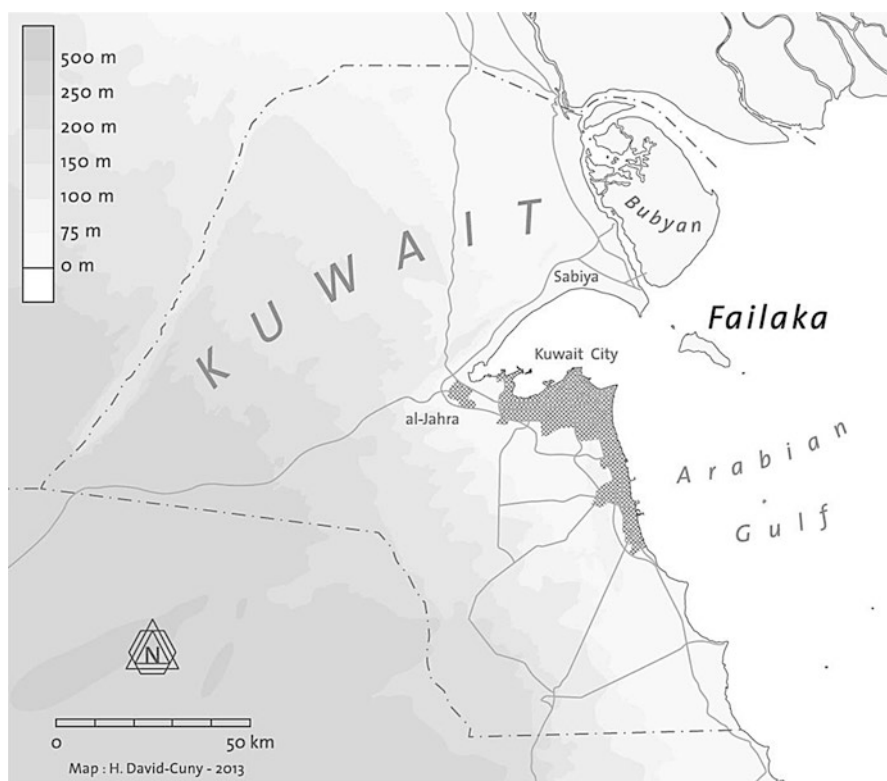


Fig. 2 Map of Kuwait and the location of Failaka Island as the first stopping point on the mouth of Shatt Al-Arab

The recent excavations by the Slovak expeditions [12] have shown that the old port of the island was located at the Al-Khidr area in the northern part. Its position, facing the direction of Al-Basra in Iraq, is considered to be a natural old harbor and a convenient stop on the maritime route along the western coastline of the Arabian Gulf.

Many natural features qualified the island as a choice to accommodate trading expeditions by traders associated with early Middle Eastern state-level societies. The island contains many water wells along with fertile soil, which supported plantations; this agricultural area constituted 70% of the island’s geography until the first half of the twentieth century [17, p. 10]. Because the island has a natural source of freshwater, its population grew steadily before the invasion of Iraq in 1990. After Iraq was expelled in 1991, the Kuwaiti government resettled the island’s inhabitants on the mainland and compensated islanders for their property. Currently, the island is a place for both military exercises and fishing activities. The public may also visit the archaeological sites.

Failaka’s initial occupation around 2000 BC is based on various finds at three sites (F6, F3, and Al-Khidr) on the island that were excavated by Danish, French, and Slovak missions (Fig. 3). A recent excavation by Danish mission has uncovered a structure beneath the second millennium BC layer that dated to Ur III period of the

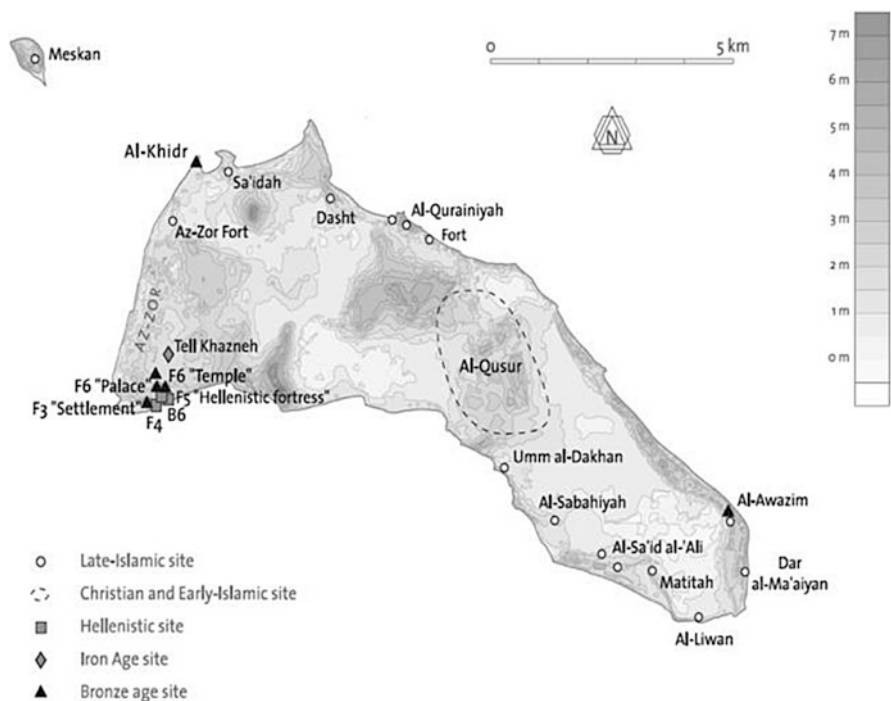


Fig. 3 Map of Failaka Island showing different archaeological sites and the well-known Bronze Age sites in the western portion of the island (F3, F6, and Al-Khidr)

late third millennium BC [18]. Some of the oldest as well as major Bronze Age sites are attributed to the Dilmun period. F3 site (F = Failaka) is an archaeological site named by the Danish expedition [16, p. 8] and is known as Tell Sa'ad or Dilmun City site. Approximately 2.90 m above sea level, F3 is a residential settlement with documented domestic activities including archaeological evidence of elite structures, skeletons of gazelles and goats, 170 round stamp seals, small stone houses, a temple, and some kilns for unknown purpose [16, p. 8, 15, p. 207, 19, p. 76]. The temple was distinguished by the discovery of altars and Sumerian inscriptions on seals. Furthermore, this sacred precinct was apparently dedicated to the god Inzak, chief god during the period of the Dilmun Kingdom from the third millennium BC [13, pp. 253–254, 15, p. 207].

Approximately 200 m east of F3 and 4.20 m above sea level, the site of F6 is also regarded as a Dilmun site. F6 is the oldest site that is associated with the Dilmun occupation on Failaka. It includes an architectural structure of a temple similar to the second millennium Barbar temples in Bahrain. Ten meters east of the temple is a Bronze Age structure that is thought to be a palace based on its size and architectural sophistication [16, 18, pp. 8–10].

The discovery of the Al-Khidr site by the Kuwaiti-Slovak expedition (2004–2009) on the coast in the northwestern portion of Failaka was also significant. This site has also revealed an early Dilmun influence in the island. This site appears to have served as a port in the early second through middle second millennium BC according to its geographical location and the numerous diagnostic ceramics, metal objects, and bituminous materials encountered [12].

2 Methodology and Samples

This study is designed to determine the scale production of Barbar pottery, to locate Barbar production centers, and to explore the circulation of nonlocal pottery during the early second millennium at Bronze Age sites. The study included ceramic sherds from Bronze Age sites on Failaka Island in Kuwait, Bahrain, Indus Valley particularly from Harappa main center in Pakistan, and Iran. Collecting samples from the aforementioned regions is necessary because of their widespread circulation throughout the Arabian Gulf region during the Bronze Age. They might be beneficial as a reference group for nonlocal sherds that may be found within Dilmun sites.

To determine the possibility of homogeneity in Barbar ceramic recipes, technology, and production, each sample group from each Failaka phase is compared to a selected sample group from Bahrain, which its periods are parallel and contemporary with Failaka periods in the second millennium. For instance, some samples were taken from the Barbar Temple IIb phase that is contemporary and parallel with the earliest phase in Failaka, Period 1 (ca. 1950 BC). Also, samples from Northeast Temple, period APR-ARU, were also selected because they are contemporary and parallel with Failaka F3 samples. The aim is to determine any recipe change synchronically and diachronically within Dilmun sites and differences between Failaka

Dilmun ceramics versus Dilmun of Bahrain. By comparing each phase, the research can shed light on the development of local-type pottery in Dilmun and possibly identify any kind of attached and independent specialists, controlling raw materials and ceramic manufacturing.

The samples analyzed in this study consists of 304 ceramic sherds and clays from various types of early Bronze Age pottery on Failaka Island in Kuwait, Bahrain, Eastern Province in Saudi Arabia, Deh Luran plain and Susiana plain in Iran, and Harappa in Pakistan (Table 1). The sampling strategy is based on using different ceramic traditions—Barbar versus Mesopotamian traditions—from various sites as a reference groups. Each reference group selected is well identified and its provenance is known, or sherds are found in kilns. For instance, Dilmun sherds from Barbar Temple and Qala’at sites are collected as a reference group of Bahrain clay, while Harappan sherds come from the pottery kilns at Mound E in the main Harappa center in Pakistan.

Table 1 Summary of all sample materials from Kuwait, Bahrain, KSA, Iran, and Pakistan

Site	Structure	Region	Sample size	Phase
Tell F6	The Palace	Failaka Island, Kuwait	16	Period 1
Tell F6	Trench E	Failaka	35	Period 1
Tell F6	Mesopotamian House	Failaka	18	Pre-Period 1
Tell F3		Failaka	11	Period 2
Tell F3		Failaka Island, Kuwait	6	Period 3A
Tell F3		Failaka	12	Period 3B
Al-Khidr		Failaka	91	Period 2A–2B
Barbar	Temple II	Bahrain	10	Period IIb
Barbar	NE Temple	Bahrain	11	APR-ARU
Qala’at		Bahrain	9	Period IIIf
Qala’at		Bahrain	5	Period IIIa
Tepe Farukhabad		Deh Luran plain, Iran	5	Sukkalmahhu Elamite
Susiana plain		Iran	8	Sukkalmahhu Elamite
Susiana plain		Iran	5	Early Middle Elamite
Susiana plain		Iran	11	Late Simashki Elamite
North Susiana		Iran	7	Proto Elamite
Harappa	Mound E	Pakistan	30	Period 3B
Harappa	Mound AB	Pakistan	3	Period Cemetery H
Clay	Kuwait, KSA, and Bahrain		11	
			Total 304	

The aim of selecting samples from various archaeological sites representing different geological parts of sociopolitical entities that participated in the Bronze Age trade and interaction is to overcome the lack of geological background of archaeologists and the procedures of obtaining geological samples. This research can provide more insight about how those reference groups from Iran and the Indus Valley are useful for fingerprinting nonlocal ceramic samples that are expected in this study. It helps in the future research to suggest obtaining or avoiding samples from these particular sites.

2.1 Portable X-Ray Fluorescence (pXRF): Sampling Preparation

For this research, the 2008 MURR calibration, which was originally designed by Robert Speakman and Michael Glascock for obsidian and other silicate materials, was conducted on the raw data obtained from pXRF at the Archaeological Science Laboratory at the University of South Florida. Speakman and Glascock began in 2006 using empirical calibration based on obsidian references to calibrate an ElvaX XRF and then developed it for the Bruker pXRF, along with an obsidian “green” filter, to be used since 2008 [20]. Thus, the data obtained by pXRF in this study is valid for the purpose of the current study and may be recalibrated in the future with other software for comparison with other studies. The matrix effect in pXRF is expected when dealing with the calibrated values. It requires standards of similar major element composition to produce accurate values, which has not been well developed for the pXRF yet. Therefore, the obsidian calibration is used for ceramics that are silicon-based.

Also, the small size of the X-ray window of pXRF (about 3×5 mm diameter) is another issue of poor representativeness and the effect of the grain size. Because the diameter of the pXRF beam width does not represent a point analysis but rather an average of a micron-scale area, it is not possible to identify a small component (matrix vs. clasts) unlike electron microprobe or LA-ICP-MS. Therefore, we analyzed multiple points in a single sample to ensure the “representativeness” and homogeneity. The analysis was designed to run pXRF multiple points similar to Chayes [21] modal analysis for thin-section analysis in which variant shots are pointed along the length and width of the potsherd and then one can calculate the average percentage of different elements. It can be also analyzed by a traditional method that measures the percentage of variant runs along a set of lines. However, following the Chayes method, a set of lines presents some difficulty in this study due to the sensitivity of the pXRF to non-flat surface. Thus, it is a challenge to set a line on each surface avoiding any apparent inclusion or décor. Due to this sensitivity and to obtain possible bulk minerals, surfaces of glazed and painted ceramic potsherds were excluded. Moreover, cooking ceramic potsherds that are diagnostic with a black-carbonized inner and/or outer surface were also excluded.

Because there is some concern about analyzing a sample that does not have a smooth flat surface, affecting the actual X-ray angle, the sherd's spot of X-ray exposure has been carefully selected, avoiding a non-flat area and visual temper inclusions. The inner and outer surfaces of the samples were analyzed and the edges as well for thick samples to overcome the potentially poor representativeness of non-homogenized samples and to ensure that the results are consistent (Fig. 4). The pXRF result confirms by comparing the elemental composition of the slip outer surface with the inner surface of the sherd that the slip material does not differ from the body clay; it suggests that the slip clay possibly was a refined version of the body. Preliminary works have been carried out to examine the accuracy of the instrument and understand the validity of the use of the instrument to the Bronze Age ceramic sherds. Ashkanani and Tykot [22] have studied a large selection of Bronze Age potsherds from Kuwait using pXRF to understand the per surface consistency and compare the plain and painted surfaces per sample. The identification

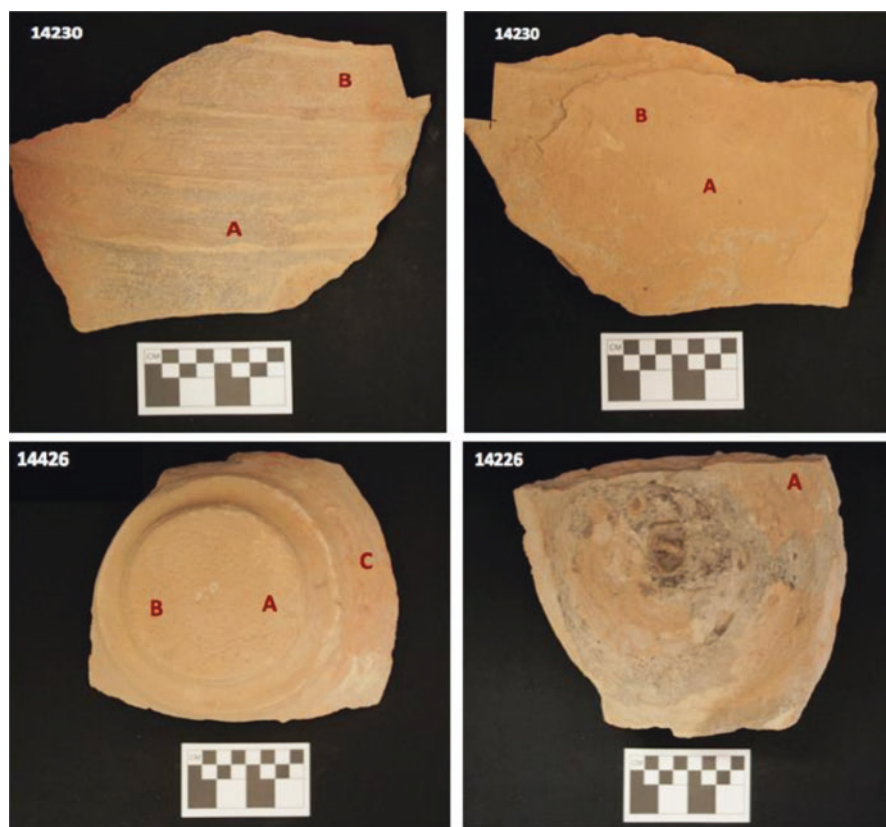


Fig. 4 Selected spots (A, B, and C) within each ceramic sherd for pXRF avoiding non-flat area. The slipped outer was selected to examine its homogeneity with the inner surface. (Photo by Hasan Ashkanani)

of each Bronze Age ceramic composition was also examined using XRD, pXRF, and ICP-MS [23]. Both works showed that the nondestructive analysis can be made on the Arabian Gulf pottery with a certain prerequisite.

The study samples were brushed to remove debris and dirt from excavation and museum storage and then were washed and allowed to dry. After the cleaning of the potsherds, the elemental composition of the surface was analyzed nondestructively using a Bruker Tracer III-SD portable XRF. The instrument was set up with a filter (12 mm Al, 1 mm Ti, 6 mm Cu) placed in the X-ray path, for a 120-s live-time count, designed to enhance data measurements of mid-Z elements in the spectrum, with settings of 40 kV and 11 μ A selected to maximize trace element analysis (Robert Tykot, personal communication 2012). The new Si (PIN) detector in the Bruker pXRF, that replaced a Si (Li) detector, supports the instrument's good performance and energy efficiency [24]. Only seven trace elements were measured and quantified as they show in the preliminary study their contribution for quantitative analysis including barium (Ba), niobium (Nb), rubidium (Rb), yttrium (Y), strontium (Sr), zirconium (Zr), and thorium (Th). They have been shown in many studies to be successful in determining sources and sub-sources of ceramic materials [25–27]. Two major elements, manganese (Mn) and iron (Fe), were excluded due to fluctuations in the measurement or values below the limits of detection determined in the preliminary results. After quantifying ceramic data using the calibration program, the values were saved in an Excel file for statistical assessment.

Each sample was set on the top of the exit window for 120 s to obtain elemental composition in parts per million (ppm) concentrations. The ceramic fragments tested are approximately 1–3 cm and completely cover the beam size of this instrument, which is about 3 \times 5 mm (Fig. 5). The inner and outer surfaces of the samples were analyzed and the edges as well for thick samples to overcome the potentially poor representativeness of non-homogenized samples and to ensure that the results are consistent. The preliminary results showed that the multiple runs on different positions within the whole sample are consistent (see Figs. 4 and 5). Peak intensities for the Ka peaks of Rb, Sr, Y, Zr, and Nb (and eliminated Fe and Mn) and La peaks of Th and Ba were calculated as ratios and converted to ppm. The data values used for each sample are reported as the average of the measurements at different positions. (contact the author).

3 Results

The assessment of the pXRF data by multivariate statistical analysis has provided valuable details about the homogeneity of Dilmun ceramics and the circulation of nonlocal pottery within the Dilmun realm. The results suggest the existence of a number of ceramic groups and illustrate the outliers. A variety of statistical applications were employed to evaluate the data collected using SPSS statistical software. Principal component analysis (PCA) was the exploratory method used to examine the correlation between chemical elements, to suggest which variables or groups of

Fig. 5 pXRF at the Archaeological Science Laboratory, University of South Florida, Tampa. The lightweight of pXRF (2 kg/4.49 lb) allows users to conduct the analysis in the laboratory or in situ. (Photo by Hasan Ashkanani)



elements are meaningful, and to account for the maximum variance in the dataset. Transformation of the dataset into logarithms was performed to standardize the data. The SPSS component matrix was useful because it contains the loading of each variable onto each factor. The results showed that only two component factors could explain to the variance 71.4%. It also showed how, for instance, Sr contributed highly (0.981) in the first component while lower in the second component (0.345).

A scatterplot was performed using PCA scores 1 and 2 that included Nb, Th, Sr, Y, Zr, Rb, and Ba, which previously showed their high contribution in the component matrix. The results show two distinct groups of ceramics (Fig. 6), while the Palace, Trench E, and the Barbar Temple were clustered together (group A). It also showed a distinct group of samples including the Mesopotamian House with a few outliers from the Barbar Temple and Trench E (group B). There were two outliers from the Palace; one was a pronounced outlier. The PCA results show the separation of shred samples between and within the archaeological sites.

The principal component analysis was followed by a cluster analysis using PCA scores, which included all seven elements (Nb, Th, Sr, Y, Zr, Rb, and Ba), for identifying natural groupings and evaluating PCA results. K-means cluster analysis was used for the clustering method because it groups all samples and then finds clusters. K-means cluster analysis is useful to test our research questions about the presence of more than two groups of ceramic sherds, as it can explore the number of groups.

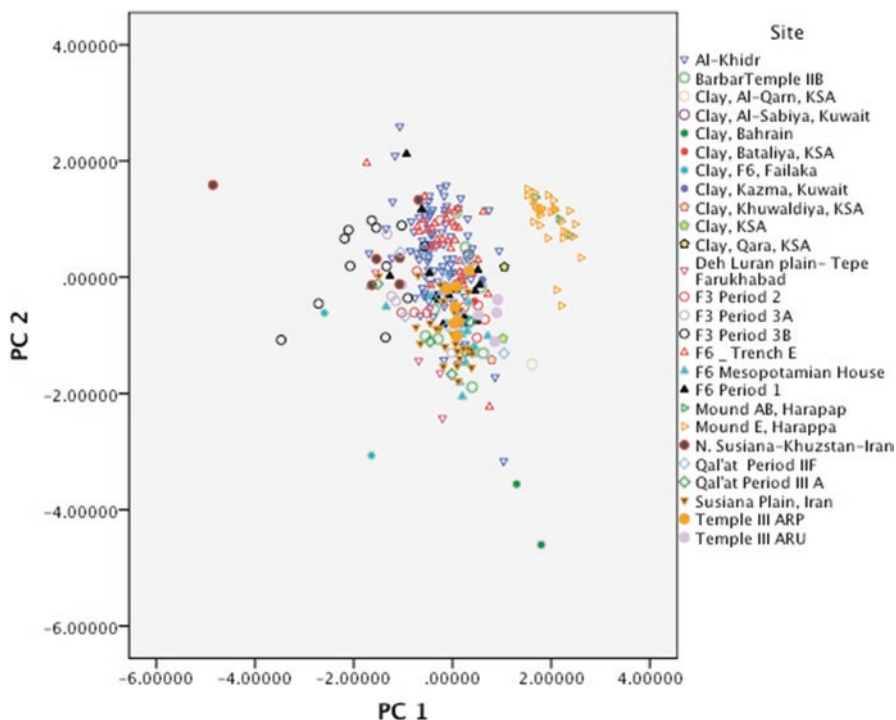


Fig. 6 Biplot derived from PCA of 304 sherd and clay samples measured by pXRF, showing variation within Failaka Island and Bahrain sites. At least two distinct groups of ceramics (Harappa vs. Dilmun) are noticed and potential outliers from Al-Khidr, F3, and F6 in Kuwait and the Deh Luran region

The ANOVA output is the most important aspect in cluster analysis as it distinguishes which factor is great and statistically significant (0.000). The cluster analysis also groups the data based on presuming a number of clusters to test the PCA scores. Five clusters have been proposed for this analysis. The number of clusters was selected based on the simple scatterplot in the exploratory analysis. The number of clusters could also be selected based on the assumption of different numbers of production centers relative to each region and/or site collection. The ANOVA results showed that all PCA factor scores are statistically significant, proposing five clusters.

Discriminant function analysis (DFA) was employed as a different quantitative technique to discriminate between groups and classify the samples into different production centers. The original log data were used for all seven elements (Nb, Th, Sr, Y, Zr, Rb, and Ba) as variables and site names as a grouping variable. Within a grouping variable, there is a step to define the range of groups and, based on that, the DFA will produce PCA scores.

I assumed a minimum of two groups to a maximum of six groups, based on the assumption of production centers that the samples that might have been made at are

limited to Dilmun of Failaka and Bahrain, Mesopotamia, the Indus Valley, and the Iranian plateau. The canonical discriminant function plot showed that the ceramic shreds and clay samples are separated into a minimum of two main groups.

Similar to the PCA component matrix, DFA also produces a matrix of function, based on the presuming groups, showing the contribution of each variable in the DF function. The results showed that there are only four significant discriminant functions. For instance, the result showed that Ba is highly contributed in DF 1 and 3, while Y is highly contributed in DF 2 and 4. The Wilk output showed that including the first discriminant function, any other functions are statistically significant (0.000), while excluding the first function, the grouping will be less significant. Based on the Wilk output, a scatterplot was performed using discriminant functions DF 1 and DF 4 (Fig. 7). The plot showed that there are at least four clusters representing a collection from the Indus Valley, Dilmun, north Susiana, and a mixed group of outliers from Failaka sites. Also, some outliers are from Al-Khidr, F3, Qala'at, north Susiana, and clay samples from Kuwait and Bahrain. Based on statistics, 78.3% of the original grouped cases are correctly classified. The percentage of correct classification of defining a range of two to six groups is higher than selecting

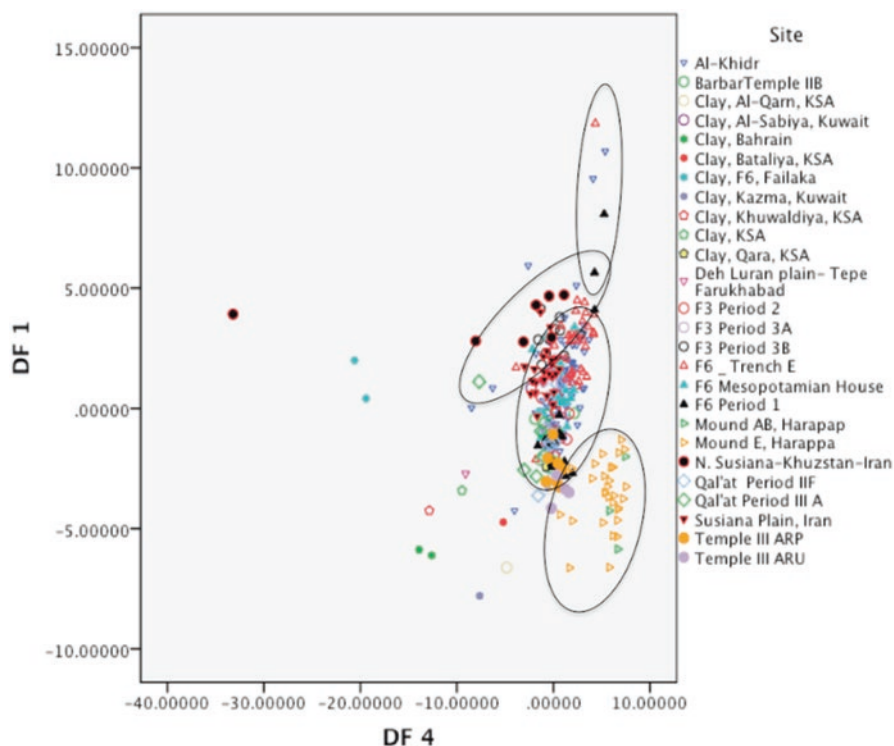


Fig. 7 Biplot of discriminant scores on discriminant function 1 and 4 showing a mixed pattern of specimens from Kuwait and Bahrain sites, along with a well-separated group of the Indus Valley. 78.3% correctly classified. Ellipses are made artificially

presumed three or four groups, which show less than 73% (~72.3–65.5%) in the pilot study.

Based on the quantitative analyses, there are at least three groups. The first group is comprised of Dilmun sherds from Kuwait and Bahrain. This cluster includes all ceramics from all phases with overlapped sherds from Susiana Plain in Iran and the Mesopotamian House on Failaka Island. The second group is comprised of sherds from Harappa Mound AB and Mound E. None of the Harappan sherds were outliers or overlapped with the samples from Failaka Island or Bahrain, except for a few samples from the NE Temple (III) ARU in Bahrain which are close with those Indus Valley collections. The third group presumably consisted of north Susiana in Iran and a few outliers from Qala'at Period IIIA of Bahrain, Al-Khidr on Failaka Island, "Trench E" at F6, and probably the Palace on Failaka Island. The others were too far from any sherd collections. They clustered alone with an exception of one clay sample that is similar to a Deh Luran plain sherd. Thus, clay samples have appeared to be unreliable as a standard to source Dilmun artifact collections as was presumed (Jonathan Kenoyer, personal communication 2011). Based on multivariate analyses, the clay itself could not be compared with the ceramic sherds as they were made of clay and additive temper to keep them from cracking or shrinking during the firing process. By combining all the research samples, it was not possible to determine properly any outliers from any individual sites or to explore any overlapping within and between sample groups. Even though the quantitative analyses showed some distinct clusters and major outliers, it was better to run multivariate analyses. In general, excluding the Harappan sherds allowed me to maximize the variation and to find any differences within the Dilmun sites. The Mesopotamian House samples are included as a reference group of Mesopotamian clay and to find properly any overlap.

3.1 Principal Component Analysis for Ceramic Sherds of All Kuwait and Bahrain Sites

A total of 224 ceramic potsherds from all Failaka Island sites and Bahrain were analyzed. The samples were selected from all Bronze Age sites on Failaka Island and Bahrain, representing all phases beginning from the early to mid-second millennium BC. The goal was to see if there were any discernable chemical groups for Dilmun pottery and if the Failaka ceramics were grouped with Bahraini collections. As with the above multivariate analyses using SPSS, transformation of the dataset into logarithms was performed to standardize the data. The results showed that three component factors could contribute to the variance which could explain 80% of the variance. It also showed, for instance, how Nb, Sr, and Th highly contribute in the first component, while Ba and Zr contribute in the second component.

A scatterplot was performed using PCA scores 1 and 2 that include Nb, Th, Sr, Y, Zr, Rb, and Ba, which previously showed their high contribution in the component

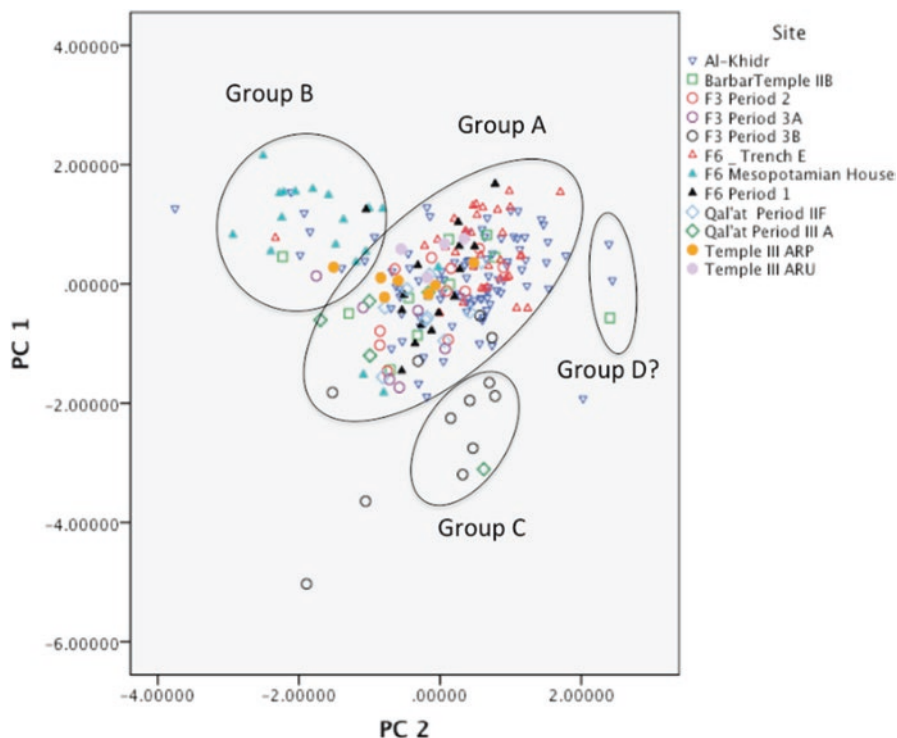


Fig. 8 Biplot derived from PCA of 224 samples. Note the match among Dilmun pottery from Kuwait and Bahrain and a few outliers from Al-Khidr and F3. Ellipses are made artificially

matrix. The results showed two distinct groups of ceramics (Fig. 8), separating Dilmun collections (Group A) from the Mesopotamian House (Group B) in which some outliers from other sites overlapped. It also showed that there were two possible groups—the F3 sherds and one sample from Qala’at—and a small group of two sherds from Al-Khidr and one from Barbar Temple. The large group consisted of all Dilmun collections from Kuwait and Bahrain and one overlapping sherd from the Mesopotamian House. The second distinct group is well separated and consisted of the Mesopotamian House collections and overlapping sherds from Al-Khidr, the Palace, Trench E, F3, Barbar Temple, and Qala’at in Bahrain. A small distinct group of F3 Period 3B was well separated as a third group. Some sherds were outliers that did not overlap with any PCA groups. Using principal components 1 and 2 showed the well separation of sherd samples between and within the archaeological sites from Failaka Island and Bahrain.

The PCA is followed by a cluster analysis using PCA scores, which included all seven elements (Nb, Th, Sr, Y, Zr, Rb, and Ba). The ANOVA output showed that the first three PCA factor scores were statistically significant ($p < 0.05$). The scores of the presumed four groups, produced by the cluster analysis, performed a scatterplot using PCA 1 and 2 and set markers. The results showed that there were two distinct groups with a few outliers.

Ceramic potsherds were grouped into four main groups, as the PCA and cluster analysis. Those groups that formed the big cluster (Group A) come from Al-Khidr, F3 Period 3A and 3B, the Palace and Trench E from Failaka Island, and from Qala'at and Temple of Barbar sites in Bahrain, with at least two overlapping samples from the Mesopotamian House. Group B consisted of samples from the Mesopotamian House on Failaka Island, with overlaps, five samples from Al-Khidr, three samples from Temple III, one sample from F3 Period 3A, and one from Trench E and F6 and F3 Period 2. Group C had eight outliers all from the F3 site Period 3B. This group appeared in the PCA plot as a potential third group and in the cluster analysis as well. Finally, a possible group D was scattered and might be clustered to consist of mixed specimens from Al-Khidr, Trench E from Failaka Island, and the Barbar Temple of Bahrain. Based on statistics, 72% of the original grouped cases were correctly classified. In addition to the four groups of potsherds, there were several outliers that appeared in the left part of the scatterplot and between group B and C. They were from Al-Khidr, F3, and the Mesopotamian House, similar to a potential group D in the multivariate analyses of Kuwait samples.

4 Discussion

4.1 *pXRF Group A*

Group A is comprised of wares from all the major Bronze Age sites on Failaka Island and from Bahrain. This group has a large number of ceramic artifacts comprised of large red-ridged jars, brown and yellowish-brown vessels, as well as red slipped and whitish to pale brown slipped feature. They have the ridged, reddish, slipped feature typical for the Bronze Age Dilmun or Barbar pottery type. Interestingly, they are grouped together based on elemental composition obtained by pXRF. This type of pottery can be further divided stylistically into identifiable subgroups based on technological production, color, grain size, and hardness. All four Dilmun fabric types (A-, B-, C-, D-ware) are clustered in this group. Also, the C-ware wheel-made which is restricted to rippled vessels such as sample No. 13642 is clustered with the handmade samples. The latter is a wheel-made greenish to yellowish, thin-sherd rippled vessel, known as rippled shoulder, [9] type 47 (Flemming Højlund, personal communication 2010).

In terms of function-space perspective, the Barbar ceramic artifacts in this research could be made from a single clay source based on pXRF results. All identical Barbar sherds that have slip or ridge or are attributed to local ceramic production are obviously made from the same clay source and/or temper materials suggesting a uniformity of land use from the early second millennium BC. There is no discernable separation between Failaka Island ceramic assemblages and the Bahrain collection. Group A comprises all local Barbar sherds even those with greenish outer (sample no. 13691) or greenish gray (e.g., nos. 14229, 14242, 14307). Also,

no separation is apparent between the red-slipped sherd and the yellowish-pale brown Barbar sherds. Moreover, the same inference can be made regarding the nature of the manufacturing of wares; there is no chemical difference between hand-made and wheel-made Barbar pottery or between some forms of pottery versus others (e.g., storage jar vs. vessel). Thus, the mixture of all Barbar ceramic forms and types from Failaka Island and Bahrain in one distinct group presents the homogeneity of Barbar ceramic recipes.

4.2 *pXRF Group B*

Ceramic potsherds of group B are comprised of samples from six archaeological sites on Failaka Island and Bahrain. These potsherds were wheel-made and highly tempered with fine material. The sand particles are seldom seen, while the colors range from pale brownish and pale greenish to light gray (Fig. 9). Some sherds have a surface of fine texture and smooth clay, while some have straw impressions

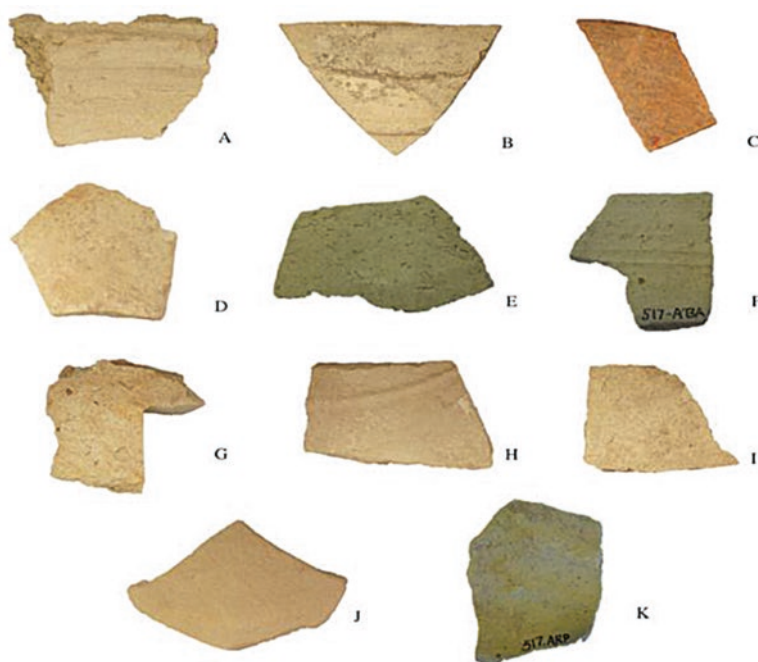


Fig. 9 Group B consisting of Mesopotamian tradition sherds, from six archaeological sites, as their colors range from pale greenish, brownish, to pale gray. Sample *A* has two ridges, *B* horizontal ribs, *C* red type, *E* Failaka Period 3A, *F* Barbar Temple II, and *K* NE Temple

(G-ware type). The G-ware group was known for being wheel-made, except for the giant storage vessels, and belongs to the Mesopotamian tradition [9, p. 106].

The majority of the group B samples came from the Mesopotamian House structure, the lowest level of the Temple at F6 site on Failaka Island as a reference group to represent Mesopotamian clay. It represents the Third Dynasty of Ur or Ur III occupation horizon (2100–2000 BC) that predates the establishment of the Dilmun colony or transit point on Failaka Island (Flemming Højlund, personal communication 2011). The similarity in chemical composition between Barbar Temple greenish sherds and the Mesopotamian House in Failaka suggests the use of the same raw material. The Mesopotamian House sherds from the Tell F6 site are useful as a group reference for Mesopotamian geology or at least for Mesopotamian origin. The Mesopotamian House sherds infer the Ur III expansion in the Arabian Gulf. It is documented that under the Ur III rulers, Mesopotamian merchants established a connection with suppliers of copper, particularly with Magan/Oman. The claim of Ur-Namma (2113–2095 BC) referred to the establishment of trade with Magan during his reign, copper in exchange for textiles [28, p. 101].

4.3 *pXRF Group C*

The pXRF group C consists of eight ceramic sherds that came from Tell F3 period 3B and one sample from Qala'at of Bahrain period IIIA (Fig. 10). Among 12 samples from Tell F3 period 3B, a total of 8 are consistently and repetitively clustered as a separated group, while 1 sample from Qala'at (no. 13693) overlaps with this group in PCA and cluster analysis but not in DFA. Interestingly, all Tell F3 period 3B samples in this group including the Qala'at sample are attributed to Mesopotamian tradition wheel-made. Five samples from tell F3 period 3B and one sample from Qala'at IIIA are categorized as E-ware type. According to Højlund, sherds of this type are well-fired, and non-oxidization gray can be seen in the core. It is tempered with medium to fine sand, and some straw has been added (no. 13656) but less than in G-ware that clearly is attributed to Mesopotamian pottery. E-ware sherds usually refer to the production of wheel-made vessels as in this group with the exception of giant jars and almost all of Mesopotamian tradition [9]. The color ranges from pale brown, reddish yellow, to pink. It has a smooth surface due to either fine slip applied or firing effect [9]. Some of this ware type could have grooves as in ceramic sample no. 13648. It has 3–11 grooves on the shoulder and upper belly and stylistically is attributed as type 97 of Mesopotamian tradition by Højlund's standard [9, p. 95].

Sample no. 13654 from the F3 site Period 3B is also clustered in group C. It has a rippled outer and D-ware type that is well-fired and medium-tempered with sand. Despite this ware type having been attributed to the Barbar tradition, the chemical analysis and statistical results confirm its Mesopotamian origin as it falls repetitively within the group C collection, with F3 Mesopotamian sherds. As it is noted from the rim setting being off in relation to the shoulder, this sherd is identical to Barbar tradition type D ware that is handmade and rounded edge, with horizontal

incised lines and yellowish-brown slip. This Dilmun style sherd that has a Mesopotamian chemical characterization would suggest the imitation of Dilmun pottery in the mid-second millennium BC. This imitation might have been produced within late Old Babylonian/early Kassite territory, before its dissemination to the Dilmun site at Tell F3. Otherwise, it is suggested that the raw materials were imported to Dilmun during the Kassite or late Old Babylonian period. The repetitive fall within group C excludes any possibility of being attributed by analytical error as it comes from the same site and same period when the Kassites conquered Old Babylonia (ca. 1590 BC) and occupied Dilmun in the fifteenth century BC.

The chemical analysis confirms its clay being distinct from the Dilmun collection of group A and even from the Mesopotamian Ur III collection of group B. Geoffrey [13, p. 136] describes this collection from his excavation of Qala'at in 1956 as thick, sand-tempered "caramel ware." The pale brown or caramel pottery marks the beginning of the 3B period in which rims with multiple grooves, knob-footed goblets, and triple-ribbed jar rims occurred.

The presence of Kassites in the Dilmun realm in the mid-second millennium BC is marked as a dramatic shift in the ancient history of the Arabian Gulf. It witnesses the Kassite domination over the Gulf and their complete control over Dilmun. With

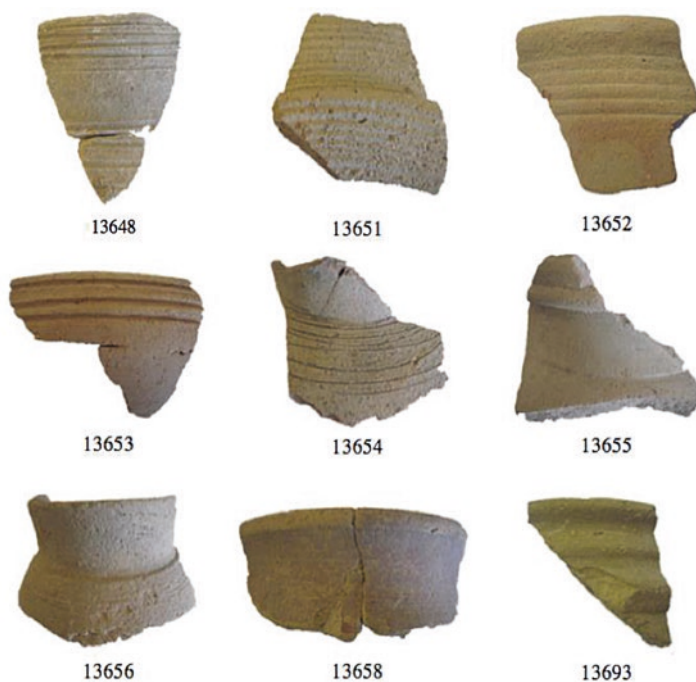


Fig. 10 All nine samples clustered with group C resemble the Mesopotamian shape. Note that the Qala'at sherd (no. 13693) is more greenish

a parallel to two expansionary episodes at the same period in Nubia by the Egyptian New Kingdom rulers and in Fars of Iran by Elamites, Kassite presence in the Gulf is characterized as colonialism. Edens [29, pp. 200–203] points out the political control of Dilmun by Kassite Babylonia in 1400 BC as some form of colonialism on the island. The latter is based on some textual evidence from Babylonia and Nippur which mention the governor of Tilmun/Dilmun, dated to perhaps 1420–1410 BC.

4.4 *pXRF* Group “Outlier”

Among 293 ceramic potsherds, a total of 10 ceramic samples did not cluster within either group A, B, or C (Fig. 11). Some of these samples were noted as being outliers or as a distinct group, called Group D in the DFA plot. However, those ten ceramic samples seem scattered without any pattern of a distinct group, except in the DF analysis of early Dilmun sites from Failaka and Bahrain. They came from four sites: a total of three samples came from the Palace in Tell F6 Period 1, one sample came from Tell F3, five samples came from Al-Khidr, and one ceramic sherd came from north Susiana in Iran. In terms of ceramic texture, the outlier samples are divided into two types, well-fired hard clay and porous non-flat surfaces. Their

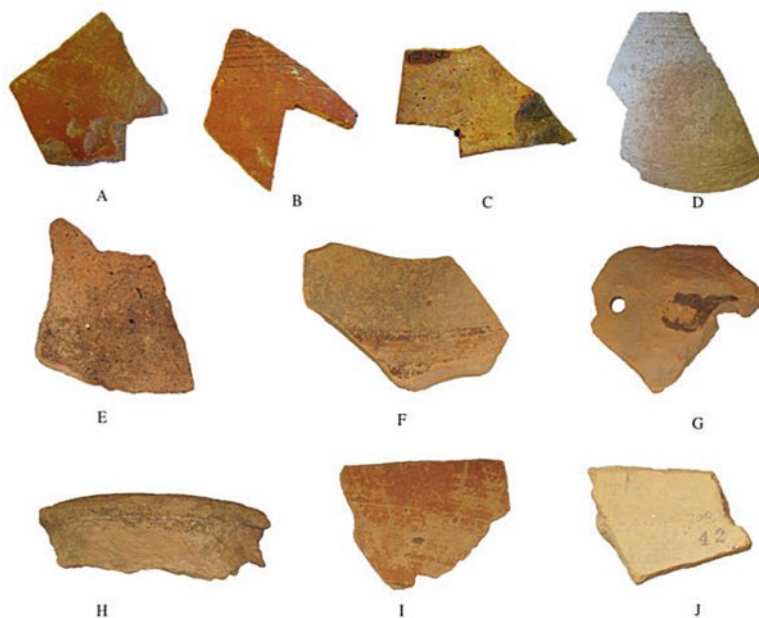


Fig. 11 Samples as outliers from F6, F3, and Al-Khidr in Kuwait and N. Susiana in Iran—scattered outside the three main *pXRF* groups

colors vary but red and reddish brown are common along with two whitish ceramic fragments.

It was assumed that sample no. 13613 from the F6 site (Fig. 11A) is unknown or had Harappan origin (Flemming Højlund, personal communication 2010). It is wheel-made, well-fired, and fine sand-tempered and has a very smooth outer surface. The small size of the sherd makes it hard to identify its cultural affiliation. Sample no. 13618 from F6 Period 1 is also reddish wheel-made and has a flat surface (Fig. 11B). It was assumed as Barbar tradition based on the red slip or paint on the outer surface (Flemming Højlund, personal communication 2010). Therefore, the outer surface was excluded from pXRF analysis, but the inner value is still very high relative to Barbar ceramic sherds of F6. Also, sample no. 13620 is another outlier from F6 Period 1 (Fig. 11C). Similar to the other two F6 samples, it was assumed as atypical and might have Harappan origin (Flemming Højlund, personal communication 2010). It has a gray slip on red ware that has fine sand temper and was well fired.

Potentially, these three ceramic potsherds could be the basis for a future study regarding the circulation of nonlocal pottery within Dilmun, particularly on Failaka Island in the early second millennium BC. The restriction of finding nonlocal pottery at F6, which is considered a governmental structure, could support one of the research arguments about the access of Failaka elites to exotic and long-distance items. Also, it would support the idea of a limited distribution of local, wheel-made, painted pottery (possibly sample no. 13618) in the early Dilmun phase on Failaka Island.

In general, using this comparative sampling strategy is very efficient in terms of providing a better understanding of the production centers, without being destructive. This strategy was effective, and the comparison between different sites and different chronological phases over the second millennium BC was possible. However, the group reference seems not applicable for the clay samples that are not overlapping with the ceramic artifices. This observation could be based on the change of the ceramic recipe after firing or due to deposition, giving a different chemical characterization away from the raw materials. Also, the temper added along with the clay paste that was averaged might have a rule to exclude clay samples from the local ceramics group. This would encourage more experimental studies in the future to compare between the same clay before and after firing. INAA was carried out on the ancient stoneware bangle samples and was compared to a single modern bangle replica made by J.M. Kenoyer using clay from the Ravi riverbed near Harappa [30, p. 68]. The results show that the potter used the same raw material. However, the quantity and quality of temper materials used in the ancient stoneware bangles that make the modern clay overlap with the ancient bangle samples must be noticed. Using different filter settings to obtain more elements in pXRF is also suggested to understand the contribution of various elements in the fingerprinting of clay and ceramics. The recent settings used here do not measure silicon (Si) that can play a role in balancing compositional groups. A recent study by Tykot et al. [31] used a new pXRF perspective analysis in combining two different settings to analyze ceramic and clay samples from northern Florida. The first setting is similar to this research while the other setting is able to obtain Si, Al, K, Ca, and Ti. This is highly recommended in the future to run different settings on the same clay

and potsherd samples as well as thin-section analysis on clay to determine the homogeneity. In conclusion, the pXRF is able to separate between and within sites in Kuwait and Bahrain and concludes that a single type of clay was used in producing Barbar tradition pottery in the second millennium BC.

5 Conclusion

This study results have demonstrated that pXRF can contribute valuable data to construct a database for chemical components of ceramics recovered from Failaka Island and Bahrain. Technically, this initial analysis shows the success of pXRF for examining the homogeneity of an artifact, identifying unknown samples, and testing the previously assumed origins for some ceramics. The pXRF device is a reliable tool to create compositional groups for production centers and to recognize ceramic centers that stylistic and descriptive methods can confuse. More data needs to be collected to identify the full range of clay variation for each production center.

Statistically, the principal component and cluster analyses successfully differentiated the samples based upon their elemental compositions and were confirmed by discriminant function analysis. The PCA shows a similar chemical compositional profile for Dilmun ceramics from Kuwait and Bahrain, suggesting a uniform chemical composition of ceramic production during the early second millennium BC. Along with PCA, discriminant analysis shows that the majority of Dilmun sherds from Failaka Island have the same compositional pattern as those from Dilmun sites in Bahrain, thus indicating they were made of the same raw material. Whatever the treatment of the outer surface or the color for the Dilmun vessels, the choice of using locally available raw materials is noticeable.

In terms of the pXRF performance, in comparison with the petrographic analysis, the pXRF ceramic group is congruous with the petrographic group for all Dilmun, Mesopotamian, and outlier groups that the Dilmun ceramic pottery is clustered in one pXRF group similar to the main group of petrographic analysis. The green and red Mesopotamian sherds found in pXRF group B are also clustered together in their petrographic thin sections. The two outliers from the pXRF group also appeared as outliers in the thin-section analysis. There are only three samples that are shown chemically as belonging to the Mesopotamian collection but grouped as outliers and one as Dilmun based on thin-section analysis. The reason for the unmatched result is due to the presence of calcareous clay in local Dilmun pottery similar to the Mesopotamian collection. One Mesopotamian sherd is assigned as an outlier petrographically due to the different clay source used within the Mesopotamian territory and metamorphic inclusions as well as volcanic.

However, the pXRF instrument is unable to identify any subgroups within local Barbar pottery. These subgroups are related to the two clay types found in Barbar tradition, iron-rich micaceous and calcareous clays. Using the current setting, on the pXRF device, with a filter (12 mm Al, 1 mm Ti, 6 mm Cu) and settings of 40 kV and 11 μ A to maximize trace element analysis of Ba, Nb, Rb, Y, Sr, Zr, and Th, the device is clearly able to cluster all local traditional pottery into one distinct group.

Using different settings in the future will provide more information about the performance of pXRF in grouping Barbar potsherds and a possible correlation with the petrographic thin-section results and other analytical techniques. Also, utilizing different calibration software and creating a certain calibration for the Arabian Gulf pottery is recommended. It would help to assess the data and compare with regular XRF as real values instead of “internally consistent.” Despite the heterogeneous surface analysis, data obtained from pXRF showed its significance lies in the partitioning of Bronze Age ceramic artifacts. The three major pXRF groups show significant agreement between the macroscopic description and the elemental composition groups. For example, Group A correlates to all Barbar tradition, Group B relates to grayish green Mesopotamian tradition, and pXRF Group C reflects the “caramel ware” of the Kassite period. Interestingly, the latter group is clearly partitioned from Mesopotamian House by the very high concentration of Sr, Ba, and Rb. The Sr element is related to plagioclase feldspar, pyroxene, and carbonate mineral, which is higher than any group. The Ba element is probably high due to rich granite, granodiorites, and other felsic igneous rocks. The Rb, which is higher than Group B, could be related to the mica content.

The compositional elements Rb, Zr, and Sr contribute more in the Barbar group than the Mesopotamian collections. Rb is associated with biotite, muscovite, granite, and hornblende. This is parallel to the rich micaceous clay and major inclusion of biotite and muscovite in Group A. Sr also appears as plagioclase feldspar and in the carbonate minerals in clay. Zr is considered a temper element not clay material.

pXRF compositional data assigned all Kuwait and Bahrain sherds to one Dilmun group. Other pXRF groups represent different pottery traditions that were circulated and flowed within Dilmun sites during the second millennium BC. The distribution of Dilmun wares within Failaka sites support the study inquiry that Dilmun administration at the main center of Bahrain exercised its power by the circulation of its materials northward to Failaka Island as an expression of economic growth and trade network. Also, the presence of nonlocal wares within elite-context site (the Palace) suggests the presence of centralized administration on the island and the control over far-distance staple to pronounce statue, power, and prestige. The uniformity of styles (Barbar ware) strongly suggests that there was a professional class of potters appeared within Dilmun entity in the beginning of the second millennium BC. The professional level, anthropologically speaking, means that potters may have been unattached and shifted gradually away from a household level of pottery production, which supports more growth of Dilmun through various means.

References

1. Potts DT (1990) *The Arabian Gulf in antiquity I. From prehistory to the fall of the Achaemenid Empire*. Clarendon Press, Oxford
2. Vine P (1993) *Bahrain National Museum*. Immel Publishing Ltd., London
3. Crawford H (1998) *Dilmun and its Gulf neighbours*. Cambridge University Press, Cambridge

4. Alster B (1983) Dilmun, Bahrain, and the alleged paradise in the Sumerian myth and literature. In: Potts D (ed) *Dilmun: new studies in the archaeology and early history of Bahrain*. Reimer, Berlin, pp 39–74
5. Larsen C (1983) *Life and land use on the Bahrain Islands: the Geoarcheology of an ancient society*. The University of Chicago Press, Chicago
6. Cornwall P (1999 [1946]) *Dilmun: the history of Bahrein Island before Cyrus*. M. Khuzai, transl. Bahrain Information services, Bahrain
7. Højlund F (1994a) Pottery from the pre-Barbar and Barbar periods (I–II). In: Højlund F, Andersen HH (eds) *Qala’at al-Bahrain: the Northern City wall and the Islamic Fortress*. JASP, Aarhus, pp 73–178
8. Højlund F (1994b) Summary and conclusions. In: Højlund F, Andersen HH (eds) *Qala’at al-Bahrain: the Northern City wall and the Islamic Fortress*. JASP, Aarhus, pp 463–481
9. Højlund F (1987) *Failaka/Dilmun: the bronze age pottery, vol 2*. Aarhus University Press, Aarhus
10. Sinopoli CM (2003) *Political economy of craft production: crafting empire in South India, c. 1350–1650*. Cambridge University Press, Cambridge
11. Al-Bader S (1978) *Mantaqat al khaliq al arabi khilal il alfin il thani wal awal qabl al milad (The Arabian Gulf Region through the second and first millennium BC)*. Author, Kuwait
12. Benediková L (2010) *Al-Khidr 2004–2009; primary scientific report on the activities of the Kuwait-Slovak Archaeological Mission*. NCCAL, Kuwait City
13. Bibby G (1969) *Looking for Dilmun*. Alferd Knope, New York
14. Calvet d’Y, Gachet J (1990) *Failaka: Fouilles Francaises*. Maison de l’Orient Mediterranean, Lyon, pp 1986–1988
15. Howard-Carter T (1972) The Johns Hopkins University reconnaissance expedition to the Arab Iranian Gulf. *Am School Orient Res* 207(Oct):6–40
16. Kjaerum P (1983) *The stamp and cylinder seals, vol 1:1*. JASP, Aarhus
17. Salem K (2006) *Gazirat Failaka ashhar el gozor il kuwaitia (Failaka Island: the most famous Kuwaiti Island)*. Author, Kuwait
18. Højlund F (2012) The Dilmun temple on Failaka, Kuwait. *Arab Archaeol Epigr* 32(2):165–173
19. Rajab J (1999) *Failaka Island: the Ikaros of the Arabian Gulf*. Tareq Rajab Museum, Kuwait
20. Speakman RJ, Steven Schakley M (2013) Silo science and portable XRF in archaeology: a response to Frahm. *J Archaeol Sci* 40(2):1435–1443
21. Chayes F (1956) *Petrographic modal analysis*. Wiley, New York
22. Ashkanani H, Tykot RH (2013) Interregional interaction and Dilmun power in the bronze age: a provenance study of ceramics from bronze age sites in Kuwait and Bahrain using non-destructive pXRF analysis. In: Armitage RA, Burton JH (eds) *Archaeological chemistry VIII, ACS Symposium Series 1147*. American Chemical Society, Washington, DC, pp 245–267
23. Stremtan C, Ashkanani H, Tykot RH, Puscas M (2014) Constructing a database for pXRF, XRD, ICP-MS and petrographic analyses of bronze age ceramics and raw materials from Failaka Island (Kuwait). In: Scott RB, Carremans M, Degryse P (eds) *Proceedings of the 39th international symposium for archaeometry, Leuven (2012)*. Centre for Archaeological Sciences, Leuven, pp 274–279
24. Shackley MS (2011) An introduction to X-ray fluorescence analysis in archaeology. In: Steven Shackley M (ed) *X-ray fluorescence spectrometry (XRF) in geoarchaeology*. Springer, New York, pp 7–44
25. Goodale N, Bailey DG, Jones GT, Prescott C, Scholz E, Stagliano N, Lewis C (2012) pXRF: a study of inter-instrument performance. *J Archaeol Sci* 39:875–883
26. Hoeck V, Ionescu C, Ghergari L, Precup C (2009) Towards mineralogical and geochemical reference groups for some bronze age ceramics from Transylvania (Romania). *Studia Universitatis Babes-Bolyai* 54(2):41–51
27. Speakman R, Little N, Creel D, Miller MM, Inanez J (2011) Sourcing ceramics with portable XRF spectrometers? A comparison with INAA using Mimbres pottery from the American Southwest. *J Archaeol Sci* 38:3483–3496

28. Astour MC (2002) A reconstruction of the history of Ebla. In: Gordon C, Rendsburg G (eds) *Eblaitica*. Eisenbrauns, Winona Lake, IN, pp 57–196
29. Edens C (1986) Bahrain and the Arabian Gulf during the second millennium B.C.: urban crisis and colonialism. In: Al Khalifa SH, Rice M (eds) *Bahrain through the ages the archaeology*. KPI Limited, London, pp 195–216
30. Dales GF (1991) Some specialized ceramic studies at Harappa. In: Meadow RH (ed) *Harappa excavations 1986–1990 a multidisciplinary approach to third millennium urbanism*. Prehistory Press, Madison, pp 61–69
31. Tykot RH, White NM, DuVernay JP, Freeman JS, Hays CT, Koppe M, Hunt CN, Wienstien RA, Woodward DS (2013) Advantages and disadvantages of pXRF for archaeological ceramic analysis: prehistoric pottery distribution and trade in NW Florida. In: Armitage RA, Burton JH (eds) *Archaeological chemistry VIII*. American Chemical Society, Washington, DC, pp 245–267

Part III
Structural Monitoring, Assessment, and
Engineering

Sustainable Design of Earthquake-Resistant Buildings Through Case Studies

Sassan Mohasseb, Niloufar Ghazanfari, and Mona Alizadeh

Case Studies

1. Construction of an Emergency Hospital in South of Switzerland.
2. Construction of the World tallest Silo in Switzerland.
3. Construction of MIT Science Building.

1 Introduction

The soil-pile-structure interaction (SPSI) plays an important role in assessing the dynamic response to seismic ground motions or vibrations internally generated within the structural system. It is very important to note that the SPSI can alter the superstructure's performance by influencing the dynamic properties of structure. A fundamental understanding of this complex phenomenon is essential for improvements of the structural design and construction practices and, as a result, for reduction of loss of life and monetary damages caused by earthquakes. Extensive field testing and experimental investigations on different aspects of pile behavior have resulted in a number of empirical and approximate analytical methods for the pile-foundation design [1–6]. In addition, other studies have resulted in more rigorous schemes for pile analysis. The results of research from various studies also back up the point that dynamic impedance of foundation is affected by several geometric and material factors such as foundation shape (i.e., disk, rectangular, strip), type of soil profile (i.e., deep uniform or multilayer deposit, shallow stratum on rock), foundation embedment (i.e., surface foundation,

In collaboration with Prof. Oral Buyukozturk MIT.

S. Mohasseb (✉) · N. Ghazanfari · M. Alizadeh
Department of Civil Engineering, Smtreeam GmbH, Zurich, Switzerland

embedded foundation, pile-foundation), shear-wave velocity, and type of loading (static, dynamic) [7, 8].

Generally, three direct numerical approaches have so far been evolved for predicting the dynamic pile behavior. The first approach represents soil as an elastic continuum; the second represents the soil-pile system by a set of discrete masses, springs, and dashpots; and the third one uses either boundary element or finite-element methods based on the actual soil properties [9, 10].

The continuum model was considered to be a generalized Winkler model. The major contribution regarding this approach was carried out by Novak [11], who introduced an approximate method based on the analytical solution of Baranov [12]. The soil was considered to be made of a set of independent infinitesimally thin horizontal layers in this model. Therefore, it automatically considered wave propagation in the horizontal direction. A set of equations for stiffness and damping ratio based on frequency-independent parameters were provided for a single pile under vertical vibration. Thereafter, further progress on this model was made by Novak et al. [13] and Dobry and Gazetas [5]. The reduction in soil stiffness and the increase in damping associated with strong shaking are sometimes modeled crudely in these analyses by making arbitrary reductions in shear moduli and arbitrary increases in viscous damping. Moreover, several researchers developed dynamic nonlinear finite-element analysis in the time domain using the full three-dimensional wave equations to investigate the seismic soil structure interaction [14] which is not feasible for engineering practice at present because of the time needed for the computations. A rigorous finite-element analysis of a pile-foundation subjected to lateral loading was done by Kaustell et al. [15].

These numerical methods have an advantage in that they can analyze the soil-pile system as a whole. Therefore, no separate analysis is required to calculate the dynamic interaction factors for pile-group analysis [16].

The major drawbacks of analytical and numerical models in prior research studies were overcome with the introduction of CONE model which applies for shallow foundations. Wolf has rearranged and extended the concept of the CONE model to cover a complete range of dynamic excitations and physical situations. This model was based on one-dimensional wave propagation in CONE segments with reflections and refractions at layer interfaces. Due to the simplification of the physical problem, the mathematics of the CONE models can be solved rigorously [17–19].

The present study investigates the effectiveness of applying the enhanced CONE model to analyze the dynamic response of pile groups in three tall and massive building projects. For this purpose, a new computer program (FCONE) was developed based on the CONE frustum model. This program utilizes the equivalent dynamic modeling concept in the analysis of soil dynamics and soil-pile-structure interaction.

2 The Concept of CONE Model

The dynamic response of pile-foundations embedded in a horizontally stratified soil profile is determined using the CONE model [19]. Linear behavior of the site is assumed; hence the soil is assumed to remain linearly elastic with hysteretic material damping during dynamic excitation. Figure 1 shows the loaded disk on the surface of a homogeneous half-space, modeled in the one-dimensional strength-of-materials approach as a truncated semi-infinite bar with a vertical axis [19].

The soil region is divided into several segments by massless rigid disks (Fig. 2). The disks will coincide with the interfaces of the half-space. In addition, further disks are selected to adequately represent the dynamic behavior. After assemblage, the dynamic stiffness matrices of all the CONE frustum segments are then calculated and subsequently assembled together with the underlying half-space to form the dynamic stiffness matrix of the corresponding backbone cone. Applying a unit load at the disk and solving for the displacement amplitudes at all disks lead to a column in the flexibility matrix $[G(w)]$ of the free field condition. Thus, the force-displacement relationship is obtained as Eq. (1), where $\{u(w)\}$ is the displacement amplitudes and $\{P(w)\}$ is the force amplitudes:

$$\{u(w)\} = [G(w)]\{P(w)\} \quad (1)$$

This procedure is repeated for all disks to obtain all columns of the dynamic flexibility matrix $[G(w)]$. The dynamic stiffness of a single cone $S_1(w)$ modeling an incident wave induced by a disk load of radius r_0 on a half-space is given by Eq. (2), where K_s is the static translational stiffness coefficient of the cone modeling the incident wave, c is the relevant wave velocity, ω is the load circular frequency, and

Fig. 1 Translational truncated semi-infinite cone model of a loaded disk on a half-space

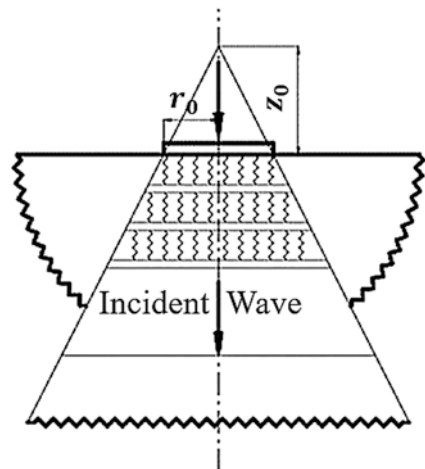


Fig. 2 Pile modeled by a stack of disks

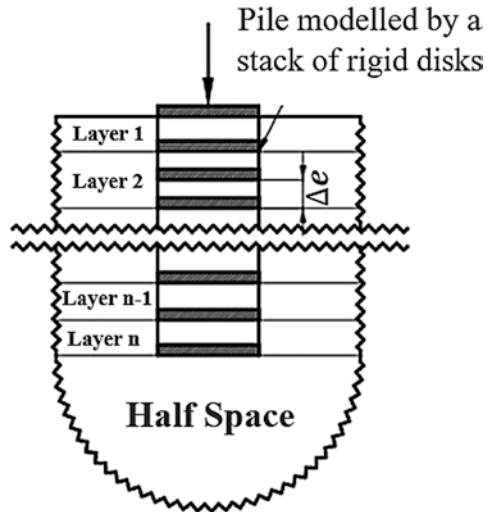


Table 1 Aspect ratios for different types of motion

Motion	Horizontal	Vertical	Rocking	Torsional
Aspect ratio	$\frac{\pi}{8}(2-\nu)$	$\frac{\pi}{4}(1-\nu)\left(\frac{c}{c_s}\right)^2$	$\frac{9\pi}{32}(1-\nu)\left(\frac{c}{c_s}\right)^2$	$\frac{9\pi}{32}$
Poisson's ratio (ν)	all ν	$\nu \leq \frac{1}{3}, \frac{1}{3} < \nu \leq \frac{1}{2}$	$\nu \leq \frac{1}{3}, \frac{1}{3} < \nu \leq \frac{1}{2}$	all ν

ρ is the soil density. The value of the aspect ratios of a particular cone is shown in Table 1 for each type of motion.

$$S_1(w) = K_s \left(1 + i \frac{wz_0}{c} \right) \quad K_s = \frac{\rho c^2 \pi r_0^2}{z_0} \tag{2}$$

The dynamic stiffness matrix of the cone frustum segments is obtained by inverting the dynamic flexibility matrix $[S^f(w)] = [G^{-1}(w)]$, and then the forces acting on the top and bottom disks and their corresponding displacements are related as:

$$\{P(w)\} = [S^f(w)]\{u(w)\} \tag{3}$$

It is well known that the behavior of a pile in a compact group is quite different from that of a single pile because of pile-soil-pile interaction. These interaction effects depend mainly on pile spacing. These dynamic interactions incorporated into the analysis by a factor which is defined as the ratio of fractional increase in displacement amplitude at receiver pile to the displacement amplitude at the loaded source pile. The dynamic normal-axial interaction factor $\alpha_v(w)$ can be obtained

from Eq. (4), where C_s = shear-wave velocity; ζ_g = hysteretic damping ratio; ω = frequency of excitation; r_0 = radius of the pile; and d = distance between two piles.

$$\alpha_v(w) = \frac{u_r^f(w)}{u_s(w)} = \sqrt{\frac{r_0}{d}} e^{-\zeta_g w \frac{d}{c_s}} e^{-i w \frac{d}{c_s}} \quad (4)$$

$$u_{\theta}^f(w) = -\sin \theta . u_r^f(90^\circ, w)$$

$$u_{\text{rad}}^f(w) = \cos \theta . u_r^f(0^\circ, w)$$

When analyzing soil-structure interaction, two types of damping have to be taken into account, namely, the geometric attenuation (radiation attenuation) that results from the distance of the excitation source to the object and the material damping due to the friction between the individual soil particles. The latter can be taken into account by substitution of G and $G(1 + 2i\zeta)$ and E by $E(1 + 2i\zeta)$, with ζ as the degree of attenuation of the soil. The material damping is independent of the excitation frequency. When the distance between the piles is large (greater than about 20 diameters), the piles do not affect each other, and the group stiffness and damping are simply the vector sums of the individual pile stiffness and damping. The dynamic stiffness matrix of the pile embedded in the half-space can be obtained by replacing the properties of the soil between two consecutive disks with the mechanical properties of the pile section. This can be performed by adding the difference between the dynamic stiffness matrix of the pile and that of the corresponding soil cylinder $[\Delta S_w]$, leading to:

$$S(w) = S^f(w) + \Delta S = S^f(w) + [\Delta K] - w^2 [\Delta M] \quad (5)$$

$$\{P(w)\} = [S(w)]\{u(w)\} \quad (6)$$

where $P(w)$ is force amplitudes and ΔK and ΔM are the difference between stiffness matrices and mass matrices of the pile and soil cylinder, respectively. Equation (6) can be written as:

$$\begin{bmatrix} P_z \\ P_x \\ P_y \\ m_z \\ m_x \\ m_y \end{bmatrix} = \begin{bmatrix} K_{vz}(w) & 0 & 0 & 0 & 0 & 0 \\ 0 & K_{hx}(w) & 0 & 0 & 0 & K_{hxy}(w) \\ 0 & 0 & K_{hy}(w) & 0 & K_{hyrx}(w) & 0 \\ 0 & 0 & 0 & K_{tz}(w) & 0 & 0 \\ 0 & 0 & K_{hyrx}(w) & 0 & K_{rx}(w) & 0 \\ 0 & K_{hxy}(w) & 0 & 0 & 0 & K_{ry}(w) \end{bmatrix} \begin{bmatrix} u_z \\ u_x \\ u_y \\ \varphi_z \\ \varphi_x \\ \varphi_y \end{bmatrix} \quad (7)$$

where v , h , r , and t denote vertical, horizontal, rocking, and torsional motions, respectively. It can be noted that coupling occurs between horizontal and rocking

motions. Each coefficient of the impedance matrix is a complex function of the excitation frequency which can be expressed in the form of real and imaginary components. Furthermore, the dynamic stiffness coefficient obtained from the analysis is then decomposed into two parts:

$$K_{ij}(w) = K_{st} [k_{ij} + ia_0 c_{ij}] \quad (8)$$

In Eq. (7), K_{st} is the static stiffness, i the imaginary unit, and k_{ij} and c_{ij} , respectively, called stiffness and damping coefficients, are dimensionless coefficients depending on the Poisson's coefficient of the soil and the frequency parameter.

$$a_0 = \frac{w(2r_0)}{C_s} \quad (9)$$

where $C_s = \sqrt{G/\rho}$ is the shear-wave velocity in the soil. Finally, the total displacement of receiver pile(i) due to lateral load of source pile(j) can be written as:

$$u_i(w) = \sum_{j=1}^{i-1} \alpha_v(d_{ij}, w) u_{jj}(w) + u_{ii}(w) + \sum_{j=i+1}^n \alpha_v(d_{ij}, w) u_{jj}(w), (i = 1, \dots, n) \quad (10)$$

or

$$u_i(w) = \frac{1}{S(w)} \left[\sum_{j=1}^{i-1} \alpha_v(d_{ij}, w) P_j(w) + P_j(w) + \sum_{j=i+1}^n \alpha_v(d_{ij}, w) P_j(w) \right], (i = 1, \dots, n) \quad (11)$$

In order to achieve a sufficient accuracy, the number of disks n has to be selected so that the length L of a pile element does not exceed about one-tenth of the shortest wavelength propagating from the pile. Because the shear-wave velocity is less than the dilatational wave velocity in the soil, the wavelength of shear waves is lesser than that of longitudinal, ones and the number of disks can be chosen as [20, 21]:

$$n \geq 1 + \frac{5}{\pi} \left(\frac{L}{2r_0} \right) a_0 \quad (12)$$

3 Case Study 1: An Emergency Hospital in South of Switzerland

The building is of a general rectangular shape with the overall dimensions of 73 meters in the longitudinal direction, 25 meters in the width direction, and a height of 35.6 meters. The building is a new reinforced concrete construction with concrete

columns. The primary lateral load-carrying system consists of three reinforced cores and an integrated reinforced concrete exterior frame system. For the earthquake resistance evaluation, a special micro zoning map and a response spectrum developed by Resonance Ltd. for Brig was used. The building is classified as a category III construction with an importance factor of 1.4. This is the highest class of building categories in Switzerland. The building was modeled in three dimensions (3D) and calculated for non-ductile behavior according to the SIA Standard 262 (2013 edition). The summary of the building characteristics and modeling assumptions is given below:

3.1 Modeling Assumptions

3.1.1 Longitudinal Direction

The earthquake loads are carried by the three reinforced concrete cores and two shear walls together with the reinforced concrete framework. As the geometry of all floors is similar, continuous transfer of earthquake loads is guaranteed from the roof to the foundation. Additionally, due to the layout and stiffness differences, the mass center and the stiffness center of the building do not match resulting in torsional stresses due to lateral earthquake effects.

3.1.2 Lateral (Short) Direction

Three reinforced concrete core and two reinforced concrete frames transfer the horizontal equivalent loads corresponding to the earthquake effects from the higher levels through the lobby level to the basements of the building. There is a concern of soft story in the building. As a result, high shear stress concentrations occur in the building due to this irregularity.

Due to the stiffness differences, the resistance of the building in the short direction is lower than that in the longitudinal direction.

3.2 Numerical Investigation

The earthquake loads are determined according to the Swiss Code SIA 260-262, Merkblatt SIA 2018. The following material characteristics have been used:

- *Concrete:* $E_c = 20,000$ Mpa (elastic modulus)
 $f'_c = 19.2$ Mpa (compressive strength).

For the seismic structural analysis, four computer programs were used:

- *ETABS* which is a well-known structural analysis and design software, CSI, Berkeley, USA.

- *OpenSees* Open system for earthquake engineering simulation. This is an earthquake simulation software based on the displacement-based structural analysis considering material nonlinearities. The program is very suitable for assessing the behavior of buildings in seismic situations. The purpose of modeling with OpenSees is to perform a nonlinear static pushover (NSP) analysis of the reinforced concrete system with concrete cores, shear walls, and the heavy concrete columns. The modeling is based on ASCE 41-13 (2014). Material nonlinearities and hysteretic behavior are considered for the elements under normal forces, bending, and shear effects. For the calculations, both force-based and displacement-based methods have been used. For the displacement-based method, ASCE 41 procedures have been implemented in the calculation of target displacements.
- *FCONE* program was a new FORTRAN program which was developed at Smtteam based on the enhanced CONE model concept for soil modeling. This program utilizes the equivalent dynamic modeling concept in the analysis of soil dynamics and pile-foundation interaction.
- *Abaqus/Cae* was used to investigate the structure response according to seismic soil-pile-structure interaction effect. The finite-element simulation phase of the present study along with a description of boundary conditions, the meshing and analysis techniques, and the materials' constitutive laws is also presented below.

3.2.1 Pile-Group Effect

When piles are used as part of a building foundation system, they are usually configured in groups to support continuous mat foundations or discrete pile caps for individual load-bearing elements. The impedance of a pile group cannot be determined by simple addition of individual pile impedances because grouped piles interact through the soil by “pushing” or “pulling” each other through waves emitted from their periphery. This is called a group effect, and it can significantly affect the impedance of a pile group as well as the distribution of head loads among individual piles in the group. Group effects depend primarily on pile spacing, frequency, and number of piles. They are more pronounced in the elastic range, and dynamic group effects decrease in the presence of material nonlinearity. Numerical analysis methods of soil-pile-structure interaction (SPSI) problems can be classified into two approaches: direct method and substructure method. In the direct method for analysis of SPSI, it is necessary to model underlying soil, foundation, and structure with best precision and accuracy since they are supposed to be analyzed together. In substructure method, soil-structure system is divided into two parts: first part is structure, and the second part is the soil that has common boundary with foundation, and each part can be modeled in detail [22]. In order to consider the influence of the piles on the dynamic response of the structure, the substructure method was used in this study. This consists of three consecutive steps:

1. Calculation of foundation input motion in the absence of superstructure inertia (kinematic interaction) includes translational displacements and rotational components.

2. Calculation of the dynamic impedances (spring and damping coefficients) for horizontal rotation and the combination of base foundation and pile system.
3. Calculation of the seismic response of the building supported on the springs and dashpots of step 2 and subjected at its base to the foundation input motion of step 1.

The method of Fan and Gazetas [7], based on the BDWF model (Beam on Dynamic Winkler Foundation), is used to determine the foundation input motion. In this method, the displacement of the pile head (U_{11}) as a function of the free-field motion (U_{ff}) is calculated as follows:

$$U_{11} = \Gamma U_{ff}$$

Here Γ is a function of spring and damping constants, frequency, mechanical characteristics of the piles such as I_p , A_p , M_p , and E_p .

A detailed study of gazetas shows that the kinematic factor $I_u = U_{11}/U_{ff}$ for small frequencies, like the first frequency of the hospital Brig (0.7 Hz), is equal to 1. This means no increase in the amplitude of the free-field earthquake motions. Therefore, in the case of the Brig hospital, the kinematic interaction effect was neglected.

The arrangement of pile group in rectangular foundation is shown in Fig. 3. In this case, both rigid and flexible foundations are considered. In fixed-base model, the structure is being analyzed without soil and foundation with fixed boundary condition to resist all displacements or rotations at the bottom.

In CONE model, the structure is built on a rigid foundation with springs and dashpots in the bottom in place of soil. The response spectrum method was used for determining the displacements and accelerations.

To determine the vertical axial load in the upper part of the piles, a finite-element model of the building was created using the ETABS program. In the modeling of the core 3D shell elements were used. The elastic modulus E of concrete has been reduced to 60% of the design value to include the effects of cracking in concrete. The (q) factor (response factor) is set to 2, and the importance factor is assumed 1.4. In 2015, a new earthquake hazard map of Switzerland (Fig. 4) was issued with a corresponding design spectrum, which was used for the present study. The modal analysis was performed to determine natural modes of frequencies for the structural model in two different conditions: namely, fixed-base behavior and behavior including SPSI (containing embedded piles with pile-group effect).

The results of ETABS analysis are given in Table 2, and the first vibration mode shape of the building with dynamic pile-group effect obtained from the ETABS is shown in Fig. 5.

Target Displacements

The calculated target displacement in long direction and short direction according to the Euronorm 8 and ASCE 41-13, 2014, are found to be 12 cm and 15 cm, respectively. These values represented the demand on the structure to have a sufficient ductility level under earthquake loads before a collapse of the building can occur.

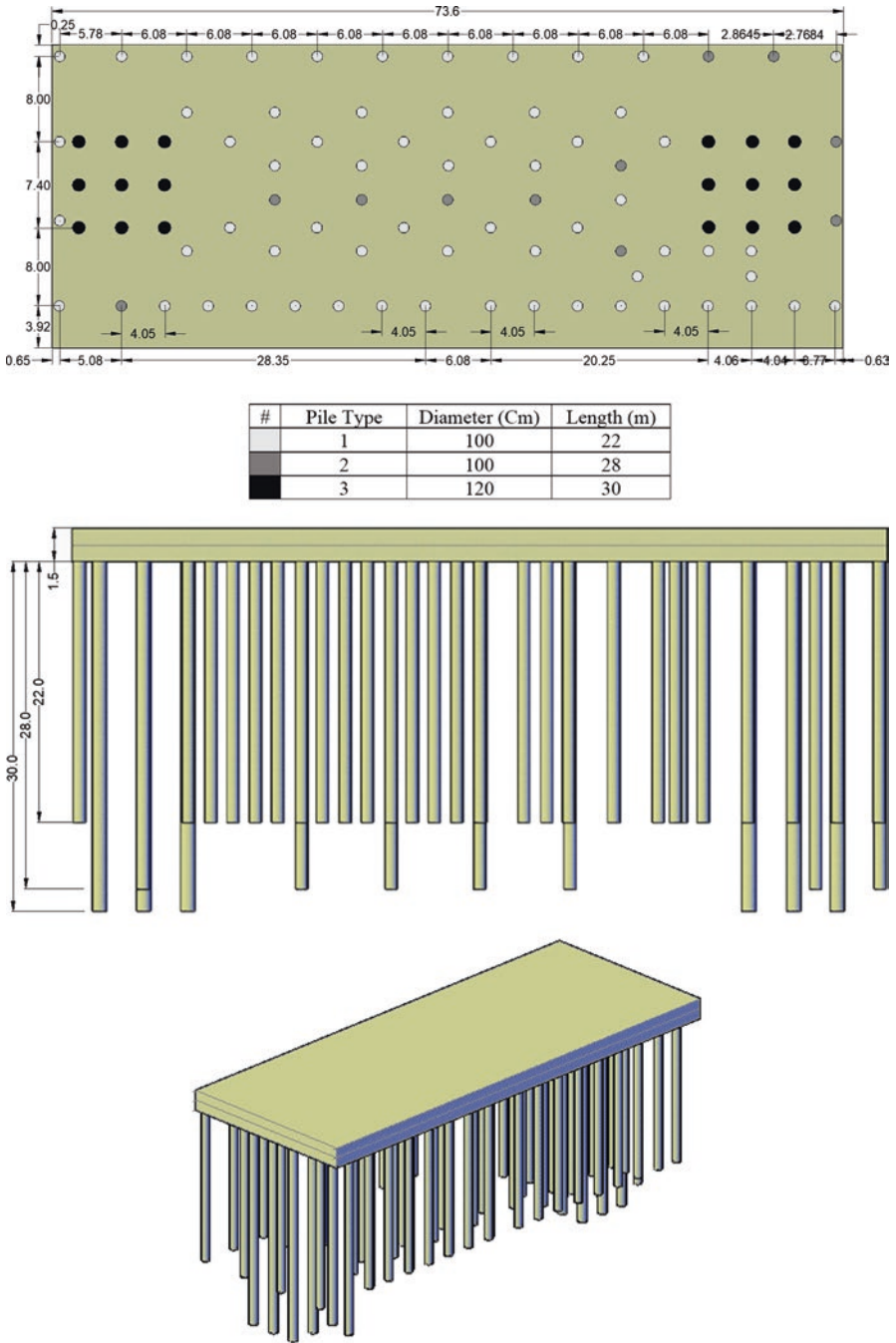


Fig. 3 The arrangement of pile group in rectangular foundation

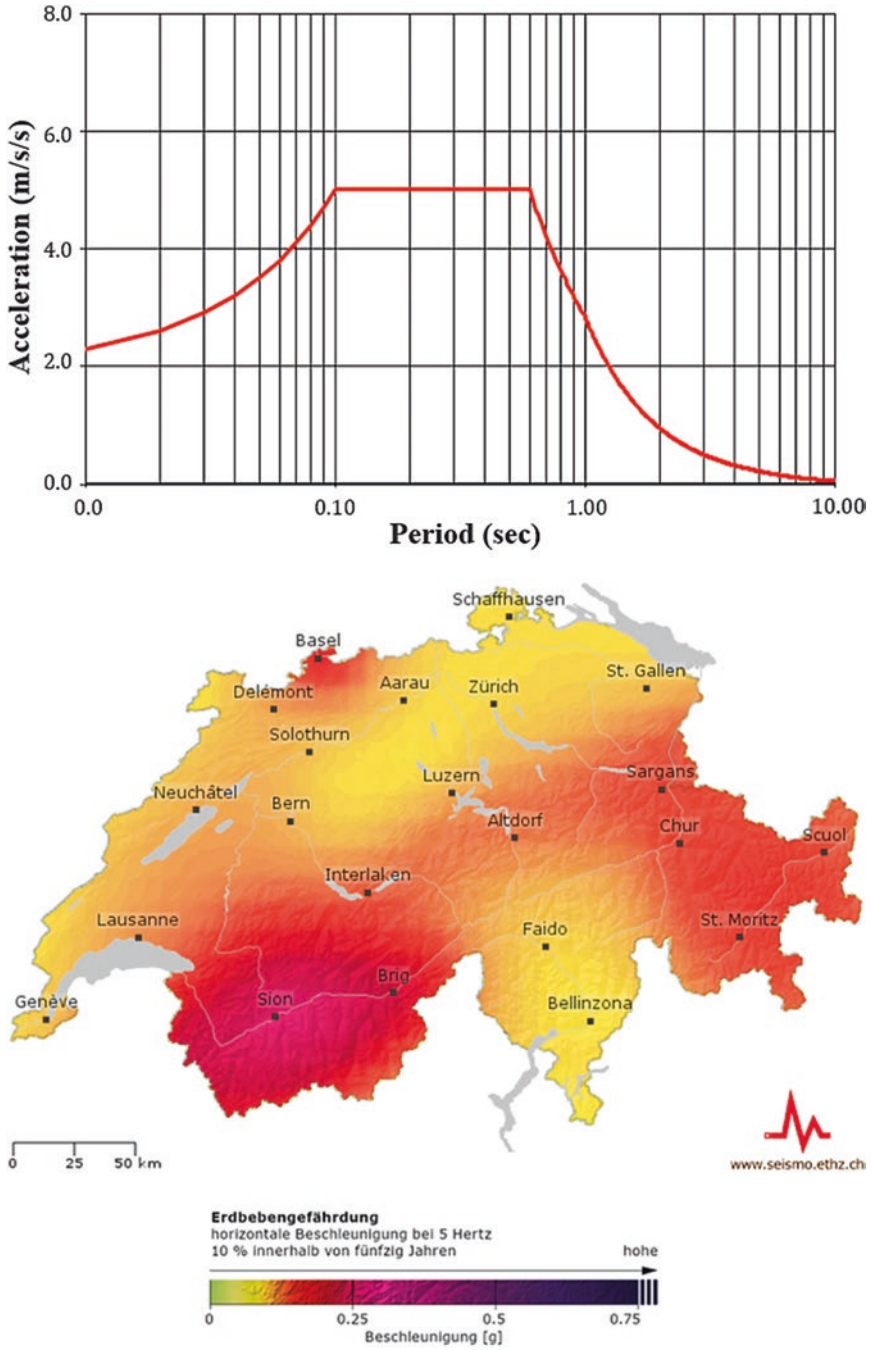


Fig. 4 The response spectrum for the Brig ground motion and the seismicity map of Switzerland

Table 2 The results of two analysis obtained from the ETABS mode

Analysis	Period of vibration (s)	The roof displacement (cm)
Fixed-base foundation (no piles)	0.7	6.5
Flexible foundation (including piles)	1.2	11.5

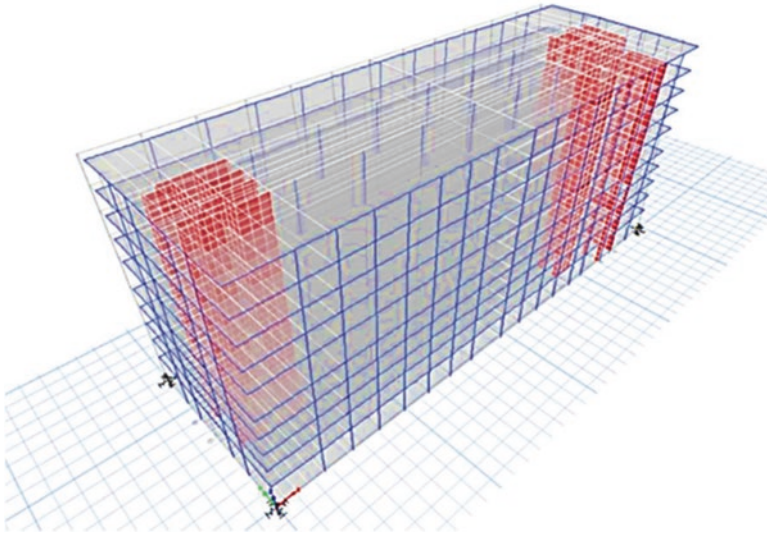


Fig. 5 The first vibration mode shape of the Brig structure (Period: 1.195)

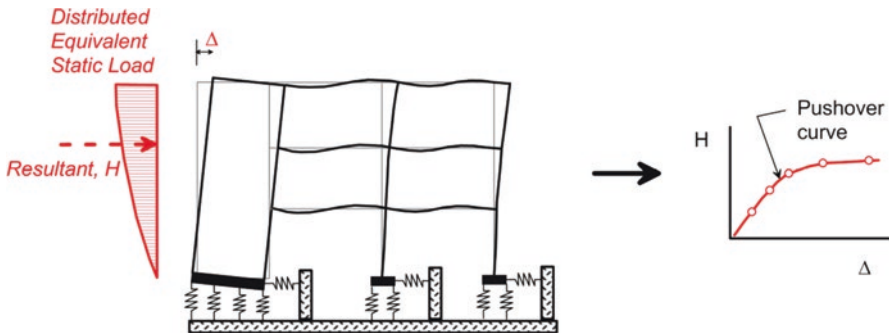


Fig. 6 Schematic illustration of a pushover analysis and development of a pushover curve for a structure with a flexible base [23]

3.2.2 Nonlinear Pushover Analysis

A pushover analysis involves the application of static lateral loads distributed over the height of the structure and calculation of the resulting displacements in a model of the SPSI system. A pushover analysis of a structure with a flexible base is schematically illustrated in Fig. 6. A nonlinear pushover analysis was reported for the

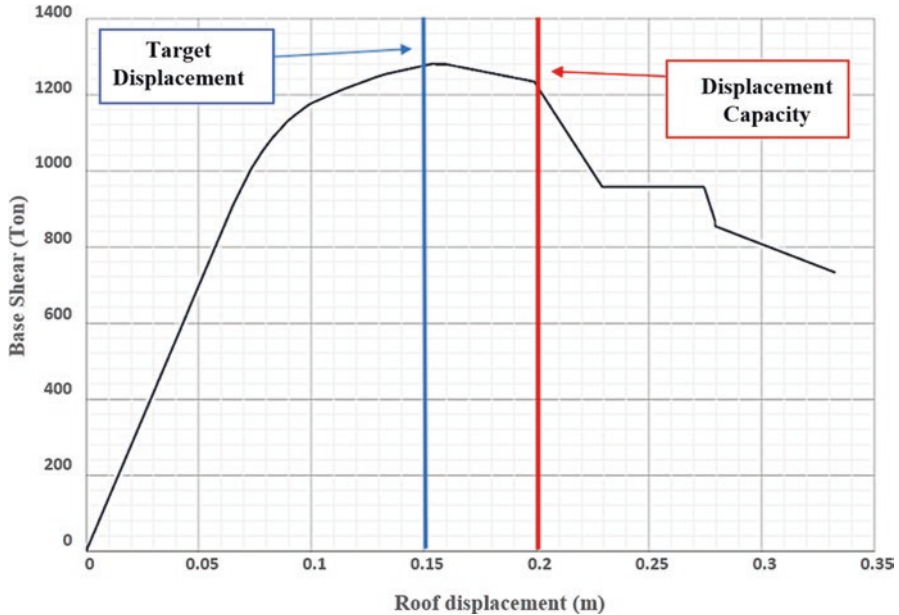


Fig. 7 The pushover curve obtained by OpenSees analysis

reinforced concrete system model of the building with the parameters defined in ASCE 41-13. Behavior of each wall was determined based on the wall thickness, the wall length, and the material properties as provided by the ETABS model. At each point on the pushover curve, the deformations of all components in the structural system are related to the reference displacement. The ETABS model has been read into OpenSees for conducting the pushover analysis.

The pushover analysis resulted in displacement capacities of 20 cm in the transverse direction and 22 cm in the longitudinal direction, as shown in Fig. 7. This compared with the target displacements, found from ASCE 41-13, of 12 cm in longitudinal direction and 15 cm in the transverse direction.

3.2.3 Dynamic Stiffness of Pile Groups

Dynamic stiffnesses (spring and damping coefficients) for a pile group are strongly frequency dependent. In the FCONE program reported in the article, the impedance matrix for different blocks (pile groups) were calculated as a function of frequency, using the CONE model concepts according to John P. Wolf [19]. For the determination of stiffness, a new method of solving dynamic interaction problems was developed wherein the seismic behavior of pile-soil-pile structure interaction (SPSI) system is investigated as a whole considering both pile-group effect and soil constitutive model. As mentioned previously, modifications of the flexibilities have to

Table 3 The mechanical characteristics of the soil

Parameter	E (MPa)	G_s (MPa)	ρ (kN/m ³)	C_s (m/s)	ν	ξ (%)
Quantity	350	125	16.45	276.00	0.4	0.05

be performed for modeling an embedded foundation since the double CONE models (especially for the vertical degree of freedom) are too flexible at large distances from the loaded disk. The pile-soil-pile interaction effect in pile group has been evaluated through the FCONE program by using the matrix of interaction factors (α_n) which is frequency dependent [24]. Results of the program for one 3×3 block under a core (i.e., spring and damper constants as a function of frequencies) are summarized in the following section.

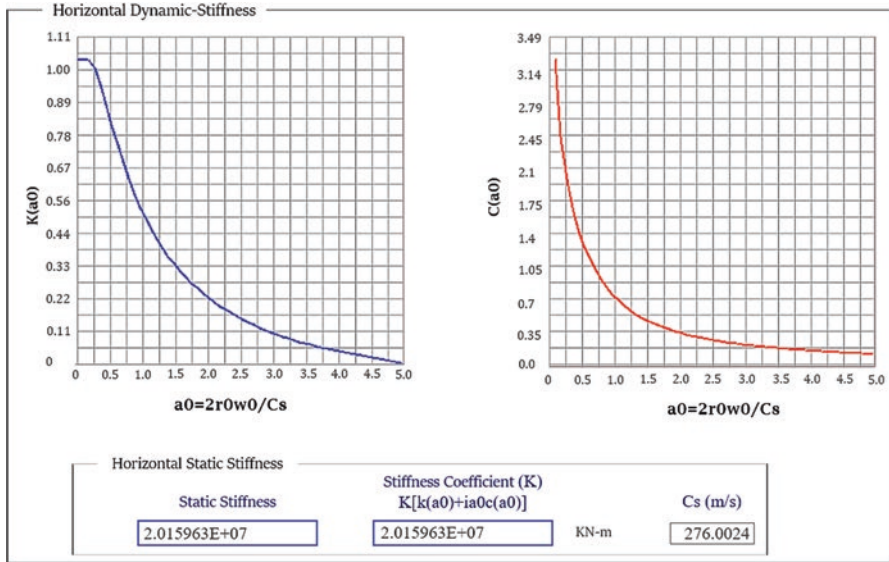
The spectral values have been reduced to take account of the radiation and material damping of the soil. It turns out that in the case of the flexible-base structure, in addition to the added rocking component to the horizontal motion of the structure, a part of the structure vibration energy will transmit to the soil layer and can be dissipated. This results in a reduction of the natural frequency in comparison with the fixed-base model and an increase of the damping (mainly due to radiation damping resulting from the wave propagation and hysteresis damping of the soil materials).

Detailed mechanical characteristics of the soil has been explained in Table 3, where E is elastic modulus, G_s is shear modulus, ρ is unit weight, C_s is shear-wave velocity, ν is Poisson's ratio, and ξ is material damping ratio. The soil region was assumed to be homogeneous with uniform shear modulus and density during analysis. The horizontal, vertical, and rotational dynamic stiffness and damping ratios of a soil layer captured by using FCONE program are shown as a function of dimensionless frequency in Fig. 8a. The dynamic stiffness coefficients of an embedded foundation such as a pile-foundation in a homogeneous half-space are sensitive to variations in the soil material damping ratio, which is in turn a function of strain amplitude. In the lower frequency range ($a_0 < 1$), considerable deviations exist for certain damping coefficient [22].

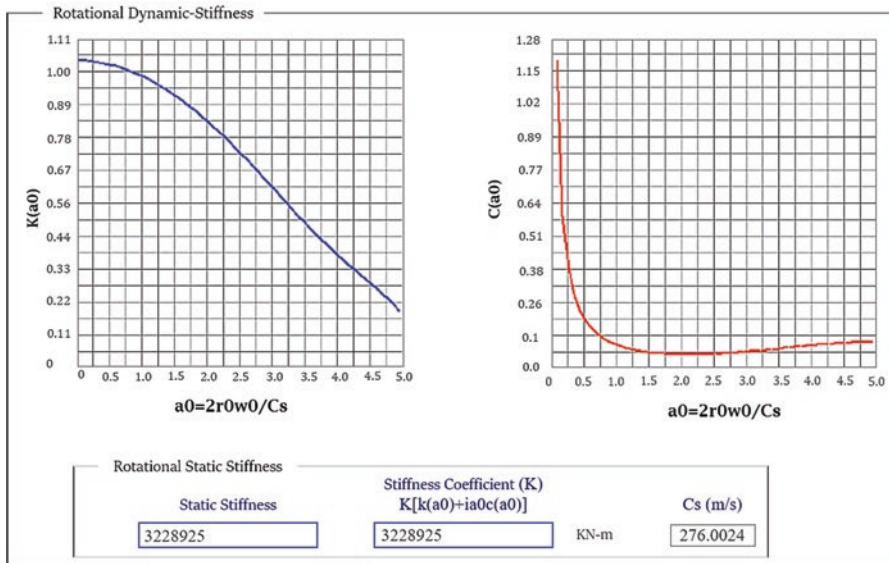
Figure 8 presents the dynamic behavior below and above the so-called cutoff frequency, where an abrupt change in response occurs. As can be seen in Fig. 8, the variation in damping coefficient at a lower frequency is much greater than that at a higher frequency.

3.2.4 The Finite-Element Simulation

The finite-element code ABAQUS/Cae model as an accurate direct way was used to investigate the seismic behavior of the structure under SPSI effect. For this purpose, the infinite soil medium is reduced to a finite region using infinite-element boundaries. In this case, an elastic perfectly plastic model was adopted for modeling the concrete piles with a modulus of elasticity of 30,000 (N/mm²). In the 3D finite-element model developed using Abaqus/Cae, both the pile and the soil were mod-

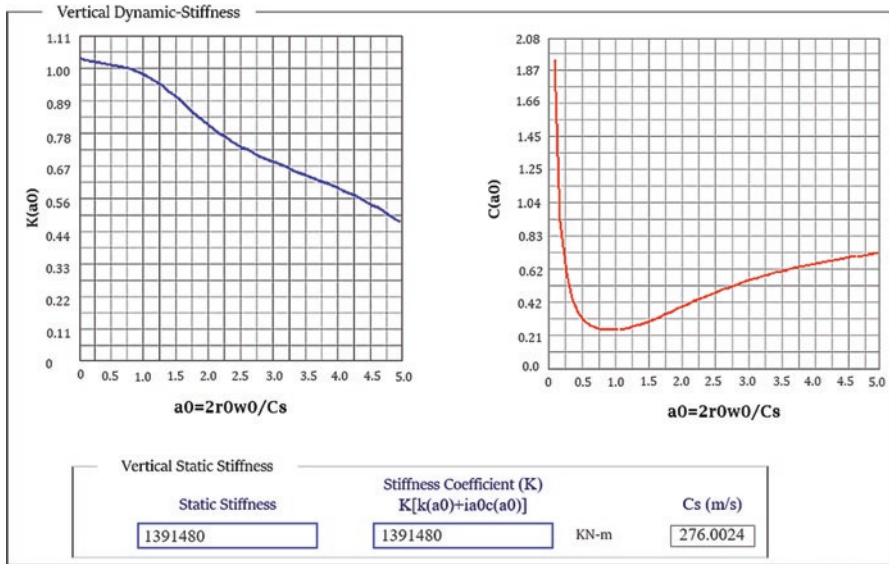


a) Horizontal Stiffness for a 3x3 Pile group



b) vertical Stiffness for a 3x3 Pile group

Fig. 8 The vertical, horizontal, and rotational dynamic stiffness for a 3 x 3 pile group. (a) Horizontal stiffness for a 3 x 3 pile group. (b) Vertical stiffness for a 3 x 3 pile group. (c) Rotational stiffness for a 3 x 3 pile group



c) Rotational Stiffness for a 3x3 Pile group

Fig. 8 (continued)

eled using eight-noded solid continuum elements (C3D8R) to account for the continuum nature of the soil. This element has quadratic shape function which is well suited to model the medium with bending dominated deformation. A too coarse mesh may deviate from the expected response, whereas a too fine mesh requires very long computational time. Hence, a relatively fine mesh was adopted for the pile, and a coarser mesh was adopted for the soil. Overall 11,089 elements for the piles and 10,205 elements for ten-story SPSI model were used. Soil was modeled using 98,400 elements, and the soil-pile interaction was modeled by defining the tangential and normal behavior of the contact surfaces in the FE model.

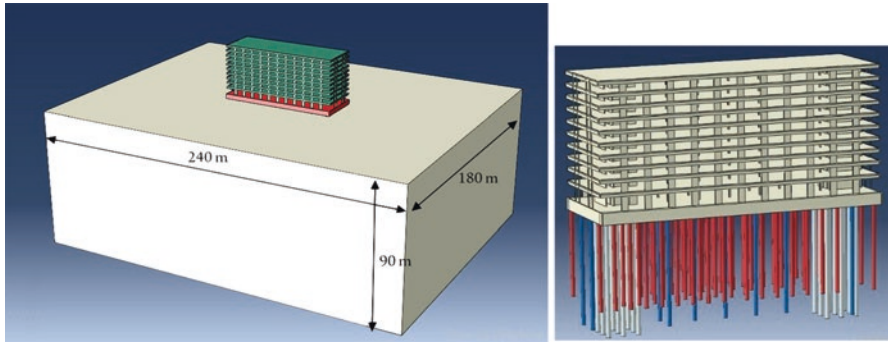
A strain hardening model using Mohr-Coulomb failure criterion was adopted for the soil which uses the five significant soil parameters, such as shear modulus (G), Poisson’s ratio (ν'), shearing resistance angle (φ'), effective cohesion (c'), and angle of dilatancy (ψ), as shown in Table 4. An angle of internal friction of 35° was used in the definition of the Mohr-Coulomb failure criterion. The geometrical details adopted for the SPSI analysis are shown in Fig. 9.

Results of 3D numerical prediction of first mode of vibration in eigenvalue analysis for both cases (fixed base and SPSI interaction) and maximum lateral displacements in short direction are shown in Figs. 10 and 11, respectively.

Table 5 provides a good comparison between the results of SPSI analysis obtained by CONE method and FEM solution, which indicates that the results of CONE method are in close agreement with FEM results. As the structural stiffness in comparison with soil or building height increases, the period rate increases as well. For first mode of vibration in modal analysis, a good tendency with negligible

Table 4 The soil parameters used in the finite-element code ABAQUS/Cae model

Elastic parameters		Plastic parameters (Mohr-Coulomb failure criterion)	
Mass density, ρ (kN/m ³)	16.45	Shearing resistance angle, φ'	34
Modulus of elasticity, E (MPa)	350	Angle of dilatancy, ψ	0.1
Poisson's ratio, ν'	0.4	Effective cohesion, c' (kPa)	22

**Fig. 9** The geometrical details of SPSI model using ABAQUS/Cae

difference was observed. Therefore, the CONE model provided reasonable accuracy of modal analysis for the high-rise building responses because the deviation was limited to 3%.

From the comparison between the maximum lateral displacements, it can be observed that the foundation displacement results obtained from CONE method give good agreement with FEM analysis results with about 6% difference, and the most difference was observed in the roof displacement with around 10%. The non-linearity of the soil medium results in increased lateral displacements of stories; however, as can be seen by comparing the results, it does not have a significant impact on the lateral displacements in this case. It can be also concluded that the maximum lateral displacement of structures increases with the increasing number of stories and the upper stories displacements are more affected with SPSI than the lower stories.

3.2.5 Dynamic Analysis of an Emergency Hospital in South of Switzerland

Specification of the free-field ground motion is one of the most important factors in SPSI analysis. A range of intensities, durations, and frequency contents were covered by selecting the ground motions to enable a comprehensive evaluation of the SPSI effect. In this research, the used earthquake excitation was the 1940 El Centro earthquake which has peak ground acceleration (PGA) of 0.349 g, commonly used

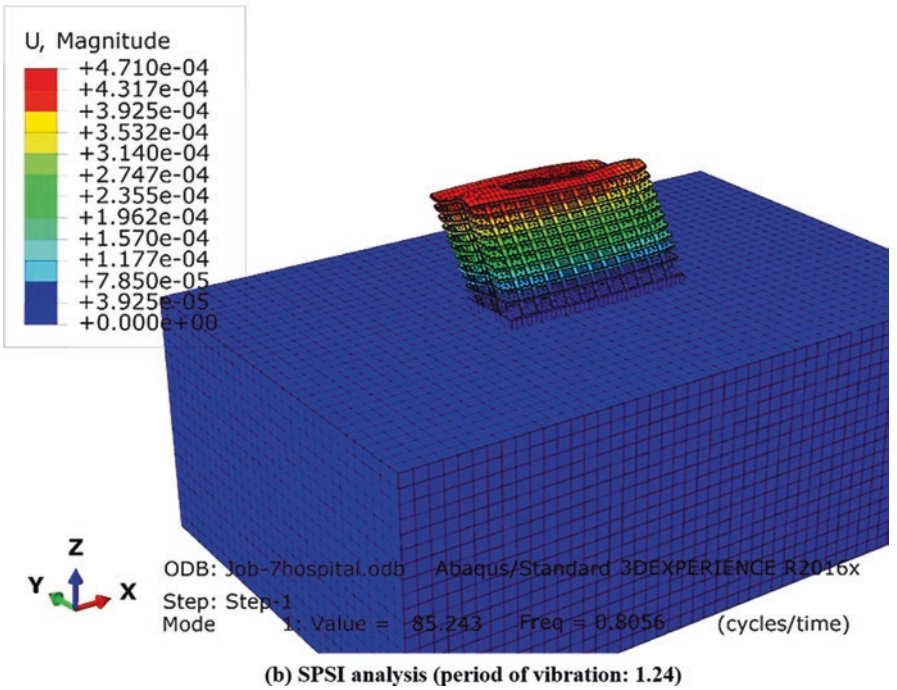
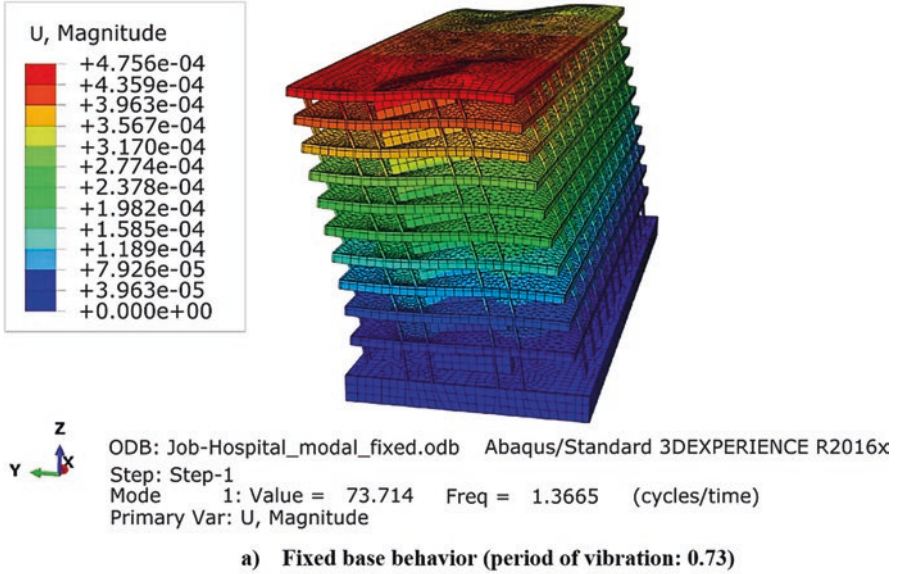


Fig. 10 The first mode of vibration in eigenvalue analysis

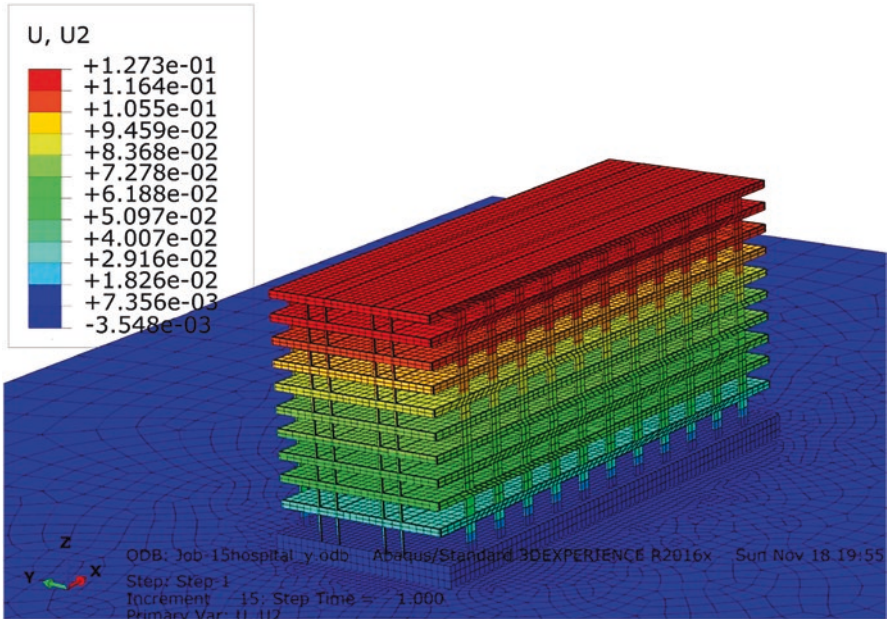


Fig. 11 The maximum lateral displacements in short direction

Table 5 Comparison between the results of SPSI analysis obtained by CONE method and FEM solution

	The period of vibration (s) (First mode)		The lateral displacement in short direction (cm)	
	Fixed base	SPSI	Foundation	The roof story
CONE model	0.7	1.20	0.28	11.50
FEM model	0.73	1.24	0.30	12.73

in structural dynamics. The ground motion records aligned in the two horizontal directions (shown in Fig. 12) were selected from the strong motion database of the Pacific Earthquake Engineering Research Center (PEER 2012).

The time history analysis was about 50-s duration consisting of 2500 steps under an actual earthquake accelerogram and a free vibration segment of 0.02 s duration. A comparison was made between the nonlinear structural response of the rigid foundation and flexible foundation models subjected to time history analysis. Under the ground motion record, the maximum lateral deflections at all stories of fixed-base and flexible models were measured by using the ETABS program. As mentioned, the significance of the displacement mechanisms was expected to depend on the excitation, soil, and structure properties. In particular, lateral displacements and story drifts of the structures resting on rather soft soils may be significantly amplified by SPSI.

The time histories of roof displacements under earthquake excitation with and SPSI effect along X and Y directions have also been demonstrated in Fig. 13.

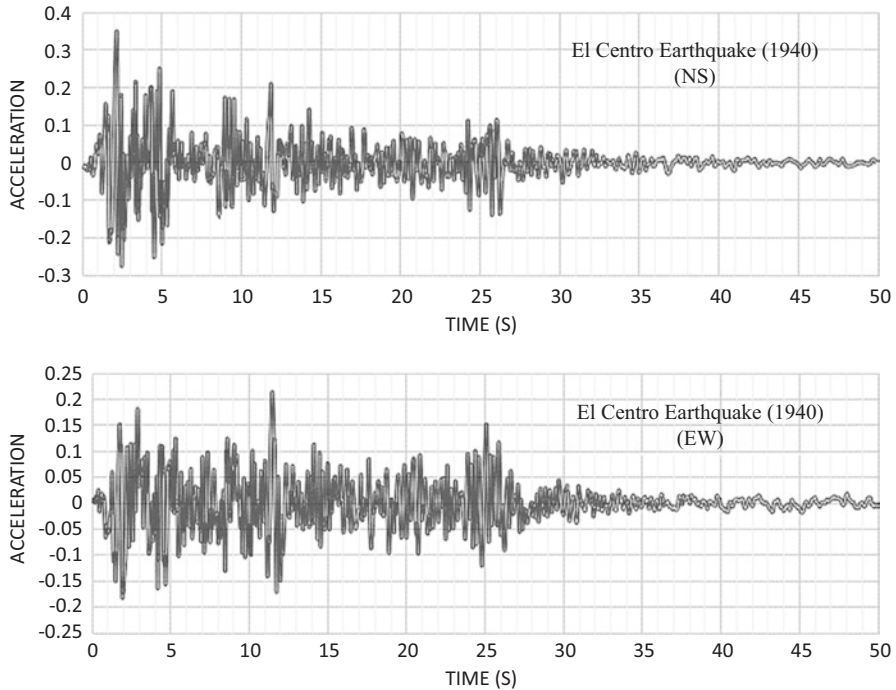


Fig. 12 Earthquake excitation: the El Centro earthquake in two horizontal direction (NS and EW)

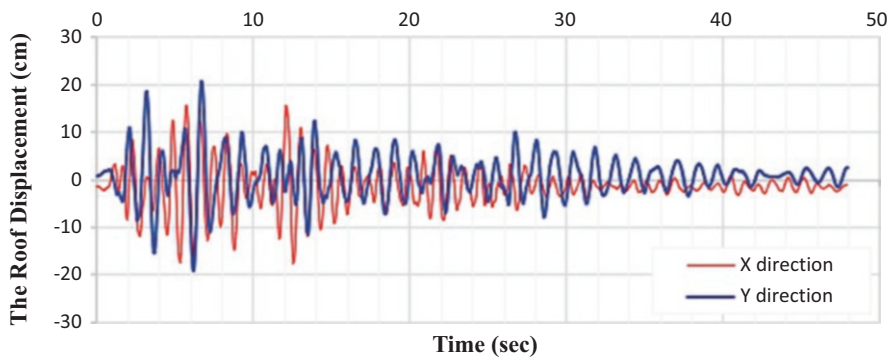


Fig. 13 The roof displacements along X and Y directions

In addition, the maximum lateral displacements and story drifts in both cases are shown versus the building floors in Fig. 14 (part a and b) and (part c and d), respectively.

From the comparison, it can be observed that the top deflection of the nine-story building (roof) with SSI effect increased by 1.77 times (and 2.12 times) than the case without taking into consideration SSI effect, along the X direction and the Y direction, respectively.

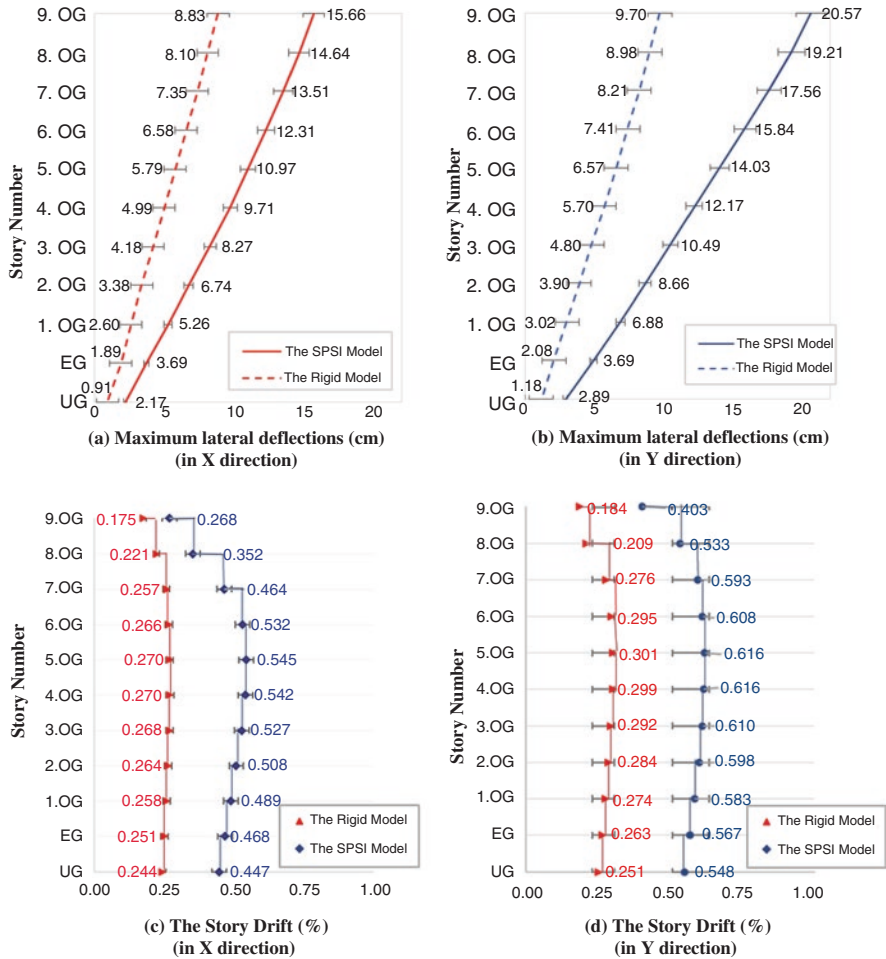


Fig. 14 The maximum lateral deflections: (a) in X direction and (b) in Y direction. The story drifts: (c) in X direction and (d) in Y direction

It should be noted that soil-structure-interaction analysis typically involves dealing with several uncertainties. The results of such dynamic analysis may require determining the limitation of material properties and models. In real engineering projects, the limitation ranges are determined in such a way that it stays on the conservative side. The uncertainties have remarkable impact on structure response, and hence it is essential to be cautious in this matter.

4 Case Study 2: Dynamic Analysis of the World Tallest Silo in Zurich, Switzerland

Silos belong to the strategic buildings in any country due to their supplying tasks. In this regard, their sustainability is essential to provide the needs of society continuously. Hence, it was necessary for Swissmill to increase the silo capacity in Zurich. The older still existing silo of Swissmill is named silo 24 and was constructed in 1924. Later, silo 57 was erected in 1957. The evaluation of projects for future capacity requirements results in increasing the capacity of the existing silo 57 by erecting the so-called Swissmill tower or Kornhaus, located in the Limmat Valley in Zurich, Switzerland.

Satellite view of the construction site is shown in Fig. 15. As it is evident, the silo is located at the riverbank. Therefore, poor soil condition would be highly expected. On the other hand, available space in order to be used as construction site was significantly limited. The other important factor, which should be noticed, is the extremely important railway bridge passing over Limmat River nearby the construction site. Any interruption or failures in silo may have catastrophic economic losses not only due to its inherent importance but also due to train transportation disturbance. All these conditions made project design, management, and execution difficult and require precise tasks.

The building's status before and after construction is shown in Fig. 16. The new parts are constructed by slip forming method in five working shifts. Moreover, the width of the silo is broadened on the roadside, and a row of cells on the riverside is replaced by a stronger new one.

At the end, the total weight became approximately equal to 80,000 tons. Considering all, the new silo is the heaviest and second tallest building in Zurich. The total sum of planning and construction costs amounts 35 million CHF, of which 25 million CHF are for the structure. The Swissmill tower belongs to Swissmill, a firm of coop production. Swissmill is the largest flour production plant in Switzerland and provides approximately 30% of the whole country's requirements by operating 800 tons of grains each day. In the current article, for the Swissmill tower, the structural concept, construction, and planning duties and seismic analysis efforts are briefly discussed.

4.1 Structural Concept

The load-bearing structure of Swissmill tower consists of two parts, the structure of the existing silo 57 and the added new structure to build up the Swissmill tower. The load-bearing structure of Swissmill tower behaves as a monolith composed by the structure of the existing silo 57 and the added new one. Generally, the gray parts in the following figures show the existing old structure, while the green parts show the added new one. Two new silo cell rows and two new transverse walls were constructed around the existing silo 57 up to a level of 42 m above terrain, as it is shown

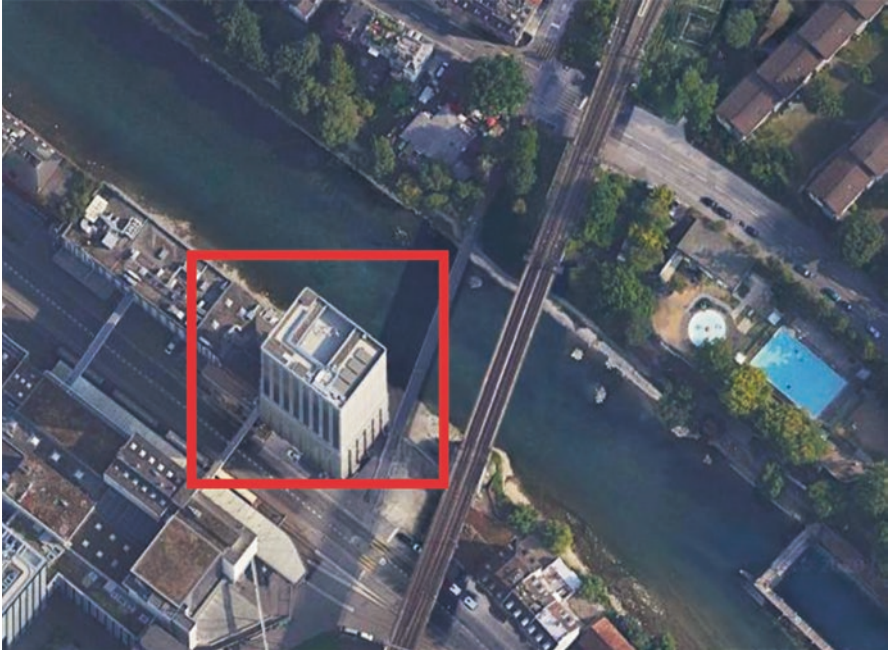


Fig. 15 Satellite view of silo's location



Fig. 16 View of the existing and new silo

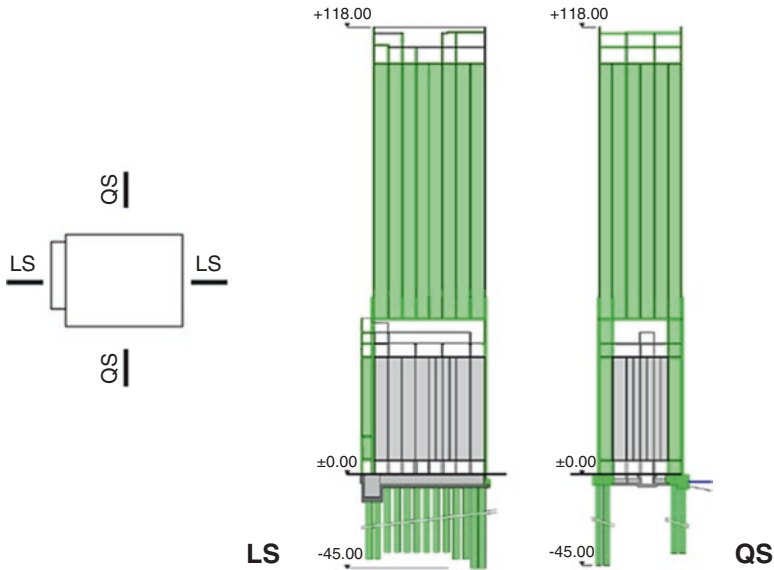


Fig. 17 Cross section (elevation view) of existing and new silo

in Fig. 17. Obviously, the big weight of the upper part is transferred to bedrock by the lower new silo cell rows and the transverse walls by the pile caps and the piles. Forty-nine piles were constructed for such aims. The diameter of piles is 1.50 m and their approximate length varies from 40 m to 50 m.

Detailed investigations of the structure of the older silo 24 have shown that it could be severely damaged or destroyed due to movements of the new Swissmill tower, in case of missing joint above the terrain. The new intermediate structure (small green part on left side in section LS) is monolithically connected to the silo 57, while it is separated from silo 24 above terrain. Thus, the old silo 24 is no longer endangered by dynamic vibrations of the new Swissmill tower. Likewise, the connection between the new intermediate structure and the old silo 24 had to be detailed in a way that no great forces are transferred to the old silo 24. In addition, the joint between silo 24 and the new intermediate structure was covered by a surrounding metal sheet in order to prevent weathering.

Because of the already mentioned poor structural condition of silo 24, it was reinforced locally by steel supports. During construction, it was found that a part of the outer wall of silo 24 is not a concrete wall as previously assumed but a masonry wall. In order to reduce risk of collapse, the masonry wall is immediately secured in the critical area by fastening of steel girders. First, the 49 piles and the 2 pile caps were constructed in construction stages 1 and 2 (red numbers 1 and 2 in Fig. 18). In these two construction stages, the two new lower cell rows and the eastern sidewall (transverse wall) were constructed up to a level of 42 m above terrain. Then, in construction stage 3 (red number 3 in Fig. 18) the old small intermediate part between silo 24 and silo 57 was replaced by a new intermediate part, and the new western transverse wall was constructed up to a level of 42 m above terrain. Later, the upper silo was erected in two construction phases (red numbers 4 and 5 in Fig. 18) due to

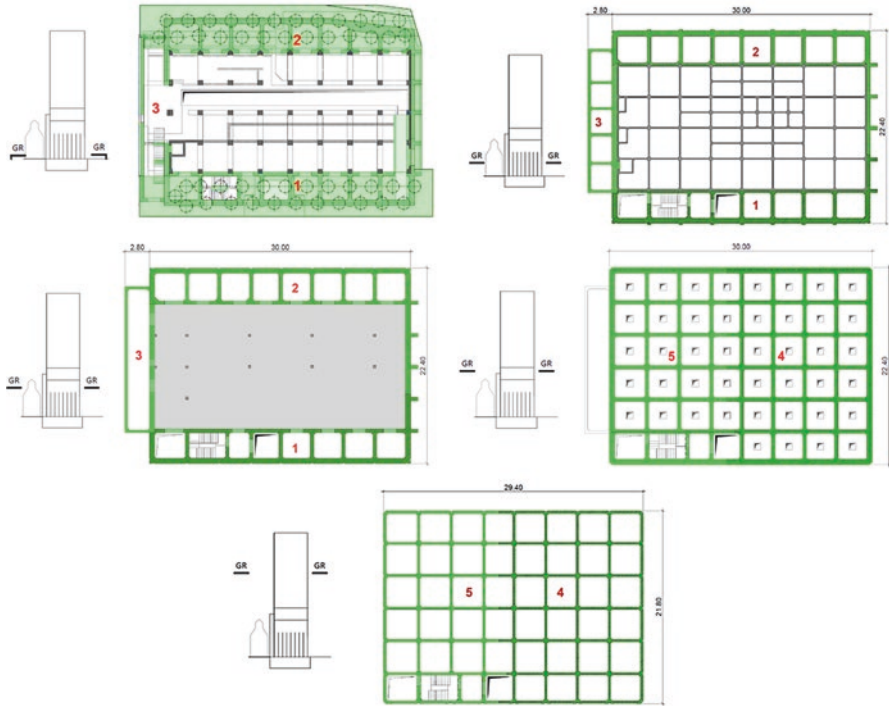


Fig. 18 Plan view on different height levels

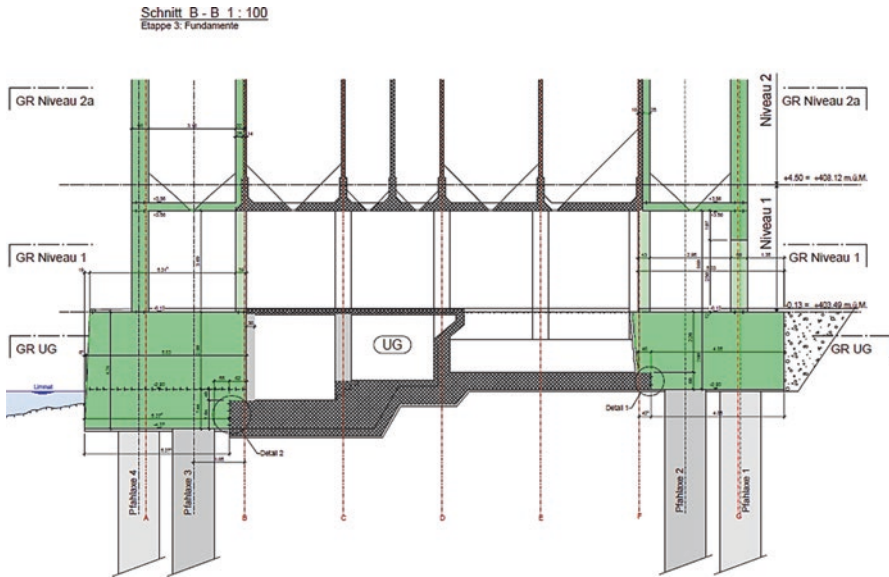


Fig. 19 Foundation section

logistical considerations. At the end, in the construction, stage 6 the upper silo was completed with the ceiling part.

One of the important challenges in the design of the project is considering interaction between soil, flat foundation of existing silo 57 and new structure including piles. Three-dimensional finite-element models are constructed to conduct dynamic analysis, of which the results will be illustrated in Sect. 4 of this paper. Foundation section and position of piles are depicted in Fig. 19.

The authorities of Zurich demanded space for a future public footpath along the river. Thus, a cantilever situation had to be made in a silo corner on the riverside. This part is highly stressed due to stress concentration from above parts. It is strengthened by thickening the outer wall and installation of complex steel reinforcement. Later and during the second phase of the construction, demanding and uniquely distinctive investigations were made regarding the stresses under heavy loads and possible dynamic effects. These studies have shown that the load-bearing structure in this silo corner must additionally be reinforced by an internal concrete structure above the pile cap. This difficult reinforcement work was carried out under direct supervision of project engineer Dr. Josef Grob. It began in mid-September 2015 and was completed in a perfect quality at the end of January 2016. Plan view and inner reinforcement of this part are shown in Fig. 20.

4.2 *Modeling and Dynamic Analysis*

Instrumentally recorded ground motions in Switzerland between 1975 and 2014 are shown in Fig. 21. As it is evident, Zurich is located in a median seismic region. Moreover, Swiss probabilistic peak ground acceleration hazard map is shown in Fig. 22. As it is evident, Zurich is between 60 and 70 cm/s^2 (0.06 – 0.07 g). Therefore, possibility of major earthquake occurrence at studying site would not be significant. In spite of that, it should be noticed that weak site soil condition can amplify earthquakes.

Such amplifications are reported in past earthquakes. For instance, the Michoacan earthquake (Mexico) of 1985 with magnitude of 8.1 had an epicenter 350 km away from Mexico City. This earthquake produced accelerations equal to 0.04 g at rock sites, while recorded accelerations at soft soil sites were up to five times greater than those at rock sites. Therefore, soil-structure interaction should be considered. Soil condition includes different layers of the site.

In order to extract demands on the building, 3D finite-element model using ADINA software is constructed and linear analysis is conducted. The model has more than 3,000,000 elements. The structure is modeled using shell and solid elements. Based on NEHRP provisions, soil-structure interaction is considered by assigning equivalent springs and dashpots located under foundation. In cases which fundamental frequency of the building is less than frequency of site, no radiation damping is expected. This phenomenon is due to existence of the cutoff frequency. First frequency of site soil is 0.9 Hz, which is greater than 0.3 Hz of the structure. Hence, no radiation damping is considered.

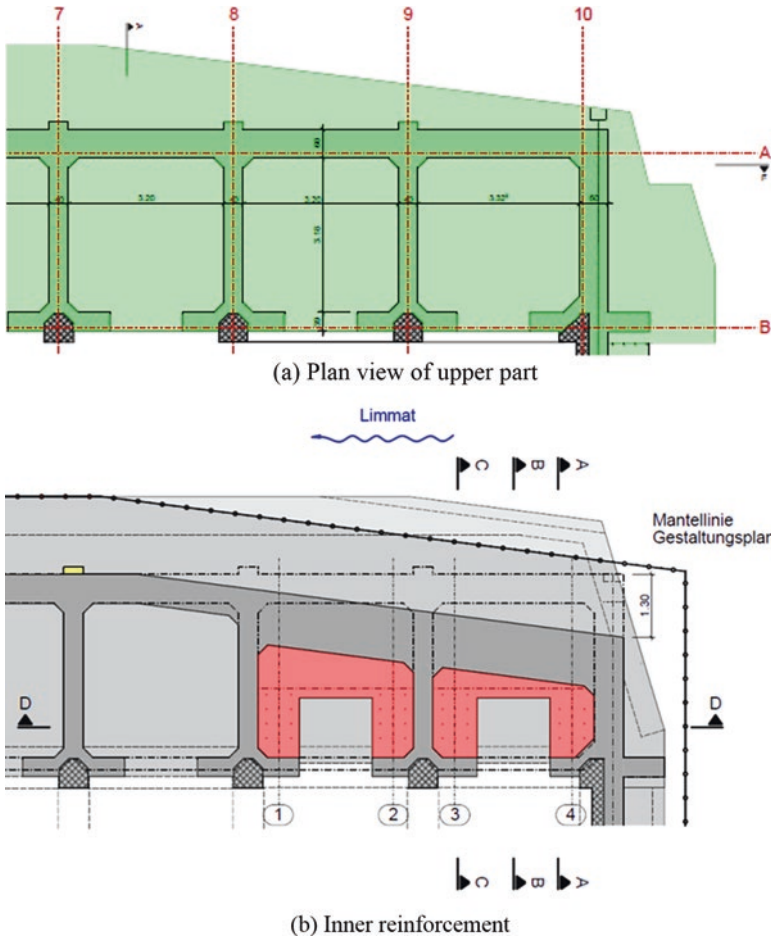


Fig. 20 Plan view of lower part with internal reinforcement. (a) Plan view of upper part. (b) Inner reinforcement

Finally, two different FEM models have been used by two different design groups. As shown in Fig. 23, the first period of vibration which was analyzed using the ETABS program increased by about 74% (from 1.72 s to 3.1 s) concerning the SPSI effect. In order to control roof displacement under possible ground motion, Duzce record is applied to the model. The maximum roof displacement approximately equals to 21 cm.

At the end, von Mises stresses and lateral displacement of piles using load combination of dead loads and earthquake are calculated. Horizontal displacement of foundation under earthquake excitation equals to 3.1 cm. In addition, axial force and bending moment of piles equal to 19,000 kN and 3430 kN m, respectively (Fig. 24).

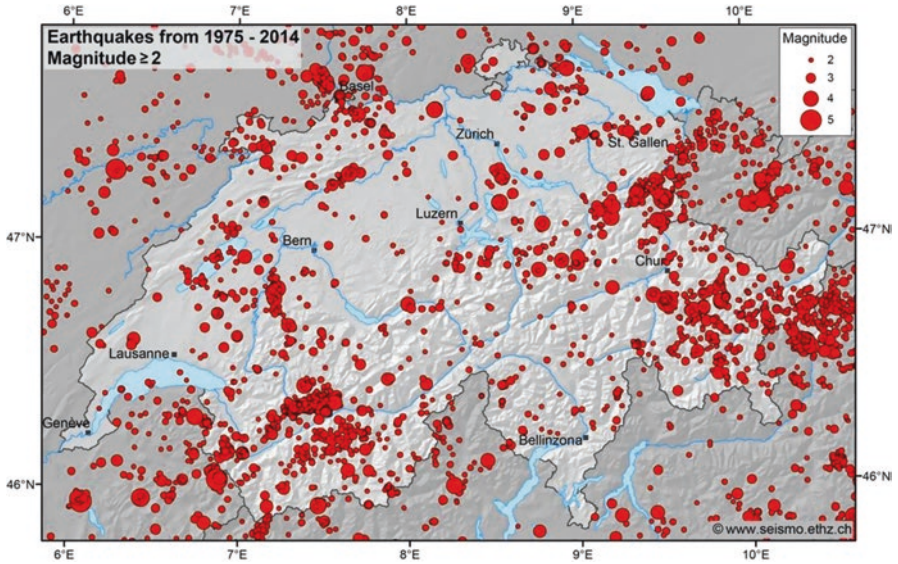


Fig. 21 Instrumentally recorded earthquakes in Switzerland between January 1975 and January 2014

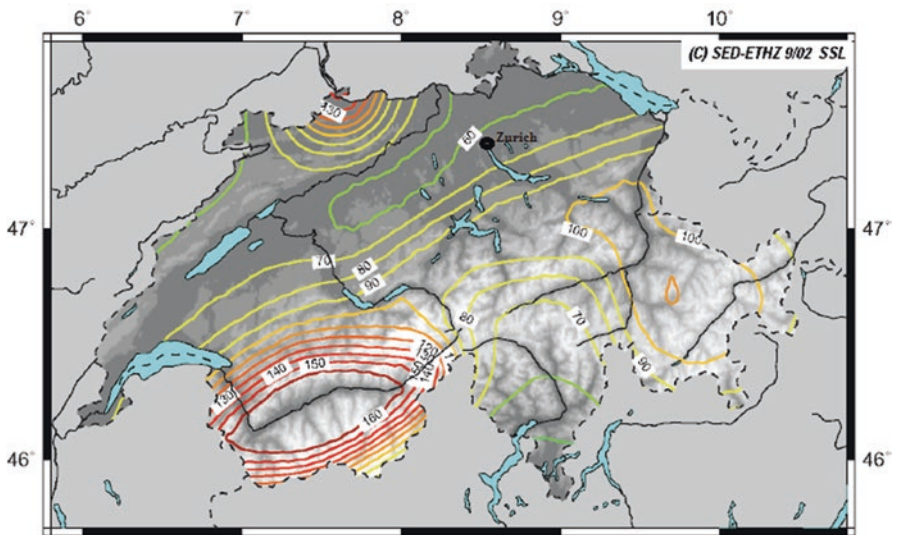


Fig. 22 Probabilistic hazard map of Switzerland showing the peak horizontal ground acceleration in cm/s^2

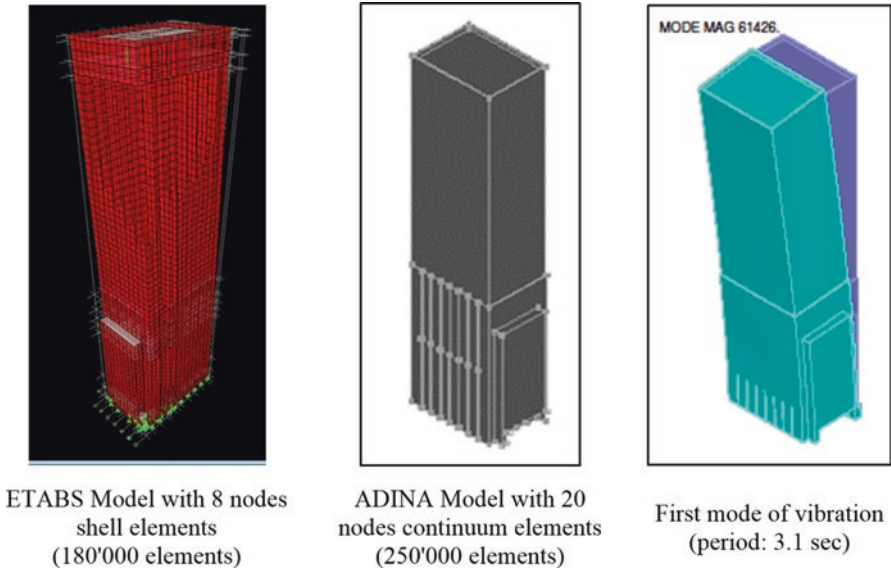


Fig. 23 Dynamic analysis of Swissmill tower using two different FEM models

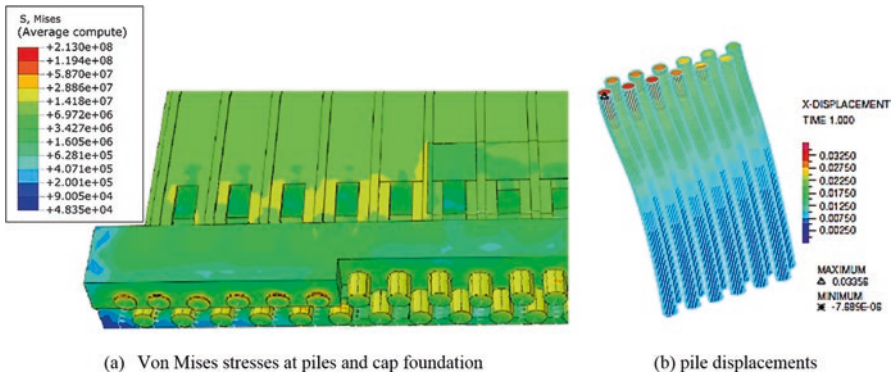


Fig. 24 Stress and displacement at foundation level

5 Case Study 3: Dynamic Analysis of the Green Building at MIT Campus

The Green building is the Building 54 at MIT campus in Cambridge, Massachusetts, USA. This building is the tallest structure in Cambridge, designed and constructed by I.M. Pei from 1962 to 1964, and came into operation in 1964. In the plan, this building has a dimension of 34 × 16.5 m. It has 20 stories with an overall height of 83 m plus a 1-story basement below ground level. The height of the first story is 10 m and the others are 3.5 m. The ground surface is approximately 6.1 m above sea level, and depth to bedrock is approximately 30.55–40.0 m below sea level. Building



Fig. 25 Image of Green building at MIT campus, Cambridge

54 includes administrative sections and classrooms for natural sciences department. As shown in Fig. 25, the building orientation in the plan has a deviation of 25° to the north. Two 25-cm-thick shear walls extending from the basement foundation level to the roof level at the two narrow ends. The underground floor has a link to the MIT colleges connecting tunnel. The structure was made of cast-in-place reinforced concrete, and the thickness of concrete slab at each story is 101 mm.

In Fig. 26, the position of the shear walls, the dimensions, and the sizes are specified. The building is placed on a concrete mat foundation with concrete pile caps that have thickness of 350 mm and loading capacity of 50 tons. The foundation dimension is 34×16.5 m. Despite the existence of doors, windows, and entrances, from the shear walls up to the roof level, the building still could be considered as a symmetric structure. Figure 27 shows a typical depth versus shear-wave velocity log from a site approximately 50 m (150 ft.) from the building (Jen 2011, personal communication; [25]).

5.1 Site Condition

Building 54 is located near the Charles River. The structure is placed on the alluvial deposits of the river. The geotechnical studies of site condition have been thoroughly performed, and the soil properties especially shear-wave velocity of the soil were determined.

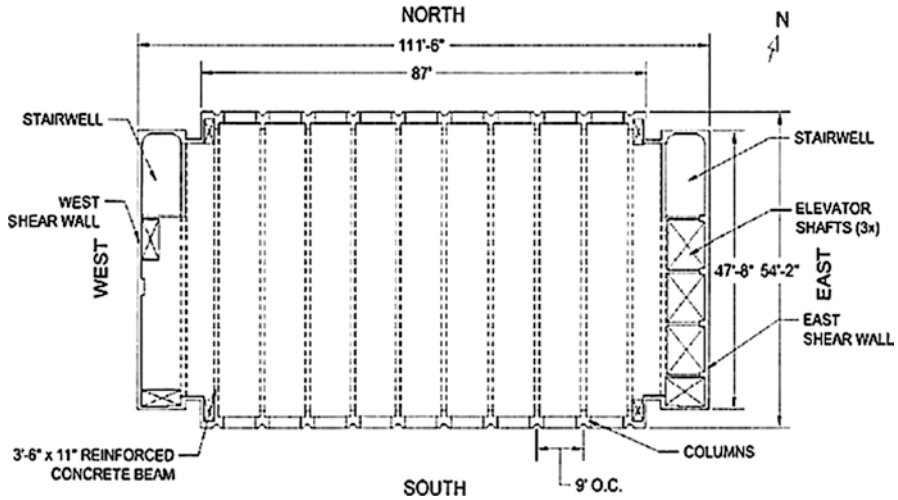


Fig. 26 The plan view of the building depicting the distribution of shear walls

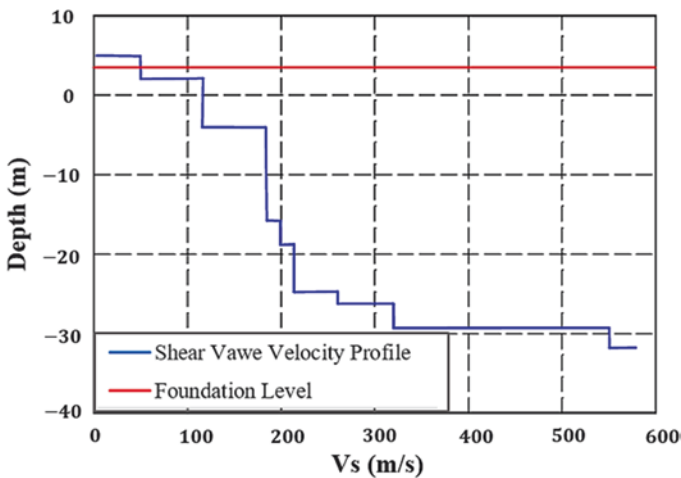


Fig. 27 Shear-wave velocity log versus depth profile of the site

The site was 6.1 m above mean sea level, and according to geotechnical studies, the shear-wave velocity varied between 100 and 600 m/s. The depth of bedrock was estimated to be around 30.55–34 m from the ground surface. Based on a shear-wave velocity boring log from a site approximately 50 m from the building (Jen 2011, personal communication; [25]), the fundamental site frequency is estimated to be ~1.5 Hz [24]. Figure 28 displays the soil profile and the wave propagation in the soil layers. Later, Trocha [26] studied the dynamic behavior of this building, again using ambient data. The natural frequencies were identified—with some differences from those identified by Çelebi et al. [24] as 0.75 Hz (first NS), 2.85 Hz (second

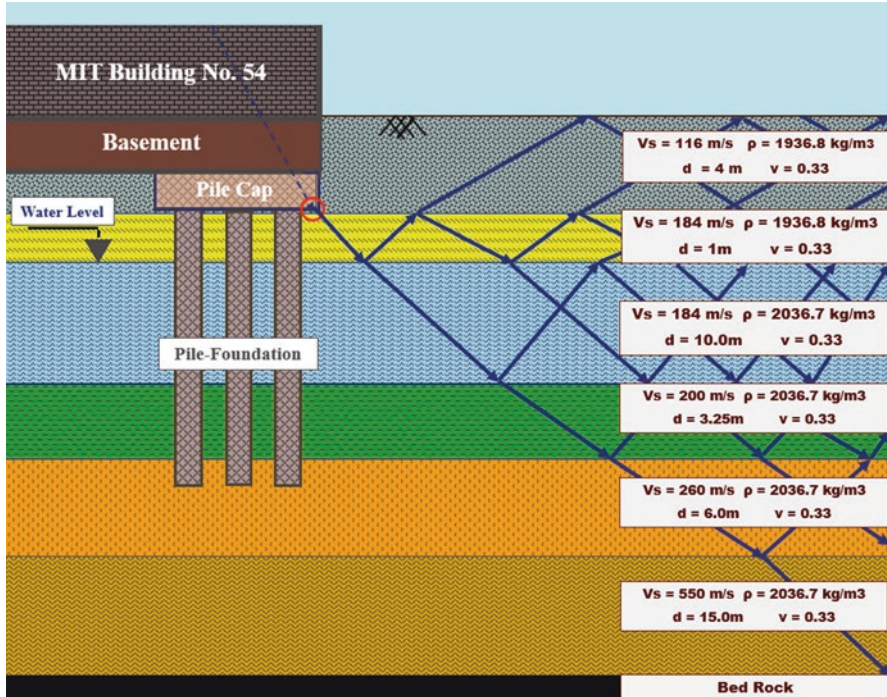


Fig. 28 The soil profile and the wave propagation in the soil layers

NS), 0.68 Hz (first EW), 2.45 Hz (second EW), and 1.45 Hz (first Tor). The fundamental frequency of the building (0.68 Hz) is less than the frequency of site; hence, no radiation damping is considered. In addition to geotechnical data, the site seismicity data were also available. In 2012, the magnitude 4.0 earthquake occurred near Hollis Center, Maine, where data recorded with accelerometers were available. In the present study, three ground motions including Hollis Center, El Centro, and Hotel Azadi were considered as input for the dynamic analysis and structure evaluation [26].

5.2 Modeling and Dynamic Analysis

The modeling of Building 54 has been performed in detail, meaning that the structure was simulated along with the surrounding soil. Computation of maximum lateral displacement for all stories of the building corresponding to the soft soil during the three mentioned earthquakes was done based on both conditions with and without SSI. Although the structure data were clear and definite, there was considerable uncertainty in soil properties which caused complex challenges in the analysis. The “springs and dashpots” method proposed by NEHRP allows evaluating the mechanical and

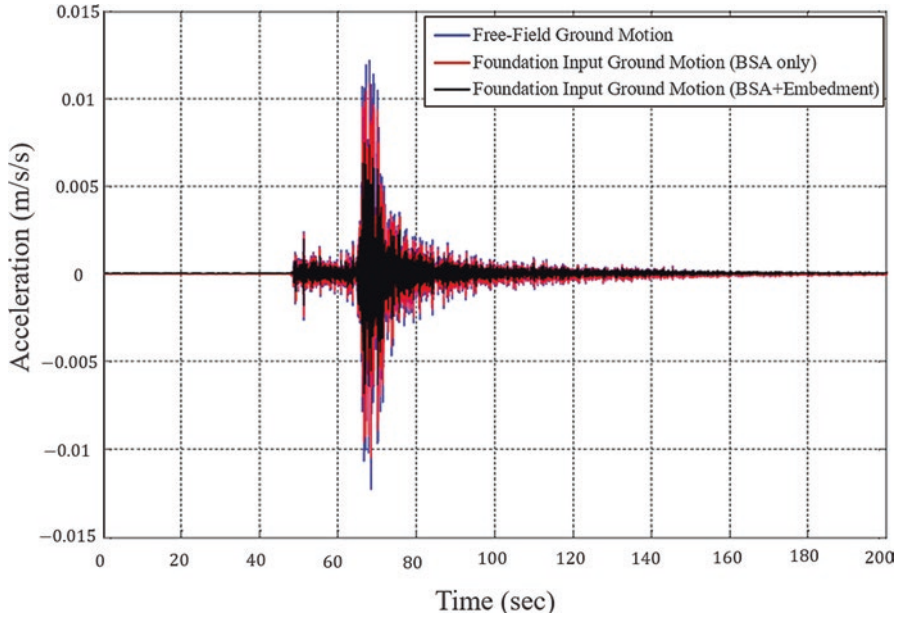


Fig. 29 The M4.0 Hollis Center earthquake (Maine) in free field, modified by BSA consideration, and modified with both BSA and embedment effect

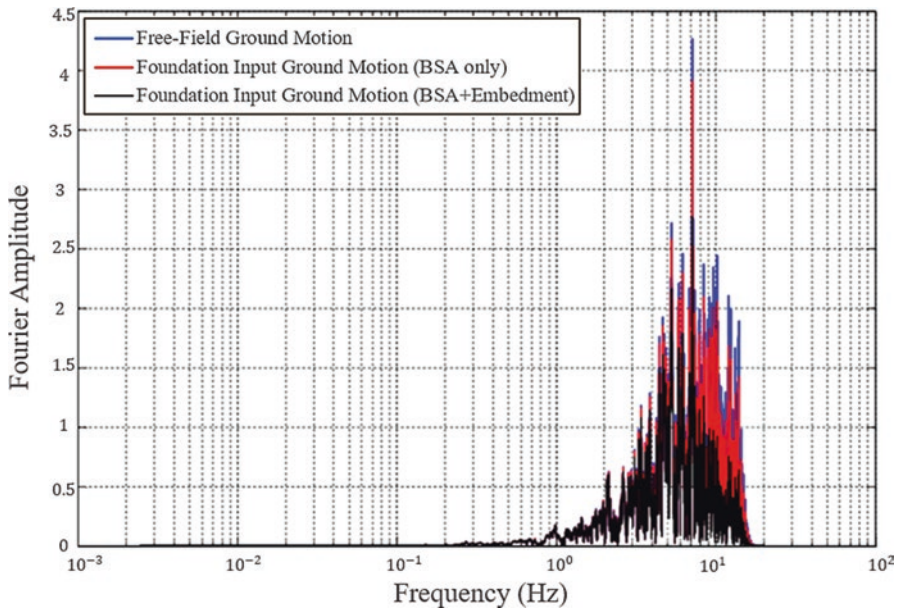


Fig. 30 Fourier transform of M4.0 Hollis Center earthquake (Maine) which transfers function of BSA and embedment is multiplied

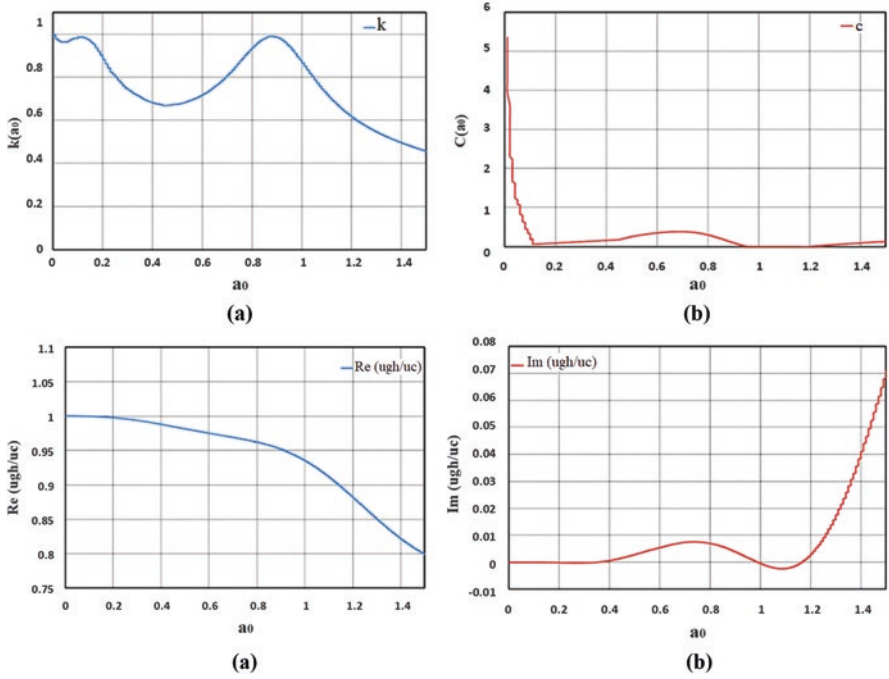
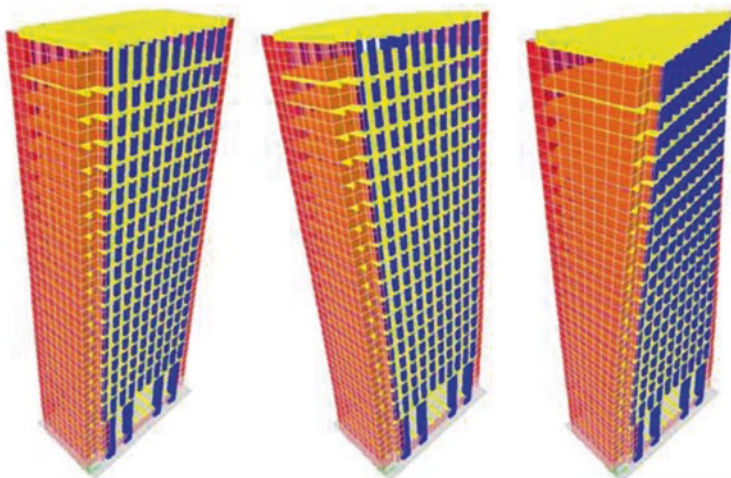


Fig. 31 The plot of dynamic stiffness coefficients and damping coefficients versus the dimensionless frequency parameter (a_0)



Mode No.	Period Fixed-Based ETABS Model (sec)	Period Flexible-Based ETABS Model (sec)	Period Çelebi <i>et al.</i> (sec)
1	1.3793	1.5319	1.47
2	0.9883	1.0938	1.33
3	0.5892	0.6303	0.4

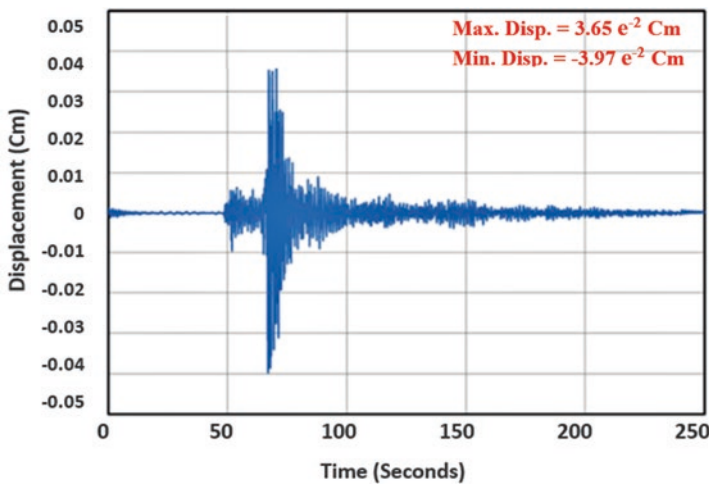
Fig. 32 The first three identified mode shapes obtained from the ETABS analysis

dynamical characteristics of soil that have been impacted by a combination of three mechanisms including footing conditions, embedment effects, and pile contributions. On the basis of the approach described above, 160 nodes are considered at the base level, and resultant of footing and pile stiffness is distributed on nodes in base level. Figure 29 depicts the acceleration records of the Hollis Center earthquake in three situations: free field, modified by base slab averaging (BSA) consideration, and modified with both BSA embedment and embedment effect. As shown in Fig. 30, the Fourier transform of these cases which transfers function of BSA and embedment is multiplied.

The dynamic analysis was conducted considering the soil-structure interaction based on CONE model. The results obtained by FCONE program are shown in Fig. 31, where dynamic stiffness coefficients and damping coefficients are plotted against the dimensionless frequency parameter $a_0 = w2r_0/c_s$.

The mentioned characterization and structure evaluation method are normally used for seismic analysis of infrastructures as it was also applied to the Building 54. The first three identified mode shapes obtained from the ETABS analysis are shown in Fig. 32, where it can be seen that the application of SSI could cause approximately 10% increase in captured periods of the building. A comparison was also made between the results of modal analysis by Çelebi et al. [24] and these 3D numerical predictions captured by using ETABS and FCONE programs. Good agreements have been achieved in the comparison of results.

In general, SSI tended to amplify the lateral deflections of the superstructures. Experienced roof displacements under excitation of considered ground motions



	Flexible-based Model (Cm)				Fixed-Based Model (Cm)			
	Min. Y	Max. Y	Min. X	Max. X	Min. Y	Max. Y	Min. X	Max. X
HC	-0.0468	0.055	-0.0402	0.0377	-0.06	0.0547	-0.0397	0.0365
HA	-29.408	31.915	-30.7	36.7	-20.94	20.26	-34.4	35.7
EC	-15.695	20.12	-28	28.2	-20.63	20.64	-17.5	17.7

Fig. 33 The roof displacements under excitation of considered ground motions with and without SSI effects

Table 6 Minimum and maximum vertical accelerations under excitation of considered ground motions with and without SSI effects

<i>Flexible-based model (m/s²)</i>				
Hollis Center	-0.173	0.151	-0.187	0.177
Hotel Azadi	-15.8	14.68	-10.6	11.0
El Centro	-10.568	7.69	-6.48	7.91
<i>Fixed-base model (m/s²)</i>				
Hollis Center	-0.305	0.358	-0.316	0.291
Hotel Azadi	-14.82	15.85	-12.4	15.2
El Centro	-10.2	11.65	-8.53	8.52

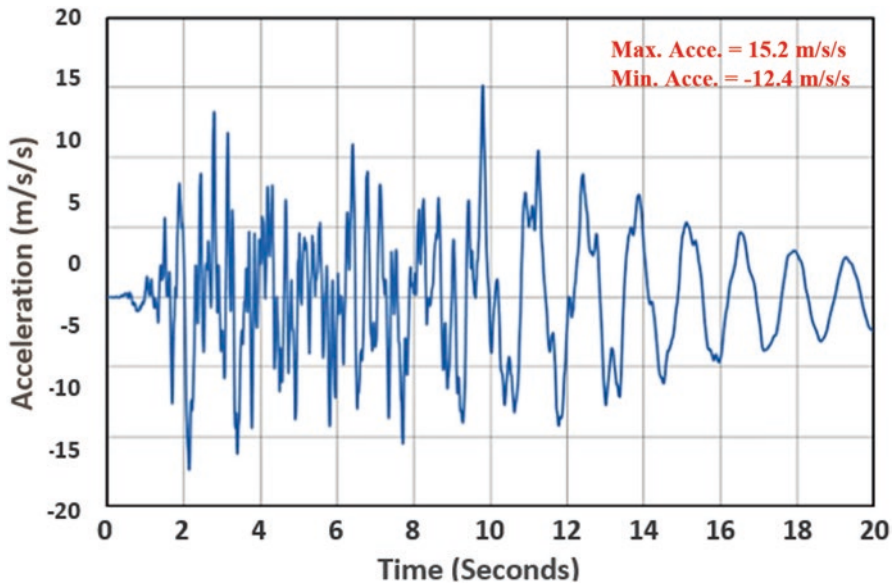


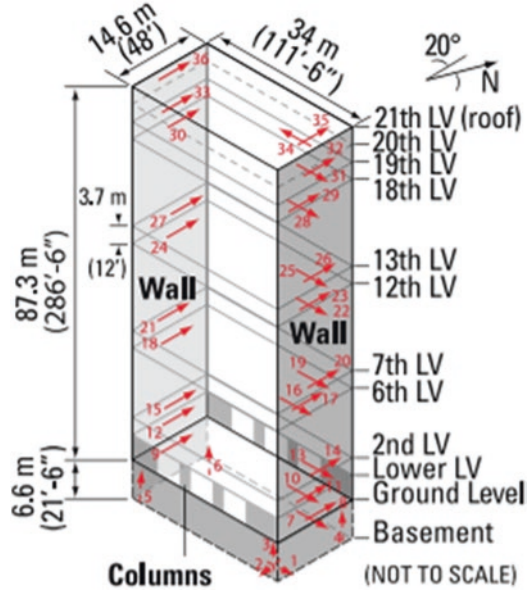
Fig. 34 The roof acceleration under Hotel Azadi ground motion

with and without SSI effects are shown in Fig. 33, where it can be seen that the displacements increased by consideration of SSI effects. To determine the sensitivity in the structure’s response from an analytical perspective, we computed both minimum and maximum horizontal accelerations under excitation of considered ground motions with and without SSI effects which were presented in Table 6.

Moreover, the roof acceleration under Hotel Azadi ground motion is plotted in Fig. 34. It can be seen that the experienced roof accelerations are decreased by consideration of SSI effect.

Figure 35 shows a schematic of the building depicting important dimensions as well as locations and orientations of the 36 accelerometers deployed throughout the building. Each accelerometer channel is connected via cable to a 36-channel central recording system. The accelerometers are distributed as three per level to capture the real acceleration values under Hollis Center ground motion excitation in a building.

Fig. 35 Distribution of accelerometers in the MIT Building 54



The simulation and dynamic analysis of the building under seismic loads were compared to measured values. It can be seen from Fig. 36 that there is a good agreement between results of the roof acceleration in X direction obtained from FEM model (ETABS) and recorded values.

6 Conclusion

The present study investigates the effectiveness of applying the enhanced CONE model to analyze the dynamic response of pile groups in three tall and massive building projects. For this purpose, we have developed a new computer program in which the seismic behavior of pile-soil-pile structure interaction on a large building is investigated as a whole considering pile-group effect and soil constitutive model according to the CONE theory. This program utilizes the equivalent dynamic modeling concept in the analysis of soil dynamics and pile-foundation interaction. The main conclusions drawn from the results are given as follows:

- The enhanced CONE model allows the nonlinearity of the near-field soil (plastic zone) to be represented by an equivalent linear manner, thereby reducing the degrees of freedom compared to FEM method and consequently reducing computational effort. The results presented in this article are obtained from substructure approach in the frequency domain which is formulated on a basis of the CONE method derived from the fundamental solution for a homogeneous, isotropic, and linear-elastic continuum. The presented model is also capable of incorporating the angular wave incidence from the far-field.

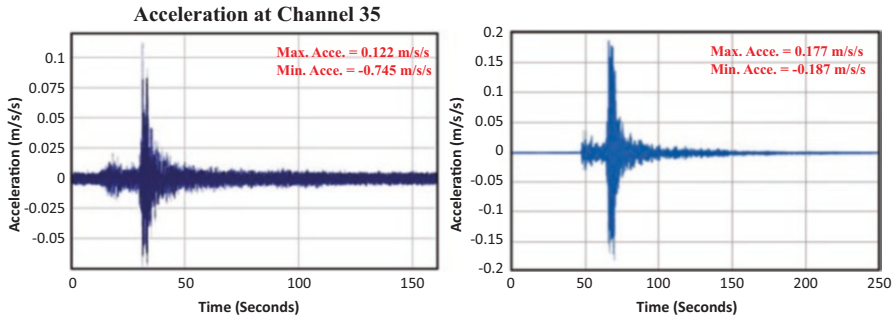


Fig. 36 Measured vs. calculated roof acceleration in X (or 1) direction under Boston ground motion excitation

- By comparing the obtained results, it can be concluded that considering the effects of the SPSI can alter the dynamic characteristics of the structural system. It is shown that the effects of soil-structure interaction are demonstrated as increasing the period of vibrations and the lateral deflections as well as decreasing the experienced roof accelerations. Consequently, the in-story drifts of structures were amplified in comparison with the fixed-base model. Therefore, ignoring the SPSI effects in such cases could affect the predicted damage level of structural and non-structural elements during an earthquake, resulting in considerable deviations.
- Linear (frequency-domain) SSI analysis can be employed for prediction of dynamic response of structures in low- to moderate-intensity shaking earthquakes such as these real cases located in a moderate-level seismic zone. Besides, the consequences might differ for extreme shaking that results in highly nonlinear soil where the nonlinear effects, including gapping, sliding, and uplift, are greatest in the immediate vicinity of the soil-structure boundary, and these cannot be captured using equivalent linear techniques.
- The capability of the CONE method to predict the dynamic SPSI effects gives it an advantage over other time-consuming rigorous methods. This approach leads to physical insight with conceptual clarity, is simple to use and solve as the mathematical solution is simplified, and provides sufficient generality (layered site, embedment, all frequencies) and acceptable engineering accuracy. The accuracy of any analysis is limited anyway, because of the many uncertainties, some of which can never be eliminated (for instance, the definition of the dynamic loads and the values of the dynamic soil properties in the analysis of a structure). The analysis with cones fits the size and economics of practical engineering projects. Thus, the results presented in this article can contribute to relevant engineers in designing safe and economical structures based on foundation vibration and dynamic SPSI analysis in practical projects whenever possible.

References

1. Craig RRJ, Kurdila AJ (2006) Fundamentals of structural dynamics. Wiley, Hoboken, NJ
2. Han Y (2002) Seismic response of tall building considering soil-pile-structure interaction. *Earthq Eng Eng Vib* 1(1):57–65
3. Guin J, Banerjee PK (1998) Coupled soil-pile-structure interaction analysis under seismic excitation. *J Struct Eng* 124(4):434–444. [https://doi.org/10.1061/\(ASCE\)0733-9445\(1998\)124:4\(434\)](https://doi.org/10.1061/(ASCE)0733-9445(1998)124:4(434))
4. Kaynia AM (1982) Dynamic stiffness and seismic response of pile groups. Doctoral dissertation, Massachusetts Institute of Technology
5. Dobry R, Gazetas G (1988) Simple method for dynamic stiffness and damping of floating pile groups. *Geotechnique* 38(4):557–574
6. Chore HS, Ingle RK, Sawant VA (2010) Building frame-pile foundation-soil interaction analysis: a parametric study. *Interact Multiscale Mechan* 3(1):55–79
7. Fan K, Gazetas G, Kaynia A, Kausel E, Ahmad S (1991) Kinematic seismic response of single piles and pile groups. *J Geotech Eng ASCE* 117(12):1860–1879
8. Ptilakis D, Dietz M, Wood DM, Clouteau D, Modaressi A (2008) Numerical simulation of dynamic soil-structure interaction in shaking table testing. *Soil Dyn Earthq Eng* 28:453–467
9. Kaynia AM, Kausel E (1991) Dynamics of piles and pile groups in layered soil media. *Soil Dyn Earthq Eng* 10(8):386–401
10. Massumi A, Tabatabaiefar HR (2007) Effects of soil–structure interaction on seismic behavior of reinforced concrete buildings with moment resisting system (using direct method). International Institute of Earthquake Engineering and Seismology (IIEES), Tehran
11. Novak M (1987) Discussion of dynamic response of arbitrarily shaped foundations: experimental verification. *J Geotech Eng* 113(11):1410–1412
12. Baranov VA (1967) On the calculation of excited vibrations of an embedded foundation. *Voprosy Dinamiki Prochnosti*. Polytechnic Institute Riga, Riga, p 14
13. Novak M, Nogami T (1977) Soil-pile interaction in horizontal vibration. *Int J Earthq Eng Struct Dyn* 5:263–281
14. Ismail S, Kaddah F, Raphael W (2018) Seismic soil structure interaction of a midrise frame structure. In International congress and exhibition “sustainable civil infrastructures: innovative infrastructure geotechnology”. Springer, Champions, p 73–88
15. Ülker-Kaustell M, Karoumi R, Pacoste C (2010) Simplified analysis of the dynamic soil–structure interaction of a portal frame railway bridge. *Eng Struct* 32(11):3692–3698
16. Sadeghi Hokmabadi A, Fatahi B, Far H, Samali B (2012) Effects of soil-pile-structure interaction on seismic response of moment resisting buildings on soft soil. In 3rd international conference on new developments in soil mechanics and geotechnical engineering. Near East University Press, Turkey
17. Pal AS, Baidya DK (2018) Dynamic analysis of pile foundation embedded in homogeneous soil using cone model. *J Geotech Geoenviron* 144(8):06018007
18. Jaya KP, Prasad AM (2004) Dynamic behaviour of pile foundations in layered soil medium using cone frustums. *Géotechnique* 54(6):399–414
19. Meek JW, Wolf JP (1994) Cone models for an embedded foundation. *J Geotech Eng* 120:60–80
20. Mohasseb S, Ghazanfari N, Hajian M, Elahi A, Karimi F (2018) Information technologies (IT) applications for construction: (case study: the tallest silo of the world in Zurich). *Am J Civil Environ Eng* 3(4):96–104
21. Mohasseb S, Nayeri A (2015) Theory to practice. Mahnevisan publication
22. Wolf JP (1985) Dynamic soil-structure interaction. Prentice-Hall, Englewood Cliffs, NJ
23. Stewart J, Crouse CB, Hutchinson TC, Lizundia B, Naeim F, Ostadan F (2012) Soil-structure interaction for building structures (no. grant/contract reports (NISTGCR)-12-917-21).

24. Çelebi M, Toksöz N, Büyüköztürk O (2014) Rocking behavior of an instrumented unique building on the MIT campus identified from ambient shaking data. *Earthquake Spectra* 30(2):705–720
25. Haley, Aldrich (1983) *Isoseismal/Geological Conditions Maps for Eastern Massachusetts*. Unpublished report to the Massachusetts Civil Defense Agency (now the Massachusetts Emergency Management Agency), Framingham, MA
26. Trocha P (2013) *Characterization of structural properties and dynamic behavior using distributed accelerometer networks and numerical modeling*. PhD Dissertation, Massachusetts Institute of Technology, Cambridge, MA

Experimental Verification of Inelastic Energy Demand Spectrum Using SDOF Steel Specimens on Shaking Table



Hümeýra Börekçi, Cem Yalçın, and Ercan Yüksel

1 Introduction

A total of 28 experimental tests were performed with hollow structural steel cross-sectional column specimens representing single degree of freedom (SDOF) system models on a shaking table. Actual scaled 1986 San Salvador earthquake ground motion data was used to excite the SDOF models. The main aim was to validate the existing energy demand spectra since shake table experimental research with varying damping ratios in nonlinear range of SDOF systems is missing in the literature. Also, developed energy demand spectra by other researchers need to be verified experimentally, especially with varying damping ratios. Two methods were used to determine damping ratio of the system. The first one was the logarithmic decrement which uses free vibration after the excitation is completed, and the second method was Chopra's [1] method which uses the hysteresis behavior during simulated earthquake excitation. Finally, Gullu's [2] proposed energy spectra, with mass-normalized energy versus natural period, corresponding to SDOF system's appropriate damping ratio were plotted, and experimentally obtained data was compared with these spectra.

H. Börekçi (✉) · C. Yalçın
Department of Civil Engineering, Bogazici University, Istanbul, Turkey
e-mail: humeýra.borekci@boun.edu.tr; yalcince@boun.edu.tr

E. Yüksel
Department of Civil Engineering, Istanbul Technical University, Istanbul, Turkey
e-mail: yukselerc@itu.edu.tr

2 Methodology

Two methods, logarithmic decrement and Chopra’s [1] method, were used to calculate the damping ratios of the specimens.

Responses of SDOF system that is subjected to ground motion are used to calculate the energy terms. A typical SDOF system that is subjected to ground motion $\ddot{u}_g(t)$ is illustrated in Fig. 1.

In this research, relative energy equation was developed from the general equation of motion since responses of SDOF system are relative to the movement of the shake table experimental setup. The energy-balance equation, which is obtained by integrating the equation of motion with the system’s incremental displacement response over the entire duration of the motion, used in this study is:

$$\int m\ddot{u}du + \int c\dot{u}du + \int f_s du = -\int m\ddot{u}_g du \tag{1}$$

where parameters m is the mass, c is the damping, and f_s is the spring force and u , \dot{u} , and \ddot{u} are the varying responses of the SDOF system as a function of duration of ground motion.

Multiplying each term of Eq. (1) by dt/dt yields:

$$\int m\ddot{u}du \frac{dt}{dt} + \int c\dot{u}du \frac{dt}{dt} + \int f_s du \frac{dt}{dt} = -\int m\ddot{u}_g du \frac{dt}{dt} \tag{2}$$

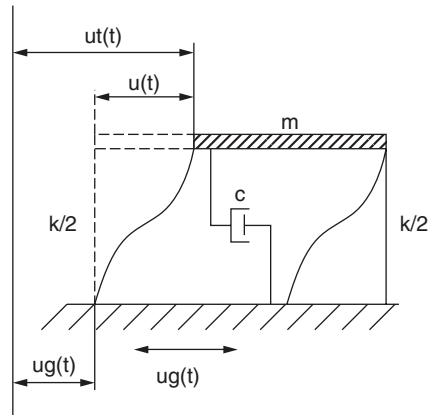
Further simplifying Eq. (2) yields:

$$\int m\ddot{u}\dot{u}dt + \int c\dot{u}\dot{u}dt + \int f_s \dot{u}dt = -\int m\ddot{u}_g \dot{u}dt \tag{3}$$

Therefore, the energy terms could be expressed as the following:

- Kinetic energy, E_k :

Fig. 1 SDOF systems that are subjected to ground motion



$$E_k = \int m\ddot{u}\dot{u}dt = \int m\dot{u}d\dot{u} = \frac{m\dot{u}^2}{2} \text{ (constant)} \tag{4}$$

- Damping energy, E_d :

$$E_d = \int c\dot{u}\dot{u}dt = c \int \dot{u}^2 dt \tag{5}$$

- Absorbed energy, E_a , is defined as the combination of strain energy (E_s) and plastic energy (E_p):

$$E_a = \int f_s \dot{u} dt \tag{6}$$

$$E_s = \frac{f_s^2}{2k} \text{ (constant)} \tag{7}$$

where k is the initial stiffness of the SDOF system.

- Input energy, E_I :

$$E_I = -m \int \ddot{u}_g \dot{u} dt = E_k + E_d + E_a \tag{8}$$

- Also, plastic energy (E_p) could be calculated from the following expression:

$$E_p = E_I - (E_k + E_d + E_s) \tag{9}$$

3 Experimental Tests

In this research, shaking table experimental study was carried out on 3 hollow structural steel cross-sectional column specimens representing single degree of freedom (SDOF) system. Actual scaled 1986 San Salvador earthquake ground motion data was used to excite the SDOF models. Specimens were excited beyond their elastic limits in order to determine responses in the inelastic range.

3.1 Experimental Study Setup and Process and Instrumentation

Experimental tests were conducted in order to validate the inelastic input energy spectrum with varying damping ratios. Figure 2 shows the test setup, instrumentation, and cross section of a typical specimen.

Two accelerometers and four strain gauges were mounted on the specimen. One of the accelerometer was installed under the mass plate while the other one on the

shake table. Two of the strain gauges were placed in front of the column, and two of them were placed at back of the column.

Also, video recording thorough testing using GoPro camera was done in order to determine responses via image processing methodology that was developed by Yardimci [3].

First data source was obtained through strain gauge readings where relative displacement responses of the specimens were calculated using basic structural mechanics theory. Accelerometer measurements were used as a second data source. Here, using mathematical integral operations, and difference between specimen and table accelerations, relative velocity and relative displacements were calculated. As a third data source, image processing software which was developed by Yardimci [3] was used. The displacement responses were directly obtained from image processing algorithm. All measurements that were obtained from these data sources were assessed and then selected for the rest of this study.

3.2 Normalized Input Energy Spectrum [2]

In 2018, Gullu [2] proposed an improved input energy spectrum verified by the shake table tests. Since this verification was carried out with constant damping ratio, varying damping ratios were tried in this study to further check the validity of Gullu’s proposed equation. The relationship between normalized input energy and period is composed of three parts, as illustrated in Fig. 3. Fourier spectrum or undamped velocity spectrum is used to determine the corner period (T_c). Ordinates

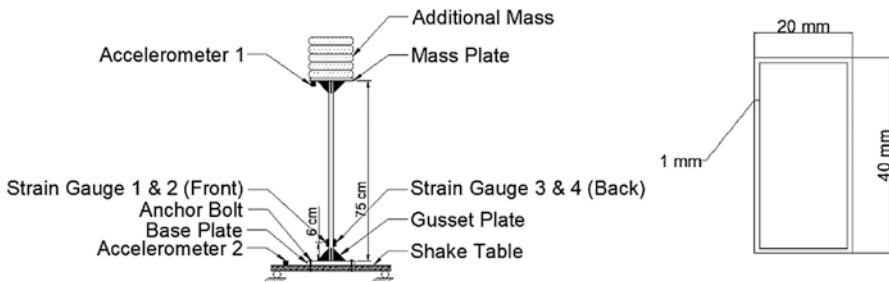
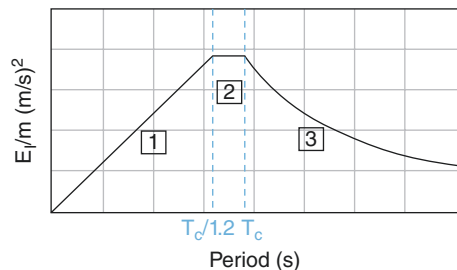


Fig. 2 Sketch of the shake table and cross section of the specimen

Fig. 3 Gullu’s mass-normalized input energy spectrum [2]



of the plateau (Sect. 2) are calculated from Eq. (10). Section 3 is the descending branch, which is created by the term of B and k parameters that were originated from Dindar [4].

$$\frac{E_I}{m} = B \sqrt{SV(\zeta)_{\max} SA(\zeta)_{@SV_{\max}} T_c I_e t_e} \left(\frac{T_c}{T}\right)^k \tag{10}$$

4 Results and Discussion

Input energy spectra were plotted for all experiments with varying damping ratios calculated from two different methods. Mass-normalized input energies were compared with these spectra plots. Figures 4, 5, and 6 show Gullu’s input energy spectra, and data plotted as dots on the graphs represent mass-normalized input energies that were obtained from experiments.

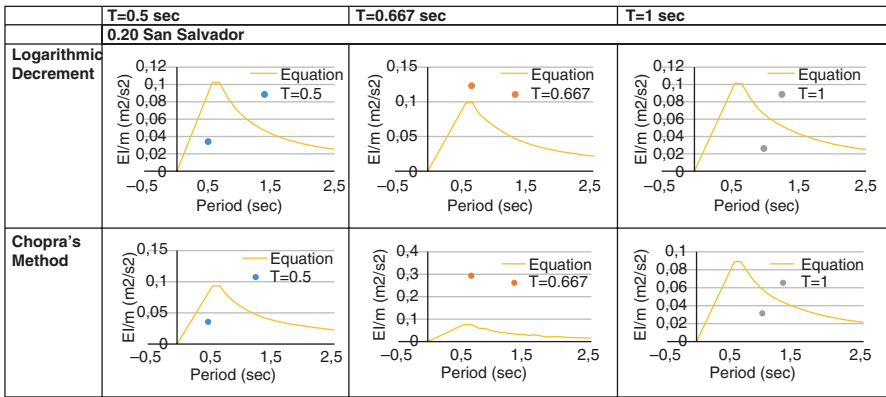


Fig. 4 0.20 San Salvador input energy spectrum

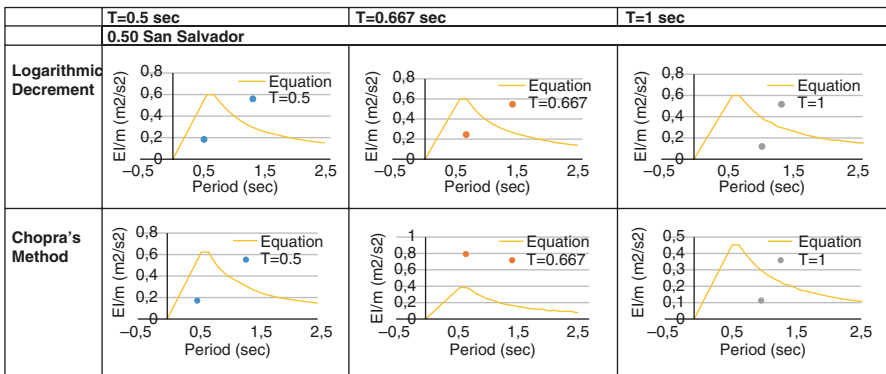


Fig. 5 0.50 San Salvador input energy spectrum

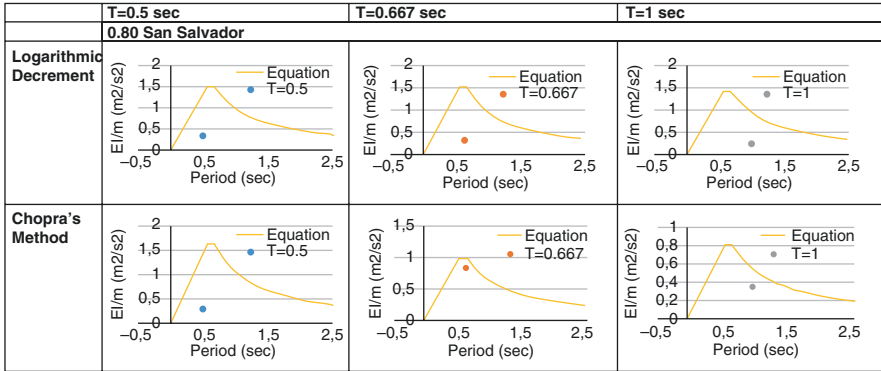


Fig. 6 0.80 San Salvador input energy spectrum

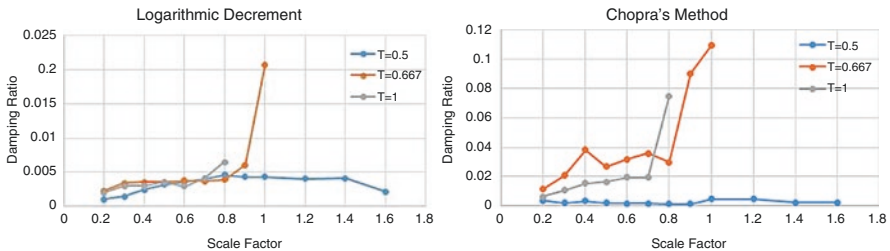


Fig. 7 Damping ratios obtained from logarithmic decrement and Chopra's methods for varying San Salvador earthquake scaling factors

Although the damping ratios calculated from Chopra's method are much greater than those damping ratios calculated from logarithmic decrement method, the trends were similar in both methods (Fig. 7). Especially at $T = 0.667$ s, the damping ratio increased dramatically, and thus, mass-normalized input energy values in all cases also increased. As far as Gullu's spectra is considered, increase in damping ratio lowered the input energy limits because it decreased the maximum spectral velocity and spectral acceleration. Therefore, input energy corresponding to corner period decreased. Also, trends in all graphs obtained from experimental data were consistent for different intensities. For periods 0.5 s and 1.0 s, mass-normalized input energies from experimental data were below the limits. Yet, for period 0.667 s, mass-normalized input energies from experimental data reached the peaks successfully, and in some cases, it exceeded the peaks far too much.

5 Conclusion

As a result of these experiments, conclusions could be drawn as the following:

- Some differences were observed between logarithmic decrement and Chopra's methods in the determination of damping ratios while their trends were similar. As the hysteretic behavior became closer to linear range, it was observed that the logarithmic decrement method somewhat yielded better results.
- Most spectral values obtained experimentally verified Gullu's spectrum. The trend of the obtained input energy data was consistent with Gullu's energy spectrum. Near the plateau region, mass-normalized input energy values were higher than those obtained around low and high period regions of the spectrum.
- It is noteworthy to mention that the data source obtained from vision-based measurements gave better results. Using Savitzky-Golay filter, derivation of displacements to obtain velocity and acceleration responses were more accurate than those obtained from accelerometer and strain gauge readings.

Acknowledgments The financial support for this project has been provided by Bogazici University Research Fund grant number BAP11164.

References

1. Chopra AK (1995) Dynamics of structures: theory and applications to earthquake engineering. Prentice Hall, Englewood Cliffs, NJ
2. Gullu A, Yüksel E, Yalçın C, Anıl Dindar A, Özkaynak H, Büyüköztürk O (2018) An improved input energy spectrum verified by the shake table tests. *Earthquake Eng Struct Dyn*:1–19
3. Yardımcı F (2018) Application of image-based sensing methods in shake table experiments. MSc thesis, Department of Civil Engineering, Bogazici University, Istanbul, Turkey
4. Dindar AA (2009) Energy-based earthquake response analysis and design of reinforced concrete sdof columns. PhD thesis, Department of Civil Engineering, Bogazici University, Istanbul, Turkey

Image-Based Dynamic Response Measurement of a Full-Scale, Multistory Structure Tested on a Shake Table



Ferit Yardımcı, Cem Yalçın, and Ercan Yüksel

1 Introduction

Most common conventional measurement devices used in shake table experimental dynamic testing of structures are accelerometers, LVDTs, LPTs, or lasermeters. As an alternative, image-based methods could be used in these experiments. These methods have some advantages over the conventional devices. High-precision, and thus expensive, mechanical devices such as LVDT and LPT affect the stiffness and damping values of specimens especially when the scale is small. Accelerometers affect the dynamic characteristics of small-scale test specimens due to its own weight. Lasermeters on the other hand are quite effective, but they need to be calibrated from time to time like other devices stated above. Contactless measurement with a video record does not create any of these mentioned problems. Above all, the tedious work of implementing all these measurement devices, including cumbersome cabling work, and collecting the response data with high-speed data acquisition system is not necessary with video records. It is quite effortless to acquire the data by a video record and process it.

The topic of image-based measurement gained popularity in recent years. The study conducted by Feng et al. [1] presented a video-based sensing method that measures the displacement. A template matching algorithm that increases the accuracy in sub-pixel level was used in this study. They conducted various tests both in laboratory and on field and used both natural (bolts and joints) and artificial targets (unique templates). They obtained successful results in both laboratory and field tests. The study conducted by Chen et al. [2] included a series of experiments in

F. Yardımcı (✉) · C. Yalçın
Department of Civil Engineering, Bogazici University, Istanbul, Turkey
e-mail: ferit.yardimci@boun.edu.tr; yalcince@boun.edu.tr

E. Yüksel
Department of Civil Engineering, Istanbul Technical University, Istanbul, Turkey
e-mail: yukselerc@itu.edu.tr

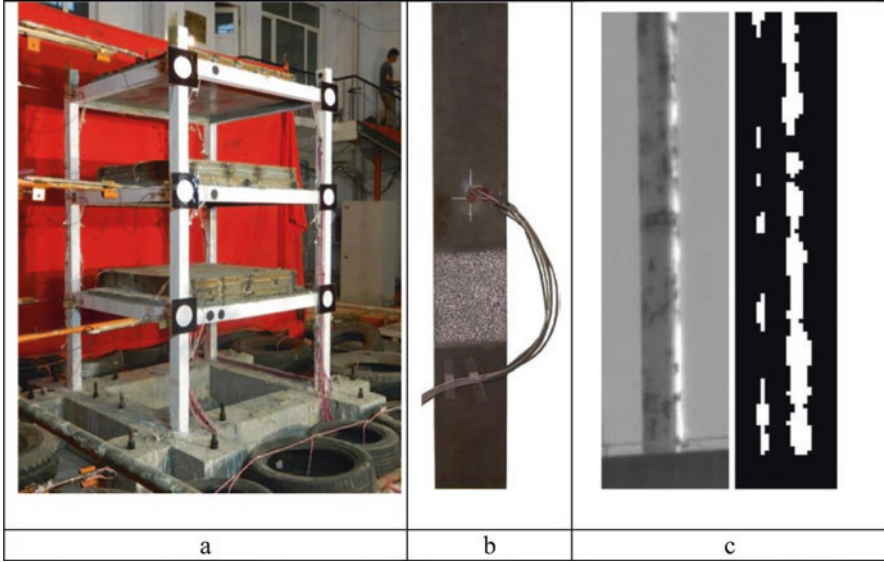


Fig. 1 Examples of studies with different tracking methods: (a) point-based, (b) DIC, (c) targetless method

which they performed the modal analysis and detected the mode shapes of various structures from video records by using targetless methods. They utilized a recently developed motion magnification technique that detects various vibration modes under dynamic loads. The comparison of results with the data received from accelerometers and laser vibrometers showed that the video-based measurements were in good correlation with those measured by conventional methods.

Main methods to obtain measurement of structural responses with video cameras could be divided into three categories [3]. These categories are point-based methods, digital image correlation (DIC) methods, and targetless methods. Figure 1 shows various studies that utilized these methods. Li et al. [4] (Fig. 1a) utilized a point-based method. Hoult et al. [5] (Fig. 1b) used DIC, and Chen et al. [2] (Fig. 1c) used targetless methods.

The main objective of this study is to extract the dynamic responses of full-scale building specimen tested on a shaking table [6] and its comparison with the acceleration results.

2 Methodology

To extract motion at each floor level, Kanade-Lucas-Tomasi (KLT) object tracking algorithm was utilized. This tracking method was originally developed by Tomasi and Kanade [7]. This powerful computer vision technique is quite efficient to

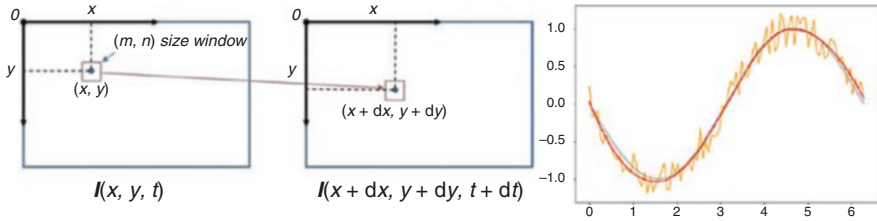


Fig. 2 (a) KLT tracking algorithm. (b) Results of Savitzky-Golay filtering

estimate the exact position of the object. Given that the background and the color or geometry of the object are, respectively, stable, the algorithm provides quite precise results. In general, tracking algorithms utilize predefined features in images. One of the greatest advantages of the KLT tracker algorithm is that it presents its own feature detection method that is compatible with the tracking algorithm of itself. Generally, these are unique features that present a contrast in the video frame. Derivation of position data with respect to time produced velocity and acceleration responses. In order to take the derivative of a discrete data, Savitzky-Golay [8] (SG) derivation operators were utilized. Position data obtained from a video have, respectively, low sampling rate compared to the conventional measurement devices. In addition, these discrete data contain noise, which leads to erroneous values while taking the derivations unless a proper operator is used. This SG filter was specifically developed to deal with such noisy data. After the derivation was complete, scaling data with a known distance provided the transformation of unit from pixel to actual responses. Figure 2 shows the search of KLT tracker in consecutive frames and effects of the SG filter.

3 Experimental Setup

The tests of this full-scale building were conducted at the University of California San Diego in 2007. It was tested on large high-performance outdoor shake table. Video records and accelerometer data are open to public.

Test building had seven floors with floor heights of 2.54 m and 4.29 m by 8.13 m of floor dimensions. Shake table applied a seismic ground motion of Northridge earthquake (1994). Since the video record was not taken for measurement purposes, optical targets that would ease the tracking task were absent. Instead, physical features such as edges or connections were utilized to virtually label in order to track each floor’s movement. Details of this project were presented in the study conducted by Waugh and Sritharan [9]. Figure 3 (<http://nheri.ucsd.edu/projects/2006-seven-story/>) shows the test building and dimensions of the test structure.

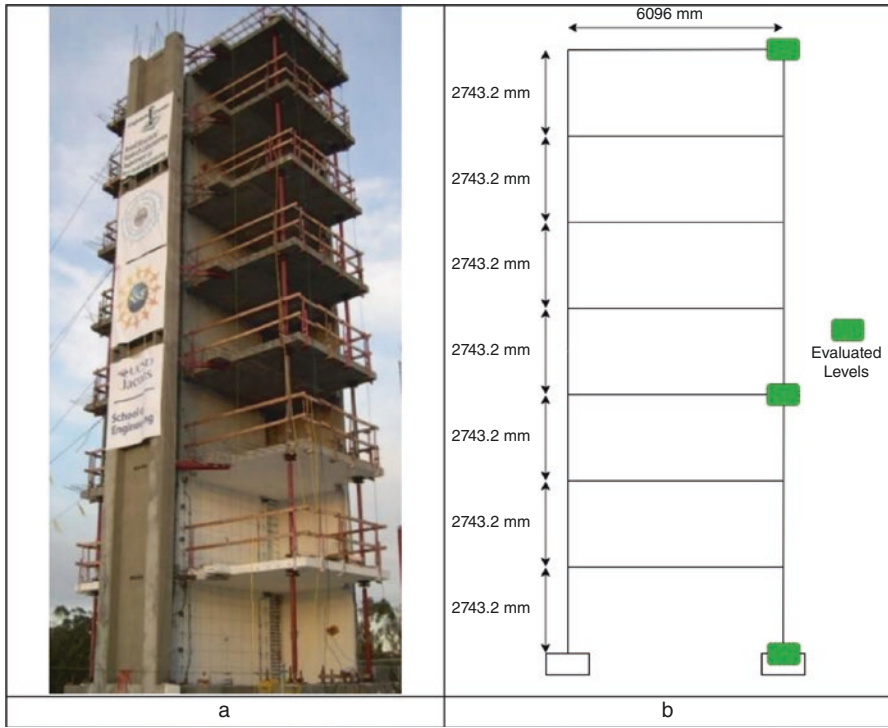


Fig. 3 (a) View of the full-scale specimen from side and (b) dimensions of the full-scale specimen

4 Results and Discussion

Even if it was not intended to provide a measurement option with this video, record provided a useful data to track the motion of each floor. Obtained data contained all responses. Acceleration data was compared with the data obtained by accelerometers at every level. Results of the KLT tracking and their comparison at ground, third, and seventh floor are presented in below figures from Figs. 4, 5, and 6.

The matching results between acceleration values obtained from the video record and given accelerometer data were quite accurate. However, some mismatches at peaks were observed and considered as a crucial problem. Peak accelerations and displacements during an earthquake are quite essential to assess structural condition after the earthquake. These mismatches were considered as result of difference between sampling rates.

These dissimilarities were relatively small on top floors, but it increased considerably as the floor level decreased. Two different reasons were considered behind this situation. First one is the responses with lower magnitude at the bottom of the test structure. As the motion increases, it is easier for algorithm to track. The second is the position of the recorder, which was closer to the top floors and received the motion of them in direct angle. This leads to better results in these top floors and worse in lower levels.

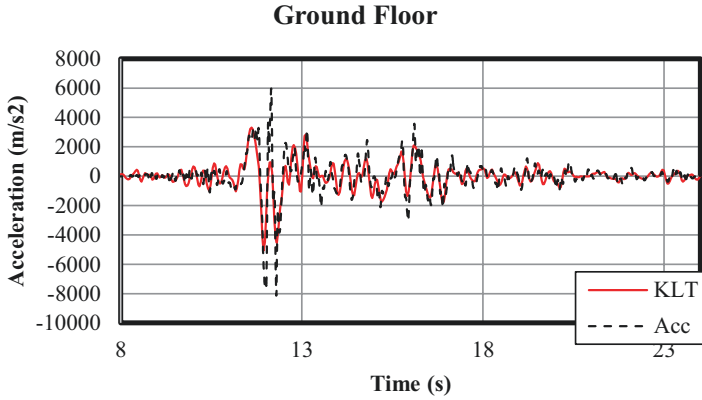


Fig. 4 Ground acceleration comparison graph of accelerometer (Acc) and video record 640p, 30 fps EQ Record: Northridge

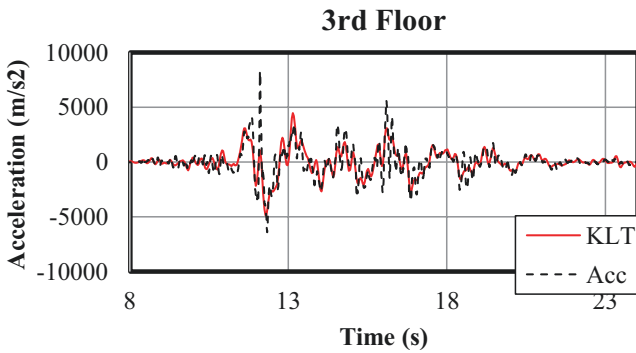


Fig. 5 Third floor acceleration comparison graph of accelerometer (Acc) and video record 640p, 30 fps EQ Record: Northridge

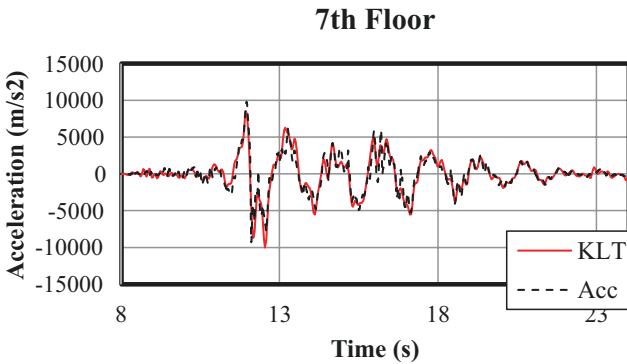


Fig. 6 Seventh floor acceleration comparison graph of accelerometer (Acc) and video record 640p, 30 fps EQ Record: Northridge

5 Conclusion

In this study, a video record of a full-scale building testing on a large shake table was processed to obtain responses under 1994 Northridge earthquake ground motion data. One of the aims of this study was to assess responses under ground motion from video records. Results showed that even if the video was not recorded for measurement purposes, it was able to provide significant information. The relative acceleration response of the upper floors (third, seventh) had matching results with the accelerometer data. However, comparison of lower floor accelerations showed some mismatches since the camera at lower stories was positioned in an oblique way.

As an optical tracker, KLT method yielded reliable results that generally match quite well with the accelerometer data. Even if there was no optical target, it was able to extract the displacements of each story.

A proper comparison between conventional measurement devices and the image-based methods should be considered based on the same sampling rate. Actual comparison of these two sources is not possible unless such sampling characteristics are equal. Significant portion of the mismatches were considered due to the difference in sampling rate. Considering the developments in the visual technology since the date of experimental record (2007), such an experiment would yield far better results today.

Acknowledgments The financial support for this project has been provided by Bogazici University Research Fund grant number BAP11164.

References

1. Feng D, Feng M, Ozer E, Fukuda Y (2015) A Vision-Based Sensor for Noncontact Structural Displacement Measurement. *Sensors* 15(7):16557–16575
2. Chen JG, Davis A, Wadhwa N, Durand F, Freeman WT, Büyüköztürk O (2017) Video Camera-Based Vibration Measurement for Civil Infrastructure Applications. *Journal of Infrastructure Systems* 23(3)
3. Baqersad J, Poozesh P, Niezrecki C, Avitabile P (2017) Photogrammetry and optical methods in structural dynamics—a review. *Mech Syst Signal Process* 86:17–34. <https://doi.org/10.1016/j.ymssp.2016.02.011>
4. Li S, Zuo Z, Zhai C, Xu S, Xie L (2016) Shaking table test on the collapse process of a three-story reinforced concrete frame structure. *Eng Struct* 118:156–166. <https://doi.org/10.1016/j.engstruct.2016.03.032>
5. Hoult NA, Andy Take W, Lee C, Dutton M (2013) Experimental accuracy of two dimensional strain measurements using digital image correlation. *Eng Struct* 46:718–726
6. UCSD (2007) Seismic response of a 7-story RC building. <http://nheri.ucsd.edu/projects/2006-seven-story/>

7. Tomasi C, Kanade T (1991) Detection and tracking of point features. Computer Science Department, Carnegie Mellon University, Pittsburgh
8. Savitzky A, Golay MJE (1964) Smoothing and differentiation of data by simplified least-squares procedures. *Anal Chem* 36:1627–1639
9. Waugh JD, Sritharan S (2010) Lessons learned from seismic analysis of a seven-story concrete test building. *J Earthq Eng* 14(3):448–469

Determination of Input Energy Profile in Structures Through Seismic Interferometry



Burak Horoz, Cem Yalçın, and Ercan Yüksel

1 Introduction

Earthquake is a random phenomenon, and thus, future occurrences cannot be exactly predicted. Historical knowledge helps in understanding the nature and occurrence time cycle. Therefore, procedures to evaluate the existing buildings and design methods have to be developed in order to overcome the effects of this phenomenon. Strength- and displacement-based analysis methods include a wide range of approaches from equivalent earthquake loading using static forces to response spectra and displacement-based with performance-based analyses. Although strength-based design is a practical method, the cumulative damage during earthquake is ignored since this approach considers only the maximum response, which is a great drawback of the procedure [1]. The significant features of an earthquake such as its duration, frequency content, and hysteretic behavior of the structures are not explicitly taken into consideration in these methods. In this study, energy-based design combined with seismic interferometry methodologies is utilized to evaluate the input energy at floor levels of the structures. The purpose of this study is to identify the amount of the input energy at floor levels, as well as its distribution among the structural members. Once the floor-wise input energy and its distribution among the members are determined, the next step would be the energy-based design and assessment of the structural members in regard to their energy absorption capacity and determining damage levels.

B. Horoz (✉) · C. Yalçın
Department of Civil Engineering, Bogazici University, Istanbul, Turkey
e-mail: burak.horoz@boun.edu.tr; yalcince@boun.edu.tr

E. Yüksel
Department of Civil Engineering, Istanbul Technical University, Istanbul, Turkey
e-mail: yukselerc@itu.edu.tr

1.1 *Energy-Based Design*

The energy-based methodology, which was initially brought up by Housner in the 1950s, includes all the features of the force- and displacement-based design methods, as well as accounts for duration, frequency content, and the hysteretic behavior of the structural members. The earthquake energy imposed on the structure is defined through its corresponding kinetic, damping, elastic, and plastic energy components, and since they are scalar quantities, addition of all these components would yield the input energy, which is the total energy demand in the structure caused by the earthquake. While earthquakes with different intensity, frequency, and duration characteristics may result in almost the same acceleration response spectra, each earthquake may result in different input energy demand imposed to the structure. Thus, design acceleration spectra used in current standards, especially in regard to permanent damage, could provide erroneous results. Input energy and contributions of energy components could be readily calculated with today's commercial and open source software such as SAP2000 and Perform3D. However, how the input energy and its components are distributed at layers of the structures is still a matter of debate.

1.2 *Seismic Interferometry*

The vibrations of a structure during an earthquake are caused by the propagation of seismic waves along the structure's height. Structural engineers tend to use vibration approaches to identify the response of structures imposed by earthquakes. Vibration methods (such as modal analysis) and wave-propagation methods are the tools of solution techniques. Wave-propagation methods are used mainly for structures that could be modeled as a continuous medium [2]. In this study, deconvolution interferometry was used to evaluate the response of models and experimental results by using impulse response functions (IRFs) at various floor levels. Another relevant study [3] focused on the deconvolution-based seismic interferometry and damage detection by keeping track of certain metrics, such as shear wave velocity, via various approaches.

IRFs are extracted using deconvolution-based interferometric approach. The reconstructed waves could be used to identify the structural parameters, such as shear wave travel velocities, modal frequencies, mode shapes, and intrinsic attenuation (damping) values. These waves could also be interpreted as the summation of the normal modes of the structure [4]. The IRFs could be extracted by deconvolving the recorded acceleration time series of a structure with respect to the ground motion. The deconvolution operation could be formulated as shown in the following Eq. (1).

$$S(z, t) = F^{-1} \left\{ \frac{y(z, \omega) y^*(z_{\text{ref}}, \omega)}{|y^*(z_{\text{ref}}, \omega)|^2 + \varepsilon} \right\} \quad (1)$$

where $S(z, t)$ is the IRF at z ; $y(z, \omega)$ is the response measurement at z in the frequency domain; $|y^*(z_{\text{ref}}, \omega)|^2$ is the power spectrum of z_{ref} ; ω is angular frequency; t is time; y_{ref} is the reference level of the building; $*$ denotes the complex conjugate; ε is a stabilizing parameter; and F^{-1} denotes the inverse Fourier transform [5].

In this study, the distribution of Input Energy between layers (floors) of the structure by using of seismic interferometry methodology was investigated.

2 Methodology

Input energy formulation could be directly related with the responses of the structures.

Akiyama [6] derived the energy formulations by multiplying the equation of motion with relative displacement as presented in Eq. (2):

$$\int m\ddot{u}(t)du + \int c\dot{u}(t)du + \int f_s(t)du = - \int m\ddot{u}_g(t)du \quad (2)$$

A two-dimensional ten-story structure was modeled in SAP2000 structural analysis software in order to determine the responses of the structure using ground excitation. A Matlab code was developed to evaluate energy-based formulations [7] and also deconvolution-based seismic interferometry mathematical operations [4]. After obtaining the acceleration-time history response of the layers of the structure, deconvolution interferometry is used to obtain IRFs for each layer with respect to reference story. Then, shear wave propagation was evaluated by using arrival picking method (APM). In the APM, the wave velocity is determined by fitting a linear line to the wave travel times versus height of the structure. The slope of the fitted line gives the shear wave velocity along the structure. The distribution of input energy along the structural layers are then assessed according to the IRFs of the layers. These IRFs were utilized in order to obtain response of the layers of the structures while using reverse operations which are based on convolution theorem, as shown in Eq. (3):

$$y(z, t) = y(z_{\text{ref}}, t) * S(z, t) = \int_0^t y(z_{\text{ref}}, \tau) S(z, t - \tau) d\tau \quad (3)$$

Akiyama's formula (Eq. 2) and convolution theorem were combined to compute the mass-normalized input energy at n th floor shown in the following equations:

$$n\text{th floor acceleration } (I^n : \text{IRF}) : \ddot{u}_g * I^n \quad (4)$$

$$n\text{th floor velocity} : \dot{u}(t) = \int_0^t \ddot{u}_g * I^n . dt \quad (5)$$

Mass-normalized input energy:

$$\frac{E_I}{m} = -\int_0^t \ddot{u}_g \dot{u} dt \quad (6)$$

For n th floor, mass-normalized input energy:

$$\frac{E_I}{m^n} = -\int \int_0^t \ddot{u}_g \cdot \dot{u}_g * I^n \cdot dt dt \quad (7)$$

3 Results and Discussion

In this study, the structural identification on multi-degree of freedom (MDOF) experiment results which were conducted by Gullu [8] and full-scale seven-story reinforced concrete building experiments at the University of California San Diego Engineering Simulations (UCSD-NEES) shake table were evaluated. Finite element models (FEM) were generated in SAP2000 and PERFORM 3D software, and dynamic response time history analysis of the structures was performed. The response of the MDOF structures under dynamic loading was evaluated and compared with the developed FEM. Acceleration, velocity, and displacement responses were then obtained to calculate the energy components. These acceleration data was then used in the seismic interferometry analysis to acquire the shear wave velocity profile and IRFs of the layers of the structure. Throughout this study, Sylmar (360°) record of the 1994 Northridge earthquake (PGA:0.91g) dataset which is called EQ4 in UCSD experiments from the whole test data was used to obtain the IRFs and shear wave velocities. Deconvolution seismic interferometry methodology was used to estimate the responses of these test results, and IRFs were created by using this methodology to find the shear wave velocity profile for these experiments. IRFs with respect to ground and top level of the UCSD full story building are presented in Figs. 1 and 2. Shear wave propagation could be clearly seen in these figures. APM was utilized to determine shear wave velocity as shown in Figs. 1 and 2. Fitting linear line obtained with the help of IRFs at the different floor levels is shown in Fig. 3 to obtain shear wave velocities (Table 1) along the structure for top and ground reference in the structure.

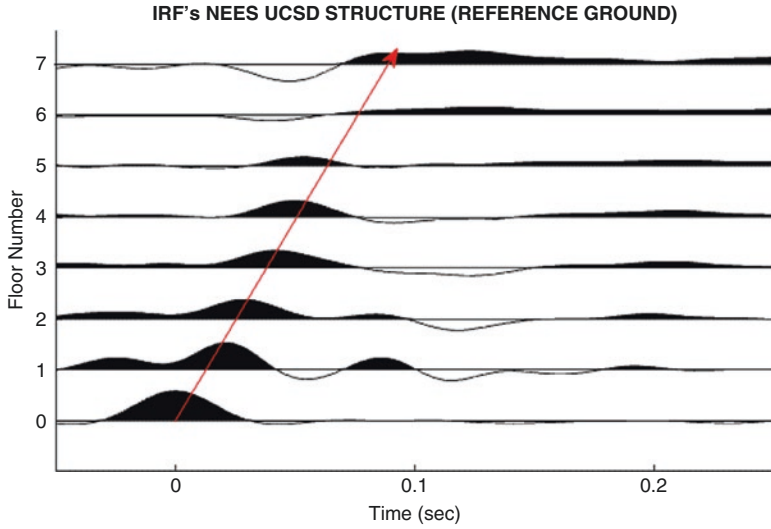


Fig. 1 IRF NEES UCSD structure (reference ground)

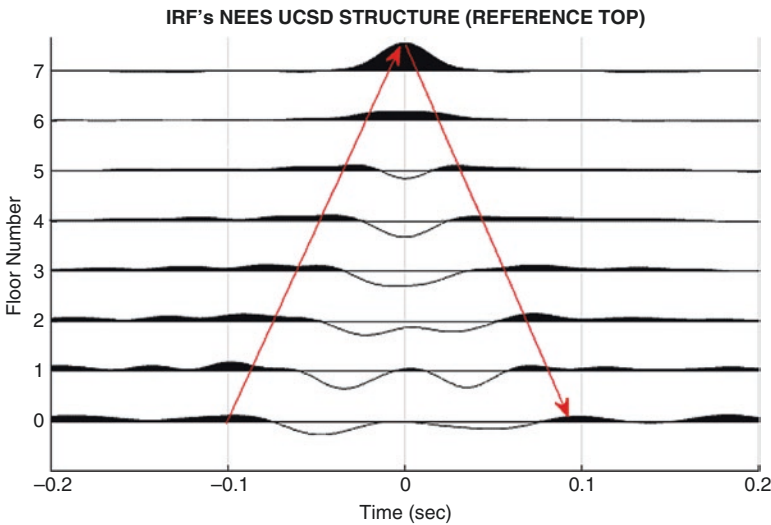


Fig. 2 IRF NEES UCSD structure (reference top)

Responses which were obtained by test results and convolution process, which utilized IRFs for stories, were compared to check the results of the developed Matlab code. In Fig. 4, the acceleration responses of the fifth floor of the UCSD full-scale test specimens obtained by the accelerometers and by using the convolution methodology were compared.

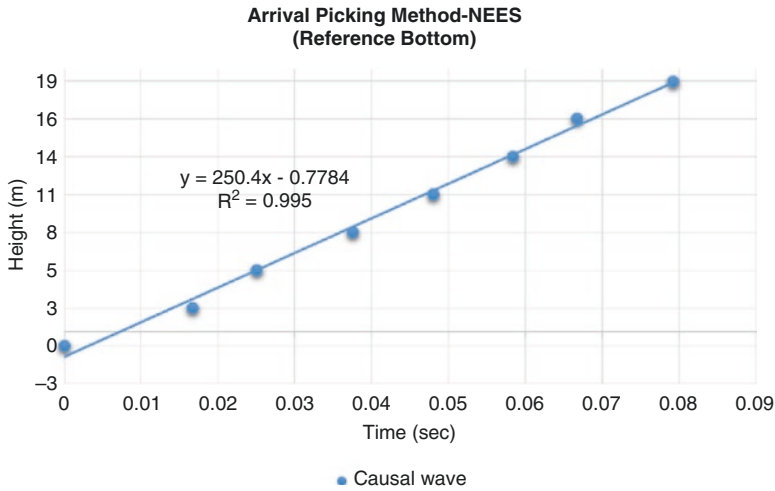


Fig. 3 Least square fitting line to obtain shear wave velocity

Table 1 Shear wave velocity for NEES UCSD structure

Velocity (m/s) (reference top-causal wave)	239.37
Velocity (m/s) (reference top-acausal wave)	237.32
Velocity (m/s) (reference bottom)	250.4

Input energy distribution along the height of the building is proposed utilizing IRFs, which are calculated using seismic interferometry methodology. Mass-normalized input energy at the floor levels for MDOF tests [8] was estimated by using Eq. (7) and shown in Fig. 5. The mass-normalized total input energy of the structure was calculated by adding up the different mass-normalized input energies at each floor level. The total input energy was also obtained from PERFORM 3D model. Comparison of mass-normalized total input energies on the structure is shown in Fig. 6.

Based on the findings, it is anticipated to advance to the next level of the energy-based design and assessment approach, which is a promising and relatively new topic. For different earthquake records, the IRFs, extent of the plasticity, and the ductility of the buildings could be estimated based on the elastic and plastic input energy at different floor levels. Moreover, the ductility-based force reduction factor (also known as the *R* factor), which is one of the most ambiguous issues in seismic codes, could be estimated in a more reliable and realistic way by employing the energy approach.

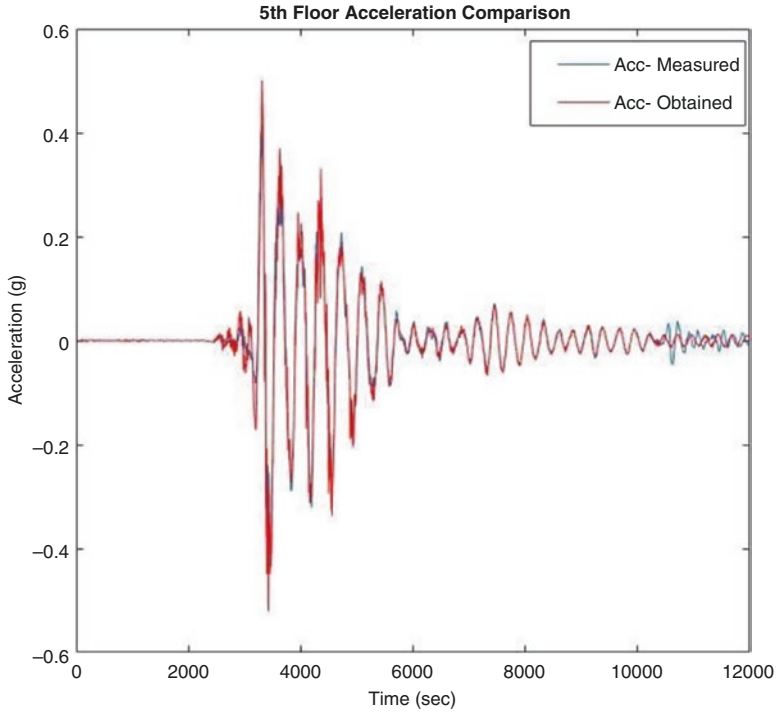


Fig. 4 Acceleration response comparison of the fifth floor of NEES-UCSD

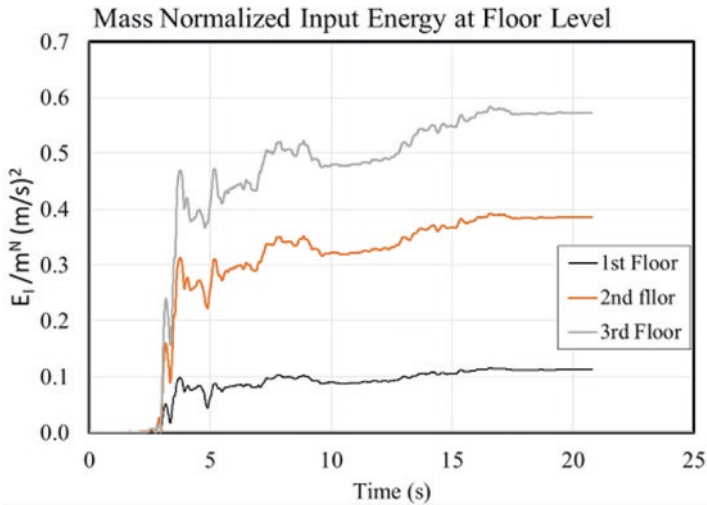


Fig. 5 Mass-normalized input energy at floor levels

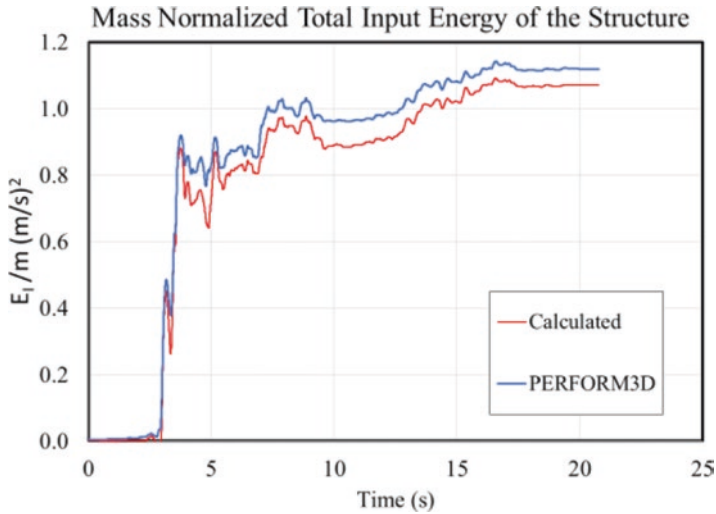


Fig. 6 Mass-normalized total input energy of the structure

4 Conclusion

Structures are designed to resist the earthquake demands. Energy-based design methodology could be considered as more favorable among other current design methodologies since it includes duration and frequency of the ground motion. When this is coupled with seismic interferometry methodology, more deterministic results could be obtained, and thus, damage levels after the earthquakes could easily be monitored and located.

The advantage of the seismic interferometry methodology is that pure dynamic characteristics, which are the effects of the soil-structure interaction and the source of excitation, could be eliminated with the deconvolution mathematical operation. As a result, shear wave velocity could be extracted from IRFs.

Input energy along the height of the building at floor levels was estimated using IRFs of the structure. Developed Matlab code was verified against other commercial software in terms of finding input energy components. Further, with this code, seismic interferometry operations were carried out, and shear wave velocity of the building was found and verified by NEES-UCSD and [8] experimental work. A good agreement with both commercial software and experimental study was obtained.

References

1. Chopra AK (1995) Dynamics of structures. Prentice Hall of India, New Delhi
2. Todorovska MI, Lee VW (1989) Seismic waves in buildings with shear walls or central core. *J Eng Mech ASCE* 115(12):2669–2686
3. Uzun M (2018) Learning structures: fusing deconvolution-based seismic interferometry with Bayesian inference for structural health assessment. Thesis dissertation, Massachusetts Institute of Technology
4. Snieder R, Şafak E (2006) Extracting the building response using seismic interferometry: theory and application to the Millikan Library in Pasadena, California. *Bull Seismol Soc Am* 96(2):586–598
5. Sun H, Mordret A, Prieto GA, Toksöz MN, Büyüköztürk O (2017) Bayesian characterization of buildings using seismic interferometry on ambient vibrations. *Mech Syst Signal Process* 15:468–486
6. Akiyama H (1985) Earthquake-resistant limit-state design for buildings. University of Tokyo Press, Tokyo
7. Dindar AA, Yalcin C, Yuksel E, Ozkaynak H, Buyukozturk O (2015) Development of earthquake energy demand spectra. *Earthquake Spectra* 31(3):1667–1689
8. Güllü A, Yüksel E, Yalçın C, Anıl Dindar A, Özkaynak H, Büyüköztürk O (2018) An improved input energy spectrum verified by the shake table tests. *Earthq Eng Struct Dyn*:1–19
9. Wapenaar K, Draganov D, Snieder R, Campman X, Verdel A (2010) Tutorial on seismic interferometry: part 1—basic principles and applications. *Geophysics* 75(5):75–195
10. Wapenaar K, Slob E, Snieder R, Curtis A (2010) Tutorial on seismic interferometry: part 2—underlying theory and new advances. *Geophysics* 75(5):75211–75227

Structural Health Monitoring System for Al-Hamra Tower in Kuwait City

Jamal Al-Qazweeni, Jafarali Parol, Hasan A. Kamal, Abdullah Al-Enezi, Ammar Bin-Nakhi, Hao Sun, and Oral Büyüköztürk

1 Introduction

Structural health monitoring (SHM) is a process of continuous condition monitoring of buildings and other infrastructures [1–3]. SHM could be employed to identify the damages occurred during and after an earthquake, due to any other natural hazards, due to aging, or due to harsh environmental conditions in bridges and tall buildings. The main advantage of SHM with real-time monitoring is the ability to assess the damage during or immediately after any catastrophic events. Structural damage will result in changes in the structural stiffness and damping. The stiffness, mass, and damping of a structural system are directly related to the natural frequencies, mode shapes, and modal damping of the structure. Shifts in natural frequency or changes in mode shapes or changes in modal damping are some indicators of damages in the structure [4–8]. These changes could be detected through SHM and vibration measurements. A good instrumentation design is vital for developing a robust SHM system.

The objective of instrumentation design task in the present work was to develop a layout and location of sensors for the structural health monitoring system for the Al-Hamra tower in Kuwait. The system aims to monitor the dynamic behavior of

J. Al-Qazweeni (✉) · J. Parol · H. A. Kamal · A. Al-Enezi
Kuwait Institute for Scientific Research, Kuwait City, Kuwait
e-mail: jqazweni@kisir.edu.kw

A. Bin-Nakhi
Kuwait University, Kuwait City, Kuwait

H. Sun
Northeastern University, Boston, MA, USA

O. Büyüköztürk
Department of Civil and Environmental Engineering, Massachusetts Institute of Technology,
Cambridge, MA, USA

the tower continuously in real time and detect and locate any changes in its structural damage. Al-Hamra tower is an 80-story, 412 m-tall reinforced-concrete structure with a unique geometry (Fig. 1). As it can be seen in the picture, uniqueness of the geometry comes from the fact that the geometry is formed by cutting a simple prismatic volume with a spiraling slice. The two cut surfaces are formed by hyperbolic-paraboloid reinforced-concrete walls that extend the full height of the building. The key effect of such a geometry is that the vertical loads create torsional moments in the building. The structural load-resisting system consists of a central shear-wall core and a perimeter moment-resisting frame with the spiraling walls of the cut. For such a building to develop, a robust instrumentation design is a challenging task.

In the context of the present project, development of the SHM system for the tower involves the following tasks:

- Design of the monitoring system (types and locations of sensors).
- Technical specifications for the instruments.
- Supervision and inspection of the installation.
- Development of a real-time data processing.
- Analysis, interpretation, and display software.
- Design and development of a structural safety warning system.
- Long-term maintenance and data analysis procedures.

Fig. 1 Al-Hamra tower in Kuwait City



However, in this section, details of the first task are presented.

2 Research Methodologies

Effective instrumentation of tall buildings involves the installation of accelerometers or other sensors at key locations throughout a structure. The number and location of sensors are very important to extract maximum information regarding the building behavior. Optimal locations in a building are obtained based on the building's geometrical and structural characteristics. Another very important factor that determines the locations is the accessibility of the chosen locations for the instrumentation.

For the Al-Hamra tower, due to its geometric shape, torsional mode is one of the most important vibration modes of the tower. The tower geometry is built in such a way that section gets twisted along the height of the building. Due to the complex geometric shape of the tower, redundant channel needs to be placed more than what is just minimum required (three) at each floor. Change of stiffness along the height of the building was an important parameter for selecting floors for instrumentation. The Al-Hamra tower was already occupied by tenants, which was another parameter considered for the instrumentation location.

Optimal sensor placement algorithm [9] has also been used to verify the instrumentation design. In the present case, the sensor layout was based on the structural and architectural drawings, visual inspection, as well as the available analytical studies already done to simulate its dynamic behavior using the finite element method. The sensor locations were chosen to identify the building's main vibration modes and their variations along the height, including two horizontal translations, rotations with respect to vertical axis, rocking motions with respect to foundation, and soil-structure interaction.

Accelerometers, tiltmeters, high-frequency GPS displacement sensors, wind sensors, and temperature sensors were used in the proposed SHM system for the Al-Hamra tower. The sampling rate for the accelerometers will be minimum 500 Hz. The data from all the sensors will be recorded synchronously (or, if recorded separately, will include a GPS time signal to allow synchronization during processing) and have a time precision of one millisecond or less. The recorders will be broadband with minimum of 24-bit resolution.

The data will be stored in a server inside the building and simultaneously transmitted to a data center at a specified location (e.g., to a server in KISR) in real time. A workstation at the data center will perform the data processing, analysis, and display operations. A two-way high-speed communication between the data center and the building will be established. In case of a power or communication failure, the recorders will be able to operate and store the data for three full days (72 h).

3 Results and Discussions

Selected floors for the instrumentations were shown in Table 1 and Fig. 2.

It can be seen from Table 1 that a total of 56 accelerometer channels and 14 tiltmeter channels and 2 GPS channels will be placed in the present monitoring system. These channels are distributed over ten floors. Tiltmeters are distributed over eight floors. The instrumentation layouts for the basement floors (B2 and B3) are depicted in Figs. 3 and 4.

In the B3 floor (Fig. 3), two tri axial sensors are placed at the diagonally opposite columns, and two uniaxial vertical sensors will be placed at the bottom of the remaining two columns. This is a typical instrumentation design for a lowest floor in order to capture the rocking motion of the tower.

The sensor layout at the ceiling of B2 floor is depicted in Fig. 4. Three biaxial sensors (six channels) are placed on this floor. It may be noted that the minimum required channels at each floor is only three. However, in the present case, three additional channels are proposed in order to capture the torsional behavior of the structure accurately. This is done due to the complex twisted geometric shape of the tower.

A typical sensor arrangement for all other remaining floors is shown (at the ceiling of the sixth floor) in Fig. 5. In these floors, three biaxial sensors are placed, and the locations are chosen at the core shear wall. In addition to the accelerometer, one biaxial tiltmeter is placed at this floor. The tiltmeter is intended to get the rotation of the tower. The locations at all instrumented floors are chosen such that the torsional behavior of the tower can be extracted accurately. It can be seen that all the floors are designed with the biaxial channels (accelerometers and tiltmeter).

Table 1 Summary of sensors and channels

Floor location	Uni-axial accel.	Bi-axial accel.	Tri-axial accel.	Bi-axial tiltmeter	GPS sensor	Wind sensor	Temperature sensor
Roof	–	–	–	–	1	1	2
76	–	3	–	1	–	–	–
65	–	3	–	1	–	–	–
54	–	3	–	1	–	–	–
42	–	3	–	1	–	–	2
29	–	3	–	1	–	–	–
16	–	3	–	1	–	–	–
6	–	3	–	1	–	–	–
B2	–	3	–	–	–	–	2
B3	2	–	2	–	–	–	–
Total number of sensors	2	24	2	7	1	1	6
Total number of channels	2	48	6	14	1	2	6

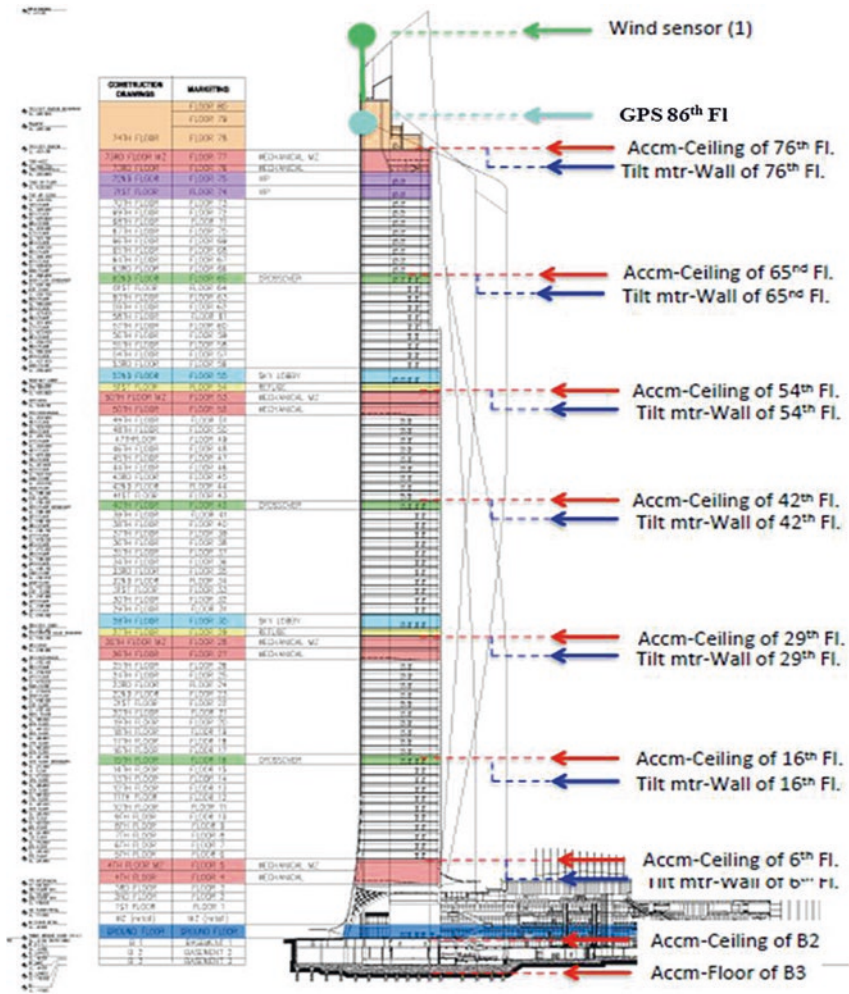


Fig. 2 Proposed instrumented floors for the Al-Hamra tower

Two GPSs are proposed, one at the top of the 86th floor and the other one at the top of the mall roof. Using the GPS, two-dimensional movements of the tower can be estimated reasonably accurately.

Wind sensors and temperature sensors will also be placed. The temperature sensors will be placed inside and outside the tower at three different floors. The purpose of the temperature sensors is to measure the temperature difference along the height and outside and inside the tower. The wind sensor is to be placed at the top of the tower hanging top above the peak point of the tower by 4–5 m.



Fig. 3 Proposed instrumented B3 floor

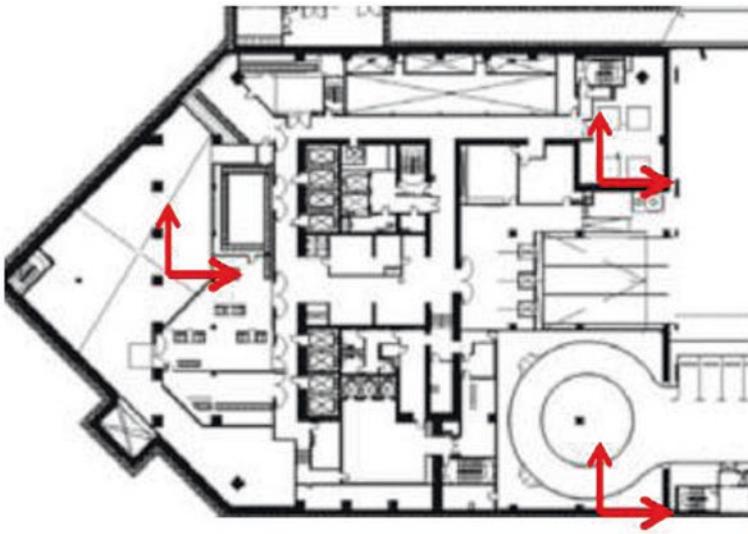


Fig. 4 Proposed instrumented B2 floor

4 Summary and Conclusion

Instrumentation design of the AL-Hamra tower is presented in this section. Visual inspection, free vibration, finite element analysis results, and optimal sensor placement algorithm were utilized for the instrumentation design. The SHM system includes accelerometer, tiltmeters, GPS sensors, wind sensors, and temperature

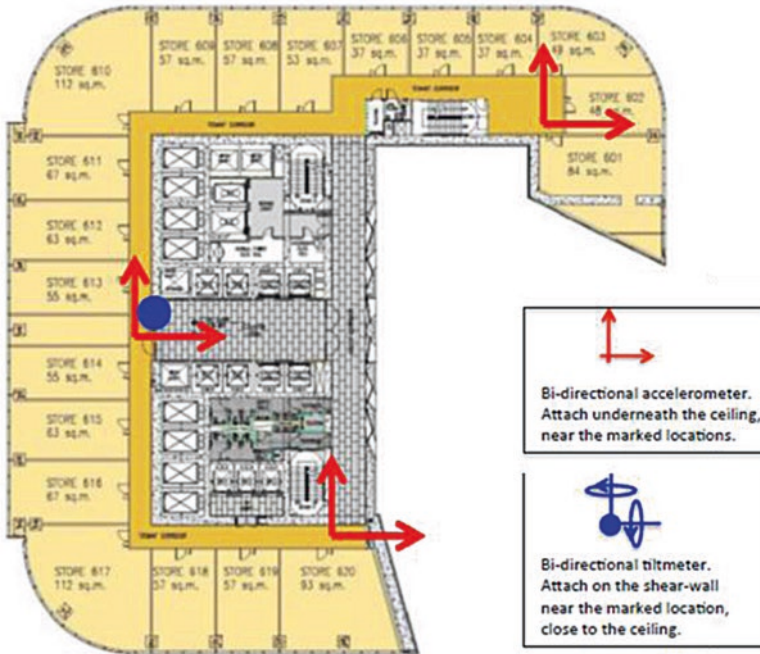


Fig. 5 Proposed typical instrumentation of higher floors (ceiling of the sixth floor)

sensors. The proposed SHM system has 84 channels. These channels are spread over ten floors. In the SHM design, special attention was paid to capture the most dominant torsional behavior of the tower.

References

1. Chang PC, Flatau A, Liu SC (2003) Review paper: health monitoring of civil infrastructure. *Struct Health Monitor* 2(3):257–267
2. Kaya Y, Safak E (2015) Real-time analysis and interpretation of continuous data from structural health monitoring (SHM) systems. *Bull Earthq Eng* 13:917–934
3. Şafak E, Çaktı E, Kaya Y (2010) Recent developments in structural health monitoring and data analysis. In: Garevski M, Ansal A (eds) *Earthquake engineering in Europe*. Springer, London, pp 331–355
4. Alampalli S, Fu G, Dillon EW (1997) Signal versus noise in damage detection by experimental modal analysis. *J Struct Eng* 123(2):237–245
5. Huth O, Feltrin G, Maeck J, Kilic N, Motavalli M (2005) Damage identification using modal data: experiences on a pre-stressed concrete bridge. *J Struct Eng* 131(12):1898–1910
6. Nair KK, Kiremidjian AS, Law KH (2006) Time series-based damage detection and localization algorithm with application to the ASCE benchmark structure. *J Sound Vibrat* 291:349–368
7. McNeill SI, Zimmerman DC (2008) A framework for blind modal identification using joint approximate diagonalization. *Mech Syst Signal Process* 22(7):1526–1548

8. Salawu OS (1997) Detection of structural damage through changes in frequency: a review. *Eng Struct* 19(9):718–723
9. Sun H, Büyüköztürk O (2015) Optimal sensor placement in structural health monitoring using discrete optimization. *Smart Mat Struct* 24(12):125034. (16 pp)

Part IV
Energy Efficiency and Life Cycle Analysis

Disaster Resilience and Sustainability of Infrastructures: Relationships and Quantification Methods



Bilal M. Ayyub

1 Introduction: Threats and Challenges

Our global society is facing many challenges that include, for example, natural, technological, and human-caused threats potentially affecting property and life, costing annually hundreds of billions of dollars. The effects of these threats are exacerbated by factors that include the following:

- Income disparity that may lead to more severe impacts on the poor than the non-poor and societal or international conflicts and disorders.
- Population growths with time-variant differences in consumption cultures that potentially may be converging toward the high ends of consumption behavior for significant population segments, thereby stressing or threatening our limited resources.
- A changing climate and growing populations with significant increases in urbanization.
- New and emerging technological threats.

Three categories of hazards are of interest: (1) natural, (2) accidental, and (3) deliberate attacks. The focus herein is on natural hazards although concepts introduced are applicable to the categories of accidental hazards and deliberate attacks. Figure 1 shows a classification of the natural hazards according to insurance industry practices. Some of these hazards are out of scope.

Resilience and sustainability as system characteristics are necessary for societal endurance and survival. Enhancing them at the element, network, community, etc. levels could lead to massive savings not only through efficiencies but also through risk reduction and expeditious recovery in case of disasters. The rational management

B. M. Ayyub (✉)

Center for Technology and Systems Management, Department of Civil and Environmental Engineering, University of Maryland, College Park, MD, USA

e-mail: ba@umd.edu

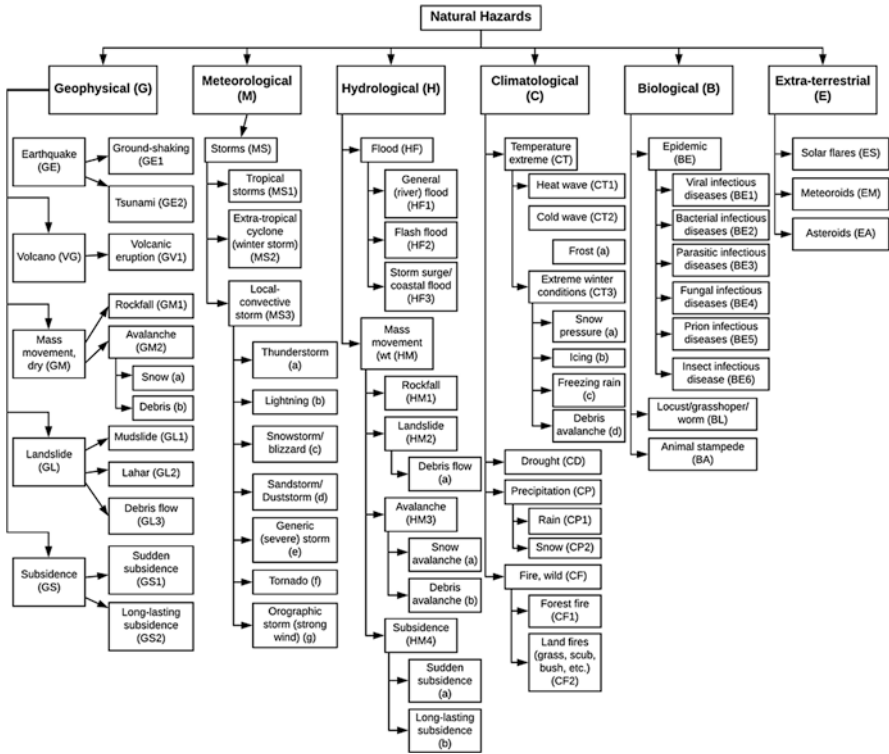


Fig. 1 A general classification of natural hazards

of such reduction and recovery is facilitated by practical and fundamental resilience and sustainability metrics. Starting with contrasting resilience and sustainability for understanding their relationships is essential for making appropriate decisions for their control in a cost-effective manner. A methodology is then proposed for analyzing and designing disaster-resilient infrastructure systems.

2 Resilience and Sustainability and Their Relationships

2.1 Resilience

The concept of resilience appears in different domains ranging from ecology to child psychology and psychiatry to infrastructure systems. It was formally introduced in ecology, defined as the persistence of relationships within a system [1], and measured by the system’s ability to absorb change-state variables, driving variables, and parameters and still persists. In discussing the philosophical basis of risk analysis, Starr et al. [2] characterized the resilience of a system as its ability to

bounce or spring back into shape or position or to recover its strength or spirits quickly.

US federal agencies generally define resilience in accordance to the Presidential Policy Directives (PPD) 8 [3] and 21 [4]. PPD 8 [3] defines resilience as “the ability to adapt to changing conditions and withstand and rapidly recover from disruption due to emergencies.” PPD 21 [4] expanded the definition to include “the ability to prepare for and adapt to changing conditions and to withstand and recover rapidly from disruptions. Resilience includes the ability to withstand and recover from deliberate attacks, accidents, or naturally occurring threats or incidents.” The National Institute of Standards Technology Community Resilience Planning Guide for Buildings and Infrastructure Systems [5] provides a similar definition.

Ayyub [6, 7] provides a comparative examination of these definitions and their suitability as a basis for resilience quantification and measurement science. A proposed definition that belongs to the intension class is that “the resilience of a system is the persistence of its functions and performances under uncertainty in the face of disturbances [6].” This definition enables the measurement of resilience through metrics by meeting the following requirements: (1) building on previous notional definitions; (2) considering initial and residual strength, i.e., capacity and robustness; (3) accounting for abilities to prepare and plan for, absorb, recover from, or adapt to adverse events; (4) treating disturbances as events with occurrence rates of stochastic processes; (5) permitting the use of several performance attributes; (6) accounting for changes over time, e.g., aging or improvements; (7) considering full or partial recovery and times to recovery; (8) considering potential enhancements to system performance after recovery; (9) being compatible with other familiar notions such as reliability and risk; and (10) enabling the development of resilience metrics with meaningful units.

For engineering systems, resilience is a system characteristic and the system can be a system of systems. For instance, to be functional after a disruption, a building needs communications, power, water, and transportation for access of its users as well as to be functional itself. Usually a water utility depends on a power utility to be functional, and a power plant requires cooling water and all depend on natural, human, social, and financial capitals for functionality.

2.2 *Sustainability*

As for sustainability, the American Society of Civil Engineers (ASCE) defines sustainability, in its Policy Statement 418 [8], as a set of economic, environmental, and social conditions in which all of society has the capacity and opportunity to maintain and improve its quality of life indefinitely, without degrading the quantity, quality, or the availability of natural, economic, and social resources. Sustainable development is the application of these resources to enhance the safety, welfare, and quality of life for all of society. Several other definitions are available as provided by Webb and Ayyub [9] with examples shown in Table 1.

Table 1 Selected sustainability definitions (adapted after [9])

Context	Definition and source
General	<p>“Creating and maintaining conditions under which humans and nature can exist in productive harmony and that permit fulfilling social, economic, and other requirements of present and future generations” [10]</p> <p>“Ability to maintain or improve standards of living without damaging or depleting natural resources for present and future generations” [11]</p>
Manufacturing	<p>“The creation of manufactured products that use processes that minimize negative environmental impacts; conserve energy and natural resources; are safe for employees, communities, and consumers; and are economically sound” [12]</p>
Green buildings	<p>“The practice of increasing the efficiency with which buildings and their sites use and harvest energy, water, and materials and protecting and restoring human health and the environment, throughout the building life cycle: siting, design, construction, operation, maintenance, renovation, and deconstruction” [13]</p>

2.3 *Contrasts and Relationships*

Fiksel [14, 15] and Redman [16] provide a discussion on contrasting elements of resilience and sustainability for systems. A resilience theory approach recognizes the following: (1) change is normal with multiple stable states; (2) experience leads to a gracefully adaptive cycle; (3) resilience originates in ecology for maintaining ecosystem services; (4) results of change are open ended and emergent; (5) resilience is concerned with maintaining system dynamics; and (6) stakeholder input is focused on desirable dynamics. On the other hand, a sustainability science approach recognizes the following: (a) this approach envisions the future and acts to make it happen; (b) it utilizes transition management approach; (c) it originates in social sciences with the presumption that a society is flawed; (d) its desired results of change are specified in advance; (e) its focus is on interventions that lead to sustainability; and (f) stakeholder input is focused on desirable outcomes.

Fiksel [14, 15] examined dynamic modeling techniques, including biocomplexity, system dynamics, and thermodynamic analysis, to investigate the impacts on ecological and human systems of major shifts such as climate change and the associated policy and technology responses. It is concluded that these techniques can yield at least a partial understanding of dynamic system behavior, enabling a more integrated approach to systems analysis, beneficial intervention, and improvement of resilience, and identified gaps and needs.

Redman’s [16] sustainability science approach is descriptive on how an engineer addresses both sustainability and resilience where resilience is treated as an aspect of sustainability during the life cycle of a project or in the management of a system, enterprise, or community. The life cycle includes conception, design, construction, operation, maintenance, and renewal or removal. The necessary steps are the following: (1) envision the future, for normal function and response to a perturbation,

and act for sustainability and resilience; (2) use a transition management approach from current to desired conditions; (3) seek desired results of change that are specified in advance; (4) focus on interventions that lead to sustainability and resilience; and (5) seek stakeholder input by focusing on desired outcomes.

Bocchini et al. [17] examined the relationships and use of life cycle costs to unify the treatment of sustainability and resilience in a common risk framework. Gillespie-Marthaler et al. [18] examined an integrative approach to conceptualizing sustainable resilience to enable alignment of adaptation and transformation strategies with desired resilience outcomes. Nelson et al. [19] presents a high-level, integrated, and dynamic framework for assessing sustainable resilience for complex adaptive systems.

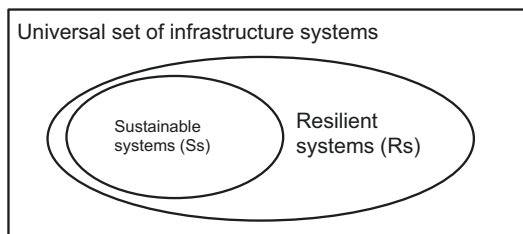
Defining the relationship between resilience and sustainability is context dependent. Two contexts are considered herein: (1) states of infrastructure systems [20] and (2) resilience and sustainability requirements for infrastructure systems. The following precepts should be captured in relating resilience and sustainability: (a) systems that are resilient might not be sustainable; (b) systems that are not resilient are not sustainable; and (c) systems that are not sustainable might be resilient. Let's introduce the following notations:

- R = resilient infrastructure systems.
- \bar{R} = non-resilient infrastructure systems.
- S = sustainable infrastructure systems.
- \bar{S} = non-sustainable infrastructure systems.

Using the first context and a Venn diagram (see Fig. 2) of two ovals representing the *states of resilient and sustainable infrastructure systems* within a rectangular universal set of infrastructure systems, the following six cases should be considered in order to identify the ones that best meet the precepts previously stated:

- Case 1. Rs and Ss are mutually exclusive resilient (Rs) and sustainable (Ss) systems, respectively.
- Case 2. Rs and Ss are independent systems.
- Case 3. Rs and Ss are systems with positive dependency.
- Case 4. Rs and Ss are systems with negative dependency.
- Case 5. Rs and Ss are systems with perfect dependency and Rs systems nested in Ss systems.

Fig. 2 Sustainable systems (Ss) and resilient systems (Rs) with perfect dependency (Case 6 of nested infrastructure systems)



- Case 6. Rs and Ss are systems with perfect dependency and Ss systems nested in Rs systems.

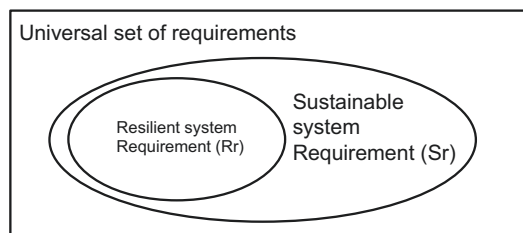
Cases 1 to 5 are inappropriate, whereas the most appropriate representation of the *states of infrastructure systems* is Case 6. Case 6, as shown in Fig. 2, is consistent with the above three precepts. The figure basically states that generally infrastructure systems that are characterized to be sustainable are best represented as a subset infrastructure systems characterized to be resilient.

Using the second context and a Venn diagram (see Fig. 2) of two ovals representing the *requirements of resilient and sustainable infrastructure systems* within a rectangular universal set of all requirements of infrastructure systems, the following six cases should be considered in order to identify the ones that best meet the precepts previously stated:

- Case 7. Rr and Sr are mutually exclusive sets of resilience requirements and sustainability requirement, respectively.
- Case 8. Rr and Sr are independent sets of requirements.
- Case 9. Rr and Sr are for systems with positive dependency between the two sets of requirements.
- Case 10. Rr and Sr are for systems with negative dependency between the two sets of requirements.
- Case 11. Rr and Sr are for systems with perfect dependency in requirements and Rr requirements nested in Sr requirements.
- Case 12. Rr and Sr are for systems with perfect dependency in requirements and Sr requirements nested in Rr requirements.

Cases 7 to 11 are inappropriate, whereas the most appropriate representation of the *states of infrastructure systems* is Case 6. Case 6, as shown in Fig. 3, is consistent with the above three precepts. The figure basically states that generally infrastructure systems that are characterized to be sustainable are best represented as a subset infrastructure systems characterized to be resilient. Note that in this requirements context, resilience requirements are contained in sustainability requirements, i.e., $Rr \subset Sr$, whereas in the system state requirement, it is the other way around, i.e., sustainable systems are nested in resilient systems as $R_s \subset S_s$.

Fig. 3 Resilient system requirements (Rr) and sustainable system requirements (Sr) with perfect dependency (Case 12 of nested sets of requirements)



3 Infrastructure Sustainability: Quantification Methods

A primary challenge in the quantification of infrastructure sustainability is its multidimensionality of attributes requiring the use of multiple units [9], as illustrated in Fig. 4. These multidimension and associated units can be addressed by using conversion relationships to a probabilistic scale of achieving a performance target as illustrated in Fig. 5. The quantification methodology consists of three steps as provided in Fig. 6. The methodology results are illustrated in Fig. 7.

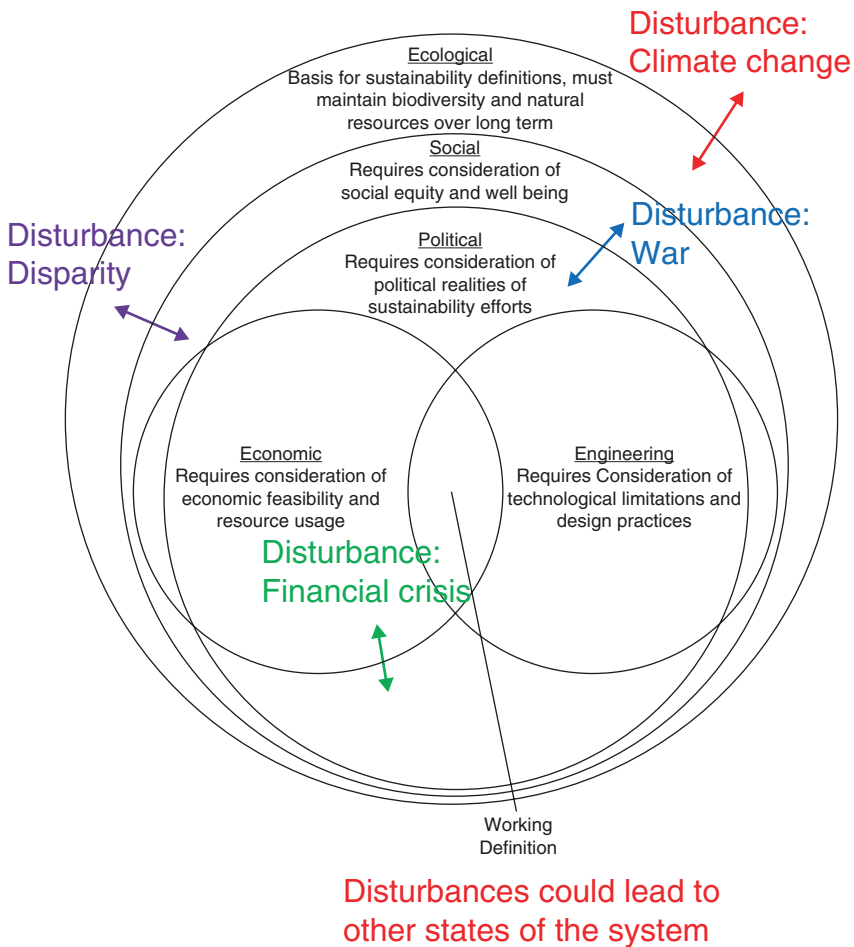
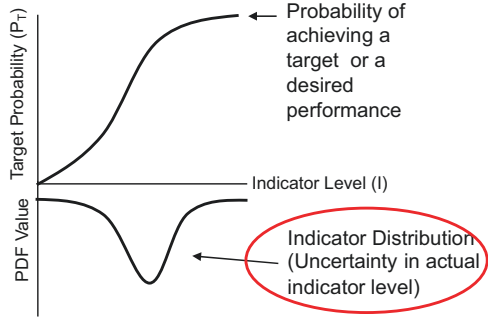


Fig. 4 Multidimensions associated with infrastructure sustainability

Fig. 5 Conversion curves to a need probability of achieving a target performance



Need probability – The probability of achieving a sustainability target. This is an exceedance probability calculated from a target distribution using a set indicator level

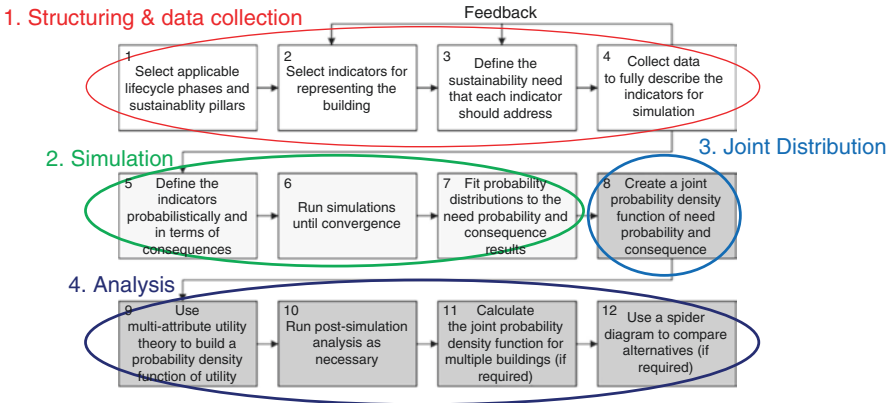
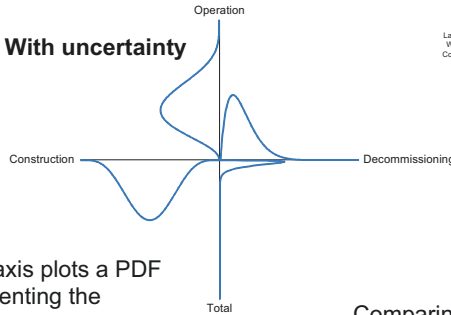


Fig. 6 A methodology for quantifying infrastructure sustainability

4 Disaster Resilience of Infrastructure: Quantification Methods

This section provides in Fig. 8 a proposed outline of a high-level methodology for resilience analysis of infrastructure systems by Ayyub [21]. It consists of the following primary steps: (1) context definition, (2) hazard identification and characterization, (3) failure probability and fragility curves estimation, (4) exposure and loss analysis, (5) economic valuation and loss accumulation, (6) risk quantification as loss exceedance probabilities, (7) extremes and uncertainty analysis, (8) risk-informed decision analysis for resilience engineering, and (9) life cycle analysis. The methodology includes also other considerations and information and data

Need probability – The probability of achieving a sustainability target. This is an exceedance probability calculated from a target distribution using a set indicator level.



Each axis plots a PDF representing the distribution of need probability for that phase.

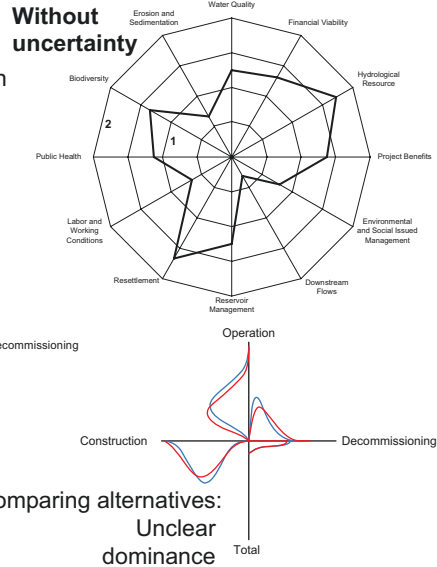


Fig. 7 Results from the methodology for quantifying infrastructure sustainability

sources. The color coding in the figure shows these steps with relationships in groups. The methodology is a top-down approach that starts with the hazard scenarios and predictions or projections, assessment, and management and design. The chapters called out in Fig. 8 are of the document by Ayyub [21].

Quantifying risk for a system brings together the probabilities and consequences in terms of a loss (L) random variable as follows:

$$L = \sum_{t=1}^T \left(\sum P(E)P(H|E)P(F|H)(L|F)e^{-it} \right) \tag{1}$$

where L = loss (L) at time t ; $P(E)$ = probability of an event (E) or related scenario at time t ; $P(H|E)$ = annual probability of a hazard (H) under the conditions defined by E ; $P(F|H)$ = probability of a failure (F) upon the occurrence of H ; $L|F$ = loss (L) upon the occurrence of; and I = annual discount rate. Accumulating the loss estimates from Eq. (1) over all the scenarios, i.e., as represented by the inner summation sign, with an appropriate discount rate (i) over a planning horizon (T), i.e., as represented by the outer summation sign, produces a total loss random variable (L) (Stanley and Ayyub 2016).

Risk management is typically based on the associated economics of design or improvement options identified for a particular decision situation based on the cost-effectiveness of an option for reducing the risk associated with the situation. As an example, in the context of extreme storms, options may include countermeasures aimed at reducing vulnerabilities of coastal lines, property and asset exposure, impact on resources and populations, and land use changes. Options also may

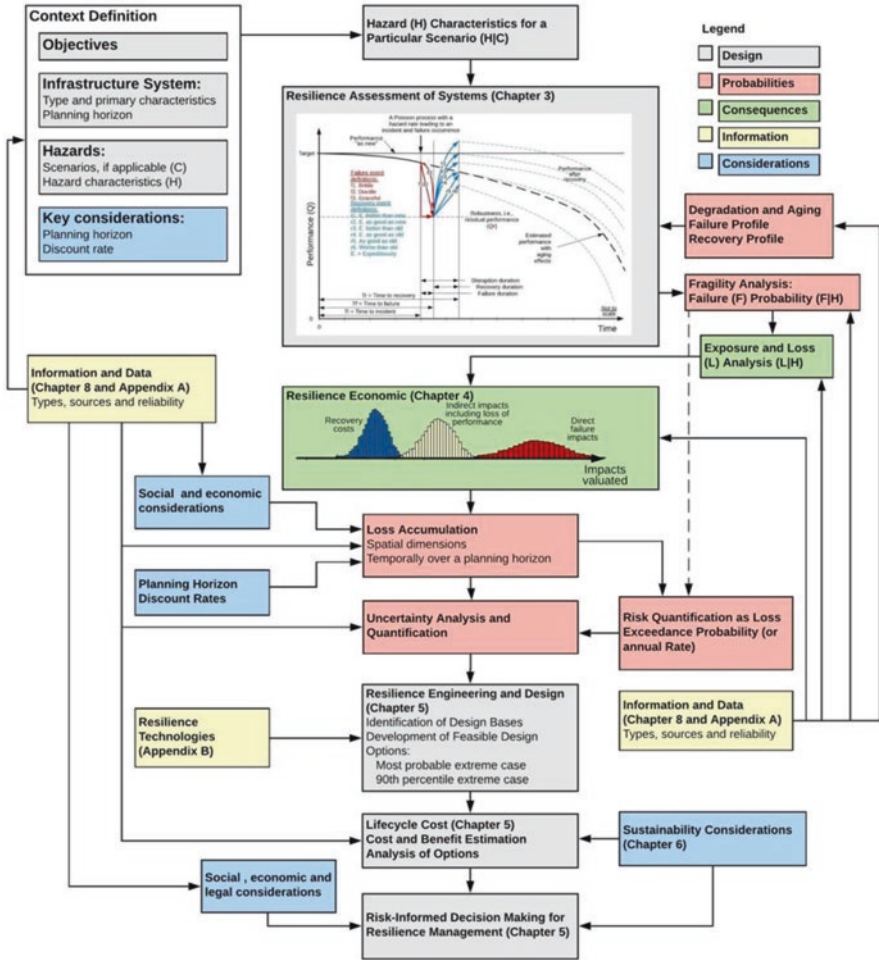


Fig. 8 Methodology for resilience analysis [21]

include consequence mitigation strategies aimed at reducing the potential consequences given the occurrence of a failure scenario [6]. The probability of realizing a favorable benefit-to-cost ratio can be represented as follows:

$$P\left(\frac{\text{Benefit}}{\text{Cost}} \geq 1\right) = 1 - P(\text{Benefit} - \text{Cost} \leq 0) \tag{2}$$

where both benefit and cost in Eq. (2) are random variables. With the knowledge of their underlying distributions, the probability of realizing a favorable benefit-to-cost ratio can be computed using reliability assessment techniques including Monte Carlo simulation. It should be noted that the uncertainty associated with the benefit

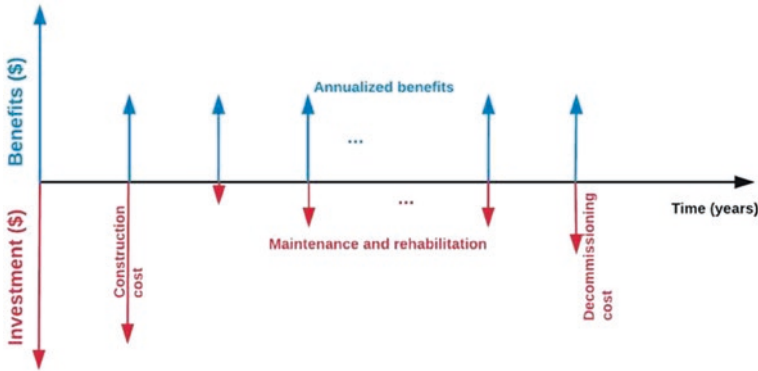


Fig. 9 Investments and benefits over an infrastructure system’s life cycle [22]

is typically greater than the uncertainty associated with the cost of the strategy. The life cycle cost analysis of an infrastructure system is illustrated in Fig. 9 in terms of a cash flow over time using a convenient time step, such as a year. The figure shows the costs, i.e., investments, as downward arrows. The upward arrows show the benefits gained on an annual basis. Typically, engineers and analysts focus on the costs, and the benefits are not expressed explicitly and considered to be a function of the costs based on economic concepts such as the willingness to pay as a basis for economic valuation of these benefits [6].

5 Disaster-Resilient Infrastructure

Resilience is defined by the Presidential Policy Directive (PPD)-8 [3] as “the ability to adapt to changing conditions and withstand and rapidly recover from disruption due to emergencies.” Measuring resilience is typically based on the performance of an infrastructure system after an external shock including the time it takes to return to initial level of performance. The concept is shown in Fig. 10, commonly called the resilience triangle, with a resilience index defined as follows:

$$\text{Resilience} = \frac{\int_{t_0}^{t_1} Q(t) dt}{100(t_0 - t_1)} \tag{3}$$

where Q is the infrastructure quality or the performance of a system, t_0 is the time of incident or disturbance occurrence, and t_1 is the time to full recovery. According to this model, the units of resilience are performance per unit time, where performance can be measured in percent according to Eq. (3). The earthquake community used Eq. (3) with a suggested approach of resilience called the four Rs defined as follows [23]:

- Robustness as the ability of the system and system elements to withstand external shocks without significant loss of performance.
- Redundancy as the extent to which the system and other elements satisfy and sustain functional requirements in the event of disturbance.
- Resourcefulness as the ability to diagnose and prioritize problems and to initiate solutions by identifying and monitoring all resources, including economic, technical, and social information.
- Rapidity as the ability to recover and contain losses and avoid future disruptions.

These properties are defined in Table 2 with reference to Fig. 10.

Another model proposed by Ayyub [6] is illustrated in a schematic representation of a system’s performance (Q) with aging effects and an incident occurrence with a rate (λ) according to a Poisson process (see Fig. 11). At time t_i , it might lead to degraded performance, called failure for convenience, of a duration ΔT_f . The failure event concludes at time t_f . The failure event is followed by a recovery event with a

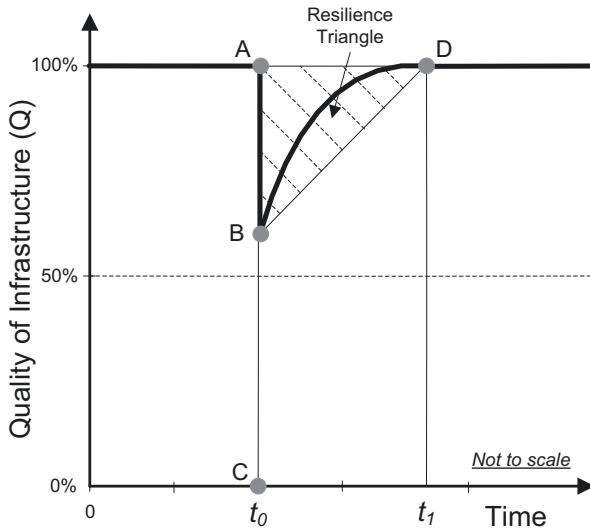


Fig. 10 Resilience properties and triangle

Table 2 Definition of resilience properties

Property	Models (points A, B, C, and D per Fig. 10)	Units	Equation number
Robustness	$Robustness = B - C$	Percentage	(4)
Redundancy	Not defined		
Resourcefulness	Not defined		
Rapidity	$Rapidity = \frac{A - B}{t_0 - t_1}$	Average recovery rate in percentage per time	(5)

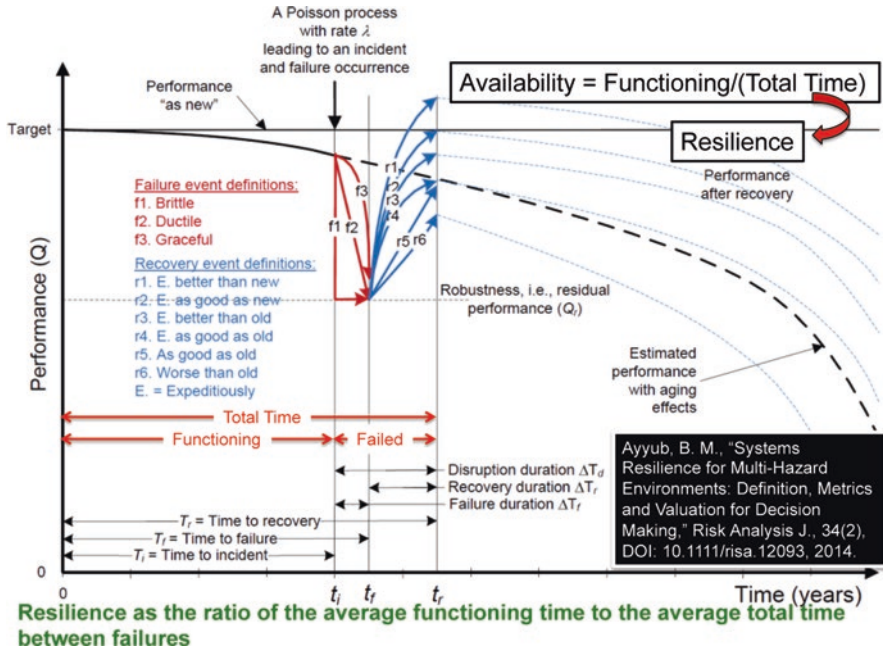


Fig. 11 Resilience measurement and metrics and associated economics [6]

duration ΔT_r . The recovery event concludes at time t_r . The total disruption (D) has a duration of $\Delta T_d = \Delta T_f + \Delta T_r$. The figure shows for illustration purposes three failure events—brittle (f_1), ductile (f_2), and graceful (f_3)—and six recovery events: expeditious recovery to better than new (r_1), expeditious recovery to as good as new (r_2), expeditious recovery to better than old (r_3), expeditious recovery to as good as old (r_4), recovery to as good as old (r_5), and recovery to worse than old (r_6). These events define various rates of change of performance of the system. The figure also shows the aging performance trajectory and the estimated trajectory after recovery. The proposed model to measure resilience is

$$\text{Resilience}(R_e) = \frac{T_i + F\Delta T_f + R\Delta T_r}{T_i + \Delta T_f + \Delta T_r} \tag{6}$$

where for any failure event (f) as illustrated in Fig. 11, the corresponding *failure profile* F is measured as follows:

$$\text{Failure}(F) = \frac{\int_{t_i}^{t_f} f dt}{\int_{t_i}^{t_f} Q dt} \tag{7}$$

Similarly for any recovery event (r) as illustrated in Fig. 11, the corresponding *recovery profile* R is measured as follows:

$$\text{Recovery} (R) = \frac{\int_{t_f}^{t_r} r dt}{\int_{t_f}^{t_r} Q dt} \tag{8}$$

The failure-profile value (F) can be considered as a measure of robustness and redundancy and is proposed to address the notion offered by Eq. (4), whereas the recovery-profile value (R) can be considered as a measure of resourcefulness and rapidity and is proposed to address the notion offered by Eq. (5). Building on the work of Mori and Ellingwood [24], the time to failure (T_f) can be characterized by its probability density function computed as follows:

$$-\frac{d}{dt} \int_{s=0}^{\infty} \exp\left[-\lambda t \left(1 - \frac{1}{t} \int_{\tau=0}^t F_L(\alpha(\tau)s) d\tau\right)\right] f_{S_0}(s) ds \tag{9}$$

where Q is defined as the system’s performance in terms of its strength (S) minus the corresponding load effect (L) in consistent units, i.e., $Q = S-L$. Both L and S are treated as random variables, with $F_L =$ the cumulative probability distribution function of L and $f_s =$ the probability density function of S . The aging effects are considered in this model by the term $\alpha(t)$ representing a degradation mechanism as a function of time t . It should be noted that the term $\alpha(t)$ can also represent improvement to the system. Equation 9 is based on a Poisson process with an incident occurrence, such as loading, rate of λ . The probability density function of T_f as shown in Eq. (9) is the negative of the derivative of the reliability function. The times T_i , T_f , and T_r are random variables as shown in Fig. 11 and are related to durations as follows:

$$\Delta T_f = T_f - T_i \tag{10}$$

$$\Delta T_r = T_r - T_f \tag{11}$$

The disruption duration is given by:

$$\Delta T_d = \Delta T_f + \Delta T_r \tag{12}$$

Figure 11 also shows the associated costs including losses, recovery cost, and indirect costs. These losses and costs should be based on total economic valuations using anthropocentric considerations.

A simplified model [7] is suggested for a fundamental case having a performance level that would be maintained and sustained over time, i.e., no aging effects, with a brittle failure profile, i.e., f1, in Fig. 11. Also, assume as-good-as-old recovery, i.e., r5 in Fig. 11. Additionally, the following assumptions are made: (1) a planning horizon (t), (2) Poisson process of stressors with a rate (λ), (3) the planning horizon related to the stressor rate as $t = 1/\lambda$, (4) failure probability (p) due to a stressor, and (5) independent failures. It should be noted that the stressors have varied intensities

and not all stressors fail the system and disrupt the system’s performance. The failure probability is denoted as p . Fundamental cases are presented in this section: the case of linear recovery and the case of step recovery; however, other cases can be treated in a similar manner.

For the fundamental case of a linear recovery, the resilience metric of Eq. (6) for one failure-causing event is basically the ratio of two areas according to this figure, i.e., the rectangular area tQ_{100} , divided by the tQ_{100} without the triangle representing the degraded performance of the system. The triangle has the sides of brittle failure and linear recovery. For a linear recovery path (r), it can be expressed as follows for one failure-inducing event:

$$\text{Linear recovery : Resilience per failure } (R_f) = 1 - \frac{(t_r - t_i)(Q_{100} - Q_r)}{2Q_{100}t} \tag{13}$$

For analytical and computational convenience, the concept of non-resilience, i.e., resilience triangle, can be introduced and defined as follows:

$$\text{Linear recovery : Non-resilience per failure } (\bar{R}_f) = \frac{(t_r - t_i)(Q_{100} - Q_r)}{2Q_{100}t} \tag{14}$$

Figure 12 provides an example of a linear recover. The relationship between R_f and \bar{R}_f is

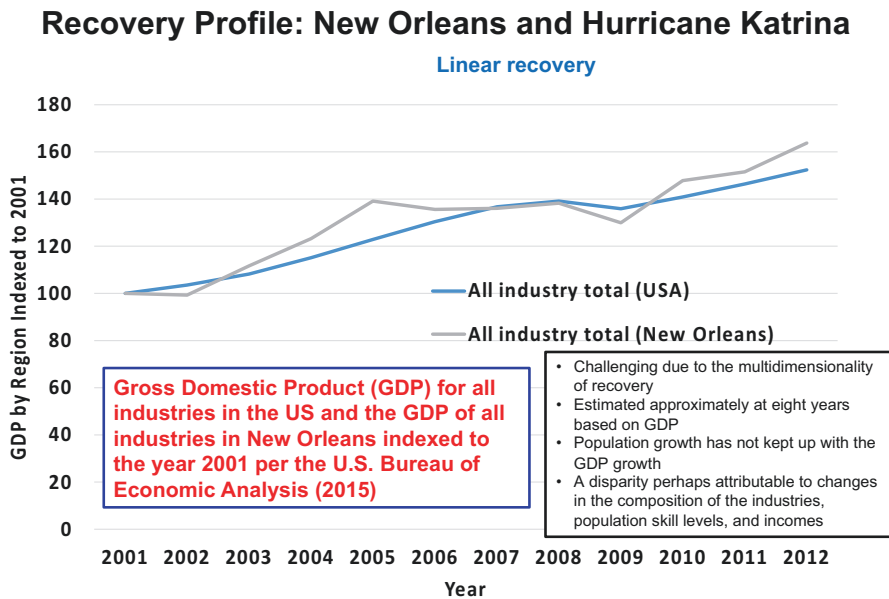


Fig. 12 Resilience measurement and metrics and associated economics [6]

$$\bar{R}_f = 1 - R_f \quad (15)$$

Equations (13) and (14) can be generalized to account for the potential of multiple occurrences of failure-inducing events x and their associated probabilities as follows:

$$\text{Resilience}(R_e) = 1 - \sum_{x=1}^{\infty} \left(\exp(-\lambda t) \frac{(\lambda t)^x}{x!} p^x \bar{R}_f^x \right) \quad (16)$$

This equation can be reduced to:

$$\text{Resilience}(R_e) = 1 - \exp(-\lambda t (1 - p \bar{R}_f)) + \exp(-\lambda t) \quad (17)$$

This model offers the simplicity and practicality desired for systems with time-invariant performance and accounts for the following: rate of events, i.e., the rate λ , of a Poisson process; probability of failure (p) given a stressor, i.e., inherent strength of the system; capacity of the system (Q_{100}); robustness of the system (Q_r); brittle failure and linear or step recovery to as-good-as-old profiles; non-resilience associated with the occurrence of a failure-inducing event; planning horizon t ; and stressor time as a result of failure-inducing event.

6 Case Study: Climate-Resilient Infrastructure

This section illustrates designing of disaster-resilient infrastructure for flooding as a result of a rising sea level due to a changing climate. In general, the design process, applicable to climate-related and other hazards, is provided in Fig. 8 [21].

The ASCE Committee on Adaptation to a Changing Climate (CACC) prepared a manual of practice of climate-resilient infrastructure [22] to meet the challenges associated with designing for a changing climate, such as non-stationarity of the characteristics of hazards.

Civil infrastructure systems traditionally have been designed for appropriate functionality, durability, and safety for climate and weather extremes during their full service lives; however, climate scientists inform us that the extremes of climate and weather have altered from historical values in ways difficult to predict or project due to non-stationarity of the characteristics of hazards and the dynamic relationship among human needs, environment and natural processes. The engineering community has a need for guidance on infrastructure analysis and design in a world in which risk profiles are changing and can be projected with varying degrees of uncertainty requiring a new design philosophy to meet this challenge.

The underlying approaches in this ASCE manual of practice are based on probabilistic methods for quantitative risk analysis, and the design framework provided focuses on identifying and analyzing low-regret, adaptive strategies to make a project more resilient. The manual starts with an overview of the driving forces and hazards associated with a changing climate; subsequent chapters in the manual provide observational methods, illustrative examples, and case studies; estimation of extreme events particularly related to precipitation with guidance on monitoring and measuring methods; flood design criteria and the development of project design flood elevations; computational methods of determining flood loads; adaptive design and adaptive risk management in the context of life cycle engineering and economics; and climate resilience technologies.

Such methods are necessary and needed for the use of engineers, researchers, planners, and other stakeholders charged with adaptive design decisions to achieve infrastructure resilience targets while minimizing life cycle costs in a changing climate.

As an example, consider the case of designing for water-level rise (WLR) due to an underlying sea-level rise (SLR) and greater levels of surges and waves. Designing infrastructure under a changing WLR based on available projections and data entails significant and time-variant uncertainty. Adaptive design methods with risk control offer a way to deal with associated uncertainties, as illustrated in the following hypothetical example of the design and construction of a rail system in a coastal region experiencing WLR owing to a changing climate with the potential for surges and waves.

Consider a hypothetical example of a proposed high-speed rail transportation between Miami and Homestead, Florida. The planning horizon is to the year 2100. Figure 13 depicts the relationship between projected SLR and its associated

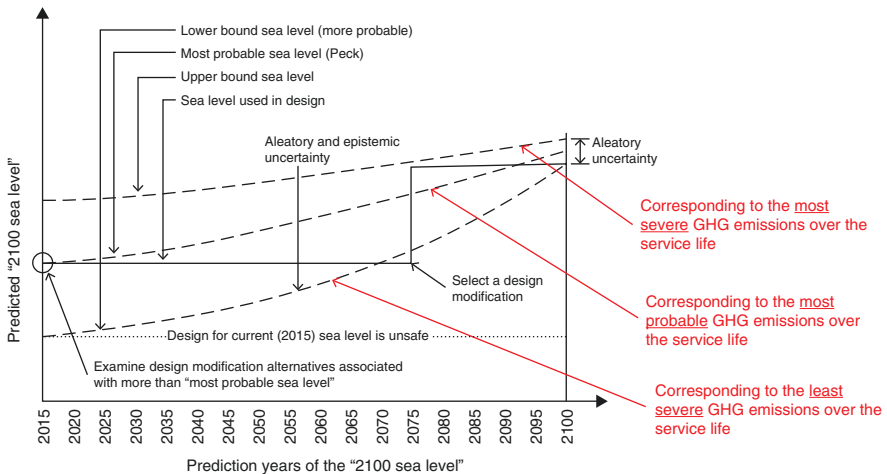


Fig. 13 Adaptive design with adaptation in 2075 with increasing water level and decreasing uncertainty [20]

uncertainty as a basis for projecting WLR [20]. The vertical axis shows the predicted sea level for the year 2100 as a function of time starting with a prediction made in the 2015. The uncertainty is assumed to decrease as the prediction year approaches the year 2100. The height of the rail bed can be based on the most-probable level, with appropriate consideration for potential needs to increase the height. Accommodating such a potential increase might require the installment of an oversized foundation system and other details to facilitate the height increase without needing to demolish the rail system itself. The sea level is tracked in future years and the height is kept the same or increased as needed. Several decision points are shown on the figure for the purpose of illustration. Such an adaptive management approach would help to counter the indecisiveness associated with great uncertainty levels. This approach can be combined with risk methods to create adaptive risk control strategies for economic and tradeoff analysis as provided by Ayyub [6, 25].

A similar approach was used for the design of the Los Angeles to San Diego (LOSSAN) Rail Corridor [26], presented in Figs. 14 and 15 [26].



Fig. 14 Los Angeles to San Diego (LOSSAN) rail corridor that follows the sea coast and crosses low-lying areas on trestles [26]

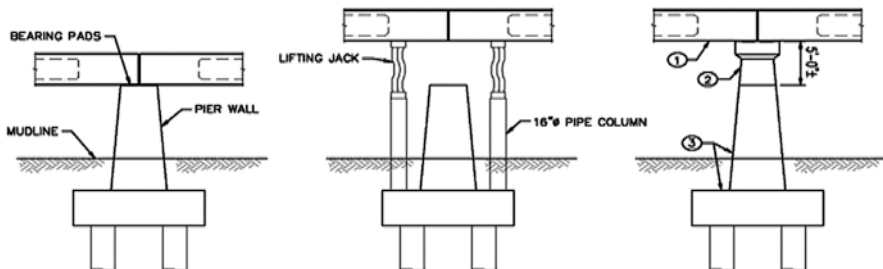


Fig. 15 LOSSAN Rail Corridor uses a Moffatt and Nichol concept of precast piers and caps to allow insertion of additional pier segments if needed to adapt to flooding hazard [26]

Acknowledgments The author acknowledges the support and facilitation of the ASCE Infrastructure Resilience Division and the ASCE Committee on Adaptation to a Changing Climate particularly their executive committee members and ASCE staff including Ms. Catherine Tehan, Mr. Jay Snyder, and Mr. John Durrant. The author acknowledges the inspirational and impactful contributions and leadership of Dr. Richard N. Wright and Professor Ted Vinson.

References

1. Holling CS (1973) Resilience and stability of ecological systems. *Ann Rev Ecol Syst* 4:1–23
2. Starr C, Rudman R, Whipple C (1976) The philosophical basis for risk analysis. *Ann Rev Energy* 1:629–662
3. Presidential Policy Directives (PPD) (2011) National preparedness. <http://www.dhs.gov/presidential-policy-directive-8-national-preparedness>. Accessed 9 Feb 2016
4. Presidential Policy Directives (PPD) (2013) Critical infrastructure security and resilience. <https://www.whitehouse.gov/the-press-office/2013/02/12/presidential-policy-directive-critical-infrastructure-security-and-resil>. Accessed 9 Feb 2016
5. National Institute of Standards Technology (NIST) (2016) Community resilience planning guide for buildings and infrastructure systems, Special Publication 1190, volume 1. <https://doi.org/10.6028/NIST.SP.1190v1>
6. Ayyub BM (2014) Systems resilience for multihazard environments: definition, metrics, and valuation for decision making. *J Risk Anal* 34(2):340–355
7. Ayyub BM (2015) Practical resilience metrics for planning, design, and decision making. ASCE-ASME J Risk Uncertain Eng Syst Part A Civil Eng. <https://doi.org/10.1061/AJRUA6.0000826>
8. American Society of Civil Engineers (ASCE) (2016) Policy statement 418. <http://www.asce.org/issues-and-advocacy/public-policy/policy-statement-418—the-role-of-the-civil-engineer-in-sustainable-development/>. Accessed 9 Feb 2016
9. Webb D, Ayyub BM (2016) Sustainable construction and manufacturing: definitions, metrics and valuations for decision making. ASCE-ASME J Risk Uncertainty Eng Syst Part A Civ Eng
10. Environmental Protection Agency (EPA) (2016) Learn about sustainability. <http://www.epa.gov/sustainability/learn-about-sustainability>. Accessed 9 Feb 2016
11. Environmental Protection Agency (EPA) (2016) EPA's report on the environment. <http://cfpub.epa.gov/roe/chapter/sustain/index.cfm>. Accessed 9 Feb 2016
12. International Trade Administration, Department of Commerce (ITA) (2016) How does commerce define sustainable manufacturing? http://www.trade.gov/competitiveness/sustainable-manufacturing/how_doc_defines_SM.asp. Accessed 9 Feb 2016
13. Environmental Protection Agency (EPA) (2016) Green buildings. <http://archive.epa.gov/greenbuilding/web/html/faqs.html>. Accessed 9 Feb 2016
14. Fiksel J (2003) Designing resilient, sustainable systems. *Environ Sci Technol* 37(23):5330–5339
15. Fiksel J (2006) Sustainability and resilience: toward a systems approach. *Sustainabil Sci Pract Policy* 2(2):14–21
16. Redman CL (2014) Should sustainability and resilience be combined or remain distinct pursuits? *Ecol Soc* 19(2):37. <https://doi.org/10.5751/ES-06390-190237>
17. Bocchini P, Frangopol DM, Ummenhofer T, Zinke T (2013) Resilience and sustainability of civil infrastructure: toward a unified approach. *J Infrastruct Syst* 20(2):04014004
18. Gillespie-Marthaler L, Nelson KS, Baroud H, Kosson DS, Abkowitz M (2018) An integrative approach to conceptualizing sustainable resilience. *Sustain Resilient Infrastruct*:1–16
19. Nelson KS, Gillespie-Marthaler L, Baroud H, Abkowitz M, Kosson DS (2019) An integrated and dynamic framework for assessing sustainable resilience in complex adaptive systems. *Sustain Resilient Infrastruct*. <https://doi.org/10.1080/23789689.2019.1578165>

20. Ayyub BM, Wright RN (2016) Adaptive climate risk control of sustainability and resilience for infrastructure systems. *J Geogr Nat Disast* 6(2). <https://doi.org/10.4172/2167-0587.1000e118>. Accessed 15 Aug 2018
21. Ayyub, B. M., Medina, M., Vinson, T., Walker, D., Wright, R. N., AghaKouchak, A., Barros, A. P., Cerino, A. C., Conray, R. P., Fields, R. E., Francis, O. P., Olsen, J. R., Samaras, C., and Vahedifard, F., 2018. *Climate-Resilient Infrastructure: A Manual of Practice on Adaptive Design and Risk Management*. Edited by B.M. Ayyub, ASCE Manual of Practice (MOP) 140, American Society of Civil Engineers, Reston, VA.
22. Ayyub BM, Medina M, Vinson T, Walker D, Wright RN, AghaKouchak A, Barros AP, Cerino AC, Conray RP, Fields RE, Francis OP, Olsen JR, Samaras C, Vahedifard F (2018) Climate-resilient infrastructure: a manual of practice on adaptive design and risk management. In: Ayyub BM (ed) ASCE manual of practice 140. American Society of Civil Engineers, Reston, VA
23. Bruneau M, Chang SE, Eguchi RT, Lee C, D T, O'Rourke AM, Reinhorn M, Shinozuka M, Tierney WAW, von Winterfeldt D (2003) A framework to quantitatively assess and enhance the seismic resilience of communities. *Earthquake Spectra* 19(4):733–752. <http://courses.washington.edu/cee518/Bruneauetal.pdf>. Accessed 8 Aug 2018
24. Mori Y, Ellingwood BR (1993) Time-dependent system reliability analysis by adaptive importance sampling. *Struct Safety* 12(1):59–73
25. Ayyub BM (2014) *Risk analysis in engineering and economics*, 2nd edn. CRC Press, Boca Raton, FL
26. Dial R, Smith B, Rosca G Jr (2014) Evaluating sustainability and resilience in infrastructure: Envision™, SANDAG, and the LOSSAN Rail Corridor. In: *Proceedings of the 2014 international conference on sustainable infrastructure*. ASCE, Reston, VA, pp 164–174

What Can GCC Countries Learn from Well-Established Green Power Markets in Other Countries?



Leila Dagher, Jenny Heeter, and Mohamad Hussein Mansour

1 Introduction

Renewable energy purchases either are typically part of a compliance-based (government-mandated) program or belong to one of the voluntary green power programs. Under government-mandated goals, electricity producers are required to generate a certain percentage of their electricity from renewable sources, while voluntary green power by definition is the voluntary purchase of RE by retail electricity customers over and above what is required from utilities by the government. The latter category includes various options, namely, utility green pricing, utility renewable contracts, unbundled RECs, competitive suppliers, community choice aggregations, power purchase agreements, and community solar. Table 1 shows a description of each of the products and to which customer class(es) it is typically available.

In terms of sales, the compliance-based market dominates the voluntary green power market in all countries. For example, in 2017 the voluntary market represented only about 26% of all US non-hydropower renewable energy sales. As of 2018, 33 countries have a government-mandated RE requirement, and at least 39 countries have some form of voluntary green power program [2].

Driven by several factors (environmental, economical, etc.), in the past few years, all six GCC countries have announced major plans to shift to cleaner renewable electricity production. These plans are essentially government-mandated goals (see next section for more details). Thus, this paper fills a gap by focusing on voluntary customer-driven RE markets - markets that are still missing in the GCC—that can complement the government-mandated objectives. Moreover, we will focus on

L. Dagher (✉) · M. H. Mansour
Institute of Financial Economics, American University of Beirut, Beirut, Lebanon
e-mail: ld08@aub.edu.lb

J. Heeter
National Renewable Energy Laboratory, Golden, CO, USA

Table 1 Voluntary green power programs

Product	Description	Customer classes
Utility green pricing	Utility customers procure green power on a month-to-month basis through an added fee on their utility bill	Residential, small commercial
Utility renewable contracts	Utility customers procure green power from their utility through a special tariff or bilateral contract, typically on a long-term basis sourced from a new renewable energy generator	Large C&I
Unbundled RECs	Retail customers buy RECs separated or “unbundled” from the underlying electricity. This category refers only to sales of unbundled RECs directly to retail customers, it excludes sales of unbundled RECs through other green power products (e.g., utility green pricing) to avoid double counting.	All, mostly C&I and institutional
Competitive suppliers	Customers in competitive electricity markets may select a green power option from an alternative retail electricity supplier	All
Community choice aggregations (CCA)	Communities aggregate their loads to collectively procure green power as a bulk purchaser through an alternative electricity supplier	All, mostly residential and small commercial
Power purchase agreements (PPA)	Customers procure green power through a long-term contract with an off-site renewable energy project	C&I, institutional*
Community solar	Customers buy a subscription in a shared solar project and accrue green power in proportion to their subscription	All, mostly residential and small commercial

Source: NREL [1]

* Residential customers may also sign on-site PPAs. Our focus is on off-site PPAs here

the green power options relevant to the residential sector, given that the residential sector constitutes around 50% (if not more) of all electricity consumed in the GCC [3].

In the voluntary market, the largest two markets have historically been utility green pricing programs and unbundled RECs [1]. Green pricing programs were first offered in the 1990s in several countries where consumers can voluntarily pay a premium for each kWh consumed to cover additional cost of generating electricity from a renewable energy source (RES) [4], while RECs are credits that represent environmental and other non-power attributes of renewable electricity and are measured in single MWh where the owner of the REC can legally claim to have purchased renewable energy. Within the USA, the commercial and industrial sectors constitute most of the voluntary market for RECs, while the residential sector’s REC purchases account for only 1% of all REC sales [1].

While the first unbundled retail REC product was sold in 1998, the first mention of “certificate trading” was in California in 1995, and some European countries had already introduced tradable attribute certificates in 1997 [5]. The number of countries that have adopted RECs since then has increased to 16 in 2005, and by 2017 there were more than 30 countries that have adopted RECs [6]. These countries

include, among others, the USA, Canada, Australia, and India. RECs can enable multiple purchasing types, including unbundled certificate trading and purchases, as well as utility products, competitive supplier products, and power purchase agreements. Countries that have adopted RECs are providing the framework for ensuring that purchasers receive what they are paying for.

2 GCC Background

With about 30% of proven crude oil reserves and about 22% of global gas reserves, the GCC states are the most important oil-producing region in the world [3]. Today, despite being considered developing economies by the United Nations [7], all six GCC countries are considered high income, with GDP per capita of at least \$16,000 (see Fig. 1) [8, 9], with Saudi Arabia and the UAE being the largest two economies [10].

The GCC countries were used to be considered as relatively small consumers of energy compared with Europe, Asia, and North America. However, with rapid economic growth and increased population, these economies have substantially increased their energy consumption. Electricity demand in the region is expected to increase by around 62% in the next decade. All six countries have ambitious plans to invest in renewable energy and energy efficiency for several reasons. First, with lower oil prices, oil exporters have seen a sharp decline in their revenues. Consequently, reducing domestic consumption of oil and gas would increase the exported share and lead to an increase in revenues. Second, renewable energy especially solar is abundant in the region and has become economically viable. Third, the GCC countries are all very high on the list on CO₂ emitters per capita and feel the urge to start curbing down on their emissions (see Fig. 2). Fourth, the GCC states are also very high on the list of electricity—and in general energy—

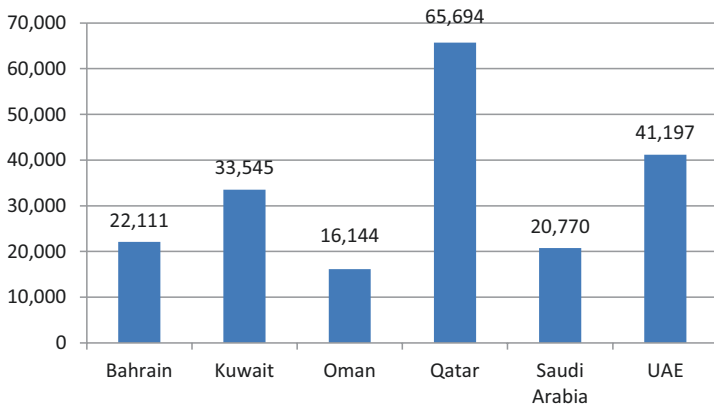


Fig. 1 GDP per capita 2017 (constant 2010 USD). Data source: World Bank [8, 9]

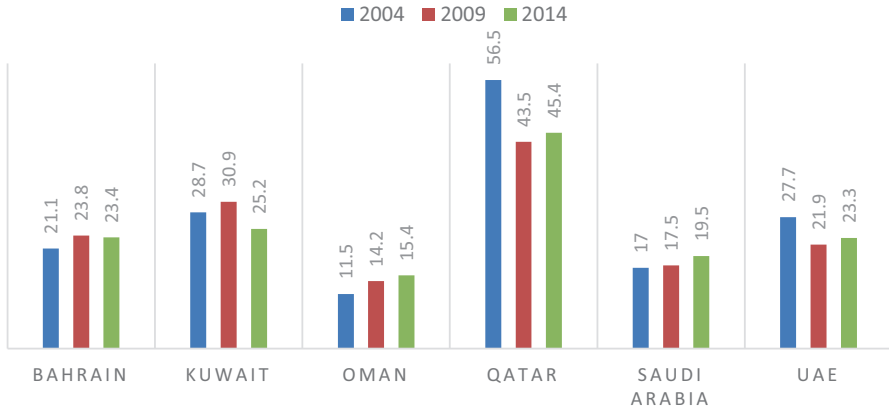


Fig. 2 CO₂ emissions (metric tons per capita). Data source: World Bank

consumption per capita due to the generously subsidized energy prices that the consumers enjoy. Current rates are provided in Fig. 3. Recently, all GCC countries have come up with plans, and some have started implementing a gradual phasing out of electricity subsidies.

Current renewable energy capacity as a percentage of total capacity as well as the goals set in each of the GCC countries is shown in Table 2. Clearly, these countries have set ambitious goals. The next section presents the economic background, followed by a detailed exposition of the electricity sector in each of the six countries, including plans to reach the RE goals.

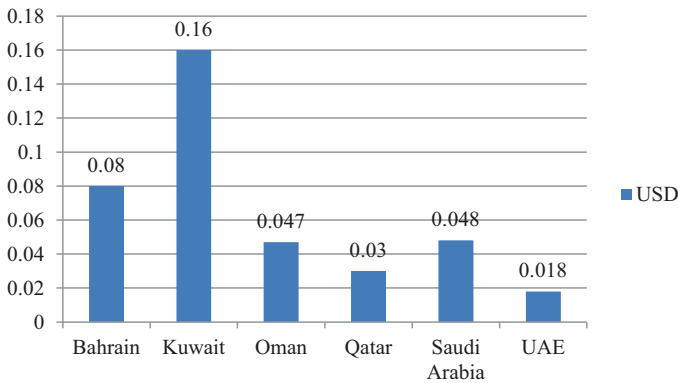


Fig. 3 Electricity rates for the residential sector (2018/2019). Data source: GCC Ministries’ websites. Note: local currency converted to USD

Table 2 Current and planned RE capacity

	Planned RE	RE share 2018
UAE	27% in 2021 and 44% in 2050	2.03%
KSA	3.45GW in 2020, 9.5 in 2023, 30% in 2030	0.18%
Qatar	200–500 MW of solar in 2020	0.42%
Oman	10% in 2025	0.12%
Kuwait	15% in 2030	0.41%
Bahrain	5% in 2025 and 10% in 2035	0.22%

Data source: IRENA [3]

2.1 Bahrain

2.1.1 Current Economic Status

Bahrain and Oman are the only two countries bordering the Persian Gulf which are not members of the Organization of the Petroleum Exporting Countries (OPEC). The Kingdom of Bahrain, a high-income country with a GDP per capita of 47,526 USD (PPP current international \$) in 2017 [8, 9], is the smallest oil producer among the Gulf Cooperation Council (GCC) nations [11]. The total primary energy supply of Bahrain in 2016 reached 2216 ktoe of primary and secondary oil and 12,031 ktoe of natural gas [5].

Due to the dependence of the energy sector completely on fossil fuel, the government aims at diversifying its energy supply sources [12]. In order to shift from dependence on oil to competing globally in including the private sector in the energy sector, Bahrain initiated its Economic Vision 2030. The “Vision” aims at attracting foreign direct investment and to increase reliance on the service sector, tourism, business services, and manufacturing and logistics.

2.1.2 Electricity Sector and Future Plans

With around 4 GW of installed generating capacity, the country is witnessing a similar trend to its neighboring countries; demand for electricity is growing rapidly to cope with the population growth and the expansion of the industrial sector. Currently, only 6 MW of the 4 GW (0.15%) are from renewable sources [3]. Although the Kingdom has initiated a number of power projects to meet the increased needs, so far only modest achievements have been reached in the renewable energy sector.

In early 2017, the Bahraini Government adopted the National Renewable Energy Action Plan (NREAP) and the National Energy Efficiency Action Plan (NEEAP). The NREAP sets a national target for the share of renewable energy (solar, wind,

and waste-to-energy) in total energy generation to reach 5% by 2025 and 10% by 2035.

To reach 5% target by 2025, Bahrain needs to have at least 200 MW of renewable-based energy. One of the projects which is part of the NREAP and NEEAP is the 100 MW Bahrain PV Park which is being developed by BAPCO. Other projects include the Bahrain PV Park 1 (200 MW), Al Dur PV Plant (3 MW), the Al Dur Wind Farm (2 MW), and the Bahrain Waste-to-Energy Project (54 MW) [3].

In total, the planned projects (359 MW) with the existing 6 MW would add up to 365 MW of renewable energy and will amount to around 9% of total energy in the country. Although the announcement of projects seems promising, however there is previous experience of such plans being shelved. One project that was announced in 2014 but its construction is still pending is the 5 MW (USD 25 million) by BAPCO to supply electricity to a few locations [3].

2.2 Kuwait

2.2.1 Current Economic Status

Kuwait is the fifth largest producer of crude oil among the 14 OPEC members and tenth largest producer in the world and holds the world's sixth largest oil reserves [13]. With a GDP per capita of USD 33,545, Kuwait is classified as a high-income country by the World Bank [8, 9] and as a developing economy by the United Nations [7]. In terms of oil production, the country was the tenth largest producer of petroleum and other liquids in 2015 [3]. In 2016, Kuwait supplied 17,659 ktoe of oil and gas and 18,176 of natural gas [14].

According to EIA [15], Kuwait has been aiming to boost stagnant production rates by implementing enhanced oil recovery measures. Despite new discoveries made, Kuwait's regulated oil sector led to a slower exploration and production. In this regard, Project Kuwait was initiated to attract foreign investors in order to boost production capacity to four million b/d by 2020 [15].

2.2.2 Electricity Sector and Future Plans

Similar to the other GCC countries, demand for electricity has been rising tremendously due to population growth and economic growth [16]. This increase in demand has raised the country's reliance on imports of natural gas. Consequently, Kuwait is trying to attract international investment for natural gas development to increase dry natural gas production to satisfy increasing domestic consumption and to reduce dependence on natural gas imports during hot climate periods [15]. With an installed generating capacity of 15.7 GW in 2015 [17, 18], Kuwait will need to reach an estimated capacity of 23 GW by 2021, requiring USD 14 Bn. of investment [19].

Both the New Kuwait Development Plan and current Five-Year Development Plan aim at diversifying the economy [15]. New Kuwait 2035 is expected to help in the creation of three new power companies with particular focus on renewable energy. The government has earmarked USD 9.9 billion. For infrastructure projects including power, and progress is being made on greenfield thermal and renewable projects [19].

In 2018, Kuwait had reached 79 MW of installed renewable-based capacity [3] or 0.4% out of total power generation capacity. The government has set a target of having renewable energy contribute 10% of the total energy mix by 2020 and 15% by 2030, from an installed capacity of 5.7 GW CSP, 4.6 GW solar PV, and 0.7 GW wind [20]. According to KUNA [20], the 10% capacity of RE in 2020 will satisfy around 3% of total energy demand. Kuwait has had several solar projects in recent years such as the Al-Dibdibah Solar PV Plant (1.5 GW) and the Shagaya (70 MW) [3].

Similar to the measures taken by other GCC countries, in May 2017, Kuwait increased the tariff in the commercial sector, and Kuwait's electricity rates were changed to rationalize consumer consumption [19]. Among the diversifying approaches, the Kuwaiti Government plans to boost the use of renewable energy, hence benefiting from more oil exports and lowering gas emissions. The savings through 2030 are estimated at USD 750 million [21].

2.3 *Oman*

2.3.1 **Current Economic Status**

Oman is the largest oil and natural gas producer in the Middle East that is not a member of the Organization of the Petroleum Exporting Countries (OPEC) [11]. Having the lowest GDP per capita among the GCC countries (USD 16,144), Oman is still considered as a high-income country [8, 9]. In 2016, Oman produced 3024 ktoe of primary and secondary oil and 21,087 of natural gas [14].

Similar to its neighbors, Oman is highly dependent on its hydrocarbon sector which accounted for 30% of Oman's GDP in 2017 [22]. In recent decades, Oman has also witnessed the regional trend in fast-rising demand for energy. Oman's geography, abundance of solar resources, and socioeconomic context have helped renewables dominate in applications that have been underexploited by its neighbors such as small-scale roof-mounted solar generation [23].

2.3.2 **Electricity Sector and Future Plans**

With 8.2 GW of electricity generation capacity in 2017 [24], Oman targets a 10% generation mix from renewables (mainly from onshore wind and solar) by 2020 which is equivalent to a capacity of 2.6 GW. In 2017, Oman reached only 17 MW

of installed renewable-based capacity which corresponds to a 0.1% share of total capacity [3].

In 2015, Oman's National Energy Strategy to 2040 was announced in line with the ambitions to diversify the energy mix in the country [3]. The 500 MW Ibri Solar Project was announced in 2017 to be the first utility-scale solar project [25]. Al Amin Solar PV Plant (100 MW) that was constructed by Petroleum Development Oman in November 2018 [3] is another example of the initiative to shift to renewables in Oman. Other smaller projects include the 50 MW wind park at Harweel and the 50 MW Dhofar I Wind Project.

In this regard, and to decrease dependence on natural gas, Petroleum Development Oman (PDO) (which is 60% owned by the state) is collaborating with the solar company GlassPoint to build a 1021 MW large-scale solar EOR project (Miraah) [26]. According to PDO [27], this project is expected to generate 6000 tons of steam per day saving up to 80% or 5.6 trillion BTUs of natural gas and to save over 300,000 tons of CO₂ emissions annually. PDO has also announced its interest to build other PV projects [27].

2.4 Qatar

2.4.1 Current Economic Status

Qatar holds the ninth largest reserves of crude oil in OPEC and the 13th largest in the world with proved reserves of crude oil estimated at 25.24 billion barrels [13]. Although the country is classified as a developing economy by the United Nations [7], Qatar has the second highest GDP per capita (USD 65,694) in the world and the highest among GCC countries [8, 9]. In 2016, Qatar supplied 318 ktOE of primary and secondary oil and 41,797 ktOE of natural gas [14].

Qatar's crude oil and lease condensate production ranks 17th in the world, with most of the country's production sent abroad as exports [13]. In terms of production, the country is the third lowest among the OPEC members, but with an increasing production of non-crude liquids—most of which are a by-product of natural gas production. With 13.7% of the world's natural gas reserves, Qatar is the world's largest exporter of LNG and the world's largest producer of gas [23] with the largest proven natural gas reserves in the region (24.5 trillion cubic meters) and the largest producer of natural gas among the GCC countries (163.3 million tons of oil equivalent) [11].

Given that a significant portion of the country's revenues come from its exports of LNG, crude oil, and petroleum products [3], Qatar, like its neighbors, relies on its energy sector to support its economy. According to the Qatar National Bank, Qatar's earnings from its hydrocarbon sector accounted for 49% of the country's total government revenues in 2014, a figure that has declined over the past 4 years [28].

The LNG expansion along with economic growth has also increased the demand for electricity which in turn made the country consider plans for significant growth

in electricity generation capacity. Similar to other GCC countries, Qatar has acknowledged the need to shift for a more sustainable energy and diversify the energy sources away from the natural resources. To this end, the country launched its Qatar's National Vision 2030 in 2008.

2.4.2 Electricity Sector and Future Plans

Qatar's total electricity generating capacity in 2017 was 8.8 GW, with demand of around 8.2 GW [29]. According to IRENA [3], Qatar reached 43 MW of installed renewable-based capacity in 2017, which amounts to 0.4% of total capacity [3].

Qatar's Second National Development Strategy 2018–2022 strategy introduces a plan that calls for an increase in the use of renewable energy, more specifically 200–500 MW of solar power, by 2020 [30]. In addition, Ayre [31] states that Qatar has expressed its intention to hold auctions for solar power projects on multiple occasions. A new solar project, which is a joint venture between Qatar Petroleum and Qatar Electricity and Water Company, is expected to start operating in December 2020 and is set to reach 1000 MW installed capacity [26]. Two other new solar power projects include the 10 MW Al Duhail Solar PV Park which has the potential to be expanded to 210 MW [3] and the PV solar panels at the Qatar Convention Centre, a 0.7 MW solar PV array [32].

With regard to regulatory framework and policy instruments, IRENA [3] reports that Qatar has been relatively slow in deploying renewables with the notable exception of biogas and municipal waste. The largest waste-to-energy facility (30 MW Mesaieed plant) in the GCC region is located in Qatar [3].

2.5 Saudi Arabia

2.5.1 Current Economic Status

The Kingdom of Saudi Arabia (KSA) is a founding member of OPEC and has the second largest reserves of crude oil in the world after Venezuela (16% of the world's proved oil reserves). It also has the world's sixth largest natural gas reserves [11]. In 2016, Saudi Arabia supplied 136,525 ktoe of oil and 74,165 ktoe of natural gas [14]. The Kingdom, a high-income country [8, 9], is the largest exporter of total petroleum liquids in the world and maintains the world's largest crude oil production capacity at roughly 12 million barrels per day [33].

KSA is the fastest-growing consumer of energy in the MENA region. Due to heavily subsidized domestic oil prices, the country relies on liquid petroleum for approximately 60% of its electricity generation [19]. Petroleum exports are a crucial component of the Saudi economy as it accounted for nearly 75% of total Saudi export value in 2016 [34]. About 60% of Saudi Government's revenues are oil based, and the real GDP growth rate fell significantly in 2016, as a result of the

slowdown in oil-driven growth that year [33]. According to the EIA [34], Saudi Arabia's oil revenues have fallen dramatically as crude oil prices have decreased since mid-2014. Increasing domestic demand for energy is also negatively affecting Saudi revenues. Saudi Arabia is setting future plans to rely less on oil and more on renewable energy.

In addition, and in order to reduce the reliance of its economy on oil, the Saudi Government launched Vision 2030, to help in gradually shifting the Saudi economy away from its dependence on oil [3]. Moreover, Vision 2030 aims to position Saudi Arabia as a leader in renewable energy while at the same time creating jobs and expanding service and knowledge-based industries [10].

In 2017, Saudi Arabia started to move to market rates by reducing subsidies on fuel and electricity [33]. As the government seeks to reform the power sector along with lifting tariffs, the state announced the liberalizing of electricity prices for both the residential and nonresidential sectors. The new prices are expected to reflect the export value of feedstock fuels and higher generation costs [19].

2.5.2 Electricity Sector and Future Plans

According to EIA [5], Saudi Arabia's total electricity installed capacity in 2017 was 83 GW. As part of Vision 2030, the National Renewable Energy Program was launched aiming for 3.45 GW of installed renewable capacity by 2020 and 9.5 GW by 2023 (10% of power generation capacity) [3]. One year after Vision 2030 was launched, the kingdom's renewable capacity in 2017 reached about 142 MW, mostly from solar PV projects (with some 2 MW of onshore wind), based on small-scale demonstrational projects, such as solar-powered buildings and parking lot installations [3]. The share of renewables in total installed power generation capacity reached 0.2% in 2018 [3].

A new city, Neom, is expected to be powered entirely by renewable energy [35].

2.6 United Arab Emirates

2.6.1 Current Economic Status

The United Arab Emirates (UAE) is among the world's ten largest oil producers [23] and is a member of the Organization of the Petroleum Exporting Countries (OPEC) and the Gas Exporting Countries Forum (GECF). The UAE is classified as a high-income country with USD 41,917 GDP per capita [8, 9]. In 2016, the UAE supplied 11,762 ktce of oil and 60,501 ktce of natural gas. In terms of oil production, in 2016 the UAE produced an average of nearly 3.7 million barrels per day of petroleum and other liquids (of which 2.9 million b/d are from crude oil), the seventh highest total in the world [34].

The UAE has also started to move to market-based pricing by reducing subsidies on fuel and electricity, which has further weakened non-oil growth [33]. Like other GCC countries facing rapid growth of domestic demand for electricity, the UAE are working to reduce their dependence on fossil fuels by embracing new energy technologies. The United Arab Emirates' Vision 2021, UAE Energy Strategy 2050, UAE Green Growth Strategy, UAE Future Strategy, and UAE Centennial Plan (2071) all highlight economic diversification and technological innovation (particularly green energy technologies) as pivotal to future development. Ultimately this will result in creating new jobs and expanding service and knowledge-based industries, turning the UAE into a regional leader in clean and sustainable energy.

The UAE leads among the GCC countries in building of smart cities. In 2017 it launched the Energy Plan 2050 to increase the contribution of clean energy and cut dependence on natural gas to generate power in line with UAE Vision 2021. In March 2017, the UAE's Ministry of Energy signed a contract with PricewaterhouseCoopers (PwC) to conduct a technical and economic study of its electricity sector. The deal is in line with the UAE's clean energy strategy. This includes plans to invest USD 163.3 billion to meet demand and aims to generate efficiency savings of around USD 190 billion.

The UAE Government is also leading efforts to raise awareness and build capacity of the private sector through the Ministry of Climate Change and Environment [36]. Such efforts are crucial in order to achieve the UAE Green Agenda 2030 and the National Climate Change Plan 2050. Green growth efforts are expected to result in 4–5.5% higher GDP growth and create 160,000 new jobs by 2030, while accelerating the country's economic diversification efforts and mitigating a substantial portion of carbon emissions [36]. With regard to environmental aspects of shifting to renewable energy, the UAE aims at reducing CO₂ emission by 30% in 2030 [37].

2.6.2 Electricity Sector and Future Plans

The UAE had a 29 GW of total electricity generating capacity in 2016 [5], in which renewable energy contributes around 2% in terms of capacity [3]. According to the UAE Government [38], by 2050, the aim is to increase the share of clean energy in the country's electricity generation capacity to 50% and to expand renewable energy capacity to reach 44 GW. Abu Dhabi and Dubai each have their own targets. Abu Dhabi aims to install approximately 1.5 GW of renewable power by 2020, constituting 7% of its power generation capacity, while the Integrated Energy Strategy of Dubai aims to install 5000 MW of renewables by 2030, constituting approximately 25% of its power generation capacity [37].

According to APICORP [39], the UAE needs to invest USD 35 billion. to meet the 17 GW capacity addition needed over the medium term. APICORP estimates that 10.4 GW of capacity additions are already in execution. The UAE is expected to highly diversify its energy sources in the power mix; it is planning to add nuclear (6%), renewable (44%), and coal-fired electricity generating capacity to accommodate rising demand, while the country currently relies primarily on natural gas [3].

Among the GCC countries, the UAE has installed the most renewable capacity by 2018 with 589 MW [3] and is the largest and fastest-growing solar market in the GCC [37].

According to AFED [36], the UAE Government is promoting public-private partnerships such that the private sector can benefit from participating in, or financing, various large-scale projects. A good example is Dubai's Mohammed bin Rashid Al Maktoum Solar Park. Developed in multiple phases, it will become the world's largest single plot solar park with a total capacity of 5000 MW—enough to power 800,000 homes—when completed in 2030.

3 Lessons from Other Countries

To better understand the GCC countries' opportunities and challenges in introducing voluntary green power markets, it is important to examine the experiences of other countries who were early adopters of green power products. Several developed countries around the world started offering voluntary green power options since the 1990s. Most of these countries introduced an energy-based product in which consumers voluntarily pay a premium for each kWh consumed to cover the additional cost of generating renewable-based electricity [5]. Although more than two decades have passed since the introduction of voluntary renewable energy, available data shows that penetration rates for green pricing programs are still very low. In the USA, one of the first adopter of voluntary-based renewable energy, participation rates are still very low; around 4% in the top 10 programs average and around 2% for the remaining programs [1]. In terms of sales, the voluntary market, including all purchasing types, only accounts for approximately 26% of all US non-hydropower renewable energy sales.

However, with the drop in RE prices, the development of RE sources is now being driven by economics rather than dependent solely on policy. New product types are being offered, many of which provide the opportunity for customers to earn a return on their investment and also source from a local RE generator, which is of interest to many large corporate purchasers. The market changes and new programs might be a game changer for the voluntary green power market.

3.1 Opportunities

Two closely related factors that have been found to impact the decision to join green power markets are (1) existing knowledge about RE environmental attributes and (2) information and marketing campaigns. According to Bird et al. [40], the success in the Netherlands can be due to the aggressive marketing campaigns. Similar evidence has been found for the USA; promoting the advantages of the green plan significantly increases green plan adoption, while promoting the disadvantages of

the gray plan also significantly increases green plan adoption [41]. MacDonald and Eyre [42] note that evidence from Australia shows the marketing campaigns done by the government provided valuable returns to green power investment. Information and knowledge of RE have also shown to be important factors in China [43] and Japan [44]. Nowadays, the spread of information through social media is easy, fast, and relatively cheap. Thus, the GCC countries can take advantage of social media to raise awareness and share information with consumers.

The source of renewable energy can also have a significant effect on WTP for green power. Sundt and Rehtanz [45] look at ten countries and their consumers' WTP for renewable energy showing that WTP depends on the source of renewable energy, where hydropower is the least valued by households, while solar is positively viewed. In line with these results, a more recent study by Bae and Rishi [46] considers both monetary and nonmonetary incentives to study what influences the consumers' uptake in green pricing programs. Results also show that the green pricing program is linked with the type of green energy resources where sources that produce fewer externalities, more jobs, and monetary incentives had a positive effect on consumer uptake. WTP was highest in fuel cells, followed by solar and wind energy [46]. This again works in favor of GCC countries given that most of the planned projects are solar or fuel cells.

Another factor that positively affects participation in the voluntary green power market is the "warm-glow" effect and the related public prestige [47]. The warm-glow effect is when people feel better about themselves by contributing or taking part in something good, like benefiting the environment [48, 49]. In Australia, most respondents select the minimum commitment possible when it comes to green products suggesting a buy-in warm-glow for carbon mitigation [50]. Social status is extremely important in the GCC states, which leads us to expect that prosocial behavior such as purchasing green power will abound.

Trust in the energy supplier or certification of the RE generation also seems to have a significant positive effect on customers' demand for green power [4, 43]. Dagher et al. [4] show that green accreditation has a positive and significant impact on green power consumption. Green accreditation is typically done by a third party to guarantee that the energy supplier is indeed generating electricity from RES. For example, in Australia, the GreenPower Accreditation Program provides verification of energy source [51], while most RE is certified by Green-e in the USA. Therefore, another recommendation for GCC countries is to make it compulsory for any RE supplier to obtain certification by one of the global leaders such as Green-e or DNV GL. Marketing and advertising campaigns for green power should highlight the use of an independent accreditation service.

With regard to the price of green energy, some researchers have argued that the demand for RESs is relatively price inelastic [4, 52, 53]). On the other hand, other studies argue that demand for RESs is affected by price. A report by Pollution Probe [54] investigates the green power market in Canada and finds that effective way to increase the residents' participation is by reducing the price of renewable electricity. The report argues that this can be done in Canada through increasing or broadening Wind Power Production Incentive. The different results between the strands of literature

can be due to the different context and country effects (USA and Canada). For example, success in Sweden is believed to be due to the availability of large quantities of existing hydropower that can be sold at relatively low prices [40]. In the USA, the green power premium has continued to fall for several years now “owing to a combination of higher prices of conventional generation fuels and lower renewable resource costs” [55]. In the USA, relatively low REC prices are one contributing factor to ongoing increases in unbundled REC sales. From 2014 to 2017, REC prices fell by more than 50%, corresponding to a period of rapidly increasing unbundled REC sales.

In general, most RE in GCC nations is expected to come from solar PV whose price has dropped to below 3 cents per kilowatt-hour (kWh) [3], and hence the premium is expected to be rather small. Recently, due to the declining RE prices, many studies are investigating the vanishing premium of green power programs.

Large green pricing programs generally charge lower premiums than smaller programs possibly due to economies of scale [1]. Given that electricity in GCC countries is monopolized by the public utility, it should be able to take advantage of the increasing returns to scale and offer relatively lower prices.

Other factors that have been found to increase WTP are income and education [43, 56, 57]; Bigerna and Polinori 2014; and Liu et al. 2013). There is agreement across the different studies looking at individual characteristics that income and education are positively correlated with WTP. This correlation can explain the different responses between rural areas typically with low education and income levels and urban areas with higher income and education levels. Given that all six GCC countries are considered high-income countries, this should play in favor of any newly established green power market.

3.2 Challenges

MacDonald and Eyre [42] review all markets of green electricity tariffs only to find that high competition markets in energy markets are found to be a key driver of green tariff success. Countries where consumers switched easily between energy producers were more likely to have high enrolment in the green power market [42]. As GCC's electricity sectors are vertically integrated national utilities, this fact will work against newly introduced green power markets. However, in the long run, it might be possible to privatize electricity (in the distribution sector at least) and hence introduce competition in the electricity market.

It is noteworthy to mention that the introduction of premium-based voluntary RE market in the GCC countries might be more challenging in a region where the energy sector has been historically subsidized by the government. Although all six countries have plans to reduce and ultimately get rid of these subsidies, this subsidization has delayed the development of RE projects. Lee and Heo [58] argue that consumers' approval and WTP are essential for implementation of green energy development. Using a contingent valuation method (CV) to study the level of

consumers' WTP in Korea, they show that public's disapproval can terminate such developmental projects. For example, the construction of transmission lines in Korea was suspended due to residents' opposition and protestors even resorting to self-immolation. If consumers oppose the reduction and removal of subsidies, this will potentially hurt green power markets.

3.3 Policy Enabling Environment

In vertically integrated electricity markets, such as those of the GCC countries, policies and programs to allow green power purchasing can be mandated by the government or implemented voluntarily by the utility.

Programs include green pricing, utility renewable contracts, community solar, and unbundled RECs (see Table 1 for program descriptions). Each program type has advantages and disadvantages. First, green pricing products, because of their short-term subscription and price premium, tend to be favored by residential and small- to medium-sized companies without large load. Larger companies tend to be more price sensitive and can find more cost-effective products such as unbundled RECs.

Second, utility renewable contracts, which typically require long-term commitments, are favored by companies that know their future electricity load and will be located in the same utility service territory for the length of the commitment. In the USA, utilities in some cases have created green tariffs in order to draw new load to their service territory, which allows them to earn greater profits. In addition to gaining new load, utilities recover their administrative costs.

Third, community solar, which may be structured similarly to a utility renewable contract, typically has the benefits of a utility renewable contract but uses a smaller, locally sourced renewable energy supply.

Finally, unbundled RECs provide a simplified structure for purchasers, in that they do not need to source renewable energy for each utility account. However, renewable generators may be reluctant to develop new projects if they are not able to secure long-term unbundled REC contracts; they must also secure contracts to sell their generation to the utility. Generators will have to determine how much risk they can take on and what contract lengths and prices (for both energy and RECs) are acceptable to them.

Regardless of which type of program is developed, supportive policies are needed to ensure customer participation. Supportive policies include creating a REC tracking system and ensuring purchases are not used for other government or utility mandates. Other policies, such as those that support RE deployment generally, can also support the market. These could include things such as streamlined permitting and interconnection for RE generators.

REC tracking systems can be developed by third parties, either with funding from a government or without. Two existing tracking systems for RECs internationally include Tradable Instruments for Global Renewables (TIGRs) system developed by APX and the International-REC (I-REC) Standard developed by a nonprofit

organization of the same name. The TIGRs tracking system supports REC issuance and tracking in Indonesia as well as nine other countries, primarily in Asia [59]. TIGRs requires that project owners report generation via a third party, for example, a power system operator, or allow APX to directly connect to project generation meters, read the generation data, and import it into TIGRs after it has been validated [59]. Under the I-REC code of conduct, a third party must audit production data before an I-REC is issued [60].

Having a robust tracking system is one component to ensure that consumers are getting what they are paying for. One of the key barriers for corporate procurement of off-site renewables is the inability to make renewable claims from purchases [61]. In countries with existing renewable energy policies or programs, for example, a renewable portfolio standard or feed-in-tariff, there is a need to ensure that customers are not paying for renewable energy that is already being claimed by someone else. A “claim” can be a formal document stating the renewable use by a given entity or a more informal marketing statement. The Green-e Energy standard provides guidance on what types of claims are double counting [62].

In some cases, REC ownership may not be clearly defined in existing policies or programs, such as a renewable portfolio standard (RPS) or feed-in-tariff (FIT), particularly if a REC system has not been used in a country previously. In those cases, parties should review all contractual documents to determine how RECs should be handled. If the FIT provides a generator with revenue, some parties may argue that the generator is giving up its renewable attributes (RECs) to the utility. Others may argue that if REC ownership is not specified, the generator should be able to keep the RECs (and sell them to others, if they so choose). In any case, the auditing process is intended to ensure that RECs are not being double-sold, double-counted, or double-claimed.

4 Concluding Remarks

In conclusion, the GCC countries are well positioned to introduce a successful voluntary green power market. To set the stage for a good uptake of green power products, (1) awareness and marketing campaigns should be launched early on, (2) certification by an international independent accreditation firm should be made compulsory, and (3) ways to maximize the public prestige factor should be identified. However, even the strongest voluntary markets around the world still suffer from low penetration rates. As noted above, this can soon change with the continuous decline in RE prices. However, in the meantime, the GCC governments can start preparing the ground for a successful introduction of voluntary green power markets.

Acknowledgments The first author would like to thank UCLA’s Institute of the Environment and Sustainability for hosting her as a visiting scholar while this article was being written. Also, funding for conference travel by the Kuwait Foundation for the Advancement of Sciences to present this work as a keynote speaker is greatly appreciated. Special thanks are due to the organizers of

the seventh International Symposium on Environment and Energy Finance Issues (Paris); the International Congress of Energy, Economy and Security (Istanbul); and the Gulf Conference on Sustainable Built Environment (Kuwait) for funding conference travel and for valuable comments by the participants.

References

1. NREL (National Renewable Energy Laboratory) (2018) Status and trends in the U.S. Voluntary green power market (2017 data). <https://www.nrel.gov/docs/fy19osti/72204.pdf>
2. IRENA (International Renewable Energy Agency) (2018) Corporate sourcing of renewables: market and industry trends. https://irena.org/-/media/Files/IRENA/Agency/Publication/2018/May/IRENA_Corporate_sourcing_2018.pdf
3. IRENA (International Renewable Energy Agency) (2019) Renewable energy market analysis: GCC 2019. https://www.irena.org/-/media/Files/IRENA/Agency/Publication/2019/Jan/IRENA_Market_Analysis_GCC_2019.pdf
4. Dagher L, Bird L, Heeter J (2017) Residential green power demand in the United States. *Renew Energy* 114:1062–1068
5. EPA (United States Environmental Protection Agency) (2019) History of voluntary markets. <https://www.epa.gov/greenpower/history-voluntary-markets>
6. Appavou F, Brown A, Epp B, Leidreiter A, Lins C, Murdock HE et al (2017) Renewables 2017 global status report. Renewable Energy Policy Network for the 21st Century. REN21, Paris
7. United Nations (2019). https://www.un.org/development/desa/dpad/wp-content/uploads/sites/45/WESP2019_BOOK-web.pdf
8. World Bank (2019) Electric power consumption (kWh per capita). <https://data.worldbank.org/indicator/EG.USE.ELEC.KH.PC>
9. World Bank (2019). <https://datahelpdesk.worldbank.org/knowledgebase/articles/906519-world-bank-country-and-lending-groups>
10. Government of Saudi Arabia (2018) National transformation program. www.vision2030.gov.sa/en/ntp
11. ESCWA (2016) Electricity sector infrastructure and energy exchange in Arab countries. <https://www.unescwa.org/sites/www.unescwa.org/files/publications/files/infrastructure-electricity-sector-regional-energy-linkages-exchange-english.pdf>
12. University of Bahrain (2018) The Kingdom of Bahrain sustainable energy policies and initiatives. Manama. www.wesii.uob.edu.bh/images/Presentations/TheKingdomofBahrainSustainableEnergyPoliciesandInitiatives.pdf
13. OPEC (Organization of the Petroleum Exporting Countries) (2018) Annual statistical bulletin. www.opec.org/opec_web/en/press_room/5027.htm
14. International Energy Agency IEA (2019). Data retrieved at <https://www.iea.org/countries>
15. EIA (2016) Country analysis brief: United Arab Emirates. www.eia.gov/beta/international/analysis_includes/countries_long/United_Arab_Emirates/uae.pdf
16. Arab Union of Electricity (2017) Statistical bulletin. www.auptde.org/Publications.aspx?CID=36&lang=en
17. EIA (2016) Country analysis brief: Bahrain. www.eia.gov/beta/international/analysis.php?iso=BHR
18. EIA (2016) Country analysis brief: Kuwait. www.eia.gov/beta/international/analysis_includes/countries_long/Kuwait/kuwait.pdf
19. Middle East Electricity (MEE) (2018) GCC power market. <https://www.middleeastelectricity.com/content/dam/Informa/Middle-East-Electricity/en/pdf/AET18DME-EJ-GCC%20Power%20Market%20Report%202018.pdf>

20. Kuwait News Agency (2018) Kuwait eyes three pctshift from renewable energy by '20 – KISR, KUNA, 23 January. www.kuna.net.kw/
21. Xinhua Net (2018) Kuwait reaffirms commitment to renewable energy, Xinhua Net, 7 May. www.xinhuanet.com/english/2018-05/07/c_137159921.htm
22. Central Bank of Oman (2017) Annual report 2017. https://www.nbo.om/en/PublishingImages/Pages/Forms/AllItems/NBO%20Annual%20Report_EN_Web.pdf
23. BP (British Petroleum) (2018) BP statistical review of world energy. www.bp.com/content/dam/bp/en/corporate/pdf/energy-economics/statistical-review/bp-stats-review-2018-full-report.pdf
24. Oman National Center for Statistics and Information (2019). Retrieved at www.ncsi.gov.om
25. Bellini E (2018) Oman reveals pre-qualified developers for 500 MW solar tender. www.pv-magazine.com/2018/04/30/omanreveals-pre-qualified-developers-for-500-mw-solar-tender/
26. RCREEE (Regional Center for Renewable Energy and Energy Efficiency) (2018) The role of (ICOs) in the reduction of GHG emission through RE & EE, and main challenges. http://www.rcreee.org/sites/default/files/current_and_future_role_of_renewable_energy_12-11.pdf
27. Petroleum Development Oman (PDO) (2018) PDO inaugurates solar car park. <https://www.pdo.co.om/en/news/press-releases/Pages/PDO%20Inaugurates%20Solar%20Car%20Park.aspx>
28. Qatar National Bank (QNB) (2012) Non-hydrocarbon 'tops 50% of Qatar GDP'. <https://www.gulf-times.com/story/421989/Non-hydrocarbon-tops-50-of-Qatar-GDP>
29. The Peninsula (2017). Retrieved at <https://thepeninsulaqatar.com/article/24/05/2017/Qatar-s-power-generation-capacity-to-surge-by-50>
30. MDPS (Ministry of Development Planning and Statistics) (2018) Qatar second national development strategy 2018-2022. www.mdps.gov.qa/en/knowledge/Documents/NDS2Final.pdf
31. Ayre J (2015) Qatar close to opening 200 MW solar tender. www.cleantechnica.com/2015/01/29/qatar-close-opening-200-mwsolar-tender-reportedly/
32. Alhaj M (2017) Implementation of rooftop solar PV in Qatar through the roof rental business model. *Modern Environmental Science and Engineering* 3(2):115–122. www.researchgate.net/publication/318397559_Implementation_of_Rooftop_Solar_PV_in_Qatar_through_the_Roof_Rental_Business_Model
33. IMF (International Monetary Fund) (2017) Gulf Cooperation Council: the economic outlook and policy challenges in the GCC countries. www.imf.org/en/Publications/Policy-Papers/Issues/2017/12/14/pp121417gcc-economic-outlook-and-policychallenges
34. EIA (2017) (U.S. Energy information administration) Country analysis brief: Saudi Arabia. www.eia.gov/beta/international/analysis_includes/countries_long/Saudi_Arabia/saudi_arabia.pdf
35. Government of Saudi Arabia (2019) Vision 2030. www.vision2030.gov.sa/en
36. Arab Forum for Environment and Development (AFED) (2018) Financing sustainable development in the Arab countries. <http://www.afedonline.org/webreport2018/AFEDReport-financingSDinArabCountries2018-.pdf>
37. ESCWA (2018) Evaluating renewable energy manufacturing potential in the Arab region: Jordan, Lebanon, United Arab Emirates. <https://www.unescwa.org/sites/www.unescwa.org/files/publications/files/evaluating-renewable-manufacturing-potential-arab-region-english.pdf>
38. UAE Government (2018) UAE Energy Strategy 2050. www.government.ae/en/about-the-uae/strategies-initiativesand-awards/federal-governments-strategies-and-plans/uaeenergy-strategy-2050
39. APICORP (Arab Petroleum Investments Corporation) (2018) Renewables in the Arab world: maintaining momentum. www.apicorp-arabia.com/Research/EnergyResearch/2018/APICORP_Energy_Research_V03_N08_2018.pdf
40. Bird L, Wüstenhagen R, Aabakken J (2002) A review of international green power markets: recent experience, trends, and market drivers. *Renew Sust Energ Rev* 6(6):513–536
41. Cardella E, Ewing B, Williams RB (2018) Green is good—the impact of information nudges on the adoption of voluntary green power plans (no. 2015-2018-151)

42. MacDonald S, Eyre N (2018) An international review of markets for voluntary green electricity tariffs. *Renew Sust Energy Rev* 91:180–192
43. Xie BC, Zhao W (2018) Willingness to pay for green electricity in Tianjin, China: based on the contingent valuation method. *Energy Policy* 114:98–107
44. Nomura N, Akai M (2004) Willingness to pay for green electricity in Japan as estimated through contingent valuation method. *Appl Energy* 78(4):453–463
45. Sundt S, Rehdanz K (2015) Consumers' willingness to pay for green electricity: a meta-analysis of the literature. *Energy Econ* 51:1–8
46. Bae JH, Rishi M (2018) Increasing consumer participation rates for green pricing programs: a choice experiment for South Korea. *Energy Econ* 74:490–502
47. Harbaugh WT (1998) What do donations buy? *J Public Econ* 67(2):269–284
48. Andreoni J (1989) Giving with impure altruism: applications to charity and Ricardian equivalence. *J Polit Econ* 97(6):1447–1458
49. Andreoni J (1990) Impure altruism and donations to public goods: a theory of warm-glow giving. *Econ J* 100(401):464
50. Ma C, Burton M (2016) Warm glow from green power: evidence from Australian electricity consumers. *J Environ Econ Manag* 78:106–120
51. GreenPower (2015) National GreenPower accreditation program status report, 2015. <http://www.greenpower.gov.au/News/Q4-2015-Quarterly-Report-released/~media/B1AD55F463D14BF8829B7EAEDB572DEF.PDF>
52. Wiser R, Olson S, Bird L, Swezey B (2005) Utility green pricing programs: A statistical analysis of program effectiveness. *Energy Environ* 16(1):47–68
53. Mewton RT, Cacho OJ (2011) Green power voluntary purchases: price elasticity and policy analysis. *Energy Policy* 39(1):377–385
54. Tampier M, Probe P (2002) Promoting green power in Canada. *Pollution-Probe*, Toronto, p 209
55. Bird L, Dagher L, Swezey B (2007) Green power marketing in the united states: a status report, 10th edn. National Renewable Energy Laboratory, Golden, CO. NREL/TP-670-42502
56. Bigerna S, Polinori P (2014) Italian households' willingness to pay for green electricity. *Renew Sustain Energy Rev* 34:110–121
57. Liu W, Wang C, Mol AP (2013) Rural public acceptance for renewable energy deployment: the case of Shandong in China. *Appl Energy* 102:1187–1196
58. Lee CY, Heo H (2016) Estimating willingness to pay for renewable energy in South Korea using the contingent valuation method. *Energy Policy* 94:150–156
59. APX (2019) TIGRs overview. <https://apx.com/tigrs-overview>. Accessed 9 Aug 2019
60. I-REC Standard (International REC Standard) (2015). http://www.irecstandard.org/assets/doc_3994.pdf. Accessed 9 Aug 2019
61. Bird L, Heeter J, O'Shaughnessy E, Speer B, Cook O, Jones T et al (2017) Policies for enabling corporate sourcing of renewable energy internationally: a 21st century power partnership report (no. NREL/TP-6A50-68149). National Renewable Energy Lab. (NREL), Golden, CO, USA
62. Center for Resource Solutions (2017) <https://www.green-e.org/docs/energy/framework/Green-e%20Framework%20for%20Renewable%20Energy%20Certification.pdf>. Accessed 9 Aug 2019

Analysis of Optimal Energy Performance for Commercial Buildings in the GCC Region

Fatemah Ashraf, Benjamin Park, and Moncef Krarti

1 Introduction

Bahrain, Kuwait, Kingdom of Saudi Arabia, Oman, Qatar, and the United Arab Emirates are countries located in the Middle East and form an alliance known as the Gulf Cooperation Council (GCC) based on economic and political agreements. The economy of these six countries depends heavily on oil and gas for domestic energy consumption and export revenues [1]. The GCC region holds almost 40% and 20% of the world's known oil and gas reserves, respectively [2]. The national GCC energy consumption has significantly increased in the last decade due to a rapid growth in population size and economic development. By 2020, the population is expected to increase by 30% from the year 2000 and reach 53.5 million, with a projected 56% increase in gross domestic product (GDP) [3]. Furthermore, international companies have established significant base operation in most GCC countries due to their relatively low prices in energy, labor, and taxes [4]. As a result, between 2000 and 2010, energy consumption attributed to buildings has doubled as outlined in Fig. 1 and is expected to increase annually by 10–15% rate until the year 2020 [2]. As clearly indicated in Fig. 1, buildings in the GCC region consume almost exclusively electricity to operate.

Table 1 shows the electrical power capacity, average electricity price, electricity annual consumption per person, and the per-capita annual carbon emission for all GCC countries obtained from various sources [1–3]. In particular, Table 1 indicates that the GCC region has 115,287 MW of available electric power generating capacity with 69% from natural gas and 31% from oil products. The GCC region is considered to be one of the world's largest per-capita contributors to greenhouse gas

F. Ashraf · B. Park · M. Krarti (✉)
Department of Civil, Environmental, and Architectural Engineering,
University of Colorado at Boulder, Boulder, CO, USA
e-mail: krarti@colorado.edu

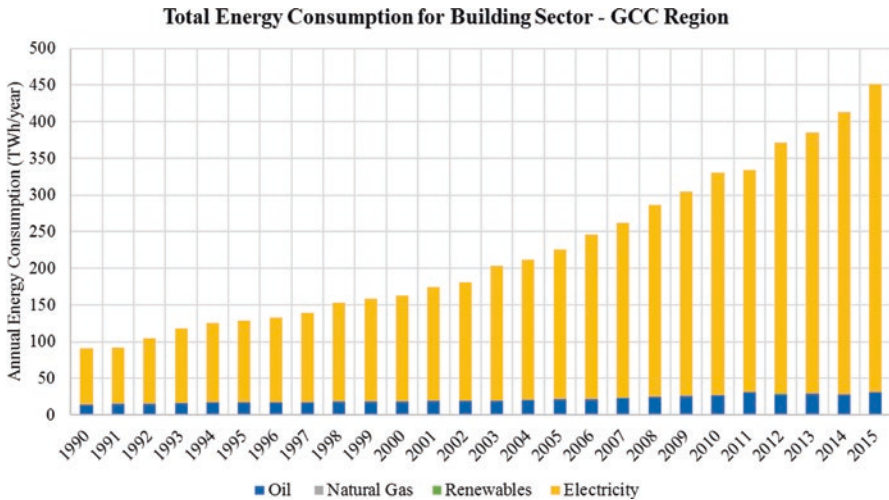


Fig. 1 Total annual energy use of the building sector in the GCC region between 1990 and 2015

Table 1 Electricity prices, energy use, and carbon emission indicators for GCC countries

Country	Cost of electricity (\$/kWh) ^a	Electricity generation capacity (MW) ^b	Electricity consumption per capita (kWh/person) ^c	Total final energy consumption per capita (TOE/person) ^c	CO ₂ emissions per capita (tons/person) ^d
Bahrain	0.008	3889	20,190	4.568	23.450
Kuwait	0.007	18,000	14,951	4.523	25.224
Oman	0.026	8750	6588	4.548	15.443
Qatar	0.022	8900	17,460	8.769	45.423
Saudi Arabia	0.013	46,400	9926	4.6	19.529
UAE	0.080	29,348	12,916	5.805	23.202
GCC	0.041	115,287	147	0.095	0.865

^aAverage prices in 2014 for residential buildings estimated based on 500 kWh of consumption [28]

^bData for 2015 obtained from IRENA [29]

^cData for 2015 obtained from IEA [1]

^dData for 2014 obtained from the World Bank [5]

emissions with all six countries accounting for the top 25 highest carbon dioxide emissions per capita [2].

The average building energy consumption per capita for the GCC region has been increasing significantly over the last two decades as illustrated in Fig. 2 especially when compared to the same metrics in the world. However, the GCC region per-capita building total energy use remains lower compared to the values reported for the EU and especially the USA as illustrated in Fig. 2a [1]. It should be noted that the building energy consumption per capita for EU and the USA has started to decline since 2009 even though they remain significantly higher than the global

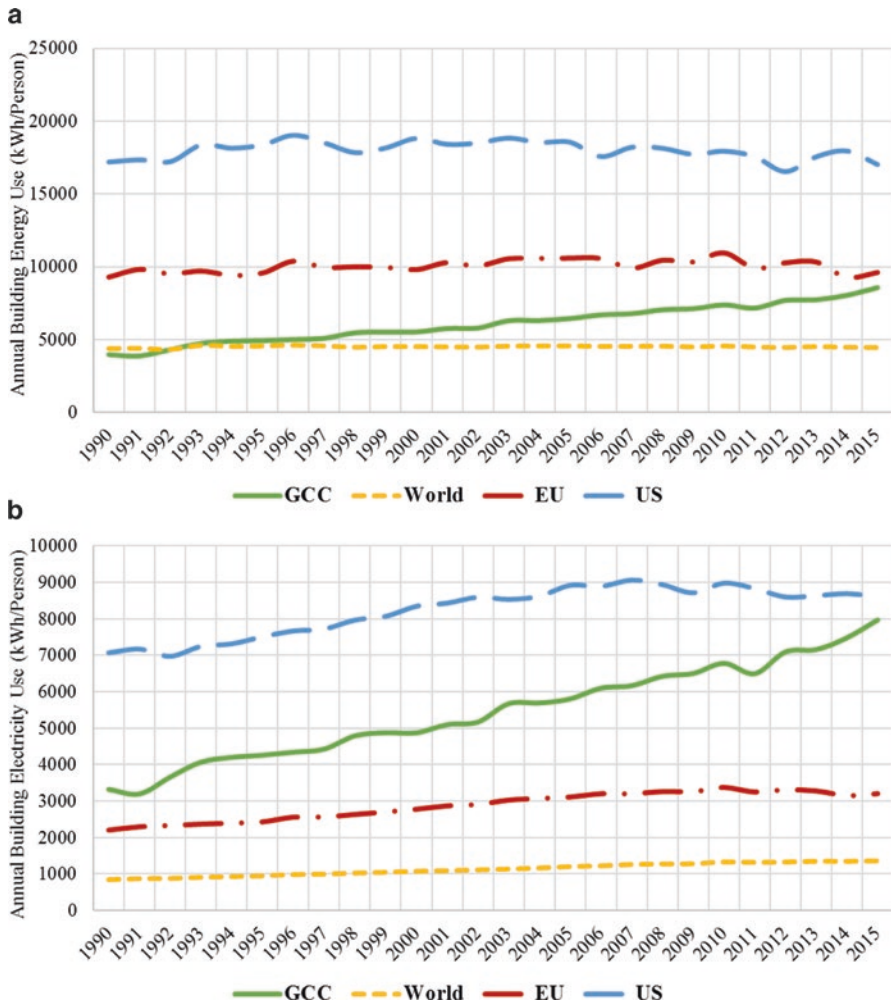


Fig. 2 Annual per-capita building (a) total final energy consumption and (b) total electricity consumption of the GCC region compared to those of the USA, EU, and world

average. The rate of increase in the GCC region is even more pronounced for the per-capita building electricity consumption compared to that observed for the world, EU, and the USA as outlined in Fig. 2b. Currently, buildings consume almost the same electricity per capita in the GCC region than that reported for the USA.

Using a commonly used building energy performance indicator, building energy use per floor area or energy use intensity (EUI) data are compiled for the GCC region and compared to those in other regions in the world as listed in Table 2 [32]. Specifically, Table 2 clearly indicated that the EUI values for the GCC have been increased significantly between 2000 and 2012 while and EUI values estimated for

Table 2 Energy use intensity (expressed in kWh/m²) for the building sector for the Arab region, world, USA, EU, China, and India estimated for 2000, 2006, and 2012

Country region	2000	2006	2012
World	200	175	165
EU	223	215	187
USA	212	207	197
China	131	108	102
India	195	180	165
Arab region ^a	196	238	273

^aEstimated using the average building floor area estimations discussed in Sect. 3.3

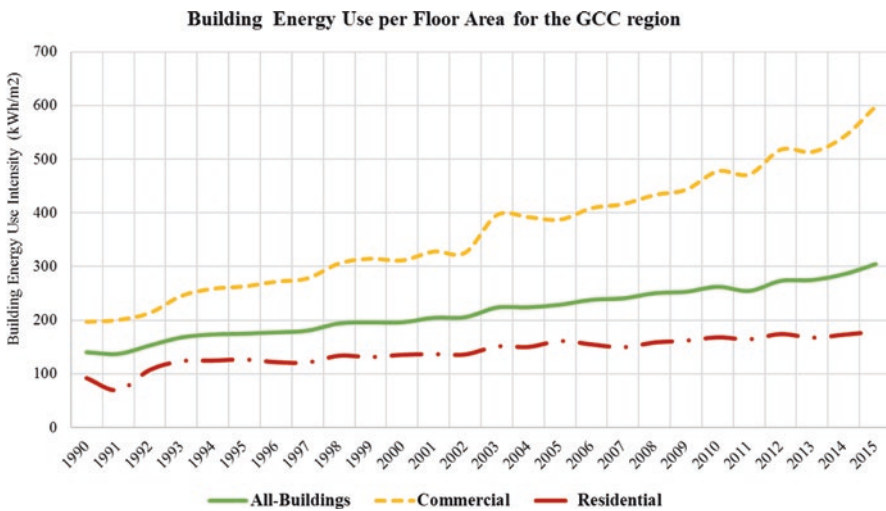


Fig. 3 Energy use intensity variations for commercial, residential, and all building types for the GCC region during the 1990–2015 period

the world, EU, USA, China, and India are generally decreasing over the same period [32]. The increase of standards of living and the lack in any substantial energy efficiency programs have been suggested as the main reasons for this decrease in energy efficiency levels of the building sector in the GCC region [32].

Figure 3 shows the EUI variations for the 1990–2015 period for the GCC region by building type. It is clear that the EUI values for the commercial buildings are significantly higher than those for the residential buildings with the difference gaps widening especially since 2000. The GCC region has seen its commercial buildings’ EUI doubled from 311 kWh/m² in 2000 to 598 kWh/m² in 2015. Meanwhile, the residential building sector EUI has slightly increased by 31% from 136 kWh/m² in 2000 in 2015. This trend is most likely attributed to the prevalent use of energy-intensive equipment in the commercial building sector including AC systems within all the GCC countries.

In this paper, potential benefits of reducing energy consumption for commercial buildings are evaluated for all the countries in the GCC region. In particular, optimized designs and energy retrofit measures are analyzed to assess their impacts for new and existing buildings in each GCC country.

First, a review of the literature is summarized to identify the various reported design and retrofit options suggested to improve the energy performance of buildings within the GCC region. Then, a detailed evaluation is described to assess the benefits for implementing energy efficiency measures for prototypical commercial buildings located in representative locations within the GCC region. A bottom-up approach is then used to estimate the impacts of scaling-up energy efficiency programs for the commercial building sector in all the GCC countries.

2 Literature Review

This section provides a brief summary of the reported studies specific to the building energy performance and potential benefits of implementing energy efficiency programs and policies for each country within the GCC region.

2.1 *United Arab Emirates*

United Arab Emirates (UAE) has experienced over the last two decades a rapid urban growth leading to significant increase in carbon dioxide emissions per capita, as well as in energy consumption. In order to maintain comfortable indoor environment, UAE requires regular air-conditioning that represents over 60% of the electrical peak demand during the summer season and 40% of the average annual energy consumption. The high space cooling demands are due to the high design temperatures (45 °C dry bulb, 30.6 °C wet bulb), humidity (70% summer, 80% winter), and solar irradiance (20 MJ/m²/day average annual global horizontal irradiance) [6]. Furthermore, the increase in the country's building energy consumption has intensified by delayed implementation and enforcement of adopted energy efficiency codes and by the relatively low energy prices [6]. Therefore, energy efficiency measures need to be applied to both new and existing buildings in order to reduce the country's energy consumption. The impacts on energy performance of UAE buildings of some design and retrofit options have been outlined by several studies reported in the literature as summarized in the following sections.

Geometric characteristics such as shape, layout, orientation, and window size can significantly affect the energy consumption of a building since they dictate exposure to climatic factors such as thermal, wind, and solar energy [6]. A study by Abounaga et al. [9] compared four residential buildings that had different building orientations in the city of Al-Ain. The study concluded that by limiting the window to wall ratio (WWR) to 1:6, and by constraining the windows to two orientations, building energy savings can reach up to 55%.

The addition of thermal insulation and/or a reduction in the absorbed solar radiation on the building's exterior surfaces can significantly reduce cooling loads. In the last decade, UAE has established prescriptive requirements for the thermal performance of building envelopes. In Dubai, U-values are restricted to a maximum of $0.30 \text{ W/m}^2\text{-K}$ for roofs and $0.57 \text{ W/m}^2\text{-K}$ for walls as required by the Dubai Green Building Regulations [6]. As for Abu Dhabi, U-values have to be lower than $0.14 \text{ W/m}^2\text{-K}$ for roofs and $0.32 \text{ W/m}^2\text{-K}$ for walls [10]. Friess et al. [11], Radhi [12], and Al-Masri et al. [13] conducted experimental analyses for residential villas located in Dubai, Al-Ain, and Abu Dhabi, respectively. They tested the effects of thermal insulation and thermal mass on the building's energy consumption. Specifically, Friess et al. [11] indicated that a villa in Dubai achieved 23% in electrical energy savings when only 50-mm EPS insulation was added to 54% of the building's enclosures, which helped reduce the wall's U-value from $2.40 \text{ W/m}^2\text{-K}$ to $0.60 \text{ W/m}^2\text{-K}$. However, when the entire villa's perimeter was insulated with additional insulation using 160-mm EPS insulation to further reduce the wall's U-Value to $0.23 \text{ W/m}^2\text{-K}$, only additional 11% of electrical savings were achieved. Radhi [12] conducted a similar experimental analysis on a villa located in Al-Ain. He concluded that a total of 19% of savings can be achieved in cooling energy use if wall and roof U-values decrease from $2.32 \text{ W/m}^2\text{-K}$ and $0.60 \text{ W/m}^2\text{-K}$ to $0.30 \text{ W/m}^2\text{-K}$ and $0.23 \text{ W/m}^2\text{-K}$, respectively. Radhi [12] also achieved a 13% reduction in cooling energy use when the concrete thickness was increased from 150 mm to 250 mm. Another study conducted by Al-Masri [13] tested the effect of adding both insulation and thermal mass on a villa located in Abu Dhabi. A total energy reduction of 3% was achieved when insulation thickness was increased from 50 mm to 100 mm. However, only 1% energy reduction was achieved when the building's thermal mass increased by changing the wall concrete layer thickness from 250 mm to 400 mm. Therefore, only adding the appropriate levels of thermal insulation and thermal mass to the building's envelope can effectively decrease the building's total energy consumption.

Solar heat gains can significantly increase the building's cooling thermal loads in UAE. Currently, Dubai Green Building Regulations requires all new buildings to have 75% of their exposed walls coated with paintings that have a minimum reflectance value of 45% and for all low and flat roofs to have a minimum Solar Reflective Index of 78 [10]. Radhi [14] tested the effect of solar heat gains on a three-story university building's wall cladding system in Dubai. Al-Sallal [15] investigated the effect of solar absorption using various landscaping options for a villa located in Abu Dhabi. He concluded that adding trees to reduce direct and reflected solar heat gains can reduce the wall and window thermal loads by 18% and 31%, respectively, and reduce the total villa's cooling energy by 6%. M. Haggag [16] studied the effect of a green wall system on energy performance of an institutional building in Al-Ain. The analysis found that the green wall helped reduce the temperature of the building's external wall by a range of $5\text{--}13 \text{ }^\circ\text{C}$ and hence reduced the building's cooling thermal loads.

Since UAE has high solar irradiance and sky illuminance levels, Dubai Green Building Regulations requires all new buildings to have 50% of their glazed walls

and be located in the northern facades. Furthermore, buildings with facades that are more than 60% glazed require a maximum U-Value and shading coefficient of 1.9 W/m²-K and 0.25, respectively, and a minimum of 0.1 light transmittance [10]. Aboulnaga [9] conducted a study on a two-story residential building in Al-Ain to test the thermal performance of various window glazing designs. A total of 55% of total energy savings were achieved when the building's windows were restricted to the northern and eastern elevations using 10–20% window to wall ratios. Al-Masri [13] evaluated the effect of window glazing type for a 14% glazed residential building in Dubai. The study indicated that 12% and 15% of energy savings were achieved when single glazed windows were modified to double and triple low-e glazed windows, respectively. Friess et al. [11] investigated the effect of changing double glazed windows to triple glazed windows with low-e and high reflectivity properties on a 21% glazed villa in Dubai. It is found that the villa's annual energy consumption decreased by 5%. Hammad et al. [17] tested the effect of adding lighting controls and external dynamic louvres on a 60% glazed small office building in Abu Dhabi. The building experienced a decrease of 28–34% in its annual energy consumption. Al-Sallal [15] also tested the effect of external shading techniques by adding vegetation outside a villa located in Abu Dhabi. He demonstrated a total of 7% reduction in total energy consumption.

Some studies analyzed the effects of introducing natural ventilation into UAE low-rise buildings. Using computational fluid dynamics (CFD) models, it is found that cooling energy can be reduced by 30% when outdoor conditions were suitable and occupants relied on natural ventilation by opening windows than turning on their air-conditioners [6]. The use of courtyards, wind towers, and solar chimneys into the building's layout can further reduce the energy consumption by 35–73%, depending on the mixed mode of ventilation strategy used [6].

2.2 Oman

Buildings in Oman account for more than 75% of Oman's total electricity consumption. It is estimated that without any energy efficiency program, Oman will experience significant increase in energy consumption and electrical peak demand to reach 55,288 GWh and 11,240 MW, respectively, by 2030 [18]. Currently, Oman has no enforceable energy efficiency programs for the building sector. Moreover, only limited reported studies have evaluated options and impacts to improve the energy performance of new and existing buildings in Oman. Krarti and Dubey [18] studied the impact of a wide range of energy efficiency measures and their effect on various residential and commercial buildings located in Oman. They found that optimal set of energy efficiency measures applied to all building types can reduce energy use and electrical peak demand by over 50% compared to current design practices [18]. Moreover, they found that a basic energy retrofit of the existing residential building stock in Oman can achieve savings of 957 GWh in annual energy consumption and 214 MW in electrical peak demand [18]. Mallela et al. [19] found

that through simulation analysis 26% in annual energy savings can be achieved for a building located in Oman when the cooling set point was increased from 20 °C to 24 °C and when lighting consumption was decreased by 25%. Malik [20] examined the impact of retrofitting lighting and air-conditioning measures on commercial and governmental building stocks in Oman. He found that reductions can reach 596 MW in electrical peak demand and 44 TWh in annual energy consumption generating up to 597 millions of dollars in savings.

2.3 Qatar

Limited analyses have reported to assess impacts of energy efficiency measures on building thermal performance in Qatar. Kharseha et al. [22] indicated that 46% reduction in total cooling thermal load can result for a building located in Qatar when (1) thermal insulation was added to the building's walls and roof, (2) the cooling set point was increased from 22 °C to 24 °C, and (3) more energy-efficient lighting fixtures were installed. Krarti et al. [21] evaluated the benefits of multiple energy efficiency measures for both new and existing buildings. The investigated energy efficiency measures include addition of thermal insulation, implementation of improved glazing, use of shading devices, installation of better efficacy lighting fixtures, increase of cooling temperature set points, and specification of high energy performance HVAC systems. As a result of optimal designs and retrofits, residential buildings can achieve savings of 58–65% in annual energy consumption and 66–70% in electrical peak demand of 7–66%. Similarly, savings obtained for commercial/governmental found to range between 56% and 60% for annual energy consumption and 61% and 65% for electrical peak demand. Krarti et al. [21] estimated that the combined impacts of improvement energy performance of new building construction and existing building stock can reduce the annual energy consumption and electrical peak demand by 11,000 GWh and 2500 MW, respectively.

2.4 Kingdom of Saudi Arabia

The building sector accounts for the majority of the total electricity consumed in the Kingdom of Saudi Arabia (KSA). Several studies and analyses have been carried out to assess the impacts of adopting renewable energy and energy efficiency programs for various KSA sectors including buildings [23]. In particular, Abd-ur-Rehman et al. [24] investigated the impact of applying the International Energy Conservation Code (IECC) as a standard residential building in Saudi Arabia. The results indicated that significant energy use savings could be achieved including 56% for space cooling, 37% for space heating, 46% for lighting, and 27% for appliances against current design practices. Furthermore, Krarti et al. [23] used a detailed simulation analysis to determine optimal sets of measures to improve the energy

performance for both new and existing buildings. Implementing and enforcing these optimal set of measures for new KSA buildings can reduce the annual energy consumption and peak demand by 1751 GWh and 468 MW, respectively. Moreover, retrofitting the existing building stock was found to be highly cost-effective and provide significant economic, environmental, and social benefits. For instance, a level 3 retrofit of residential building stock can results in an annual decrease of 1.3 million tons in carbon emissions [23]. However, level 2 and level 3 retrofit programs require significant investments to be implemented with estimated costs of \$104 billion and \$207 billion, compared to level 1's \$10 billion. Therefore, implementing level 1 retrofits on the country's entire building stock can be highly cost-effective. Finally, utilizing energy efficiency programs on KSA's residential and commercial building can save 27% and 30% on energy consumption and electrical peak demand, respectively [23].

2.5 Kuwait

Buildings in Kuwait consume 70–80% of the country's generated electrical power. Air-conditioning systems account for the majority of the consumed energy, since Kuwait is situated in a desert climate with an average ambient air temperature of 45 °C and intense solar radiation that can reach up to 940 W/m² on horizontal surfaces during the summer [8]. Krarti [7] investigated the impact of implementing and retrofitting new and existing buildings with energy efficiency measures. A base case model for a villa was used, and the building operations and schedules were collected from surveys in order to establish an analysis of the impact of retrofitting residential buildings on the country's energy consumption, peak demand, and carbon dioxide emissions. The building characteristics of the base case model were modified to match the Ministry of Electricity and Water's (MEW) energy code for buildings established in 1983 against the energy code for buildings established in 2010 [25]. Energy-efficient measures included adding wall and roof thermal insulations, modifying window types, implementing shading devices and techniques, reducing lighting wattage per square feet, adding 8.2 ft. of fence walls around the building, and utilizing HVAC equipment with a higher coefficient of performance (COP). As a result, the 2010 energy code for buildings achieved 23% of energy savings compared to the 1983 energy code since it had more stringent requirements. Implementing and enforcing optimal design and operating strategies from the 2010 energy code on new construction can reduce the annual energy consumption and peak demand by 164 GWh and 94 MW as well as decrease the annual emissions of carbon dioxide by 143×10^3 tons. Furthermore, an additional study conducted by Ameer and Krarti [26] confirmed that implementing the current Energy Conservation Code of Practice in comparison with MEW's 1983 energy code can yield a total of 22% in energy savings annually, as well as decrease the electrical peak demand by 24%, and decrease the carbon dioxide emissions by 17 tons per year for each individual residential building in Kuwait.

However, Krarti [7] recommended that in order to further improve the energy efficiency of the building sector in Kuwait, the Ministry of Electricity and Water should update the energy code every five years to incorporate more stringent requirements and to perform energy efficiency retrofits for the residential buildings and then for the entire building sector in Kuwait. As a result, significant economic and environmental benefits can be achieved in Kuwait if both residential and commercial buildings adopt the stringent requirements.

2.6 Bahrain

The building sector in Bahrain consumes the majority of the total annual energy, with residential and commercial buildings accounting for 54% and 29% of the total energy consumed, respectively [27, 28]. However, only limited energy efficiency standards have been adopted in Bahrain to reduce energy consumption in the building sector especially for the existing building stock. Radhi [27] investigated the benefits of retrofitting a governmental building in Bahrain and found that 30% of monthly energy savings can be achieved by adding insulation to the roof and walls and installation of high efficiency lights and equipment. Furthermore, retrofitting the building's operation measures such as raising the set point temperature yielded 15–40% of savings in heating and cooling loads [28].

2.7 Review Summary

Countries in the Gulf Cooperation Council (GCC) have been witnessing a major development in their urban and socioeconomic growths which result in a significant increase in their energy demand. The building sector is responsible for a significant fraction of the increased energy consumption. Based on the reported analyses for the building sector, Table 3 summarizes the range of energy savings for each GCC country when energy efficiency measures are implemented mostly in residential buildings.

Table 3 Range of reported energy savings for improved buildings in the GCC region

Country	Range of energy savings	Sources/references
Bahrain	28–71%	[27, 28]
Kingdom of Saudi Arabia (KSA)	27–56%	[23, 24]
Kuwait	22–42%	[7–26]
Oman	57–66%	[18]
Qatar	58–65%	[21]
United Arab Emirates (UAE)	46–59%	[6]

As noted throughout the literature review, the reported analyses are mostly limited to improving the energy performance of residential buildings within the GCC region. It is the aim of the study presented in this paper to evaluate and assess the impact of providing optimal design and retrofit energy efficiency alternatives for new and existing commercial buildings in the GCC region. The results of the analysis can be suitable to investigate the effect of scaling-up energy efficiency programs to promote high performance residential and commercial buildings on the energy consumption for the entire GCC's building stock.

3 Analysis Methodology

A prototypical commercial building model developed by the US Department of Energy (DOE) was used to represent a medium-sized office building located in a hot and dry climate zone similar to that of the GCC region [29]. Specifically, the building model complied with ASHRAE standard 90.1 as well as American National Standards Institute (ANSI) and Illuminating Engineering Society (IES) codes [29]. In this study, the DOE prototypical commercial building model established for KSA conditions was adjusted in order to be suitable as a baseline model for all six GCC countries and assess the building's energy performance using detailed simulation analysis [30]. A series of parametric analyses were performed on the building in each individual country to test the effect of providing design and retrofit alternatives on the building's energy consumption, electrical peak demand, and carbon dioxide emissions. Finally, the building energy performance was optimized based on a life-cycle cost (LCC) analysis to select the energy efficiency measures that can minimize LCC value while minimizing the annual building energy consumption.

3.1 Commercial Building's Baseline Features

The commercial building model considered for the various analyses consists of a 16-story, 26,572 m² medium office building, comprised of four perimeter zones and a core zone that make up 40% and 60% of the total floor area, respectively, as shown in Fig. 4.

Each story is 50 m long and 33 m wide and has a floor to floor height of 4 m, as specified in the AECOM Middle East Property and Construction Handbook [31]. Table 4 lists the percent area each space type occupies in the commercial building. As indicated in Table 3, 70% of the building is composed of open and private offices, while the remaining 30% is distributed between conference rooms, restrooms, equipment rooms, and a lobby.

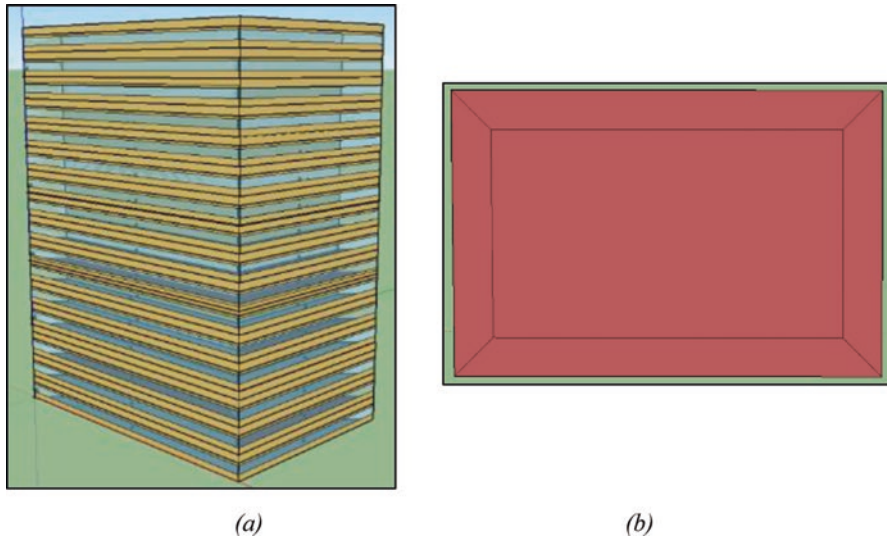


Fig. 4 Office building energy model. (a) 3D rendering and (b) thermal zones

Table 4 Percent area of building's space types

Space type	Percent area
Open plan office	40%
Executive office	30%
Corridor	10%
Lobby	5%
Restrooms	5%
Conference room	4%
Mechanical/electrical room	4%
Copy room	2%

3.1.1 Construction

Details and specifications of the building's constructions for walls, roofs, and floors were determined from the construction practices in the GCC region [7, 18, 23, 26, 28] as well as the US Department of Energy's Analysis of Building Envelope Construction specific to KSA [32, 33]. The construction layers in the baseline model did not include any insulation in order to mimic practices for the existing buildings in the GCC region, as well as to test the effect of adding insulation on the building's energy performance. Table 5 displays the materials and properties of the exterior wall's construction layers. The construction layers of the exterior walls yielded a total U-Value of 2.6 W/m²-K. Furthermore, Table 6 displays the materials and properties of the roof's construction layers. The construction layers of the roof yielded a total U-Value of 4.6 W/m²-K. Finally, the building's foundation was constructed using an unheated 203 mm concrete slab.

Table 5 Thermal properties of the exterior wall constructions

(38 × 89) mm steel frame walls at 0.41 m O.C.	Thickness (m)	Conductivity (W/m-K)	Resistance (m ² -K/W)	Density (kg/m ³)	Specific heat (J/kg-K)
Outdoor air film coefficient	–	–	0.030	–	–
25 mm Stucco	0.025	0.72	0.035	1856	840
16 mm Gypsum Board	0.016	0.16	0.099	800	1090
Air gap	0.016	4.80	0.003	–	–
16 mm Gypsum Board	0.016	0.16	0.099	800	1090
Indoor air film coefficient	–	–	0.122	–	–

Table 6 Thermal properties for the exterior roof constructions

Roof construction	Thickness (m)	Conductivity (W/m-K)	Resistance (m ² -K/W)	Density (kg/m ³)	Specific heat (J/kg-K)
Outdoor air film coefficient	–	–	0.031	–	–
Built-up roofing	0.009	0.16	0.059	1120	1460
Air gap	0.016	4.80	0.003	–	–
Metal decking	0.001	45.28	0.000	7824	500
Indoor air film coefficient	–	–	0.122	–	–

3.1.2 Fenestration

Despite the high temperatures and solar irradiance in the GCC region, some existing buildings still have low performance windows that contribute to buildings’ high solar loads. Therefore, the baseline model incorporated single-pane, 3-mm clear glass windows that had a total U-value of 7.1 W/m²-K, a solar heat gain coefficient (SHGC) of 0.82, and a visible transmittance (VT) of 0.76 [29]. Furthermore, the building had 33% of evenly distributed window to wall ratio (WWR) throughout the northern, southern, eastern, and western orientations. Finally, no shading techniques or fins were implemented on the baseline design.

3.1.3 Internal Loads

Based on the prototypical building model that followed ANSI/ASHRAE/IES Standard 90.1, the number of occupants was estimated at 18.6 m²/person. Furthermore, the equipment power density was rated at 8 W/m², complying with the Ministry of Electricity and Water’s Energy Conservation Program in Kuwait [25]. According to AECOM’s Middle East Property and Construction Handbook [31], some countries in the GCC region are still using a range of 12–15 W/m² of lighting

power density based on their local specifications. Therefore, in order to test the effect of lighting power density on the building's energy performance, the baseline model incorporated 2214 luminaires, with three fluorescent lamps per luminaire, and yielded a total of 15 W/m^2 of lighting power density.

3.1.4 HVAC System

The commercial building's summer and winter set points are set at $24 \text{ }^\circ\text{C}$ and $21 \text{ }^\circ\text{C}$, respectively, as defined in the local specifications of the GCC countries in AECOM's Middle East Property and Construction Handbook [31]. The infiltration rate is set at 0.25 ACH as defined by the Kuwaiti Ministry of Electricity and Water's Energy Conservation Program [25]. Furthermore, the Energy Conservation Program specifies a maximum infiltration flow rate of 1.5 L/s/m^2 for all fenestrations. Based on the prototypical building model that followed ANSI/ASHRAE/IES Standard 90.1, and the Ministry of Electricity and Water in Kuwait, medium office buildings are eligible to utilize air-cooled HVAC systems [25]. Therefore, the building's cooling and heating loads are met by packaged rooftop air-conditioning units with VAV boxes that include electric reheat coils and dampers. The packaged rooftop units accommodate DX cooling coils, fans, filters, dampers, and control systems that help route air to the designated zones around the building through a series of ductwork. The VAV boxes with the reheat coils help adjust the airflow rate and temperature in order to cool or heat the zone and meet the desired set point. A coefficient of performance (COP) of 2.3 is used for the DX cooling coils in order to investigate the COP's impact on the building's energy performance and consumption. Finally, electricity is used as a primary source of energy in order to cool and heat the building, and natural gas is used for domestic hot water.

3.2 Parametric and Sensitivity Analyses

A series of parametric and sensitivity analyses were performed on the prototypical commercial building in order to assess the impact of each individual energy efficiency measure on the building's total energy consumption, electrical peak demand, and carbon dioxide emissions. Energy efficiency measures include improving the building's envelope construction, glazing, WWR, shading techniques, HVAC efficiency, and internal loads. Table 7 displays the options used to improve the building's performance for each category of energy efficiency measures as well as their implementation costs and the references considered to estimate these costs.

The first and second energy efficiency measures included adding insulation to the building's exterior wall and roof insulation to improve the building envelope's resistance to heat flow. The range of R-values implemented in the analysis was derived from ASHRAE 90.1 [29] and based on the availability of insulation materials in the GCC region. Furthermore, the Ministry of Electricity and Water's Energy

Table 7 List of energy efficiency measures and their cost of implementation

Energy efficiency measure		Initial cost	References
Exterior wall insulation (m ² -k/W)	R1.9	\$11.79/m ²	[26, 34]
	R2.3	\$15.31/m ²	
	R3.3	\$22.02/m ²	
	R4.4	\$29.45/m ²	
Roof insulation (m ² -k/W)	R1.9	\$11.79/m ²	[26, 34]
	R2.3	\$15.31/m ²	
	R3.3	\$22.02/m ²	
	R4.4	\$29.45/m ²	
Window glazing	Double tinted	\$203/m ²	[26, 34]
	Double reflective	\$210/m ²	
	Double tinted, low E, spectrally selective	\$294/m ²	
WWR	10%	Depends on glazing type	[26, 34]
	20%	Based on glazing	
	50%	Based on glazing	
	10% E-W, 20% S, 33% N	Based on glazing	
Shading projection	0.2 m	\$0/m ²	[26, 34]
	0.5 m	\$16.94/m ²	
	0.7 m	\$40.84/m ²	
Cooling COP	3	\$2122/RTU	[26, 35]
	4	\$2759/RTU	
	5	\$3862/RTU	
Infiltration rate	% reduction	\$0.54/LM	[35]*
Lighting power density	10 W/m ²	\$6.95/LED lamp	[35]*
	8 W/m ²	\$4.99/LED lamp	
	5 W/m ²	\$9.98/LED lamp	
Set point	25 °C (C)/20 °C (H)	\$0	[26]
	26 °C (C)/19 °C (H)	\$0	
Pump’s motor efficiency	50%	\$211.66	[35]
	70%	\$291.66	
	90%	\$312.62	

Note: References with [*] do not include the labor rate but are accounted for in the optimization analysis

Conservation Program specifies a maximum wall U-value of 0.48 W/m²-K and a maximum roof U-value of 0.34 W/m²-K, in which both U-value requirements can be satisfied by adding R1.9 and R2.3 insulation, respectively.

The third energy efficiency measure assessed the effect of upgrading the window’s glazing by improving the window’s U-value and reducing the SHGC. The types of window constructions implemented in the analysis were derived from the Ministry of Electricity and Water’s Energy Conservation Program and based on the availability of these window construction types in the GCC region [25]. Table 8 lists

Table 8 List of improved window glazing types

EEM 3: window glazing		
Window construction	U-value (W/m ² -K)	SHGC
Single glazing, 3 mm clear glass, metal without thermal break	7.10	0.82
Double tinted (Blue) glazing, with 6 mm air gap	3.52	0.40
Double reflected glazing, with 13 mm air gap	2.44	0.25
Double tinted, low E, spectrally selective glazing, with 13 mm argon gap	1.36	0.23

the four glazing types considered for both the parametric and optimization analyses carried out for this study.

The fourth energy efficiency measure assessed the effect of providing design alternatives such as increasing, decreasing, or altering the window to wall ratio on several building orientations. The baseline design's WWR was set at 33%, and the building's performance is evaluated based on WWRs ranging from 10% to 50%. Furthermore, design considerations had to also be balanced between introducing more daylight into the building and considering heat gain during the summer and heat loss during the winter. Therefore, the building's performance is also evaluated based on WWR design modifications across various building orientations. The northern wall witnessed a WWR of 33% to provide diffused illumination and to maximize the amount of daylighting introduced into the building. Furthermore, a 20% WWR was applied to the southern wall, and a 10% WWR was applied to the eastern/western walls. Therefore, the building's energy performance is being evaluated based on higher WWR on the northern/southern exposures and limited WWR on the eastern/western exposures.

The fifth energy efficiency measure included adding overhangs to help reduce the solar load and to help diffuse daylighting prior to entering the building. To block the path of the sun coming from direct high solar angles, overhangs were added on the southern exposure. Furthermore, tilted overhangs were also added to the eastern and western exposures to block the path of the sun coming from direct low solar angles. The building's energy performance is being evaluated based on the effect of increasing the projection factor of the overhangs.

It is crucial to test the effect of improving the HVAC system's cooling COP since all six countries in the GCC region are dominated by air-conditioning systems. Therefore, the building's energy and HVAC performance is being evaluated based on the effect of improving the system's COP. However, since the medium office building is using a DX air-cooled system, a COP of 3, 4, and 5 does not necessarily mean the HVAC system will perform at its full rated COP capacity due to the harsh climate in the GCC region characterized by high outdoor temperatures during the summer.

The Ministry of Electricity and Water's Energy Conservation Program specified a maximum fenestration infiltration flow rate of 1.5 L/s/m² [25]. However, the prototypical commercial building model assigned a fenestration infiltration flow rate of

0.3 5 L/s/m². Therefore, the seventh energy efficiency measure investigates the effect of reducing the infiltration flow rate from the baseline design, as specified by the Ministry's Energy Conservation Program, to the infiltration flow rate assigned in the prototypical building model, in increments of 25%.

As noted earlier, all countries in the GCC region are still using a range of 12–15 W/m² of lighting power density based on their local specifications, according to AECOM's Middle East Property and Construction Handbook [31]. Therefore, EEM 8 tests the effect of reducing the lighting power density from 15 W/m² to 5 W/m². The baseline model incorporated 2214 luminaires, with (3) - 4 ft. fluorescent lamps per luminaire, and yielded a total of 15 W/m² of lighting power density. In order to reduce the lighting power density and maximize energy savings, all fluorescent lamps were upgraded to 4-ft LED lamps that can fit in the existing luminaires. Furthermore, installing the LED lamps does not require any rewiring and can work off of the existing ballast voltage.

The ninth energy efficiency measure investigates the effect of widening the dead-band and decreasing the zone airflow rate by increasing the cooling set point and decreasing the heating set point by 1 °C on the building's performance and energy savings. Although some people might not accept a temperature set point of 26 °C for cooling and 19 °C for heating, it is important for people in the GCC region to implement a cultural shift by increasing awareness and proposing policy changes in order to improve the energy performance of commercial buildings.

The prototypical medium office building model specified a pump-motor efficiency of 30% for the building's water distribution system. Therefore the tenth, and final, energy efficiency measure investigates the effect of improving the pump's motor efficiency from 30% to 90% on the building's consumption and energy savings.

3.3 Building Optimization Analysis

An optimization analysis is performed to select all feasible and implementable energy efficiency measures using both life-cycle cost (LCC) analysis and total building energy use savings. Equations (1) and (2) display the formulas used to calculate the LCC for the baseline model and energy efficiency measures [36]. Equation (3) displays the formula used to calculate the simple payback period (SPP) of implementing the energy efficiency measures.

$$\text{Life Cycle Cost}(\$) = \text{Initial Cost}(\$) + \text{Energy Cost}(\$) \times \text{USPW} \quad (1)$$

$$\text{USPW} = \frac{1 - (1 + r_d)^{-n}}{r_d} \quad (2)$$

$$\text{SPP} = \frac{\text{Initial Costs}}{\text{First Year Savings}} \quad (3)$$

where USPW = uniform series present worth, r_d = discount rate, n = period (years).

The life-cycle cost analysis was performed using a discount rate of $r_d = 5\%$ and a life cycle of $n = 35$ years for the baseline design and all the energy efficiency measures, resulting in USPW = 16.4 [36]. A sensitivity analysis was also performed to assess the impact of the life-cycle period and discount rate, as discussed in the Optimization Analyses Results section. The building's energy cost is calculated using the energy usage (kWh) obtained from simulating the model in EnergyPlus [30] and multiplying the usage by the energy cost (\$/kWh) for each country, as provided in Table 1. The implementation cost of each measure was calculated based on values provided by reference materials, manufacturers, and RS means [7, 18, 23, 26, 28, 34, 35]. Costs were typically given in terms of dollars per square meter or calculated per piece of equipment as noted in Table 6.

4 Selected Results

4.1 Baseline Design's Results

The baseline design model was simulated in EnergyPlus [30] using six different weather files that represent the countries of Bahrain (Manama), Kingdom of Saudi Arabia (Riyadh), Kuwait (Kuwait City), Oman (Muscat), Qatar (Doha), and the United Arab Emirates (Dubai). The total energy consumption, electrical peak demand, and carbon dioxide emissions were the three main results considered in the analysis. However, additional simulation results are considered including thermal loads, thermal comfort levels, and energy end-use distributions. Figures 5 and 6 display the total site and source energy consumed by the prototypical office building located in each GCC country.

Specifically, Fig. 5 displays the net site energy of the 16-story medium office building for each individual country in the GCC region. The total annual energy consumed by each country range from 251 to 268 kWh/m²/year, with an average annual consumption rate of 265 kWh/m²/year. Thus, the building yielded an average electricity consumption rate of 263 kWh/m²/year for all six countries, which is significantly higher than 182 kWh/m²/year, the average annual electricity consumed by US commercial buildings with comparable building floor space [37]. Bahrain and the Kingdom of Saudi Arabia have the highest and lowest energy consumption, respectively, while the remaining countries follow a similar pattern of electricity and gas consumption.

Figure 6 displays the net source energy of the 16-story medium office building for each individual country in the GCC region. The source energy includes the total kWh used to generate, distribute, and consume electrical power. The net source

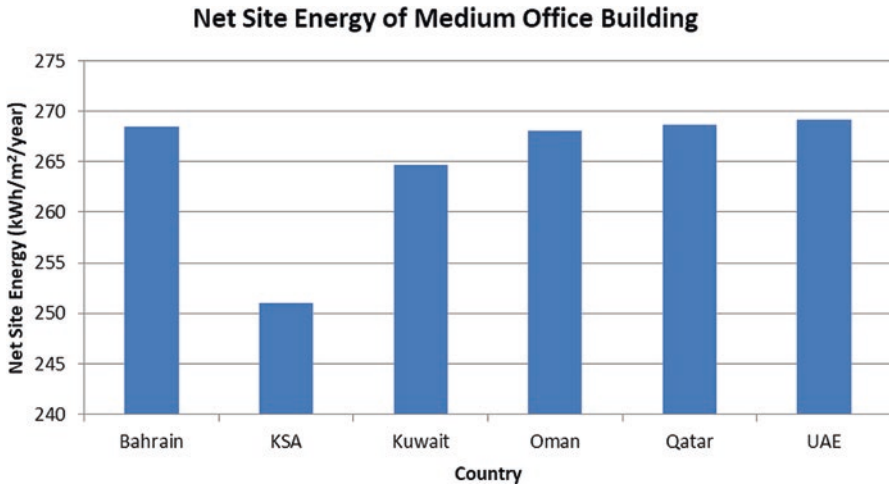


Fig. 5 Net site energy of medium office building in the GCC region

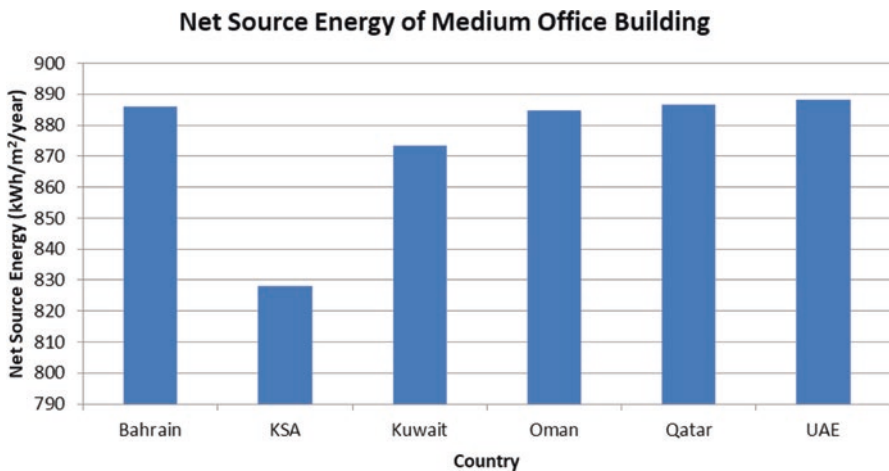


Fig. 6 Net source energy of medium office building in the GCC region

energy was calculated using a fuel source energy factor of 3.3 [7, 23, 26]. Therefore, for every unit of energy consumed on site, 3.3 units of energy are consumed in generation and distribution, and the process hence develops a site to source ratio of 3.3.

Figure 7 shows the end-use electricity distribution specific to the prototypical office building for all the GCC countries. As predicted, cooling energy consumes the majority of electricity, ranging from 44 to 49% of the total electricity consumed. Although the office building energy consumption is dominated by space cooling, the results indicate that a range of 15–18% of the total electricity consumed goes

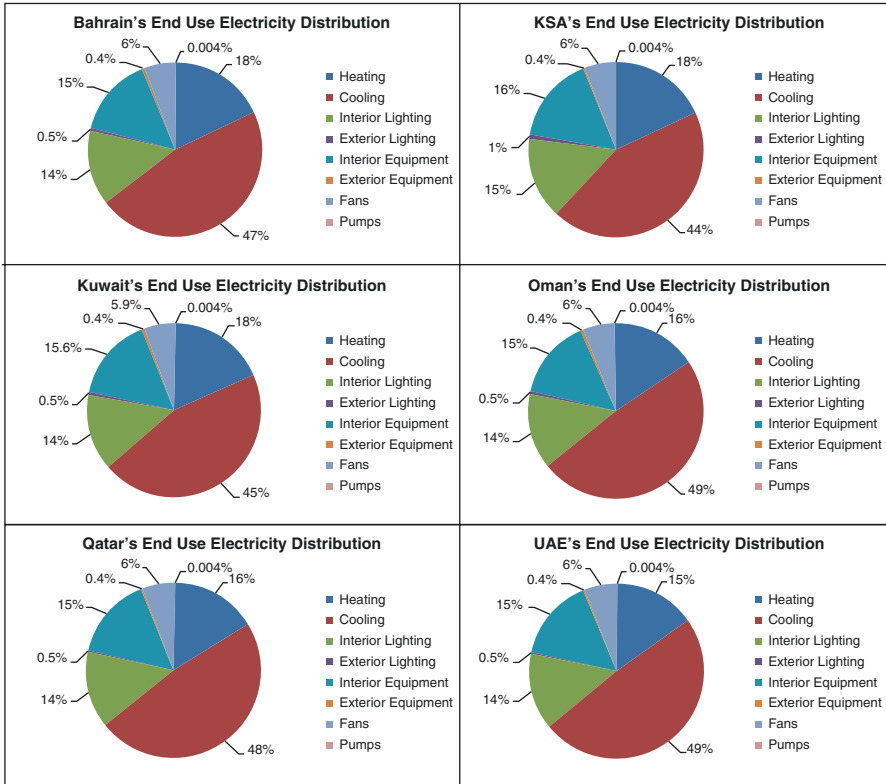


Fig. 7 End-use electricity distribution of GCC countries

toward space heating. Since countries in the GCC region typically tend to overcool their buildings (i.e., have cooling set point temperatures of less than 24 °C), the VAV reheat coils warm up the air in order to meet the set point and ensure the occupant’s thermal comfort. Furthermore, interior lighting and equipment consume an average of 14% and 15% of the total electricity consumed, respectively, and the rest of the electricity goes toward fans, pumps, exterior lighting, and exterior equipment.

Building zones maintain 24 °C cooling and 21 °C heating set points during the building’s occupied periods, which are scheduled from Sunday to Thursday, 7 am to 10 pm [38]. The building’s HVAC system is scheduled to meet a set point of 27 °C for cooling and 16 °C for heating during unoccupied periods, including weekends and holidays.

One of the three main objectives of the analysis is to assess the building’s electrical peak demand in order to reduce and/or eliminate power outages in some areas around the GCC region and to reduce the number of power plants operating throughout the region. The electrical peak demand is calculated based on the maximum wattage acquired during a billing cycle that is made up of 15-min intervals. Figure 8 displays the annual electrical peak demand for each of the individual countries. The

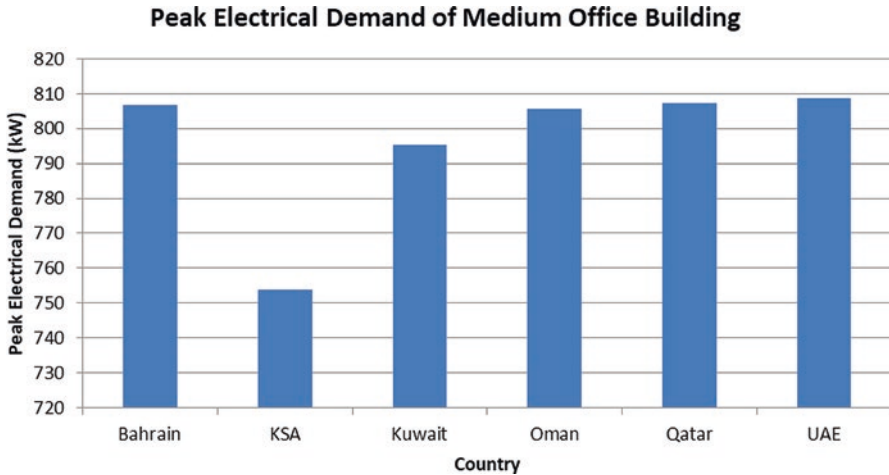


Fig. 8 Electrical peak demand of medium office building in the GCC region

annual electrical peak demand for each country ranges from 753 to 806 kW, with an average annual rate of 796 kW. Similar to the trend found in energy consumption, Bahrain and the Kingdom of Saudi Arabia exhibit the highest and lowest electrical peak demand, respectively, while the remaining countries have similar levels of electrical peak demand.

Figure 9 indicates the amount of carbon dioxide emissions released into the atmosphere, annually. The annual carbon dioxide emissions released into the atmosphere for each country range from 4,205,364 to 4,500,139 kg, with an average annual rate of 4,441,955 kg. Bahrain and the Kingdom of Saudi Arabia experience the highest and lowest carbon dioxide emissions, respectively, while the remaining countries follow similar patterns of released emissions.

4.2 Parametric Analyses Results

A series of parametric analyses were performed on the office building in order to study the impact of each individual energy efficiency measure on the building’s total energy consumption, electrical peak demand, and carbon dioxide emissions [39]. Energy efficiency measures include improving the building’s envelope construction, glazing, WWR, shading techniques, HVAC efficiency, and internal loads. The results obtained for the six GCC countries show very similar patterns on the impacts of all the measures considered in the analysis on the office building annual energy consumption, electrical peak demand, and carbon dioxide emission savings as those shown in, respectively, Figs. 10, 11, and 12 for Bahrain.

In particular, Fig. 10 presents the total energy consumption savings when each individual energy efficiency measure listed in Table 7 is implemented separately.

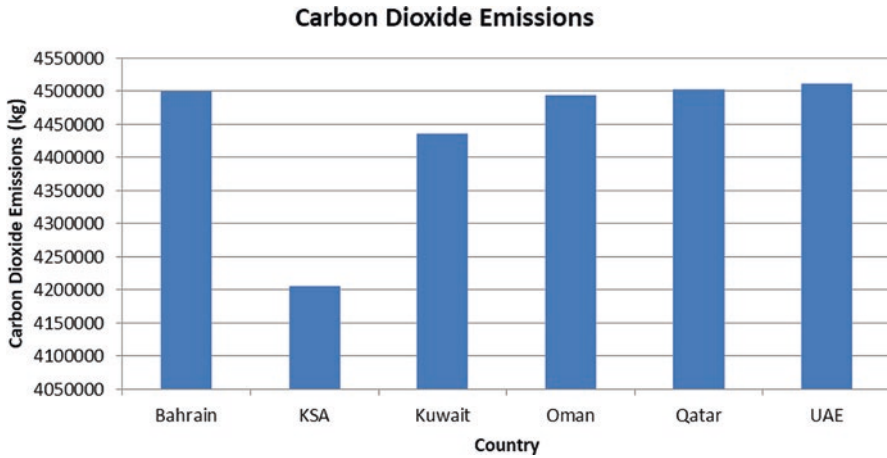


Fig. 9 Carbon dioxide emissions released into the atmosphere

Upgrading the HVAC's cooling COP had the highest impact on the total annual energy savings, saving up to 27% in the total energy consumed by the office building. Changing the temperature set point provides savings range of 17–25% in annual energy consumption, while installing double reflective glazing or double tinted, low-e, spectrally selective glazing leads to energy savings range of 17–25%. Adding exterior wall insulation, overhangs, and reducing the WWR and the lighting power density also had a noticeable impact on the building's performance, providing a range of 6–15% in energy use savings. Measures that had the least amount of energy savings for the office building included adding roof insulation, reducing the infiltration rate, and upgrading the pump's motor efficiency.

Figures 11 and 12 display the impact of individual energy efficiency measures on the electrical peak demand and carbon dioxide emissions released. Both figures follow the same trend as Fig. 10 and provide similar percent savings for the same energy efficiency measures.

4.3 Optimization Analyses Results

An optimization analysis for each GCC country was developed for the office building by selecting and combining energy efficiency measures into the building's baseline design using an LCC analysis and total energy use savings. Equations (1) and (2) were used to calculate the LCC for the baseline model and energy efficiency measures. Equation (3) was used to calculate the simple payback period (SPP) using the initial costs and first-year savings. All initial costs were utilized using the values found in Table 7.

The LCC values and simple payback periods for each individual measure for the countries of Bahrain, Kingdom of Saudi Arabia, Kuwait, Oman, Qatar, and the

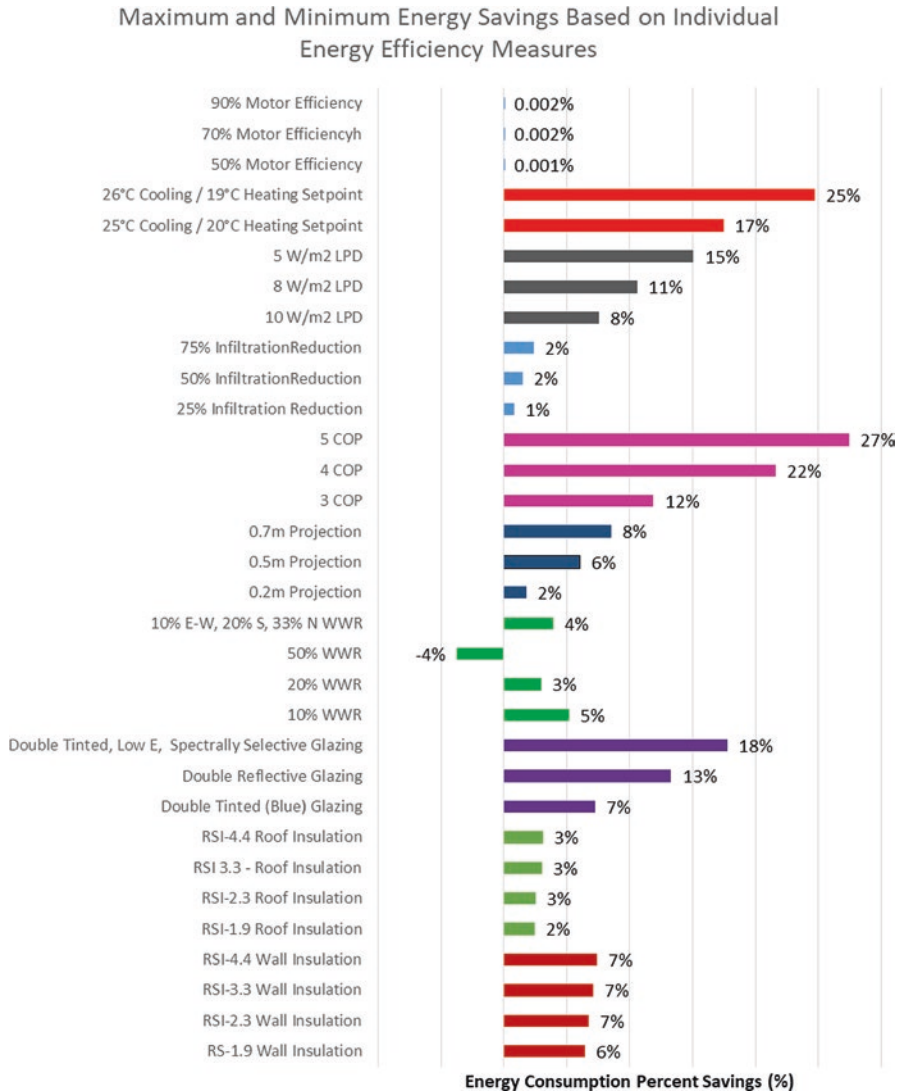


Fig. 10 Savings of annual energy consumption based on individual efficiency measures

United Arab Emirates are displayed in Table 18. Cost-effective and high impact energy efficiency measures are identified and considered in the optimization analysis based on the sequential search technique [18]. The optimization results are presented in the form of Pareto graphs showing the LCC values and the percent source energy savings for all the combinations of energy efficiency measures. These results are briefly discussed for each GCC country in the following sections. Furthermore, the results of a sensitivity analysis performed to evaluate the impact of the life-cycle period and discount rate indicate slight changes in the selection of the optimal sets of energy efficiency measures for all GCC countries.

Maximum and Minimum Peak Demand Savings Based on Individual Energy Efficiency Measures

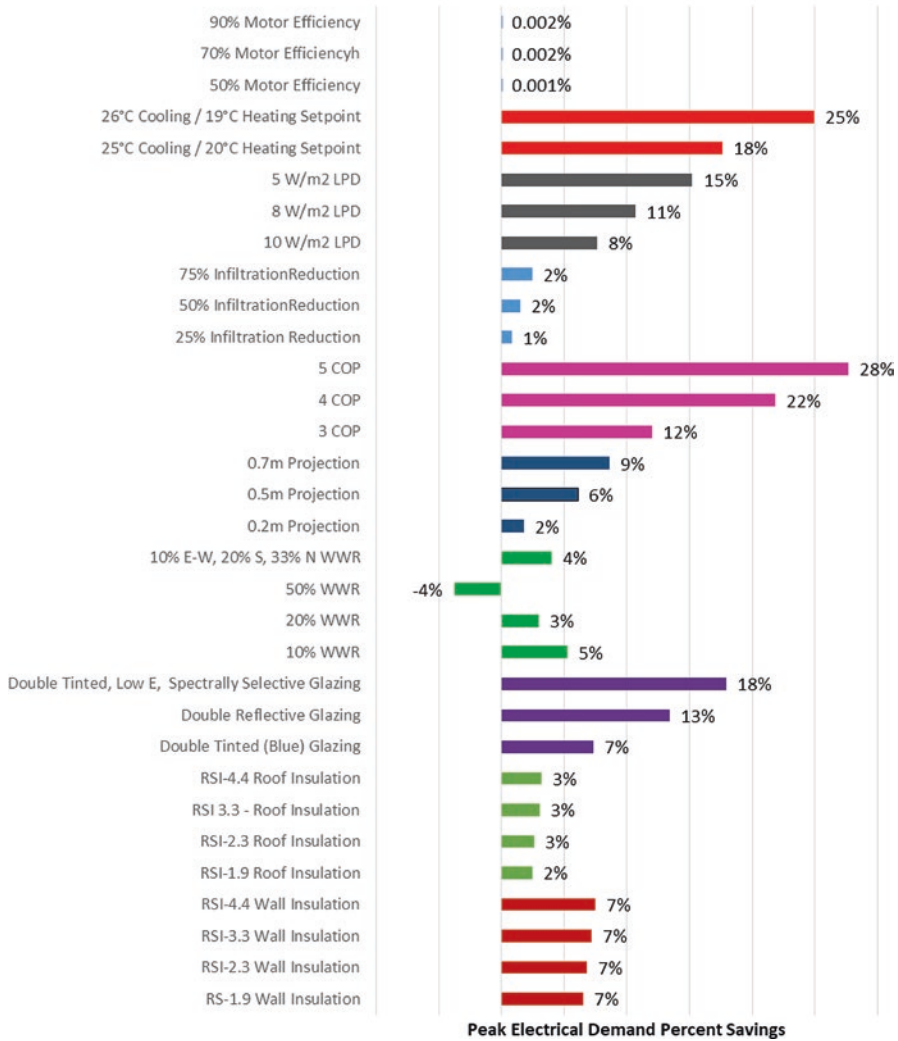


Fig. 11 Savings in electrical peak demand based on individual energy efficiency measures

4.3.1 Bahrain

Figure 13 displays the results of the office building optimization analysis for Bahrain. Implementing the cost-effective measures from Table 9 yielded an optimal point, as shown by the red dot in Fig. 13. Increasing the exterior wall and roof insulation and improving the window glazing type resulted in high energy savings, but high life-cycle costs, respectively. Table 10 displays the optimal point's imple-

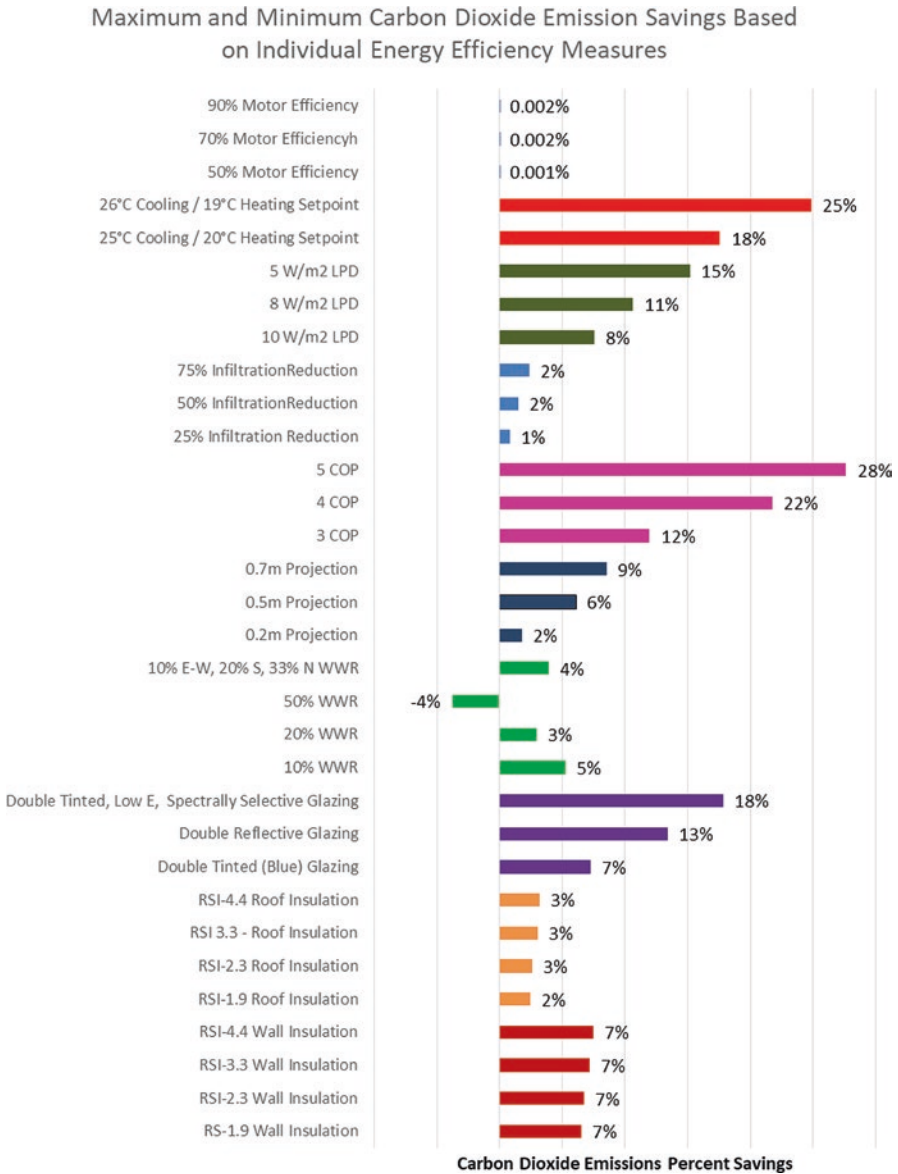


Fig. 12 Savings in carbon dioxide emissions based on individual energy efficiency measures

mented energy efficiency measures, along with the total LCC and SPP for the combined measures. The optimized office building design configuration yielded total savings of 63% in energy consumption, electrical peak demand, and carbon dioxide emissions. The comparative performance of the optimized building’s energy performance against the baseline model is displayed in Table 11.

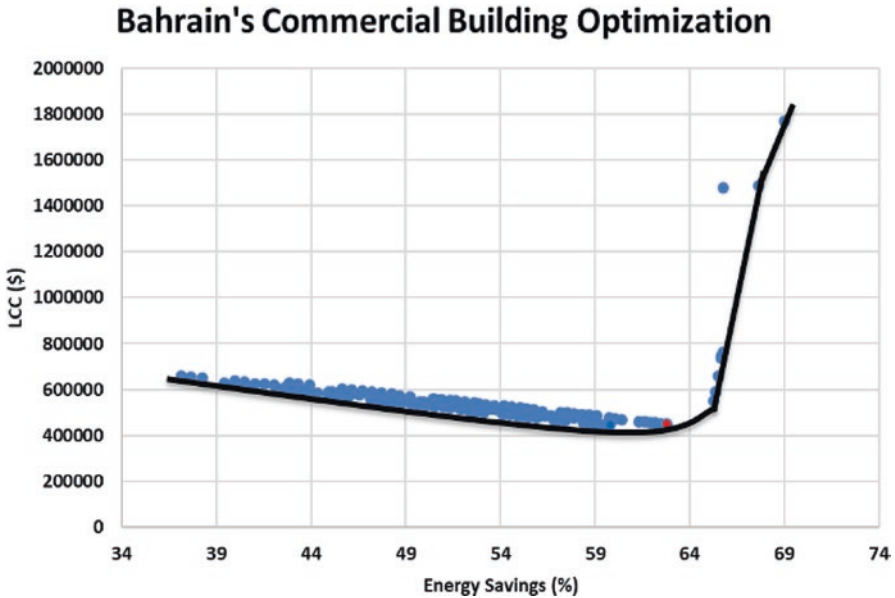


Fig. 13 Bahrain's office building optimization Pareto path

4.3.2 Kingdom of Saudi Arabia

Figure 14 displays the results of the optimization analysis for the office building located in Riyadh, KSA. The optimal set of energy efficiency measures yielded an optimal design as shown in red dot in Fig. 14. Increasing the exterior wall insulation, improving the window glazing type, and reducing the window to wall ratio resulted in high energy savings, but high life-cycle costs, respectively. Table 12 lists the optimal point's implemented energy efficiency measures, along with the total LCC and SPP for the combined measures. The optimized building yielded a total of 62% in savings regarding energy consumption and carbon dioxide emissions and 63% in savings toward the electrical peak demand. The indicators for the optimized building's performance against the baseline model are displayed in Table 13.

4.3.3 Kuwait

Figure 15 illustrates the optimization analysis results for the office building located in Kuwait City with the optimal set of energy efficiency measures shown in red. Increasing the exterior wall and roof insulation, improving the window glazing type, and reducing the window to wall ratio resulted in high energy savings, but high life-cycle costs, respectively. The optimal point's implemented energy efficiency measures, along with the total LCC and SPP for the combined measures, are dis-

Table 9 Bahrain’s life-cycle cost analysis and simple payback period

EEM type	EEM	LCC(\$)	ΔLCC(\$)	Simple payback period (years)
Baseline	Baseline design model	934,417	–	–
Exterior wall insulation	R1.9 m ² -K/W	999,593	65,176	34
	R2.3 m ² -K/W	10345B0	100,163	42
	R3.3 m ² -K/W	1,102,220	167,302	53
	R4.4 m ² -K/W	1,173,342	244,424	74
Exterior roof insulation	R1.9 m ² -K/W	931,370	–3047	14
	R2.3 m ² -K/W	935,933	1566	17
	R3.3 m ² -K/W	942,523	3106	21
	R4.4 m ² -K/W	953,957	19,540	27
Glazing type	Double tinted (blue) glazing, with 6 mm air gap	1,530,022	645,605	172
	Double reflected glazing, with 13 mm air gap	1,543,141	613,724	97
	Double tinted, Low E, spectrally selective glazing, with 13 mm Argon gap	1,301,671	367,254	102
WWR	10%	1,011,460	77,043	42
	20%	1,153,315	223,397	150
	50%	1,597,745	663,327	–293
	10% E-W, 20% S, 33% N	1,147,704	213,236	111
Shading techniques	0.2 m	913,036	–16,331	0
	0.5 m	373,352	–55,565	0
	0.7 m	353,412	–76,005	1
COP	3.0	329,367	–104,550	1
	4.0	740,663	–193,750	1
	5.0	639,312	–245,105	1
Infiltration rate	25% reduction	927,952	–6466	2
	50% reduction	921,502	–12,916	1
	75% reduction	913,179	–21,239	1
Lighting power density	10 W/m ²	910,432	–23,936	11
	8 W/m ²	363,999	–65,413	6
	5 W/m ²	359,991	–74,426	3
Setpoint change	25 °C (C)/20 °C (H)	771,221	–163,196	0
	26 °C(C)/19 °C(H)	703,429	–230,939	0
Pump’s motor efficiency	50%	934,617	200	293
	70%	934,693	275	239
	90%	934,711	293	267

played in Table 14. The optimized building yielded a total of 62% in energy savings and 63% in electrical peak demand and carbon dioxide emission savings as summarized in Table 15.

Table 10 Bahrain’s optimal set of energy efficiency measures for the office building

EEM type	Energy efficiency measures	LCC (\$)	ΔLCC (\$)	SPP (years)
Exterior wall insulation	No insulation	449,626	-484,791	2.8
Exterior roof insulation	R1.9 m ² -K/W			
Glazing type	Single glazing, 3 mm clear glass			
WWR	33%			
Shading techniques	0.7 m			
COP	5			
Infiltration rate	75% reduction			
Lighting power density	5 W/m ²			
Setpoint change	26 °C (C)/19 °C (H)			
Pump’s motor efficiency	30%			

Table 11 Bahrain’s optimal design benefits vs. baseline office building

Bahrain	Baseline	Optimized	% Savings
Annual energy consumption (kWh/m ² /year)	268	100	63%
Annual electrical peak demand (kW)	807	295	63%
Annual carbon dioxide emissions (kg)	4,500,139	1,653,941	63%

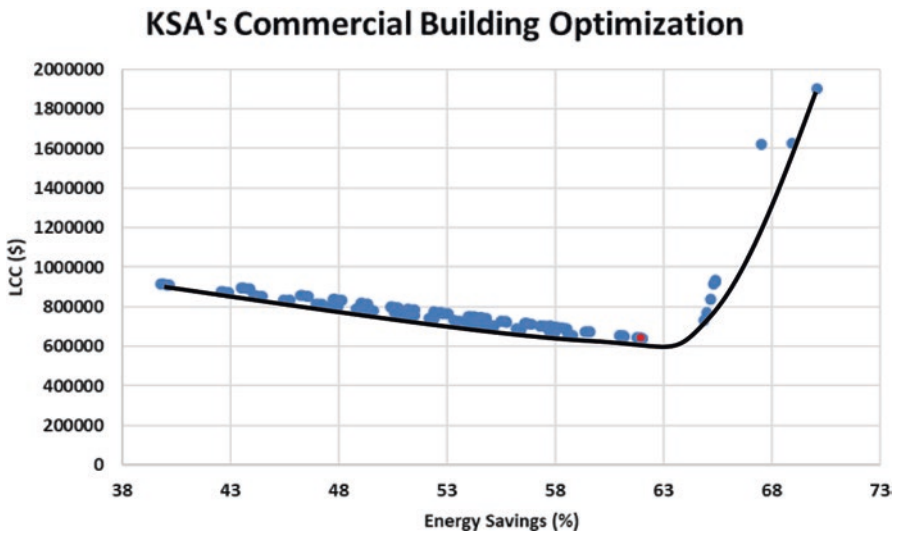


Fig. 14 KSA’s office building optimization Pareto path

Table 12 KSA’s optimal set of energy efficiency measures for the office building

EEM type	Energy efficiency measures	LCC (\$)	ΔLCC (\$)	SPP (years)
Exterior wall insulation	No insulation	641,928	-777,691	1.9
Exterior roof insulation	R1.9 m ² -K/W			
Glazing type	Single glazing, 3 mm clear glass			
WWR	33%			
Shading techniques	0.7 m			
COP	5			
Infiltration rate	75% reduction			
Lighting power density	5 W/m ²			
Setpoint change	26 °C (C)/19 °C(H)			
Pump’s motor efficiency	30%			

Table 13 KSA’s optimal design benefits vs. baseline office building

KSA	Baseline	Optimized	% Savings
Annual energy consumption (kWh/m ² /year)	251	95	62%
Annual electrical peak demand (kW)	754	282	63%
Annual carbon dioxide emissions (kg)	4,205,364	1,579,589	62%

4.3.4 Oman

The optimization analysis results for the office building located in Oman are displayed in Fig. 16 with the optimal design configuration specified in red. Increasing the exterior wall insulation and improving the window glazing type yielded high energy savings, but high life-cycle costs, respectively. The optimal point’s implemented energy efficiency measures, along with the total LCC and SPP for the combined measures, are displayed in Table 16. The optimized building yielded a total of 67% in savings regarding energy consumption, electrical peak demand, and carbon dioxide emissions. The performance metrics of the optimized building’s performance against the baseline model is displayed in Table 17.

4.3.5 Qatar

Figure 17 summarizes the Pareto graph associated with the optimization analysis results for the office building located in Doha, Qatar. The optimal design is identified in red in Fig. 16. Increasing the exterior wall insulation and improving the window glazing type yielded high energy savings, but high life-cycle costs, respectively. The optimal point’s implemented energy efficiency measures, along with the total LCC and SPP for the combined measures, are displayed in Table 18. The optimized building yielded a total of 67% in savings regarding energy consumption and carbon dioxide emissions and 68% in savings regarding electrical peak demand. The comparative results of the optimized building’s performance against the baseline model are displayed in Table 19.

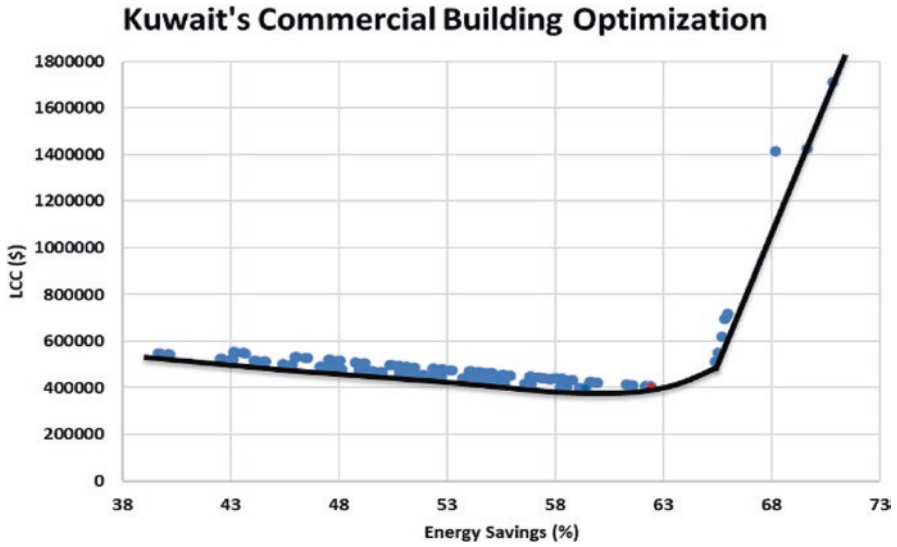


Fig. 15 Kuwait’s building optimization Pareto path

Table 14 Kuwait’s optimal set of energy efficiency measures for the office building

EEM type	Energy efficiency measures	LCC (\$)	ΔLCC (\$)	SPP (years)
Exterior wall insulation	No insulation	404,687	−401,495	3.3
Exterior roof insulation	R2.3 m ² -K/W			
Glazing type	Single glazing, 3 mm clear glass			
WWR	33%			
Shading techniques	0.7 m			
COP	5			
Infiltration rate	75% reduction			
Lighting power density	5 W/m ²			
Setpoint change	26 °C (C)/19 °C (H)			
Pump’s motor efficiency	30%			

Table 15 Kuwait’s optimal design benefits vs. baseline office building

Kuwait	Baseline	Optimized	% Savings
Annual energy consumption (kWh/m ² /year)	265	99	62%
Annual electrical peak demand (kW)	795	294	63%
Annual carbon dioxide emissions (kg)	4,436,798	1,645,681	63%

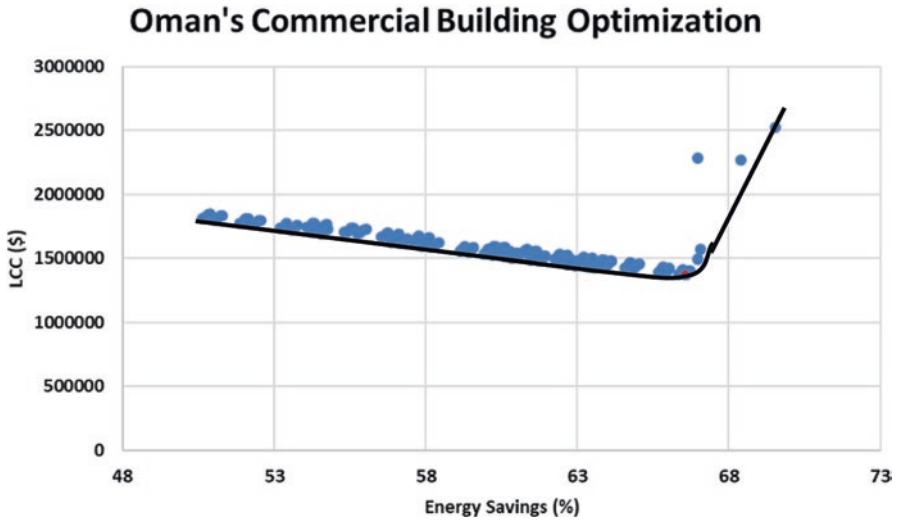


Fig. 16 Oman’s building optimization Pareto path

Table 16 Oman’s optimal set of energy efficiency measures for the office building

EEM type	Energy efficiency measures	LCC (\$)	ΔLCC (\$)	SPP (years)
Exterior wall insulation	R1.9 m ² -K/W	1,372,236	-1,660,561	2.9
Exterior roof insulation	R2.3 m ² -K/W			
Glazing type	Single glazing, 3 mm clear glass			
WWR	10%			
Shading techniques	0.7 m			
COP	5			
Infiltration rate	75% reduction			
Lighting power density	5 W/m ²			
Setpoint change	26 °C (C)/19 °C (H)			
Pump’s motor efficiency	30%			

Table 17 Oman’s optimal design benefits vs. baseline office building

Oman	Baseline	Optimized	% Savings
Annual energy consumption (kWh/m ² /year)	268	90	67%
Annual electrical peak demand (kW)	806	264	67%
Annual carbon dioxide emissions (kg)	4,494,087	1,480,313	67%

Table 18 Qatar’s optimal set of energy efficiency measures for the office building

EEM type	Energy efficiency measures	LCC (\$)	ΔLCC (\$)	SPP (years)
Exterior wall insulation	R1.9 m ² -K/W	1,204,564	-1,367,012	3.4
Exterior roof insulation	R1.9 m ² -K/W			
Glazing type	Single glazing, 3 mm clear glass			
WWR	10%			
Shading techniques	0.7 m			
COP	S			
Infiltration rate	75% reduction			
Lighting power density	5 W/m ²			
Setpoint change	26 °C (C)/19 °C (H)			
Pump’s motor efficiency	30%			

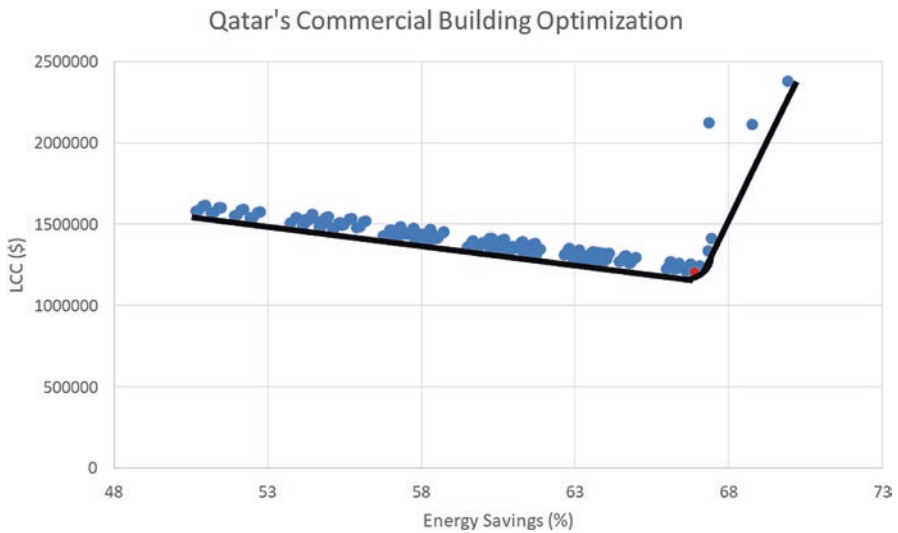


Fig. 17 Qatar’s building optimization Pareto path

Table 19 Qatar’s optimal design benefits vs. baseline office building

Qatar	Baseline	Optimized	% Savings
Annual energy consumption (kWh/m ² /year)	269	89	67%
Annual electrical peak demand (kW)	807	262	68%
Annual carbon dioxide emissions (kg)	4,503,541	1,469,814	67%

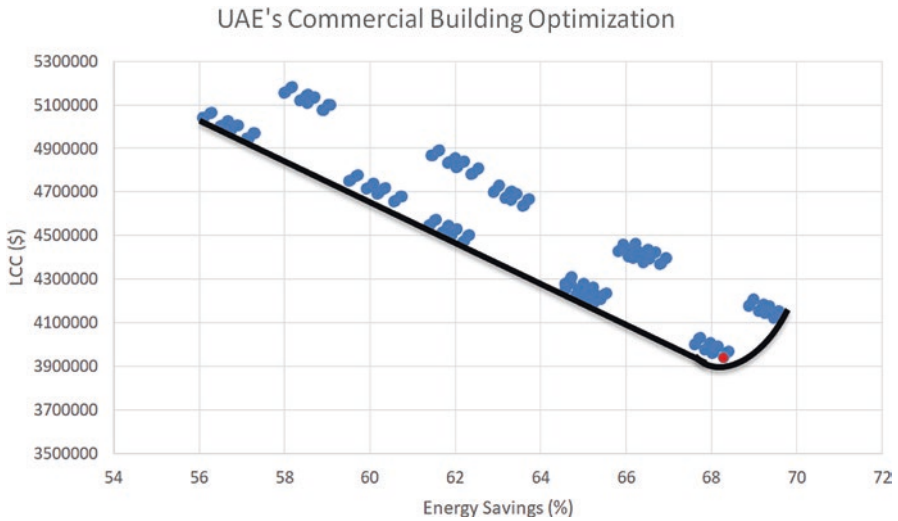


Fig. 18 UAE’s building optimization Pareto path

Table 20 UAE’s optimal set of energy efficiency measures for the office building

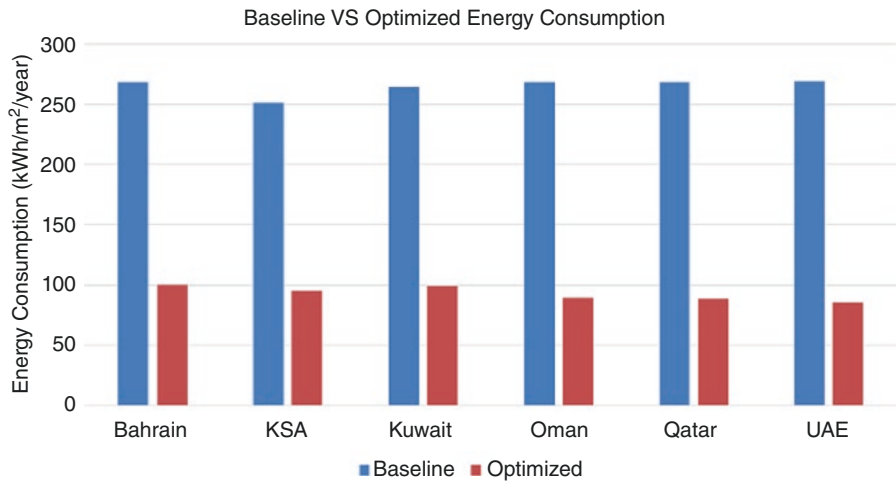
EEM type	Energy efficiency measures	LCC (\$)	Δ LCC (\$)	SPP (years)
Exterior wall insulation	R1.9 m ² -K/W	3,937,311	-5,430,910	2.5
Exterior roof insulation	R1.9 m ² -K/W			
Glazing type	Double reflective glazing			
WWR	10%			
Shading techniques	0.7 m			
COP	5			
Infiltration rate	75% reduction			
Lighting power density	5 W/m ²			
Setpoint change	26 °C (C)/19 °C (H)			
Pump’s motor efficiency	30%			

4.3.6 United Arab Emirates

Figure 18 summarizes the optimization analysis results obtained for the office building located in Dubai, UAE. The optimal set of energy efficiency measures, along with the total LCC and SPP for the combined measures, are displayed in Table 20. The optimized building yielded a total of 68% in energy savings and 69% in savings regarding electrical peak demand and carbon dioxide emissions. The performance indicators of the optimized building’s performance against the baseline model are displayed in Table 21.

Table 21 UAE's optimal design benefits vs. baseline office building

UAE	Baseline	Optimized	% Savings
Annual energy consumption (kWh/m ² /year)	269	85	68%
Annual electrical peak demand (kW)	809	251	69%
Annual carbon dioxide emissions (kg)	4,511,799	1,409,765	69%

**Fig. 19** Annual energy consumption savings for optimized office building in GCC countries

4.3.7 Summary of Optimization Analysis

The optimization analysis results for all the GCC countries indicate that the energy performance of office buildings can be significantly improved through the implementation of common and proven energy efficiency measures into the building's baseline model. The improved office building designs can yield a range of 62–69% savings in annual energy consumption, electrical peak demand, and carbon dioxide emissions with payback periods of 1.9–3.4 years. Figure 19 displays a graphical representation of the difference between the baseline and the optimized office building annual energy consumption per floor area. The energy consumption in all six countries is reduced significantly after applying feasible energy efficiency measures and can hence result in lower production, distribution, and consumption of energy.

Figures 20 and 21 illustrate the difference between the baseline and optimized office building's electrical peak demand and carbon dioxide emissions for all six GCC countries. Optimizing the building energy performance helped to reduce significantly electrical peak demand and carbon dioxide emissions for all GCC countries. Therefore, the improved designs will not only result in a significant decrease in the office building's energy bills, but the electric utilities will also experience less pressure to meet the peak demand, and GCC region will reduce their contribution to the world's environmental footprint.

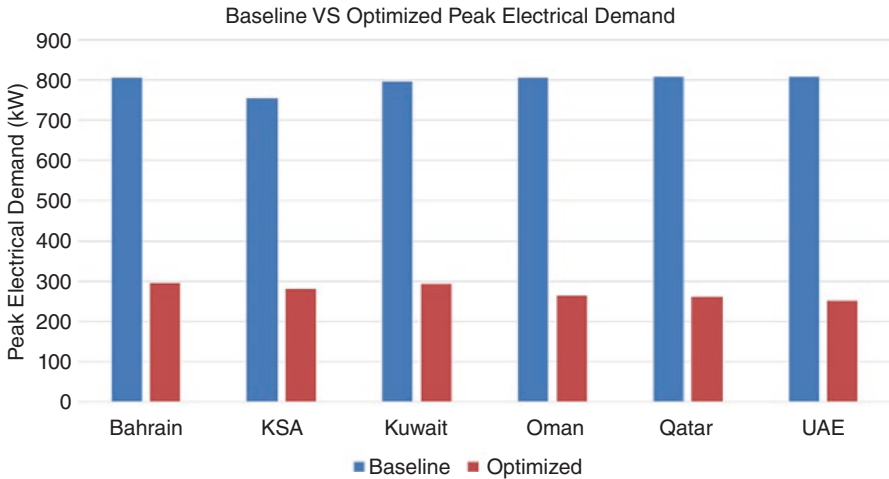


Fig. 20 Electrical peak demand savings for optimized office building in GCC countries

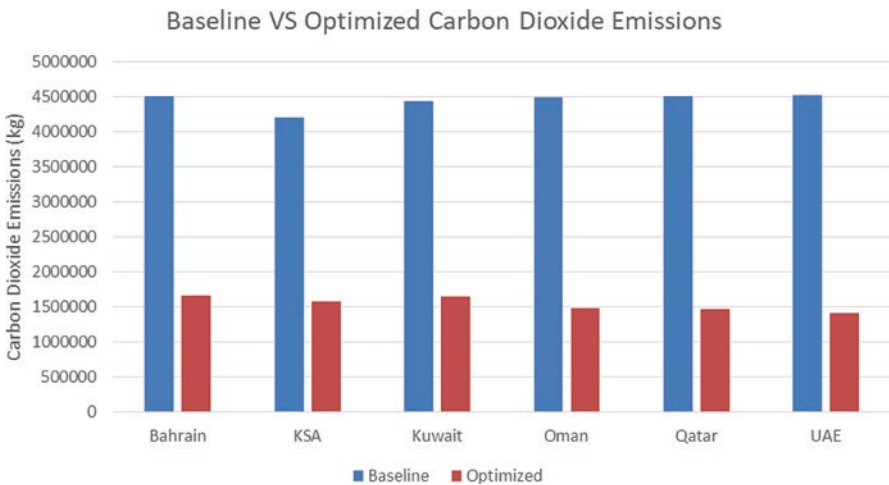


Fig. 21 Carbon dioxide emission savings for optimized office building in GCC countries

5 Summary and Conclusions

Countries in the Gulf Cooperation Council (GCC) region have been witnessing a major development in their urban and socioeconomic growth leading to significant increase in energy consumption and electricity demand especially for the building sector. Since commercial buildings contribute significantly to the building stock’s energy consumption and carbon dioxide emissions, a series of parametric and sensitivity analyses were performed on a prototypical commercial building in order to assess the impact of individual energy efficiency measures on the building’s total

Table 22 Potential savings from the optimization analysis of commercial buildings

Country	Energy savings	Electrical peak demand savings	Carbon dioxide emissions savings
Bahrain	63%	63%	63%
KSA	62%	63%	62%
Kuwait	62%	63%	63%
Oman	67%	67%	67%
Qatar	67%	68%	67%
UAE	68%	69%	69%

energy consumption, electrical peak demand, and carbon dioxide emissions. An LCC analysis helped develop a list of feasible energy efficiency measures in order to optimize the energy performance of the office building. The optimized building designs resulted in savings ranging between 62% and 69% in annual energy consumption, electrical peak demand, and carbon dioxide emissions as summarized in Table 22 for all GCC countries.

Improving the building's envelope constructions, glazing, WWR, shading techniques, HVAC efficiency, and internal loads can significantly improve the building's energy performance.

Future work concerns implementing a water-cooled HVAC system instead of a DX air-cooled HVAC system and implementing renewable energy sources to help decrease the GCC's heavy reliance on fossil fuels and address a post-oil future. Not only does the shift in energy sources benefit the economic aspect of the region, but also improve their high contribution to the world's environmental footprint. The GCC region has significant solar and wind resources to be suitable for integrating renewable energy technologies with buildings to achieve net or even positive energy designs and retrofits. As an initial step to improve the energy performance of buildings, it is crucial for GCC countries to update their local energy efficiency codes regularly and to impose more stringent specifications and requirements in terms of building constructions and systems in order to reduce energy consumed in both residential and commercial buildings.

References

1. Munawwar S, Ghedira H (2014) A review of renewable energy and solar industry growth in the GCC region. *Energy Procedia* 57:3191–3202
2. Bhutto AW, Bazmib AA, Zahedi G, Klemes J (2014) A review of progress in renewable energy implementation in the Gulf Cooperation Council countries. *J Clean Prod* 71. <https://doi.org/10.1016/j.jclepro.2013.12.073>
3. The Economist (2010) The GCC in 2020: resources for the future, volume 2010. The Economist Intelligence Unit Limited: Geneva. http://graphics.eiu.com/upload/eb/GCC_in_2020_Resources_WEB.pdf. Accessed 3 Mar 2018
4. Saif I (2009) The oil boom in the GCC countries 2002–2008: old challenges, changing dynamics. *Carnegie papers* 15. Carnegie Middle East Center, Washington, DC

5. Krarti M, Ihm P (2016) Evaluation of Net-Zero energy residential buildings in the MENA region. *Sustain Cities Soc* 22:116–125
6. Friess WA, Rakhshan K (2017) A review of passive envelope measures for improved building energy efficiency in the UAE. *Renew Sust Energ Rev* 72:485–496
7. Krarti M (2015) Evaluation of large scale building energy efficiency retrofit program in Kuwait. *Renew Sust Energ Rev* 50:1069–1080
8. Al-Ajmi FF, Hanby VI (2008) Simulation of energy consumption for Kuwaiti domestic buildings. *Energy Buildings* 40(6):1101–1109
9. Aboul-Naga M, Al-Sallal KA, Diasty RE (2000) Impact of city urban patterns on building energy use: Al-Ain City as a case study for hot-arid climates. *Architect Sci Rev* 43(3):147–158
10. Estidama (2016) Insulation products and systems for PEARL villa rating. <http://estidama.upc.gov.ae>. Accessed 18 Apr 2018
11. Friess WA, Rakhshan K, Hendawi TA, Tajerzadeh S (2012) Wall insulation measures for residential villas in Dubai: a case study in energy efficiency. *Energy Buildings* 44:26–32
12. Radhi H (2009) Evaluating the potential impact of global warming on the UAE residential buildings—a contribution to reduce the CO2 emissions. *Build Environ* 44:2451–2462
13. Al-Masri A, Abu-Hijleh B (2012) Courtyard housing in midrise buildings: an environmental assessment in hot-arid climate. *Renew Sust Energ Rev* 16:1892–1898
14. Radhi H (2010) On the optimal selection of wall cladding system to reduce direct and indirect CO2 emissions. *Energy* 35:1412–1424
15. Al-Sallal KA, Al-Rais L, Dalmouk MB (2013) Designing a sustainable house in the desert of Abu Dhabi. *Renew Energy* 49:80–84
16. Haggag M, Hassan A, Elmasry S (2014) Experimental study on reduced heat gain through green facades in a high heat load climate. *Energy Buildings* 82:668–674
17. Hammad F, Abu-Hijleh B (2010) The energy savings potential of using dynamic external louvers in an office building. *Energy Buildings* 42:1888–1895
18. Krarti M, Dubey K (2017) Energy productivity evaluation of large scale building energy efficiency programs for Oman. *Sustain Cities Soc* 20:12–22
19. Mallela V, Solanki P, Al-Harasi Y (2010) Regulation of energy demands via DSM policies: a case study in Oman. *Can J Elect Electron Eng*:54–59
20. Malik AS (2007) Impact on power planning due to demand-side management (DSM) in commercial and government sectors with rebound effect—a case study of central grid of Oman. *Energy* 32(11):2157–2166
21. Krarti M, Ali F, Alaidroos A, Houchati M (2017) Macro-economic benefit analysis of large scale building energy efficiency programs in Qatar. *Int J Sustain Built Environ* 6(2):597–609
22. Kharseha M, Al-Khawajaa M, Ferri Hassanib F (2015) Comparison between different measures to reduce cooling requirements of residential building in cooling-dominated environment. *Energy Buildings* 88:409–412
23. Krarti M, Dubey K, Howarth N (2017) Evaluation of building energy efficiency investment options for the Kingdom of Saudi Arabia. *Energy* 134:595–610
24. Abd-ur-Rehman HM, Al-Sulaiman FA, Mehmood A, Shakir S, Umer M (2018) The potential of energy savings and the prospects of cleaner energy production by solar energy integration in the residential buildings of Saudi Arabia. *J Clean Prod* 183:1122–1130
25. MEW (2014) Energy conservation program -code of practice. Ministry of Electricity and Water for Kuwait, Kuwait. Report No. MEW/R-6/2014. <https://www.mew.gov.kw/Files/MediaLibrary/TheCode.pdf>. Accessed 4 Mar 2018
26. Ameer B, Krarti M (2016) Impact of subsidization on high energy performance designs for Kuwaiti residential buildings. *Energy Buildings* 116:249–262
27. Radhi H (2008) A systematic method for optimising the energy performance of buildings in Bahrain. *Energy Buildings* 40(7):1297–1303
28. Krarti M, Dubey K (2018) Benefits of energy efficiency programs for residential buildings in Bahrain. *J Build Eng* 18:40–50

29. ASHRAE (2013) ASHRAE Standard 90.1-2013, ANSI/ASHRAE/IES Standard. Energy standard for buildings except low-rise residential buildings. American Society for Heating, Refrigerating and Air Conditioning, Atlanta, GA
30. EnergyPlus, a whole-building energy simulation tool, energyplus.net. <https://energyplus.net/>. Accessed 10 Jan 2018
31. AECOM (2017) Middle east property and construction handbook. AECOM, Abu Dhabi
32. Winiarski DW, Halverson MA, Jiang W (2007) Analysis of building envelope construction in 2003 CBECS. Report no. PNNL-2380, by Pacific Northwest National Laboratory. https://www.pnnl.gov/main/publications/external/technical_reports/pnnl-20380.pdf. Accessed 15 Apr 2018
33. Winiarski DW, Jiang W, Halverson MA (2006) Review of pre- and post-1980 buildings in CBECS—HVAC equipment, report no. PNNL-20346, by Pacific Northwest National Laboratory. https://www.pnnl.gov/main/publications/external/technical_reports/PNNL-20346.pdf. Accessed 12 Apr 2018
34. Al Anzi A, Al Shammeri B (2010) Energy saving opportunities using building energy simulation for a typical Mosque in Kuwait. Paper no. ES2010-90478, proceedings of ASME 2010 4th international conference on energy sustainability, volume 2, Phoenix, Arizona, USA, May 17–22, 2010
35. RS Means (2018) Building construction costs. <https://www.rsmeans.com/>. Accessed 5 Mar 2018
36. Ozbay K, Parker NA, Jawad D, Hussain S (2003) Guidelines for life cycle cost analysis, Federal Highway Administration. U.S. Department of Transportation, Washington, DC
37. Commercial Buildings Energy Consumption Survey (CBECS) (2012) U.S. energy information administration. <https://www.eia.gov/consumption/commercial/data/2012/index.php?view=consumption#c23-c32>. Accessed 10 Mar 2018
38. ASHRAE (2010) ANSI/ASHRAE standard 55-2010, thermal environmental conditions for human occupancy. American Society for Heating, Refrigerating and Air Conditioning, Atlanta, GA
39. JEPlus—an EnergyPlus simulation manager for parametrics, jeplus.org. <http://www.jeplus.org/wiki/doku.php?id=start>. Accessed 10 Apr 2018

Nanocomposite Windows Converting Solar Power into Electricity for Self-Sustaining Buildings



A. M. Darwish, S. S. Sarkisov, and D. N. Patel

1 Introduction

There is increasing public and private interest in the adoption of green energy technologies, of which solar will be a prime player. As it becomes desirable to generate energy at the point of demand, it is also more apparent that additional features beyond electrical performance play an important role in solar power: aesthetics and safety. Because of their adaptability and attractive appearance, there is a growing interest in luminescent solar concentrator (LSC) devices for use in buildings [1]. LSCs are large polymer/glass windows filled/coated with luminescent materials that absorb sunlight and re-emit it at a longer wavelength. The window acting as an optical waveguide redirects the re-emitted radiation to small edge-attached photovoltaic (PV) cells to generate electricity (Fig. 1). Because the LSC area exposed to sunlight is much larger than the edges, LSCs can greatly increase the flux of radiation incident onto the perimeter PV devices and increase the photocurrent, acting as a solar concentrator. In building-integrated applications, LSCs can be introduced without compromising a building's aesthetic value.

Despite advancements in design, wide use of LSCs has long been hindered by the lack of suitable emitters. Organometallic chromophores suffer from limited spectral coverage, while organic dyes and conventional core-only colloidal quantum dots [2, 3] exhibit a large overlap between the absorption and emission spectra (small Stokes shifts), which leads to strong reabsorption of the guided luminescence in large-area LSCs [4]. Therefore, a higher-performance luminophore would be needed for the

A. M. Darwish (✉)
Dillard University, New Orleans, LA, USA

S. S. Sarkisov
SSS Optical Technologies, LLC, Huntsville, AL, USA

D. N. Patel
Oakwood University, Huntsville, AL, USA

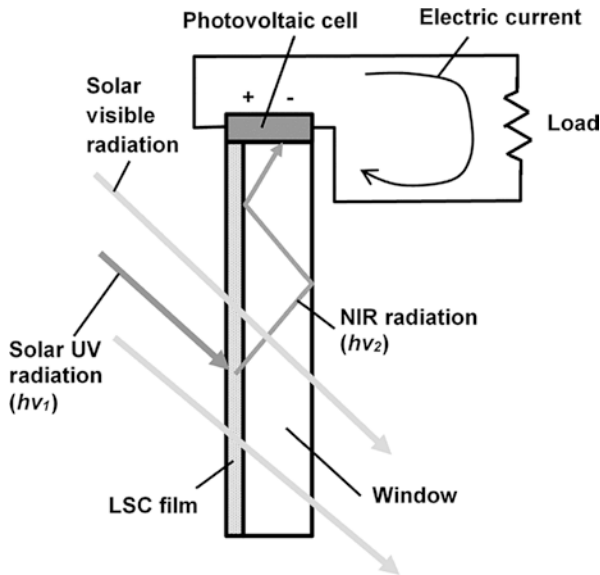


Fig. 1 Conceptual schematic of a luminescent solar concentrator (LSC). The nanoparticles of a luminescent material in the nanocomposite LSC film absorb incident UV sunlight (wide dark gray arrows; photons with energy $h\nu_1$, where h is the Planck's constant and ν_1 is the frequency of UV radiation) and re-emit the light at a longer wavelength (narrow dark gray zig-zag arrow; photons with energy $h\nu_2$, where ν_2 is the frequency of NIR radiation) in a window guiding it to a photovoltaic cell attached to the window edge

technology to advance. Compounds (halides, oxides, and fluorides) doped with ions of rare-earth (RE) elements can be considered as a potentially suitable alternative to address the issue [5–9]. They have a broad absorption spectrum covering a significant portion of the solar radiation spectrum, high spectral conversion efficiency, and low reabsorption. Additionally, they are environmentally stable, nontoxic, and do not require the usage of toxic materials for their synthesis. The RE-based lumino-phores must be embedded in a host, such as optically transparent resin, polymer, or glass. The host material must be shaped up either in the form of a coating or sheet/plate to be integrated with PV cells attached to the edges in order to implement an LSC. Suitable host material should have low optical losses, be durable, and inexpensive. And the technology of making large-size LSCs must be cost efficient.

Polymers have been studied as host materials for LSCs based on RE-compounds and demonstrated low optical losses in a wide optical spectrum from UV to near-infra-red (NIR) [5, 10]. They encapsulated the particles of the lumino-phores well and isolated them from ambient moisture. The LSC layer deposition was limited to dip wetting of the substrate (glass plate) with a polymer solution with the nanoparticles of the RE-phosphor added. The disadvantages of such a process were that (1) the thickness of the coating was no less than 100 μm and poorly controlled; as a result it was not possible to create anti-reflection interference coatings with periodically varying refractive index with a thickness of half-wavelength $\lambda/2$ (few

hundred nanometers); (2) it was not possible to vary the concentration of the luminescent phosphor and other nano-additives along and across the plane of the LSC in order to optimize its performance depending on its designated location and use in the building.

In this chapter, material and fabrication aspects of polymer nanocomposite films for luminescent solar concentrators doped with nanoparticles of RE-based fluorides and deposited using vacuum and open-air pulsed-laser deposition (PLD) are discussed.

2 Polymer Nanocomposite LSC Films Deposited in Vacuum

2.1 Fabrication

The LSCs were fabricated in vacuum using the concurrent multi-beam, multi-target pulsed laser deposition and matrix-assisted pulsed laser evaporation (CMBMT-PLD/MAPLE) process, which is a further development of the conventional PLD. For the last three decades, PLD has been intensively used for deposition of many kinds of otherwise hard-to-deposit (for instance, due to prohibitively high melting/vaporization temperatures) materials, such as oxides, nitrides, carbides, metals, superconductors, electro-optic and piezoelectric materials, etc. [11]. The technology, in its variation of the matrix-assisted pulsed laser evaporation (MAPLE), has been used for making polymer and other organic coatings [12–22]. In MAPLE, a frozen solution of a polymer in a volatile solvent becomes a laser target. The main portion of the laser energy is absorbed by the solvent and not by the solute, and no photochemical reaction occurs between the former and the latter. The energy of the laser beam absorbed by the solvent is converted to thermal energy, which heats the polymer but causes the solvent to vaporize. As the solvent molecules escape into the gas phase, the polymer molecules gain sufficient kinetic energy via collisions with the evaporating solvent molecules and enter the gas phase as well. This can result in the deposition process with no significant degradation of the polymer. In the case of fabrication of polymer nanocomposites, MAPLE targets are usually prepared as nanocolloids of the additives of interest in the initial polymer solutions. Combining components of different nature, such as polymers and inorganic substances, in the same target and ablating them with the same laser beam rarely results in nanocomposite films of fair quality. The laser beam energy and wavelength cannot fit all the components in the mixture. Also, the proportion of the components in the film is dictated by the target and cannot be altered in the process. It thus follows that, despite some encouraging results for single-component films, conventional single-beam, single-target PLD or MAPLE techniques are poorly suitable for composite films made of materials of different nature. Further improvement is a new variant of PLD called the concurrent multi-beam, multi-target PLD (CMBMT-PLD), which deposits different materials simultaneously with different laser beams producing overlapping plumes. In the case of polymer-inorganic nanocomposite films, at least

one of the laser beams and the target must be suitable for deposition of the polymer, such as MAPLE. This combined process can be designated the acronym CMBMT-PLD/MAPLE [23–46]. The advantages of this process with respect to other methods of making multicomponent polymer nanocomposite films are: (1) precise control of film thickness, (2) wide range of variation of fractional volume of the components, and (3) possibility of variation of mixing proportion of the components during deposition. The last improvement of the process was its open-air variant suitable for making LSC nanocomposite films on large substrates [46].

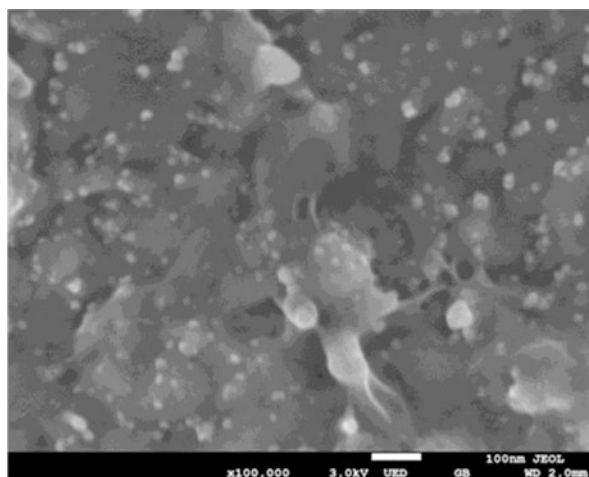
In the CMBMT-PLD/MAPLE process at Dillard University, the inorganic target was a pellet made of compressed powder of compound $\text{NaYF}_4:\text{Yb}^{3+},\text{Er}^{3+}$. The MAPLE target was a solution of polymer poly(methyl methacrylate), known as PMMA, in chlorobenzene at a proportion of 1 g solids per 10 mL liquids filtered with 0.2 μm filter. The solution was poured into a copper cup of the MAPLE target assembly and frozen in liquid nitrogen (LN). The laser source was a Spectra Physics Quanta Ray Nd:YAG Q-switched Pro-250-50 laser with a pulse repetition rate of 50 Hz, 750 mJ energy per pulse at the 1064 nm fundamental wavelength, and 400 mJ energy per pulse at the 532 nm second harmonic. The inorganic target was ablated with the 532-nm beam. The fluence was tuned up between 0.8 and 1.0 J/cm^2 per pulse. The MAPLE target was evaporated with the 1064-nm beam. The fluence ranged from 0.84 to 2.4 J/cm^2 per pulse. The volume fraction of the inorganic nanoparticles in the polymer matrix did not exceed 1%. The deposition time was 3.0 min. The thickness of the deposited films was approximately 150 nm as measured with an Atomic Force Microscope. The films were deposited at glass substrates at room temperature in vacuum. The inorganic target was rotated during the irradiation of laser beam. The substrate-target distance was maintained about 35 mm.

Phosphor $\text{NaYF}_4:\text{Yb}^{3+},\text{Er}^{3+}$, the material of the inorganic PLD target and the luminophore for LSC, have been used before by the authors for making polymer nanocomposite upconversion emitters (the concentration of Yb^{3+} ions was $\sim 2\%$, $\text{Er}^{3+} \sim 20\%$) [23–46]. However, in order to efficiently convert sunlight into NIR radiation via the mechanism of downconversion (quantum cutting), the proportions of the RE ions in the phosphor were chosen to be: Er $\sim 3\%$; Yb – from $\sim 1\%$ to 5% [9]. Powders of phosphor were synthesized using the economic wet process, which in its essence is the coprecipitation in the presence of Na_2 -ethylenediaminetetraacetic acid (EDTA). In a typical procedure, 2.1 g of NaF (0.05 mol) was dissolved in 60 ml of deionized water. Another solution was prepared by mixing together $a \times 16$ mL of 0.2-mol/L aqueous solution of YCl_3 , $b \times 16$ mL of 0.2-mol/L solution of YbCl_3 , $c \times 16$ mL of 0.2-mol/L solution of ErCl_3 , and 20 mL of 0.2-mol/L EDTA aqueous stock solution to form the metal-EDTA complex ($c = 1 - (a + b)$). The complex solution was injected in the NaF solution quickly, and the mixture was stirred vigorously for 1 h at room temperature. After stirring, the mixture was allowed to stay overnight for the precipitate to settle. The precipitate was collected and washed several times with distilled water and anhydrous ethanol. In the second stage of the process, the precipitate was dried under vacuum to remove any traces of water. The resulting microcrystalline powder had the doping rate according to formula $\text{NaY}_a\text{F}_4:\text{Yb}^{3+}_b,\text{Er}^{3+}_c$. For instance, the proportion Er (3%)Yb (1%) corresponded to

2.2 Results and Discussion

Fabricated polymer nanocomposite LSC films were characterized in terms of their morphology, microstructure, and optical properties. Figure 3 presents high-resolution scanning electron-microscope (SEM) image of the polymer nanocomposite LSC film of PMMA+NaYF₄:Yb³⁺,Er³⁺ deposited on glass substrate. As can be seen from Fig. 3, the luminophore nanoparticles (small white spots) in the polymer host have an average size of 10–50 nm. The LSC polymer nanocomposite films, as deposited, have a roughness of ~50–200 nm. They might need post-deposition heating above the polymer glass transition temperature of ~120 °C to be smoothed. Figure 4 presents the X-ray diffraction (XRD) spectrum of the two-component composite film made of PMMA and the nanoparticles of NaYF₄: Yb³⁺, Er³⁺ with the diffraction peaks attributed to the hexagonal β -phase of NaYF₄. This indicates that the monocrystalline nanoparticles of the luminophore were transferred in the polymer matrix during the CMBMT-PLD/MAPLE intact and their crystalline structure did not change. Figure 5 presents the fluorescence spectrum of the polymer nanocomposite LCS film pumped by a 457-nm Ar-ion laser. The laser simulated the sun with its UV and blue radiation, poorly producing a photo-electric current in silicon PV cells. The luminophore in the film was able to downconvert the laser radiation in NIR radiation with a spectrum at least 300 nm away from the laser spectral peak. There is no indication of possible strong re-absorption of the UV-blue radiation by the luminophore. Figure 6 shows the short-wave component of the NIR fluorescence spectrum of LSC downconversion luminophore NaYF₄:Er³⁺, Yb³⁺ in the film pumped with a 457-nm Ar-ion laser. The spectral peaks in the range from 600 to 910 nm can be more likely attributed to the transitions of the ions of Erbium from their excited states to the ground state ⁴I_{15/2} (Fig. 2). Figure 7 shows the long-wave component of the NIR fluorescence spectrum of LSC downconversion luminophore NaYF₄:Er³⁺,Yb³⁺ in the film pumped with a 457-nm Ar-ion laser. The spectrum

Fig. 3 Scanning electron-microscope (SEM) image of the polymer nanocomposite LSC film of PMMA doped with the nanoparticles of NaYF₄:Yb³⁺,Er³⁺ deposited on glass substrate at 100 k magnification



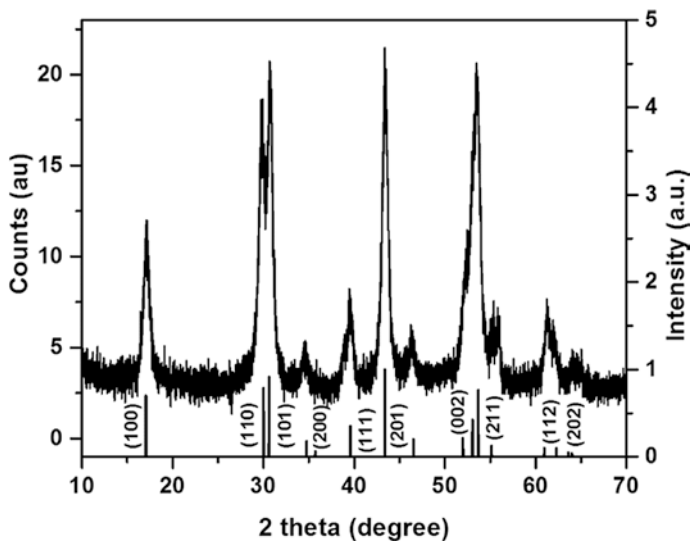


Fig. 4 XRD spectrum of the two-component composite film made of PMMA and the nanoparticles of $\text{NaYF}_4:\text{Yb}^{3+}, \text{Er}^{3+}$ with the diffraction peaks that can be attributed to hexagonal β -phase of NaYF_4 . For comparison, computed XRD spectrum of hexagonal β -phase of NaYF_4 (JCPDS card No. 77-2042) is shown at the bottom. Indices (hkl) mark the diffraction peaks associated with corresponding atomic planes

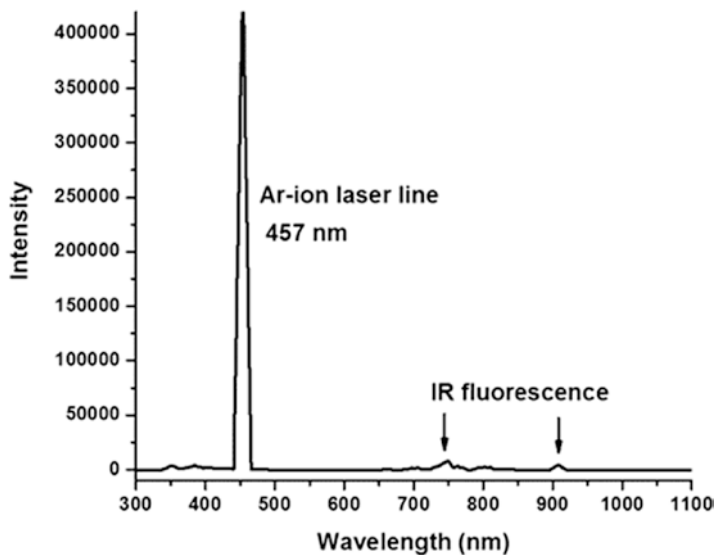


Fig. 5 Fluorescence spectrum of LCS downconversion lumiphore $\text{NaYF}_4:\text{Er}^{3+}, \text{Yb}^{3+}$ in the polymer nanocomposite film pumped with a 457-nm Ar-ion laser

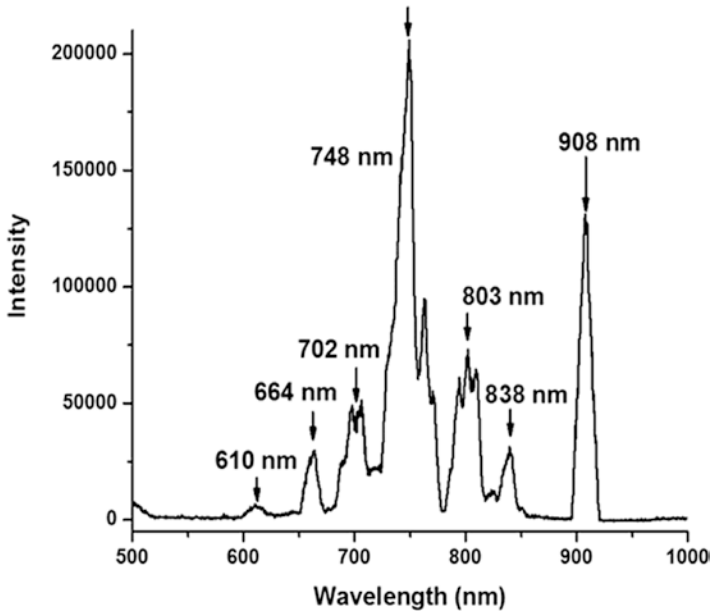


Fig. 6 Short-wave component of the NIR fluorescence spectrum of LSC downconversion lumiphore $\text{NaYF}_4:\text{Er}^{3+}, \text{Yb}^{3+}$ pumped with a 457-nm Ar-ion laser

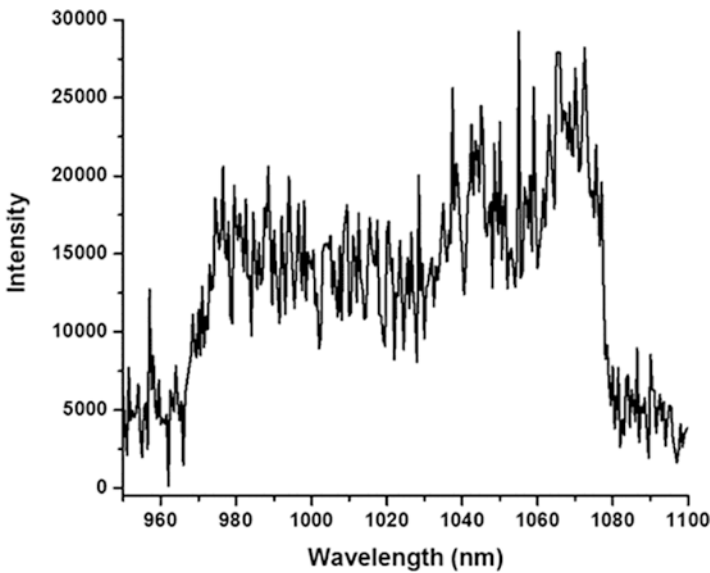


Fig. 7 Long-wave component of the NIR fluorescence spectrum of LSC downconversion lumiphore $\text{NaYF}_4:\text{Er}^{3+}, \text{Yb}^{3+}$ pumped with a 457-nm Ar-ion laser

more likely corresponds to the transitions of the ions of Ytterbium excited via the two above-mentioned cross-relaxation mechanisms of downconversion (Fig. 2) to ground state $^5F_{7/2}$. So the proposed luminophore dopant of the polymer nanocomposite film is suitable for the task of converting sunlight in the NIR radiation acceptable by silicon PV cells in LSCs.

3 Polymer Nanocomposite LSC Films Deposited in Ambient Air

3.1 Fabrication

The advantage of the open-air deposition is the ability to coat wide-area window-size substrates. The study was concentrated on the survivability of the polymer host of the films at the deposition in open air. Polymer PMMA (Fig. 8) was assumed as a suitable host for the downconversion luminophore in the polymer nanocomposite LSC films. One can see in the chemical formula of PMMA molecule (Fig. 8) a number of chemical bonds that can be broken due to oxidation in atmospheric oxygen during the PLD process. This might result in possible decomposition of the polymer. The actual open-air PLD target was a plastic microscope slide, treated, UVT (UV transmittable) acrylic; (75 × 25 × 1.1 mm); Catalog #260226 from Ted Pella, Inc. The surface of the slide is tissue culture treated by using a dry treatment

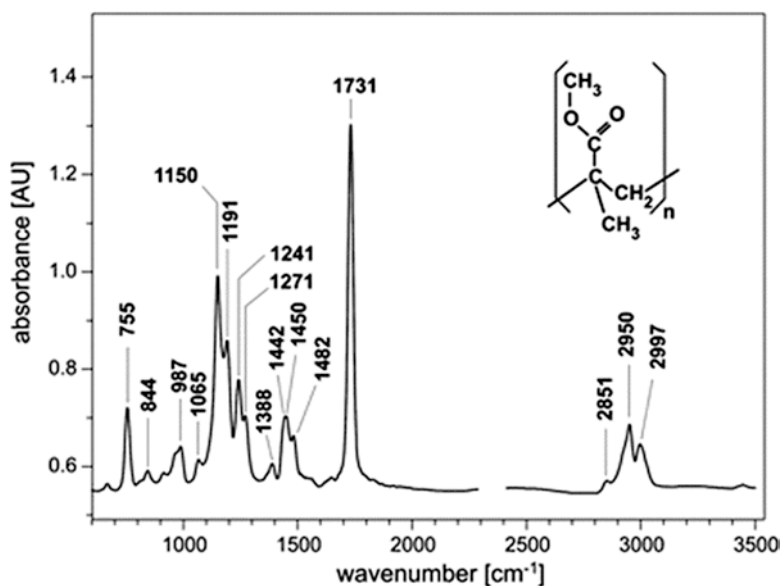


Fig. 8 Typical FTIR absorption spectrum of polymer PMMA [47]

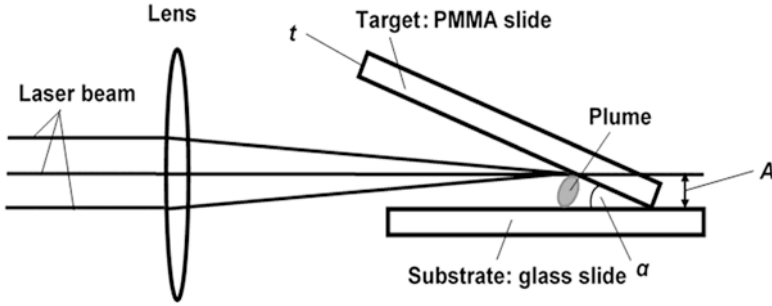


Fig. 9 Schematic of the open-air PLD of PMMA polymer film

of gas plasma, gamma sterilized. A typical FTIR absorption spectrum of PMMA is also presented in Fig. 8.

The experimental setup to test the suitability of PMMA for the open-air PLD process is presented in Fig. 9. Experiments were conducted to investigate how the integrity of the polymer host was affected by the open-air PLD process. The polymer film was deposited in open air using Continuum Surelite SL III-10 Q-switched Nd:YAG laser. Laser pulse had energy $E = 0.9$ J at a wavelength $\lambda = 1064$ nm, pulse duration was $\tau = 5$ ns. Laser beam diameter $D = 10$ mm. The lens had a focal length $f = 50$ mm. Pulse average power $P = E/\tau = 1.8 \times 10^8$ W = 0.18 GW. Beam radius in the focus w_0 .

$$w_0 = \left(\frac{2\lambda}{\pi} \right) \left(\frac{f}{D} \right) = 3.4 \text{ } \mu\text{m}.$$

Average beam intensity in the focus I_0 .

$$I_0 = \frac{P}{(\pi w_0^2)} = 5.0 \times 10^{14} \text{ W / cm}^2.$$

Target thickness was $t = 1$ mm; material: PMMA slide; target tilt angle $\alpha = 5^\circ$; substrate: microscope glass slide; distance from the laser spot on the target to the substrate $A \approx 2$ mm; time of ablation (exposure to laser beam): 5 min. With a pulse repetition rate of 10 Hz, the ablation took 3000 laser pulses.

3.2 Results and Discussion

The morphology of the open-air deposited PMMA coatings was investigated using optical microscopy with an optical AmScope M400 Monocular Compound microscope, a WF10× Eyepiece, 40×–400× Magnification, anti-mold optics, tungsten illumination, bright field, Abbe condenser, coarse and fine focus, and plain stage

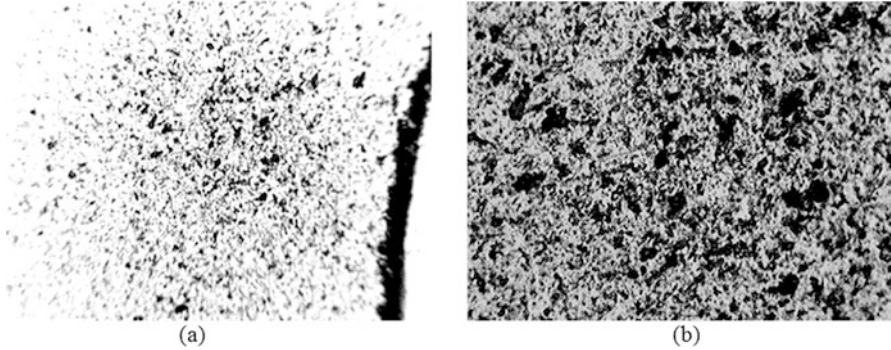


Fig. 10 Microscope image of the acrylic coating on glass substrate right after open-air PLD (at 532-nm harmonic) with (a) $\times 40$ magnification (objective $\times 4$) and (b) $\times 100$ magnification (objective $\times 10$). Dark band on the right in image (a) is the print made by $\times 40$ objective that occasionally touched the coating

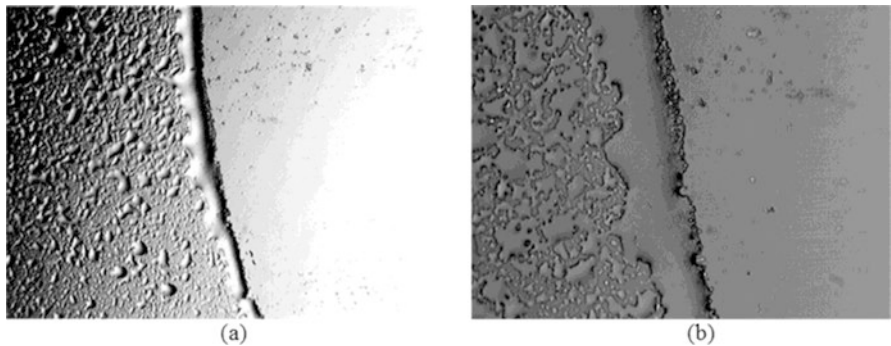


Fig. 11 Microscope image of the PLD made PMMA coating on glass substrate presented in Fig. 10 right after melting on a hot plate at $90\text{ }^{\circ}\text{C}$ with (a) $\times 40$ magnification, dimensions: $X = 2257\text{ }\mu\text{m}$, $Y = 1674\text{ }\mu\text{m}$, and (b) $\times 100$ magnification, dimensions: $X = 903\text{ }\mu\text{m}$, $Y = 670\text{ }\mu\text{m}$

with AmScope Mu 400 CCD camera. The microscope images of the coating as deposited (initially, using the laser second harmonic at 532-nm) are presented in Fig. 10. The dimensions of the images in Fig. 10a are: horizontal $X = 2257\text{ }\mu\text{m}$, vertical $Y = 1674\text{ }\mu\text{m}$. The dimensions of the image in Fig. 10b are: horizontal $X = 903\text{ }\mu\text{m}$, vertical $Y = 670\text{ }\mu\text{m}$. The coating is partial. It was made by 15-min exposure to 532-nm laser pulses, pulse energy 0.024 J (37.5 times less than at 1064 nm). Melting the coating depicted in Fig. 10 on a hot plate at $90\text{ }^{\circ}\text{C}$ did not create a continuous film (Fig. 11). The droplets coalesced, but there was not enough material to produce continuous coating. Then open-air PLD of acrylic material was conducted by the more energetic 1064-nm pulses for 5 min. After melting on a hot plate at $90\text{ }^{\circ}\text{C}$, the droplets coalesced to create a continuous film as presented in Fig. 12.

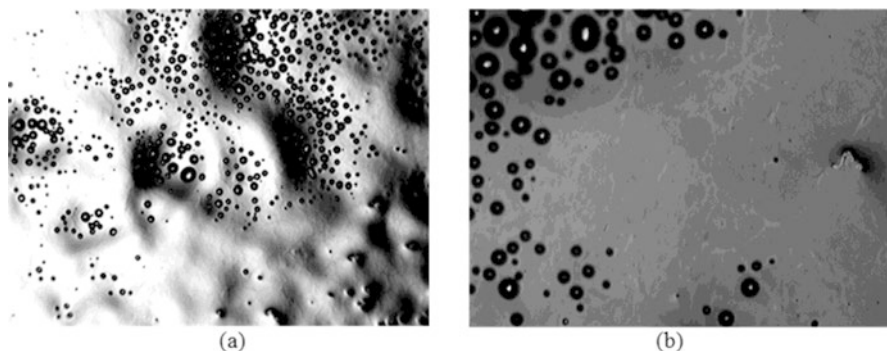


Fig. 12 Microscope image of the PLD made (1064-nm pulses, 5-min exposure) acrylic coating on glass substrate right after melting on a hot plate at 90 °C with (a) $\times 40$ magnification, dimensions: $X = 2257 \mu\text{m}$, $Y = 1674 \mu\text{m}$, and (b) $\times 100$ magnification, dimensions: $X = 903 \mu\text{m}$, $Y = 670 \mu\text{m}$. The images of boiling air bubbles are seen as small circles

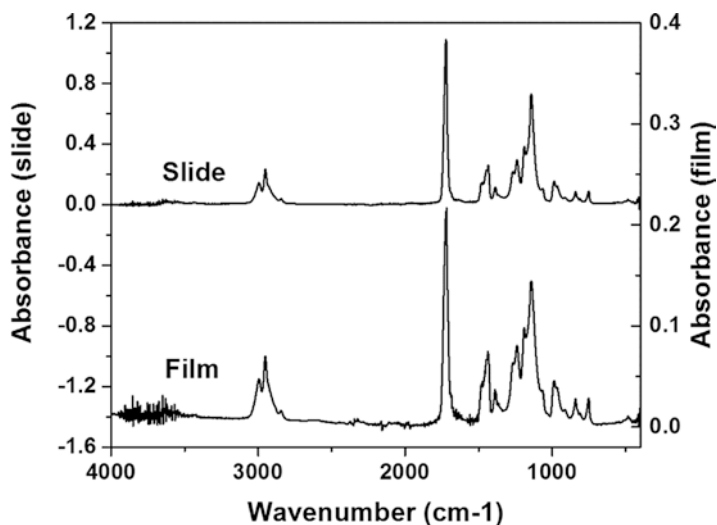


Fig. 13 FTIR absorption spectra of the acrylic slide used as a PLD target and the PLD-deposited acrylic film on glass slide

FTIR absorption spectra of the acrylic slide used as a target for PLD ablation (reference) and the resulting PLD film (Fig. 13) were taken with the Nicolet iS5 FTIR spectrometer from Thermo Scientific (ThermoFisher) with an iD7 ATR diamond anvil attachment. Comparison of the FTIR spectrum of the film against the spectrum of the slide indicates that there was no noticeable decomposition of the molecules of the acrylic polymer during the open-air PLD process.

4 Conclusions

1. Downconversion luminophore NaYF₄:Er³⁺, Yb³⁺ selected for LSCs has low reabsorption: Stokes shift between the spectrum of absorption and fluorescence is no less than 300 nm.
2. The luminophore is chemically stable and can be transferred to the polymer matrix during the CMBMT-PLD/MAPLE process, preserving its crystalline structure.
3. The luminophore nanoparticles in polymer PMMA host have an average size of 10–50 nm. The LSC polymer nanocomposite films as deposited (in vacuum) have a roughness of ~50–200 nm. They need postdeposition heat-induced melting to be smoothened.
4. PMMA host of the nanocomposite LSC film deposited using open-air PLD process was found to preserve its chemical integrity. The open-air PLD coating of large window-size substrates was proven to be feasible.

The obtained results might find applications in the improvement of building energy efficiency.

Acknowledgments Dr. A.M. Darwish and his research team at Dillard University appreciates financial support from US Air Force Office of Scientific Research Grant F9550-18-1-0364 AFOSR and Army Research Office Grant W911-19-1-0451 and partial support from Minoriy Health and Health Disparity Research Center (MHHDR) at Dillard University.

References

1. Debije M (2017) Luminescent solar concentrators. Luminescent solar solutions. Semiconductor solutions. *Nat Photon* 11:143–144
2. Krumer Z, Pera SJ, van Dijk-Moes RJA, Zhao Y, de Brouwer S, Groenvelde E, van Sark WGJHM, Schropp REI, de Mello Donega C (2013) Tackling self-absorption in luminescent solar concentrators with type-II colloidal quantum dots. *Sol Energy Mater Sol Cell* 111:57–65
3. Pietryga JM, Park Y-S, Lim J, Fidler AF, Bae WK, Brovelli S, Klimov VI (2016) Spectroscopic and device aspects of nanocrystal quantum dots. *Chem Rev* 116:10513–10622
4. Giebink NC, Wiederrecht GP, Wasielewski MR (2011) Resonance-shifting to circumvent reabsorption loss in luminescent solar concentrators. *Nat Photon* 5:694–701
5. Wang T, Zhang J, Ma W, Luo Y, Wang L, Hu Z, Wu W, Wang X, Zou G, Zhang Q (2011) Luminescent solar concentrator employing rare earth complex with zero self-absorption loss. *Sol Energy* 85:2571–2579
6. Park WJ, Oh SJ, Kim JK, Heo J, Wagner T, Strizik L (2014) Down-conversion in Tm³⁺/Yb³⁺ doped glasses for multicrystalline silicon photo-voltaic module efficiency enhancement. *J Non-Cryst Solids* 383:181–183
7. TenKate OM, Krämer KW, Van der Kolk E (2015) Efficient luminescent solar concentrators based on self-absorption free, Tm²⁺ doped halides. *Sol Energy Mat Sol Cells* 140:115–120
8. Xia W, Jin X, Yang X, Xiao S (2016) Down conversion of Er³⁺-Yb³⁺ couple in Y₂BaZnO₅. *Opt Mat* 54:294–299
9. Verma A, Sharma SK (2017) Down-conversion from Er³⁺-Yb³⁺ codoped CaMoO₄ phosphor: a spectral conversion to improve solar cell efficiency. *Ceram Int* 43:8879–8885

10. Meinardi F, Ehrenberg S, Dharmo L, Carulli F, Mauri M, Bruni F, Simonutti R, Kortshagen U, Brovelli S (2017) Highly efficient luminescent solar concentrators based on earth-abundant indirect-bandgap silicon quantum dots. *Nat Photon* 11(3):177–186
11. Yan D (ed) (2016) Applications of laser ablation. Thin film deposition, nanomaterial synthesis and surface modification. InTech, Rijeka, Croatia
12. Constantinescu C, Rotaru A, Nedelcea A, Dinescu M (2015) Thermal behaviour and matrix-assisted pulsed laser evaporation deposition of functional polymeric materials thin films with potential use in optoelectronics. *Mat Sci Semiconduct Process* 30:242–249
13. Caricato AP, Cesaria M, Leo C, Mazzeo M, Genco A, Carallo S, Tunno T, Massafra A, Gigli G, Martino M (2015) Very low roughness MAPLE-deposited films of a light emitting polymer: an alternative to spin coating. *J Phys D Appl Phys* 48(13):135501
14. Aronne A, Bloisi F, Calabria R, Califano V, Depero LE, Fanelli E, Federici S, Massoli P, Vicari LPMR (2015) Lipase biofilm deposited by matrix assisted pulsed laser evaporation technique. *Appl Surf Sci* 336:196–199
15. Iordache F, Grumezescu V, Grumezescu AM, Curutiu C, Ditu LM, Socol M, Ficai A, Truşcă R, Holban AM (2015) Gamma-cyclodextrin/uscnic acid thin film fabricated by MAPLE for improving the resistance of medical surfaces to *Staphylococcus aureus* colonization. *Appl Surf Sci* 336:407–412
16. Matei A, Constantinescu C, Mitu B, Filipescu M, Iona V, Ionita I, Ionita I, Brajnicov S, Alloncle A-P, Emandi A, Dinescu M (2015) Laser printing of azo-derivative thin films for non-linear optical applications. *Appl Surf Sci* 336:200–205
17. Stiff-Roberts AD, McCormick RD, Wangyao G (2015). Material properties and applications of blended organic thin films with nanoscale domains deposited by RIR-MAPLE, In Proceedings of SPIE, vol 9350. SPIE, Bellingham, WA, p 935007
18. Grumezescu V, Andronesu E, Holban AM, Grumezescu AM, Socol G, Iordache F, Maniu H, Chifiriuc MC (2015) MAPLE fabrication of thin films based on kanamycin functionalized magnetite nanoparticles with anti-pathogenic properties. *Appl Surf Sci* 336:188–195
19. Caricato AP, Anni M, Cesaria M, Lattante S, Leggieri G, Leo C, Martino M, Perulli A, Resta V (2015) MAPLE-deposited PFO films: influence of the laser fluence and repetition rate on the film emission and morphology. *Appl Phys B Lasers Opt* 19(3):453–461
20. Wangyao G, Atewologun A, Stiff-Roberts AD (2015) Hybrid nanocomposite thin films deposited by emulsion-based resonant infrared matrix-assisted pulsed laser evaporation for photo-voltaic applications. *Org Electron Mat, Phys, Chem Appl* 22:98–107
21. Janković A, Eraković S, Ristoscu C, Mihailescu N, Duta L, Visan A, Stan GE, Popa AC, Husanu MA, Luculescu CR, Srdić VV, Janačković D, Mišković-Stanković V, Bleotu C, Chifiriuc MC, Mihailescu IN (2015) Structural and biological evaluation of lignin addition to simple and silver-doped hydroxyapatite thin films synthesized by matrix-assisted pulsed laser evaporation. *J Mater Sci Mater Med* 26:1–14
22. Paun IA, Acasandrei AM, Luculescu CR, Mustaciosu CC, Ion V, Mihailescu M, Vasilea E, Dinescu M (2015) MAPLE deposition of polypyrrole-based composite layers for bone regeneration. *Appl Surf Sci* 357:975–984
23. Darwish AM, Sagapolutele MT, Sarkisov SS, Patel D, Hui D, Koplitz B (2013) Double beam pulsed laser deposition of composite films of poly(methyl methacrylate) and rare earth fluoride upconversion phosphors. *Composites B* 55:139–146
24. Darwish AM, Sagapolutele MT, Wilson S, Sarkisov SS, Patel D, Koplitz B, Hui D (2013) Double pulse laser deposition of polymer nanocomposite films for optical sensors and light emitting applications, In Proceedings of ICCE-21. Twenty first annual internal conference on composite/nano Engineering, July 21–27, 2013 Tenerife, Canary Islands, Spain, ed. by David Hui, Paper 181
25. Darwish AM, Wilson S, Sarkisov SS, Patel D (2014) Double pulse laser deposition of polymer nanocomposite $\text{NaYF}_4:\text{Tm}^{3+}, \text{Yb}^{3+}$ films for optical sensors and light emitting applications. In Photonic Fiber and Crystal Devices: Advances in Materials and Innovations in Device Applications VII. Proceedings of SPIE, vol. 8847. SPIE, Bellingham, WA, p 884702

26. Darwish AM, Burkett A, Blackwell A, Taylor K, Sarkisov SS, Patel D, Koplitz B, Hui D (2015) Polymer-inorganic nano-composite thin film upconversion light emitters prepared by double-beam matrix assisted pulsed laser evaporation (DB-MAPLE) method. *Composites B* 68:355–364
27. Darwish AM, Wilson S, Blackwell A, Taylor K, Sarkisov SS, Patel D, Koplitz B, Hui D (2014) New double-beam matrix assisted pulsed laser evaporation (DB-MAPLE) method for making polymer nano-composite coatings. In *Proceedings of ICCE-22. Twenty Second Annual International Conference on Composites or Nano-Engineering*, July 13–19, 2014, Malta, ed. by David Hui
28. Darwish AM, Burkett A, Blackwell A, Taylor K, Walker V, Sarkisov SS, Koplitz B (2014) Efficient upconversion polymer-inorganic nanocomposite emitters prepared by the double beam matrix assisted pulsed laser evaporation DB-MAPLE. In *Photonic Fiber and Crystal Devices: Advances in Materials and Innovations in Device Applications VIII. Proceedings of SPIE*, vol. 9200. SPIE, Bellingham, WA, p 92000C
29. Patel D, Lewis A, Wright D III, Lewis D, Valentine R, Valentine M, Wessley D, Sarkisov SS, Darwish AM (2015) Optical properties and size distribution of the nano-colloids made of rare-earth ion-doped NaYF₄. In *Optical Components and Materials XII. Proceedings of SPIE* vol. 9359. SPIE, Bellingham, WA, p 93591L
30. Darwish AM, Wilson S, Blackwell A, Taylor K, Sarkisov SS, Patel DN, Koplitz B (2015) Ammonia Sensor based on polymer-inorganic nano-composite thin film upconversion light emitter prepared by double-beam pulsed laser deposition. *Amer J of Mat Sci* 5(3A):8–15
31. Darwish AM, Wilson S, Blackwell A, Taylor K, Sarkisov SS, Patel D, Mele P, Johnson MW, Zhang X, Koplitz B (2015) Polymer-inorganic nanocomposite thin film emitters, optoelectronic chemical sensors, and energy harvesters produced by multiple-beam pulsed laser deposition. In *Photonic Fiber and Crystal Devices: Advances in Materials and Innovations in Device Applications IX. Proceedings of SPIE*, vol. 9586 SPIE, Bellingham, WA, p 958602
32. Darwish AM, Wilson S, Blackwell A, Taylor K, Sarkisov SS, Patel D, Mele P, Koplitz B (2015) Multi-beam pulsed laser deposition: new method of making nanocomposite coatings. in *Photonic Fiber and Crystal Devices: Advances In Materials and Innovations in Device Applications IX. Proceedings of SPIE* vol. 9586 (SPIE, Bellingham, WA, p 958605
33. Darwish AM, Wilson S, Blackwell A, Taylor K, Sarkisov S, Patel D, Mele P, Koplitz B, Hui D (2015) Multi-beam pulsed laser deposition of nanocomposite films as a new additive manufacturing process. In *Proceedings of ICCE-23. Twenty Third Annual International Conference on Composites or Nano-Engineering*, July 12-17, 2015, Chengdu, China. Ed. by David Hui
34. Darwish AM, Wilson S, Blackwell A, Taylor K, Sarkisov SS, Patel D, Mele P, Koplitz B, Hui D (2016) Triple-beam triple-target pulsed laser deposition of polymer nanocomposite films with rare-earth and AZO additives. In *Proceedings of ICCE-24. Twenty Fourth Annual International Conference on Composites/Nano-Engineering*, July 17–23, 2016, Haikou, Hainan Island, China, ed. by David Hui
35. Patel D, Sarkisov SS, Darwish A, Ballato J (2016) Optical gain in capillary light guides filled with NaYF₄: Yb³⁺, Er³⁺ nanocolloids. *Opt Express* 24(18):21147–21158
36. Darwish AM, Moore S, Mohammad A, Alexander D, Bastiana T, Dorlus W, Sarkisov SS, Patel DN, Mele P, Koplitz B (2016) Organic-inorganic nano-composite films for photonic applications made by multi-beam multi-target pulsed laser deposition with remote control of the plume directions. In *Photonic Fiber and Crystal Devices: Advances in Materials and Innovations in Device Applications X. Proceedings of SPIE*, vol. 9958. SPIE, Bellingham, WA, p 995802
37. Darwish AM, Moore S, Mohammad A, Alexander D, Bastian T, Dorlus W, Sarkisov SS, Patel D, Mele P, Koplitz B, Hui D (2017) Polymer nano-composite films with inorganic upconversion phosphor and electro-optic additives made by concurrent triple-beam matrix assisted and direct pulsed laser deposition. *Composites B* 109:82–90
38. A. M. Darwish, S. S. Sarkisov, D. N. Patel, Concurrent multi-target laser ablation for making nano-composite films. Chapter 6. in *Applications of laser ablation – thin film deposition, Nanomaterial Synthesis and Surface Modification* by D. Yang, InTech, Rijeka,, Croatia, 2016). p. 129

39. Darwish AM, Sarkisov SS Method and apparatus for multi-beam pulsed laser deposition of thin films. US Provisional Patent Application No. 61/850,330, Filed 2/14/2013
40. Darwish AM, Mele P, Sarkisov S Nano-composite thermo-electric energy harvester and fabrication method thereof. US Provisional Patent Application No. 62/071,116, Filed 9/15/2014
41. Darwish AM, Sarkisov SS Multiple beam pulsed laser deposition of composite films. US Patent Application No. 14/158,567, Priority date Feb 14, 2013, Filed 1/17/2014, Publication No. US 2014/0227461 A1, Pub. Date 8/14/2014
42. Darwish AM, Sarkisov SS Multiple beam pulsed laser deposition of composite films. US Patent Application No. 14/506,685, Filed 10/15/2014
43. Darwish AM, P. Mele, S. S. Sarkisov, Nano-composite thermo-electric energy converter and fabrication method thereof. US Patent Application No. 14/853,674, Filed 9/14/2015
44. Darwish AM, Sarkisov SS, Method and apparatus for open-air multi-beam multi-target pulsed laser deposition. US Provisional Patent Application No. 62/389,086, Filed 2/17/2016
45. Darwish AM, Mele P, Sarkisov SS, Nano-composite thermo-electric energy converter and fabrication method thereof. US Patent Application No. 14/853,674, Priority date 9/15/2014, Filed 9/14/2015, Publication No. US 2016/0056361 A1, Pub, Date 2/25/2016
46. Darwish AM, Sarkisov S, Method and apparatus for open-air pulsed laser deposition. US Patent Application No. 15435778, Filed 2/17/2017
47. Dazzi A, Deniset A, Lasch P (2013) Minimizing contributions from scattering in infrared spectra by means of an integrating sphere *Analyst* 138(14):4191–4201

Atrium Design and the Science of Daylighting: A Comparative Field Study



Sadiqa Al Awadh and Ihab Elzeyadi

1 Introduction

The design of a building is greatly influenced by stakeholders' attitudes and outlooks on the roles the building is expected to fulfill. The utilitarian role views the building as an organizational container, a necessary overhead which should involve the minimum of expenditure; the public relations role portrays the building as a corporate symbol of prestige, with the emphasis on dominant location and impressive exterior image; the industrial relations role deems the building as a tool of personnel relations with interior standards of comfort and safety, conveying concern for the workforce; the instrument role regards the building as an instrument of efficiency with layouts and services consciously designed to aid performance and support internal communications; the inspirational role perceives the building as an inspirational force that expresses high standards of attainment sought of all staff and a commitment to excellence [1]. Since buildings are ultimately designed and constructed for human end users, it is critical that they not only satisfy environmental and economic expectations, but also meet indoor environment requirements. Indoor environmental parameters that influence occupant well-being include visual, thermal conditions, air quality, ergonomics, and acoustics. Studies have shown that people spend more than 90% of their time indoors [2]. This highlights the need to design indoor environments that enhance occupant well-being by creating a connection to the outdoors.

S. Al Awadh (✉) · I. Elzeyadi
University of Oregon, Eugene, OR, USA
e-mail: ihab@uoregon.edu

2 Daylight Instrumental Metrics

The following luminous quantities are some of many that have been extensively used in the literature for the assessment of daylight and the luminous environment [3, 4]. The distinct luminous characteristics of daylight are determined by its spectrum, color, quantity, and directionality; knowing these light factors, one can replicate the luminous distribution [5]. Other light factors, including timing, duration, and history, are temporal characteristics of daylight. These are mostly dependent on a building's occupancy pattern, which vary from one person to another [6].

The most familiar and widely used photometric unit of measure for light is photopic lux. It quantifies illuminance, the total power of light falling on a detector surface from any direction as perceived by a standard human observer [7]. What primarily started as a means to assess the daylight conditions needed to provide minimally adequate daylight levels in Europe resulted in the development of one of the earliest metrics for daylight performance. The Daylight Factor (DF) is the ratio of internal illuminance at a point in a building to the unshaded, unobstructed, external horizontal illuminance under standard CIE overcast sky conditions—expressed as a percentage [8]. An average DF of 2% across a given space is usually required for it to be considered sufficiently daylit. This metric, which was not developed with the intention to accurately assess daylight performance, does not account for different sky conditions and is not sensitive to building orientation, geographic location, or sun position. To address the shortcomings of this overly simplified metric, more complex hourly daylight metrics were developed and adopted.

Daylight Autonomy (DA), first defined by Reinhart, is the percentage of occupied time of the year when a minimum work plane illuminance threshold of 500 lux can be maintained by daylight alone [9]. It uses work plane illuminance as an indicator of whether there is sufficient daylight in a space so that an occupant can work by daylight alone. This metric is somewhat problematic as it proposes binary thresholds which might unjustly differentiate spaces based on measurements of light changes that may not be perceived by the human visual system. This was further developed and standardized to what is known as Spatial Daylight Autonomy (sDA) which is a percentage of analyzed area that meets a minimum horizontal daylight illuminance level for a specified fraction of the operating hours of the year [10]. A commonly used benchmark is to achieve 300 lux for 50% of the time, $sDA_{300/50\%}$.

With these metrics, there is little emphasis on the evaluation of the potential risk of excessive sunlight penetration; this led to the development of the Annual Light Exposure (ASE). It is defined as the cumulative amount of visible light incident on a point of interest over the course of a year, measured in lux hours per year. It describes the potential for visual discomfort in interior work environments by quantifying the percentage of analyzed points that receive at least 1000 lux for at least 250 occupied hours per year. Daylit spaces predicted to have more than 10% ASE are considered to have “unsatisfactory visual comfort,” spaces with less than 7% are considered “nominally acceptable” and spaces with less than 3% are considered “clearly acceptable.” Both the sDA and ASE metrics described above are commonly

referred to as the Dynamic Daylighting Metrics and adopted by IES as standards of measurements in practice [10]. These were expanded to incorporate aspects of occupant behavior and preference based on field research and reports of occupants' use of user-operated shading devices. Useful Daylight Illuminances (UDI) determine when daylight levels are "useful" for the occupant, that is, neither too dark (<100 lux) nor too bright (>2000 lux) [11].

A high or nonuniform distribution of brightness in the field of view can cause what are usually categorized into three levels of glare: disability glare, discomfort glare, and veiling glare [12, 13]. Detecting and evaluating the dynamic patterns of luminance in daylight spaces and mapping how these patterns may affect the comfort and behavior of occupants is complex. It not only relies on the brightness of the source, but also depends on the size of the source, the viewer's position and the overall surrounding scene luminance. Despite the extent of how unreliable glare metrics utilized in the field can be [14], the outlined modes of measurements are frequently used. They currently provide the closest predictive performance of daylight spaces designers are capable of reaching [15].

The Daylight Glare Probability identifies glare sources as detected by contrast ratios—above 0.45 is intolerable, below 0.3 is barely perceptible. The CIE Glare Index is an index used for luminaire sources of glare, it requires both direct and diffuse illuminances—above 28 is intolerable, below 13 is barely perceptible. The Daylight Glare Index is another index used that considers glare from the sky viewed through a window—above 31 is intolerable, below 18 is barely perceptible. Visual Comfort Probability is the percentage of people predicted to feel comfortable with the luminous environment.

These commonly used metrics clearly reflect the academic research, lighting design, and manufacturing communities' priorities in relation to defining daylighting. Relatively simple illuminance measurements are considered to be sufficient for meeting visual task needs, minimizing discomfort and maximizing energy savings. Though determining the impacts of illuminance levels in the luminous environment is essential, what about the other dimensions of daylight? Do these illuminance-based metrics unjustly overshadow the other components of daylight?

3 Occupant Well-Being as a Design Criteria

Most of the metrics and building standards have been derived from and based on our understanding of the function of the rods and cones in our eyes. They essentially focus on quantitative and instrumental aspects of light. Similarly, occupant well-being and human health models have mostly assessed the luminous environment for visual effects of glare [16], flicker [17], and perceptual health based on the meaning that occupants give to lit environments [18]. Glare and flicker we found to be the main environmental variables to be correlated with the occurrence of headaches, eye symptoms, fatigue, and difficulty concentrating. These were referenced in the definition of lighting quality but not adequately defined with established metrics.

There remain a number of unexplained parameters about our relationship with light. Though we are familiar with the rods and cones, which are responsible for image forming, not everyone is familiar with intrinsically photosensitive retinal ganglion cells (ipRGCs), which are found at the back of our retina. These are responsible for non-image-forming or nonvisual functions, both physiological and psychological, which include regulating the circadian biological clock and hormones, body temperature, heart rate, vitamin D synthesis, mood, stress, depression, and alertness.

These nonvisual benefits of daylight that affect well-being are stimulated by a different light action spectrum. The common measurement of illuminance, photopic lux $V(\lambda)$, describes the spectral sensitivity of one aspect of human cone-based vision, which peaks at 555 nm. The spectral sensitivities of nonvisual circadian systems peak at 490 nm. Optimal light for vision differs from optical radiation appropriate for nonvisual responses [19]. Since there has been recent discovery of ipRGCs, these nonvisual components should be taken into consideration and designers should incorporate human biological impacts of light as a design criterion. It is important to investigate how architecture can act as a mediating component between these quantitative instrumental, physiological health effective aspects and the qualitative psychological perception aspects of light to enhance occupant well-being (Fig. 1) .

3.1 Daylight Health Effective Metrics

Since the common measure of illuminance, photopic lux $V(\lambda)$, describes the spectral sensitivity of one aspect of human cone-based vision, it has limited utility. As previously mentioned, the spectral sensitivities of the visual and nonvisual systems (peaked at 555 nm and 490 nm, respectively) are different. Thus, illuminance-based photopic lux metrics are not appropriate to evaluate nonvisual responses. Researchers and professionals in the field have resorted to developing a set of metrics, simulation, field study methods, and technological tools for new daylight health effective modes of measurements.

The biological effects of light on humans are usually translated from spectral power distributions and measured in “equivalent melanopic lux,” a proposed alternate flux density metric that is weighted to the *ipRGCs*’ luminous efficiency function, which peaks at 490 nm and is based on the action spectrum of melanopsin instead of the cones’ photopic luminous efficiency function $V(\lambda)$. The latter function peaks at 555 nm and is based on the response of foveal, long- and middle-wavelength sensitive cones, which is the case with traditional lux [20]. This translation is used to understand how much the spectrum of a light source stimulates ipRGCs and affects the circadian system. The equivalent melanopic lux metric has been adopted by the WELL Building Standard [21]. It states that lighting in workplace breakrooms is required to maintain an average of at least 250 equivalent melanopic lux.

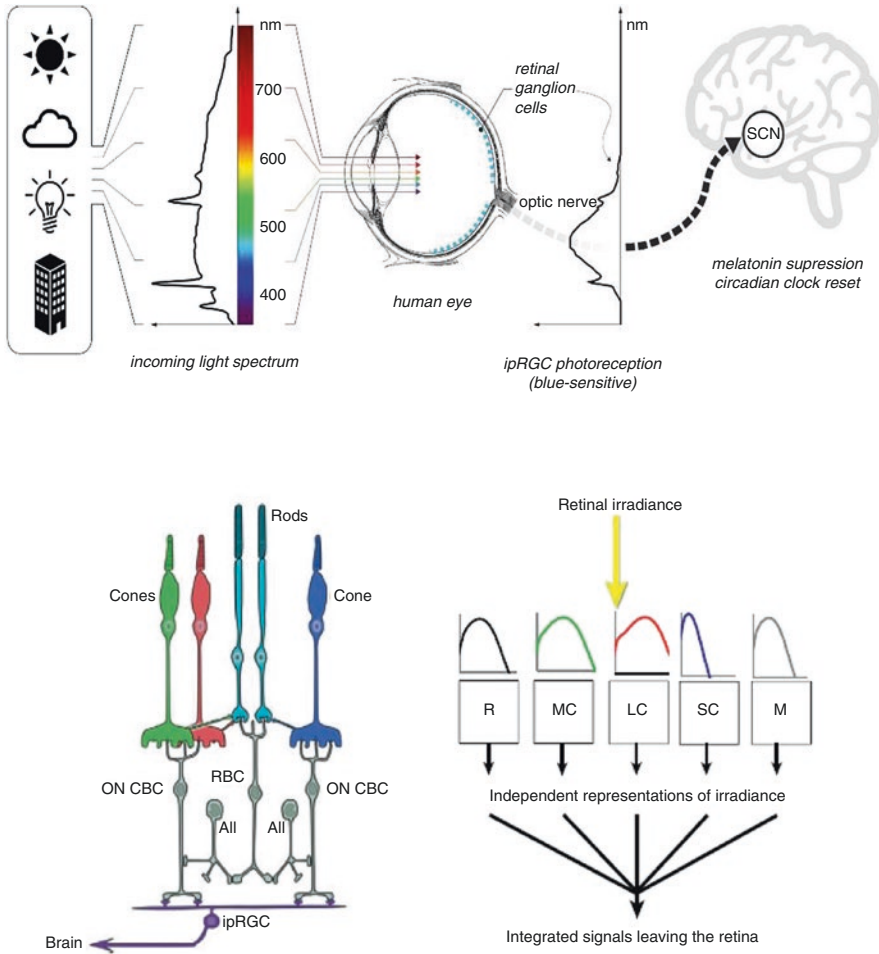


Fig. 1 Schematic of retinal circuitry and photoreceptive mechanisms in humans [19]

The Lighting Research Center at Rensselaer Polytechnic Institute has also proposed a metric, known as “the circadian stimulus,” for applying circadian light in the building environment [22]. It uses irradiance weighted by the spectral sensitivity of every retinal phototransduction mechanism that stimulates the biological clock as measured by nocturnal melatonin suppression. The metric is derived from a transformation of circadian light into relative units, from 0 to a response saturation of 0.7, and is directly proportional to nocturnal melatonin suppression after 1 h of light exposure (0–70%). The recommended levels for circadian stimulus are greater than 0.3 during the day and less than 0.1 in the evening.

Though the science behind these metrics may be difficult to understand for designers who have not specialized in lighting, it should not be a reason to adopt the

simpler, alternate approaches that either disregard health effective light or are knowingly inaccurate, unreliable, and without validation.

4 Field Study

The aim of this study is to compare the daylighting performance of two different atrium geometries inside two educational buildings of similar size and spatial typologies and yet of different atrium geometries. Both buildings excel in sustainable design strategies employed, green technologies, and have accomplished LEED certifications but have not been assessed with daylight health metrics. The two buildings selected for this study are: The Lewis Integrative Science Building (LISB), which has achieved LEED Platinum certification, and Straub Hall, which has achieved LEED Gold certification. Both buildings are located at the University of Oregon campus, Eugene, Oregon (ASHRAE Climate Zone 4C). They both employ atriums to enhance daylight availability and encourage social interaction. This study assesses how these two different atrium typologies, but with similar goals, perform differently in terms of daylight availability for visual task needs and occupant well-being.

The Lewis Integrative Science Building (LISB), opened in 2012, is a home to research oriented toward the human brain, molecular biology, nanotechnology, and solar energy. The building, with an area of 107,000 gross square feet, consists of four occupied stories, a subterranean level, and a fifth floor, which contains mechanical equipment. It is comprised of faculty offices as well as office space for graduate and postdoctoral students, collaboration and meeting spaces, and more than 30,000 ft² of wet labs, dry labs, an MRI facility, ERPS booths, and other instrument labs.

It was designed by HDR Inc. and THA Architects with the design intent to achieve LEED Platinum certification by incorporating energy savings, including solar shading, daylight harvesting, night flush cooling, immense solar panels, and heat from an adjacent utility tunnel. The research facility uses about 58% less energy than conventionally designed buildings of similar size and function. Based on metered data, a baseline building of similar size and function would typically have a total energy consumption of 264.64 kBTU/ft²/year. The Lewis Integrative Science Building's metered energy consumption for several consecutive years is as follows: 161.49 kBTU/ft²/year (2013), 182.63 kBTU/ft²/year (2014), 169.75 kBTU/ft²/year (2015).

The primary component of interest in this building is the four-story, rectangular atrium elongated in an East-West orientation. This serves as the heart of the building for circulation, to encourage interaction between scientists from different disciplines, and allows daylight to penetrate the building from within (Fig. 2).

Straub Hall was originally a u-shaped building which consisted of six separate units that surrounded a central room and served as the main male's residence hall on campus. Since the building was unsuccessful in meeting current American Disability

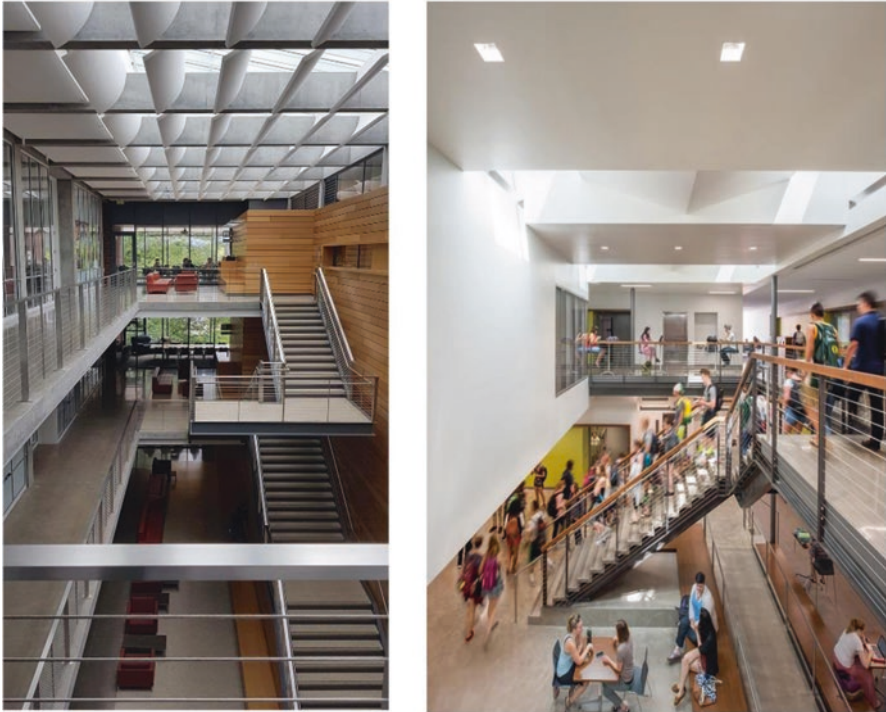


Fig. 2 Lewis Integrative Science Building atrium (left); Straub Hall atrium (right). (Source: Author, <http://rowellbrokaw.com/uo-straub-hall/>)

Association regulations and several internal systems began to fail, a comprehensive renovation of Straub Hall and a classroom expansion was undertaken by Rowell Brokaw Architects in collaboration with Opsis Architecture.

What is especially commendable about Straub Hall is how the building acclimated to user needs and adapted to its change of function over time. This places a strong emphasis on sustainability by conserving and transferring embodied energy whilst still addressing the historical preservation aspect of the retrofit project. Though parts of the building required a complete gut to be rebuilt, that was a more cost-effective solution. A new north-south path through to the daylit stair improves circulation. The commons and stair together form a two-story heart where students and faculty can interact outside class. The deferred maintenance, expansions, and additions included approximately 1000 total classroom seats in a two-story building totaling over 58,000 ft².

Upon completion, Straub Hall was awarded with LEED Gold-level certification. It was also 35% more energy-efficient than the adopted Oregon Energy Code requirements and baseline building performance according to Appendix G of ANSI/ASHRAE/IESNA Standard 90.1–2007. Based on an energy performance analysis of Straub Hall's total energy utilization intensity, the results show an EUI of

61.27 kBTU/ft²/year in 2016 and 72.32 kBTU/ft²/year in 2017, whereas comparative Oregon code is at 100 kBTU/ft²/year. The breakdown of energy resource consumption by fuel type demand from lowest to highest is as follows: natural gas, steam, chilled water, electricity.

The field study was conducted on a typical morning and afternoon of ASHRAE climate zone 4C, characterized with overcast sky conditions. The study employed spot measurements using a handheld spectroradiometer (Asensetek Lighting Passport; accuracy: $x, y: \pm 0.002$, Illuminance: $\pm 3\%$, CCT: $\pm 2\%$). Illuminance levels and spectral power distribution measurements were taken at several points within the atriums on both horizontal plane and vertical plane at the North, East, West, and South cardinal points. The collected data were interpreted by computing visual comfort and chronobiological light metrics. The computed metrics included: Daylight Factor (DF), Daylighting Autonomy (DA₃₀₀), Annual Solar Exposure (ASE), Daylighting Glare Probability (DGP), Circadian Stimulus (CS), and Equivalent Melanopic Lux (EML).

Seating chart logs and occupant surveys questioning seating choices and preference provided specific data that quantified behavioral assessments. These data documented which seats were occupied most from 9 am to 3 pm on two different days for varying sky conditions and class schedules.

5 Results

Findings related to both atriums performance are broken down into three sets: daylight factor and illuminance levels, circadian stimulus, and equivalent melanopic lux metrics. Each location point reports the measurements for both horizontal plane and vertical plan at the North, East, West, and South cardinal points at one point in time for the morning (9-11 am) and afternoon (1-3 pm) hours. In the tables, cells that are shaded in gray indicate that measurement did not meet the benchmarks. The daylight factor benchmark was set at 2%, illuminance levels at 300 lux, circadian stimulus at 0.3, and equivalent melanopic lux at 250 EML.

Illuminance level measurements taken on the horizontal plane tend to be greater than those in the vertical plane facing different directions. This misconception can be misleading to designers as they make assumptions that meeting 300 lux benchmark for the horizontal plane is sufficient. Some tasks require occupants to look in different vertical directions. Accordingly, designers must take into consideration different views and planes. It is also noted that meeting 300 lux benchmark is not a strong indicator of maintaining 0.3 circadian stimulus or 250 EML benchmark. Both circadian stimulus and equivalent melanopic lux biological benchmarks appear to be more difficult to meet than the visual task illuminance level benchmark requirements. In some cases, space conditions may require more or less illuminance levels. Designers should predict how these changes will be reflected in creating biologically bright or dark spaces.

5.1 *Lewis Integrative Science Building*

An elongated atrium provides favorable conditions at specific times of the day and at different orientations. The elongated atrium in the Lewis Integrative Science Building performed poorly on the lower levels, especially during the morning hours. This critical observation hinders the atrium's performance since the circadian stimulus benchmarks are not met during the morning hours, when it is most vital. The horizontal illumination levels meet the benchmarks more than the vertical measurements. This may satisfy some task requirements, but, since the walls surrounding the atrium are predominantly made of glass, it would be beneficial for the adjacent areas to receive daylight too. In this case, the atrium elongated East-West is a wise design decision to allow some light to reach the adjacent heavily used lab areas. The upper floors have more space designated for socializing, studying, and collaborating. These seating areas benefit from the highest illumination levels and circadian entrainment. As for the entire atrium volume, different light levels in various floors allow for adaptability of user behavior (Figs. 3 and 4) .

5.2 *Straub Hall*

The first floor consists of classrooms, a lobby area, and, more importantly, the atrium. Data collected indicate that there are very contrasting illumination levels between these zones. The bright atrium benefits from the skylight and marginally fails to meet the benchmarks during the afternoon hours. It is also noted that seating areas in the hallways fail to meet the benchmarks. This was rather surprising since side lighting is hypothetically more effective than top lighting on the first floor. Alternatively, the lobby area creates a calm, dark environment. It remains consistently dark throughout the day under varying sky conditions. The exception is the seating area, which is directly under a concealed skylight providing a strip of daylight. Results from the circadian stimulus calculator proved that the same seating areas that meet 300 lux benchmark predominantly meet 0.3 circadian stimulus benchmark. This is reportedly due to the added benefit daylight had over the electric lighting's poor performance.

The second floor has one main circulation axis which runs down the hallway. Seating areas are allocated on either side, conveniently placed outside the classrooms. Side lighting for seating area in the South was slightly more effective during the morning hours, given the orientation. Especially noticeable was how the use of the projector screen in the meeting room down the hallway drastically affected the brightness of the hallway as the screen blocked the South sun. Top lighting generally proved to be a successful strategy as it allowed seating areas right below to maintain higher illumination levels as opposed to the row of seats that received little daylight.



Fig. 3 Lewis Integrative Science Building plan with measurement points [23]

Point	DF		Illuminance (lux)									
			Horizontal		Vertical							
			N	E	S	W						
1	4%	2%	273	718	33	79	125	234	20	100	34	195
2	4%	1%	285	332	15	48	122	149	29	115	32	139
3	3%	1%	226	227	15	39	76	74	76	66	33	110
4	5%	1%	367	397	36	41	115	56	36	36	55	220
5	1%	0%	101	152	22	21	18	51	10	31	82	143
6	3%	0%	186	92	6	25	24	86	38	33	70	85
7	1%	0%	70	96	19	18	36	137	25	24	48	53
8	1%	0%	84	105	29	45	46	124	20	50	74	221
9	6%	1%	407	490	31	64	74	100	207	338	128	302
10	8%	2%	552	871	65	118	173	340	232	349	118	300
11	5%	2%	340	614	53	184	201	436	185	436	125	874
12	3%	3%	190	118	88	257	72	482	77	374	244	1602
13	18%	5%	1478	210	136	375	127	592	420	117	300	760
14	10%	4%	714	453	121	321	318	637	616	1015	297	575
15	7%	4%	819	1659	95	260	315	728	546	92	259	652
16	16%	2%	692	679	122	215	331	587	541	745	125	707
17	2%	1%	163	578	66	86	201	673	120	351	249	1119

Point	Circadian Stimulus (CS)									
	Horizontal		Vertical							
	N	E	S	W						
1	0.12	0.5	0.03	0.08	0.18	0.26	0.03	0.17	0.03	0.17
2	0.14	0.38	0.02	0.04	0.18	0.21	0.02	0.1	0.03	0.13
3	0.8	0.31	0.01	0.06	0.09	0.12	0.11	0.06	0.03	0.14
4	0.41	0.4	0.04	0.03	0.16	0.06	0.03	0.05	0.05	0.2
5	0.15	0.18	0.02	0.01	0.02	0.07	0.01	0.03	0.12	0.18
6	0.2	0.14	0.01	0.02	0.02	0.15	0.04	0.02	0.1	0.12
7	0.04	0.12	0.03	0.01	0.05	0.2	0.02	0.03	0.08	0.04
8	0.11	0.15	0.02	0.04	0.06	0.21	0.02	0.03	0.11	0.26
9	0.43	0.47	0.04	0.08	0.12	0.16	0.28	0.39	0.19	0.4
10	0.47	0.55	0.08	0.15	0.2	0.27	0.29	0.67	0.16	0.41
11	0.87	0.48	0.08	0.22	0.27	0.41	0.2	0.4	0.18	0.052
12	0.2	0.54	0.13	0.63	0.09	0.39	0.09	0.4	0.42	0.59
13	0.6	0.64	0.18	0.24	0.018	0.45	0.41	0.57	0.035	0.51
14	0.53	0.62	0.17	0.24	0.4	0.47	0.48	0.55	0.4	0.46
15	0.54	0.61	0.14	0.28	0.85	0.5	0.47	0.54	0.42	0.49
16	0.51	0.51	0.17	0.27	0.86	0.46	0.47	0.52	0.18	0.51
17	0.16	0.42	0.1	0.5	0.2	0.48	0.14	0.87	0.42	0.58

Point	Equivalent Melanopic Lux (EML)									
	Horizontal		Vertical							
	N	E	S	W						
1	265.8	696	26.4	61.3	119	210.8	12	68.7	23.6	149.2
2	284.9	338.5	12.8	34.8	119	144.5	19.8	84.7	23.9	106.6
3	226.1	228.3	11.7	24.3	53.1	70.9	68.9	47.9	25	95.3
4	378.7	385.9	28.8	29	107	44.8	25.8	20.6	42.9	195.4
5	97.1	134.9	16.8	14.5	11.2	49.2	5.4	13	76.4	128.5
6	191.3	88.1	3.9	16.3	18.4	87.7	31.5	21.7	65.3	76
7	41.6	46.1	10.5	11.2	18.2	144.5	9.5	10.3	45.6	35.5
8	42	59.1	19.2	32.6	39.4	127.8	9.2	33.5	70	206.7
9	427.2	519.4	27.9	54.3	70.9	99.8	208.4	347.8	124.6	290.7
10	559.2	906.6	54.4	104.7	176.3	331	224.8	331.7	108.8	269.1
11	330.9	594.3	48.8	166.7	199.3	417.5	181.7	406.9	119.9	805.7
12	152.3	1007.7	83.3	2274.8	63.1	423.5	60.7	322.3	243.6	1158
13	1319.8	2218	127.6	337.8	119.5	554.4	411.6	1137.2	295.3	733.4
14	762	1403.1	115	302.3	303.2	601.7	599.3	1057.5	289	554.2
15	832.8	1609	89.9	234.9	314.6	694.3	553.1	898.8	254.7	639.9
16	696	697.4	114.4	205.7	324.9	554.9	546	757.4	118.5	701.4
17	122.7	492	62.9	770.5	189.3	636.4	97.4	333.3	247.5	1148.8

Fig. 4 Lewis Integrative Science Building measurement points that met benchmark requirements; the cells shaded in gray did not meet the benchmarks

The behavioral assessment identified that greater illumination levels and views to the outdoors were not the most important factors for occupants when making a decision for their desired seating area. It appeared that there were other prevailing factors, including furniture type and layout, the type of activity students are undertaking (studying, socializing, eating, waiting), whether they are in groups or looking to sit as individual occupants, if the area is in a quiet zone or within main circulation axes. Though the data collected shows that most people gravitated towards the well-lit areas, there were some anomalies that indicated some people preferred darker areas. In order to pinpoint which factor best explains these occurrences, more studies with controlled variables would be desired (Figs. 5 and 6).

6 Discussion

This field study has provided insight into building design focused on occupant well-being. Though the study addressed light levels, health, and occupant behavior separately, it seems that the three domains overlap. The main takeaway from the illuminance level data collection was that skylights played a major role in increasing daylight within the building floor plate by allowing the spaces under them to meet sDA300/50%. benchmarks. In addition, spaces that met this benchmark correspondingly met the 0.3 circadian level recommendations. In other cases, electric lighting did not suffice to meet both requirements.

Architecture plays a major influential role in how much light exposure occupants receive and how they behave inside buildings. On a larger exterior scale, light penetrating building's interior can be predetermined by the surrounding environment's exterior reflectance. This can be mediated with the building's orientation and facade design by altering window parameters: ratio, size, position, glazing type, and whether shading devices will be allocated.

Architectural design parameters of buildings should respect cyclical nature of light, the specific spectrum of daylight and the intensity of light that people are exposed to. Not all daylighting practices have followed the chronobiological fundamentals of daylighting. Daylight apertures and the glazing material allocated should distort the daylight spectrum only minimally. Very few studies have looked at the circadian potential of transmitted light through different glazing types. Although some types of glazing provide a comparable amount of transmitted photopic light, the amount of transmitted circadian light can be very different. In one study, the differences between light transmittance and circadian transmittance of several materials have been assessed [24]. In some cases the glazing transmittance of light in the nonvisual photoreception region can be so small that it may disrupt circadian rhythms or cause other health problems for occupants. This was especially evident with tint colors, such as bronze, which reduce the blue light component of daylight. The study concluded that further research should be undertaken to determine the health and well-being benefits associated with spectral filters in daylighting of buildings.

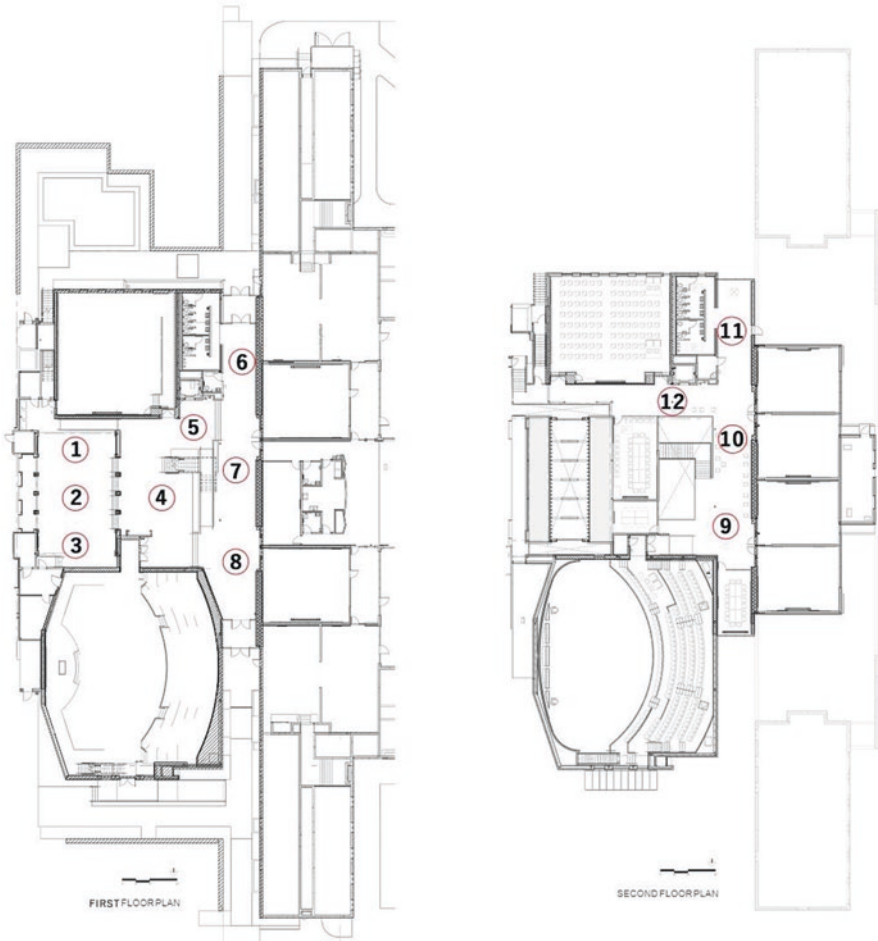


Fig. 5 Straub Hall plan with measurement points [23]

On the interior scale, light penetrating the building’s envelope is either enhanced or diminished based on the indoor spatial configuration, surface properties, and interior reflectance. Designers can also modify indoor light exposure through the use of electric lighting. They specify the light source type, spectral properties, and position. Occupants have the freedom to distance themselves from certain light sources or, based on the degree of control they have, to operate light switches.

To increase daylight availability, designers often resort to increasing glazing percentages. This can be problematic in several climatic regions as they have to compensate for heat gain or loss with mechanical systems, which decrease energy efficiency. In addition, problems could arise with visual discomfort metrics such as glare. Most of the light metrics and building standards used by the design industry have been derived from and based on the rods and cones, which essentially focus on

Point	DF		Illuminance (lux)									
			Horizontal		Vertical							
					N		E		S		W	
1	0%	0%	52	50	44	42	25	30	40	42	34	28
2	0%	0%	48	50	43	42	29	27	45	44	20	21
3	0%	0%	62	27	42	43	27	26	40	40	30	22
4	2%	2%	268	181	92	92	71	66	115	87	109	94
5	2%	2%	272	242	146	133	101	95	68	62	82	99
6	2%	3%	273	278	171	158	53	64	78	135	71	122
7	2%	2%	227	192	97	106	108	121	60	104	39	42
8	2%	2%	206	214	75	65	35	43	131	116	56	92
9	1%	5%	190	556	78	64	66	53	42	60	207	108
10	1%	1%	179	81	89	98	60	16	68	63	82	75
11	1%	2%	190	181	196	372	72	65	48	63	44	69
12	2%	2%	209	249	62	111	146	176	107	131	185	163

Point	Circadian Stimulus (CS)										
	Horizontal		Vertical								
			N		E		S		W		
1	0.05	0.05	0.05	0.05	0.04	0.03	0.04	0.04	0.04	0.04	0.03
2	0.04	0.05	0.04	0.04	0.02	0.02	0.04	0.04	0.04	0.02	0.02
3	0.06	0.03	0.04	0.04	0.02	0.02	0.05	0.05	0.03	0.03	0.02
4	0.8	0.2	0.09	0.1	0.07	0.07	0.13	0.1	0.1	0.08	0.08
5	0.2	0.26	0.13	0.12	0.11	0.1	0.08	0.07	0.07	0.09	0.09
6	0.24	0.24	0.19	0.17	0.07	0.04	0.07	0.12	0.06	0.11	0.11
7	0.2	0.17	0.1	0.1	0.09	0.1	0.06	0.1	0.04	0.04	0.04
8	0.19	0.19	0.07	0.06	0.06	0.05	0.14	0.13	0.05	0.08	0.08
9	0.21	0.45	0.09	0.06	0.05	0.04	0.04	0.06	0.2	0.14	0.14
10	0.15	0.08	0.1	0.1	0.05	0.01	0.06	0.06	0.1	0.08	0.08
11	0.17	0.19	0.2	0.7	0.07	0.07	0.04	0.06	0.04	0.07	0.07
12	0.19	0.2	0.05	0.11	0.14	0.17	0.11	0.15	0.17	0.16	0.16

Point	Equivalent Melanopic Lux (EML)									
	Horizontal		Vertical							
			N		E		S		W	
1	38.1	36.8	36.4	35.4	20.9	21.7	28.8	30.6	26.6	21.7
2	33.4	35.8	31.5	30.3	19.4	17.9	34.4	32.9	14	15.6
3	46.1	20.8	29.7	30.1	18.8	18.6	34.1	34.1	23.4	17.2
4	244.7	163.1	69.8	71.3	54.5	50.6	92.2	69.1	76	65.2
5	242.5	206.1	100.6	91.6	77.9	70.7	54.2	49.1	57.3	72
6	197.6	197.8	135	121.8	28.3	40.1	52.7	93.8	48.9	85.6
7	158.5	134.2	71.6	75.2	70.9	81.8	43.1	73.8	28.1	31
8	146.5	151.1	54.1	44.6	21	19.3	99.4	91.5	38	62.9
9	162.9	528	62.7	48.9	45.1	37.1	29.7	45.4	190.9	95.6
10	122.8	57.9	70.1	74.5	42.3	11.2	50.5	44.9	69.1	57.8
11	134.3	144.8	171.8	336.2	52.2	52	34.6	45.4	32.3	52.9
12	150.2	187.1	42.7	79.2	103.1	130.4	82.5	108.7	130.2	122.3

Fig. 6 Straub Hall measurement points that met benchmark requirements; the cells shaded in gray did not meet the benchmarks

quantitative and instrumental aspects of light, such as having enough light for task performance, avoiding glare and visual discomfort, and maximizing energy savings. Though the field has primarily addressed daylight architecturally in terms of these daylight distribution, visual comfort, and energy efficiency metrics, there has been a recent increased interest in the health and well-being components. This is partly

due to the recent discovery of the *ipRGCs*, which are responsible for non-image-forming or nonvisual functions, both physiological and psychological. The field has acknowledged the physiological and psychological impacts of daylight on occupants by developing health effective metrics, simulation models, field study methods, wearable technology, and building standards and benchmarks. Studies have looked at the architectural parameters that influence daylight availability and have investigated occupant physiological and psychological responses to the daylight exposure received. This is especially important in the case of office working environments where occupant alertness and well-being has an impact on productivity and financial gains.

In addition to the measurement findings of the atrium field studies, it is important to consider the function and role of the space typology. The success of the atrium design lies not only in its daylighting parameters, but in the opportunity it creates as an intermediate condition between interior and exterior spaces. Fomenting social activity might be more influenced by the space's furniture, its arrangement, views across space, and proximity to paths. Nonetheless, if the design's intent is to create an atrium space to be occupied by building users for extensive periods of time, it is vital for designers to assess the human well-being and biological aspects of daylight in addition to the instrumental metrics. This will help with the considerations for their proper use and pitfalls suggesting that, indeed, atriums of one form do not fit all buildings.

7 Conclusion

The study provides a proof-of-concept approach to investigate the fundamentals of measuring the circadian potential of a space based on daylight availability from an architectural standpoint in the field, it is important to investigate how much exposure occupants receive from the available daylight based on their behavior within building spaces. A successful building should be designed systematically by paying attention to occupant behavior and expected user patterns in order to maximize comfort and well-being of all users during all times of the year. Humans should not have to adapt to poorly designed building layouts that deprive them from the biological benefits of daylight. Instead, buildings should be designed based on human behavior to maximize availability of beneficial daylight exposure. This requires designers to pay more attention to occupant's view sheds and viewing preferences within the indoor building layout in order to determine if occupants really do receive adequate daylight, or whether they do not, despite meeting building performance benchmarks.

Chronobiological and physical light measurement assessment tools need to be carefully selected in accordance with the assessment goal. Each measurement protocol has its own strengths, weaknesses, and specific sensitivities to different components of human responses and light characteristics, making it more or less suitable and valid within a specific testing context. Most research on circadian patterns

related to lighting is performed in controlled laboratory environments. Little is known about the variability of circadian light within buildings and natural environments in the field. Researchers are continuously working on developing frameworks and models to best integrate nonvisual effects at different times through field studies and simulations. As could be seen from the presented results, researchers have to make decisions on what approach to adopt based on the methods' applicability, research design, and focus area.

References

1. Raw G (1992) Sick building syndrome: a review of the evidence on causes and solutions. HM Stationery Office, Richmond
2. Frontczak, M. W., Pawel 2011. Literature survey on how different factors influence human comfort in indoor environments. *Build Environ*, 46, 922-937
3. Mardaljevic J, Hescong L, Lee E (2009) Daylight metrics and energy savings. *Light Res Technol* 41:261-283
4. Reinhart CF, Mardaljevic J, Rogers Z (2006) Dynamic daylight performance metrics for sustainable building design. *Leukos* 3:7-31
5. Van Bommel WJM (2006) Non-visual biological effect of lighting and the practical meaning for lighting for work. *Appl Ergon* 37:461-466
6. Khademagha P, Aries M, Rosemann A, Van Loenen E (2016) Implementing non-image-forming effects of light in the built environment: a review on what we need. *Build Environ* 108:263-272
7. Serra R (1998) Daylighting. *Renew Sust Energy Rev* 2:115-155
8. Moon P (1942) Illumination from a non-uniform sky. *Illum Energies (NY)* 37:707-726
9. Reinhart CF (2004) Lightswitch-2002: a model for manual and automated control of electric lighting and blinds. *Sol Energy* 77:15-28
10. Hescong L, Wymelenberg VD, Andersen M, Digert N, Fernandes L, Keller A, Loveland J, Mckay H, Mistrick R, Mosher B (2012) Approved method: IES Spatial daylight autonomy (SDA) and annual sunlight exposure (ASE). IES-Illuminating Engineering Society, New York, NY
11. Nabil A, Mardaljevic J (2005) useful daylight illuminance: a new paradigm for assessing daylight in buildings. *Lighting Res Technol* 37:41-57
12. Vos JJ (1984) Disability glare-a state of the art report. *CIE J* 3:39-53
13. de l'Eclairage CI (2004) Ocular lighting effects on human physiology and behaviour. CIE Technical Report, 158
14. Kent M, Fotios S, Altomonte S (2018) Experimental biases in discomfort glare evaluations. 34th International Conference on Passive and Low Energy Architecture (PLEA), PLEA, 2018
15. Konis K, Selkowitz S (2017) The role of metrics in performance-based design. effective daylighting with high-performance facades. Springer, New York, NY
16. Wallace LA, Nelson CJ, Dunteman G (1991) Workplace characteristics associated with health and comfort concerns in three office buildings in Washington, DC (No. PB-91-211342/XAB). Environmental Protection Agency, Research Triangle Park, NC (United States). Atmospheric Research and Exposure Assessment Lab
17. Salinas JL (1982) Artificial light and occupational health. *Occup Health Nurs* 30:13-15
18. Kim A, Schiavon S, Graham L, Ko WH (2016) Lighting for circadian health: survey module and non-invasive open-source wearable sensor system. Center for the Built Environment (CBE)

19. Lucas RJ, Peirson SN, Berson DM, Brown TM, Cooper HM, Czeisler CA, Figueiro MG, Gamlin PD, Lockley SW, O'hagan JB, Price LLA, Provencio I, Skene DJ, Brainard GC (2014) Measuring and using light in the melanopsin age. *Trends Neurosci* 37:1–9
20. Enezi JA, Revell V, Brown T, Wynne J, Schlangen L, Lucas R (2011) A “Melanopic” spectral efficiency function predicts the sensitivity of melanopsin photoreceptors to polychromatic lights. *J Biol Rhythm* 26:314–323
21. Institute IWB (2019) Well Building Standard V2
22. Mariana Figueiro MR (2017) Quantifying circadian light and its impact [Online]. Architectural Lighting. Available: https://www.archlighting.com/technology/quantifying-circadian-light-and-its-impact_o
23. Floor Plan Database (2019) University of Oregon: The High Performance Environments Lab (HiPE)
24. Hraska J (2015) Chronobiological aspects of green buildings daylighting. *Renew Energy* 73:109–114

Early Adopter Nation for Electric Vehicles: The Case of Iceland



Andri Ottesen and Sumaya Banna

1 Introduction

Rising the production and usage of electric vehicles (EVs) has been suggested as a possible scheme to lessening fuel consumption and greenhouse gas (GHG) emissions to mitigate the effect of climate change. Automobile transport is the second biggest contributor to GHG emissions among all sectors [1]. Consequently, governments across the globe play an essential role in technological transitions by introducing EVs' penetration into the markets.

The European Automobile Manufacturers Association (EAMA) has categorized electric vehicles into three types: BEV (Battery Electric Vehicles), EREV (Extended Range Electric Vehicles), and PHEV (Plug-in Hybrid Electric Vehicles). BEV is a vehicle which uses battery as the only power source. EREV is a car that utilizes battery as a primary source of energy for short daily trips and utilizes the hydrocarbon combustion engine for longer daily trips and/or trips that do not rely on high speed, and the battery is charged while driving on the combustion engine. PHEVs are like EREVs where the battery is charged by plugging it into a power source just like BEVs. The technology of lithium-ion batteries is the most optimal and effective solution for electric vehicles due to high energy densities. Battery aging has become one of the greatest concerns for the users and producers of electric vehicles. Other factors, such as discharging situations, humidity, and temperature, may also influence the performance and capacity of the battery. Range Anxiety (RA) is an issue for the driver of an electric car and is usually termed as the fear of becoming trapped in with the discharged battery that can take up to 8 h to fully charge. RA is the most

A. Ottesen (✉)
Australian College of Kuwait, Mishref, Kuwait
e-mail: a.ottesen@ack.edu.kw

S. Banna
American University of Kuwait, Salmiya, Kuwait

prominent barrier in the adoption of electric vehicles in Iceland. Therefore, it is becoming the greatest concern for the manufacturing companies in Iceland. The second biggest concern of consumers of EVs (BEVs and PHEVs) is rapid depreciation, which can be as high as 30–50% compared to regular vehicles. The lack of battery and charging standards and high replacement cost of the battery limits the utility of EVs to about 8 years versus an average of 13 years for combustion engine vehicles. However, regarding battery lifetime and cost, there have been major improvements and the trend is expected to continue. The third main obstacle for plug-in EVs is the lack of infrastructure, including home-based and public-based charging facilities and reliable electrical grid to support myriads of vehicles being charged at the same time. The price of electricity also plays a part whether it is from a sustainable source or made from hydrocarbons such as oil or gas. Taxation of gasoline is an additional factor.

2 Literature Review

Prior studies focused on early adopters of EVs by profiling the consumers socio-economic indicators and identifying factors and motives, which influence the purchasing decision. For instance, Trommer et al. [2] explained the socioeconomic differences between early adopters of electric vehicles (EVs) and buyers of conventional vehicles in Germany by their attitudes towards new technologies, their mobility, and their awareness of ecological issues. The early adopters were found to have a higher average income, a higher level of education and more cars per household. Boston et al. [3] conducted massive data analysis related to the charging and driving behavior for the case of North American Ford full battery electric vehicles and plug-in hybrid electric vehicles. The results indicated that customers were selecting vehicles with attributes and functionality that were appropriate for their lifestyle.

Consistently, Hardman et al. [4] compared high-end and low-end adopters of battery electric vehicles among North American owners. They found that each group has a different socio-economic profile. There are also some psychographic differences. Furthermore, high-end adopters viewed their vehicles more preferentially than low-enders. The high-end adopters were more likely to continue with ownership of battery electric vehicles in subsequent purchases. They suggested that time to refuel and range for low-end battery electric vehicles should be improved in order to increase chances of drivers continuing with BEV ownership.

Besides profiling early adopters by socio-economic factors, several studies also attempted to identify the main consumer incentives for buying EVs. The results suggest that the perceived financial benefits, such as reducing costs, environmental benefits, and regulatory advantages, played a key role in the purchasing decision.

Some studies concluded that factors such as cost and performance had a greater influence on the purchasing decision. For instance, Krupa et al. [5] surveyed 911 consumers and found that there was the strongest motivation to accept plug-in hybrid electric vehicles in US markets. However, those who were most open to this

type of vehicle preferred to save at least 500USD annually in gas. Similarly, Levay et al. [6] examined the effect of fiscal incentives on market penetration of electric vehicles. They conducted pairwise comparison of total cost of ownership to analyze how cost and EV sales are related in the European region. They found that negative total cost ownership-sales relationship varied across car segments in the Netherlands, France, and UK. Bjerkan et al. [7] described the role of incentives for promoting Battery Electric Vehicle (BEV) adoption in Norway and determined what incentives were critical for deciding to buy a BEV and what groups of buyers responded to different types of incentives. They found that price reduction is the most critical incentive in promoting EV adoption. A comparative state to state study on potential EV users in the USA found that although sustainability and environmental benefits of EVs have some influence on their adoption, financial incentives also played critical part. Soltani-Sobh et al. [8] analyzed the electric vehicles adoption across the USA. They demonstrated that electricity prices were negatively associated with EV use while urban roads and government incentives were positively correlated with the states' electric vehicle market share.

An international panel data collected from 31 countries, including some European countries, China, UK and USA on time series from 2011 to 2015, indicated that the relative price of electric vehicle compared to internal combustion engine vehicle, driving range, and the number of models available in markets were correlated to the market share of electric vehicles. On the other hand, relationship between recharging infrastructure—an important factor for electric vehicle adoption in many studies—and market share of electric vehicles turned out to be insignificant in this study [9].

To sum up, many of the reported studies were based on preference surveys, which attempted to identify and describe potential EV buyer socio-economic factors and motive indicators. Only a limited number of studies addressed actual owners of EVs and were based on the interview approach and/or mixed approach—survey and interview. Furthermore, most of the studies analyzed the adoption of only certain kinds of EVs: battery electric vehicles (BEVs) and—in the case of just a few studies—plug-in hybrid electric vehicles (PHEVs). While countries such as the USA and Norway already have the initial results of comprehensive studies carried out among owners of EVs, it is in Iceland that no significant analysis of actual owners and users of EVs have been undertaken so far. Therefore, the current study aims to bridge the gap in the existing literature reviews by identifying various needs of actual owners in different types of electric vehicles in Iceland using the mixed approach.

3 Objectives and Challenges

The purpose of this study was to investigate private consumer market readiness for electric vehicles in Iceland for the period 2012–2018 and evaluate market readiness and growth opportunities. The study investigated various market segments, includ-

ing those based on demographic characteristics of customers such as gender, age, educational-level, income, urban vs. rural, family type and size and prior car ownership. The demographic information would form a foundation for qualitative predictions of the future development scenarios until year 2018. To reach the goal of this project, the main research question was investigated and answered along with relevant subsequent questions, such as: “What are the factors that explain the growth of the number of electric vehicles in the private consumer market in 2012–2018?” According to recent a CNN report [10], Iceland took the second place in implementing EVs after Norway. In 2019, EVs in Norway outsold gas and diesel vehicles, with 58.4% of new automobiles sold.

The relevant subsequent questions were also: “What are the prevailing market segments?” and “Is the trend likely to continue for the next 5 years in Iceland?” To answer these subsequent questions, a follow-up research was conducted using in-depth interviews at the beginning of 2019. These interviews had the objective to explore how predictive the original study was, and whether there were any discrepancies. The interviews provided significant insights into consumer experiences, their greatest disappointments, revelations and whether they anticipated any benefits from electric vehicles soon. Finally, there was a discussion if the experience of Iceland as an early adopter nation could be extended to other countries. If so, what would be the limitations and success factors?

4 Methodology: The Instruments and Participants

Originally, to achieve the objectives of this research, the survey questionnaire was created through an online survey platform in 2018. This generated 237 completed responses from participants with a 98.75% response rate. Participants were selected randomly at the main shopping centre in Kringlan to provide their responses for an online survey. The list is gathered from willing participants of Facebook chat room—Rafbílar á Íslandi. The selection strived to capture a collection of the largest EV owner groups regarding the above-mentioned categories. The participants were between ages 17 and 70 with the majority (45%) between ages 26 and 35. There were more female than male participants (nearly 62%), and around 80% resided in urban areas. The majority of the sample had a partner or were married (74%), had children (74%) and close to half of the participants had 2–3 children (46%). A vast majority were car owners (93%) and were divided between small vehicles (20%), medium vehicles (43%) and SUVs (25%). While almost 90% of participants used their cars daily, nearly 70% of participants used cars many times during the day. The income level of the participants was distributed between low, medium and high with the majority in the medium level. The educational level ranged from high school to higher education, with the majority with university degree (40%). The survey was presented and completed by the participants in the Icelandic language and translated by the researchers. The survey comprised of 21 questions where participants rated their preference in order of importance, in terms of vehicle safety, Capital Expenses

(CAPEX), Operating Expenses (OPEX), Range Anxiety (RA), charging facilities anxiety, reselling anxiety, battery life anxiety, level of knowledge/comfort about EVs and the possibility of purchasing electric vehicle over the next 6 years.

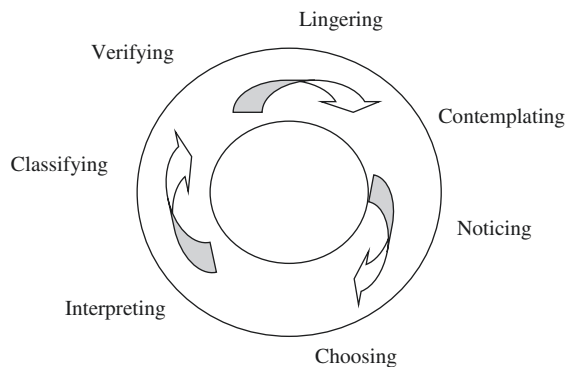
The follow-up study was conducted in early 2019 using in-depth interviews with 5 participants based on the so-called Vancouver School Approach to Qualitative Research (see below). There were 15 open-ended questions, ranging from overall experience of owning and operating EVs, if they would repurchase, the greatest disappointments and most pleasant surprises, limitations and outlook. Five owners of EVs (Nissan Leaf 2013, Kia Soul 2016, Nissan Leaf 2017, Nissan Leaf 2016, and Kia Soul 2017) were interviewed. In-depth interviews were also conducted with the electric car specialists at the Icelandic Ministry of Transport and Icelandic New Energy Think Tank.

5 Qualitative Research Approach: Implementation of Vancouver School Phenomenology

Phenomenology is a “way of thinking about knowledge – a philosophical and theoretical viewpoint – how do we know what we know” (Bozzi 1990; Mortari and Tarozzi n.d., p.5). The central aim of the Vancouver School phenomenology is to provide an interpretation of human subjectivity instead of letting data in any study speak for itself. The Vancouver School is a blend of description, interpretation, clarification and construction of human experience [11]. Figure 1 shows seven steps of the research process for Vancouver School phenomenology, namely silence, reflection, identification, selection, interpretation, construction and verification. It can be depicted as a circle.

Furthermore, the seven-step process can be further broken down into 12 sub-steps as follows:

Fig. 1 The seven steps of Vancouver School Phenomenology



5.1 Step 1: Selection of Dialogue Researchers (The Sample)

The underlying assumption when choosing dialogue researchers, also known as co-researchers, in Vancouver School is that people who have experience with phenomenon are viewed as the source of knowledge for their understanding of the phenomenon. It is also assumed that it is necessary to choose participants from both gender groups and various ethnicity groups to avoid biased research findings. It is also important to have enough co-researchers with relevant experiences because one of the main criticisms of phenomenology is that data collection often falls short of the holistic picture of the problem.

The choice of participants/co-researchers is pivotal. The two-step procedure is required firstly to discover the depth of knowledge of the problem and secondly the width of it. For the first step the experts in the field are carefully selected for their experience and deep insights of the phenomena. Here two experts were selected for depth interview: Asta Thorleifsdottir—Senior Advisor at Transportation and Infrastructure Department at Ministry of Transportation and Local Government, and Anna Margret Korneliusdottir—Project Manager at Icelandic New Energy Think Tank. For the second, width-of-knowledge part, six users of the most popular BEV brands Nissan Leaf (2013, 2016, and 2017 models) and Kia Soul (2016 and 2017 models) were selected. The researchers tried to get more user data for private BEV car owners before the year 2015, but, as shown in Fig. 2, the number of BEVs in private ownership was very low and most BEV owners at that time were companies that bought the BEVs as some kind of image-making scheme. These corporate users were not interviewed per suggestion of the co-researchers as their views did not represent today's issues regarding BEVs (Table 1).

5.2 Step 2: Phenomenology Starts in Tranquility

As Spiegelberg [12] has noted, “phenomenology begins in silence” (p. 693). It means that this silence is re-entered again and again throughout the study. This silence is a reflective silence where a researcher contemplates the phenomenon at hand. The goal of this silence is that the researcher opens up, sharpens his/her receptive faculties and is ready to hear something new. We must empty ourselves in order to be able to take in something new. It is a specific view of things that aim at revealing aspects hidden from usual viewpoints by habit. It requires leisure (“*époche*”) in order to exclude preconceptions about the thing under consideration. The interviewer who usually has made some preconceived notions about the process and the outcome of the interview needs to take time to lay them aside before he/she begins asking questions that might compromise the findings. It is important for a researcher to write down before an interview the probable outcome and then compare it with the findings to single out biases and prejudgments, which he might accept instead of denying them. Research diary is helpful in keeping our personal experiences and

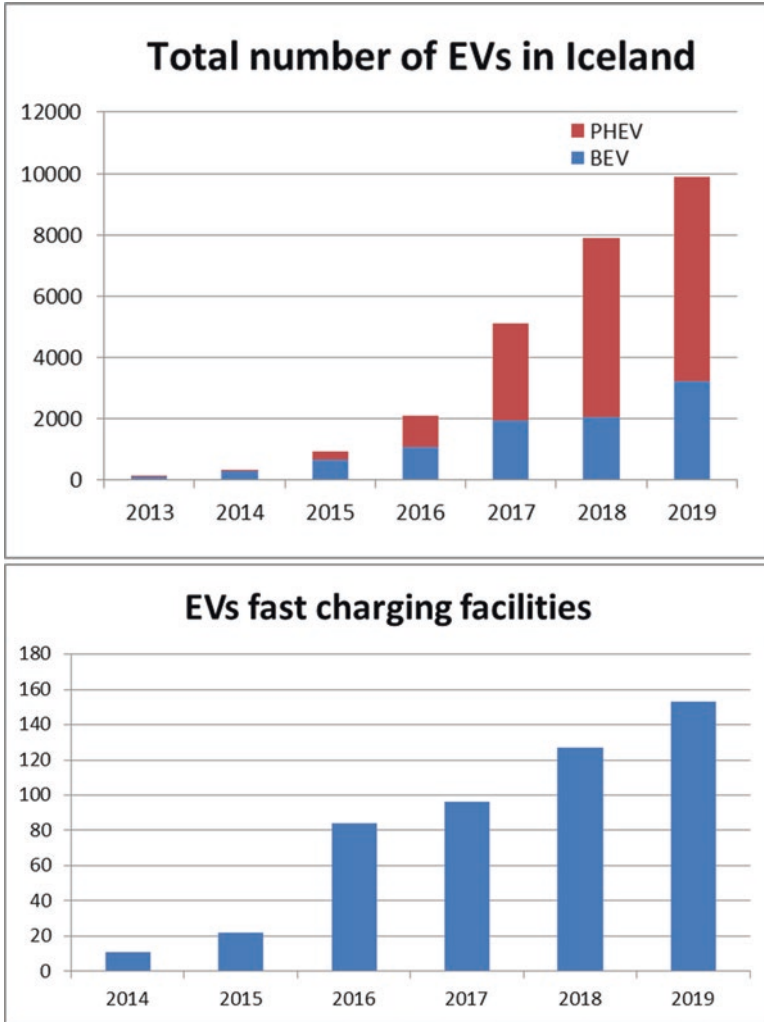


Fig. 2 Left: 18.5% of all new vehicles sold in Iceland in 2018 were electric, the highest percentage in the world apart from Norway (estimated to reach over 50% of new vehicles in 2019). Right: fast-charging stations have followed the increase of EVs. The cost of a fast-charging station (36 kV) is around 26.500 USD plus installation [19]

opinions about the phenomenon and preventing the interviewer from inferring with the testimony of the co-researcher.

The researcher is greatly encouraged to read as much information about the topic beforehand as possible, which increases the likelihood of panorama view. It also makes sure that the researcher does not stop the co-researcher seemingly deviating from the phenomenon when they might indeed be talking about the core of it. The researcher must be very open to hear about new ideas and perspectives, which is a

Table 1 BEV owners that were interviewed in March 2019

Vehicle type	Model	User's gender	Age of the BEV owners	Family size	Urban vs. rural	Only car
Nissan Leaf	2013	Male	42	Married with 3 children	Urban	No
Nissan Leaf	2016	Male	50	Single	Urban	Yes
Nissan Leaf	2017	Female	43	Married, with 2 children	Rural	No
Nissan Leaf	2018	Female	42	Married, with 2 children	Urban	No
Kia Soul	2016	Male	42	Married, with 2 children	Urban	No
Kia Soul	2017	Male	60	Married, with 3 children	Rural	No

point that must be always mentioned. Creating the situation of trust, impartiality and sense of importance when the co-researcher can be completely sincere is the situation that is most likely to reap results [13]. Here, establishing trust, impartiality and mutual respect are at the core of this approach. Luckily, academic researchers are often given this trust as it was in this case.

5.3 Step 3: Starting a Dialogue (The Data Collection)

In Vancouver School, data are collected through true dialogues. Dialogue is defined by the Vancouver school as a constructive discussion where both researchers respect each other and experience absolute freedom of speech and listening. The researchers perceive each participant as an expert. The whole data collection starts as a subjective interaction when researchers value each other's personality and are free to speak and listen and engage. These interviews will demand full attention from the researcher for as long as 3 h. Hence, the researcher decides to be in good physical as well as mental state to keep the senses sharp throughout the whole interview. The researcher needs to be interactive and ask how, why, when, what, where, for whom questions for clarification when full understanding is not clear. "Dance of a dialogue" is a term that is used in such instances. The researcher usually starts the interview with a simple open question while establishing trust and getting the co-researcher to be more interactive. When the intellectual bridge into the world of the co-researcher has been built, more narrow and specific questions start to surface for better understanding of the phenomenon. Here, 15 open-ended questions were asked to 6 EV owners that corresponded with the original survey in the areas of anxieties and concerns, various aspects of the CAPEX and OPEX; battery charge range; reliability; charging time; charging facilities; battery lifetime; environment

protection; quality of driving, such as torque and soundlessness; and finally if the user would buy another EV based on their experience of the current one.

5.4 Step 4: Defining the Answers, Expression and Terminology

Data collection and data analysis is done concurrently according to the Vancouver School. Although, proportions shift in favour of the analysis when all interviews have been conducted. All conversations are taped and typed up word to word. It is important to take notes and time all interviews that are recorded on the tape as well as silences, laughter or other expressions. If the researcher does not write the interview, it is important that the he/she listens to the interview about three times from the recorder because it enables the researcher to “live” with the data. This step of “living with the data” is extremely important and should be taken most conscientiously with an open mind. If this is done well, the invested time pays off generously. Here, the 6 BEV owners and the 2 experts were interviewed using Skype and Facebook video-chat rooms, which was enough but not preferable compared to face to face interaction environment.

5.5 Step 5: Finding the Theme: Putting Ideas Into Words, Coding

Data analysis and scrutiny are next in the hermeneutics process after the transcripts have been typed up. The researcher needs to read the transcripts at least once without making marks or comments. Then the researcher marks the important parts and summarizes them into a few words and codes the themes (usually on the margin). If the data analysis is done correctly, the co-researchers will more likely agree with the outlined description of the phenomenon, although the style and structure may vary. Much like two artists creating portraits of the same person with very different methods, but if the techniques are good, the person can be recognised from the paintings. In our study, several themes started to emerge as the actual usage was compared to expectations before purchasing the BEVs.

5.6 Step 6: Starting to See a Holistic Picture from Everyone’s Perspective

During this phase, the researcher summarizes the theme and the core from each interview. Each researcher needs to be constantly asking about what message the co-researcher is trying to convey, and how can this experience be summarized from

his/her own perspective. From that information, a mental model is formed for everyone, which must be consistent with both the individual and the research material, but further rests on insights, logical thinking and conception should be conducted. Insight refers to understanding the situation as a holistic picture. Logical thinking is the ability to study and scrutinize ideas critically while ranking their proportional importance to the project. Conception means here that one ought to turn the attention inwards and look at ideas, as they appear on a “movie screen” of the mind. In our study, the differences started to appear between genders, as the two females appreciated more the lack of engine sound while driving but, on the other hand, the four male drivers liked most the torque and acceleration of the car. Both genders liked the maintenance free feature as the engine has no moving parts: one of the owners mentioned “maintenance free and the only fluid that needed to be replaced was the window wiper fluid.”

5.7 Step 7: Verifying the Holistic Picture with the Co-researcher

It is important for the researchers to realize that their selective mindset model reflects to some extent their own preconceptions as they tend to ignore what they do not pay attention to. Therefore, the research biases are always the phenomena that sneak into data analysis. Therefore, it is important that each researcher in cooperation with each co-researcher verify and validate each case construction by comparing different dialogues to find “common threads” and differences between them. In this way we allow the phenomenon to establish itself in our consciousness and “gradually crystallize before our inner eye” ([12], p. 716). Based on our study, the outcomes of the interviews were sent to two specialists for concerns and comments. They both agreed on the findings and backed up one of the observations that women, especially young women, were more environmentally concerned than men with regard to purchasing BEVs.

5.8 Step 8: Realizing the Main Theme of Whole Research Outcome

This step focuses on turning all the mental models of the co-researchers into overlapping clusters of themes that are supposed to answer questions, such as “what was the essence of the combined experiences from their perspectives,” and decide whether they fit actual data. To achieve the goal of this process, the researcher needs to use all seven intellectual proponents of the discovery phase as shown in Fig. 1. This final analysis must be supported always by the actual data and give the data “equal rights without favouritism.” However, it is the researcher’s responsibilities to

translate the insider's mental information into common terminology for the outsiders to understand. Phenomenological research aims on expansion of the knowledge base on human phenomena. The researcher needs to be very critical of their own assumptions and conjectures and be ready to change the theme and subsequent themes if needed. Ingenuous self-criticism is practiced by defining the ability to separate one's personal goals and feelings from the research itself to increase the validity of research findings. This area was particularly interesting as the first author of this study has worked in the field of renewable fuels that was competing with electricity as clean energy. He started with negative biases against mass implementation of BEVs that he had noticed and then always be aware to strictly follow evidence-based reasoning and constantly pursue impartiality in his questions and approaches towards interviewers.

5.9 Step 9: Comparing the Outcome with the Data

After the results and the themes are constructed, they are compared with the research materials in terms of any discrepancies and to verify if some topics are missing and should be included. The researcher needs to take the viewpoint of an independent reviewer or a journal editor who is evaluating the research regarding procedures and practices. Here, a second literature review was necessary to compare the findings of this study. However, since the field of empirical research of studying private EV driving is still in its infancy, research into something like life cycle costs of EVs compared to combustion engine is hard to find as it depends on the total usage of the electric battery that has a factory guarantee of 8 years only. There are very few privately driven EVs that are old enough to empirically access the true life cycle cost of EVs as very few are significantly older than the 8-year factory guarantee. Today, it is only assumed that EV battery lasts only 8 years, which remains the largest life cycle cost compared to 13 years average lifetime of combustion engine vehicles. If the battery lasts up to 13 years without significantly dropping its power charge capabilities, then the life cycle cost would lower significantly. This data will however not be available until about 5 years from now. This is especially relevant in conditions that are colder than the constant factory environmental condition of around 20° average temperature with minimal wind condition. However, Green Car Reports [14] state that EV battery may expect to retain 70 per cent of its original charging capacity after 8 years, which might be enough for some EV users.

5.10 Step 10: Finding an Appropriate Name for the Outcome That Prescribes the Result and Its Interpretation

The naming process includes summarizing the themes into a few catchy words. The name should reflect the experience of the co-researcher. The seven intellectual proponents of the discovery phase as well as insights, logic thinking and conception parts are also useful for this process. Here, the description from one female user was adopted when she mentioned that driving without engine was like “riding a magic carpet” and for a male user that gearless fast acceleration, the torque, was like “driving a muscle car.”

5.11 Step 11: Verifying the Research Outcome and Interpretation with Some of the Co-researchers

It is helpful when the co-researchers look over the summarized write-up of the study. It is important to explain that the outcome might be different from the individual interviews. The final draft of written findings was then shared with the experts for final comments.

5.12 Step 12: Writing Up the Result for the Readers

The Vancouver School of thoughts stresses that every voice must be heard, and each viewpoint of every co-researcher must be noted from a diversity perspective because every experience is different. The co-researchers should not feel isolated from the result or the findings. The report is a testimony of the co-researcher’s story, which proves for the readers that the findings are fact based. The researchers act as a storyteller by borrowing the voices and transferring them into readable text. If the original voices and sentiments are in place, the readers of the report are more likely to accept and acknowledge the findings. The purpose of this study was to borrow the experiences and feelings of EV drivers from the early adopter nation of Iceland with a cold climate.

6 Validity and Credibility of the Vancouver School of Thoughts

Writing up the findings is viewed as knowledge contribution. However, the future will decide whether the contribution is significant or convincing enough in the long-run to have a lasting impact. Validity and credibility are largely based on positioning.

Sound logic is always a subject for criticism; convincing logic silences these critiques; and overwhelming logic eliminates the critiques because they will be busy asking themselves why they did not think of that. Kvale [15] explained that an expert validating qualitative research and describing a better dialogue can be characterized as the one searching for the true meaning of the term “defensible knowledge claim”. In qualitative research, the researcher is a “measurement instrument”: two researchers could balance each other in that respect. A research triangulation occurs when two or more researchers combine their resources and abilities and reduce the probability of errors.

7 Threats to Validity and Credibility

The researcher needs to be constantly asking themselves the questions: “Did I understand it correctly?” and “Is that the real issue or does the problem lie deeper?” A co-researcher who is experienced could help the researcher in finding the answers to these questions. There are four sets of threats that are dangerous to validity and credibility of qualitative research:

- Holistic fallacy—When the researchers think they have discovered the holistic picture of the phenomenon, but co-researchers are too few and several interviews are needed to reach a “saturation point”, which must be defined.
- Elite bias—When the researchers have not tried selecting the right well-experienced co-researchers. The findings tend to be defective and faulty.
- “Going native”—When the researcher goes too close to the phenomenon to be able to use the “critical eye of an outsider”. Deep passion and sympathy can cloud judgment in that respect.
- Premature closure—When the researcher does not have enough time to analyse the data and rushes to judgment. This might discredit the validity of the whole research.

To summarize, the Vancouver School of thoughts strives to integrate tools that help increase the quality of the research by constantly evaluating the data collection, data analysis and placement of the findings.

8 Findings of the Research

Safety is the most concerning attribute because batteries in BEVs can catch fire that can be hard to extinguish. In a cold country like Iceland this is not too much of a concern compared to other hot-climate countries like Kuwait.

OPEX is the second concern for prospective EV owners. One liter of gasoline in Iceland costs 220 ISK. That is about 15 ISK for every driven km (assuming 7 L/100 km), which is five times more than the equivalent cost of electric charge for

1 km driven. This cost savings is particular to Iceland as this country is one of the lowest resellers of electricity for 7.3 ikr per kwh (Orka Heimilanna, 2019). On the contrary, it would cost up to three times more per km to use electricity. Even in the European Union there is no such savings as the price of electricity is low only in Eastern European countries, including Estonia, Poland, Romania, Hungary, Lithuania and Bulgaria, but the gasoline prices are also lower as they levy lower taxes [16].

Another cost that is significantly lower is maintenance cost, but the BEV engine has no moving parts or fluids and hardly needs any maintenance. One of the participants reported that the only fluid refill and the maintenance he had conducted for 3 years was to change the fluid for the window wipers. The life of the battery remains a major OPEX concern. Data on the actual battery life in Iceland is inconclusive, as most BEVs have not been in use for more than 8 years, which is the factory warranty. However, the charge testing of the early editions from 2012 indicated that the charge has not significantly dropped, probably due to cold conditions in Iceland. This suggests that the battery would last well over 8 years guaranteed and up to 13 years which is the average age of a combustion engine. However, the opposite is likely to be true for hot countries as hot climate kills car batteries faster due to water loss, heat distortion and increased corrosion [17].

CAPEX is also a major concern when buying BEVs or PHEVs. The Government of Iceland does not levy import excise duty on EVs, compared to 30–45% on conventional vehicles depending on their CO₂ emissions, and does not charge the 25% VAT under the import value of six million ISK. As a result, EVs are competitively priced compared to combustion engine vehicles, and without these concessions most EVs would be priced out of the market [18]. The government of Norway is even more generous and additionally cancels fees for toll roads and fast lanes used by EVs. This might explain why Norway has now higher percentage of new cars as EVs. However, the opposite is also true: the lack of such generous concession could also explain low adaptation of EVs in the rest of the world.

Range anxiety is a major factor and one of the most disappointing aspects of operating EVs in Iceland. Because of the cold and windy conditions, drivers are expecting up to 30% lower range per electric charge. More so in cold weather when the heater is in operation, as it drains the battery much faster. These factors impact drivers in the countryside more than city dwellers, who drive on an average of 40 km/day and are for the most part not bothered by a lower range, which is usually from 100 to 200 km per charge for the older models. The optimal temperature for driving EVs is around 20 °C, when neither heater nor air conditioner must be used (this drains the battery and limits available kilometers driven per charge). New editions of EVs have bigger battery options that are popular. Many of the participants of the interview stated that they wished to have an option of a large battery when they bought their EVs, as it caught them by surprise how large the range reduction (km driven on one charge of electricity) was when using the heater. This will become more of an important factor when using air-conditioners, as cooling by 1° requires more energy than heating. Operating either the car-heater or air conditioning will

significantly lower the driving range. Thus, outdoor temperature around 20 °C will be considered optimal as neither heating nor cooling is needed.

The lack of charging facilities is the most commonly given excuse for not buying an EV. It is essential to have overnight access to an electric outlet that is linked to a meter that measures the electricity usage charged to the owner. According to the owners' manuals of most EVs, it would take 7–8 h to fully charge. However, this charging time is based on an optimal electric system load condition when a few people are using electricity. Many EV owners complain that it takes them 10–12 h to fully charge their EVs, especially if they live in an apartment building with other inhabitants charging their vehicles. For those who do not manage to fully charge their vehicles overnight, a wide net of fast-charging facilities where 80% charge can be obtained in 20–30 min is available in Iceland and growing month by month [19].

Quality of driving is one reason drivers say, “once you go electric – you never go back”. Generally, male drivers state that the major advantage of electric vehicles is the torque (fast and smooth acceleration) because of the absence of a gear box. Women, on the other hand, stated that the noiselessness is the main factor: “with no engine sounds it is like riding a magic carpet”.

What is “a Typical EV” driver the first group is largely single women who buy cheaper versions of EVs. Environmental concern is one of the main reasons for their choice, particularly contributing to greenhouse gases, such as CO₂. The second group is bigger, and it is comprised of middle-class families that already have a combustion engine car. They generally tend to live in their private or terraced houses in the suburbs of Reykjavik, the capital city, and drive 50–150 km to work per day. They state that fuel savings is their main reason for their EV purchase. Their EV is generally priced higher than 4.5 million ISK.

9 Conclusion and Managerial Implication

While the Icelandic and Norwegian governments will continue to provide generous Capex and OPEX concessions towards EV owners, their number of EVs is likely to grow. If these governments halt their financial support towards EVs owners, the growth is likely to stall. Other countries that do not give similar concessions as Iceland and Norway will not see similar growth in number of EVs. Iceland and Norway are not with the rest of the world in terms of levying some of the highest taxes on gasoline. This results in the highest gasoline prices in the world while the price of electricity is one of the lowest because of low production cost passed over to consumers. OPEX fuel savings in using EVs is higher than in any other country. The highest cost today is the cost of EV itself, which is assumed to depreciate in 8 years. Due to high cost of the battery vs. the cost of the car, most people will rather replace the car rather than replace the battery. The lifetime of the battery thus dictates the lifetime of the car. It remains to be seen if the lifetime of batteries in cold countries will significantly exceed 8 years and last up to 13 years, which is the same

as the lifetime of an average combustion engine car, making depreciation cost the same.

Real-world studies of the lifetime of electric car batteries in various weather and climate conditions is a topic for further studies. Not only the lifetime of the battery remains a factor, but also the cost and the efficiency of storing energy and fast charging. Availability of private and public charging facilities as well as general infrastructure improvements in delivering electricity is needed if EVs are going to become a standard. In 2009, the author interviewed the CEO of Mitsubishi Heavy Industries and the CEO of Pure Mobility Cars (Driving Sustainability Reykjavik, 2009) about when EVs would become the mainstream option for the general public. The CEO of Mitsubishi stated that it would probably take 25 years or about until 2032 and the CEO of Smart Car said that in 10 years, or by 2019 EVs would account for 1% sales of new cars in the world. Iceland and Norway clearly are the early adoption nations for EVs. For the rest of the world it is likely that the prediction of the CEO of Mitsubishi Motors and Smart Car will come true.

References

1. European Environment Agency (2012) Annual European Union greenhouse gas inventory 1990–2010 and inventory report 2012. ISBN 978-92-9213-316-0 Luxembourg, Office for Official Publications of the European Communities
2. Trommer S, Jaraas J, Kolarova V (2015) Early adopters of electric vehicles in Germany unveiled. EVS28 International Electric Vehicle Symposium and Exhibition 1. Korea. Retrieved from https://www.researchgate.net/publication/312283413_Early_adopters_of_electric_vehicles_in_Germany_unveiled
3. Boston D, Werthman A (2016) Plug-in vehicle behaviors: an analysis of charging and driving behavior of Ford plug-in electric vehicles in the real world. *World Electr Veh J* 8:926–935
4. Hardman S, Shiu E, Steinberger-Wilckens R (2016) Comparing high-end and low-end early adopters of battery electric vehicles. *Transp Res A* 88:40–57
5. Krupa JS, Rizzo DM, Epptein MJ, Lanute BD, Gaalema DE, Lakkaraju K, Warrender CE (2014) Analysis of a consumer survey on plug-in hybrid electric vehicles. *Transp Res A Policy Pract* 64:14–31
6. Levy PZ, Drossinos Y, Thiel C (2017) The effect of fiscal incentives on market penetration of electric vehicles: A pairwise comparison of total cost of ownership. *Energy Policy* 105:524–533
7. Bjerkan KY, Norbech TE, Nordtomme ME (2016) Incentives for promoting Battery Electric Vehicle (BEV) adoption in Norway. *Transp Res D* 43:169–180
8. Soltani-Sobh A, Heaslip K, Stevanovic A, Bosworth R, Radivojevic D (2017) Analysis of the electric vehicles adoption over the United States. *Transp Res Procedia* 22:203–212
9. Kim S, Lee J, Lee C (2017) Does driving range of electric vehicles influence electric vehicle adoption? *Sustainability Journal* 9:1783. Retrieved from www.mdpi.com/journal/sustainability
10. CNN (2019). For the first time ever, electric vehicles outsold gas and diesel vehicles in Norway. Retrieved from <https://edition.cnn.com/2019/04/04/world/norway-zero-emission-vehicles-trnd/index.html>
11. Schwandt TA (1994) Handbook of qualitative research. In: Denzin NK, Lincoln YS (eds) *Constructivist, interpretivist approaches to human inquiry*. Sage, Thousand Oaks
12. Spiegelberg H (1984) *The phenomenological movement: a historical introduction*. Kluwer Academic Publishers

13. Halldorsdottir S (2000) The Vancouver school of doing phenomenology. Retrieved from <http://staff.unak.is/not/sigrundur/The%20Vancouver%20School.pdf>
14. Green Car Reports (2019). Retrieved from <https://greencarreports.com>
15. Kvale S (1989) To validate is to question. In: I. K. (ed) issues of validity in qualitative research. Studentlitteratur, Lund, pp 73–92
16. Eurostats (2019) Retrived from <https://www.ec.europa.eu>
17. RACQ (2019) Car battery myths and facts. Retrieved from <https://www.racq.com.au/cars-and-driving/products-and-services/batteries/battery-myths>
18. Wappelhorst S, Tietge U (2018) Iceland is one of the world's most interesting electric vehicle markets. ICCT The International Council on Clean Transportation. Retrieved from <https://the-icct.org/blog/staff/iceland-ev-market-201807>
19. European Alternative Fuel Observatory (2019) Ministry of Transport. Retrieved from <https://www.eaf.eu/alternative-fuels/overview>

3D Numerical Modeling for Assessing the Energy Performance of Single-Zone Buildings with and Without Phase Change Materials

Hamed H. Saber and Ali E. Hajiah

1 Introduction

The phenomenon of global warming is one of the problems we currently face. This phenomenon has led to many environmental issues, including higher atmospheric temperatures, increased intensity of precipitation, and increased greenhouse gas emissions. Buildings and other engineered structures are responsible for a large portion of the global and local impacts of climate change. In regions with harsh climatic conditions, a substantial share of energy is used for heating and cooling buildings [1]. The energy consumption of the building sector is high and although the situation differs from country to country, buildings are responsible for about 30–40% of the total energy demand [2]. In Europe, however, buildings are responsible for 40–50% of energy use and the largest share of energy in buildings is used for heating [3].

Kuwait has experienced substantial building construction activities in recent decades, which cause significant strain on the country's electricity grid. Al Tayyar [4] reported that the annual electrical peak demand has doubled to 15,000 MW in the period between 2000 and 2015, and the Ministry of Energy and Water (MEW) expects this number to double again by 2030 attributing 70% of this growth to new housing projects. Regarding the distribution of electricity consumption by end-user sector in Kuwait, Krarti, and Hajiah [5] reported that the building sector represents 90% of the electricity consumption of the country. The authors also reported that the

H. H. Saber (✉)

Jubail University College, Royal Commission of Jubail and Yanbu,

Jubail Industrial City, Kingdom of Saudi Arabia

e-mail: saberh@ucj.edu.sa

A. E. Hajiah

Research Scientist, Energy and Building Research Center, Kuwait Institute for Scientific Research, Shuwaikh, Safat, Kuwait

e-mail: ahajiah@kisir.edu.kw

residential sector (including privately owned residences and rental apartment units) were responsible for over 70% of Kuwait's electrical peak power demand in 2004.

Reinhart et al. [6] have shown that in established residential neighborhoods in Kuwait about half of the electricity use and 70% of peak demand in buildings stem from cooling energy demand and the growing peak demands have led to recurring summer blackouts in some residential areas. The energy and power demand in Kuwait between 2008 and 2009 has increased at a rate of 6% per year, suggesting the peak power demand could reach 27 GW in 2025 if the same trend persists [7]. Also, the study by Alotaibi [8] has shown that the annual energy consumption per capita in Kuwait is among the highest in the world (13,000 kWh/person). While this use of energy can be partly attributed to the harsh summer climate, other contributing factors include inefficient construction practices and equipment, as well as energy-intensive lifestyle choices [9].

Given that Kuwait is an oil-exporting country, a further expansion in the residential sector requires more need for generating electrical power. However, oil is the country's only natural resource and its main source of revenue [7], and while as late as 1980 only 10% of the produced energy was consumed locally, this percentage was close to 40% in 2015. As such, it is important to design Kuwaiti building envelopes with the intent of achieving energy savings to help reduce building operating loads and thus the demand for energy over time. To reach this goal, the energy conservation code of Kuwait's Ministry of Electricity and Water [7] established several recommendations to enhance the energy efficiency of buildings (including insulation, glazing, lighting, and ventilation requirements) and to reduce power ratings of air-conditioning systems. This study focuses on the energy performance of the whole building envelope that includes roofing and wall systems with and without Phase Change Materials (PCMs).

Regarding the energy performance of Kuwaiti residential buildings, Al-ajmi and Hanby [10] conducted a study to investigate the energy consumption in which only traditional sensible construction materials were considered. That study proposed several features that could be adopted to achieve more energy-efficient buildings, including (1) reducing uncontrolled air infiltration rates, (2) control the sizes of windows and their orientations and placements in the facades, and (3) the use of certain treatments for glazing to reduce solar heat gain coefficients. To enhance the energy performance of residential buildings, many studies explored the incorporation of Phase Change Materials (PCMs) in these buildings.

PCM is a material that undergoes melting/freezing at a nearly constant temperature resulting in storing/releasing an amount of energy due to the latent heat involved in the solid-liquid phase change processes, called latent heat of fusion. As such, PCM can be used in the applications of thermal energy storage. PCMs are mainly classified as organic, inorganic, and eutectic. For a given thermal energy storage application, the selection of a PCM mainly depends on its melting/freezing temperature and its latent heat of fusion; additionally, this PCM should have desirable thermophysical, kinetic, chemical, and economic properties as suggested by some researchers [11, 12]. Several building applications of PCMs can be found in the

literature, including PCM-enhanced wallboards, PCM bricks, PCM-enhanced concrete systems and mortars, and PCM Trombe walls.

Many authors have investigated the advantages of incorporating PCMs in buildings, and several numerical and experimental studies have been carried out to assess the thermal performance of different PCM-based wallboards [11–27]. Also, a number of studies have provided important information about the optimization of a paraffin-based wallboard for building applications, and also showed the importance of several aspects that can be considered in the assessment of the heat transfer with solid-liquid phase change through PCM-based wallboards [18–20].

Under several European weather conditions, Soares et al. [28] used EnergyPlus and GenOpt tools to investigate the impact of incorporating PCM-wallboards on the heating and cooling energy loads of residential rooms having lightweight steel framing. By considering a number of design parameters such as the thickness and location of the PCM-drywalls, air-infiltration rates, solar gains, internal gains, and set-points, Soares et al. [28] concluded that PCM-wallboards can contribute to the annual cooling and heating energy savings in a passive way. Another numerical result by Saffari et al. [29] showed that PCMs improved the cooling and heating energy loads for buildings subjected to climates of Madrid.

A renovated office building in Lyon was monitored for a period of 1 year by Kuznik et al. [30] to investigate the potential of a PCM-wallboard constituted of 60 wt% of microencapsulated paraffin within a copolymer where a room was equipped with PCM-wallboards in the lateral walls and in the ceiling, and another room, identical to the first one, was not equipped but also monitored. The results of that study showed that the use of PCM-wallboards resulted in an enhancement in the thermal comfort of occupants [30]. In a Mediterranean residential building, Mandilaras et al. [31] evaluated experimentally the impact of PCM-wallboards on the thermal performance of this building. The results of that study showed that the thermal mass of the walls can be enhanced during late spring, early summer, and fall when the PCM-wallboards have gone through melting-freezing processes (i.e., PCMs were activated).

In summary, several studies concerning the application of white roofing systems have been carried out to investigate the potential energy savings, and risk of condensation and mold growth in these roofing systems (e.g., see [32–36]). A full study that investigated the incorporation of PCMs in white roofing systems subjected to the weather conditions of Kuwait city is available in [37]. Furthermore, many studies regarding the application of PCM-wallboards in the wall systems of buildings have been carried out in order to investigate the effect of incorporating PCM-wallboards on the energy performance in these buildings. However, no guidelines about the incorporation of PCM-wallboards in heavyweight construction subjected to the dry desert climate conditions of Kuwait were found in the literature. Low-rise heavyweight construction is common in Kuwait and, regarding the residential sector, low-rise buildings are the most representative Kuwaiti buildings. As such, this category of buildings is used in this study.

2 Objectives

This study investigates the potential energy savings as a result of incorporating PCMs in the wall and roofing systems of single-zone buildings when these buildings are subjected to the weather conditions of Kuwait. To maximize the contribution of PCM on the energy savings, this material should change its phase from solid to liquid (i.e., melting) and from liquid to solid (i.e., freezing) in long periods during the year. As such, the melting/freezing temperature of the PCM is one of the key parameters that has a direct impact on the energy performance of buildings having PCM. For buildings subjected to Kuwaiti climates, the questions are: (1) what is the optimum temperature of a PCM for maximizing the energy savings? and (2) what is the amount of energy savings as a result of using PCM? To answer these questions, the main objectives of this study are to:

1. Conduct numerical simulations for the cases of single-zone buildings as these are the cases of single-story buildings. In this study, windows with different overall WWR (10–70%) are located in more than one orientation. Windows are modeled with different U-values (or R-values) and different SHGC (see Table 1).
2. Conduct numerical simulations for reference single-zone buildings without drywall, and with drywall but without PCM. The obtained results are needed to determine the contribution to energy savings due to using PCM inside drywall versus not using PCM inside drywall.
3. For a given PCM drywall thickness, conduct numerical optimization to determine the optimum melting temperature of the PCM for Kuwaiti weather.

3 Problem Description, Numerical Model, and Design Variables

To quantify the amount of energy savings as a result of using PCM-drywalls in the wall and roofing systems (see Fig. 1), two reference wall systems and two reference roofing systems were considered. The two reference wall systems are called “Ref Wall 1” and Ref Wall 2,” and the two reference roofing systems are called “Ref Roof

Table 1 Different types of glazing for different Window-to-Wall Ratios (WWRs) in accordance with the Kuwaiti Building Energy Code [7]

Case	WWR	Glazing type required	U-factor (W/(m ² K))	SHGC
W1	10%	6 mm double-tinted	3.42	0.36
W2	20%	6 mm double-reflective	3.38	0.254
W3	30%	6 mm double-reflective	3.38	0.254
W4	40%	6 mm double-reflective	3.38	0.254
W5	50%	6 mm double-spectrally selective	1.71	0.23
W6	60%	6 mm double-spectrally selective	1.71	0.23
W7	70%	6 mm double-spectrally selective	1.71	0.23

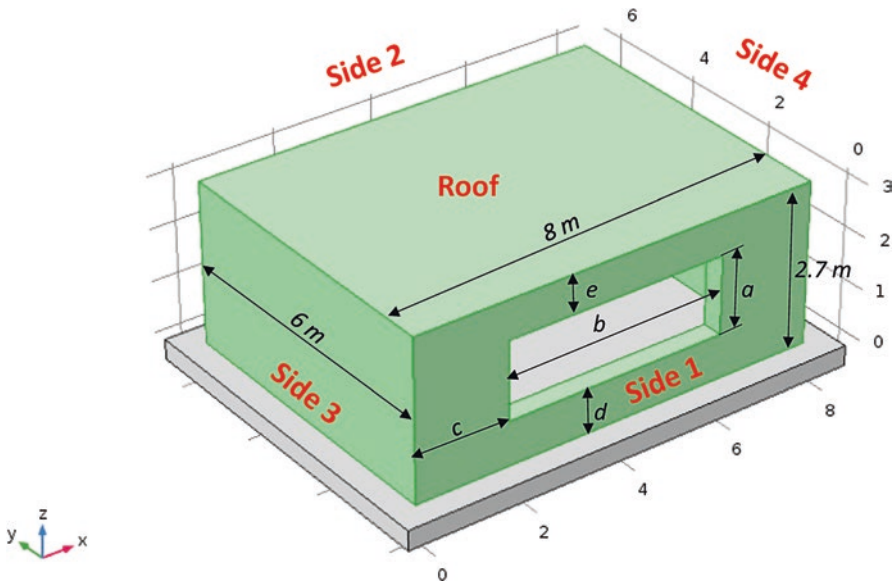


Fig. 1 Schematic and dimensions of air-conditioned single-zone building

1” and “Ref Roof 2.” As shown Figs. 2 and 3, Ref Wall 1 and Ref Roof 1 are similar to the Test Wall and the Test Roof, respectively, but without drywalls. Additionally, Figs. 2 and 3 show that Ref Wall 2 and Ref Roof 2 are also similar to the Test Wall and the Test Roof, respectively, but with drywalls only (i.e., without PCM).

3.1 Model Development and Benchmarking

It is expensive and time consuming to perform mid- and full-scale experiments in fields or laboratories in order to assess the long-term hygrothermal performance of building envelopes. As such, a numerical model that was previously developed is used in this study to assess the moisture and energy performance of different building components and assemblies.

This model solves simultaneously the moisture transport equation, the energy equation, the surface-to-surface radiation equation (e.g., surface-to-surface radiation in the enclosed airspace), and the air transport equation in the various material layers. The air transport equation is the Navier-Stokes equation for the space layers (e.g., air cavities), and the Darcy equation (Darcy Number, $D_N \leq 10^{-6}$) and Brinkman equation ($D_N > 10^{-6}$) for the porous material layers. The Heat, Air, and Moisture (HAM) equations were discretized using the Finite Element Method (FEM). To gain confidence in the model and thus simulation results, the model was extensively benchmarked against experimental results from the evaluation of a number of

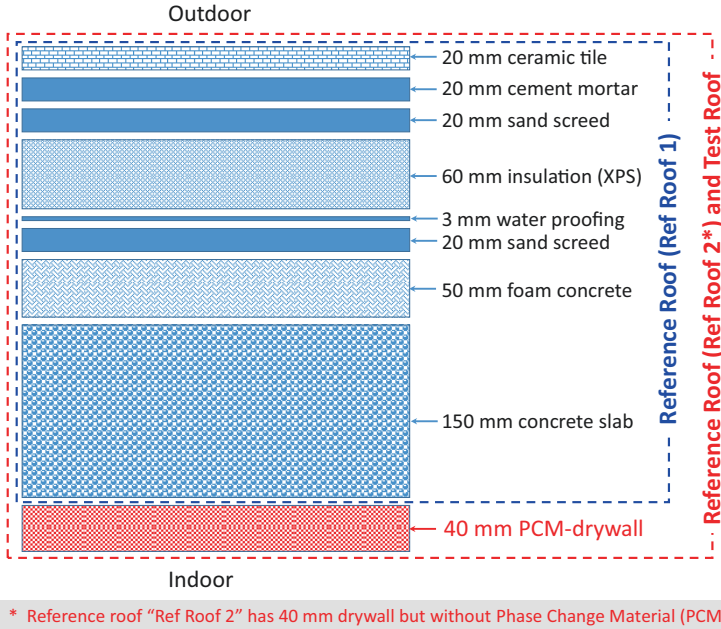


Fig. 2 Schematics of the reference and test roofing systems [37]

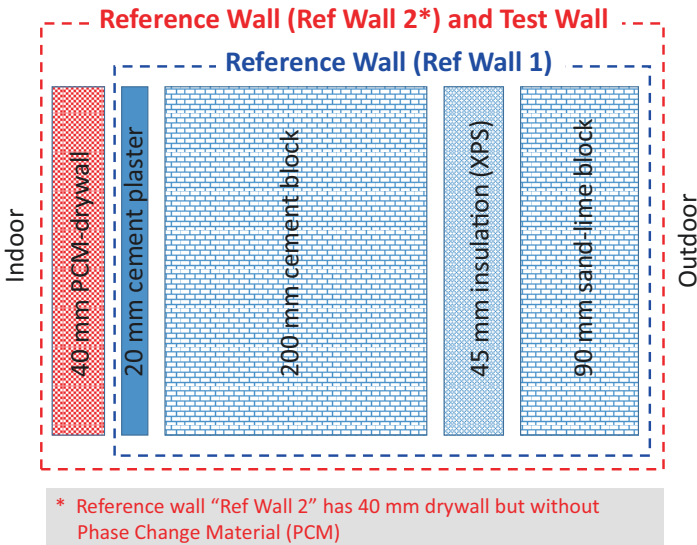


Fig. 3 Schematics of the reference and test wall systems

different building components and assemblies. More details about the model are available in previous publications (e.g., see [38–47]).

In building applications that are similar to this study, the experimental tests by Maref et al. [48–50] were used to validate the present model. In these tests, full-scale laboratory experiments were conducted in indoor and outdoor climatic chambers in order to assess the hygrothermal performance of wall specimens. The measured temperature and relative humidity (RH) in these climatic chambers for both indoor and outdoor conditions were within ± 0.5 °C and $\pm 1\%$ RH, respectively. A series of tests for the wall specimens were mainly focused on the drying process of wood-based sheathing material, a key component of light wood-frame construction. The full-scale specimens consisted of wall assemblies having dimensions of 2.43×2.43 m. The tests were conducted over a sufficiently long period of time so as to permit gravimetric quantification of the change in the total moisture content of critical wall specimen components under the drying process. The model predictions were in good agreement with the experimental data. The full details of model validations with the test data by Maref et al. [48–50] are available in Saber et al. [36]. In addition, as provided in [51], the model was validated in several applications that are related to building components and assemblies that contain enclosed airspaces such as wall and roofing systems with reflective insulations, as well as fenestration systems such as double glazing windows, curtain walls, and skylight devices. The model predictions were also in good agreement with test data (see [51] for more details).

3.2 *Window-to-Wall Ratios*

In this study, seven WWRs of the main solar-oriented windows are considered. The energy impact of incorporating different PCM-drywalls of 40 mm thick and having a latent heat of 100 kJ/kg with different melting temperatures is considered so as to determine the optimum melting temperature for achieving the highest energy savings. A 4×7 fully air-conditioned air space cases (28 in total) at an indoor set point temperature of 24 °C with seven WWRs facing the four cardinal directions were considered. The interior air volume remains as per the ASHRAE 140 standard [52] with the interior dimensions of $8 \text{ m} \times 6 \text{ m} \times 2.7 \text{ m} = 129.6 \text{ m}^3$. To reflect current, relatively dense, deep floor plan residential construction practices in Kuwait in which most spaces have windows with one orientation, the windows with different WWRs were concentrated on one side. The total floor area of the room is 48 m^2 with a slab-on-grade foundation. All vertical surfaces are considered as external walls with no obstruction from neighboring buildings.

In accordance with the requirements of the Kuwaiti Building Energy Code [7], Table 1 shows the specific glazing types for different WWR values. To prevent the boost of cooling energy demand when increasing the area of the fenestration systems, Table 1 shows that the higher the value of the WWR, the more selective the

requirements of the glazing type, with lower U-factor and SHGC values. The different WWRs are obtained by changing the fenestration area as shown in Fig. 1.

3.3 Wall and Roofing Systems

According to Al-ajmi and Hanby [10], the traditional roofing system is almost universal in Kuwait and the exterior walls are mainly of two types: Autoclaved Aerated Concrete (AAC) walls and concrete block walls called “classical walls.” The latter exterior wall is cheaper, widely available, locally produced, and structurally stronger than AAC. However, AAC has the advantage of acting as thermal insulation, but there are few factories producing these blocks in Kuwait. This study considers classical walls in its numerical simulations. Figure 2 shows a cross section and dimensions of the reference and test roofing systems. A full study was recently conducted on these roofing systems to investigate their energy and long-term moisture performance for a wide range of short-wave solar absorption coefficient of rooftops [37]. Figure 3 shows a cross section and dimensions of the reference and test wall systems. Also, the thermal properties of the construction materials for both the roofing and wall systems are obtained from [10].

Figures 2 and 3 show that the PCM-enhanced model is attained by including a PCM-drywall on the indoor surfaces of the wall and roofing systems. In this study, the wall system with PCM-drywall is called “Test Wall,” and the roofing system with PCM-drywall is called “Test Roof.” Currently, there are many PCM products available in the markets (see [53] for more details). In this study, hypothetical PCM-drywalls of 40 mm thick are assumed to have a latent heat of 100 kJ/kg but with different melting temperatures (22–29 °C), and their thermal conductivities are considered different for the solid phase (0.18 W/mK) and the liquid phase (0.14 W/mK) [53].

4 Methodology

A study presented in another paper in these proceedings for reflective and nonreflective roofing systems showed that the PCM-drywall having a melting temperature of 24 °C has resulted in the lowest cooling, heating, and total energy loads compared to other PCM-drywalls with different melting temperatures when these roofing systems were subjected to the weather conditions of Kuwait City [37]. In this study, numerical simulations were conducted for the different wall systems shown in Fig. 3 when these systems are also subjected to the weather conditions of Kuwait City and facing the four cardinal directions (see side 1 through side 4 in Fig. 1). For the Test Wall, different melting temperatures (22–29 °C) for PCM-drywall were considered so as to determine the optimum melting temperature for maximizing the amount of energy savings. Similar to the previous study [37], the temperature, heat flux, and moisture distributions in the wall systems (Ref Wall 1, Ref Wall 2 and Test

Wall, see Fig. 3) were obtained by solving the energy equation and moisture equation in different layers [38–47]. The predicted heat fluxes on the indoor surfaces of these wall systems were used to determine the monthly and yearly heating and cooling energy loads.

As will be shown later, a melting temperature (T_m) of 24 °C for PCM-drywalls has resulted in the lowest energy loads for: (1) different Test Wall systems located in the different cardinal directions (side 1 through side 4), and (2) different Test Roof systems having different reflective materials with a wide range of short-wave solar absorption coefficients ($\alpha_s = 0.88\text{--}0.2$) [37]. In this study, the Test Wall having PCM-drywall with $T_m = 24$ °C is called the Optimum Test Wall. Whereas, the Test Roof having PCM-drywall with $T_m = 24$ °C is called the Optimum Test Roof (see [37]).

In accordance with the Kuwaiti Building Energy Code [7], different types of glazing for different Window-to-Wall Ratios (WWR = 10%–70%), as provided in Table 1, were considered in this study. Using Ref Wall 1, Ref Wall 2, and the Optimum Test Wall shown in Fig. 3, and Ref Roof 1, Ref Roof 2, and the Optimum Test Roof shown in Fig. 2, numerical simulations were conducted for single-zone buildings when the different windows (W1 through W7, see Table 1), were located in different cardinal directions/orientations (side 1 through side 4). Twenty eight numerical simulation cases “SI-WJ”, where I = 1, 2, 3, and 4, and J = 1, 2, 3, 4, 5, 6, and 7, were conducted for single-zone buildings. Note that SI-WJ refers to the simulation case of window WJ (i.e., W1 through W7, see Table 1) when it is located in side I (i.e., side 1 through side 4) and no windows in the other sides. For example, the simulation case “S2-W5” refers to the case of window W5 (Table 1) when it is located in side 2 (i.e., S2) and no windows in the other sides (i.e., side 1, side 3, and side 4).

5 Results and Discussion

This section presents the results of the numerical simulations for different cases of single-zone buildings as these are the cases of single-story buildings when different overall WWR (10%–70%) are located in more than one orientation. To quantify the amount of energy savings due to incorporating PCM in single-zone buildings, the simulation results include the cases for: (1) reference single-zone buildings without drywall and (2) reference single-zone buildings with drywall but without PCM.

5.1 Yearly Energy Loads of Different Wall Systems

For Test Wall having a wide range of PCM melting temperatures, T_m (22–29 °C), the monthly cooling, heating, and total energy loads were used to determine the yearly cooling energy loads and yearly total energy loads (yearly cooling energy loads + yearly heating energy loads). The obtained results for the yearly cooling energy

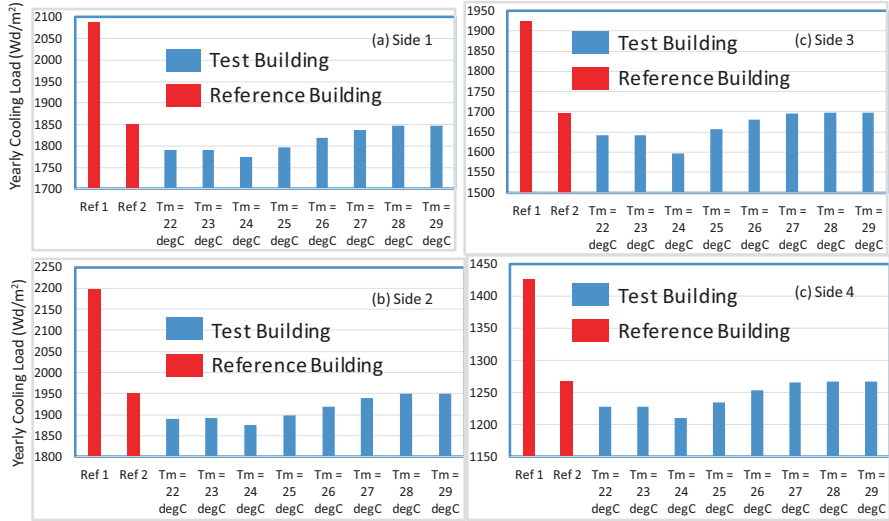


Fig. 4 Effect of the PCM melting temperature on the yearly cooling loads of wall located in different sides (Side 1 through Side 4)

loads are shown Fig. 4a (side 1), Fig. 4b (side 2), Fig. 4c (side 3), and Fig. 4d (side 4). Also, the results of the yearly total energy loads are shown in Fig. 5a (side 1), Fig. 5b (side 2), Fig. 5c (side 3), and Fig. 5d (side 4). For the Test walls in different cardinal directions (side 1 through side 4), these figures show that the Test Wall having PCM-drywall with a melting temperature of 24 °C has resulted in the lowest yearly cooling load and yearly total load. As such, this Test Wall is called “Optimum Test Wall.”

5.2 Comparison of the Energy Loads of Optimum Test Wall against Reference Walls

Figures 4 and 5 show the effect of the PCM melting temperature on the yearly cooling loads, and yearly total loads, respectively, of Ref Wall 1, Ref Wall 2 and Test Wall when they are located in different sides. For different wall systems located in side 1, the contributions to the yearly cooling loads for Ref Wall 1, Ref Wall 2, and Test Wall with PCM-drywall having $T_m = 24\text{ °C}$ (i.e., Optimum Test Wall) were 2087.1 Wd/m², 1848.5 Wd/m² and 1774.9 Wd/m², respectively (Fig. 4a). Consequently, the contributions to the yearly cooling load for Optimum Test Wall was, respectively, 17.6% and 4.1% lower than that for Ref Wall 1 (i.e., without dry-wall) and Ref Wall 2 (i.e., with dry-wall but without PCM). As shown in Fig. 5a, the contributions to the yearly total energy loads of Ref Wall 1, Ref Wall 2, and Optimum

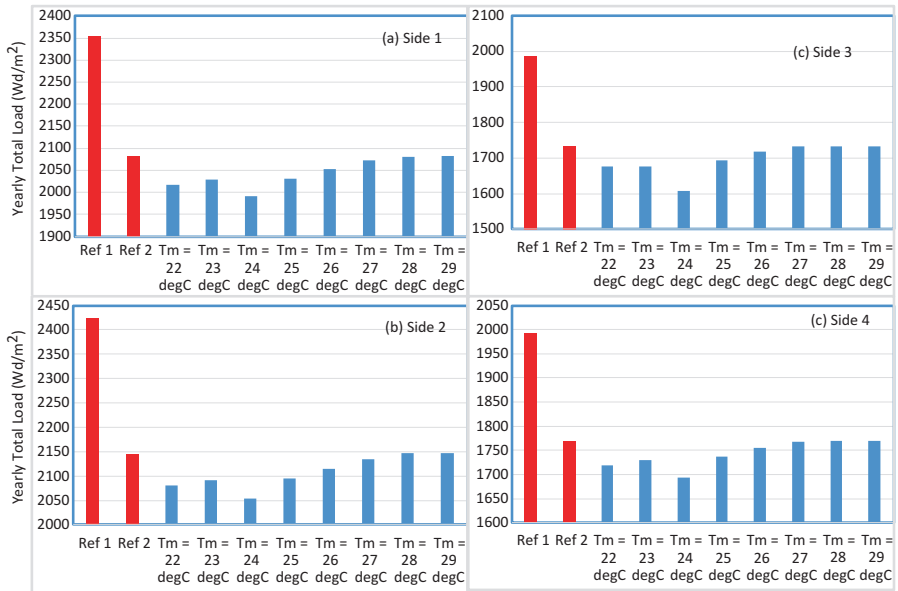


Fig. 5 Effect of the PCM melting temperature on the yearly total loads of walls located different sides (Side 1 through Side 4)

Test Wall were 2354.1 Wd/m², 2082.7 Wd/m², and 1991.2 Wd/m², respectively. These have resulted a contribution to the yearly total load for the Optimum Test Wall at 18.2% and 4.6% lower than that for Ref Wall 1 and Ref Wall 2, respectively.

The corresponding results for Ref Wall 1, Ref Wall 2, and Optimum Test Wall when they are located in side 2, side 3 and side 4 are summarized in Table 2. The contributions to the yearly cooling load for Optimum Test Wall were 17.2% and 4.0% (side 2), 20.5% and 6.2% (side 3), and 17.9% and 4.7% (side 4) lower than that for Ref Wall 1 and Ref Wall 2, respectively. In addition, the contributions to the yearly total load for this Optimum Test Wall was 18.0% and 4.5% (side 2), 23.6% and 7.9% (side 3), and 17.6% and 4.4% (side 4) lower than that for Ref Wall 1 and Ref Wall 2, respectively.

In summary, for the different wall systems considered in this study and located in the different cardinal directions (side 1 through side 4), it was observed that the Test Wall having PCM-drywall with melting temperature of 24 °C, called “Optimum Test Wall,” has the lowest cooling and total energy loads. For different cardinal directions for the wall systems (side 1 through side 4), the ranges of the contributions to the yearly cooling load for this Test Wall were 17.2–20.5% and 4.0–6.2% lower than that for Ref Wall 1 and Ref Wall 2, respectively. Also, the ranges of the contributions to the yearly total loads for this Test Wall were 17.6–23.6% and 4.4–7.9% lower than that for Ref Wall 1 and Ref Wall 2, respectively.

Table 2 Contributions to the yearly cooling load and yearly total load for different wall systems located in different sides

Wall location	Ref Wall 1		Ref Wall 2		Optimum Test Wall	
	Cooling load (Wd/m ²)	Total load (Wd/m ²)	Cooling load (Wd/m ²)	Total load (Wd/m ²)	Cooling load (Wd/m ²)	Total load (Wd/m ²)
Side 1	2087.1	2354.1	1848.5	2082.7	1774.9	1991.2
Side 2	2197.7	2422.6	1950.4	2145.9	1875.2	2053.9
Side 3	1926.3	1985.6	1697.1	1733.7	1598.0	1606.5
Side 4	1426.0	1991.7	1266.1	1768.6	1209.8	1693.3

6 Yearly Energy Loads

For different combinations of windows located in the different cardinal directions/orientations with different WWRs, the numerical simulations were conducted for roofing systems having different reflective materials with different short-wave solar absorption coefficients, namely, $\alpha_s = 0.88$ (black/conventional roof), $\alpha_s = 0.6$, $\alpha_s = 0.4$, and $\alpha_s = 0.2$. For different values of the short-wave solar absorption coefficients of the rooftops (α_s), the obtained results of the yearly total loads are provided in Fig. 6 ($\alpha_s = 0.88$), Fig. 7 ($\alpha_s = 0.6$), Fig. 8 ($\alpha_s = 0.4$), and Fig. 9 ($\alpha_s = 0.2$). These figures provide the yearly total loads for three types of buildings, namely:

1. Building with no drywall in the wall and roofing systems. This type of building is referred to as “Ref Building 1.”
2. Building with drywall but without PCM in the wall and roofing systems. This type of building is referred to as “Ref Building 2.”
3. Building with PCM-drywall having melting temperature of 24 °C in the wall and roofing systems. This type of building is referred to as “Test Building.”

As shown in Figs. 6 through 9, decreasing the short-wave solar absorption coefficient for the rooftops has resulted in a decrease in the yearly total loads. Furthermore, for a given short-wave solar absorption coefficient for the rooftop, these figures show that the Test Buildings have the lowest yearly total loads.

6.1 Effect of Window Orientation on the Yearly Energy Loads

For the properties of different windows with different WWRs as provided in Table 1, when these windows were located in the four cardinal directions, Figs. 6a–d through 9a–d show that the window case of W1 (WWR = 10%, U-factor = 3.42 W/(m²K) and SHGC = 0.36) has resulted in the lowest yearly total loads. While the window case of W4 (WWR = 40%, U-factor = 3.38 W/(m²K) and SHGC = 0.254) has resulted in the highest yearly total loads. For example, for the window case W4 located in side 1 (i.e., S1-W4) in single-zone buildings having a roofing system with short-wave solar absorption coefficient of 0.88 (i.e., black/conventional roof), the yearly cooling loads for Ref Building 1, Ref Building 2, and Test Building were,



Fig. 6 Yearly total loads with PCM at an optimum melting temperature of 24°C and without PCM for the cases of windows located in (a) Side 1, (b) Side 2, (c) Side 3 and (d) Side 4 with roof having $\alpha_s = 0.88$

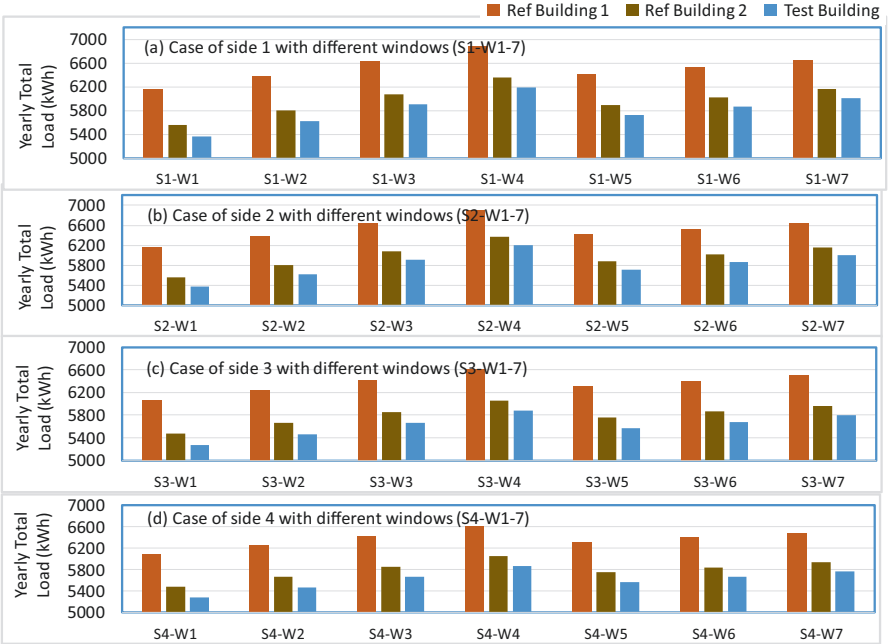


Fig. 7 Yearly total loads with PCM at an optimum melting temperature of 24°C and without PCM for the cases of windows located in (a) Side 1, (b) Side 2, (c) Side 3 and (d) Side 4 with roof having $\alpha_s = 0.6$

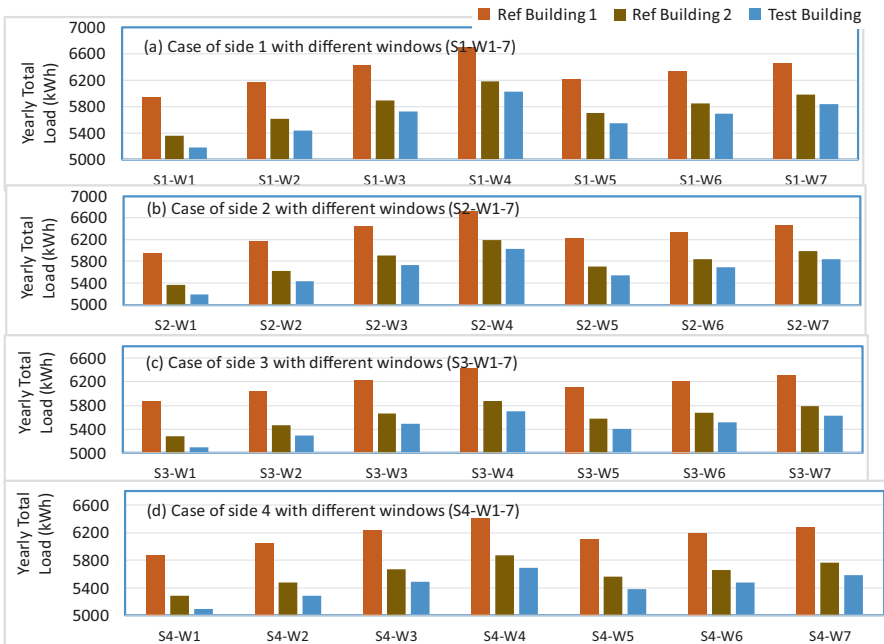


Fig. 8 Yearly total loads with PCM at an optimum melting temperature of 24°C and without PCM for the cases of windows located in (a) Side 1, (b) Side 2, (c) Side 3 and (d) Side 4 with roof having $\alpha_s = 0.4$

respectively, 6360.7 kWh, 5872.9 kWh, and 5701.8 kWh, and the corresponding yearly total loads were, respectively, 7173.2 kWh, 6637.2 kWh, and 6449.5 kWh (Fig. 6a). However, replacing the window case W4 located in side 1 by the window case W1 located in the same side (i.e., side 1) has resulted in lower yearly cooling loads for Ref Building 1, Ref Building 2, and Test Building (5841.7 kWh, 5308.9 kWh, and 5116.5 kWh, respectively) by 8.9%, 10.6%, and 11.4%, and lower yearly total loads (6450.8 kWh, 5856.6 kWh, and 5635.2 kWh, respectively) by 11.2%, 13.3%, and 14.5%.

For a given cardinal direction (side 1 through side 4) and a short-wave solar absorption coefficient for the rooftop (0.88, 0.6, 0.4 and 0.2), Fig. 6 through Fig. 9 show that the order of the window cases starting from that resulting in the lowest energy load to that resulting in the highest energy load are as follows:

1. W1 (WWR = 10%, U-factor = 3.42 W/(m²K) and SHGC = 0.36).
2. W2 (WWR = 20%, U-factor = 3.38 W/(m²K) and SHGC = 0.254).
3. W5 (WWR = 50%, U-factor = 1.71 W/(m²K) and SHGC = 0.23).
4. W6 (WWR = 60%, U-factor = 1.71 W/(m²K) and SHGC = 0.23).
5. W3 (WWR = 30%, U-factor = 3.38 W/(m²K) and SHGC = 0.254).
6. W7 (WWR = 70%, U-factor = 1.71 W/(m²K) and SHGC = 0.23).
7. W4 (WWR = 40%, U-factor = 3.38 W/(m²K) and SHGC = 0.254).

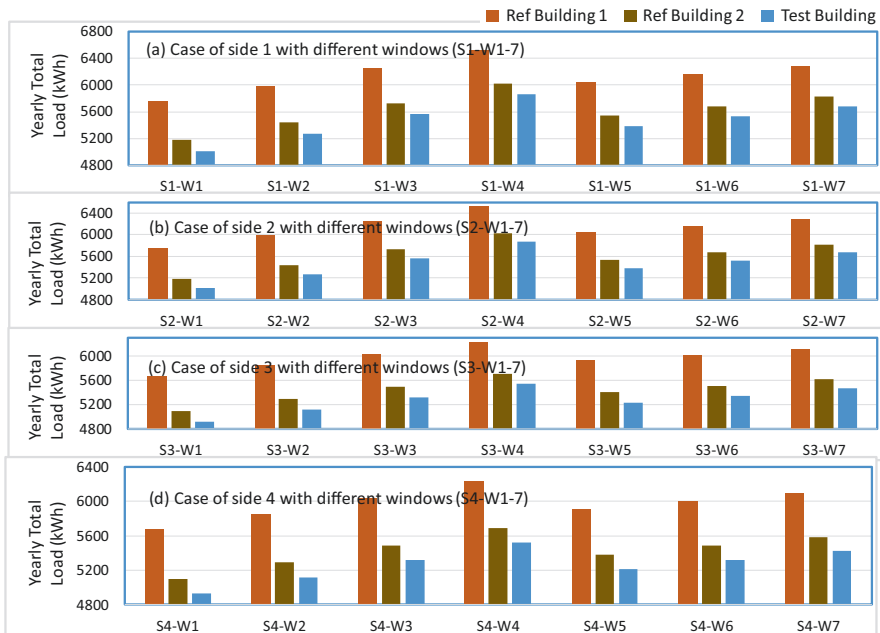


Fig. 9 Yearly total loads with PCM at an optimum melting temperature of 24°C and without PCM for the cases of windows located in (a) Side 1, (b) Side 2, (c) Side 3 and (d) Side 4 with roof having $\alpha_s = 0.2$

As shown in Figs. 6 through 9, for a given window case (W1 through W7, see Table 1) and a short-wave solar absorption coefficient for the rooftop, locating the window in the cardinal direction of side 4 has resulted in the lowest yearly total loads. Whereas, locating the window in the cardinal direction of side 2 has resulted in the highest yearly total loads. For example, for the window case W4 located in side 2 (i.e., S2-W4) in single-zone buildings having a roofing system with short-wave solar absorption coefficient of 0.88 (i.e., black/conventional roof), the yearly total loads for Ref Building 1, Ref Building 2 and Test Building were 7181.1 kWh, 6636.2 kWh and 6447.0 kWh, respectively, (Fig. 6b). Just only relocating the same window in side 4 (i.e., S4-W4) instead of side 2 has resulted in lower yearly total loads for Ref Building 1, Ref Building 2, and Test Building (6901.3 kWh, 6328.6 kWh, and 6122.3 kWh, respectively, Fig. 6d) by 4.1%, 4.9%, and 5.3%.

6.2 Effect of Short-Wave Solar Absorption Coefficient of the Roofing Systems on the Yearly Energy Loads

For a given cardinal direction of the window in single-zone buildings, decreasing the short-wave solar absorption coefficient of the roofing system has resulted in decreasing the energy loads. Also, for a given cardinal direction of the window, the

window cases W1 and W4, respectively, have resulted in the lowest and highest energy loads compared to the other window cases for different single-zone buildings. For example, for the window case S1-W1 in the Ref Building 1, decreasing the short-wave solar absorption coefficient from 0.88 to 0.2 (Fig. 9a) has resulted in decreasing the yearly total energy load by 12.3%. For the window case S1-W4 in the Ref Building 1, decreasing the short-wave solar absorption coefficient from 0.88 to 0.2 has resulted in decreasing the yearly total energy load by 10.1%.

Decreasing the short-wave solar absorption coefficient from 0.88 to 0.2 for the window case S1-W1 in the Ref Building 2 has resulted in decreasing the yearly total energy load by 13.0%. For the window case S1-W4 in the Ref Building 2, decreasing the short-wave solar absorption coefficient from 0.88 to 0.2 has resulted in decreasing the yearly total energy load by 10.2%. For the window case S1-W1 in the Test Building 2, decreasing the short-wave solar absorption coefficient from 0.88 to 0.2 has resulted in decreasing the yearly total energy load by 12.4%. For the window case S1-W4 in Test Building 2, decreasing the short-wave solar absorption coefficient from 0.88 to 0.2 has resulted in decreasing the yearly total energy load by 9.9%.

7 Comparison of Energy Performance of Reference Buildings with Test Building

For single-zone buildings, comparisons of the energy performance for reference buildings (Ref Building 1 and Ref Building 2) and the Test Building having PCM-drywall with melting temperature (T_m) of 24 °C (in which the energy loads are the lowest compared to other melting temperatures) are shown in Fig. 6 through Fig. 9 for yearly total loads. As indicated earlier, locating the windows in the cardinal direction of side 4 and side 2, respectively, have resulted in the lowest and highest energy loads.

For a given short-wave absorption coefficient for the roofing (α_s) and cardinal direction for the window, these figures clearly show that the energy performance for the Test Building are lower than that for Ref Building 1 and Ref Building 2. For example, for $\alpha_s = 0.88$ (i.e., black roof), the yearly total loads for Ref Building 1, Ref Building 2, and the Test Building for the window case S2-W1 (i.e., window W1 located in side 2) were, respectively, 6454.6 kWh, 5856.6 kWh, and 5636.8 kWh. Thus, the yearly total load for the Test Building were 14.5% and 3.9% lower than that for Ref Building 1 and Ref Building 2, respectively. By relocating the same window (i.e., W1) in side 4 instead of side 2 (i.e., window case S4-W1), the yearly total loads for Ref Building 1, Ref Building 2, and the Test Building were, respectively, 6376.0 kWh, 5771.4 kWh, and 5544.9 kWh; consequently, the yearly total load for the Test Building were 15.0% and 4.1% lower than that for Ref Building 1 and Ref Building 2, respectively.

For $\alpha_s = 0.88$, the yearly total loads for Ref Building 1, Ref Building 2, and the Test Building for the window case S2-W4 (i.e., window W4 located in side 2) were, respectively, 7181.1 kWh, 6636.2 kWh, and 6447.0 kWh. Thus, the yearly total load for the Test Building were 11.4% and 2.9% lower than that for Ref Building 1 and Ref Building 2, respectively. By relocating the same window (i.e., W4) in side 4 instead of side 2 (i.e., window case S4-W4), the yearly total loads for Ref Building 1, Ref Building 2, and the Test Building were, respectively, 6901.3 kWh, 6328.6 kWh, and 6122.3 kWh; consequently, the yearly total load for the Test Building were 12.7% and 3.4% lower than that for Ref Building 1 and Ref Building 2, respectively.

8 Summary and Conclusions

In this study, numerical simulations were conducted to investigate the potential energy savings as a result of using Phase Change Materials (PCMs) in the wall and roofing systems of single-zone buildings when these buildings were subjected to weather conditions of Kuwait. In accordance with the requirements of the Kuwaiti Building Energy Code, seven Window-to-Wall Ratios (WWRs) of the main solar-oriented window facade were considered in the study, where the ranges of WWR, U-factor, and SHGC were 10–70%, 1.71–3.42 W/(m²K), and 0.23–0.36, respectively. For the different wall systems considered in this study and located in the different cardinal orientations (side 1 through side 4), it was observed that the Optimum Test Wall having PCM-drywall with a melting temperature of 24 °C has the lowest yearly total energy loads compared to Ref Wall 1 (without drywall) and Ref Wall 2 (with drywall but without PCM). The results showed that the contributions to the yearly total loads for the Optimum Test Wall located in the different cardinal directions were, respectively, 17.6–23.6%, and 4.4–7.9% lower than that for Ref Wall 1 and Ref Wall 2.

When the windows were located in the four cardinal directions for single-zone buildings, the results showed that the window case of W1 (WWR = 10%, U-factor = 3.42 W/(m²K) and SHGC = 0.36) has resulted in the lowest yearly total loads. However, the window case of W4 (WWR = 40%, U-factor = 3.38 W/(m²K), and SHGC = 0.254) has resulted in the highest yearly total loads. Also, locating the window in the cardinal direction of side 4 has resulted in the lowest yearly total loads. Whereas, locating the window in the cardinal direction of side 2 has resulted in the highest yearly total loads. Using reflective materials with lower short-wave solar absorption coefficients in the roofing systems of different buildings (Ref Building 1, Ref Building 2, and Test Buildings) have resulted in a decrease in the yearly total energy loads for single-zone buildings. Finally, depending on the cardinal directions of the windows, the results showed that the total energy loads for the Test Building were up to 15% and 5% lower than that for Ref Building 1 and Ref Building 2, respectively.

References

1. Al-Homoud MS (2005) Performance characteristics and practical applications of common building thermal insulation materials. *J Build Environ* 40:353–366. <https://doi.org/10.1016/j.buildenv.2004.05.013>
2. Vrachopoulos MG, Koukou MK, Stavlas DG, Stamatopoulos VN, Gonidis AF, Kravvaritis ED (2012) Testing reflective insulation for improvement of buildings energy efficiency. *Cent Eur J Eng* 2(1):83–90. <https://doi.org/10.2478/s13531-011-0036-3>
3. European Commission, Green public procurement thermal insulation technical background report. Report for the European Commission – DG Environment by AEA, Harwell, Owner, Editor: European Commission, DG Environment-G2, B-1049, Brussels, 2010
4. AL Tayyar I (2015) Success program save energy in mew, internal presentation Kuwait Ministry of Energy and Water
5. Krarti M, Hajiah A (2011) Analysis of impact of daylight time savings on energy use of buildings in Kuwait. *Energy Policy* 39:2319–2329
6. Reinhart CF, Cerezo C, Jones N, Hajiah A, Al-Mumin A (2015) Kuwait 2030: A Blueprint for Managing Kuwait's Building-related Energy Needs. Presentation to the Kuwait Foundation for the Advancement of Sciences (KFAS), Kuwait, Dec 3, 2015
7. Ministry of Electricity and Water, Energy Conservation Program – Code of Practice, MEW, R-6, 2nd ed. (2010)
8. Alotaibi S (2011) Energy consumption in Kuwait: prospects and future approaches. *Energy Policy* 39:637–643
9. Al-Mumin A, Khattab O, Sridhar G (2003) Occupants' behavior and activity patterns influencing the energy consumption in the Kuwaiti residences. *Energy Buildings* 35:549–559
10. Al-ajmi FF, Hanby VI (2008) Simulation of energy consumption for Kuwaiti domestic buildings. *Energy Buildings* 40:1101–1109
11. Cabeza LF, Castell A, Barreneche C, de Gracia A, Fernández AI (2011) Materials used as PCM in thermal energy storage in buildings: a review. *Renew Sust Energ Rev* 15(3):1675–1695
12. Soares N, Costa JJ, Gaspar AR, Santos P (2013) Review of passive PCM latent heat thermal energy storage systems towards buildings' energy efficiency. *Energy Buildings* 59:82–103
13. Khudhair AM, Farid MM (2004) A review on energy conservation in building applications with thermal storage by latent heat using phase change materials. *Energy Convers Manag* 45(2):263–275
14. Zhang Y, Zhou G, Lin K, Zhang Q, Di H (2007) Application of latent heat thermal energy storage in buildings: state-of-the-art and outlook. *Build Environ* 42(6):2197–2209
15. Tyagi VV, Buddhi D (2007) PCM thermal storage in buildings: a state of art. *Renew Sust Energ Rev* 11(6):1146–1166
16. Zhu N, Ma Z, Wang S (2009) Dynamic characteristics and energy performance of buildings using phase change materials: a review. *Energy Convers Manag* 50(12):3169–3181
17. Sharma A, Tyagi VV, Chen CR, Buddhi D (2009) Review on thermal energy storage with phase change materials and applications. *Renew Sust Energ Rev* 13(2):318–345
18. Kuznik F, Virgone J, Noel J (2008) Optimization of a phase change material wallboard for building use. *Appl Therm Eng* 28(11–12):1291–1298
19. Kuznik F, Virgone J (2009) Experimental investigation of wallboard containing phase change material: data for validation of numerical modeling. *Energy Buildings* 41(5):561–570
20. David D, Kuznik F, Roux J-J (2011) Numerical study of the influence of the convective heat transfer on the dynamical behaviour of a phase change material wall. *Appl Therm Eng* 31(16):3117–3124
21. Baetens R, Jelle BP, Gustavsen A (2010) Phase change materials for building applications: a state-of-the-art review. *Energy Buildings* 42(9):1361–1368
22. Kuznik F, David D, Johannes K, Roux J-J (2011) A review on phase change materials integrated in building walls. *Renew Sust Energ Rev* 15(1):379–391

23. Osterman E, Tyagi VV, Butala V, Rahim NA, Stritih U (2012) Review of PCM based cooling technologies for buildings. *Energy Buildings* 49:37–49
24. Zhou D, Zhao CY, Tian Y (2012) Review on thermal energy storage with phase change materials (PCMs) in building applications. *Appl Energy* 92:593–605
25. Pomianowski M, Heiselberg P, Zhang Y (2013) Review of thermal energy storage technologies based on PCM application in buildings. *Energy Buildings* 67:56–69
26. de Gracia A, Cabeza LF (2015) Phase change materials and thermal energy storage for buildings. *Energy Buildings* 103:414–419
27. de Gracia A, Navarro L, Castell A, Cabeza LF (2015) Energy performance of a ventilated double skin facade with PCM under different climates. *Energy Buildings* 91:37–42
28. Soares N, Gaspar AR, Santos P, Costa JJ (2014) Multi-dimensional optimization of the incorporation of PCM-wallboards in lightweight steel-framed residential buildings in different climates. *Energy Buildings* 70:411–421
29. Saffari M, de Gracia A, Ushak S, Cabeza LF (2016) Economic impact of integrating PCM as passive system in buildings using Fanger comfort model. *Energy Buildings* 112:159–172
30. Kuznik F, Virgone J, Johannes K (2011) In-situ study of thermal comfort enhancement in a renovated building equipped with phase change material wallboard. *Renew Energy* 36(5):1458–1462
31. Mandilaras I, Stamatidou M, Katsourinis D, Zannis G, Founti M (2013) Experimental thermal characterization of a Mediterranean residential building with PCM gypsum board walls. *Build Environ* 61:93–103
32. Bludau C, Zirkelbach D, Kuenzel HM (2009) Condensation problems in cool roofs. *Interface J RCI XXVII(7)*:11–16
33. Bludau C, Künzel HM, Zirkelbach D (2010) Hygrothermal performance of flat roofs with construction moisture. In: Eleventh International Conference on Thermal Performance of the Exterior Envelopes of Whole Buildings (Buildings XI Conference), held in December 4–9; 2010. Clearwater, Florida, USA
34. Saber HH, Swinton MC, Kalinger P, Paroli RM (2012) Long-term hygrothermal performance of white and black roofs in North American climates. *J Build Environ* 50:141–154. <https://doi.org/10.1016/j.buildenv.2011.10.022>
35. Saber HH, Swinton MC, Kalinger P, Paroli RM (2011) “Hygrothermal simulations of cool reflective and conventional roofs”, 2011 NRCA International Roofing Symposium, Emerging Technologies and Roof System Performance, held in Sept. 7–9, 2011, Washington D.C., USA
36. Saber HH, Maref W, Hajiah AE (2019) Hygrothermal performance of cool roofs subjected to Saudi climates. *J Front Energy Res* 7(39):1–24. <https://doi.org/10.3389/fenrg.2019.00039>
37. Hajiah AE, Saber HH (2019) Long-term energy and moisture performance of reflective and non-reflective roofing systems with and without PCM under Kuwaiti climates. In: Gulf Conference on Sustainable Built Environment, GSBKW-2019, held in March, 10–13, 2019, Kuwait
38. Saber HH, Maref W (2015) Risk of condensation and mould growth in wood-frame wall systems with different exterior insulations. In: Building Enclosure Science & Technology Conference (BEST4 Conference), held in April 12–15, 2015, Kansas City, Missouri, USA
39. Saber HH, Maref W, Abdulghani K (2014) Properties and Position of Materials in the Building Envelope for Housing and Small Buildings, Report No. A1-004615.1, NRC-Construction, Ottawa, Canada, December 31 2014. <https://www.bchousing.org/research-centre/library/building-science-reports/building-envelope-for-housing&sortType=sortByDate>
40. Saber HH, Maref W, Lacasse MA, Swinton MC, Kumaran MK (2010) Benchmarking of hygrothermal model against measurements of drying of full-scale wall assemblies. In: International Conference on Building Envelope Systems and Technologies, ICBEST 2010, held in Vancouver, BC, June 27–30, 2010. pp 369–77
41. Saber HH, Maref W, Elmahdy AH, Swinton MC, Glazer R (2010) 3D thermal model for predicting the thermal resistances of spray polyurethane foam wall assemblies. In: Eleventh International Conference on thermal performance of the exterior envelopes of whole buildings (Buildings XI Conference), held in Dec 4–9; 2010. Clearwater, Florida, USA

42. Saber HH, Maref W, Elmahdy AH, Swinton MC, Glazer R (2012) 3D heat and air transport model for predicting the thermal resistances of insulated wall assemblies. *Int J Build Perform Simul* 5(2):75–91
43. Saber HH, Maref W, Armstrong M, Swinton MC, Rousseau MZ, Gnanamurugan G (2010), Benchmarking 3D thermal model against field measurement on the thermal response of an insulating concrete form (ICF) wall in cold climate. In: Eleventh International Conference on thermal performance of the exterior envelopes of whole buildings (Buildings XI Conference), held in Dec 4–9; 2010. Clearwater, Florida, USA
44. Saber HH, Swinton MC (2010) Determining through numerical modeling the effective thermal resistance of a foundation wall system with low emissivity material and furred-airspace. In: 2010 International Conference on building envelope systems and technologies, ICBEST 2010. British Columbia, Canada: Vancouver; June 27–30, 2010. pp 247–57
45. Saber HH, Maref W, Swinton MC, St-Onge C (2011) Thermal analysis of above-grade wall assembly with low emissivity materials and furred airspace. *J Build Environ* 46(7):403–414
46. Saber HH, Maref W, Swinton MC (2011) Numerical investigation of thermal response of basement wall systems with low emissivity material and furred airspace. In: 13th Canadian conference on building science and technology (13th CCBST) conference. Canada: Winnipeg; May 10–13, 2011
47. Saber HH, Maref W, Swinton MC (2012) Thermal response of basement wall systems with low emissivity material and furred airspace. *J Build Phys* 35(2):353–371
48. Maref W, Lacasse MA, and Booth DG (2004) Large-scale laboratory measurement and benchmarking of an advanced hygrothermal model. In: Proceeding of CIB 2004 Conference, May 2–7, 2004, Toronto, ON, pp. 1–10
49. Maref W, Booth DG, Lacasse MA, Nicholls M (2002) Drying experiment of wood-frame wall assemblies performed in the climatic chamber EEEF: specification of equipment used in eef-environmental exposure envelope facility. IRC Research Report, pp 1–42, October 18, 2002 (RR-105). <https://nrc-publications.canada.ca/eng/view/fulltext/?id=d0b86027-1114-4028-abe4-f1de489d2aa6>
50. Maref W, Lacasse MA (2009) Drying response of wood-frame construction: laboratory and modelling. *Journal of ASTM International (JAI)* 7(1). Second Symposium on Heat-Air-Moisture Transport: measurements and implications in buildings, Vancouver, BC. April 19, 2009, pp 1–12
51. Saber HH, Maref W, Hajiah AE (2019) Effective R-value of Enclosed reflective space for different building applications. *J Build Phys*. <https://doi.org/10.1177/1744259119880306>
52. ANSI/ASHRAE (2004) Standard 140-2004, Standard method of test for the evaluation of building energy analysis computer programs, GA: American Society of Heating, Refrigerating, and Air-Conditioning Engineers, Atlanta, 2004
53. Soares N, Christoph F, Reinhart CF, Hajiah A (2017) Simulation-based analysis of the use of PCM-wallboards to reduce cooling energy demand and peak-loads in low-rise residential heavyweight buildings in Kuwait. In: *Building Simulation*. Tsinghua University Press and Springer-Verlag, Berlin

Role of Green Buildings in Reduction of Energy Consumption



Mohamed F. Hamoda

1 Introduction

Residential housing construction is growing rapidly to cope with increasing population and progressing economy in many countries. In order to satisfy housing/building needs, the construction and housing sectors are increasing rapidly [1]. This is accompanied by increasing consumption of natural resources in general and energy in particular and calls for development of sustainable solutions. Buildings account for nearly 40% of total energy usage worldwide and up to 38% of global CO₂ emissions. Green buildings use 30% less energy than conventional buildings and research indicates that every US\$1 invested into energy efficiency avoids more than US\$2 in energy supply costs. Heating, ventilation, and air conditioning (HVAC) systems are the main energy consumers for buildings especially in warm climates [2]. According to USGBC, the current worldwide mix of energy resources is weighted heavily toward oil, coal, and natural gas. However, in addition to emitting greenhouse gases, these resources are also nonrenewable and their quantities are limited, or they cannot be replaced as fast as they are consumed. When it comes to energy use, buildings play a very large role since they approximately use 40% of the total energy used in the United States [3].

In the state of Kuwait, there has been increasing consideration toward enforcing environmental requirements and energy conservation. Kuwait is among the countries of high yearly energy consumption per capita with an average of 13,081 kW h/capita/year which is increasing at a rate of 8% annually, which also results in a high yearly CO₂ emissions per capita. Internal cooling is the largest part of energy consumption. Due to the hot climate in Kuwait, including dry areas, this aggressive climate uses air conditioning to cool buildings to a satisfactory level and provide comfort. Therefore, it is important to create solutions that reduce the energy

M. F. Hamoda (✉)

Department of Civil Engineering, Kuwait University, Kuwait, Kuwait

requirements of air conditioning, such as using effective insulation and using solar energy. On the other hand, the residential water consumption is also high in Kuwait and the per capita water consumption reached up to 475 L/capita/day in 2015 based on Kuwait Ministry of Electricity and Water yearbook [4]. Furthermore, sustainable housing can be defined as “that which effectively integrates low energy design with materials, which have minimal environmental or ecological impact (in manufacture, use and disposal) whilst maintaining social diversity” [5]. Conventional buildings use large amounts of energy, water, and raw materials [6]. Additionally, they generate large quantities of waste and emit harmful greenhouse emissions, such as CO₂, with a value that exceeds 400 ppm according to the National Oceanic and Atmospheric Administration (NOAA) [7]. According to the US Green Building Council [5], the percentages of consumption resulting from conventional buildings are 38% for CO₂ emissions, 13.6% for potable water, and 73% for electricity. On the other hand, the concept of green buildings has gained much attention in recent years. A green building is defined as one which uses less water, optimizes energy efficiency, conserves natural resources, generates less waste, and provides healthier spaces for occupants, as compared to a conventional building [5]. In essence, it is an environment-friendly building that is built and operated to satisfy the goals of energy efficiency, water conservation, material efficiency, indoor air quality, waste management, and reduced environmental impact.

This study examined, in a simplified way, the main features and energy savings of a new residential development in Kuwait consisting of 12 luxury villas with a modern avant-garde design, luxury qualities, and exceptional finishing to satisfy the LEED (Leadership in Energy and Environmental Design) certification. Each villa occupies 500 m² of land and has four bedrooms and four bathrooms. The study is intended to present a simple and accessible tool to motivate construction engineers and builders about the different merits of green buildings and seeks to push for sustainability. Cost estimates are not included since cost figures vary according to place.

2 Methodology

The building considered in this study is a private villa under construction, in a project of 12 villas (Fig. 1). The villa satisfies the Kuwaiti housing demands of a large living hall, multiple bedrooms, bathrooms kitchen, garage, and a surrounding garden. It is designed to accommodate a family of six persons, as a basis for determining water consumption and waste generation quantities. For energy calculations, the main focus is in lowering operational energy by:

1. Installation of solar panels
2. Better thermal insulation
3. Energy-efficient HVAC machinery
4. Utilization of naturally occurring light



Fig. 1 View of the studied villa

Table 1 Outdoor and indoor design conditions [8]

Parameter	Summer (°C)		Winter (°C)	
	Outdoor	Indoor	Outdoor	Indoor
DBT	46.2	23.9	10	18.3
WBT	24.0	17.0	5	11.6
RH	60%	50%	40%	30%

To calculate the peak cooling demand, the annual cooling, and electrical energy requirements, it is essential to generate hourly data profiles for parameters that have significant on the hour-to-hour cooling demand of the building. These parameters are the dry-bulb temperature (DBT), wet-bulb temperature (WBT), wind speed, and global solar radiation according to the guidelines set by the Ministry of Electricity and Water in Kuwait [8].

Kuwait meteorological data over the past several years show an appreciable difference between weather conditions in the interior hot and dry regions and the coastal hot and humid regions, particularly in the summer season. Moreover, there are different sets of outdoor and indoor design conditions. The villa under study is built in interior zone of Kuwait, and the outdoor and indoor design conditions are presented in Table 1 [8].

3 Results and Discussion

3.1 Energy Efficiency

The main elements include (1) PV (photovoltaic) solar energy system, (2) HVAC system, and (3) lighting.

3.1.1 PV Solar System

After calculating an assumed power consumption, it was determined that each villa will need 14 modules in which each is 6 kW PV module. The solar PV system is illustrated in Fig. 2.

Solar photovoltaic system sizing (Table 2):

1. Determining power consumption
2. Sizing the PV panels
3. Inverter sizing
4. Battery sizing
5. Solar charge controller sizing

The PV type selected is monocrystalline silicon PV, which is made from high-quality silicon cells to convert the largest amount of solar energy into electricity.

This type has a high durability and long lifespan, with an efficiency of 18.3%. The panels are provided with a self-cleaning mechanism to remove dust since dust storms frequently occur in Kuwait. This project shows how we can generate energy (renewable energy source) through solar panels to provide the electricity needed for the building. Excess energy will be generated in the summer month which could be supplied to the city network for revenue.

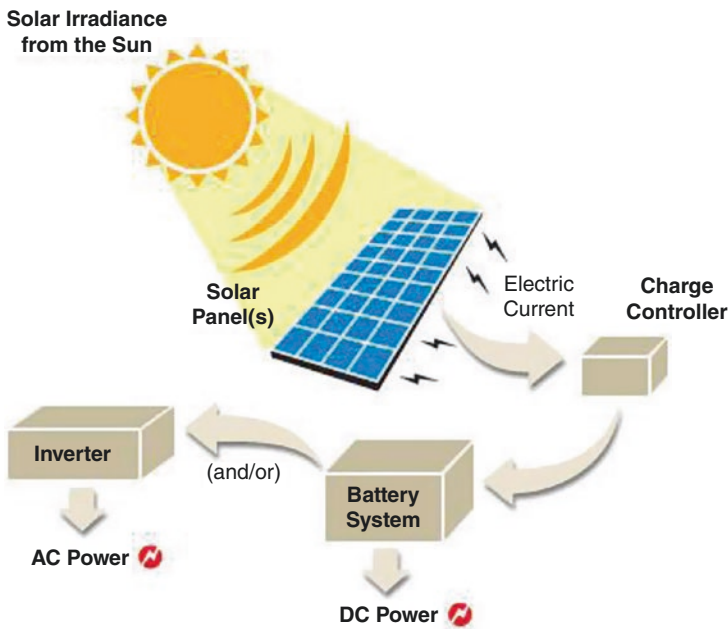


Fig. 2 PV energy supply system

Table 2 Power requirements and PV system calculations

The system will be powered by PV module with:		12 Vdc	
		320 Wp	
Appliances	Quantity	Watts	Q*Watt
Fridge	1	80	80
Oven	1	3000	3000
Microwave	1	1000	1000
Electric Kettle	1	2200	2200
Toaster	1	800	800
Television	3	150	450
Steam iron	1	2100	2100
Clothes Washer	1	1800	1800
Clothes Dryer	1	1000	1000
LED lights	40	8	320
chandelier	2	300	600
Air conditioner	3 tons	3500	3500
Laptop	3	20	60
mobile phone charger	6	4	24
Vacuum Cleaner	1	200	200
Ventilator Fan	2	18	36
Sum			17170
total PV panels energy needed (Total Wh/day * 1.3		103788 * 1.3 =	
total Wp of PV panel capacity needed =		134924.4 / 3.4 =	
number of PV paneeles needed =		39683.6 / 320 =	
So this system should at least powered by		125	modu
		320	Wp PV n
inverter Sizing			
total Wof all appliances =	17170 * 1.25 =	21462.5	Watt
the inverter size (watt) > or =		21463	
Battery sizing			
Nominal battery voltage(V) =	12		
Days of autonomy =	3		
Battery capacity =	(103788*3)/(0.85*0.6*12)		
Total Ampere-hours required (Ah) =	50876.471		

PV module specification:

$P_m = 320 \text{ Wp}$

$V_m = 36 \text{ Vdc}$

$I_m = 8.89 \text{ A}$

$V_{oc} = 45 \text{ A}$

$I_{sc} = 9.6 \text{ A}$

Nominal battery voltage = 12 V

Days of autonomy = 3 days

Battery capacity = 50,877 A h

3.1.2 HVAC System

The HVAC system was divided into zones and the HAP 5.01 program was used in calculations. For each zone, all HAP inputs for each area and the space properties were determined based on ASHRAE (American Society of Heating, Refrigeration and Air Conditioning Engineers) guidelines. The total annual HVAC cooling loads as calculated show cost savings of about 30%.

Air conditioning is vital to buildings in Kuwait for the long summer season in Kuwait with warm to hot weather prevailing for almost 9 months, whereas heating may be needed over a 3-month period. On the other hand, it is important to have periodic ventilation to maintain good indoor air quality and that vents and ducts for bathrooms and kitchens should be separated. In order to calculate air conditioning cooling load for the purpose of sizing A/C equipment, the thermal mass of the building envelop, the hourly outdoor temperature, solar radiation, and other weather parameters were assumed and an energy simulation program was used. An excel sheet was formatted to determine power requirements and make PV system calculations. Meanwhile, in order to determine the HVAC cooling loads in the building, the Hourly Analysis Program (HAP 5.01) was used based on ASHRAE. This software simulates energy use, designs the HVAC system, and computes the operating costs.

3.1.3 Lighting

For LED light bulbs required (depending on the area of each room), Table 3 presents the details depending on the area and function of each room, to which other areas (e.g. halls, corridors, etc.) are added to estimate the total power demand for lighting. In addition, the design includes use of sensors and control devices to have optimal use of lighting in the villa and reduce consumption of electricity.

3.1.4 Insulation

The most common locations for insulation in a building are exterior walls, unfinished attic and basement spaces, and floors above exposed spaces (e.g. above garages). Closed-cell spray polyurethane foam (SPF) insulation systems are self-adhering, two-component products that are spray-applied on site. The material is a rigid insulation system. The recommended insulation is presented in Table 4.

Air leakage occurs when outside air enters and conditioned air leaves the house, this will cause trouble with the indoor air quality when it comes to moisture levels, and having small particles inside the building such as dust, these particles can cause allergic reactions to people with asthma (Fig. 3).

The climate in Kuwait is considered to be hot and humid, which brings the need of having dehumidifiers in the villa. The recommended device to be is called Keystone KSTAD70B as shown in Fig. 4. It is energy efficient, has an above-normal

Table 3 LED (light-emitting diode) light bulb requirements

Room type	Area (m ²)	Number of LED 8 W lighting
Bedroom 1	12	4
Bedroom 2	20	6
Living room	25	10
Kitchen	6	2
Bathroom	4	2

Table 4 Recommended insulation system

Type of insulation	Application on	Advantage
White bricks	Exterior walls	Heat and fire insulation—reduces the usage of AC by isolating heat
Sprayed foam	Interior walls	Insulation for irregular shaped areas—waterproof—soundproof
Low-E coating windows	Windows	Reflects heat only passes light

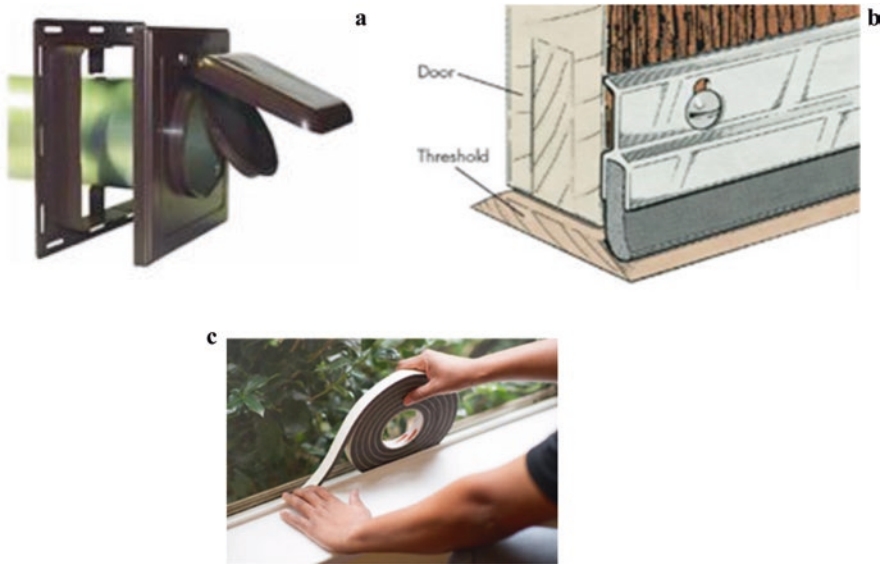


Fig. 3 Control of air leakage. (a) Cover for kitchen exhaust fan. (b) Sealing gasket for doors. (c) Sealing strips for windows

Fig. 4 Keystone KSTAD70B dehumidifier



moisture removal rate, and is the most quiet. Installation of double-glass, low-e windows, and proper shading are considered. Furthermore, greenery and use of in-house plantation is of particular importance in improving indoor air quality.

3.2 Water Efficiency

Water consumption depends on indoor and outdoor usage. The highest indoor water usage is in kitchens and bathrooms, while the outdoor water usage is landscape irrigation. High water consumption is also accompanied by generation of large quantities of wastewater to be collected and properly treated in order to protect the environment and public health.

3.2.1 Reduction of Water Consumption

This could be achieved through utilization of water saving fixtures such as infrared taps, shower heads with aerators, and toilet flushing tanks as presented in Table 5. One important fixture is the infrared tap (Fig. 5), which, if compared with normal conventional taps, not only saves about 50% of water used but also about 15% of energy used to produce and convey the treated water [4]. This, in turn, will result in up to 60% in long-term cost savings.

3.2.2 Greywater Recycling

Greywater may be defined as gently used water from bathroom sinks, showers, tubs, and washing machines. It is not water that has come into contact with faeces, urine, and organic wastes in toilets and urinals which is known as blackwater. It makes up

Table 5 Water saving fixtures

Fixture	Percentage water saved (%)	Where it is used	Amount of water used per year (L) (standard)	Amount of water saved per year (L)
Shower aerator	55	7 bathroom sinks, 1 kitchen sink	90,000	49,500
Infrared sensor taps	70	7 bathroom sinks, 1 kitchen sink	49,500	34,650
e-Shower heads	70	5 showers	270,000	189,000
Evadrop	70	5 showers	189,000	132,300
Edyn smart gardening	40	Indoor and outdoor gardens	80,000	32,000
Flushing	37	5 toilets	130,000	48,100

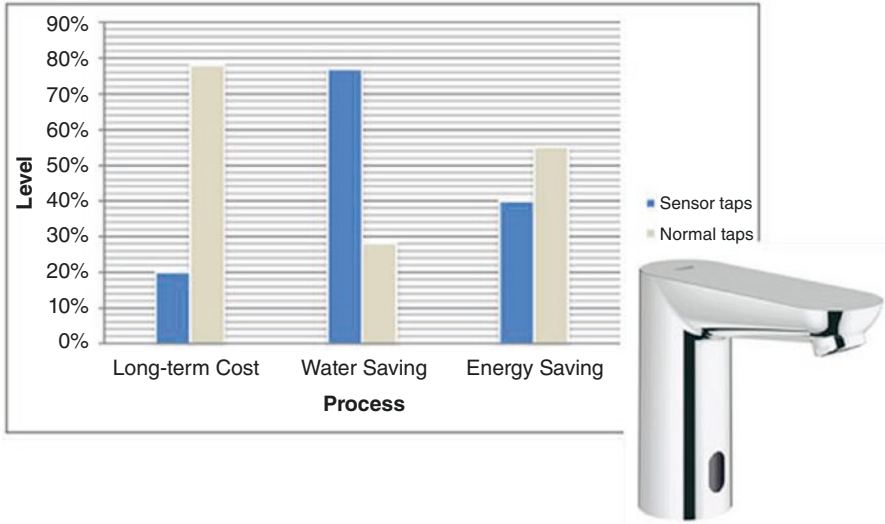


Fig. 5 Potential savings from use of infrared taps

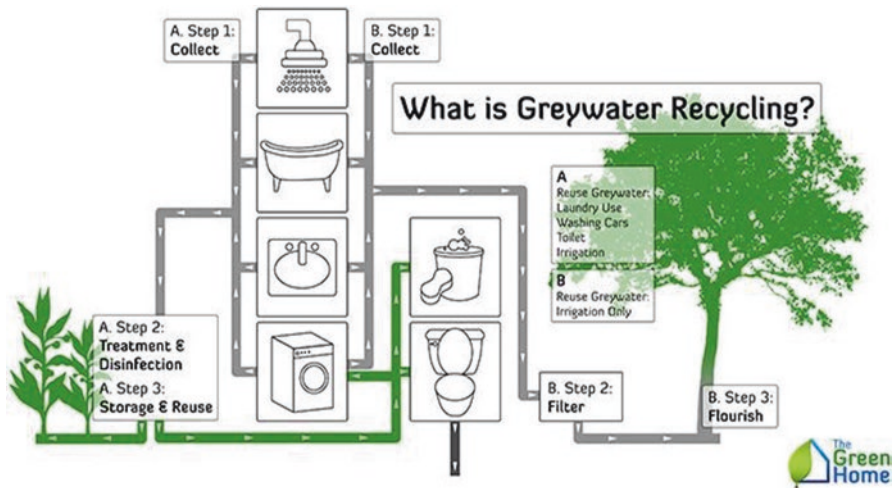


Fig. 6 Greywater recycling steps (adapted from Green Home)

about 65% of the total wastewater produced by the household and may be a good source of water for reuse for toilet flushing and landscaping. Greywater is collected and treated by filtration to remove traces of dirt, food, grease, hair, and certain household cleaning products (Fig. 6). According to USGBC, the use of greywater for toilet flushing, landscaping, and car washing saves up to 30% of residential water use [5].

3.3 Solid Waste Management

Solid waste management in green buildings is an important issue especially in Kuwait where the waste generation rate per person is high and studies show an average rate of 1.5 kg/person/day [9]. Waste separation at home is essential for waste recycling, thus food, paper, metals. Table 6 presents the energy savings from material recycling of residential solid waste where specialized companies in each component exist in Kuwait. The food component of residential solid waste in Kuwait being 55% is the highest, whereas the paper component is about 15% and other recyclable materials range from 5% to 10% [9]. On this basis and information presented in Table 6, it is estimated that, on the average, material recycling will result in an indirect energy savings of 12%.

3.4 Energy Simulation

Analysis of energy efficiency measures were conducted using the software EnergyPlus [10–12] which is the most authoritative and has been extensively used and validated by research community. It has several user interface add-ons (with Design Builder being one). It is essentially the accumulation of 60 years of experience by US department of energy. Others also exist that might suit this application but the EnergyPlus program is the most authoritative and has been extensively used and validated by research community.

The program has three main components, namely, a simulation manager, a heat balance simulation module, and a building system's simulation module. Many assumptions were made for input data. The simulation assumptions for materials are summarized in Table 7. The other major data input is weather. The data files were easily read as spreadsheets. All assumptions made according to MEW [8] and ASHRAE [13] codes. The building energy was simulated using EnergyPlus for the purpose of checking the design considering the mass of the building envelop, the outdoor temperatures, solar radiation, and other weather parameters [8].

The assessment of building cooling loads and demands was the first step that carried in the building energy simulation analysis. For each thermal zone, the calculation procedure started from the analysis of the related heat flows which depend on

Table 6 Energy savings from material recycling of residential solid waste

Material	Energy saving (%)
Aluminium	95
Cardboard	24
Glass	5–30
Paper	50
Plastic	70
Steel	60

Table 7 Thermal properties of the materials used in the building

Material	Materials conductivity (W/m K)	Density (kg/m ³)	Specific heat (J/kg K)
Concrete block	0.51	1400	1000
Concrete slab	1.13	1400	1000
Brick	0.56	1200	900
Wood flooring	0.14	650	1200
Foam insulation	0.04	10	1400
Roof	1.08	1200	900
Glass	1.06	2500	750

heat conduction through walls, internal and external convection and radiation, sun radiation transmission through fenestration, and heat gains due to building equipment and occupants and ventilation. The cooling indoor air set point temperature is 24 °C which is continually kept by the HVAC system.

The EnergyPlus building system-simulation module, with a variable time step, calculates heating and cooling system and plant and electrical system response [12]. This integrated solution provides more accurate space temperature prediction crucial for system and plant sizing, occupant comfort, and occupant health calculations. Integrated simulation also allowed to evaluate realistic system controls, moisture adsorption and desorption in building elements, radiant heating and cooling systems, and inter-zone air flow. HVAC equipment templates specified a common HVAC subsystem loop air, chilled water, hot water, or refrigeration. Templates for the eight LEED baseline systems were included.

3.5 Total Energy Savings

Based on the data presented in this study and the design of the green building, a total of 40% of direct energy savings (through energy conservation) and about 25% of indirect energy savings (through water conservation and solid waste recycling) are expected in a villa of 500 m² of total area. This is accompanied by reduction in CO₂ emissions as a greenhouse gas contributing to global warming, since for each kWh saved, 7.07 × 10⁻⁴ MT (metric tons) of CO₂ emissions is prevented. Meanwhile, in terms of cost savings associated with reduction in demand on electricity, it is not an easy task to determine such cost savings since the subsidized price of electricity and government financial support in Kuwait has a very large impact on the cost per house. Meanwhile, according to MacNaughton et al. [14], using Harvard Co-BE calculator and applying the social cost of carbon and the social cost of atmospheric release to translate these reductions into health benefits, LEED-certified buildings in the United States, Germany, India, China, Turkey, and Brazil have already saved \$7.5 B in energy costs and averted 33 MT of CO₂, from entering the atmosphere, which amounts to \$5.8 B in the year 2016. It also prevented between 172 and 405

premature deaths in the United States. However, adoption of the greenhouse approach is not limited to cost savings in energy but rather to maintain a high indoor air quality and healthy living environment for inhabitants of a green building.

4 Conclusions

1. The selected PV type was monocrystalline silicon PV, which is made from highly ordered silicon cells, proved to be effective. This PV type converts the largest amount of solar energy into electricity and is suitable for limited space areas. It has a long lifespan and a high level of durability. Each panel has 300 W power, with an efficiency of 18.3%.
2. In terms of lighting, the saving percentages for energy consumption per day and the annual cost were approximately 86% and 54%, respectively. These percentages were the result of replacing normal lights with LED lights, including timers and sensors.
3. For the HVAC design, the HAP simulation for the green buildings, with respect to the conventional buildings, indicates a reduction in the HVAC cooling load by 25%. This reduction is the result of using high-quality EcoBuild insulation and double-glass low-e windows filled with argon. Moreover, an environmentally efficient duct that contains 80% recyclable glass was installed.
4. By using low-flow water units (i.e. showerheads and kitchen and lavatory tap aerators), the total house water consumption was reduced by 30%. Additionally, by recycling greywater for irrigation, washing cars, cleaning courtyards, and flushing toilets, the water consumption was reduced by 16%. Thus, the overall water savings, in terms of consumption and bill cost, were 46%.
5. A total of 40% of direct energy savings (through energy conservation) and about 25% of indirect energy savings (through water conservation and solid waste recycling) are obtained in a villa of total area of 500 m². This is accompanied by reduction in CO₂ emissions as a GHG contributing to global warming.

Acknowledgments The author would like to thank his students Ms. Basma Al-Sabah and Ms. Noor Al-Kandari in the course Sustainability and Green Engineering, in the Civil Engineering Department, Kuwait University. Their assistance is very much appreciated.

References

1. Baldwin AN, Loveday DL, Li B, Murray M, Yu W (2018) A research agenda for the retrofitting of residential buildings in China—a case study. *Energy Policy* 113:41–51
2. Fasiuddin M, Budaiwi IM (2011) HVAC system strategies for energy conservation in commercial buildings in Saudi Arabia. *Energ Buildings* 43(12):3457
3. Holmes S (2017) How LEED saves energy, LEED v4 energy saving. US Green Building Council, Washington, DC

4. MEW (2015) Statistical yearbook: electrical energy. Ministry of Electricity and Water, Kuwait
5. USGBC (2016) Benefits of green building. U.S. Green Building Council, Washington, DC
6. Franzoni E, Volpi L, Bonoli A, Spinelli R, Gabrielli R (2018) The environmental impact of cleaning materials and technologies in heritage buildings conservation. *Energy Buildings* 165:92–105
7. ESRL (2018) What is the global greenhouse gas reference network? Global Monitoring Division, Earth System Research Laboratory, Boulder, CO. Available from <https://www.esrl.noaa.gov/gmd/ccgg/about.html>
8. MEW (2018) Energy conservation code for buildings. MEW/R-6/2018. Ministry of Electricity and Water, Kuwait
9. Hamoda MF (2017) Management of discarded produce from supermarkets and hypermarkets. *Int J Environ Waste Manag* 20(3):264–282
10. Basarkar M, Pang X, Wang L, Haves P, Hong T (2011) Modeling and simulation of HVAC Results in EnergyPlus. Lawrence Berkeley National Laboratory, Berkeley, CA
11. Crawley DB, Lawrie LK, Winkelmann FC, Buhl WF, Huang YJ, Pederson CO, Strand RK, Liesen RJ, Fisher DE, Witte MJ, Glazer J (2001) EnergyPlus: creating a new-generation building energy simulation program. *Energy Buildings* 33:319–331
12. See R, Haves P, Sreekanthan P, O'Donnell J, Basarkar M, Settlemyre K (2011) Development of a user interface for the ENERGYPLUS whole building energy simulation program. In: Proceedings of 12th Conference of International Building Performance Simulation Association, Sydney, Australia, 14–16 November, 2011, pp 2919–2926
13. ASHRAE (2018) Energy-efficient design of low-rise residential buildings. Standard ANSI/ASHRAE/IES Standard 90.2-2018. The American Society of Heating, Refrigerating and Air-Conditioning Engineers, Atlanta, GA
14. MacNaughton P, Cao X, Buonocore J, Cedeno-Laurent J, Spengler J, Bernstein A, Allen J (2018) Energy savings, emission reductions, and health co-benefits of the green building movement. *J Expo Sci Environ Epidemiol* 28:307. 12 pages

Long-Term Energy and Moisture Performance of Reflective and Non-reflective Roofing Systems with and Without Phase Change Materials Under Kuwaiti Climates



Ali E. Hajiah and Hamed H. Saber

1 Introduction

This paper mainly focuses on the performance of only one part of the building envelope, which is the roofing system with and without Phase Change Materials (PCMs). Many investigators [1–16] have shown that green and reflective roofs can save energy, mitigate urban heat islands, slow global warming by decreasing greenhouse gas emissions, and reduce local air pollution while increasing thermal comfort. The effects of globally installing white roofs were assessed using an urban canyon model coupled to a global climate model [11]. The results of that study showed that the annual mean heat island decreased by 33%, and the urban daily maximum temperature decreased by 0.6 °C and daily minimum temperature by 0.3 °C.

Roofing systems with potential energy savings and low risk of moisture-related problems can help reduce the energy requirements for operating buildings, thereby reducing operating costs and contributing to the fight against global warming [17–19]. In order to enhance the roof's contribution to environmental requirements, “green” roofing has evolved into one of two categories: highly reflective or “cool” roof systems and vegetative roof systems. Bentz [19] presented a practical decision-making process for selection and design of a sustainable or green, reroofing system. In that study, the author considered various assemblies currently available in the markets, compared the advantages and disadvantages of each, and illustrated

A. E. Hajiah (✉)

Research Scientist, Energy and Building Research Center, Kuwait Institute for Scientific Research, Shuwaikh, Safat, Kuwait
e-mail: ahajiah@kisir.edu.kw

H. H. Saber

Jubail University College, Royal Commission of Jubail and Yanbu,
Jubail Industrial City, Kingdom of Saudi Arabia
e-mail: saberh@ucj.edu.sa

© Springer Nature Switzerland AG 2020

A. Bumajdad et al. (eds.), *Gulf Conference on Sustainable Built Environment*,
https://doi.org/10.1007/978-3-030-39734-0_26

453

which assemblies meet cool roofing and vegetative roofing guidelines. That study also offered a good understanding of “green” roof options that is viable to reroofing [19].

For reflective roofs, the DOE-2 building energy simulation program was used to investigate the impact of roof reflectivity on the cooling and heating energy use for buildings in the USA [20]. That study showed that the estimated annual electricity savings was about 10.0 TW h with a net savings of about \$750 M in annual energy payments, and the peak electricity power reduction was about 7 GW. In support of inclusion of reflective roofs in the proposed ASHRAE standard SSPC 90.2, simulation results including the annual electricity and fuel use for a prototypical single-family one-storey house indicated that increasing the roof reflectivity from 20% to 60% is worth over half of the roof insulation in hot climates [21]. Recently, Levinson and Akbari [22] conducted energy simulations (no moisture transport was accounted for) to determine the annual heating and cooling energy uses of four commercial building prototypes in 236 US cities. Those simulations were conducted by substituting a cool roof with solar reflectivity of 0.55 (solar absorptivity of 0.45) and for a conventional grey roof with solar reflectivity of 0.20 (solar absorptivity of 0.8). The results showed that using cool roofs resulted in annually energy cost saving per unit conditioned roof area ranging from \$0.126/m² in West Virginia to \$1.14/m² in Arizona (\$0.356/m² nationwide).

Ray and Glicksman [12] developed a thermal model which was used to assess the energy savings of cool and green roofs. Their results showed that the potential energy savings are highly sensitive to roof type, climate, and amount of insulation. For example, for a one-storey building in Boston with a modified-bitumen roof and 2.7 m² K/W (15.3 ft² °F h/BTU) roof insulation, 13% in cooling and heating energy can be saved by doubling the insulation, whereas 12% can be saved if a green roof is installed instead. In Lisbon, however, the same additional amount of roof insulation on the same building resulted in approximately no energy savings, while the installation of a green roof results in a 26% reduction in energy use [12].

It is important to design roofing systems that can simultaneously lead to energy savings and a low risk of moisture-related problems. Moisture accumulation, over time, can damage some roofing materials and reduce the effective thermal resistance of the roofing system, resulting in higher energy costs and a shortened service life of the roofing system. Normally, short-wave solar radiation can dry out the roofing system during the daytime and summer. The amount of short-wave energy absorbed by the roof depends on the reflectivity of its surface. Thus, solar reflectivity is the significant characteristic for selecting cool roof coating [23]. Because cool (white) roofs have low short-wave solar absorption coefficients, they maintain lower temperatures than dark (black) roofs, and so they may provide less heat to dry out moisture. This may cause cool roofs built in cold climate locations to be more susceptible to moisture accumulation [13]. This phenomenon has been observed in both cool and dark roofs in cold climates [14].

Ennis and Kehrer [24] investigated the effect of roof membrane colour on moisture accumulation in low-slope commercial roof systems. That study focused on mechanically attached, highly reflective, single-ply roof systems with black and white TPO/PVC membrane, installed on low-slope (less than 2:12) structures in cold climates. Hygrothermal simulations were conducted for the climates of Boston, Albany, Chicago, Cleveland, and Detroit for a period of 1 year. In that study, a short-wave solar absorption coefficient of 0.3 and 0.9 was considered for the white roof and black roof, respectively. A vapour permeance for metal deck of 0.75 perms was used to account for leakage due to screws. The simulation results showed that all roofs accumulate moisture underneath the exterior TPO/PVC membrane during the winter and dried out completely in the summer. Also, it was observed that the amount of accumulated moisture for white roofs in winter was more than twice the amount for black roofs due to less solar energy gain needed for the dry-out process [24].

Bludau et al. [25] conducted hygrothermal simulations to investigate moisture build-up in white and black roofs under different climatic conditions (Phoenix, AZ; Chicago, IL; Anchorage, AK; and Holzkirchen, Germany). The simulations were conducted for a period of 5 years with short-wave solar absorption coefficients of 0.88 for black roofs and 0.2 for white roofs. That study showed that black roofs always run with lower moisture compared to white roofs. In the case of roofing system with initial construction moisture, Bludau et al. [26] investigated the hygrothermal performance of dark, bright, and shaded flat roofs where 2 L/m² of water was added before the roof was sealed from above. In that study, a short-wave solar absorption coefficient of 0.9 was considered for the dark roof. For the white roof, a measured short-wave solar absorption coefficient of 0.2 was considered. The dark roofs showed the largest surface temperature and humidity fluctuations, including comparatively high heat fluxes during summer. The surface temperature and drying potential were low in roofs with bright and shaded surfaces. Additionally, roofs with bright surface showed even lower temperatures and also smaller drying potential than roofs with shaded surface.

Saber et al. [27, 28] conducted hygrothermal simulations to investigate the moisture accumulation over time as well as energy use of white and black Modified-Bitumen (MOD-BIT) roofing systems when these roofs were subjected to different outdoor climates of North America with different heating degree days, namely, Toronto (ON), Montreal (QC), St John's (NL), Saskatoon (SK), Seattle (WA), Wilmington (AZ), and Phoenix (AZ). Results showed that black roofs always perform with lower moisture than white roofs. For the outdoor climates of St John's and Saskatoon, the black roofs have no risk of moisture damage. In these locations, the simulations suggest that the white roofs could lead to longer-term moisture-related problems. For the outdoor climates of Toronto, Montreal, Seattle, Wilmington, and Phoenix, the simulation results showed that the white roofs have a low risk of experiencing moisture damage. The yearly heating loads of the white roof were slightly higher than that of the black roof. Conversely, the yearly cooling loads of the black roof were much higher than that of the white roof. Thus, buildings with white roofs in these locations are predicted to result in a net yearly energy savings compared to buildings with black roofs.

2 Objectives

The main objectives of this task study are to:

- (a) Predict the long-term energy and moisture performance of black roofing systems with and without PCM-drywalls when these roofing systems are subjected to the weather conditions of Kuwait.
- (b) Repeat (a) above for white roofing systems with and without PCM-drywalls and having different values of the short-wave solar absorption coefficients ranging from 0.2 to 0.6.
- (c) Use the results obtained in (a) and (b) above to determine the potential energy savings as result of using PCM-drywalls in white roofing systems with low risk of moisture accumulations as compared to black roofing systems.

3 Approach, Numerical Model, and Simulation Parameters

A previously developed and extensively validated numerical model is used in this study to assess the performance of the roofing systems with and without PCMs. The model simultaneously solves the highly coupled heat, air, and moisture (HAM) transport equations in building envelope [29–39]. These equations are discretized using the finite element method (FEM). Most recently, this model was validated by comparing its predictions with the test data of full-scale test assemblies [37, 38]. Thereafter, the model was used to assess the energy and long-term moisture performance of white and black roofs when these roofs were subjected to the climatic conditions of the Eastern Province of Saudi Arabia (more details are available in [37]). In addition, as provided in [39], the model was validated in several applications that are related to building components and assemblies that contain enclosed airspaces such as wall and roofing systems with reflective insulations and fenestration systems such as double glazing windows, curtain walls, and skylight devices. The model predictions were also in good agreements with test data (see [39] for more details).

As indicated earlier, white roofing systems use bright surfaces to reflect a significant portion of the incident short-wave solar radiation, which lowers the surface temperature compared to black roofing systems. As well, buildings with white roofing systems in hot climates (e.g. see [27, 28]) resulted in a net yearly energy savings compared to buildings with black roofing systems. With and without PCM, the questions are as follows: (a) Do white roofing systems lead to moisture-related problems in Kuwaiti climates? and (b) What are the amount of energy savings as result of using white roofing systems instead of black roofing systems? To answer these questions, numerical simulations were conducted for roofing systems shown in Fig. 1 in order to assess and compare the energy and hygrothermal performance of white and black roofing systems with and without PCM-drywall.

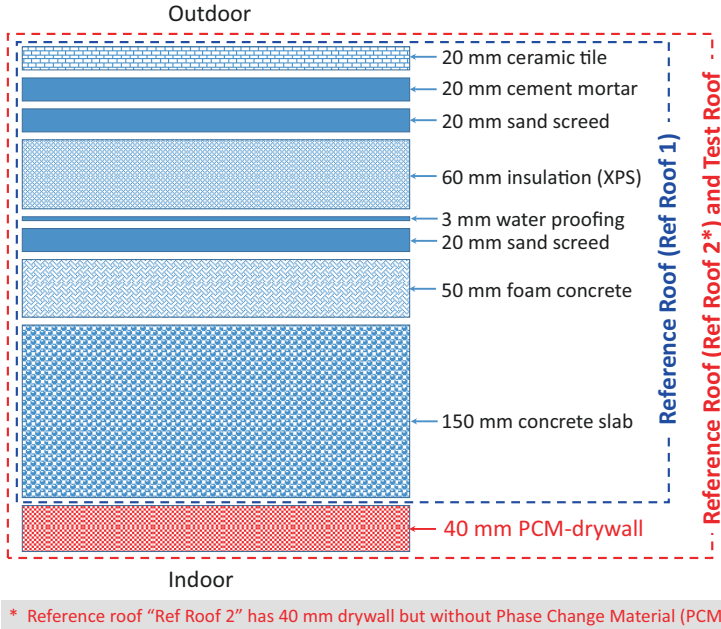


Fig. 1 Schematics of the reference and test roofing systems

Figure 1 provides a description of three roofing systems. The reference roofing system called in this paper “Ref Roof 1” consists of a number of layers, namely, ceramic tile (20 mm thick), cement mortar (20 mm thick), sand screed (20 mm thick), XPS thermal insulation (60 mm thick), water proofing (3 mm thick), another sand screed (20 mm thick), foam concrete (50 mm thick), and concrete slab (150 mm thick). The test roofing system, called “Test Roof”, is similar to Ref Roof 1 but includes an additional layer which is PCM-drywall (40 mm thick). However, to quantify the contribution of having PCM in the drywall on the energy performance, another reference roofing system, called “Ref Roof 2”, is considered in this paper, which is identical to the Test Roof but with drywall only (i.e. without PCM).

3.1 Indoor and Outdoor Conditions

The indoor relative humidity (RH) values that were used in this study are based on the simple method of ASHRAE 160 [40] (40% RH in winter and 70% in summer). The indoor air temperature was assumed constant during the whole year by considering indoor set-point temperature of 24 °C. For the outdoor conditions, all roofing systems provided in Fig. 1 were subjected to the weather conditions of Kuwait city.

3.2 Initial Conditions and Simulation Period

Conducting hygrothermal simulation for a roofing system, subjected to a climatic condition, requires knowing the initial conditions (i.e. at time = 0) for both the temperature and moisture content distributions inside the roofing system. Normally, these initial conditions are not known and hence should be assumed [4, 6, 25–28]. In this study, for each roofing system, time = 0.0 corresponded to January 1st at 00.00 at which the initial temperature in all material layers was assumed equal 10 °C. Also, the initial moisture content in all material layers was assumed to correspond to 50% RH [27, 28].

To predict the long-term hygrothermal performance of each roofing system, the numerical simulations were conducted for a long time period which was five (5) years. In case of the moisture accumulation continues to increase over time after 5 years, the period of simulation was extended so as to predict the long-term performance of the roofing systems. Because the initial conditions were assumed as indicated above, the first year in the simulation period was used as a conditioning year for the roofing system. As such, the energy and moisture performance of the roofing system with and without PCM was assessed from the results of the simulation period after excluding the results of the first year [27, 28].

3.3 Material Properties

The hygrothermal properties (e.g. air permeability, vapour permeability, thermal conductivity, etc.) of all materials of different roofing systems were obtained from the references [41, 42].

3.4 Short-Wave Solar Absorption Coefficient

For most conventional/black roofing systems, the short-wave solar absorption coefficient is 0.88 [25–28]. As the white roofing systems would have different values of short-wave solar absorption coefficients (α_s), this study was conducted for different values of α_s ranging from 0.2 to 0.6.

3.5 Properties of PCM

As shown in Fig. 1, the PCM-enhanced model is attained by including a PCM-drywall on the indoor surface of the roofing system. In this paper, the roofing system with PCM-drywall is called “Test Roof”. As provided in [43], there are many PCM

products available in the markets. In this study, hypothetical PCM-drywall of 40 mm thick is assumed to have a latent heat of 100 kJ/kg but with different melting temperatures (22–27 °C). The thermal conductivities of the PCM-drywall are 0.18 W/m K and 0.14 W/m K for the solid phase and liquid phase, respectively [43]. Also, the density of the PCM-drywall is 700 kg/m³.

4 Methodology

The temperature, heat flux, and moisture distributions in the roofing systems were obtained by solving the energy equation and moisture equation in different layers [29–36, 44–46]. In this study, numerical simulations were conducted for three roofing systems (Ref Roof 1, Ref Roof 2, and Test Roof; see Fig. 1) with XPS insulation thickness of 60 mm and for a wide range of the short-wave solar absorption coefficient (0.88, 0.6, 0.4, and 0.2). Because one of the objectives of this study is to investigate the moisture accumulation over time within the roofing systems, the numerical simulations for different roofing systems were conducted for a period of 5 years. When it was observed that the moisture accumulation continues to increase over time after 5 years, the period of simulation was extended so as to determine the number of years behind which no moisture accumulation increases over time. In all numerical simulations, the weather data of year 2017 was repeated in the different years of the simulation period.

It is important to point out that using the weather data of different years in the simulation period (e.g. 5 years) may result in moisture accumulation over time within the roofing system. The main reason(s) of the moisture accumulation over time could be due to the differences in the weather data from one year to another and/or due to the hygrothermal properties of different layers of the roofing systems. To exclude the effect in the differences of the weather data from one year to another, however, the weather data of one year was repeated for subsequent years. As such, any moisture accumulation over time would be due to the hygrothermal properties of different layers of the roofing system (i.e. not due to the differences in the weather data from one year to another). In all simulations, time = 0 corresponds to January 1st.

For a given short-wave solar absorption coefficient of reflective material, dirt/dust accumulation on the surfaces of this material would increase its short-wave solar absorption coefficient. As such, the considered range of α_s (0.88–0.2) in this study covers the types of reflective materials having $\alpha_s \geq 0.2$ with and without dirt/dust accumulation.

Since no reflective materials are installed on the rooftops of the conventional roofing systems, the short-wave solar absorption coefficient is 0.88 [25, 27, 28]. Numerical simulations were conducted to predict the energy performance when these roofs were subjected to the weather conditions of Kuwait city. The numerical simulations were conducted for Ref Roof 1, Ref Roof 2, and Test Roof (Fig. 1) for different short-wave solar absorption coefficients, $\alpha_s = 0.88, 0.6, 0.4, 0.2$.

In cold climates, the sources of heating loads in residential buildings are usually obtained using heaters or furnaces that use fossil fuel, whereas the sources of the cooling loads are obtained using coolers or A/C systems that use electrical energy. Because of the difference in prices per thermal unit between the fossil fuel and electrical energy, the cooling energy load and heating energy load should be provided separately [25, 27, 28]. However, in hot climates such as that in Kuwait, the source of both heating loads and cooling loads in residential buildings are obtained using heaters, coolers, or A/C systems that use electrical energy. Consequently, the total energy loads in hot climates are reported in this paper as the sum of the cooling loads and the heating loads as provided in Figs. 6b, 7b, 8b, and 9b.

5 Results and Discussions

This section provides the results of the hygrothermal performances of white and black roofing systems when these roofing systems were subjected to the outdoor climates of the Kuwait city.

5.1 *Effect of Short-Wave Solar Absorption Coefficient on the Hygrothermal Performance*

For the Test Roof with PCM-drywall having melting temperature of 24 °C when it is subjected to the outdoor climate of Kuwait city, Fig. 2 shows the average hourly relative humidity in all layers of roofing system. Also, Fig. 3 shows the average hourly relative humidity in the insulation layer of roofing system. As shown in these figures, the conventional/black roof ($\alpha_s = 0.88$) runs with lower moisture compared to the white roofs with different short-wave solar absorption coefficient (α_s). Many previous studies have also shown that black roofs always run with lower moisture compared to white roofs (e.g. see [4, 6, 25–28]).

During the first 5 years, Figs. 2 and 3 show that moisture increases in the roofing system from year-to-year with different short-wave solar absorption coefficients. For the case of short-wave solar absorption coefficient greater than 0.2, no moisture accumulation occurs from year-to-year after 4 years. However, for short-wave solar absorption coefficient of 0.2, moisture accumulation was still increasing after 5 years on a year-to-year basis of comparison of moisture. As such, the periods of simulations were extended up to 10 years for white roofing system with short-wave solar absorption coefficient of 0.2. As shown in Figs. 2 and 3, no moisture accumulation occurs from year-to-year after 9 years for the white roof with short-wave solar absorption coefficient of 0.2.

It is important to point out that no risk of condensation and mould growth occurs when the relative humidity is below 80% (see [29, 44–46] for more details). As

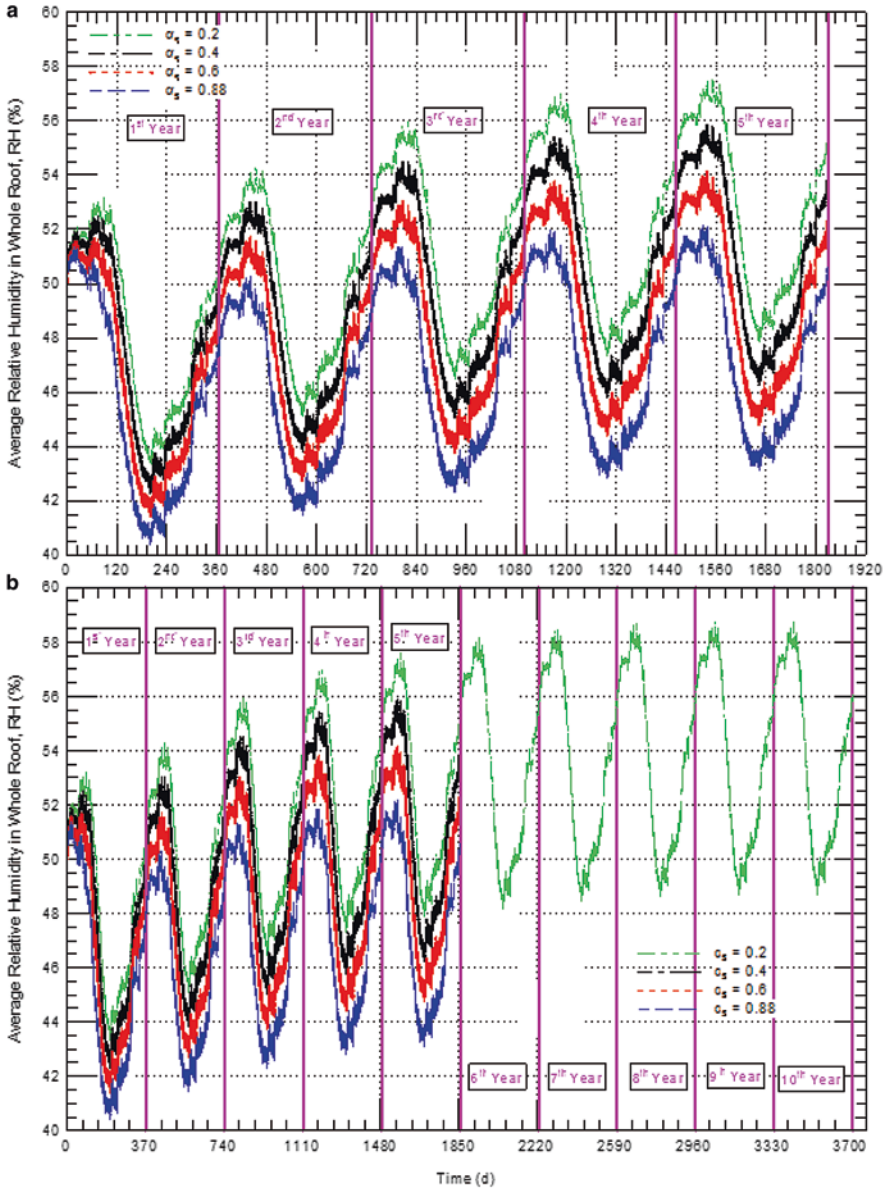


Fig. 2 (a, b) Average hourly relative humidity in the whole roofing systems with different short-wave solar absorption coefficients (α_s) with PCM-drywall of melting temperature of 24 °C

shown in Figs. 2 and 3, the highest relative humidities in the black and white roofing systems are well below 80%. As such, no risk of condensation and mould growth occur in these roofing systems when they were subjected to the weather conditions of Kuwait city.

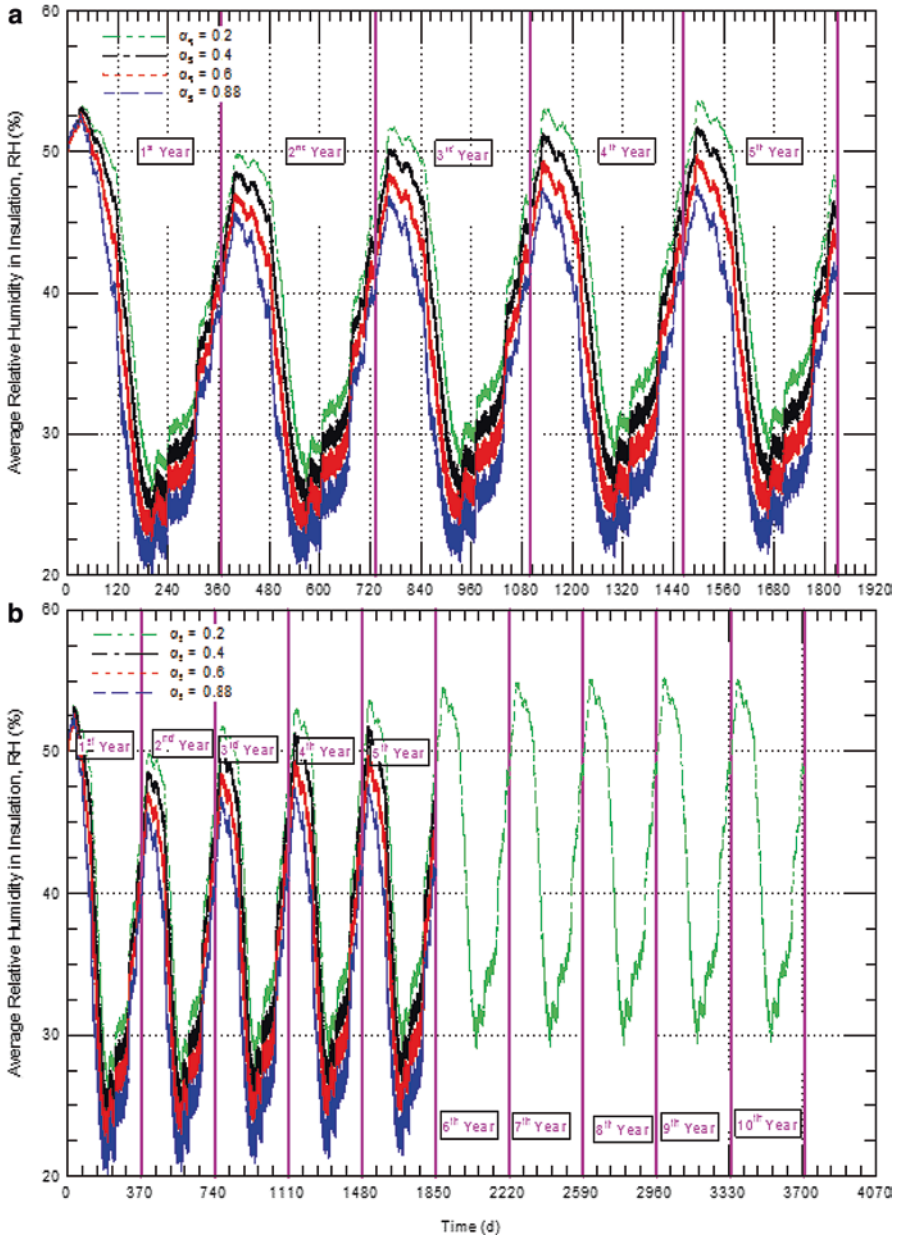


Fig. 3 (a, b) Average hourly relative humidity in the insulation materials of the roofing systems with different short-wave solar absorption coefficients (α_s) with PCM-drywall of melting temperature of 24 °C

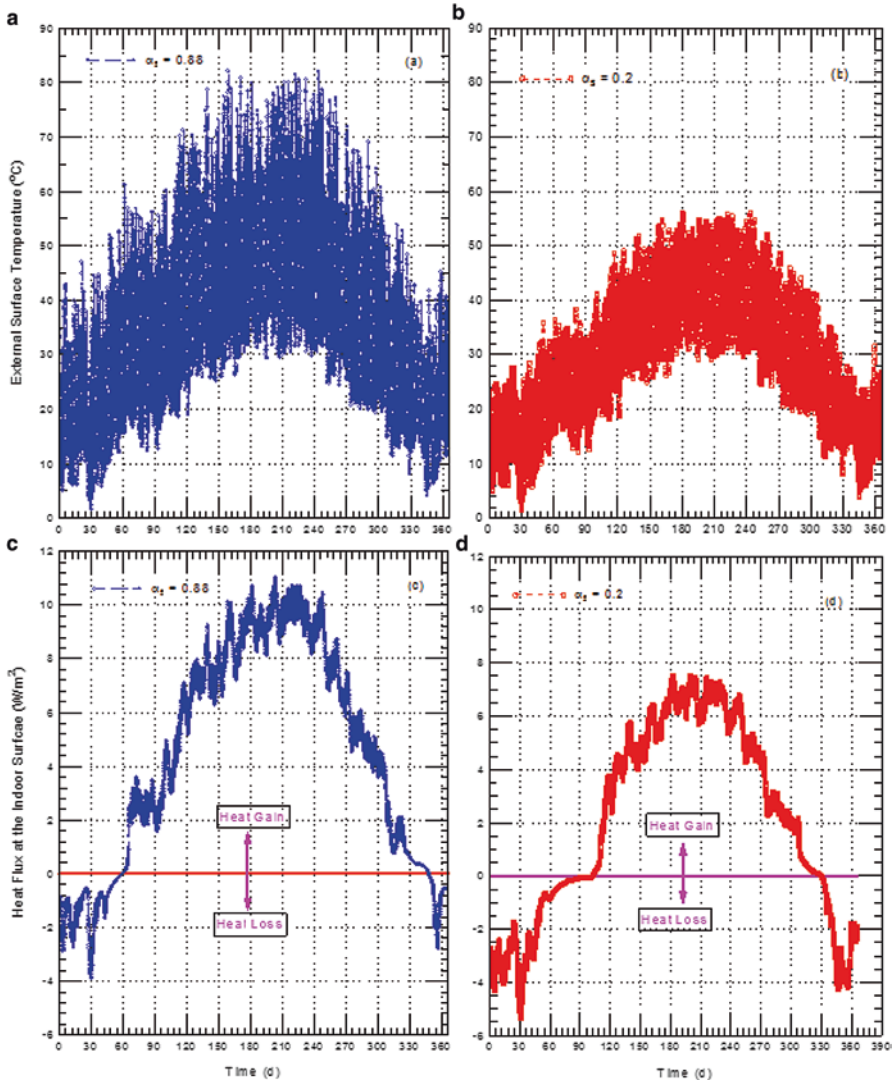


Fig. 4 (a–d) Comparison of hourly external surface temperature and heat flux at the indoor surface of conventional/black roof ($\alpha_s = 0.88$) and white roof ($\alpha_s = 0.2$) for the roofing systems with PCM-drywall of melting temperature of 24 °C

Figure 4a, b shows comparisons of the hourly external surface temperature of the conventional/black roof with $\alpha_s = 0.88$ and white roof with $\alpha_s = 0.2$ for the Test Roof with PCM having melting temperature of 24 °C and latent heat of melting of 100 kJ/kg. Furthermore, for a different values of short-wave solar absorption coefficients ($\alpha_s = 0.88, 0.6, 0.4,$ and 0.2), Fig. 5 shows the monthly average external surface temperature for these roofing systems.

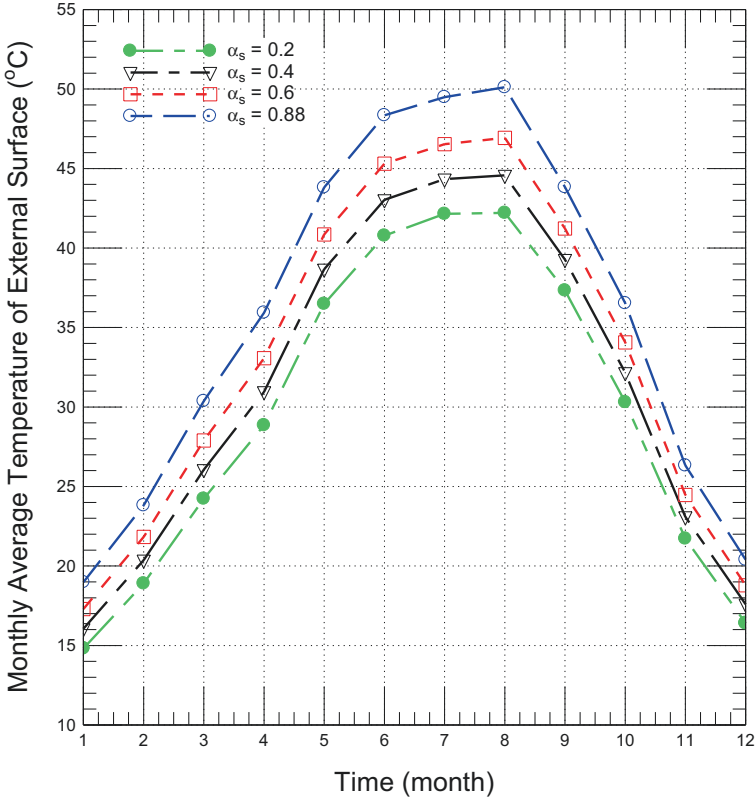


Fig. 5 Comparison of monthly average external surface temperature of conventional/black roof ($\alpha_s = 0.88$) and white roof of different short-wave solar absorption coefficients (α_s) for roofing system with PCM-drywall of melting temperature of 24 °C

Due to the high short-wave solar absorption coefficient of the black roof of $\alpha_s = 0.88$ (Fig. 4a), its surface temperature was found through numerical simulations to be significantly higher than that of the white roof of $\alpha_s = 0.2$ (Fig. 4b). The highest surface temperatures of the black roofs were found to be 84.7 °C compared to 56.1 °C for the white roofs of $\alpha_s = 0.2$. For all roofing systems, during night-time, the surface temperatures of both black and white roofs were approximately the same. Figure 5 shows that the highest monthly average surface temperatures of the roofing system with different short-wave solar absorption coefficients occurred in the month of August followed by the month of July.

Figure 4c, d shows comparisons of the hourly heat flux on the indoor surface of black roof of $\alpha_s = 0.88$ and white roof of $\alpha_s = 0.2$. In these figures, a zero heat flux represents the case of no heat entering or leaving the building through the roof. Note that when the heat flux is positive, it is called “heat gain” (i.e. heat into the building where the system contributes to the cooling load). Moreover, when the heat flux is negative, it is called “heat loss” (i.e. heat out of the building where the

system contributes to the heating load). Due to the higher surface temperature of black roof, its heat gain is significantly higher than that for white roof. During the whole year, the hourly highest heat gain for the black roof with $\alpha_s = 0.88$ was 11.025 W/m^2 , which was about 1.467 times that for white roof with $\alpha_s = 0.2$ (7.514 W/m^2). Furthermore, the corresponding highest hourly heat loss of the black roof was 3.919 W/m^2 , which was about 0.733 times that for the white roof (5.347 W/m^2). As such, black roofs require higher cooling loads than that for white roofs. On the other hand, black roofs require lower heating loads than that for white roofs.

In summary, buildings with white roofs would require more heating load during the winter time than buildings with black roofs. Conversely, buildings with white roof would require less cooling load in the summer time than buildings with black roofs.

For different values of short-wave solar absorption coefficients ($\alpha_s = 0.88, 0.6, 0.4, 0.2$), numerical simulations were conducted to predict the hourly heat flux on the indoor surface of the three roofing systems under considerations (Ref Roof 1, Ref Roof 2, and Test Roof; see Fig. 1). For the Test Roof, the numerical simulations were conducted for PCM-drywall of different melting temperatures (latent heat = 100 kJ/kg). The predicted heat fluxes on the indoor surfaces of these roofing systems were used to determine the monthly and yearly accumulation of energy loss (i.e. heating energy load, $E_{H,L}$) and the monthly and yearly accumulation of energy gain (i.e. cooling energy load, $E_{C,L}$). The yearly $E_{H,L}$ represents the area above the curve of the negative heat flux only during a period of 1 year (Fig. 4c, d), whereas the yearly $E_{C,L}$ represents the area under the curve of the positive heat flux only during a period of 1 year (Fig. 4c, d). These values were obtained by the following numerical integrations:

$$\begin{aligned}
 E_{H,L} &= \int_{t=0}^{t=365 \text{ day}} \begin{pmatrix} q_{\text{ind,surf}} & \text{if } q_{\text{ind,surf}} < 0 \\ 0 & \text{if } q_{\text{ind,surf}} \geq 0 \end{pmatrix} dt, \quad \text{and} \\
 E_{C,L} &= \int_{t=0}^{t=365 \text{ day}} \begin{pmatrix} q_{\text{ind,surf}} & \text{if } q_{\text{ind,surf}} > 0 \\ 0 & \text{if } q_{\text{ind,surf}} \leq 0 \end{pmatrix} dt.
 \end{aligned}
 \tag{1}$$

Equation (1) above was also used to determine the monthly heating and cooling loads where the integration periods were conducted over each month during the whole year.

6 Energy Performance of Different Roofing Systems

Comparisons of the energy performance of the white roofing systems of different short-wave solar absorption coefficients with the black/conventional roofing systems are provided and discussed in this section. For different values of short-wave solar absorption coefficients of different roofing systems (Ref Roof 1, Ref Roof 2,

and Test Roof with PCM having melting temperature of 24 °C), Fig. 6a ($\alpha_s = 0.88$), Fig. 7a ($\alpha_s = 0.6$), Fig. 8a ($\alpha_s = 0.4$), and Fig. 9a ($\alpha_s = 0.2$) show the monthly cooling energy load (+ve values) and the monthly heating load (-ve values).

For a given short-wave solar absorption coefficient, these figures show the monthly cooling loads are significantly higher than the monthly heating loads. The highest cooling loads occurred in the month of August, followed by the month of July, whereas the highest heating loads occurred in the month of January, followed by the month of December. For each roofing system, Figs. 6a, 7a, 8a, and 9a show that the cooling energy load decreases as the short-wave solar absorption coefficient decreases. For example, the cooling load in the month of August for the Ref Roof 1 (without drywall) decreases from 331.6 Wd/m² to 289.2 Wd/m², 258.4 Wd/m², and 227.2 Wd/m² as the short-wave solar absorption coefficient decreases from 0.88 to 0.6, 0.4, and 0.2, respectively (Figs. 6a, 7a, 8a, and 9a). This represents reductions in the cooling energy loads by 14.7%, 28.3%, and 46.0% as a result of decreasing the short-wave solar absorption coefficient from 0.88 to 0.6, 0.4, and 0.2, respectively.

The cooling load in the month of August for the Ref Roof 2 (with drywall) decreases from 306.3 Wd/m² to 265.7 Wd/m², 237.4 Wd/m², and 208.7 Wd/m² as the short-wave solar absorption coefficient decreases from 0.88 to 0.6, 0.4, and 0.2, respectively (Figs. 6a, 7a, 8a, and 9a). This represents reductions in the cooling energy loads by 15.3%, 29.0%, and 46.8% due to decreasing the short-wave solar absorption coefficient from 0.88 to 0.6, 0.4, and 0.2, respectively. Furthermore, for the Test Roof (with PCM-drywall having melting temperature of 24 °C), the cooling load in the month of August decreases from 298.2 Wd/m² to 260.1 Wd/m², 232.5 Wd/m², and 204.2 Wd/m² as the short-wave solar absorption coefficient decreases from 0.88 to 0.6, 0.4, and 0.2, respectively (Figs. 6a, 7a, 8a, and 9a), and this represents reductions in the cooling energy loads by 14.6%, 28.3%, and 46.0% due to decreasing the short-wave solar absorption coefficient from 0.88 to 0.6, 0.4, and 0.2, respectively.

Figures 6b, 7b, 8b, and 9b show that the months of the highest total energy loads of different roofing systems having different short-wave solar absorption coefficients occurred in July and August. However, the months of lowest total energy loads depended on the value of short-wave solar absorption coefficient. For example, the lowest energy loads for the roofing systems having short-wave solar absorption coefficient of 0.88 (i.e. black/conventional roofs) occurred in February, whereas that for the roofing systems having short-wave solar absorption coefficient of 0.2 occurred in March.

6.1 Yearly Energy Loads of Different Roofing Systems

The results provided in Figs. 6, 7, 8, and 9 as well as those results for Test Roof having a wide range of PCM melting temperature, T_m (22–27 °C) for the monthly cooling energy loads, monthly heating energy loads, and monthly total energy

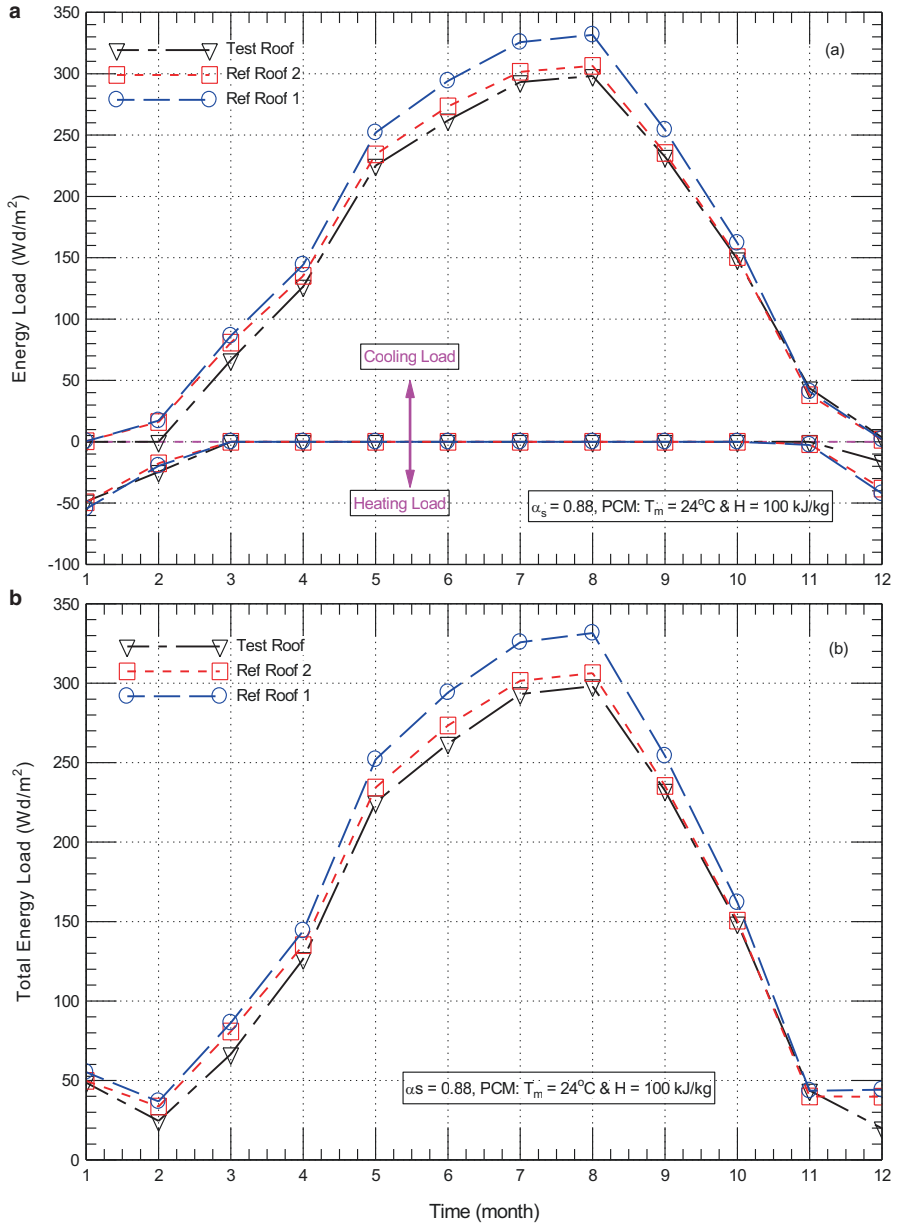


Fig. 6 (a, b) Comparison of monthly energy loads of the test roof with PCM of $T_m = 24^\circ\text{C}$ and $H = 100 \text{ kJ/kg}$ and the reference roofs for $\alpha_s = 0.88$

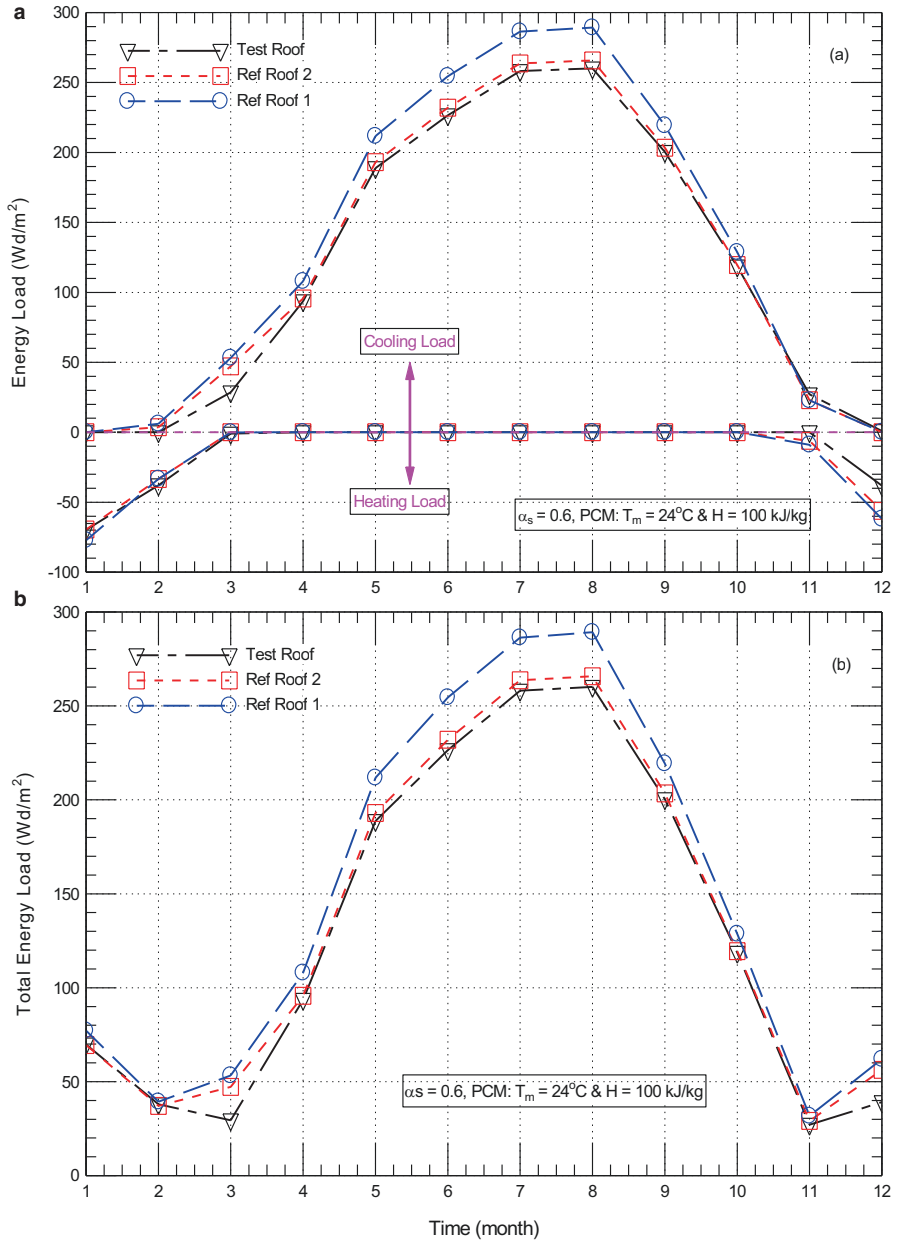


Fig. 7 (a, b) Comparison of monthly energy loads of the test roof with PCM of $T_m = 24^\circ C$ and $H = 100 \text{ kJ/kg}$ and the reference roofs for $\alpha_s = 0.6$

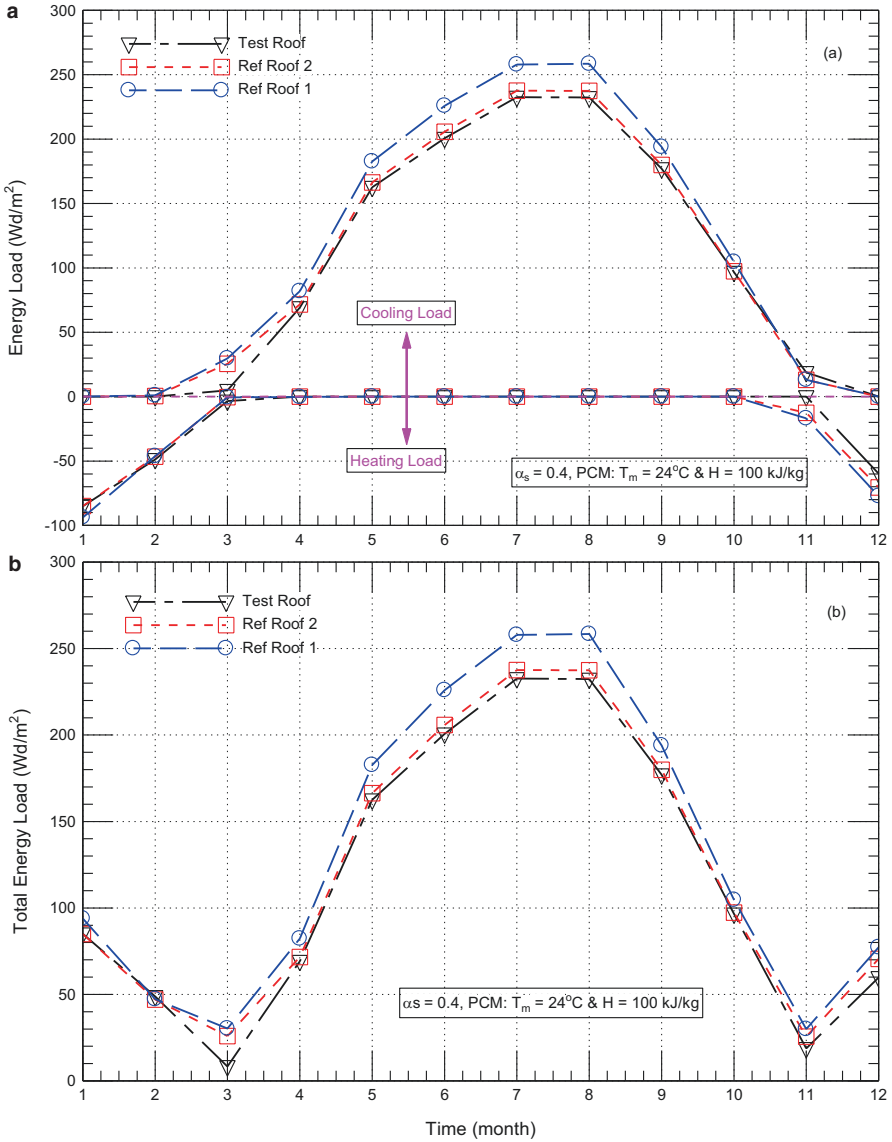


Fig. 8 (a, b) Comparison of monthly energy loads of the test roof with PCM of $T_m = 24^\circ C$ and $H = 100$ kJ/kg and the reference roofs for $\alpha_s = 0.4$

loads were used to determine the yearly cooling energy loads, yearly heating energy loads, and yearly total energy loads. The obtained results are provided in Fig. 10 ($\alpha_s = 0.88$), Fig. 11 ($\alpha_s = 0.6$), Fig. 12 ($\alpha_s = 0.4$), and Fig. 13 ($\alpha_s = 0.2$). As shown in Figs. 10, 11, 12, and 13 for different roofing systems, decreasing the short-wave solar absorption coefficient has caused a decrease in the yearly cooling loads and

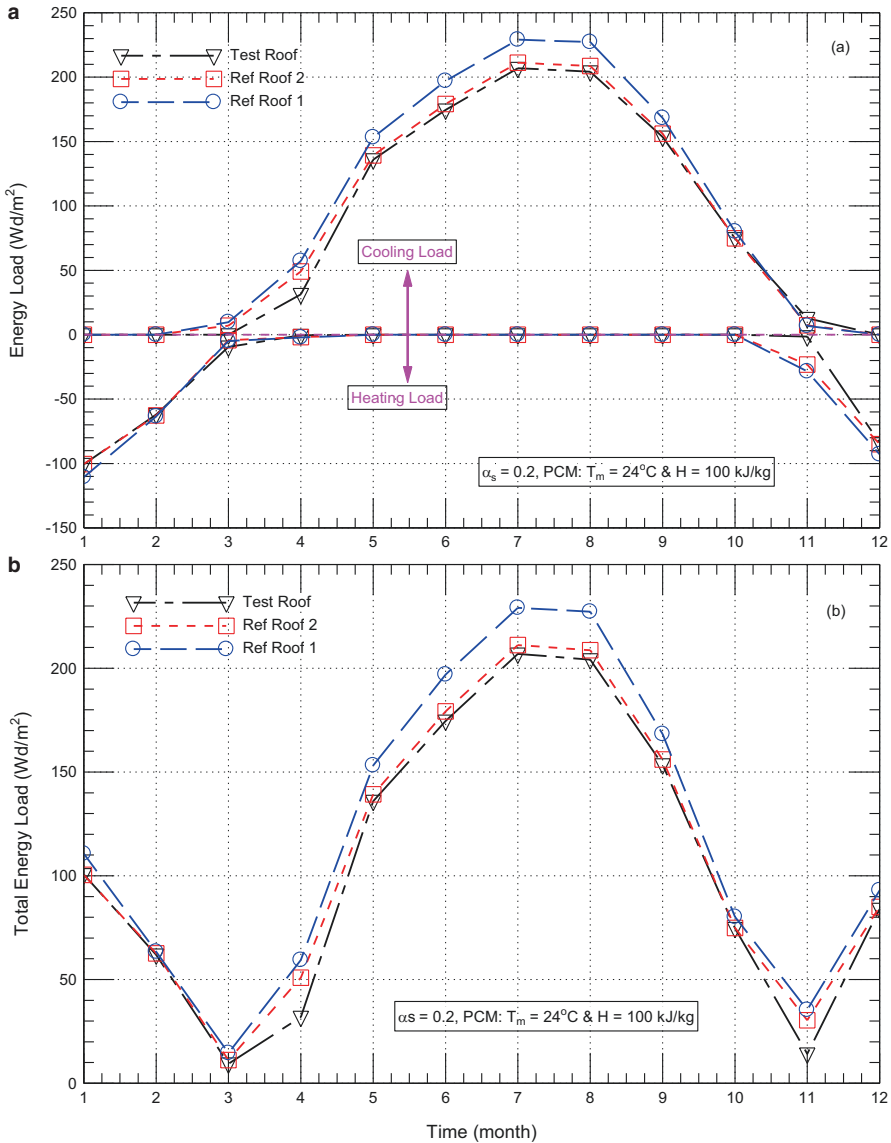


Fig. 9 (a, b) Comparison of monthly energy loads of the test roof with PCM of $T_m = 24^\circ\text{C}$ and $H = 100 \text{ kJ/kg}$ and the reference roofs for $\alpha_s = 0.2$

an increase in the yearly heating loads. The decrease in the yearly cooling loads outweighs the increase in the yearly heating loads resulting in a net decrease in the yearly total loads by decreasing the short-wave solar absorption coefficient. For a given short-wave solar absorption coefficient for the Test Roof, Figs. 10, 11, 12,

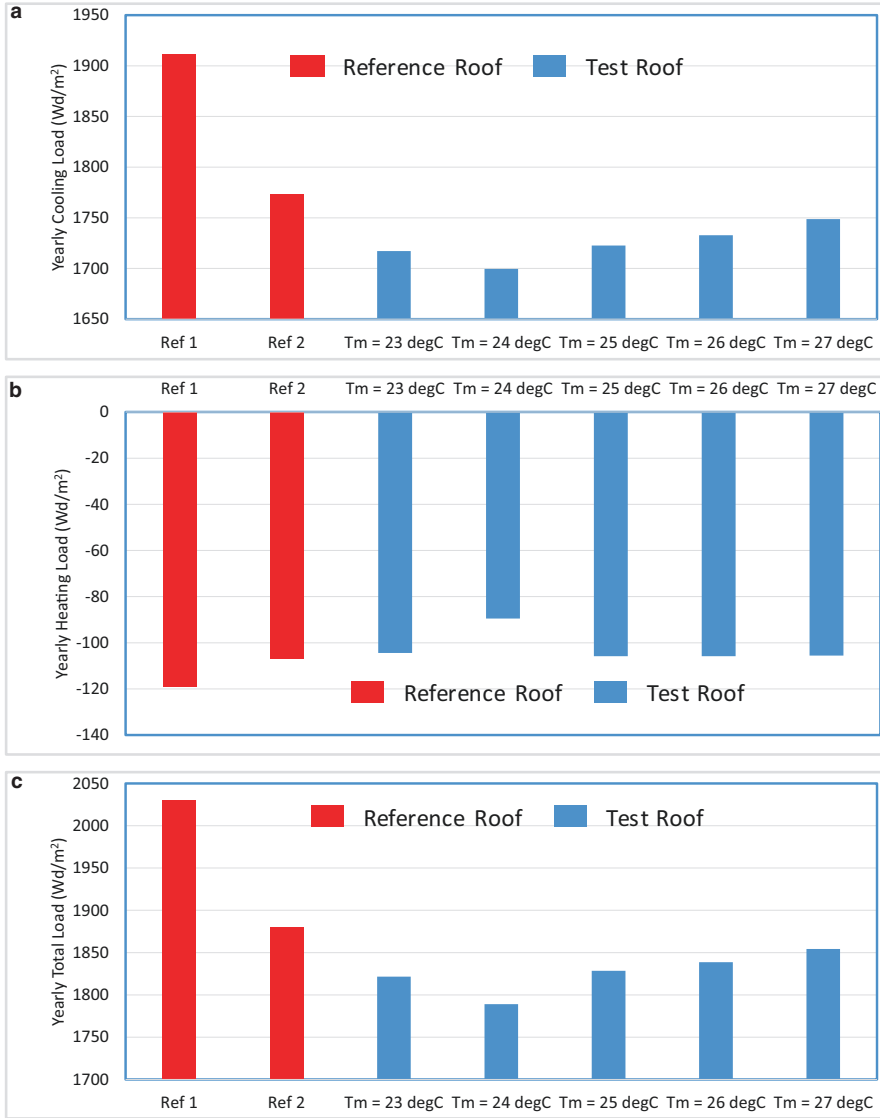


Fig. 10 (a–c) Yearly energy loads of reference and test roofing systems with $\alpha_s = 0.88$

and 13 show that the Test Roofs having PCM-drywall with a melting temperature of 24 °C resulted in the lowest yearly energy loads.

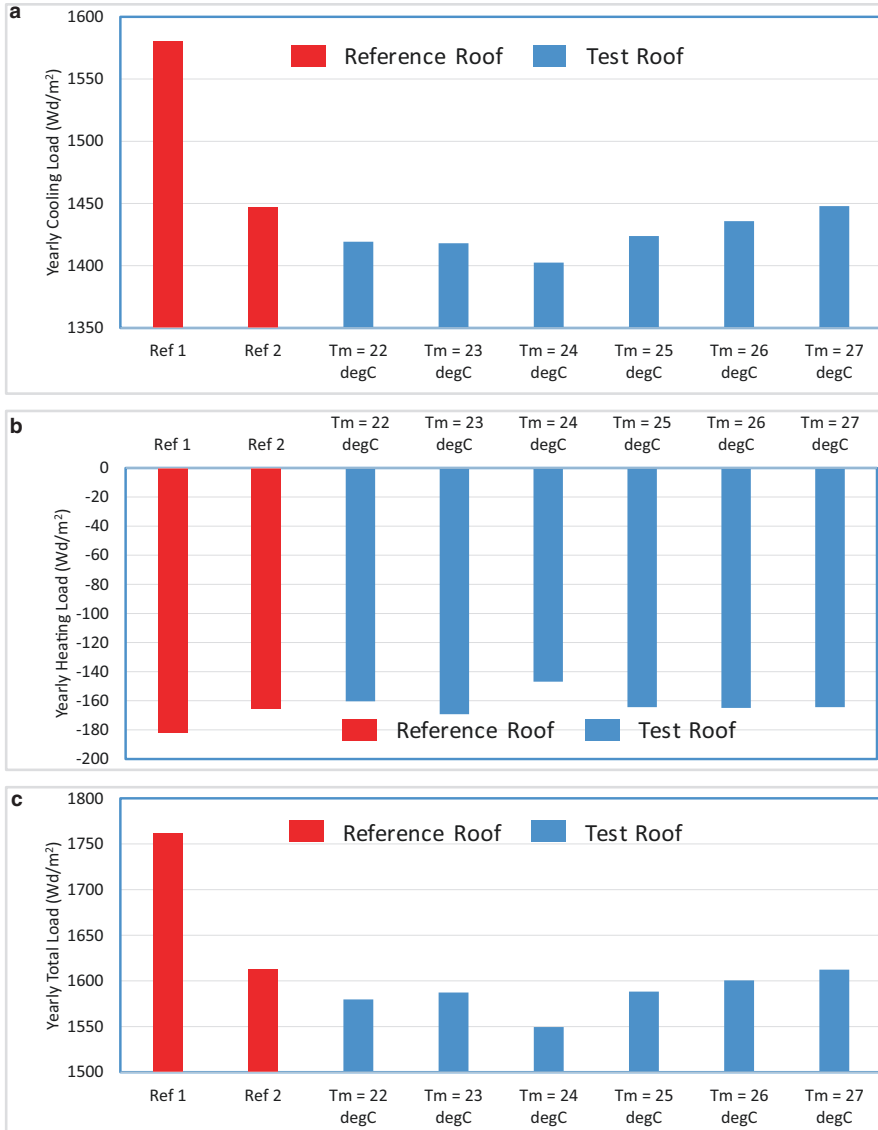


Fig. 11 (a–c) Yearly energy loads of reference and test roofing systems with $\alpha_s = 0.6$

6.2 Yearly Cooling Loads of Different Roofing Systems

Figures 10, 11, 12, and 13 show the yearly energy loads (cooling loads, heating loads, and total loads) for different short-wave solar absorption coefficients (α_s). For the Test Roof, these figures show that the PCM-drywall having melting tem-

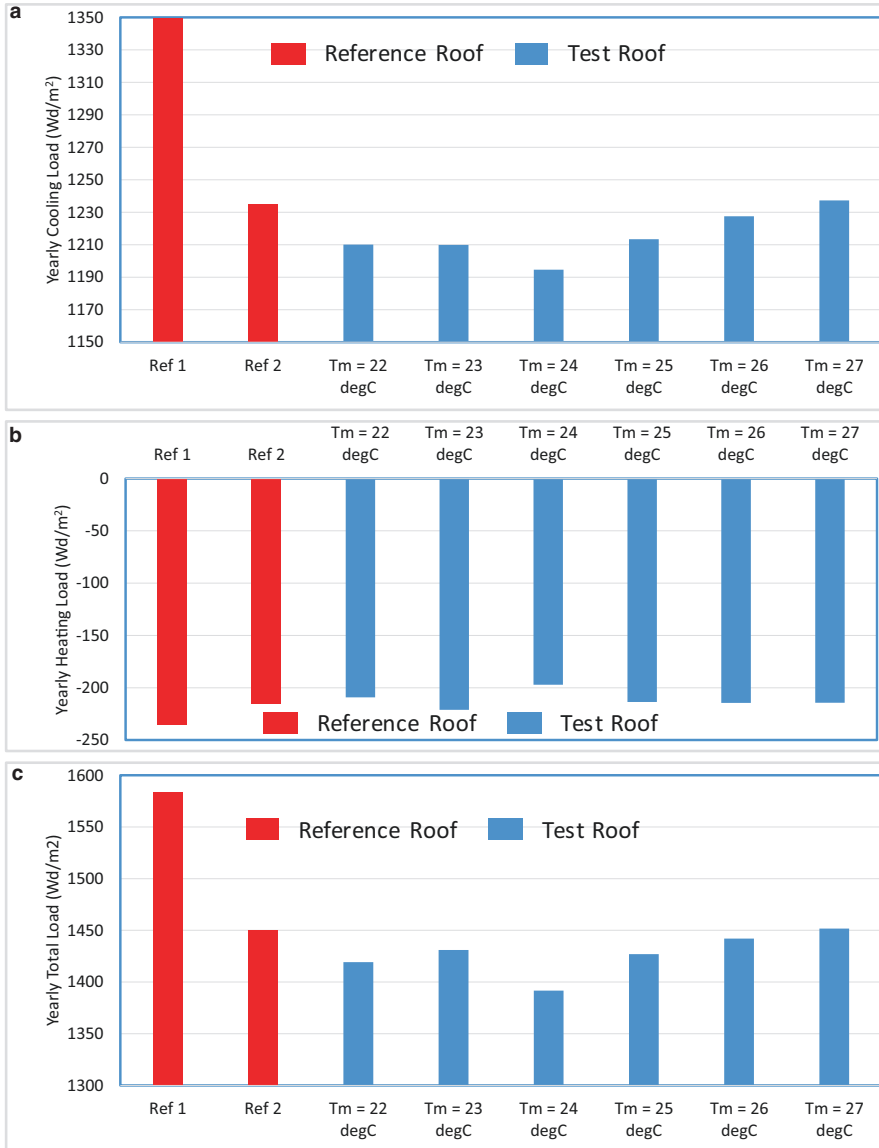


Fig. 12 (a–c) Yearly energy loads of reference and test roofing systems with $\alpha_s = 0.4$

perature (T_m) of 24 °C has resulted in the lowest energy loads for different values of short-wave solar absorption coefficients. For all roofing systems considered in this study (Ref Roof 1, Ref Roof 2, and Test Roof; see Fig. 1), Figs. 10a, 11a, 12a, and 13a show that the yearly cooling loads decrease with decreasing the short-wave solar absorption coefficient. Conversely, Figs. 10b, 11b, 12b, and 13b show

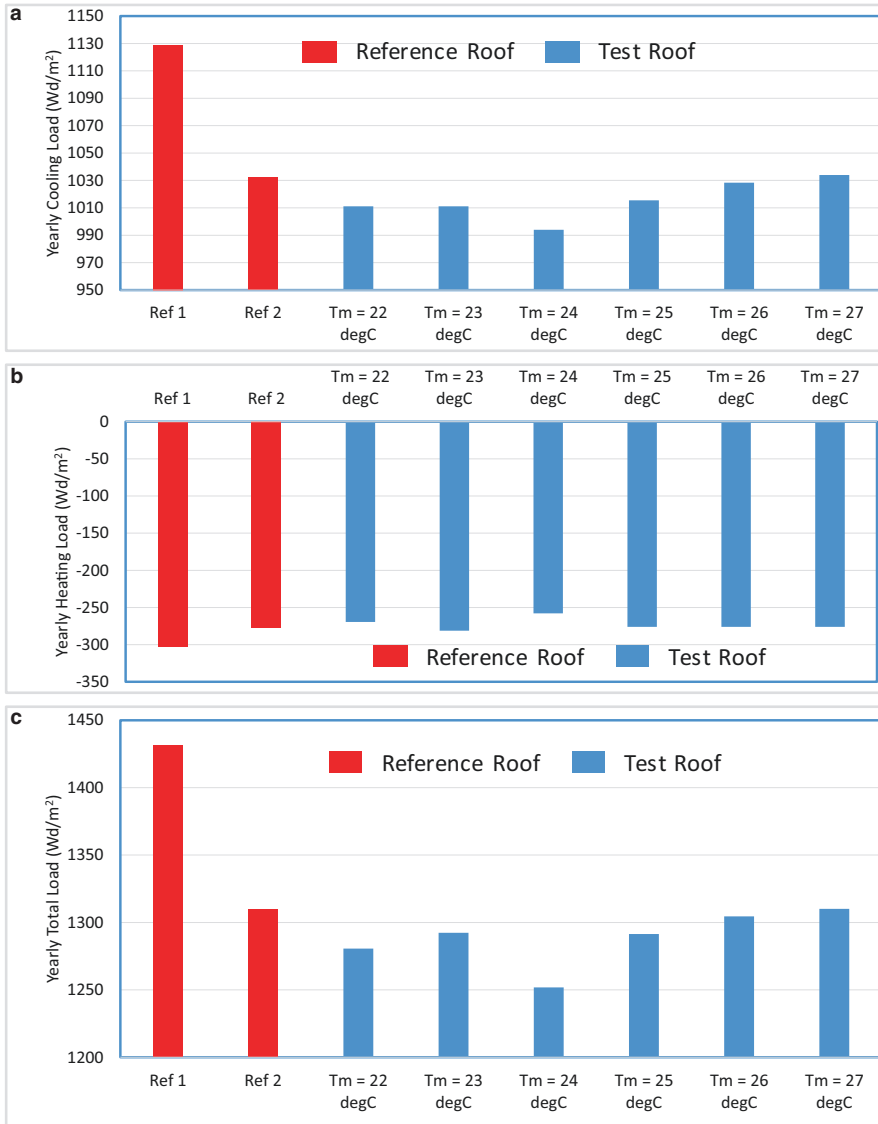


Fig. 13 (a–c) Yearly energy loads of reference and test roofing systems with $\alpha_s = 0.2$

that the yearly heating loads increase with decreasing the short-wave solar absorption coefficient. However, the yearly total energy loads decrease with decreasing short-wave solar absorption coefficient (Figs. 10c, 11c, 12c, and 13c).

For a short-wave solar absorption coefficient of 0.88 (black/conventional roof), the yearly cooling loads for Ref Roof 1, Ref Roof 2, and Test Roof with PCM-drywall having $T_m = 24\text{ }^\circ\text{C}$ were 1910.9 Wd/m², 1773.4 Wd/m², and 1699.7 Wd/m²,

respectively (Fig. 10a). Consequently, the yearly cooling load for this Test Roof ($T_m = 24\text{ }^\circ\text{C}$) was 12.4% and 4.3% lower than that for Ref Roof 1 (without drywall) and Ref Roof 2 (with drywall but without PCM), respectively. Similarly, Fig. 10b shows that the yearly heating loads of Ref Roof 1, Ref Roof 2, and Test Roof with PCM-drywall having $T_m = 24\text{ }^\circ\text{C}$ were 119.0 Wd/m², 106.9 Wd/m², and 89.5 Wd/m², respectively. Thus, the yearly heating load for this Test Roof was 33.0% and 19.4% lower than that for Ref Roof 1 and Ref Roof 2, respectively. As shown in Fig. 10c, the yearly total energy loads of Ref Roof 1, Ref Roof 2, and Test Roof with PCM-drywall having $T_m = 24\text{ }^\circ\text{C}$ were 2029.9 Wd/m², 1880.3 Wd/m², and 1789.2 Wd/m², respectively. Thus, the yearly total load for this Test Roof was 13.5% and 5.1% lower than that for Ref Roof 1 and Ref Roof 2, respectively.

The corresponding results for the Ref Roof 1, Ref Roof 2, and Optimum Test Roof (i.e. $T_m = 24\text{ }^\circ\text{C}$) having different values of the short-wave solar absorption coefficients, α_s of 0.6, 0.4, and 0.2 are summarized in Table 1. Based on the results provided in this table, the contributions to the yearly cooling load for Optimum Test Roof were 12.6% and 3.2% ($\alpha_s = 0.6$), 12.9% and 3.4% ($\alpha_s = 0.4$), and 13.6% and 3.9% ($\alpha_s = 0.2$) lower than that for Ref Roof 1 and Ref Roof 2, respectively. However, the contributions to the yearly heating load for Optimum Test Roof were 23.5% and 12.5% ($\alpha_s = 0.6$), 19.3% and 9.1% ($\alpha_s = 0.4$), and 17.4% and 7.6% ($\alpha_s = 0.2$) lower than that for Ref Roof 1 and Ref Roof 2, respectively. Additionally, the contributions to the yearly total load for Optimum Test Roof were 13.7% and 4.0% ($\alpha_s = 0.6$), 13.8% and 4.2% ($\alpha_s = 0.4$), and 14.3% and 4.6% ($\alpha_s = 0.2$) lower than that for Ref Roof 1 and Ref Roof 2, respectively.

In summary, for the different roofing systems considered in this paper, it was observed that white roofs experienced an increase in the heating load compared to that with black roofs. However, the decrease in the cooling load for white roofs was typically much greater than the increase in yearly heating load. These observations were in agreements with many previous studies (e.g. see [25–28]). For the Test Roof, the results showed that the PCM-drywall with melting temperature of 24 °C has resulted in the lowest cooling, heating, and total energy loads compared to other melting temperatures.

6.3 Comparison of Energy Performance of Reference Roofing Systems with Test Roofing System

Comparisons of the energy performance for reference roofing systems (Ref Roof 1 and Ref Roof 2) and the test roofing system (Test Roof) having PCM-drywall with melting temperature (T_m) of 24 °C are shown in Fig. 14a (yearly cooling loads), Fig. 14b (yearly heating loads), and Fig. 14c (yearly total loads). Note that the results of the yearly cooling loads (Fig. 14a) and yearly heating loads (Fig. 14b) were used to obtain the results of yearly total loads shown in Fig. 14c. For a given

Table 1 Yearly cooling loads, yearly heating loads, and yearly total loads of different roofing systems having different values of short-wave solar absorption coefficients (α_s)

α_s	Ref Roof 1	Ref Roof 2	Test Roof ^a
Yearly cooling load (Wd/m ²)			
0.88	1910.9	1773.4	1699.7
0.6	1579.9	1446.8	1402.5
0.4	1349.1	1234.9	1194.6
0.2	1128.9	1032.5	994
Yearly heating load (Wd/m ²)			
0.88	119	106.9	89.5
0.6	181.4	165.3	146.9
0.4	235.1	215.1	197.1
0.2	302.6	277.3	257.8
Yearly total load (Wd/m ²)			
0.88	2029.9	1880.3	1789.2
0.6	1761.3	1612.1	1549.4
0.4	1584.2	1450	1391.7
0.2	1431.4	1309.8	1251.8

^aPCM melting temperature, $T_m = 24$ °C

short-wave absorption coefficient (α_s), these figures show that the energy loads of the Test Roof are lower than that of the Ref Roof 1 and Ref Roof 2.

As shown in Fig. 14c for the Ref Roof 1, decreasing the short-wave solar absorption coefficient from 0.88 (i.e. black/conventional roof) to 0.2 has resulted in decreasing the yearly total energy load by 42% (from 2029.9 to 1431.4 Wd/m²). For the Ref Roof 2, Fig. 14c shows that decreasing the short-wave solar absorption coefficient from 0.88 to 0.2 has resulted in a decrease in the yearly total energy load by 44% (from 1880.3 to 1309.8 Wd/m²). Similarly, for the Test Roof having PCM-drywall with melting temperature of 24 °C, decreasing the short-wave solar absorption coefficient from 0.88 to 0.2 has resulted in decreasing the yearly total energy load by 43% (from 1789.2 to 1251.8 Wd/m²).

It is important to design a cost-effective roofing system with a satisfactory energy performance. Figure 14c shows that the same yearly total load (1880.3 Wd/m²) of the black/conventional Ref Roof 2 (i.e. with drywall but without PCM) can be achieved by using the Ref Roof 1 (i.e. without drywall) with a reflective material having $\alpha_s = 0.73$. A further decrease in α_s from 0.73 to 0.2 for the Ref Roof 1 would result in a decrease in the yearly total load by 31% (i.e. from 1880.3 to 1431.4 Wd/m²). Figure 14c shows that the same yearly total load (1789.2 Wd/m²) of the black/conventional Test Roof having PCM-drywall with melting temperature of 24 °C can be achieved by using the Ref Roof 1 (i.e. without drywall) with a reflective material having $\alpha_s = 0.63$. A further decrease in α_s from 0.63 to 0.2 for the Ref Roof 1 would result in a decrease in the yearly total load by 25% (i.e. from 1789.2 to 1431.4 Wd/m²).

Last but not the least, an engineering cost study should follow this study in Kuwait with the purpose of arriving at cost effective roofing systems that use

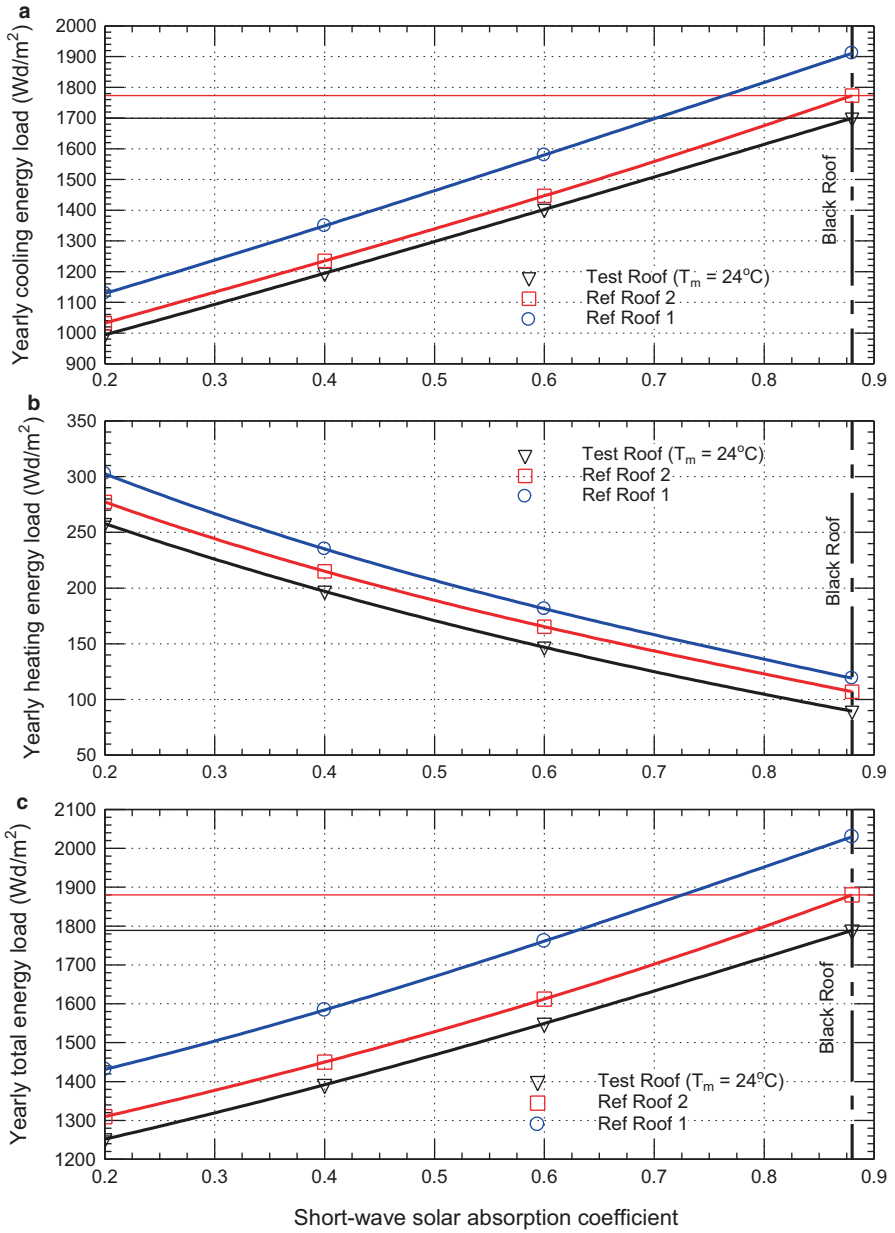


Fig. 14 (a–c) Comparison of the yearly energy loads of Ref Roof 1, Ref Roof 2, and Test Roof having PCM with $T_m = 24^\circ\text{C}$

reflective material technology and PCM for residential and commercial buildings. In that cost study, all possibilities provided in this study should be investigated in terms of the prices of reflective materials with different short-wave solar absorption coefficients and PCM with different latent heat and melting temperature as well as the prices of different types of energies (fossil fuels and electrical energy) that are needed for furnaces, heaters, coolers, and A/C systems.

7 Summary and Conclusions

In this paper, numerical simulations were conducted to investigate the hygrothermal performance of white and black roofing systems with and without Phase Change Materials (PCMs). The roofs considered in this paper were three (3) roofing systems, namely, (a) reference roof without drywall called "Ref Roof 1", (b) reference roof with drywall but without PCM called "Ref Roof 2", and (c) roofing system with PCM-drywall having latent heat of 100 kJ/kg and different melting temperatures, called "Test Roof". These roofing systems were subjected to the climate of Kuwait city.

In order to find out whether white roofs could lead to moisture-related problems, the numerical simulations were conducted for a period of 5 years. When the moisture accumulation was still increasing after 5 years on a year-to-year basis of comparison of moisture, the period of simulation was extended up to 10 years. Results showed that black roofs always perform with lower moisture than white roofs. For all roofing systems, moisture accumulation occurred from year to year. For the case of reflective material having short-wave solar absorption coefficient of 0.88 (i.e. black/conventional roof), no moisture accumulation occurred from year to year after 4 years. However, for reflective material having short-wave solar absorption coefficient of 0.2, no moisture accumulation occurs from year to year after 9 years. Since the highest relative humidities in the black and white roofing systems were below 80%, no risk of condensation and mould growth occur in these roofing systems.

The numerical simulations were conducted for the Test Roof having PCM-drywall of different melting temperatures. The results of the Test Roof having reflective materials with different short-wave solar absorption coefficients showed that the melting temperature of 24 °C has resulted in the lowest cooling energy loads, heating energy loads, and total energy loads. Additionally, the results showed that white roofs experienced an increase in the heating energy loads compared to black roofs. However, the decrease in the cooling energy loads for white roofs were typically much greater than the increase in the heating energy loads. As such, white roofs have resulted in a net energy savings compared to black roofs. These observations were in agreements with many previous studies.

Within the simulation period of whole year, the results showed that the months of the highest total energy loads for different roofing systems having reflective materials with different short-wave solar absorption coefficients occurred in July

and August. However, the months of lowest total energy loads depended on the value of short-wave solar absorption coefficient. For the Ref Roof 1, Ref Roof 2, and Test Roof having PCM-drywall with melting temperature of 24 °C, decreasing the short-wave solar absorption coefficient from 0.88 (i.e. black/conventional roof) to 0.2 has resulted in decreasing the yearly total energy load by 42–44%.

For Ref Roof 1, Ref Roof 2, and Test Roof having PCM-drywall with melting temperature of 24 °C and different short-wave solar absorption coefficients (0.88, 0.6, 0.4, and 0.2), the yearly cooling load for the Test Roof was 12.4–13.6% and 3.2–4.3% lower than that for Ref Roof 1 and Ref Roof 2, respectively. Correspondingly, the yearly heating load for the Test Roof was 17.4–33.0% and 7.6–19.4% lower than that for Ref Roof 1 and Ref Roof 2, respectively. As well, the yearly total load for the Test Roof was 13.5–14.3% and 4.0–5.1% lower than that for Ref Roof 1 and Ref Roof 2, respectively.

It is important to design a cost-effective roofing system with a satisfactory energy performance. As such a number of options were explored in this paper for designing roofing systems with reflective materials and PCMs. The main outcome of this study has shown the capabilities of using reflective materials with different short-wave solar absorption coefficients and PCMs with different melting temperature for enhancing the energy performance of the roofing systems. Finally, it is important to emphasize that the results presented in this paper apply to specific roofing systems under the climatic conditions of Kuwait city.

References

1. Al-Homoud MS (2005) Performance characteristics and practical applications of common building thermal insulation materials. *J Build Environ* 40:353–366. <https://doi.org/10.1016/j.buildenv.2004.05.013>
2. Vrachopoulos MG, Koukou MK, Stavlas DG, Stamatopoulos VN, Gonidis AF, Kravvaritis ED (2012) Testing reflective insulation for improvement of buildings energy efficiency. *Cent Eur J Eng* 2(1):83–90. <https://doi.org/10.2478/s13531-011-0036-3>
3. European Commission (2010) Green public procurement thermal insulation technical background report. Report for the European Commission – DG Environment by AEA, Harwell, Owner. European Commission, DG Environment-G2, Brussels
4. Krarti M, Hajiah A (2011) Analysis of impact of daylight time savings on energy use of buildings in Kuwait. *Energy Policy* 39:2319–2329
5. Zirkelbach D, Schafaczek B, Künzel H (2010) Long-term hygrothermal performance of green roofs. In: Eleventh International Conference on Thermal Performance of the Exterior Envelopes of Whole Buildings XI, Clearwater, FL, USA, 4–9 December 2010
6. Solecki WD, Rosenzweig C, Parshall L, Pope G, Clark M, Cox J et al (2005) Mitigation of the heat island effect in urban New Jersey. *Environ Hazard* 6(1):39–49
7. Ismail A, Samad MHA, Rahman AMA (2011) The investigation of green roof and white roof cooling potential on single storey residential building in the Malaysian climate. In: Proceedings of World Academy of Science, Engineering and Technology, vol 76, pp 129–137
8. Jo JH, Carlson J, Golden JS, Bryan H (2010) Sustainable urban energy: development of a meso-scale assessment model for solar reflective roof technologies. *Energy Policy* 38(12):7951–7959

9. Levinson R, Akbari H, Berdahl P, Wood K, Skilton W, Petersheim J (2010) A novel technique for the production of cool colored concrete tile and asphalt shingle roofing products. *Sol Energy Mater Sol C* 94(6):946–954
10. Xu T, Sathaye J, Akbari H, Garg V, Tetali S (2012) Quantifying the direct benefits of cool roofs in an urban setting: reduced cooling energy use and lowered greenhouse gas emissions. *Build Environ* 48:1–6
11. Oleson KW, Bonan GB, Feddema J (2010) Effects of white roofs on urban temperature in a global climate model. *Geophys Res Lett* 37(3):L03701
12. Ray S, Glicksman L (2010) Potential energy savings of various roof technologies. In: Eleventh International Conference on Thermal Performance of the Exterior Envelopes of Whole Buildings XI, Clearwater, FL, USA, 4–9 December 2010
13. Urban B, Roth K (2010) Guidelines for selecting cool roofs. U.S. Department of Energy, Energy Efficiency and Renewable Energy, Building Technologies Program, Washington, DC
14. Hutchinson T (2009) Cool roofing challenging what's cool. In: *Eco-structure*. Available from <http://www.eco-structure.com/cool-roofing/challenging-whats-cool.aspx>. Accessed May 2017
15. Desjarlais AO (1995) Self-drying roofs: what?! No dripping! In: Proceedings of Thermal Performance of Exterior Envelopes of Buildings VI, Clearwater, FL, USA, pp 763–773
16. Desjarlais AO, Petrie TW, Childs PW, Atchley JA (1998) Moisture studies of a self-drying roof: tests in the large-scale climate simulator and results from thermal and hygric models. In: Proceedings of the Thermal Performance of the Exterior Envelopes of Buildings VII, Clearwater, FL, USA, pp 41–54
17. McHugh B, Petrick R (2011) Chicago's green and garden roofing codes and technology. In: Proceedings of the 2011 International Roofing Symposium, Washington, DC, USA, 7–9 September 2011
18. Durhman A, Collins M, McGillis WR (2011) Utilizing green technology and research to assess green roofing benefits. In: Proceedings of the 2011 International Roofing Symposium, Washington, DC, USA, 7–9 September 2011
19. Bentz SP (2011) Decision-making process for green options in reroofing. In: Proceedings of the 2011 International Roofing Symposium, Washington, DC, USA, 7–9 September 2011
20. Akbari H, Konopacki S, Pomerantz M (1999) Cooling energy savings potential of reflective roofs for residential and commercial buildings in the United States. *Energy* 24(5):391–407
21. Akbari H, Konopacki S, Parker D (2000) Updates on revision to ASHRAE standard 90.2: including roof reflectivity for residential buildings. In: Proceedings ACEEE Summer Study on Energy Efficiency in Buildings, vol 1, pp 11–111
22. Levinson R, Akbari H (2010) Potential benefits of cool roofs on commercial buildings: conserving energy, saving money, and reducing emission of greenhouse gases and air pollutants. *Energy Effic* 3(1):53–109
23. Brehob E, Desjarlais A, Atchley J (2011) Effectiveness of cool roof coatings with ceramic particles. In: Proceedings of the 2011 International Roofing Symposium, Washington, DC, USA, 7–9 September 2011
24. Ennis M, Kehrner M (2011) The effects of roof membrane color on moisture accumulation in low-slope commercial roof systems. In: Proceedings of the 2011 International Roofing Symposium, Washington, DC, USA, 7–9 September 2011
25. Bludau C, Zirkelbach D, Kuenzel HM (2009) Condensation problems in cool roofs. *Interface* XXVII(7):11–16
26. Bludau C, Kuenzel HM, Zirkelbach D (2010) Hygrothermal performance of flat roofs with construction moisture. In: Eleventh International Conference on Thermal Performance of the Exterior Envelopes of Whole Buildings XI, Clearwater, FL, USA, 4–9 December 2010
27. Saber HH, Swinton MC, Kalinger P, Paroli RM (2012) Long-term hygrothermal performance of white and black roofs in North American climates. *J Build Environ* 50:141–154. <https://doi.org/10.1016/j.buildenv.2011.10.022>
28. Saber HH, Swinton MC, Kalinger P, Paroli RM (2011) Hygrothermal simulations of cool reflective and conventional roofs. In: 2011 NRCA International Roofing Symposium, Emerging Technologies and Roof System Performance, Washington, DC, USA, 7–9 September 2011

29. Saber HH, Maref W (2015) Risk of condensation and mould growth in wood-frame wall systems with different exterior insulations. In: Building Enclosure Science & Technology Conference (BEST4 Conference), Kansas City, Missouri, USA, 12–15 April 2015
30. Saber HH, Maref W, Lacasse MA, Swinton MC, Kumaran MK (2010) Benchmarking of hygrothermal model against measurements of drying of full-scale wall assemblies. In: International Conference on Building Envelope Systems and Technologies, ICBEST 2010, Vancouver, BC, Canada, 27–30 June 2010, pp 369–377
31. Saber HH, Maref W, Elmahdy AH, Swinton MC, Glazer R (2012) 3D heat and air transport model for predicting the thermal resistances of insulated wall assemblies. *Int J Build Perform Simulat* 5(2):75–91. <https://doi.org/10.1080/19401493.2010.532568>
32. Saber HH, Maref W, Armstrong M, Swinton MC, Rousseau MZ, Gnanamurugan G (2010) Benchmarking 3D thermal model against field measurement on the thermal response of an insulating concrete form (ICF) wall in cold climate. In: Eleventh International Conference on Thermal Performance of the Exterior Envelopes of Whole Buildings (Buildings XI Conference), Clearwater, FL, USA, 4–9 December 2010
33. Saber HH, Swinton MC (2010) Determining through numerical modeling the effective thermal resistance of a foundation wall system with low emissivity material and furred-airspace. In: International Conference on Building Envelope Systems and Technologies, ICBEST 2010, Vancouver, BC, Canada, 27–30 June 2010, pp 247–257
34. Saber HH, Maref W, Swinton MC, St-Onge C (2011) Thermal analysis of above-grade wall assembly with low emissivity materials and furred airspace. *J Build Environ* 46(7):403–414
35. Saber HH, Maref W, Swinton MC (2011) Numerical investigation of thermal response of basement wall systems with low emissivity material and furred airspace. In: 13th Canadian Conference on Building Science and Technology (13th CCBST) Conference, Winnipeg, MB, Canada, 10–13 May 2011
36. Saber HH, Maref W, Swinton MC (2012) Thermal response of basement wall systems with low emissivity material and furred airspace. *J Build Phys* 35(2):353–371. <https://doi.org/10.1177/1744259111411652>
37. Saber HH, Maref W, Hajiah AE (2019) Hygrothermal performance of cool roofs subjected to Saudi climates. *J Front Eng Res* 7:39. <https://doi.org/10.3389/fenrg.2019.00039>. Available from <https://www.frontiersin.org/articles/10.3389/fenrg.2019.00039/full>
38. Saber HH, Hajiah AE (2019) 3D numerical modeling for assessing the energy performance of single- and two-zone buildings with and without phase change materials. In: Gulf Conference on Sustainable Built Environment, GSBEKW-2019, Kuwait, 10–13 March 2019
39. Saber HH, Maref W, Hajiah, AE (2020) Effective R-value of Enclosed reflective space for different building applications. *J Build Phys* 43(5):398–427. <https://doi.org/10.1177/1744259119880306>
40. ASHRAE (2003) Handbook – Applications, chapter 3 – commercial and public buildings. American Society of Heating, Refrigerating and Air Conditioning Engineers, Inc, Atlanta, GA
41. Mukhopadhyaya P, Kumaran MK, Lackey J, Normandin N, van Reenen D, Tariku F (2007) Hygrothermal properties of exterior claddings, sheathing boards, membranes and insulation materials for building envelope. In: Proceedings of Thermal Performance of the Exterior Envelopes of Whole Buildings X, Clearwater, FL, USA, 2–7 December 2007, pp 1–16
42. Kumaran MK, Lackey J, Normandin N, Tariku F, van Reenen D (2004) A thermal and moisture transport property database for common building and insulating materials. Final Report from ASHRAE Research Project 1018-RP. National Research Council Canada, Ottawa, ON, pp 1–229
43. Soares N, Reinhart CF, Hajiah A (2017) Simulation-based analysis of the use of PCM-wallboards to reduce cooling energy demand and peak-loads in low-rise residential heavy-weight buildings in Kuwait. In: Building simulation. Tsinghua University Press; Springer, Beijing; Berlin. <https://doi.org/10.1007/s12273-017-0347-2>
44. Saber HH, Lacasse MA, Moore TV (2017) Hygrothermal performance assessment of stucco-clad wood frame walls having vented and ventilated drainage cavities. In: Advances in hygrothermal performance of building envelopes: materials, systems and simulations. ASTM STP1599. ASTM International, West Conshohocken, PA, pp 198–231. <https://doi.org/10.1520/STP159920160100>

45. Saber HH, Lacasse MA, Ganapathy G, Plescia S, Parekh A (2016) Risk of condensation and mould growth in highly insulated wood-frame walls. In: The 13th International Conference on Thermal Performance of the Exterior Envelopes of Whole, Buildings XIII, Clearwater, FL, USA, 5–8 December 2016
46. Lacasse MA, Saber HH, Maref W, Ganapathy G, Plescia S, Parekh A (2016) Field evaluation of thermal and moisture response of highly insulated wood-frame walls. In: The 13th International Conference on Thermal Performance of the Exterior Envelopes of Whole, Buildings XIII, Clearwater, FL, USA, 5–8 December 2016

Gender Differences in Thermal Comfort and Satisfaction in Offices in GCC and Asia



Madhavi Indraganti

1 Introduction

Gender equality is “smart economics” [1]. Reduced gender discrimination and women in the workforce positively impact the economic development of a nation. However, women’s labor force participation in Asia remains low and shows a downward trend despite improved female education and significant economic growth [1]. For example, in India female employment rate is lower than in any big economy barring Saudi Arabia and is falling [2]. A report says that India would be 27% richer if more women there worked. This is mainly due to lack of suitable jobs and conducive job environments [1].

Thermal comfort is a subjective feeling and is not a temperature set point. Several thermal and non-thermal factors contribute to it, such as air quality, lighting, noise levels etc. Several researchers across a wide range of building and climate types recorded marked differences in occupant comfort perceptions of both sexes [3–5]. Therefore, there cannot be a one-size-fits-all solution that is totally acceptable by both men and women [3–5].

The rentier states in the GCC have abundantly available fuel resources leading to extravagant energy consumption patterns. Their unique socio-political obligations compel them to have subsidized and cheap energy tariffs [6], which further exacerbate the energy use [7]. At the same time increasing population and consumerism transformed the Gulf states into key energy users [8]. The ecological footprint of this region is changing very rapidly. This is a major challenge. Qatar ranks the highest in electricity consumption per capita in the world [9].

Thermal comfort reports from the real-life office buildings from the affluent Gulf Cooperation Council (GCC) countries are scarce. Indraganti and Boussaa con-

M. Indraganti (✉)
Qatar University, Doha, Qatar
e-mail: madhavi@qu.edu.qa

ducted yearlong field studies in offices in Qatar and presented an adaptive thermal comfort model for GCC [10]. However, the gender differences in comfort perception in GCC offices have not been investigated yet.

In this context, the paper aims to (a) study the effect of age, gender, and body mass index on indoor environmental satisfaction and comfort temperature in offices in Qatar and (b) compare the same with other office environments in India, Japan, and other Asian countries.

2 Methods and Field Survey

This paper relies on the thermal comfort field study data the first author collected in offices in Doha [10], India [11], and Japan [12]. For drawing broader comparisons, the paper makes use of the thermal comfort field data from offices in Asia made available through ASHRAE Database II [13].

Doha (N25° 17' and E51° 32') is the capital of Qatar, a small peninsula in the Arabian Sea. It has hot desert climate and long hot-humid summer (May–September). Winter is mild (December–February) while Spring (March, April) and Autumn (October, November) are warm. The field study was conducted in ten air-conditioned office buildings in Doha during 01-2016 to 01-2017 resulting in 3742 sets of comfort data. Five of these buildings are government office buildings and the rest are private buildings. Each dataset consisted of occupant responses to a detailed paper questionnaire and simultaneous measurements of environmental parameters.

The data from Indian offices was collected from 28 office buildings located in two cities Chennai (N13°04' and E80° 17', warm humid wet land coastal climate) and Hyderabad (N17°27' and E78° 28' with composite climate) during 01-2012 to 02-2013. We collected 6042 datasets during the survey. The survey was done in naturally ventilated (NV), mixed mode (MM), and fully air-conditioned buildings. A total of 1352 sets of data were collected when the buildings were run in naturally ventilated mode and 4310 sets in air-conditioned (AC) mode. About 10% data was collected during power outages when ACs were off and windows were closed. This data is eliminated from analysis.

The data from four office buildings in Japan was collected in a paper-based thermal comfort field survey done in Tokyo (N35°41' 22.22" and E139° 41' 30.12") in humid subtropical climate during 07-2012 to 09-2012. A total of 2402 sets of data were collected (432 in NV mode and 1979 in AC mode).

All the questionnaires consisted of three sections: (1) personal identifiers such as code name, age, and gender; (2) thermal comfort responses such as current thermal sensation, preference, and acceptability; and (3) response to other environmental parameters such as air movement, humidity, etc.

While the subjects filled the questionnaires, the field surveyor simultaneously measured the following parameters using calibrated digital instruments: (1) air temperature, (2) relative humidity, (3) globe temperature, (4) air velocity, and (5) CO₂

Table 1 Descriptive statistics of the investigated subject sample

Survey	Gender	Sample size (<i>N</i>)	Age (years)		Body surface area (kg/m ²)		Clothing insulation (clo)	
			Mean	SD	Mean	SD	Mean	SD
Doha	Male	2558	36.0	8.286	1.88	0.15	0.75	0.135
	Female	1184	31.3	7.685	1.65	0.14	0.95	0.309
Chennai	Male	2037	29.6	8.61	1.79	0.14	0.67	0.039
	Female	870	31.3	9.527	1.56	0.13	0.81	0.109
Hyderabad	Male	2394	32.5	9.202	1.79	0.14	0.68	0.036
	Female	747	29.3	8.17	1.59	0.13	0.74	0.113
Tokyo	Male	1231	38.0	12.786			0.63	0.061
	Female	1171	40.8	11.555			0.62	0.09

concentration. These were taken at a height of 1.1 m following ASHRAE Class II protocols. The methods, instrument details, and sensitivities were elaborated for Doha [10], India [11], and Japan [12].

2.1 The Subject Sample

The subject sample consisted of acclimatized subjects working in the surveyed buildings within the age group of 18–70 years. In all the surveys, a larger sample size was collected from males. Females provided 31.6% of total data in Doha, 29.9% in Chennai, 23.8% in Hyderabad, and 48.8% in Tokyo. The mean age of the male sample varied from 29.6 to 38 years, whereas the mean age of the female sample varied from 29.3 to 40.8 years. Clothing insulation of female subjects was generally higher in all the surveys except in Tokyo. The descriptive statistics of the investigated sample is shown in Table 1.

2.2 Measurement of Other Environmental Parameters

Thermal comfort is a multi-dimensional paradigm that, besides the four prime variables, depends on several other environmental parameters. Therefore, measuring the occupant sensation and preferences for other environmental parameters is also important. With this objective, we measured the sensation and preference for various other environmental parameters in these three surveys using the scales as shown in Table 2.

The table also shows the subjective thermal comfort scales used for measuring thermal sensation, thermal preference, and thermal acceptability. In all the surveys, thermal sensation was measured with ASHRAE's 7-point sensation scale with 0 at neutral and +3 at hot and −3 at very cold. Thermal preference was measured with Nicol's 5-point scale as shown in Table 2. Thermal acceptance was measured using a binary scale with 0 being acceptable and 1 being unacceptable.

0	Neither high nor low	Neither humid nor dry	Neither bright nor dim	Neither noisy nor quiet	Neither bad nor good	No change	No change	No change	No change	Normal	Satisfied
-1	Slightly high	Slightly dry	Slightly dim	Slightly quiet	Slightly bad	A bit less air movement	A bit more humid	A bit brighter	A bit noisier	Slightly lower than normal	
-2	High	Dry	Dim	Quiet	Bad	Much less air movement	Much more humid	Much brighter	Much noisier	Much lower than normal	
-3	Very high	Very dry	Very dim	Very quiet	Very bad						
Surveys adopted	D; C; H; T	D; C; H; T	D	D	D; C; H	D; C; H; T	D; C; H; T	D	D	D; C; H; T	D

D Doha, *C* Chennai, *H* Hyderabad, *T* Tokyo

2.3 *Determination of Proxy Scales for Measuring Environmental Satisfaction*

We determined proxy binary scales for environmental satisfaction using the sensation votes on thermal comfort, humidity sensation, lighting sensation, noise level, and indoor air quality. We considered the votes in the central three categories as satisfied (coded as 0) and dissatisfied (coded as 1). Those preferring no change in the air movement are coded as satisfied (coded as 0), the rest as dissatisfied (coded as 1). In order to make a wider comparison, we used the ASHRAE Database II consisting of office buildings in Asia [13]. This data consisted of 11,551 sets of data collected from offices contributed by ten researchers across Asian cities such as Seoul ($N = 262$), Bangkok ($N = 1157$), Makati ($N = 277$), Singapore ($N = 817$), Ahmedabad ($N = 1507$), Bangalore ($N = 1151$), Chennai ($N = 878$), Delhi ($N = 1388$), Shimla ($N = 1406$), Ilam ($N = 345$), Tokyo (118), Jaipur (596), Jakarta ($N = 572$), and Harbin ($N = 77$).

3 Results and Discussion

3.1 *Outdoor and Indoor Environments of the Surveyed Environments*

During the survey period, the outdoor temperature varied widely in Doha (range: 18–39 °C, mean: 30.8 °C) and moderately in Chennai (range: 24.5–35.5 °C; mean: 28.9 °C), Hyderabad (range: 21.5–34.5 °C; mean: 26.7 °C) and Tokyo (20.5–30.2 °C; mean: 27.6 °C). Indoor environments varied widely under natural ventilation mode and much lesser in air-conditioned mode during the survey period in these cities. Descriptive statistics of the outdoor and indoor environments is shown in Table 3. Doha experienced higher humidity ratios and lower indoor temperatures compared to Chennai (also a coastal climate) as shown in Fig. 1 and also the other cities as shown in Table 3. The indoor air movement in Doha was much lower compared to the other three surveyed cities Chennai, Hyderabad, and Tokyo. It was reported that the air movement in Chennai, Hyderabad, and Tokyo was higher than that of Doha as is also shown in Table 3 [4].

We estimated the comfort temperature using the Griffiths' method for each thermal comfort vote, taking 0.5 as the Griffith's coefficient. Mean indoor comfort temperature was found to be 24.0 °C in Doha (range: 13.6–31.7 °C). The same in AC environments in Chennai, Hyderabad, and Tokyo was 26.9 °C (range: 17–34.9 °C), 25.7 °C (range: 17.1–34.8 °C), and 27.4 °C (range: 19.8–35.3 °C), respectively. Similarly, the mean comfort temperature in NV environments in Chennai, Hyderabad, and Tokyo was 28.6 °C (range: 21.1–33.7 °C), 27.9 °C (range: 19.9–37.7 °C), and 27 °C (range: 18.8–38.3 °C), respectively.

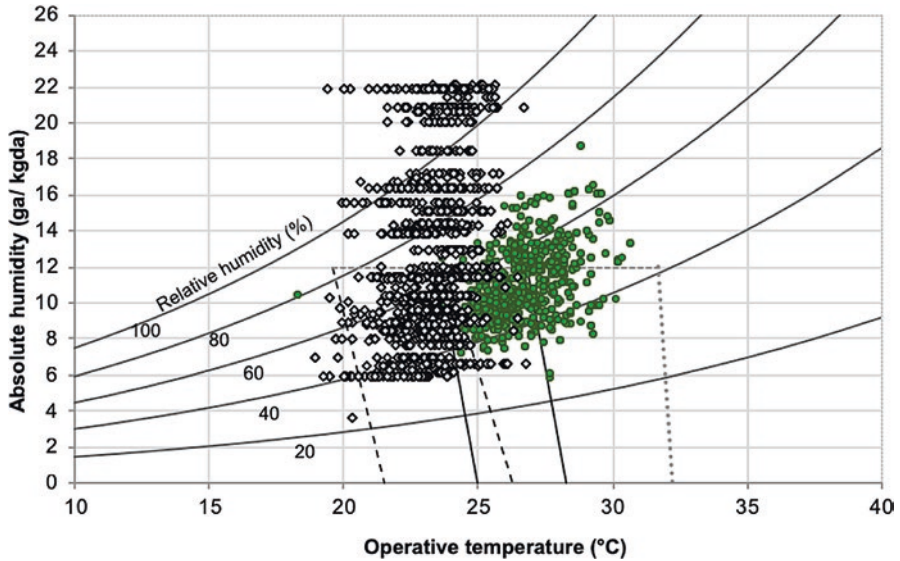


Fig. 1 Indoor environmental data of Doha (black diamond) and Chennai-AC (green square) for comparison superimposed over the psychrometric chart

3.2 Gender Differences in Subjective Thermal Responses

In Doha, majority of the subjects felt cooler sensations, voting on the cooler side of the sensation scale, more so women. About 19.4% women voted on the cooler side of discomfort against 12.7% men. We can also note that all the subjects in general voted on the cooler side of the scale in other surveys as well, such as Chennai and Hyderabad, in contrast to Tokyo, as seen in Table 4. This reflects some amount of overcooling in the air-conditioned environments. Table 4 shows another interesting feature with regard to women’s discomfort in both cooler and warmer side of the sensation scale in Doha.

A significantly higher percentage of women compared to opposite gender felt both cold and heat discomfort (at 95% CI), as they voted for (−3) very cold and (2) hot sensations. Also, the mean thermal sensation of female subjects was found to be the lowest in Doha compared to other surveys: Chennai, Hyderabad, and Tokyo. Karyono [5] also observed men expressing warmer sensations than women in Indonesian offices. This finding is in contrast to the finding of Fanger [14] who noted no significant gender differences in thermal feeling in climate chamber experiments with college age subjects.

Women displayed similar thermal preference vote as can be seen in Fig. 2. In Doha, Chennai, and Hyderabad surveys, the mean thermal preference of female subjects is significantly lower than that of males at 95% CI. Women preferred much warmer environments than men. In Doha, the mean thermal preference for men was

Table 3 Descriptive statistics of outdoor and indoor environmental variables in various cities surveyed

Variable	Doha		Chennai		Hyderabad		Tokyo							
	AC (N = 3742)	NV (N = 132)	AC (N = 2522)	NV (N = 1220)	AC (N = 1788)	NV (N = 423)	AC (N = 1979)	NV (N = 1979)						
	Mean	SD	Mean	SD	Mean	SD	Mean	SD						
T_o	30.8	6.54	26.9	2.71	28.9	2.77	25.4	2.98	27.544	3.94	25.9	2.16	28.0	1.67
T_i	23.8	1.18	29.7	2.22	26.5	1.52	29.0	1.89	26.110	1.64	29.3	1.43	27.9	1.10
T_g	23.4	1.21	29.5	2.10	26.7	1.40	28.7	1.98	25.607	1.69	29.4	1.54	27.9	1.13
RH	45.4	6.87	59.7	5.51	50.1	7.48	43.1	11.08	45.580	10.82	52.6	6.39	50.9	4.41
AH	8.2	1.28	15.7	2.73	10.8	1.96	10.7	2.66	9.479	2.06	13.4	1.58	11.9	1.24
V_a	0.04	0.06	0.5	0.33	0.2	0.20	0.1	0.21	0.049	0.08	0.2	0.15	0.3	0.16
CO ₂ level (ppm)	1337	332	821	622	1370	460	860	291	962	311	613	167	1149	413
Noise level (dB)	57.8	6.73												
Lighting level (lux)	361.3	280.38												
Tc	24.0	2.61	28.5	2.42	26.8	2.91	27.9	2.59	25.735	2.50	27.0	2.53	27.4	2.23

T_o , outdoor daily mean temperature (°C); T_i , indoor air temperature (°C); T_g , indoor globe temperature (°C); T_c , indoor air conditioned, NV naturally ventilated, NV standard deviation (g_a/kg_{da}); V_a , air velocity (m/s); T_{co} , comfort temperature (°C)

RH, relative humidity (%); AH, absolute humidity

Table 4 Gender differences in the frequency distribution of thermal sensation vote (TSV) (voting percentage) in various surveys in AC mode

TSV	Doha		Chennai		Hyderabad		Tokyo	
	Male (N = 2558)	Female (N = 1184)	Male (N = 1782)	Female (N = 740)	Male (N = 1420)	Female (N = 368)	Male (N = 986)	Female (N = 993)
-3	2.9	11.6	0.9	0.8	0.3	0.8	1	0.4
-2	9.8	7.8	12	18.2	8.9	12	2.9	4.4
-1	28.7	22.6	28.8	29.5	28.7	27.4	18.5	17.7
0	39.7	35.6	32	20.8	35.4	36.4	41.3	44.3
1	11.8	8.4	12.4	11.4	14.2	12.2	24	23.1
2	4.7	10.9	8	10.8	8.2	8.2	5.4	4.7
3	2.3	3.2	5.8	8.5	4.4	3	6.9	5.3
Mean TSV	-0.29	-0.33	-0.09	-0.1	-0.04	-0.16	0.28	0.21

Values in bold indicate the voting difference between the genders in the survey being statistically significant at 95% confidence interval (CI)

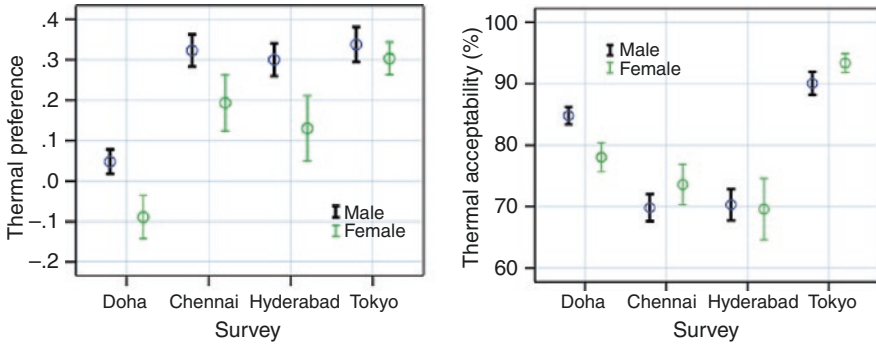


Fig. 2 Gender differences in mean thermal preference vote (TP) and thermal acceptance (%) in various surveys in AC mode. Error bars indicate 95% CI around the mean

at 0.05 (indicating a preference towards cooler environments) while the same for women was -0.09 (indicating a preference towards warmer environments). On the contrary, the other three surveys had both men and women preferring cooler environments albeit at different levels as can be seen in Fig. 2.

Thermal acceptance is another subjective measure of thermal environment. It is measured as a binary variable. ASHRAE recommends 80% acceptance in thermal environments [15]. Similar to thermal preference, we found statistically significant gender differences in thermal acceptance in Doha (at 95% CI) in contrast to other three surveys: Chennai, Hyderabad, and Tokyo. In Doha, 84% males found the office environments acceptable in average against 78% female subjects accepting the same (Fig. 2). Thermal acceptance depends on several factors of which indoor temperature could be the one. Lower acceptance among female occupants can be related to the lower temperatures being maintained in Doha and the resulting lower sensation vote on the cooler side of discomfort, compared to other offices in other cities.

Linear regression of TSV versus indoor globe temperature in Doha returned two significantly different gradients for male and female subjects. These are 0.174 K^{-1} (standard error SE: 0.020 , $p < 0.001$) and 0.3 K^{-1} (SE: 0.033 , $p < 0.001$), respectively. Higher slope for female subjects indicates that female subjects are more sensitive to thermal variations than those of the opposite gender. For example, a unit change in sensation vote needed 3.3 K variation of the indoor temperature in female subjects, while the same change occurred at 5.6 K change in indoor conditions for male occupants. Interestingly, these differences are more pronounced as the subjects moved away from the mean thermal conditions experienced in the offices. In other three surveys, differences in thermal sensitivity of males and females were not statistically significant.

3.3 Comfort Temperature: Variations with Gender and Age and Body Mass Index (BMI)

We noted statistically significant differences (at 95% CI) in the mean comfort temperature between genders in Doha. The mean comfort temperature of male and female occupants was 24.1 °C (SD = 2.426) and 23.7 °C (SD = 2.963), respectively. On the contrary, we found slightly higher comfort temperature for female subjects in Hyderabad survey (mean = 26.1 °C; SD = 2.396) in AC mode. Male subjects in Hyderabad recorded 0.4 K lower comfort temperature compared to their counterparts and the difference is significant at 95% CI. In Chennai and Tokyo, the comfort temperature for both genders was around 3 K higher than in Doha and gender differences are not significant.

We divided the subjects into two age groups: under and over 25 years. Interestingly, the mean comfort temperature of female subjects (22.6 °C) in Doha within the younger age group is significantly lower (by 0.9 K) than of their male counterparts. On the contrary, an Indian study reported [4] females under 25 years age having significantly higher comfort temperature when compared to males. Interestingly, older female subjects in Doha expressed comfort at 1.5 K higher than younger females as shown in Fig. 3. This difference is statistically significant at 95% CI. This finding assumed significance in designing appropriate environments mostly used by younger subjects such as academic facilities.

Similarly, older males had significantly higher comfort temperature (by 0.7 K) than younger males. It could be attributed to the fact that younger age subjects were engaged in activities producing a wider range of metabolic heat than older subjects who were mostly found in sedentary activities, although the differences in the mean value of the younger and older subjects are not statistically significant in both genders in Doha.

It may be possible that in air-conditioned environments, subjects' acclimatization to the narrower thermal regime matters. Brager and de Dear [16] demonstrated that people who were exposed to a small range of temperatures (mostly through HVAC systems) developed high expectations for homogeneity and cool temperatures and were soon critical of the subsequent thermal variations indoors.

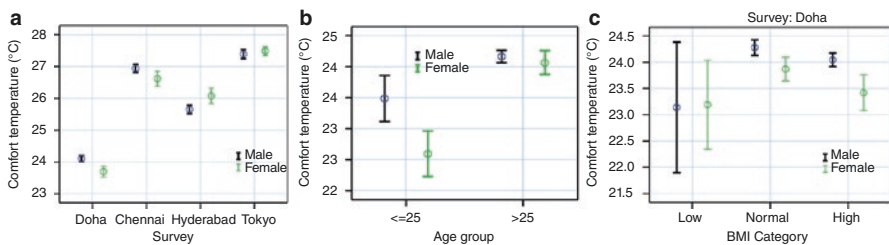


Fig. 3 Gender differences in mean comfort temperature in (a) various surveys and (b) age group (c) BMI category in AC mode. Error bars indicate 95% CI around the mean

We considered the subject sample under three categories of body mass index (BMI): low ($\text{BMI} < 18 \text{ kg/m}^2$), normal ($18 \text{ kg/m}^2 < \text{BMI} < 25 \text{ kg/m}^2$), and high ($\text{BMI} > 25 \text{ kg/m}^2$) [17]. Women subjects in normal and high BMI categories in Doha are found to have significantly lower comfort temperature than men in the respective BMI category. The gender difference in comfort temperature for BMI normal and high categories was 0.4 K and 0.6 K, respectively. We found no gender difference in low BMI category in Doha survey. No significant gender differences in comfort temperature with respect to BMI categories are noted in Chennai and Hyderabad surveys.

3.4 Comfort Temperature: Gender and Clothing Variations

It is important to note major differences in clothing insulation of the male and female subjects in the Middle Eastern and Indian environments, which in part explain their variations in comfort temperature. Except Tokyo survey, female subjects had significantly higher clothing insulation. The difference (0.2 clo) is very pronounced in Doha survey than in other surveys. To place in perspective, this is close to the insulation of a light sweater. It is important to note that due to strong cultural influences, women in Middle Eastern offices are required to wear modest clothing which often included head cover scarves, full-sleeved shirts, and abayas. The differences in mean clothing insulation of subjects wearing non-Western outfits (such as thobe, ghutra, abaya, hijab, salwar-kameez, etc.) are significantly higher than of Western outfits. Albeit not stringent, women in Indian offices too had similar modesty requirements in dressing (Fig. 4).

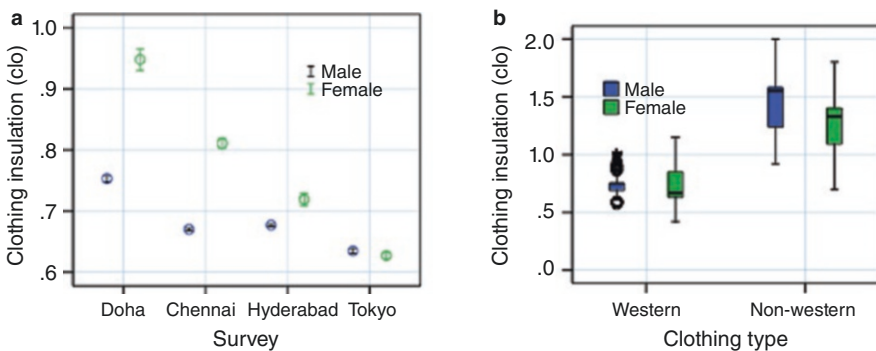


Fig. 4 Gender differences in mean clothing insulation (a) various surveys and (b) box plot showing the differences in clothing insulation for Western and non-Western ensembles for both genders in Doha survey. Error bars indicate 95% CI around the mean

3.5 Environment Satisfaction in Asian Offices: Gender Variations

We estimated the proportions of dissatisfaction in both genders using various proxy environment satisfaction parameters as shown in Fig. 5. It can be noted that women are more dissatisfied in terms of all environment satisfaction parameters considered, and there are significant differences in thermal comfort, noise level, and lighting level satisfaction. We estimated the odds ratio for these satisfaction variables using the binary logistic function in SPSS V22. It was found that female subjects in Asia are 37.3% ($p < 0.001$, $N = 22,343$) more likely to be dissatisfied with their thermal comfort sensation with the predictive accuracy being 79%. Similarly, we noted the likelihood of women being dissatisfied with ambient noise level to be 49.8% ($p < 0.001$, $N = 3742$) with the predictive accuracy being 73.3%. Much alike, women were more likely to be dissatisfied with lighting level too (probability of dissatisfied women: 52.6%, $p < 0.001$, $N = 3742$, prediction accuracy: 76.9%). On the contrary, women are less probable (9.2%) to complain about indoor air quality ($p < 0.001$). Interestingly, Kim et al. also noted similar sensitivities among women for sound privacy, temperature, noise, and visual privacy based on the analysis of a large database collected from offices in the USA [3].

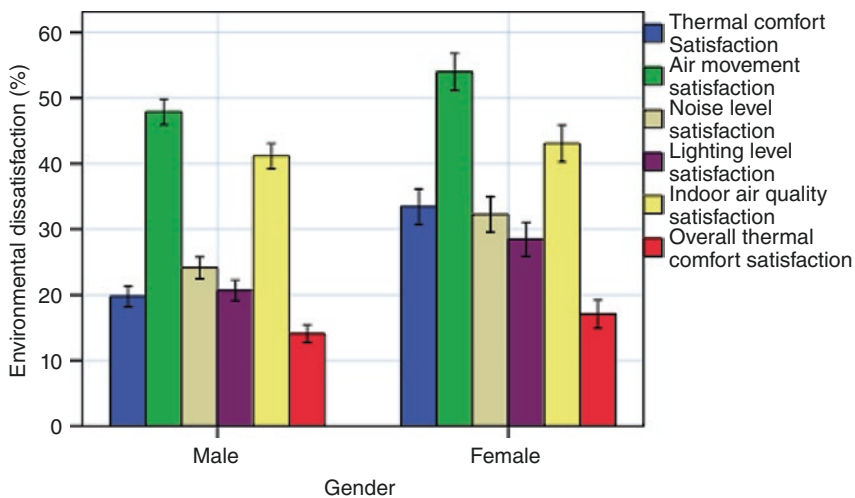


Fig. 5 Gender differences in mean dissatisfaction for various environment satisfaction parameters in Asian offices. Error bars indicate 95% CI around the mean

4 Concluding Remarks

This paper discussed the effect of age, gender, and body mass on thermal comfort perception and comfort temperature in the offices in Doha while comparing with similar data from Indian and Japanese offices. We relied on our recent field study data.

In general, more women felt cold and heat discomfort in the Doha survey. Based on all four surveys (Doha, Chennai, Hyderabad, and Tokyo), women preferred to have warmer environments in Doha. Similarly, thermal acceptance in women is also found to be lower in Doha. It can be explained by the fact that very low indoor temperatures being maintained in Doha could in part have contributed to the higher level of dissatisfaction. Further, we noted female subjects in Doha having significantly higher clothing insulation compared to the rest, owing to more stringent dress code and prevalent cultural practices.

Comfort temperature of female subjects in Doha is significantly lower than of men as compared to other cities studied. Women in younger age groups (≤ 25 years) and females in normal and high body mass index categories also had significantly lower comfort temperature compared to their male counterparts in Doha.

We estimated the environmental satisfaction using proxy parameters generated from subjective environmental sensation measurements in publicly available ASHRAE II database for Asian office buildings. It is found that Asian women are more likely to be dissatisfied with thermal comfort sensation, lighting level, noise level, and indoor air quality than men.

This study highlights the stark gender differences in comfort perceptions of female subjects in work environments in various Asian offices. Some of these differences, although not of great engineering significance, call for an attitudinal change in the design of personal environmental controls. These controls should be made available for female subjects in order to enhance their satisfaction with various environmental parameters. Only then our office environments will be inclusive. This is imperative to enhance the dwindling women's labor force participation in Asia.

Acknowledgments The author acknowledges Japan Society for Promotion of Science, The University of Tokyo, Qatar University, and the ASHRAE Database II and all the subjects for their respective contributions to the collection of the data and making the online research repositories available.

References

1. de Mattos FB, Chaudhary R (2016) Women labour force participation in Asia trends and issues, in transformation of women at work in Asia an unfinished development agenda. Sage, London, pp 23–48
2. The Economist (2018) A job of her own: culture and the labour market keep India's women at home. *Economist*:14–17
3. Kim J, de Dear R, Cândido C, Zhang H, Arens E (2013) Gender differences in office occupant perception of indoor environmental quality (IEQ). *Build Environ* 70:245–256

4. Indraganti M, Ooka R, Rijal HB (2015) Thermal comfort in offices in India: behavioral adaptation and the effect of age and gender. *Energ Buildings* 103:284–295
5. Karyono TH (2000) Report on thermal comfort and building energy studies in Jakarta, Indonesia. *Build Environ* 35:77–90
6. Rodriguez S, Pant M, Flores JC (2015) Energy price reforms in the GCC: what can be learned from international experiences? IMF, Washington, DC
7. Fattouha B, El-Katiria L (2013) Energy subsidies in the Middle East and North Africa. *Energ Strat Rev* 2(1):108–115
8. Clemente J (2015) The middle east's growing oil demand problem. In: *Forbes*
9. International Energy Agency (IEA) (2017). Available from <http://energyatlas.iea.org/#!/profile/WORLD/QAT>
10. Indraganti M, Boussaa D (2018) An adaptive relationship of thermal comfort for the Gulf Cooperation Council (GCC) countries: the case of offices in Qatar. *Energ Buildings* 159:201–212, 2018
11. Indraganti M, Ooka R, Rijal HB, Brager GS (2014) Adaptive model of thermal comfort for offices in hot and humid climates of India. *Build Environ* 74(4):39–53
12. Indraganti M, Ooka R, Rijal HB (2013) Thermal comfort in offices in summer: findings from a field study under the 'setsuden' conditions in Tokyo, Japan. *Build Environ* 61:114–132
13. Ličina VF, Cheung T, Zhang H, de Dear R et al (2018) Development of the ASHRAE global thermal comfort database II. *Build Environ* 142(9):502–512
14. Fanger PO (1970) *Thermal comfort, analysis and applications in environmental engineering*. Danish Technical Press, Copenhagen
15. ASHRAE (2010) ANSI/ASHRAE Standard 55-2010. Thermal environmental conditions for human occupancy. ASHRAE, Atlanta, GA
16. Brager G, de Dear R (2000) A standard for natural ventilation. *ASHRAE J* 42(10):21–28
17. WHO (2004) BMI classification. WHO, Geneva. Available from http://apps.who.int/bmi/index.jsp?introPage=intro_3.html. Accessed 26 May 2014

Part V
Educational Issues

Exploiting Building Information Model and Other Technologies in Facilities Management of an Educational Facility



Mohamed M. Salem, Taha A. Ahmed, Anas A. AlSarmini,
and Sana A. El-Azzeh

1 Introduction

There has been a huge economic and environmental need to manage both new and existing buildings efficiently, and it is the reason why it has been found that projects have high costs associated with the phase of operation in construction projects that account for more than 80% of total project costs [8].

Facilities management (FM) has a huge impact on the facility environment and workflow, making it a critical issue, particularly in educational facilities. Effective FM has the potential to improve the learning process, as it should provide comfort and a high-quality environment for all users. Achieving this high level of quality environment, traditional FM methods, which depend on manual work, 2D drawings and unconnected information, should be replaced by a newer, more efficient approach.

From the point of view of facility management (FM), there is a need to optimize the management of the building life cycle. A US study conducted by Jordani [3] and Rundell [6] showed that almost two-thirds of the project's estimated costs were lost due to inefficiencies during operation and maintenance phases. Current practices have shown that key challenges have arisen, such as the development of operational life cycle management, some of which are related to information collection and sharing [2].

Despite existing technologies, a full FM system has not been fully implemented in many facilities around the world. A study by the National Institute of Standards and Technology [5] on the loss of efficiency due to lack of interoperability between computer-aided design (CAD), engineering and facility management software systems is estimated at \$15.8 billion per year in the US capital facilities industry. Almost \$9 billion of \$15.8 billion per year is linked to the operation and maintenance

M. M. Salem (✉) · T. A. Ahmed · A. A. AlSarmini · S. A. El-Azzeh
Civil Engineering Department, Australian College of Kuwait, Kuwait, Kuwait
e-mail: msalem@ack.edu.kw; t.ahmed@ack.edu.kw; s.azzeh@ack.edu.kw

phase of the life cycle of the facility. This means that using FM technologies is not enough, as these technologies should be used in a better way, focusing on accessing information in an efficient, accurate and faster way.

BIM technology aims to integrate processes throughout the entire life cycle of a building. The main objective of BIM is to provide a more efficient business process, associated project and site management methodologies, including the full facilitation of construction knowledge throughout the building's life cycle [4].

BIM has also proved its efficiency in FM in many case studies around the world. A case study conducted at the University of Southern California shows that using BIM with real-time data was able to save up to 80% in operation and maintenance practices [7].

Azhar et al. [1] stated that BIM may allow facility managers to enter the decision-making process at a much earlier stage, where they can impact the design and construction phases. However, once the BIM is passed on to FM, not all data in the model will be helpful for the management of the facility during its operational stage as the model may be overloaded with unnecessary information. The information is then exchanged with multiple other software systems, such as computer-based management applications, energy management systems, electronic document management systems and building automation systems.

As for building automation systems, the level of automation in buildings has risen steadily in recent years. This is due to the continuing demand for more comfort and convenience, as well as the benefits building automation brings with regard to cost savings and managing energy.

There are a variety of automation systems for heating, ventilating and air conditioning. To ensure these systems run smoothly and economically, they are fitted with sophisticated controllers, which are often interconnected with each other and to a control centre. These control systems optimize energy consumption and enable support and maintenance personnel to carry out their jobs more efficiently. Another example of automation is automatic lighting control. Exterior lights are often linked to motion detectors, so if someone approaches them, they automatically turn on.

The Australian College of Kuwait (ACK) consists of five existing buildings and a new building under construction. ACK facilities department is using conventional way of FM. This makes it a perfect candidate for implementing new FM technologies. This research aims to showcase the potential values of using new technologies in FM department through developing a Building Information Modeling (BIM) and inventory and maintenance management systems as well as using maintenance and operational sensors in selected locations within the campus.

2 Methodology

This case study was done on Building 3 at the Australian College of Kuwait (ACK) to implement the proposed FM technologies to improve the facilities management department's work. This building was chosen for two reasons. First, the area of the

building is the smallest in comparison to all other existing buildings on campus, which improves the accuracy of the obtained results. Second, the building is easily accessible, which helps in data collection. The building area is approximately 1117 m² and consists of one ground floor only. The building includes a workshop, six classrooms, two bathrooms, facilities management department offices and an electrical room. The services of the building include electrical, HVAC, plumbing and drainage. The building was built in 2003.

Several face-to-face interviews were conducted with ACK facilities management department personnel in order to understand the current work practices and to find out the gaps and areas of improvements within their department. Based on the interview results, it was decided that the research should focus on the operation and maintenance parts of ACK facilities management department. This can be done by offering the best possible solutions to suit them by taking into consideration their current practice and work implementation processes. Thus, a Building Information Model (BIM), maintenance system integrated with the BIM, maintenance and operational sensors and inventory management system were used to complete the study.

2.1 Building Information Model (BIM)

Building Information Modeling (BIM) is to model all the building information to make it accessible to all project participants during the life cycle of the building. BIM development process begins with gathering and reviewing the available drawings of the building then conducting several visits to the building to gather any missing information and finally updating the drawings. The as-built drawings were used as a base to build the BIM. The BIM “shown in Figs. 1, 2, 3, and 4” was established using a commercial software package (Autodesk Revit 2019 version), as the

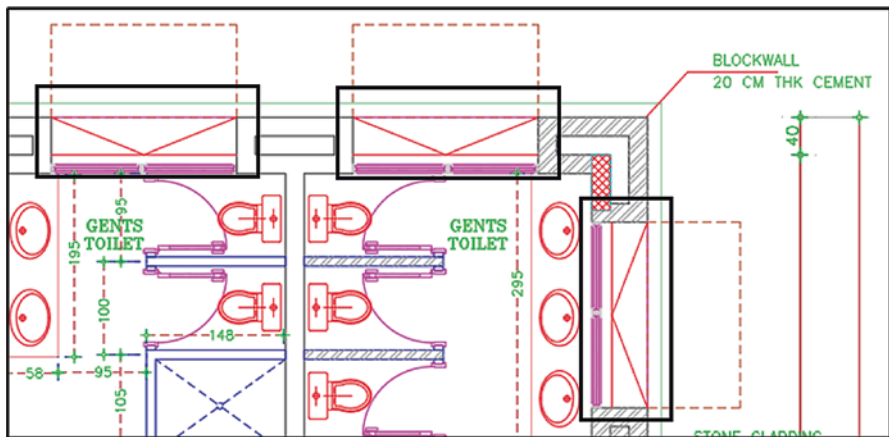


Fig. 1 Sample error in the provided 2D drawings that has been fixed (window in the bathrooms)

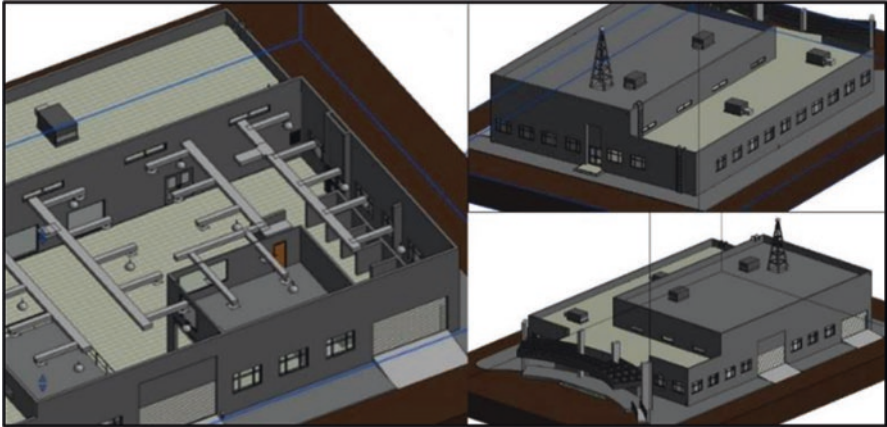


Fig. 2 Screenshots of the developed BIM

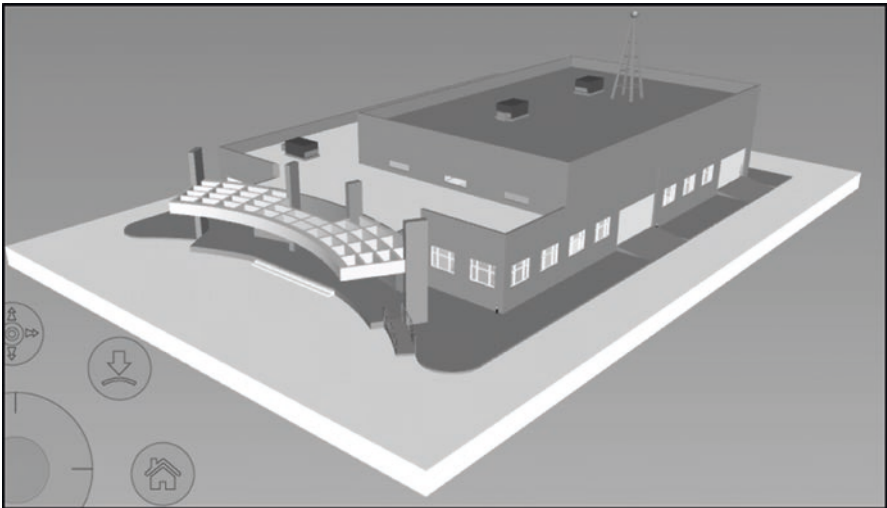


Fig. 3 Screenshot of the developed BIM

software incorporates BIM, while other packages like 3D Max and Maya offer general model design functionality.

Field inspections were done, including taking photos, videos, notes and field measurements in order to gather the essential missing information. One of the examples was a sample error in the provided two-dimensional (2D) drawings which showed there were three windows in the bathrooms “shown in Fig. 1”, which was found incorrect after the field inspection.

The Level of Details (LOD) for the developed model is 500, which means it represents the as-built model. The model was developed using 2D drawings and



Fig. 4 Screenshot showing an internal part of the developed BIM

field inspections in addition to considering all other ACK FM requirements. RetroBIM framework was adopted for this research study. RetroBIM framework was developed by G. Carbonari et al. [9].

The developed BIM was used as a centre of organized data for the investigated building. It was also integrated in other parts of this study such as the maintenance system.

2.2 Maintenance System Integrated with BIM

ACK current maintenance workflow is a traditional manual and time-consuming process, which includes several management steps and processing a significant amount of paperwork in order to finish a single maintenance task. The proposed solution to improve this traditional workflow was to consolidate all these steps into one single step using a mobile application and a computer software. This enhances the accuracy and reduces the time needed to complete any maintenance task. In this study, several applications were investigated in order to select an application that can fit ACK facilities management system.

The research team selected a maintenance application called BIM 360 Field to be used instead of the traditional maintenance workflow process. This BIM 360 Field is a commercial cloud system by Autodesk Company, which allows the users to access, import and update assets information from a mobile device. Additionally, it can support the maintenance program by scheduling asset inspections, including a checklist based on a particular procedure, which has the name of the technicians assigned to the maintenance and monitor compliance with a work order. The

selection of BIM 360 Field is due to its simple user's interface and low cost. The BIM 360 Field is usually used in construction works. However, it was found that this application can meet all of ACK facilities management requirement.

The BIM was exported to BIM 360 Field after doing all the needed configurations. The BIM 360 Field provides access to information from a personal computer or a mobile device.

Switching the maintenance workflow from a manual task to a faster and accurate electronic way significantly improved the maintenance work practices as shown in Table 1 and Figs. 5, 6, and 7.

2.3 Building Automation

This section gives an overview of the types of sensors installed in Building 3. The sensor nodes of the software interface have been provided by GateLink which has a wide range of low power sensor modules that can be used for both household and industry applications.

Smart thermostats were installed in Building 3 (Fig. 8). They are designed for remote configuration, and there are no manual adjustment buttons which prevents the cooling or heating system from being tampered with or left in an energy wasting state.

Wireless temperature sensors were also used to accurately measure temperature. These sensors are monitoring ambient temperatures around the sensor's physical location. The system also allows the facility manager to set a maximum and minimum temperature range for both occupied and non-occupied states. The facility manager can set the frequency of readings and the ability to send alerts via SMS text and/or email (Fig. 9). The system will save energy and reduce the overall energy

Table 1 Comparison between the old and new way of maintenance workflow

Old way	New way
Technicians receive the work order by a phone call or text message	Technicians receive the work orders on their portable device and can view and comment before starting the actual work
Technicians can update the work order through manual papers which have the risk of losing it, and also the needs to be hand-delivered to the facilities manager	Technicians have a portable device which allows them to better communicate with their facilities managers as shown in "Fig. 5"
Technicians don't have a full knowledge about the locations they are working in	Technicians can view maintenance locations and their surroundings as shown in "Fig. 6"
Facilities managers use papers and manual planning to plan maintenance schedules	Facilities managers can easily create electronic maintenance schedules with checklist reminders
Facilities managers have to enter the information manually and depend on manual work to monitor all the tasks and review the status of all maintenance work	Facilities managers can monitor and review the status of all maintenance tasks at any time (Fig. 7)

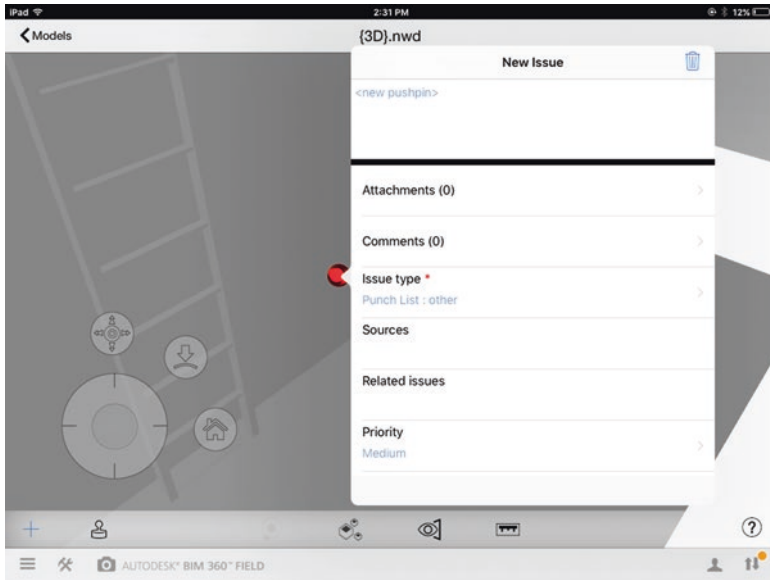


Fig. 5 Screenshot of the portable device screen showing a work order creation with one click on the subject



Fig. 6 Screenshot of the portable device viewing the locations and everything around it

cost by allowing the cooling or heating system go into a power saving mode if an area is not in use.



Fig. 7 Facilities manager is discussing maintenance task with a technician

Fig. 8 Smart thermostat



Motion sensors were also installed to auto-detect occupied areas (Fig. 10). The sensors use a sensing technology to accurately detect movements made by people within 16.4 ft (5 m) range. Lights will be turned off automatically if the rooms are unoccupied. This is an excellent solution for educational buildings that are typically unoccupied in several instances where classrooms, labs and workshops are not utilized during the working hours.

The motion sensors can also be used for security purposes if a movement detect outside usual working hours.

The GateLink Ethernet gateway was also installed to allow the wireless sensors to communicate with the iGateLink™ Online Wireless Sensor Monitoring and Notification System without the need for a computer (Fig. 11). The sensor nodes send the event logs to the GateLink Hub which in turn communicates with the iGateLink server.

Sensors and devices have been installed and tested. The sensors and devices cost \$13,000, and energy consumption year 2018 for Building 3 is \$9628 (ACK FM department). The potential savings cannot be measured at this stage due to time

Fig. 9 Wireless temperature sensor



Fig. 10 Wireless motion sensor



limitation. However, a full investigation will be conducted on the effect of the installed automation system on energy saving potential.

2.4 Inventory Management System

Several face-to-face interviews were conducted with inventory management personal to understand the whole work process which concluded that current workflow is slow, inaccurate and time-consuming complex data spreadsheets, stores are not connected, manually entered data process, inability to track assets or stock parts, inability to access any information in the stores and invoices being archived using traditional scanning method.

Fig. 11 Ethernet gateway

The study aimed to solve the above issues as well as to provide new features, such as quantity on hand, stock inventory report, alerts when reaching the maximum or minimum quantity, adding new units, adding more than one location for any building's section, check-in and checkout list, immediate access to asset locations, cost reduction from idle allocation assets, data integration with mobile devices through utilizing barcode scanners, assets tracking system, producing management reports and records to auditing purposes.

In order to set all the proposed features, an intensive research for the most appropriate system was conducted. It was found that the commercial software named as "Bar Cloud System" can successfully complete all the proposed tasks. This electronic system is easy to install and use. The main benefits of the system are to re-link databases, restore inventory management, track assets and fix errors. In order to import all the FM data and information in the new system, a data redefining process was done for all the facilities' assets, stock and spare parts inventory. Additionally, the redefining process included creating new labels and codes for all the mentioned parts.

The new developed inventory system is connected to the developed BIM. Also it is accessible through the portable device that facilities management team carry around as shown in Fig. 12.

2.4.1 Assets

The redefining process of assets included new assets codes, which consisted of numbers and letters. These new codes were listed in an excel spreadsheet, which later on was imported into the new database system. The old assets codes used to



Fig. 12 Showing a technician accessing Bar Cloud System through a portable device and using assets barcode scanning feature

have only numbers, for example, the code for “Student Folding Table” was “1”; however it was changed to “A-000001”. The letter “A” represents the word “Assets”. The new assets coding procedure made it easy and faster for the technician to record and organize the data in the system.

2.4.2 Stock and Spare Parts Inventory

Similarly, the stock and spare parts inventory data provided by the FM department were modified and redefined. The data modifications process included rearranging the parts based on the family to which they belong (consumables, carpentry, electrical, plumbing, HVAC, civil parts and furniture), which were listed under a new column called category ID as shown in Table 2. The changes that have occurred are the adjustments of stock number as shown in Table 3 to stock item number as shown in Table 2. Now, it can be seen that the stock item number became more descriptive as it describes the item type, in the code cell. Also, previous items, which were known as code and description, were combined together into one item type code in order to reduce the amount of unnecessary data and to combine the same category items under one list.

In order to avoid additional expenses, numerical accumulation and misuse of storage areas, maximum and minimum quantities limits of each item must be previously determined and included in the system. The determination of maximum and minimum quantities can be done based on the time of delivery by vendors, the life span, the extent of consumption and storage capacity. Additionally, the cost of each item was recorded and categorized accordingly, which then was included in the total budget. This can be seen in Table 2.

Finally, after finalizing all the data modifications and preparation, the data was imported into the system and linked to their corresponding fields.

Table 2 Sample of Excel sheet data for stock and spare parts after the modifications

Stock Item #	Stock Description	Description Short	ID Category	Item Type Code	Description General	Class ID	Balance Quantity	Stock Minimum	Stock Maximum	Cost	Location ID Default
ELT/LMP/MT1000	Street Light Lamp	Spares	Electrical	CODE # MT1000-LAMPS & TUBES	250w	Consumables	6	5	24	12,000	BD-2/Warehouse
ELT/LMP/MT1001	Street Light Lamp	Spares	Electrical	CODE # MT1000-LAMPS & TUBES	400w	Consumables	32	10	32	8,000	BD-2/Warehouse
ELT/LMP/MT1002	CFL 865 lamp 2pin Cool Day Light	Spares	Electrical	CODE # MT1000-LAMPS & TUBES	26w	Consumables	240	100	300	2,000	BD-2/Warehouse
ELT/LMP/MT1003	CFL 865 lamp 4pin Cool Day Light	Spares	Electrical	CODE # MT1000-LAMPS & TUBES	26w	Consumables	490	100	500	2,500	BD-2/Warehouse

Table 3 Sample of Excel sheet data for stock and spare parts as provided before the modifications

Stock #	Code	Description	Short Description	Generic Description	Class ID	Quantity Balance
1	CODE # MT1000	LAMPS & TUBES				
2	ELT/LMP/MT1000	Street Light Lamp	Spares	250w	Consumables	6
3	ELT/LMP/MT1001	Street Light Lamp	Spares	400w	Consumables	32
4	ELT/LMP/MT1002	CFL 865 lamp 2pin Cool Day Light	Spares	26w	Consumables	240

3 Results

This case study aimed to show how BIM system can be used effectively to meet all the FM requirements in an educational facility using the proper technologies and in an appropriate way to improve the current practices. Also, it provides a foundation for future improvements of the facilities management department at the Australian College of Kuwait. Furthermore, it also showed that the facilities management team were able to implement the new proposed technologies. The study included developing a Building Information Model (BIM), maintenance system integrated with the BIM, installing automation sensors and inventory management system.

The BIM provided a one centralized and accessible location of information. Also, it provided an easy way to understand the hierarchy and organization of facilities for newly joined FM members. It also laid the foundation for future improvements such as mobile localization of building resources, digital asset with real-time data, space management, renovation/retrofit planning and feasibility studies, maintainability studies, energy analysis and control and safety/emergency management [10].

The integrated maintenance system with the BIM provided smoother workplace environment, fast and easy access to FM information, digitization of the whole maintenance process and easy generation of maintenance reports.

4 Conclusions

Since not all new buildings are designed and constructed using BIM, the suggested RetroBIM framework offers a methodology that can be applied by facility managers to help them apply BIM in FM tailored requirements. The created model would not

only support the building's operation but would also act as an enabler for data interpretation and assessment.

In fact, BIM has several applications and has been used for some time now, in particular for design and construction however, the creation of models for existing buildings is not a common process, and the availability of BIMs during operation is limited. Thus, the RetroBIM framework was developed to extend BIM's advantage into practice, demonstrating a new approach to implementing information models that can be tailored to the need of management and the building.

The created BIM was tested and used by the FM department at ACK, and they have provided positive feedback on the applicability and usefulness of the model.

Installing a building automation system that controls various occupied classrooms may have the ability to save energy. There is still a lot of research to be accomplished in the field of building automation and with a system such as GateLink system, and ACK may be able to progress through automation into the next phases of energy savings.

The inventory management system helped in assets management by providing better ways to perform day-to-day assets' transactions, to easily view assets' data and to simplify the inventory management work. It also helped in stock and spare parts management through the electronic receiving of inventory and purchasing orders and performing day-to-day stock and spare items transactions.

Acknowledgement The authors would like to thank the Facilities Department personnel at the Australian College of Kuwait (ACK) for providing the necessary data and their endless support to this research study. Also, they would like to thank Mr. Waleed AlKuzbari and Ms. Zahraa Abul, ACK students, for their significant contribution in this case study.

References

1. Azhar S, Nadeem A, Mok JYN, Leung BHY (2008) Building Information Modelling (BIM): a new paradigm for visual interactive modelling and simulation for construction projects. In: Proceedings of the First International Conference on Construction in Developing Countries: Advancing and Integrating Construction Education, Research & Practice, Karachi, Pakistan, pp 435–446
2. Cardellino P, Finch E (2006) Evidence of systematic approaches to innovation in facilities management. *Journal of Facilities Management* 4(3):150–166. <https://doi.org/10.1108/14725960610673742>
3. Jordani D (2008) BIM: a healthy disruption to a fragmented and broken process. *Journal of Building Information Modelling* 2:24–26
4. Kymell W (2008) Building information modeling planning and managing construction projects with 4D CAD and simulations. McGraw-Hill, New York, NY
5. NIST (2019) National Institute of Standards and Technology | NIST. Available from <https://www.nist.gov/>. Accessed 12 Mar 2019
6. Rundell R (2006) How can BIM benefit facilities management? In: Primeedge. Available from <http://www.cadalyst.com/cad/building-design/1-2-3-revitbim-and-fm-3432>

7. Davtalab O (2017) Benefits of real-time data driven BIM for FM departments in operations control and maintenance. In: *Computing in civil engineering 2017*. American Society of Civil Engineers, Reston, VA, pp 202–210. <https://doi.org/10.1061/9780784480823.025>
8. Costin A, Pradhanananga N, Teizer J, Marks E (2012) Real-time resource location tracking in building information models (BIM). In: *Cooperative Design, Visualization, and Engineering 9th International Conference*, Osaka, Japan, 2–5 September 2012
9. Carbonari G, Stravoravdis S, Gausden C (2015) Building information model implementation for existing buildings for facilities management: a framework and two case studies. In: *WIT transactions on the built environment*. WIT Press, Southampton, pp 395–406. <https://doi.org/10.2495/BIM150331>
10. Nicał A, Wodyński W (2016) Enhancing facility management through BIM 6D. *Procedia Engineering* 164:299–306. <https://doi.org/10.1016/j.proeng.2016.11.623>

Shifting the Learning of Engineering Mechanics and Dynamics Paradigm from Hands-On Experiments to Mobile Virtual Labs



Anwar Alroomi

1 Introduction and Background

Statics, Mechanics, and Dynamics are considered very important and fundamental courses in both Civil Engineering and Mechanical Engineering. Also, they are considered as main prerequisites for different design and analysis courses. Thus, it's very important that students capture and thoroughly understand the main concepts of these fundamental courses. Recently, researchers found that learning using the one technique or method that fits all is no longer applicable anymore [1]. Using virtual labs and mobile apps help in facilitating learning and competency development by allowing the users to test and compare different scenarios and experiments setting that might be difficult to perform due to time and cost constraints [2]. In addition, Jiang et al. [3] found that lack of practical examples, accessible materials, and timely interactions and feedback from the instructor are considered as the main three factors affecting students learning and knowledge resulting in low passing grades in the course.

Recently many educators have been geared toward developing virtual learning environments to enhance and improve learning techniques and facilitate the knowledge and competency development process among students. Learning environments have been defined by Al-Emran et al. [4] who stated that "Homan and Wood (2003) defined mobile learning as the technology that changed the way students communicate, interact, and behave with each other and their perceptions toward their learning." Meanwhile, Matias and Wolf [5] stated that mobile learning extends to the learning that is facilitated across multiple contexts using portable mobile devices.

Material covered in AM 317 Mechanics Lab are beam deflection, force in a truss member, bending stress in a beam, torsion test, buckling, springs in series and

A. Alroomi (✉)

Department of Civil Engineering and Construction Management, California State University, Northridge, CA, USA

e-mail: anwar.alroomi@csun.edu

© Springer Nature Switzerland AG 2020

A. Bumajdad et al. (eds.), *Gulf Conference on Sustainable Built Environment*,
https://doi.org/10.1007/978-3-030-39734-0_29

515

parallel, mechanics vibration of a rigid beam with viscous damping, vibration of coupled pendulums, two-pinned arch, and dynamic unbalance (AM 317 Lab Manual [6]). As students with varying level of knowledge and competency learn at different base, and with the limited time to perform experiments and the high cost of equipments, the hands-on experimental sometimes is inefficient to demonstrate the entire picture and achieve the desired learning outcomes. In addition, with advancement of technology and availability of mobile devices and accessibility of mobile applications, mobile devices are proven to be an effective means used in education due to their computational power and accessibility [3].

In a study, Al-Emran et al. [4] found that using and adopting mobile learning frameworks have a positive impact on the learning environment due to their availability, flexibility, usability, maintainability, functionality, reliability, connectivity, user interface, and security. In addition, mobile learning can enhance the interaction and collaboration among peers and students/faculty relationships [7]. In addition, a study by Holotescu et al. [8] stated that education is now facing the challenge of online learning approaches, openness toward social media, and open educational resources and online course. Educators must adapt technologies and mobile sources to close gap between the traditional learning and online/mobile learning. In addition, they found that the developed app helped in improving the digital skills for different users as they continue using the app. Cukierman et al. [9] stated that utilizing online/mobile technologies facilitates the learning process and interactions between users and mobile devices laboratories (apps) by allowing the users to customize their own experiments based on their needs. Finally, providing diverse learning means can help universities in retaining first year engineering students within the major.

The purpose of this study is to improve STEM education practices and curricula by improving the learning environment and practices to achieve the desired learning outcomes. This study will help students to explore and utilize open web resources and e-learning platform for STEM education, provide a mean to assess the practicality of e-learning platforms in STEM field, provide alternatives to hands-on experiments in STEM field, and identify inexpensive means to facilitate STEM education.

2 Methodology

In this paper we will present the modeling process for two experiments out of ten hands-on experiments taught at AM 317 course as shown in Table 1. Both experiments which are the springs in series and parallel (Exp 6) and the two-pinned arch (Exp 9) were first performed as hands-on experiments to collect data, perform the necessary calculations, and finally develop the required charts and report the results. Then, using Qdex interface, both experiments were coded. Figure 1 shows a sample code in Qdex interface for experiment 6 “springs in series and parallel.” Qdex is a platform developed by Quanser engineers to empower educators to create innovative

Table 1 AM 317 mechanics lab experiments

Experiment title	Status
Exp 1: Beam Deflection	In progress
Exp 2: Force in a Truss Member	In progress
Exp 3: Bending Stress in a Beam	In progress
Exp 4: Torsion Test	In progress
Exp 5: Buckling	In progress
Exp 6: Springs in Series and Parallel	Developed
Exp 7: Mechanics Vibration of a Rigid Beam with Viscous Damping	In progress
Exp 8: Vibration of Coupled Pendulums	In progress
Exp 9: Two-Pinned Arch	Developed
Exp 10: Dynamic Unbalance	In progress

content for their students that are considered time and cost effective. Qdex offers a helpful mean to design, develop, and publish models. The developed models can help in better understanding and visualizing our experiment design output and improve the learning process. The simulation features represent the mathematical solver and the express evaluator with real-time technical simulations. It also allows to store images, YouTube videos, animated GIFs (Graphics Interchange Format). In addition, the simulated experiments developed in Qdex are available for free for faculty and students to share and compare models using a web browser or a mobile app for both Android and iPhone systems. Qdex can be used as a learning platform for mathematical and science material in STEM fields.

Experiment 6 Springs in Series and Parallel This experiment is designed to (1) study the relationship of springs connected in series and parallel and determine the equivalent spring constant and (2) study the asymmetric loading of parallel springs (AM 317 Lab Manual). Also, in experiment 6, students are required to understand the different types of spring combinations (in series or in parallel) behavior when loaded and determine the spring constant k using Hooke's law:

$$F = k\Delta$$

where

F = applied force

Δ = the resulting displacement

Figure 2 shows the Qdex mobile model for the springs in series and parallel experiment. The mobile model consists of six parts. The first part shows the objectives of experiment and learning outcomes. It is followed by a brief background and theory to help the students understand what is expected, what equations will be used, and what the expected results are. The third section lists all the equipment required for the hands-on procedure. The fourth section shows the detailed procedure for the hands-on experiment. The fifth section shows the different spring connections whether in series and/or in parallel along with the equation used for data


```

<section>
<title>I. OBJECTIVES</title>
<p>I. 1 To study the relationship of springs connected in series and parallel and determine the equivalent spring constant.</p>
<p>I. 2 To study the unsymmetrical loading of parallel springs.</p>
</section>
<section>
<title>II. BACKGROUND</title>
<p>Springs are devices that can store and release energy. Because of these properties, springs are very important in engineering. It is therefore essential that engineers understand the different types of springs combinations behave when loaded.</p>
<p>Springs can be combined in series, parallel and in a combination of the series and parallel. Each spring or spring system can be characterized it spring constant <math>k</math>. The spring constant can be determined by use of Hooke's Law:</p>
<equation>

$$F = k\Delta x$$

</equation>
<p>where</p>
<p> $F$  = applied force</p>
<p> $\Delta x$  = the resulting displacement</p>
</section>
<section>
<title>III. EQUIPMENT</title>
<p>III.1 Assorted springs, hooks and aluminum bars.</p>
<p>III.2 Steel scales</p>
<p>III.3 Steel frame</p>
</section>
<section>
<title>IV. PROCEDURE</title>
<p>IV.1 Determine the spring constant for each individual spring using Eq. 6.1. When determining the spring constant, be sure the spring has an initial load sufficient to separate the coils and remove the pretension. Determine the deflection due to several loads and take the average value for the spring constant,  $k$ . You may fit a linear trend line to the force-deflection data to obtain the spring constant.  $k$  will be the slope  $m$  of the trend line ( $y=mx+b$ ) and  $b$  is the initial preload required to separate the coils of the spring.</p>
<p>IV.2 Set up the spring system shown in Figure 1,2 and 3 to determine the equivalent spring constant for each system.</p>
<p>IV.3 Construct the spring system shown in Figure 4 and determine the equivalent spring constant. You will need to use two pairs of springs with matching spring constants to obtain good results.</p>
</section>
<title>Figure 1 and Equations</title>
<image src="resources/fig1.jpg" style="medium" />
<button name="myEbony" content="Show Equations 8.2,8.3,8.4">
<onClick>
if myEbony.Text == "Show Equations 8.2,8.3,8.4" then
myEpOneStack.Style.Visibility = "visible"
myEbony.Text = "Hide Equations 8.2,8.3,8.4"
elseif myEbony.Text == "Hide Equations 8.2,8.3,8.4" then
myEpOneStack.Style.Visibility = "collapsed"
myEbony.Text = "Show Equations 8.2,8.3,8.4"
end
</onClick>
</button>
<stack name="myEpOneStack" style="collapsed">
<equation>

$$F_1 = F_2 = F_3$$

</equation>
<equation>

$$\Delta x_1 = \Delta x_2 = \Delta x_3 = \frac{F_1}{k_1} + \frac{F_2}{k_2} = \frac{F_3}{k_3}$$

</equation>
<equation>

$$k_{eq} = \frac{F_3}{\Delta x_1 + \Delta x_2} = \frac{F_3}{\frac{F_3}{k_1} + \frac{F_3}{k_2}} = \frac{F_3}{F_3 \left( \frac{1}{k_1} + \frac{1}{k_2} \right)}$$

</equation>
</stack>
</section>
<section>
<title>Experimental VS Theoretical K Averages</title>
<xyPlot>
<axis dim="x" auto="fixed" min="0" max="5">
<title>Experiments</title>
</axis>
<axis dim="y" auto="fixed" min="0" max="7">
<title>Average k (lb/in)</title>
</axis>
<series draw="line">
<data>0 0; 1 0.53416667; 2 1.45833333; 3 3.96416667; 4 5.415</data>
</series>
<series draw="line">
<data>0 0; 1 0.60666667; 2 1.37166667; 3 2.73166667; 4 3.45</data>
</series>
</xyPlot>
<p>Red = Experimental K Average</p>
<p>Blue = Theoretical K Average</p>
</section>

```

Fig. 1 Experiment 6 coding in Qdex web-based interface

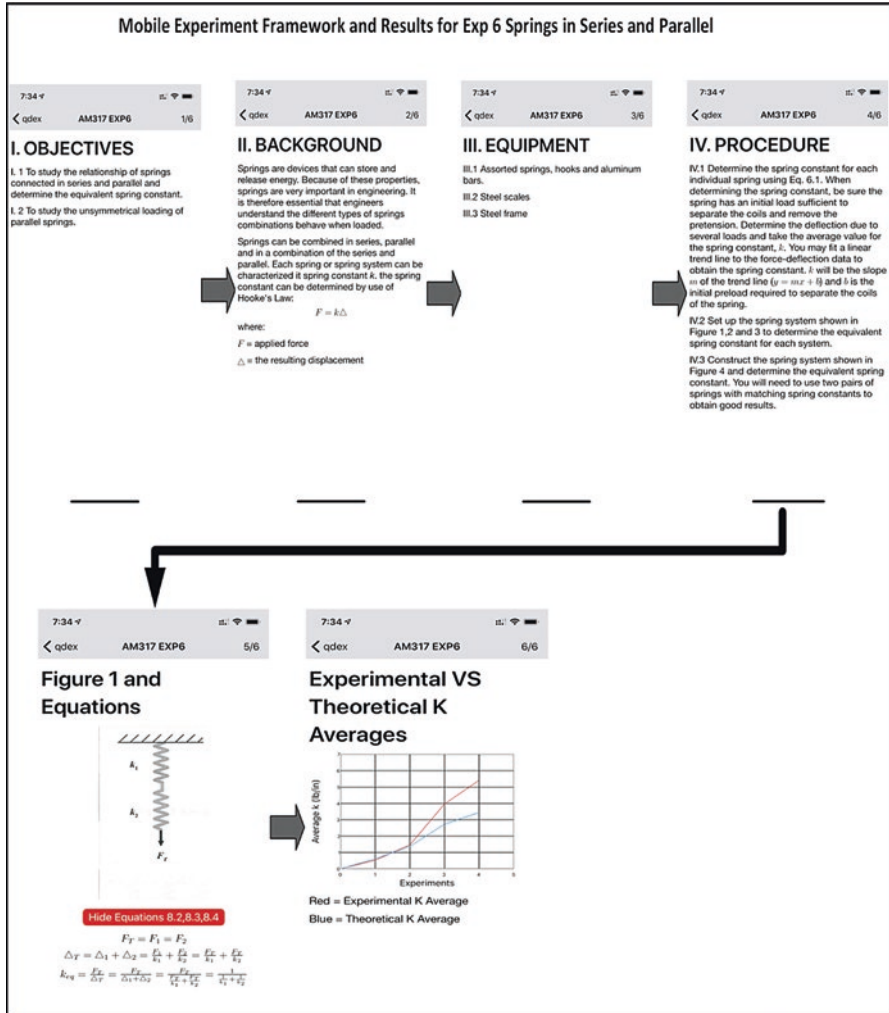


Fig. 2 Qdex mobile model for Experiment 6 springs in series and parallel

analysis, to help the user visualize the experimental connection and how it affects the use of the equation to calculate the spring constant (k). The final section shows the graphical solution which illustrates the difference between the theoretical and the experimental spring constants (k).

The coding process of this experiment is still under modifications. The research team is working on adding different spring's options and layouts. Also, the team is in the process to enable the users to show all calculation table and results comparisons. The Qdex model provided an alternative means to the students to learn and visualize the difference in results and compare their hands-on experiment results

with different groups and determine the percentage error between theoretical and experimental values.

Experiment 9 Two-Pinned Arch This experiment aims to help students (1) explore and understand the relationship between the load and the horizontal reaction force in a two-pinned arch, (2) determine the horizontal thrust force and reaction influence lines for a point load moving across a two-pinned arch, and (3) determine the horizontal thrust force for a uniformly distributed load in a two-pinned arch (AM 317 Lab Manual).

The horizontal thrust force for a given load p at location x is calculated by (AM 317 Lab Manual)

$$H_B = \frac{5Px}{8rL^3} (L^3 + x^3 - 2Lx^2)$$

where

H_B = the horizontal thrust reaction at B (N)

P = the load (N)

L = the span of the arch (m)

x = the load location, distance from the left-hand side support (m)

r = the rise of the arch (m)

The thrust force is calculated using the following equation (AM 317 Lab Manual):

$$H_B = \frac{wL^2}{8r}$$

where

H_B = the horizontal thrust reaction at B (N)

w = the intensity of uniform distributed loads (N/m)

L = the span of the arch (m)

r = the rise of the arch (m)

Figure 3 shows the Qdex mobile model for the two-pinned arch experiment. The mobile model consists of five parts. The first part shows the objectives of experiment and learning outcomes. It is followed by a brief introduction, background, and theory to help the students understand what is expected, what equations will be used, and what the expected results are. The third section lists all the equipment required for the hands-on procedure. The fourth section shows the detailed procedure for the hands-on experiment. The fifth section shows the data collected and analysis results for the experiment along with graphical illustrations for the experimental versus theoretical thrusts determined in this experiment. In addition, the percentage error between the theoretical and experimental results was calculated. The developed mobile model helped in visualizing different scenarios forces and provided a mean to better understand the thrust behavior and concept.

Mobile Experiment Framework and Results for Exp 9 Two-Pinned Arch

I. OBJECTIVES

- 1.1 To explore the relationship between the loads and the horizontal reaction force in a two-pinned arch.
- 1.2 To determine the horizontal thrust force and reaction influence lines for a point load moving across a two-pinned arch.
- 1.3 To determine the horizontal thrust force for a uniformly distributed load on a two-pinned arch.

II. INTRODUCTION and BACKGROUND

The main advantage an arch has over a beam, is that it can carry a much larger load. Historically arches were important because they could be constructed using small, easily carried blocks of brick or stone rather than using a massive, monolithic stone beam or lintel. Romans used the semicircular arch in bridges, aqueducts, and large-scale architecture. In most cases they did not use mortar, relying simply on the precision of their stone finish. When an arch is loaded by gravity forces, the pressure acts downward on the arch and has the effect of compressing it together instead of pulling it apart. A free-body diagram of the arch supports shows the arch requires both horizontal and vertical reaction forces (Figure 2). This horizontal reaction force, called thrust, can cause the arch to collapse if it is not properly restrained.

One of the disadvantages of the arch resisting loads in compression is the possibility that the arch may buckle. Any practical arch design would include analysis involving stress, deflection and buckling. To perform such analysis, reaction forces shear and moment diagrams are needed for a given load case. Since the arch is indeterminate, having more unknown reactions forces than equilibrium equations, methods such as the flexibility method are required to determine the reaction forces.

Structures test frame
Digital force display and power supply
Aluminum arch
Hangers and weights
Scale




Figure 1 In Loads Arch




Figure 2 Free-Body Diagram of Two Pinned Arch

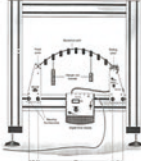


Figure 3 Test Frame and Two Pinned Arch Setup

IV. PROCEDURE

- Visually inspect all parts of the test frame (including electrical leads) for damage or wear.
- Check that electrical connections are correct and secure.
- Check that all components are secured correctly and fastenings are sufficiently tight.
- Check the four securing thumb screws are in the position show in Figure 3 and the rolling pivot on the right is gently resting against the load cell.
- Make sure the digital force display is on and the force transducer is connected from the socket marked "Force Output" on the right support, to the Digital Force Display "Force Input 1".
- Carefully zero the force meter using the dial on the right-hand side support. Gently apply a small load with a finger to the crown of the arch and release. Zero the meter again if necessary.

NEVER apply excessive loads to any part of

TABLES

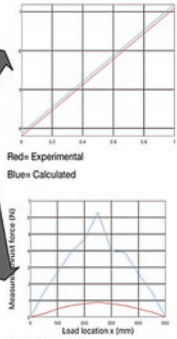
Rise of arch, r (m)	1 m
Length of arch, L (m)	5 m

added mass		100 gm	500 gm
Hanger mass	10 gm	10 gm	
Total mass	110 gm	510 gm	
Total weight	1.08 N	5 N	

Load location x (mm)	Measured thrust force for 100 gm load (N)	Measured thrust force for 500 gm load (N)
0	0	0

Total mass of hangers (gm)	Units/m distributed load (N/m)	Meas used thrust force (N)	Calculated thrust force (N)	% Error
540	90 gm	1.24 N/m	3.875 N	1.94 %
1080	90 gm	2.3 N/m	7.1 N	1.22 %

Experimental vs Calculated



Red = Experimental
Blue = Calculated

Blue = 500 gm load
Red = 100 gm load

Fig. 3 Qdex mobile model for Experiment 9 two-pinned arch

3 Conclusions and Recommendations

This study is still under development; however, the initial developed models for both experiments were very promising and easily coded and developed by freshman and junior students. The results indicate that Qdex is very effective in providing a variety of ways to design, develop, and publish models for structural mechanics and dynamics with less costs and risks. This study will enrich the classroom activities and provide wider range of learning possibilities, which will have positive impact on our learning methodology and outcomes. In addition, this study will help students to strengthen their understanding of the theoretical concepts and improve their

self-learning capabilities. The results of this study will help in advancing students learning of the subject (mechanics/dynamics) and how to design and use virtual technology. The study is in early stages; out of ten experiments required for the course, only two were coded and presented in this paper. Once the analysis of all experiments is completed, evaluation and recommendations regarding the utilization of virtual technology will be made. Also, a comparison between effectiveness of the adaptation of virtual learning environments and mobile apps in leveraging learning topics as mechanics and dynamics will be evaluated.

The study shows high potential in adopting virtual mobile model to enhance learning practices and escalate the capturing and transfer process of the knowledge and competency taught in mechanics courses. Future work will be geared toward implementing the developed models in the mechanics' lab and evaluate the effectiveness of mobile models of the experiments and compare the results to the performed hands-on experiments.

Acknowledgments The authors would like to thank the funding from AIMS² – Attract, Inspire, Mentor, and Support Students grant at California State University, Northridge, and both undergraduate AIMS² students assisted in this study Alexis Sierra and Omar Lopez for their dedicated efforts.

References

1. Alroomi A, Jeong D, Oberlender G (2016) Evaluation of methods to retain cost estimating competencies using structural equation modeling. *J Manag Eng* 32(1):04015026
2. Preston J (2012) Using virtual gaming environment in strength of materials laboratories. American Society for Engineering Education, Washington, DC
3. Jiang Z, Maxwell A, Merchant Z (2018) Using mobile learning to improve low success rate in engineering courses. American Society for Engineering Education, Washington, DC
4. Al-Emran M, Elsherif H, Shaalan K (2015) Investigating attitudes toward the use of mobile learning in higher education. *Comput Hum Behav* 56:93–102
5. Matias A, Wolf D (2013) Engaging students in online courses through the use of mobile technology. In: *Cutting-edge technologies in higher education*, vol 6, Part D. Emerald Group Publishing Limited, Bingley, pp 115–142
6. California State University, Northridge (n.d.) AM 317 mechanics lab manual. Available from <http://www.csun.edu/engineering-computer-science/civil-engineering-construction-management/mechanics-laboratory>
7. Dascalu M, Bodea C, Lytras M, De Pablos P, Burlacu A (2014) Improving e-learning communities through optimal composition of multidisciplinary learning group. *Comput Hum Behav* 30:362–371
8. Holotescu V, Vasiiu R, Andone D (2018) A critical analysis of mobile applications for learning. Study case: virtual campus app. *BRAIN* 9:110. Special issue on Educational Psychology. ISSN 2067-8957
9. Cukierman U, Agüero M, Silvestri S, Delmonte R, Drangosch J, Corrao L, Ferrando D, Saclier L (2017) Bridging the gap between first-year students and engineering: a novel application of mobile technologies for improving mathematics and physics learning. In: 2017 7th World Engineering Education Forum (WEEF)

Index

A

- AASHTO T378 test, 115
- Abaqus/Cae model, 220
- Acceleration comparison graph
 - ground, 265
 - seventh floor, 265
 - third floor, 265
- Acceleration data, 264
- Accelerations vs. displacements, 264
- Accelerometers, 281
- ACICO Industries Company (ACC), 78
- Age, 484, 485, 489, 493, 494, 496
- Aging effects, 302
- AI-based—formulation methods, 44
- Air conditioning, 440
- Air-conditioned (AC) mode, 484
- Al-Hamra tower, 279
 - B2 floor, 284
 - geometric shape, 281
 - higher floors, 285
 - instrumentation design, 284
 - instrumented floors, 282, 283
 - sensors and channels, 282
 - SHM system, 281
 - structure, 280
- Air leakage, 445
- Air transport equation, 423
- Alkali silica reactivity, 88
- Aluminosilicate nanoparticles
 - BET microstructural analysis, 149, 152
 - characterization, 147
 - in situ Raman spectroscopy, 148, 149
 - materials and methods, 146
 - metakaolin, 145
 - nanoindentation test, 152, 154
 - silica and alumina, 146
 - volcanic ash, 145
- AM 317 Mechanics Lab, 515–517, 520
- Ambient air, polymer nanocomposite LSC films deposition
 - acrylic coating, 377
 - advantage, 375
 - FTIR absorption, 378
 - microscope image, 377, 378
 - morphology, 376
 - polymer PMMA, 375, 376
- American Disability Association, 388–389
- American National Standards Institute (ANSI), 339
- American Society of Civil Engineers (ASCE), 291
- Annual heating, 454
- Annual Solar Exposure (ASE), 384, 390
- ANSI/ASHRAE/IESNA Standard 90.1-2007, 389
- Arabian Gulf
 - archaeological record, 185, 186
 - Bronze Age, 191
 - Kassite domination, 204
 - Mesopotamian House sherds, 203
 - pottery, 195, 208
 - trade network, 187, 188
 - western coastline, 190
- Architectonic monument
 - conservation/restoration, 173
 - financial aspects, 179, 183
 - fundamental documents, 173
 - ICOMOS, 174
 - issues, 173
 - Poland, 174
 - preservation works, 173
 - Torun

- Architectonic monument (*cont.*)
 Cathedral of SS, 182
 Copernicus House, 181
 Gothic Town Hall, 181
 Leaning Tower, 180
 old town, 180
- Architectural geometry, 46
- The Arctic city
 CFRP cables, 67
 “City in the Arctic”, 66
 “Shadow in the Desert”, 67
 technical data, 66, 67
- Arrival picking method (APM), 271
- Artificial intelligence (AI), 32
- ASHRAE guidelines, 443
- ASHRAE standard SSPC 90.2, 454
- Asphalt Mixture Performance Tester (AMPT), 111
- Asphalt pavement analyzer (APA) test
 ANSYS simulation, 117, 118
 evaluated asphalt mixtures, 115, 116
 power law model, 115, 117
 rutting behavior, 119
 rutting performance properties, 115
- Assets, 510, 511
- Atomic-scale engineering, 35, 36
- Australian College of Kuwait (ACK), 502, 503
- Autoclaved Aerated Concrete (AAC) walls, 426
- Automobile transport, 401
- B**
- Bahrain
 building optimization analysis, 352, 354
 buildings, 338
 economic status, 313
 electricity sector, 313
 energy efficiency measures, 356
 LCC, 355
 renewable-based energy, 314
- Bar Cloud System, 510, 511
- Barbar pottery
 archaeological sites, 193
 Bronze Age sites, 191
 homogeneity, 191
 Mesopotamian traditions, 192
- Base slab averaging (BSA), 245, 247
- Baseline design model, 346
 objectives, 348
- Battery electric vehicles (BEVs), 401–403,
 406, 408–411, 413, 414
- Battery life anxiety, 405
- Beam on Dynamic Winkler Foundation (BDWF model), 221
- BET microstructural analysis, 149, 152
- Big data (BD), 32, 34
- BIM 360 Field, 505, 506
- Bingham non-Newtonian fluid, 133
- Bioinspired engineering, 39
- Bitumen emulsions, 167
- Bituminous emulsions, 162
- Black roofs, 430, 433, 434, 460, 463
 cooling loads, 465
 indoor surface, 464
 lower moisture, 455
 surface temperature, 464, 465
 yearly cooling loads, 455
- Blackwater, 446
- Body mass index (BMI), 493, 494
- Brinkman equation, 423
- Bronze Age
 Bahrain Island, 185
 ceramic artifacts, 208
 ceramic sherds, 194
 Danish expedition, 191
 Failaka Island, 199, 201
 Kuwaiti ceramics and ceramic technology, 188
 pottery, 192
 pottery production, 186
 trade and interaction, 193
- Building automation, 506–508
- Building automation systems, 502
- Building information model (BIM), 51, 52
 ACK, 502, 503
 building automation, 506, 508
 efficiency, 502
 field inspections, 504
 FM, 502
 inventory management system, 510, 511
 life cycle, 502, 503
 maintenance system, 505–507
 sample error in 2D, 503, 504
 screenshots, 504, 505
 software package, 503
 technology, 502
- Building system’s simulation module, 448
- Building’s constructions, 340
- C**
- Cable-Stayed Stork Bridge, 62
- Calcium-aluminum-silicate-hydrate (C-A-S-H) gels, 145
- Capital expenses (CAPEX), 404–405, 414
- Carbon fiber-reinforced polymer (CFRP)
 cables, 74
 comprehensive assessment, 73

- laminates, 60–62
- long-span lightweight bridges, 58
- strengthening
 - brittle material, 60
 - Cable-Stayed Stork Bridge, 62
 - chronological development, 62
 - Ibach Bridge, Lucerne, 60–62
 - Pedestrian Bridge Kleine Emme, 65
 - Posttensioned Dintelhaven Highway Bridge, 66
 - steel-reinforced concrete, 60
 - Verdasio Bridge, 63
- sustainability, 71–73
- tendons, 58
- Visions 1970s and 1980s (*see* Visions 1970s and 1980s)
- Center for Natural Resources and the Environment (CNRE), 20
- Charging facilities, 415
- Charging facilities anxiety, 405
- CIE Glare Index, 385
- Circadian stimulus (CS), 387, 390
- Civil Engineering, 515
- Civil infrastructure systems, 304
- Climate-resilient infrastructure, 304–306
- Clothing variations, 494
- CMBMT-PLD/MAPLE process, 369, 370, 372, 379
- Coding process, 519
- Coefficient of performance (COP), 342
- Cohesive–frictional force field (CFFF), 5
- Cohesive–frictional granular pile
 - binder intensity index, 43, 44
 - compressive strength, 43
 - formulation, 42
 - optimization source, 42
 - populations, 42, 43
 - scaling relations, 42
- Comfort temperature
 - age, 493, 494
 - BMI, 493, 494
 - clothing variations, 494
 - gender, 493, 494
 - gender variations, 495
- Commercial building model, 339
- Committee on Adaptation to a Changing Climate (CACC), 304
- Common threads, 410
- Compressed earth block (CEB)
 - advantages, 158
 - disadvantages, 158
 - load-bearing wall systems, 157
 - mix designs
 - compressive strength, 166, 167
 - DTF, 167
 - stabilizers, 161–163
 - testing protocol, 164
 - native soil and stabilizers mixtures, 157
 - natural ability, 157
 - plant fibers, 158
 - soil gradation, 158, 160, 167
 - sustainable alternative technique, 157
- Computational fluid dynamics (CFD)
 - models, 335
- Computer-aided design (CAD), 501
- Computer-based management
 - applications, 502
- Computer program (FCONE), 214
- Concrete
 - BIM, 51, 52
 - binding phase, 27
 - CO₂ emission, 30
 - cohesive–frictional granular pile, 42–44
 - construction, 44–45
 - construction industry, 30
 - conventional reinforcement, 48, 49
 - extensive use, 27
 - materials science, 31–34
 - modern built environment, 27
 - nanoengineering, 35–39
 - OPC, 30
 - SCMs, 39–42
 - smart design, 46, 47
 - technical progress, 28
 - UHPC, 29
- Concrete formulation, 42, 51
- Concurrent multi-beam, multi-target PLD (CMBMT-PLD), 369
- CONE model
 - damping, 217
 - disk load, 215
 - dynamic excitation, 215
 - dynamic response, 249
 - dynamic stiffness matrices, 215–217
 - impedance matrix, 218
 - near-field soil, 249
 - one-dimensional strength-of-materials approach, 215
 - pile-soil-pile interaction, 216
 - soil-structure interaction, 250
 - stiffness and damping coefficients, 218
- Construction
 - environmental advantages, 45
 - interest, 45
 - materials, 45
 - modern sector, 44
 - SCM, 45
 - skills and traditions, 45

Consumer experiences, 404
 Contingent valuation method (CV), 322
 Conventional reinforcement, 48, 49
 Conventional roof, 430, 433, 460, 463
 surface temperature, 464
 Convolution theorem, 272
 Coolers A/C systems, 460
 Cooling energy loads, 454, 460, 465–469, 472, 476, 478
 Cooling load, 419, 421, 426, 427
 Cool roofs, 419, 421, 425–430, 432
 in annually energy cost, 454
 in cold climates, 454
 energy savings, 454
 short-wave solar absorption
 coefficients, 454
 with solar reflectivity, 454
 Co-researchers, 406, 408
 Curtain walls, 456
 Cycle greenhouse gas (GHG), 7

D

Darcy equation, 423
 Darcy–Weisbach friction factor, 131
 Dark (black) roofs
 lower temperatures, 454
 Dark roofs
 in cold climates, 454
 Data analysis, 409
 Data collection, 408, 409
 Date tree fiber (DTF), 163, 167, 168
 Daylight
 apertures, 394
 architecture plays, 394
 ASE, 384
 availability, 395, 397
 characteristics, 384
 CIE Glare Index, 385
 CS, 390
 cyclical nature, 394
 DA, 384
 Daylight Glare Index, 385
 DF, 384
 distribution, 396
 factor, 390
 field studies, 388–390
 glare probability, 385
 health impacts, 386, 388
 illuminance level measurements, 390
 instrumental metrics, 384–385
 Lewis Integrative Science
 Building, 391–393
 nonvisual benefits, 386

 parameters, 397
 photometric unit, 384
 sDA, 384
 Straub Hall, 391, 394–396
 UDI, 385
 visual comfort probability, 385
 Daylight autonomy (DA), 384
 Daylight factor (DF), 384, 390
 Daylight Glare Index, 385
 Daylight glare probability, 385
 Daylighting autonomy (DA), 390
 Daylighting Glare Probability (DGP), 390
 Deconvolution, 270–272, 276
 Defensible knowledge claim, 413
 Density functional theory (DFT), 32
 Department of Energy (DOE), 339
 Descriptive statistics, 485
 Dialogue, 408, 409
 Dialogue researchers, 406, 408
 Digital image correlation (DIC) methods, 262
 Digital skills, 516
 Dilmun
 Arabian Gulf, 187
 ceramic characterization, 187
 civilization, 185
 culture, 186
 Failaka Island, 189–190
 pottery production, 186, 187
 pXRF (*see* X-ray fluorescence spectrometer (pXRF))
 sociopolitical authority, 188
 Sumerian literature, 185
 Sumerian paradise myths, 185
 thin-section analysis, 207
 trade network, 186
 Dirt/dust accumulation, 459
 Disaster-resilient infrastructure, 299
 aging effects, 302
 assumptions, 302
 density function, 302
 economics, 301, 303
 failure-causing event, 303
 failure event, 300
 failure-profile value, 302
 performance, 301
 properties, 300
 properties and triangle, 300
 recovery event, 300
 reliability function, 302
 time-invariant performance, 304
 Discriminant function analysis (DFA), 197
 DOE-2 building energy simulation program, 454
 Double glazing windows, 456

- Dry-bulb temperature (DBT), 441
- Drying shrinkage test (DST), 81
- Dynamic Daylighting Metrics, 385
- Dynamic modeling techniques, 292
- Dynamic stiffness, 225, 226
- Dynamics, 515, 516, 521, 522

- E**
- Earthquake, 269
- Earthquake engineering, 264
- Economic growth, 483
- Educational facilities, 501, 508, 512
- Effective insulation, 440
- Eight-noded solid continuum elements (C3D8R), 228
- Electric vehicles (EVs)
 - adoption, 403
 - BEVs, 401, 402
 - buying, 402
 - CAPEX, 414
 - challenges, 403, 404
 - cost and performance, 402
 - driver, 415
 - EAMA, 401
 - early adopters, 402
 - EREVs, 401
 - instruments, 404, 405
 - lack of charging facilities, 415
 - life cycle cost, 411
 - lithium-ion batteries, 401
 - objectives, 403, 404
 - OPEX, 413, 414
 - owners, 405
 - participants, 404, 405
 - PHEVs, 401, 402
 - plug-in, 402
 - preference surveys, 403
 - production and usage, 401
 - quality of driving, 415
 - RA, 401
 - range anxiety, 414, 415
 - safety, 413
 - types, 403
 - utility, 402
 - Vancouver School Approach to Qualitative Research (*see* Vancouver School Approach to Qualitative Research)
- Electrical energy, 460
- Electricity consumption, 419
- Electricity generation, 420
- Electricity prices, 403
- Electronic document management systems, 502

- Elite bias, 413
- Embodied energy coefficients (EEC), 7
- Emissions and Embodied Energy (EE), 7
- Energy and power demand, 420
- Energy-based methodology, 270
- Energy conservation, 420, 439
- Energy consumption, 419
- Energy demand spectra, 253
- Energy efficiency
 - goals, 440
 - HVAC system, 443, 444
 - insulation, 444–446
 - lighting, 444
 - PV solar energy system, 442, 443
- Energy efficiency measures, 342–345, 351–353
- Energy-efficient buildings, 420
- Energy equation, 423
- Energy management systems, 502
- Energy performance
 - cooling energy load, 466
 - cooling loads, 466–469
 - monthly heating load, 466
 - reference buildings, 434, 435
 - test roofing systems, 471–477
 - yearly cooling loads, 472, 474–476
 - yearly energy loads, 466, 470–474, 477
- EnergyPlus program, 448
- Energy savings, 440, 448–450, 453–456, 478
- Energy simulation, 448, 449
- Energy use intensity (EUI), 331, 332
- Enhanced operational energy efficiency, 7
- Environment satisfaction
 - in Asian offices, 495
- Environmental parameters, 484–487, 496
- Equivalent Melanopic Lux (EML), 386, 390
- ETABS, 219
- Ethernet gateway, 510
- Ethylenediaminetetraacetic acid (EDTA), 370
- European Automobile Manufacturers Association (EAMA), 401
- Extended range electric vehicles (EREVs), 401

- F**
- Face-to-face interviews, 503
- Facilities management (FM), 501–503, 505, 506, 510–513
- Failaka Island
 - archaeological sites, 190
 - Bronze Age structure, 191
 - Danish mission, 190
 - geographical description, 189

- Failaka Island (*cont.*)
 rocky coastlines, 189
 Slovak expeditions, 190
 water wells, 190
- FCONE program, 220
- Feed-in-tariff (FIT), 324
- Fenestration systems, 425
- Field studies, daylight, 388–390
- Finite element (FE) model
 ANSYS model, 120
 APA test (*see* Asphalt pavement analyzer (APA) test)
 asphalt admixtures, 109
 asphalt mixtures, 120
 research methodology
 ANSYS model, 111
 task I, 111
 task II, 111, 112
 task III, 112
 task IV, 114
 task V, 115
 rutting, 109–110
 structural behavior, 111, 120
- Finite element method (FEM), 249, 272, 423, 456
- Finite-element simulation
 C3D8R, 228
 FEM analysis, 229
 infinite soil medium, 226
 SPSI analysis, 228
 strain hardening model, 228
 3D numerical prediction, 228
- Fiscal incentives, 403
- Flexibility matrix, 215
- Flicker, 385
- Fourth Industrial Revolution, 31, 32
- Full-scale specimen, 264
- G**
- GCC countries, 311
 carbon dioxide emission, 363
 carbon emission indicators, 330
 commercial building sector, 333
 commercial buildings, 364
 electrical demand savings, 363
 electricity demand, 311
 electricity prices, 330
 electricity sectors, 322
 end-use electricity, 348
 end-use electricity distribution, 347
 energy consumption savings, 362
 energy efficiency, 311
 energy use, 330
 green power products, 324
 program descriptions, 323, 324
 public utility, 322
 RE, 322
 RE capacity, 313
 social media, 321
- GCC region
 analysis methodology, 339
 building energy use, 332
 building sector, 330
 carbon dioxide emissions, 350
 construction types, 343
 electrical demand, 349
 energy savings, 338
 EUI, 332
 export revenues, 329
 glazing types, 344
 HVAC systems, 342
 insulation materials, 342
 internal loads, 341
 office building, 347
 per-capita building electricity consumption, 331
 per-capita building energy consumption, 331
- Gender, 493, 494
 equality, 483
- Gender differences
 subjective thermal responses, 489, 491, 492
- Gender variations, 494, 495
- Glare, 385
- Glazing transmittance, 394
- Global CO₂ emissions, 439
- Global positioning system (GPS), 6, 21
- Global solar radiation, 441
- Global warming, 419, 453
- Gradient anchorage system, 59
- Granulated blast furnace slag (GBFS), 40
- Green buildings
 and construction sectors, 439
 concrete pile caps, 242
 DBT, 441
 definition, 440
 energy conservation, 439
 energy efficiency (*see* Energy efficiency)
 energy savings, 440, 449, 450
 energy simulation, 448, 449
 environmental/ecological impact, 440
 environmental requirements, 439
 environment-friendly, 440
 features, 440
 geological description, 242
 internal cooling, 439

- MIT campus, 241, 242
 - modeling and dynamic analysis
 - accelerometer channel, 248
 - BSA, 247
 - ETABS analysis, 246, 247
 - FCONE program, 247
 - maximum lateral displacement, 244
 - roof acceleration, 248, 250
 - SSI effects, 247, 248
 - natural resources, 439
 - nonrenewable, 439
 - operational energy, 440
 - outdoor and indoor design conditions, 441
 - shear-wave velocity, 242, 243
 - site condition, 242–244
 - solid waste management, 448
 - water efficiency, 446, 447
 - WBT, 441
 - Green Car Reports (2019), 411
 - Green energy technologies, 367
 - Green power
 - customer demand, 321
 - factors, 320
 - residential sector, 310
 - WTP, 321
 - Green pricing programs, 310
 - Green roofing, 453
 - Green roofs
 - energy savings, 454
 - Green technologies, 388
 - Greenhouse emissions, 440
 - Greywater recycling, 446, 447
 - Gross domestic product (GDP), 329
 - Ground granulated blast-furnace slag (GGBS)
 - ASR and ACR, 81
 - cement replacement, 89
 - compressive strength, 90
 - concrete mixtures, 78, 80
 - durability, 90
 - experimental program
 - alkali silica reactivity test, 82
 - compressive strength test, 81
 - drying shrinkage test, 82
 - sulphate attack, 83
 - water absorption test, 82
 - water penetration test, 82
 - influence, 90
 - mineral slag, 78
 - mixture design
 - aggregates, 79
 - binder, 78
 - outcomes
 - alkali silica reactivity, 88
 - compressive strength, 84
 - drying shrinkage, 87
 - 25% GGBS incorporation, 85
 - sulphate resistance, 88, 89
 - water absorption, 85, 87
 - water penetration, 85
 - workability, 83, 84
 - preparation/casting/curing regimes, 81
 - sulphate content, 78, 81
 - Ground motion modeling and structural monitoring
 - analysis, 6
 - computational modeling, 6
 - excitation, 7
 - GPS, 6
 - high-fidelity computational model, 6
 - model-based predictions, 6
 - safety and reliability, 6
 - tall buildings, 6
 - Gulf Cooperation Council (GCC), 313, 483
 - Gullu's energy spectrum, 258, 259
- H**
- Hazards, categories of, 289
 - Health impacts
 - metrics, 386, 388
 - Heat, air and moisture (HAM), 423, 456
 - Heat balance simulation module, 448
 - Heat flux, 464
 - Heat gain, 464
 - Heat loss, 464
 - Heating energy loads, 454, 455, 460, 465, 466, 472, 475, 476, 478, 479
 - Heating load, 419, 421, 426, 427
 - Heating, ventilation and air conditioning (HVAC) systems, 439, 443, 444
 - Herschel–Bulkley (H-B) model, 130, 131
 - Herschel–Bulkley (H-B) fluids, 125
 - High amplitude (HiAm) anchorage system, 57
 - Highly reflective/cool roof systems, 453, 454
 - Historic heritage
 - architectonic objects (*see* architectonic monuments)
 - care, 170
 - geographical/historical features, 171
 - idea, 170
 - immovable monuments, 170
 - material, 170
 - monuments, 171
 - national, 171
 - object definition, 170
 - protection, 171
 - theoretical principles, 173
 - treasury, 171

- Historic heritage (*cont.*)
 UNESCO heritage sites
 geographic displacement, 172
 gulf region, 172
 Holistic fallacy, 413
 Holistic picture, 409, 410
 Hooke's law, 517
 Hot-mix asphalt (HMA), 115
 Hourly Analysis Program (HAP 5.01), 444
 Human end users, 383
 Hydropower, 322
 Hygrothermal performance
 short-wave solar absorption
 coefficient, 460–465
 Hygrothermal simulations, 455
- I**
 Iceland, 402–404, 407, 412–416
 Illuminating Engineering Society (IES), 339
 Image-based measurement, 261
 Immovable monuments, 170
 Impulse response functions (IRFs), 270, 273
 Independent reviewer/journal editor, 411
 Indoor environments
 design, 383
 Infrared taps, 446, 447
 Infrastructure sustainability
 methodology, 296, 297
 multidimensions, 295
 quantification, 295
 Ingenuous self-criticism, 411
 Institute for Lightweight Structures (IL), 66
 Instrument role, 383
 Insulation, 444–446
 Internal cooling, 439
 International Council on Monuments and Sites (ICOMOS), 174
 International Energy Conservation Code (IECC), 336
 Inter-zone air flow, 449
 Intrinsically photosensitive retinal ganglion cells (ipRGCs), 386
 Inventory management system, 509–511
- J**
 Jamming, 49
- K**
 Kanade-Lucas-Tomasi (KLT), 262
 Keystone KSTAD70B, 444, 445
 Kingdom of Saudi Arabia (KSA)
 building optimization, 356
 buildings, 336, 337
 energy efficiency measures, 354, 357
 optimal design benefits vs. baseline office building, 357
 KLT tracking algorithm, 263
 Kuwait, 419, 420
 buildings, 337, 338
 economic status, 314
 electricity sector, 314, 315
 energy efficiency measures, 358
 optimal design benefits vs. baseline office building, 358
 Kuwait archaeology
 Arabian Gulf, 187
 archaeological materials, 188
 Barbar period, 187
 Barbar ware types, 188
 Mesopotamian pottery, 188
 prestige items, 188
 Qala' at site, 187
 sociopolitical complexity, 188
 wheel-made pottery, 188
 wheel-turntable pottery, 187
 Kuwait Foundation for the Advancement of Sciences (KFAS), 20
 Kuwaiti Building Energy Code, 427
 Kuwait Institute for Scientific Research (KISR), 3, 8, 13
 Kuwaiti-Slovak expedition, 191
 Kuwait-MIT Collaborative Signature Project achievements, 20, 21
 focus areas, 20
 Visiting Scientist Exchange Program, 20
 Kuwait Portland Cement Company (KPCC), 78
 Kuwait University (KU), 3, 8, 10, 13
- L**
 Laminar Herschel–Bulkley (H-B) fluid flows, 132
 Latent heat of fusion, 420
 Leadership in Energy and Environmental Design (LEED) certification, 440
 Learning environments, 515
 LEED certification, 388, 389
 Level of details (LOD), 504
 The Lewis Integrative Science Building (LISB), 388, 389, 391–393
 Life-cycle cost (LCC), 299, 339, 345, 346
 Light-emitting diode (LED) light bulbs, 444
 Lighting, 444
 Lithium-ion batteries, 401

- Load transfer media (LTM), 58, 59
- Logical thinking, 410
- Los Angeles to San Diego (LOSSAN), 306
- Luminescent solar concentrators (LSCs)
- applications, 367
 - disadvantages, 368
 - higher-performance lumiphore, 367
 - layer deposition, 368
 - nanoparticles, 368
 - organometallic chromophores, 367
 - polymer nanocomposite (*see* Polymer nanocomposite LSC films deposition)
 - RE elements, 368
 - window acting, 367
- M**
- Machine learning (ML) algorithms, 33, 34
- Maintenance and operational sensors, 502, 503
- Maintenance system, 505–508
- Market readiness, 403
- Market segments, 403
- Massachusetts Institute of Technology (MIT), 3
- Mass-normalized input energy, 272, 275, 276
- Materials Genome Initiative (MGI), 33
- Materials science
- big data analytics, 32
 - composition–structure–property, 33, 34
 - evolution, 32
 - Fourth Industrial Revolution, 31
 - MGI, 33
- Mathematical solver, 517
- MATLAB code, 130, 132
- Matrix-assisted pulsed laser evaporation (MAPLE), 369, 370
- Measurement instrument, 413
- Mechanical Engineering, 515
- Mechanics, 515–517, 521, 522
- Megajoules (MJ), 7
- Mental models, 410
- Mesopotamian tradition, 208
- Mesoscale engineering, 36, 38
- Metakaolin
- Advanced Cement Technologies, 146
 - aluminosilicate NPs, 152
 - C-A-S-H phases, 153
 - N₂ adsorption–desorption isotherms, 148
 - supplementary cementitious material, 145
- Metakaolinite, 42
- Metrics
- and building standards, 385
 - daylight instrumental, 384–385
 - definition, 385
- Ministry of Energy and Water (MEW), 419, 420, 440
- MIT-Kuwait Signature Project (SP1) CNRE, 20
- collaborative and multidisciplinary research, 12, 13
 - enhanced operational energy efficiency, 7
 - ground motion modeling and structural monitoring, 6–7
 - infrastructure, 15
 - 3KMP, 16, 18
 - Kuwait seismic condition, 18, 19
 - multidisciplinary research, 3
 - nanoengineered sustainable construction materials, 4, 5
 - objectives, 3
 - performance and safety, 15
 - sustainable micro- and nano-cement additives, 4
- team and activities
- benefits, 11
 - capacity building, 8, 10
 - collaboration, 8
 - educational impact, 10
 - Gulf Conference on Sustainable Built Environment, 12
 - industry development, 11
 - managerial challenges, 11
 - outreach, 10
 - researchers, 8
 - students, 8
- Mixed mode (MM), 484
- Mobile, 515–517, 519–522
- Mode shapes, 279
- Modified-Bitumen (MOD-BIT) roofing systems, 455
- Modular compact rheometer (MCR), 124
- Mohr-Coulomb failure criterion, 228
- Moisture adsorption, 449
- Moisture desorption, 449
- Moisture transport equation, 423
- Molecular dynamics (MD), 32
- Multi-beam PLD, 369
- Multi-degree of freedom (MDOF), 272
- Multi-target PLD, 369
- N**
- Nanocomposite construction material
- LSCs (*see* Luminescent solar concentrators (LSCs))
- Nanoengineered sustainable construction materials, 5

- Nanoengineering
 - atomic-scale engineering, 35, 36
 - bioinspired engineering, 39
 - mesoscale engineering, 36, 38
 - Nanofluids
 - density, 133
 - effects, 124
 - non-Newtonian fluids, 129
 - rheological properties, 125, 134
 - single-and two-phase flows, 126
 - viscosity, 133
 - volumetric concentrations, 124
 - Nanoindentation test, 152, 154
 - Nanoparticles
 - application, 124
 - coagulations effects, 126
 - concentration, 136
 - friction reduction, 124
 - lubrication additives, 123
 - nanostructure, 136
 - Navier–Stokes equation, 125
 - Newtonian water-based fluids, 132
 - pipelines and lubrication systems, 125
 - rheological behavior, 125
 - role, 123, 124
 - shapes and sizes, 124, 134
 - volume fraction, 134
 - National Energy Efficiency Action Plan (NEEAP), 313
 - National Institute of Standards and Technology (NIST), 501
 - National Oceanic and Atmospheric Administration (NOAA), 440
 - National Renewable Energy Action Plan (NREAP), 313
 - National treasury, 171
 - Natural frequency, 279
 - Natural hazards
 - classification, 289, 290
 - Natural pozzolan
 - advantage, 94
 - clinker, 94, 105
 - formulations, 94
 - PAP, 102
 - physical properties, 96
 - valorization, 93
 - X-ray diffraction, 95, 97
 - Naturally ventilated (NV), 484
 - Navier–Stokes equation, 423
 - Near-infrared (NIR) radiation, 368, 370–372, 375
 - Network arch bridge, 74
 - New ecological cementitious material
 - cement, 94
 - clinker, 94
 - mechanical properties
 - capillary absorption, 103, 104
 - cement mortar, 101
 - compressive strength, 104
 - porosity, 102
 - methods
 - capillary absorption methods, 99
 - compressive strength methods, 100
 - porosity methods, 99
 - mixing water, 98
 - natural pozzolan, 93, 95, 105
 - physicochemical properties
 - chemical compositions, 100
 - physical–chemical, 100, 101
 - polymeric admixture, 94, 97
 - sand, 98
 - Non-image-forming, 397
 - Nonlinear pushover analysis, 224, 225
 - Nonlinear static pushover (NSP) analysis, 220
 - Nonmaterial heritage, 170
 - Non-Newtonian fluid flow simulations
 - agglomeration, 134
 - analytical expression, 134
 - ANSYS fluent, 133
 - condition, 134
 - nanoparticles, thermophysical
 - properties, 133
 - particle sizes, 136
 - pressure contours, 136
 - pressure drops, 136
 - velocity vectors, 136
 - viscosity, 133
 - Nonreflective roofing system, 426
 - Nonvisual functions, 397
 - Normalized input energy spectrum, 256
- O**
- Occupant well-being, 385, 386, 388, 394
 - Office building energy model, 340
 - Office buildings, 483, 484, 488, 496
 - Oil-based mud (OBM), 123
 - Oman
 - building optimization, 359
 - buildings, 335, 336
 - economic status, 315
 - electricity sector, 315, 316
 - energy efficiency measures, 359
 - optimal design benefits vs. baseline office building, 359
 - Online course, 516
 - Open educational resources, 516
 - OpenSees, 220

- Operating expenses (OPEX), 405
- Operational energy, 440
- OPEX, 413, 414
- Optimal sensor placement algorithm, 281
- Optimization analysis, 345, 362
- Optimum moisture content (OMC), 166
- Optimum Test Wall
 - PCM-drywall, 427
 - vs. reference walls, 428–430
- Ordinary Portland Cement (OPC), 7
- Organization of the Petroleum Exporting Countries (OPEC), 313
- Origami patterning, 48
- Origamics, 47
- Outdoor climates, 455

- P**
- Pacific Earthquake Engineering Research Center (PEER 2012), 231
- Paraffin-based wallboard, 421
- Parallel wire bundles (PWB), 57
- Parametric analyses, 349
- Parametric and sensitivity analyses, 342
- PCM-drywall, 458
- Performance-based engineering and reliability, 20
- Petrographic thin-section analysis, 187
- Phase Change Materials (PCMs)
 - advantages, 421
 - applications, 420, 421
 - benchmarking, 423, 425
 - classification, 420
 - conditions and simulation period, 458
 - design parameters, 421
 - energy consumption, 419
 - energy performance, 420, 434, 435
 - FEM, 456
 - global warming, 419
 - HAM, 456
 - indoor and outdoor conditions, 457
 - Kuwait, 419, 420
 - latent heat of fusion, 420
 - material properties, 458
 - melting/freezing, 420
 - melting/freezing temperature, 422
 - methodology, 426, 427, 459, 460
 - MEW, 419, 420
 - model development, 423, 425
 - numerical model, 456
 - objectives, 422, 456
 - properties, 458, 459
 - reference roofing systems, 422
 - reference wall systems, 422
 - roofing system, 422–424, 426
 - short-wave solar absorption, 458
 - single-zone buildings, 427–429
 - wallboards, 421
 - wall system, 422–424, 426
 - WWRs, 425, 426
 - yearly energy loads, 430–434
- Photometric unit, 384
- Photoreceptive mechanisms, 387
- Photovoltaic (PV) solar energy system, 442, 443
- Photovoltaic solar power, 367
 - to generate electricity, 367
 - silicon, 372, 375
 - window edge, 368
- Pile-group effect
 - BDWF model, 221
 - ETABS program, 221
 - fixed-base behavior, 221
 - group effect, 220
 - rectangular foundation, 221, 222
 - response spectrum method, 221, 223
 - soil-structure system, 220
 - target displacement, 221
- Plug-in hybrid electric vehicles (PHEVs), 401–403, 414
- Poisson process, 300
- Polycarboxylate (PAP), 102
- Polyester fiber (PES), 67
- Polymer nanocomposite films, 370, 372, 373, 375, 379
- Polymer nanocomposite LSC films deposition
 - ambient air (*see* Ambient air)
 - in vacuum (*see* Vacuum)
- Polymer poly(methyl methacrylate) (PMMA)
 - chemical formula, 375
 - in chlorobenzene, 370
 - composite film, 372, 373
 - FTIR absorption spectrum, 375, 376
 - open-air deposited, 376
 - open-air PLD process, 376
 - polymer nanocomposite LSC film, 372
- Polymeric admixtures, 97
- Portable X-ray fluorescence (pXRF)
 - ANOVA results, 197
 - Archaeological Science Laboratory, 193, 196
 - Barbar pottery, 207
 - Bronze Age ceramic composition, 195
 - Bruker Tracer III-SD portable XRF, 195
 - compositional elements, 208
 - DFA, 197, 198
 - elemental composition, 194
 - group A, 201, 202

- Portable X-ray fluorescence (pXRF) (*cont.*)
- group B, 202, 203
 - group C, 203–205
 - group outlier
 - ceramic sherds, 206
 - clay and ceramics fingerprinting, 206
 - comparative sampling strategy, 206
 - DF analysis, 205
 - Harappan origin, 206
 - nonlocal pottery, 206
 - thin-section analysis, 207
 - homogeneity, 207
 - matrix effect, 193
 - multivariate analyses, 199
 - multivariate statistical analysis, 195
 - PCA, 196, 207
 - petrographic analysis, 207
 - quantitative analysis, 195, 199
 - thin-section analysis, 193
 - X-ray window, 193
- Power law model, 119
- Premature closure, 413
- Presidential Policy Directives (PPD), 291
- Pressure sensor measurements, 142
- Principal component analysis (PCA), 195
- ceramic potsherds, 201
 - cluster analysis, 200
 - Dilmun collections, 200
 - goal, 199
 - mixed specimens, 201
 - scatterplot, 199
- Private consumer market, 404
- Proxy scales, 488
- Pseudoplastic, 131
- Pulsed-laser deposition (PLD)
- film, 378
 - inorganic target, 370
 - microscope image, 377, 378
 - multi-beam, 369
 - multi-target, 369
 - open-air, 375–377
 - single-target, 369
- pXRF compositional data, 208
- Q**
- Qatar
- building, 336
 - building optimization, 360
 - economic status, 316, 317
 - electricity sector, 317
 - energy efficiency measures, 360
 - optimal design benefits vs. baseline office building, 360
- Qdex, 516–521
- Qoptimization analysis, 350, 351
- Quality of driving, 415
- Quasi-homeopathic introduction, 29
- R**
- Range anxiety (RA), 401, 405, 414, 415
- Rare-earth (RE) elements, 368
- Realistic system controls, 449
- Real-time technical simulations, 517
- Recycled aggregate concrete (RAC)
- compressive strength, 77
 - durability, 78
 - GBBS (*see* Ground granulated blast-furnace slag (GGBS))
 - mechanical properties, 77
 - NAC, 77
 - SCM, 77
- Recycled coarse aggregate (RCA), 84
- Ref Roof 1, 457, 478
- Ref Roof 2, 457
- Reference buildings, 434, 435
- Reference roofing, 457, 467–470
- Reference roofing systems, 422
- Reference wall systems, 422
- Reflective coatings, 453–456, 459, 476, 478, 479
- Reflective roofing system, 426
- Relative humidity (RH), 425
- Renewable energy source (RES), 310
- Renewable portfolio standard (RPS), 324
- Reselling anxiety, 405
- Resilience, 289, 290
- definition, 291
 - engineering systems, 291
 - infrastructure systems, 293, 294
 - requirements, 291, 294
 - risk framework, 293
- Resilience analysis
- benefit-to-cost ratio, 298
 - infrastructure systems, 296
 - methodology, 296, 298
 - probabilities, 297
- Resilience index, 299
- Resilience theory, 292
- Resilience vs. sustainability, 293
- Resilient systems (Rs), 293
- Response measurement, 261, 266
- Retinal circuitry, 387
- Reynolds apparatus
- CFD simulations, 125
 - H-B model, 130, 131
 - laminar flows, 127

- nanofluid flows, 124, 126
 - peristaltic pump, 126
 - pressure drop, 127, 129
 - pressure drop measurements, 126
 - Reynolds number, 126
 - rheological properties, 136
 - schematic, 130
 - viscometer, 125
 - Risk management, 297
 - Robotic construction, 49, 50
 - Robust tracking system, 324
 - Roofing systems, 422–424, 426
 - bright surfaces, 456
 - construction moisture, 455
 - description, 457
 - design, 454
 - energy performance (*see* Energy performance)
 - energy savings, 453
 - in hot climates, 456
 - hygrothermal properties, 459
 - indoor surface, 465
 - low-slope commercial, 455
 - moisture-related problems, 453
 - insulation layer, 460
 - moisture accumulation, 459
 - numerical simulations, 459
 - PCM-drywall, 463, 464
 - PCMs (*see* Phase Change Materials (PCMs))
 - reference and test, 457
 - reflective insulations and fenestration systems, 456
 - rooftops, 459
 - single-ply, 455
 - white and black, 460
 - Royal Castle, Warsaw, 177
 - after renovation, 178
 - after restoration, 178
 - Rutting
 - HMA, 109
 - repeated load test, 110
 - simulative test, 110
 - static creep test, 110
- S**
- Safety, 413
 - San Salvador input energy spectrum, 257, 258
 - Saudi Arabia (KSA)
 - economic status, 317, 318
 - electricity sector, 318
 - Savitzky-Golay filter, 259
 - Savitzky-Golay (SG) derivation, 263
 - Scanning electron microscopy (SEM), 124
 - Sea-level rise (SLR), 305
 - Seismic analysis, 234, 247
 - Seismic interferometry, 270
 - advantage, 276
 - deconvolution-based, 271
 - mass-normalized input energy, 272
 - methodology, 271
 - Sensor locations, 281
 - Shake table testing, 263, 266
 - Short-wave solar absorption, 427, 458
 - Short-wave solar absorption coefficient
 - hygrothermal performance, 460–465
 - roofing systems, 433, 434
 - Short-wave solar radiation, 454
 - Side lighting, 391
 - Silicon PV cells, 372, 375
 - Silos
 - intermediate structure, 236
 - modeling and dynamic analysis, 238, 239
 - physical description, 234
 - reinforcement work, 238
 - satellite view, 234, 235
 - seismic analysis, 234
 - steel girders, 236
 - structural condition of silo 24, 236
 - Swissmill, 234, 236
 - three-dimensional finite-element models, 238
 - train transportation disturbance, 234
 - Zurich, 238
 - Simulation manager, 448
 - Single degree of freedom (SDOF) system
 - aim, 253
 - damping ratio, 253, 258
 - ground motion, 254, 255
 - input energy spectra, 257
 - normalized input energy spectrum, 256
 - process and instrumentation, 255, 256
 - San Salvador earthquake ground motion data, 255
 - Single-ply roof systems, 455
 - Single-zone buildings, 422, 423, 427, 430, 433–435
 - Optimum Test Wall, 428–430
 - yearly energy loads, 427, 428
 - Skylight devices, 456
 - Skylights, 394
 - Smart economics, 483
 - Smart thermostat, 508
 - Social media, 516
 - Software systems, 502

- Soil-pile-structure interaction (SPSI)
 - CONE model (*see* CONE model)
 - finite-element analysis, 214
 - foundation shape, 213
 - role, 213
 - Winkler model, 214
 - Solar energy, 440, 450
 - Solar heat gain coefficient (SHGC), 341, 422, 426, 430, 435
 - Solar power
 - aesthetics and safety, 367
 - Solar radiation, 444, 448
 - Solar Reflective Index, 334
 - Solar reflectivity, 454
 - Solid waste management, 448
 - South Dakota Department of Transportation (SDDOT), 115
 - Spatial Daylight Autonomy (sDA), 384
 - Spectral downconversion
 - mechanism, 370, 371
 - NIR fluorescence, 373
 - long-wave component, 372, 374
 - luminophore NaYF₄:Er³⁺, Yb³⁺, 372, 373
 - short-wave component, 372, 374
 - phosphor, 371
 - polymer PMMA, 375
 - solar UV light, 371
 - Spectral sensitivity, 386
 - SSI analysis, 250
 - STEM education, 516
 - Stock and spare parts inventory, 511–513
 - Stone monument restoration, 173
 - Straub Hall, 388, 389, 391, 394–396
 - Strength-based design, 269
 - Structural health monitoring (SHM), 279
 - advantage, 279
 - Al-Hamra tower (*see* Al-Hamra tower)
 - instrumentation, 281
 - tasks, 280
 - Structural material quantity (SMQ), 7
 - Students learning, 515
 - Submerged floating tunnel (SFT), 70, 74
 - Supplementary cementitious materials (SCM), 7, 8, 77
 - C-(A)-S-H-type hydrates, 41
 - definition, 39
 - durability and mechanical performance, 40
 - families, 40
 - Metakaolinite, 42
 - Surface-to-surface radiation equation, 423
 - Surveyed environments
 - outdoor and indoor, 488–490
 - Sustainability, 289, 291, 440
 - definition, 169, 291, 292
 - development, 291
 - environmental issues, 169
 - infrastructure systems, 293, 294
 - requirements, 294
 - risk framework, 293
 - Sustainability science approach, 292
 - Sustainable development, 169
 - Sustainable systems (Ss), 293
 - Swiss Commission for Technology and Innovation (CTI), 60
 - Switzerland emergency hospital
 - building description, 218
 - category III construction, 219
 - dynamic analysis, 229, 231
 - dynamic stiffness, 225, 226
 - finite-element simulation, 226–229
 - lateral (short) direction, 219
 - longitudinal direction, 219
 - nonlinear pushover analysis, 224, 225
 - pile-group effect, 220–221
 - structural analysis, 219
- T**
- Tall building, 279, 281
 - Test building, 263
 - Test Roof, 426, 457, 458
 - Test roofing systems, 471–477
 - Test Wall, 426
 - Thermal comfort field study
 - ASHRAE Database II, 484
 - calibrated digital instruments, 484
 - Doha, 484
 - environmental parameters, 485–487
 - gender differences, 489, 491, 492
 - and non-thermal factors, 483
 - office buildings (*see* Office buildings)
 - outdoor and indoor environments, 488–490
 - paper-based, 484
 - proxy scales, 488
 - subject sample, 485
 - subjective feeling, 483
 - temperature, 493, 494
 - Thermal model, 454
 - Thermal properties
 - exterior roof constructions, 341
 - exterior wall constructions, 341
 - ThermoFisher, 378
 - Third Kuwait Master Plan (3KMP), 16, 18
 - 3D-printing technologies, 50
 - Three biaxial sensors, 282
 - Tiltmeters, 282
 - Time-consuming rigorous methods, 250

- Topology optimization, 46
- TPO/PVC membrane, 455
- Tracking methods, 262
- Tradable Instruments for Global Renewables (TIGRs) system, 323
- Turzno Palace, 176
 - after restoration works, 175
 - before restoration works, 175
 - concert hall, 176

- U**
- Ultrahigh-performance concrete (UHPC), 29
- Ultrahigh-performance-fiber-reinforced concrete (UHPFRC), 46–47
- United Arab Emirates (UAE), 333
 - building optimization, 361
 - CFD, 335
 - economic status, 318, 319
 - electricity sector, 319, 320
 - energy efficiency measures, 361
 - geometric characteristics, 333
 - optimal design benefits vs. baseline office building, 362
 - solar irradiance, 334
 - thermal insulation, 334
 - thermal loads, 334
- University of California San Diego
 - Engineering Simulations (UCSD-NEES), 272–275
- Urban canyon model, 453
- Urban development, 15
- US Green Building Council (USGBC), 440
- Useful daylight illuminances (UDI), 385
- User satisfaction, 483

- V**
- Vacuum, polymer nanocomposite LSC films
 - deposition
 - characterization, 372
 - fabrication
 - CMBMT-PLD, 369
 - CMBMT-PLD/MAPLE, 369, 370
 - downconversion mechanism, 371
 - EDTA, 370
 - energy level, 371
 - energy transfer, 371
 - Er³⁺ ion, 371
 - MAPLE, 369, 370
 - microcrystalline powder, 370
 - phosphor, 370
 - PMMA, 370
 - polymer nanocomposites, 369
 - fluorescence spectrum, 372, 373
 - NIR fluorescence
 - long-wave component, 372, 374
 - short-wave component, 372, 374
 - SEM, 372
 - XRD spectrum, 372, 373
- Vancouver School phenomenology
 - coding, 409
 - co-researchers, 412
 - credibility, 412, 413
 - data analysis, 409
 - data collection, 409
 - description, 405
 - dialogue (the data collection), 408, 409
 - dialogue researchers, 406, 408
 - holistic picture, 409, 410
 - naming process, 412
 - research outcome, 410, 411
 - research process, 405
 - in silence, 406–408
 - tranquility, 406–408
 - validity, 412, 413
 - words, 409
 - writing up, 412
- Vegetative roof systems, 453
- Vehicle safety, 404
- Vibration of buildings, 281
- Video-based measurements
 - categories, 262
- Virtual labs, 515
- Virtual learning, 515, 522
- Visible transmittance (VT), 341
- Visions 1970s and 1980s
 - The Artic city, 66–68
 - Gibraltar CFRP bridges, 69
 - Gibraltar submerged tunnel, 69–71
- Visual comfort probability, 385
- Volcanic ash (VA), 7
 - aragonite, 149
 - load–displacement curve, 152
 - pozzolanic cement additives, 145
 - Raman shifts, 149
 - sulfate-based phases, 154
 - Super Burkani factory, 146
- Voluntary green power market, 309, 320
- Voluntary green power programs, 309, 310
 - customer class, 309

- W**
- Wall systems, 422–426
 - reflective insulations and fenestration systems, 456
- Wallboards, 421

Warm-glow effect, 321
Warm-mix asphalt (WMA), 115
Water-based mud (WBM), 123
Water cement ratio (w/c), 87
Water conservation, 440, 449, 450
Water consumption, 446
Water efficiency
 greywater recycling, 446, 447
 indoor and outdoor usage, 446
 water consumption, 446
Water-level rise (WLR), 305
Weather conditions, 426
Wet-bulb temperature (WBT), 441
White roofs, 455
 surface temperatures, 464
Wind speed, 441
Window orientation
 yearly energy loads, 430, 432, 433
Window-to-wall ratios (WWRs), 333, 341,
 422, 425, 426, 435
Wireless motion sensor, 508, 509
Wireless temperature sensor, 509

X

XPS insulation, 459
X-ray diffraction (XRD) spectrum, 372, 373

Y

Yearly cooling loads, 455, 469, 472,
 474–476, 479
Yearly energy loads, 427, 428, 466,
 470–474, 477
 cardinal directions/orientations, 430
 Ref Building 1, 430
 Ref Building 2, 430
 short-wave solar absorption coefficient,
 433, 434
 Test Building, 430
 wall systems, 427, 428
 window orientation, 430, 432, 433

Z

Zagros Fold–Thrust Belt (ZFTB), 6